

AN ABSTRACT OF THE THESIS OF

Warren A. Bartel for the degree of Master of Science in Civil Engineering presented on March 14, 1996. Title: Modelling, Validation and Simulation of Multi-Degree-of-Freedom Nonlinear Stochastic Barge Motions.

Abstract approved: Redacted for Privacy
Solomon C.S. Yim

Recent developments in estimation of the survivability of a U.S. Navy transport barge in random seas are extended to improve accuracy. The single Degree-of-Freedom (DOF) model of a extreme roll response of a barge used in previous research is replaced by a 3-DOF roll-heave-sway model to include linear and nonlinear static and kinematic coupling between roll, sway and heave. The predominant nonlinearity in the model arises in an improved approximation of the roll righting moment and heave buoyant restoring force by coupling roll with heave. Kinematic coupling is introduced by allowing extreme displacements and rotations in the barge response.

System coefficients in the 3-DOF roll-heave-sway model and a simpler 2-DOF roll-heave model are identified by comparing time domain simulations with measured physical model tests of barge motions. Predictions of the 3-DOF and 2-DOF models are compared to measured test data for the case of random waves.

Monte Carlo simulations of the equations of motions are performed to predict the reliability of the barge in an operational sea state for a specified mission duration. Use of parallel computer processing is found to make this a viable option for stability

estimations as we move into the next century. The stochastic nature of the ocean waves are modeled via filtered white noise. Estimations of the joint probability of the barge responses are presented after application of density estimation kernels. Both the 3-DOF roll-heave-sway model and 2-DOF roll-heave model are tested and compared.

Last, examples are provided of some observed nonlinear behavior of the barge motions for variation in damping or ocean wave amplitude. Transient and intermittent chaotic responses are observed for deterministic input waves and quasiperiodic cases are illustrated.

**Modelling, Validation and Simulation of Multi-Degree-of-Freedom
Nonlinear Stochastic Barge Motions**

by

Warren A. Bartel

A THESIS

submitted to

Oregon State University

in partial fulfillment of
the requirements for the
degree of

Master of Science

**Presented March 14, 1996
Commencement June 1996**

Master of Science thesis of Warren A. Bartel presented on March 14, 1996

APPROVED:

Redacted for Privacy

Major Professor, representing Civil Engineering

Redacted for Privacy

Chair of Department of Civil Engineering

Redacted for Privacy

Dean of Graduate School

I understand that my thesis will become part of the permanent collection of Oregon State University libraries. My signature below authorizes release of my thesis to any reader upon request.

Redacted for Privacy

Warren A. Bartel, Author

ACKNOWLEDGEMENT

Many thanks to Dr. Solomon C.S. Yim, my major professor, for allowing me to perform this research under his guidance. His knowledge, experience and ideas significantly affected the evolution of this research. I thank him for providing the graduate research assistantship throughout my stay at OSU.

Thanks to Dr. Robert T. Hudspeth and Dr. Satish Reddy for serving as committee members and for their expertise and guidance. I thank Dr. Daniel F. Farkas for serving as the Graduate Council Representative.

Thanks to Dr. Huan Lin for his many useful ideas and to graduate student, Mr. Shafik Salamor, for providing so much assistance in computer programming and showing interest to continue this research effort.

I will take this opportunity to express my sincere thanks to Dr. Rueybin Chiou of NFESC, Dr. John W. Leonard of the University of Connecticut, and Mr. Paul Palo of NFESC for their encouragement and recommendations for graduate school.

I thank the management at NFESC, Mr. Norm Albertsen, Mr. Mike Atturio and Mr. David Shields and Ms. Barbara Trotter for all their assistance.

Thanks to Dr. Erick Huang and Mr. Paul Palo for making the experimental data available for our use.

Many thanks to Dr. Robert Miller and Ms. Sally Goodlett of the OSU Oceanography Department for their modelling demonstrations and technical support on use of PVM and the Monte Carlo method. Special thanks to Sally for all her time and showing me "the way" of parallel programming.

Thanks to Dr. Michael Quinn and Mr. Ken Ferschweiler of the OSU Computer Science Department for use of the Meiko CS-2 supercomputer. This computer support is made possible by National Science Foundation Grant CDA-9216172.

Partial support from the Office of Naval Research Grant N00014-92-J-1221 and the Naval Facilities Engineering Service Center Contract N47408-94-C-7426 are gratefully acknowledged.

DEDICATION

To Allen, Jane, Ellen, Matt and Sarah

TABLE OF CONTENTS

	<u>Page</u>
1. INTRODUCTION	1
1.1 Problem Definition	1
1.2 Objective	2
1.3 Research Approach	2
1.4 Background	4
1.5 Related Ship Motion Studies	5
2. EQUATIONS OF MOTION	10
2.1 Modelling Assumptions	10
2.2 Roll-Heave-Sway Model	11
2.2.1 Rigid Body Relationships	11
2.2.2 Addition of Relative Motion Hydrostatic Terms	14
2.2.3 Addition of Relative Motion Hydrodynamic Terms	22
2.3 Roll-Heave Model	30
2.4 Roll Model	31
3. NUMERICAL SOLUTION OF EQUATIONS OF MOTION	32
3.1 First Order Differential Equations	32
3.1.1 Deterministic Excitation Formulation	34
3.1.2 Measured Excitation Formulation	35
3.1.3 Filtered White Noise Formulation	35
3.2 Time Domain Solution Method	36

TABLE OF CONTENTS (Continued)

Page

4. IDENTIFICATION OF SYSTEM COEFFICIENTS	37
4.1 Potential Theory Estimates and Experimental Data	37
4.1.1 Potential Theory	37
4.1.2 Physical Model Test Data	38
4.2 Identification for Roll-Heave-Sway Model	44
4.2.1 Test SB26, Regular Waves, H=6 ft, T=5 s	46
4.2.2 Test SB29, Regular Waves, H=7 ft, T=8 s	48
4.2.3 Test SB30, Regular Waves, H=6 ft, T=10 s	51
4.3 Identification for Roll-Heave Model	63
4.3.1 Test SB26, Regular Waves, H=6 ft, T=5 s	65
4.3.2 Test SB29, Regular Waves, H=7 ft, T=8 s	68
4.3.3 Test SB30, Regular Waves, H=6 ft, T=10 s	75
4.4 Summary of Results	80
5. COMPARISON OF NUMERICAL PREDICTIONS WITH MEASURED DATA	81
5.1 Roll-Heave-Sway Model with Random Waves	82
5.1.1 Measured Input, $H_s=4.7$ ft, $T_p=8.2$	82
5.1.2 Filtered Noise Input, $H_s=4.7$ ft, $T_p=8.2$ s	94
5.2 Roll-Heave Model with Random Waves	103
5.2.1 Measured Input, $H_s=4.7$ ft, $T_p=8.2$	103
5.2.2 Filtered Noise Input, $H_s=4.7$ ft, $T_p=8.2$ s	107
5.3 Summary of Results	119

TABLE OF CONTENTS (Continued)

Page

6. STOCHASTIC RESPONSE ESTIMATIONS BY MONTE CARLO METHOD	120
6.1 Algorithm Description	121
6.1.1 Stochastic Differential Equation Model	121
6.1.2 Pseudo Random Number Generation	121
6.1.3 Parallel Program Algorithm	122
6.1.4 Simulation Parameters	124
6.2 3-DOF Roll-Heave-Sway Model Monte Carlo Simulations	124
6.3 2-DOF Roll-Heave Model Monte Carlo Simulations	127
7. OBSERVED SENSITIVE NONLINEAR BEHAVIOR	138
7.1 Transient Chaotic Response	138
7.2 Intermittent and Complete Chaotic Response	140
7.3 Roll List Response	140
7.4 Wave Height Sensitivity	151
8. CONCLUDING REMARKS	175
8.1 Summary	175
8.2 Recommendations for Future Research	178
8.2.1 Modelling and Analysis	178
8.2.2 Computational Efficiency Studies	179
8.2.3 Analysis Tools	180
8.2.4 User Friendliness	180
8.2.5 Naval Architect and Mariner Guidance	180
BIBLIOGRAPHY	181
APPENDICES	184

LIST OF FIGURES

<u>Figure</u>		<u>Page</u>
2.1	Coordinate System Definition	13
2.2	Geometric States for Combined Roll-Heave	15
2.3	Four Main States for Combined Roll-Heave	17
2.4	Righting Moment Surface, Analytical Method	19
2.5	Heave Restoring Force Surface, Analytical Method	20
2.6	Relative Motion System	23
4.1	Added Mass and Damping for Sway	39
4.2	Added Mass and Damping for Heave	40
4.3	Added Inertia and Damping for Roll	41
4.4	Measured and Predicted Response, H=6 ft, T=5 s	47
4.5	Phase Plane for Roll and Roll Velocity, H=6 ft, T=5 s	49
4.6	Roll Spectral Densities, H=6 ft, T=5 s (semilog)	50
4.7	Measured and Predicted Response, H=7 ft, T=8 s	52
4.8	Roll vs Wave, H=7 ft, T=8 s	53
4.9	Roll vs Heave, H=7 ft, T=8 s	54
4.10	Heave vs Wave, H=7 ft, T=8 s	55
4.11	Phase Plane for Roll and Roll Velocity, H=7 ft, T=8 s	56
4.12	Roll Spectral Densities, H=7 ft, T=8 s (semilog)	57
4.13	Measured and Predicted Response, H=6 ft, T=10 s	58

LIST OF FIGURES (Continued)

<u>Figure</u>		<u>Page</u>
4.14	Roll vs Sway, H=6 ft, T=10 s	59
4.15	Heave vs Wave, H=6 ft, T=10 s	60
4.16	Phase Plane for Roll and Roll Velocity, H=6 ft, T=10 s	61
4.17	Roll Spectral Densities, H=6 ft, T=10 s (semilog)	62
4.18	Measured and Predicted Response, H=6 ft, T=5 s	66
4.19	Heave vs Wave, H=6 ft, T=5 s	67
4.20	Phase Plane for Roll and Roll Velocity, H=6 ft, T=5 s	69
4.21	Roll Spectral Densities, H=6 ft, T=5 s	70
4.22	Measured and Predicted Response, H=7 ft, T=8 s	71
4.23	Roll vs Wave, H=7 ft, T=8 s	72
4.24	Roll vs Heave, H=7 ft, T=8 s	73
4.25	Wave vs Heave, H=7 ft, T=8 s	74
4.26	Phase Plane for Roll and Roll Velocity, H=7 ft, T=8 s	76
4.27	Measured and Predicted Response, H=6 ft, T=10 s	77
4.28	Roll vs Heave, H=6 ft, T=10 s	78
4.29	Phase Plane for Roll and Roll Velocity, H=6 ft, T=10 s	79
5.1	Measured and Predicted Response, Hs=4.7 ft, Tp=8.2 s	85
5.2	Measured and Predicted Response, Hs=4.7 ft, Tp=8.2 s	86
5.3	Roll vs Wave, Hs=4.7 ft, Tp=8.2 s	87

LIST OF FIGURES (Continued)

<u>Figure</u>		<u>Page</u>
5.4	Heave vs Wave, $H_s=4.7$ ft, $T_p=8.2$ s	88
5.5	Phase Plane for Roll and Roll Velocity, $H_s=4.7$ ft, $T_p=8.2$ s	89
5.6	Wave Spectral Densities, $H_s=4.7$ ft, $T_p=8.2$ s	90
5.7	Roll Spectral Densities, $H_s=4.7$ ft, $T_p=8.2$ s	91
5.8	Heave Spectral Densities, $H_s=4.7$ ft, $T_p=8.2$ s	92
5.9	Sway Spectral Densities, $H_s=4.7$ ft, $T_p=8.2$ s	93
5.10	Wave Histograms, $H_s=4.7$ ft, $T_p=8.2$ s	95
5.11	Roll Histograms, $H_s=4.7$ ft, $T_p=8.2$ s	96
5.12	Heave Histograms, $H_s=4.7$ ft, $T_p=8.2$ s	97
5.13	Measured and FWN Predicted Response, $H_s=4.7$ ft, $T_p=8.2$ s	98
5.14	Measured and FWN Predicted Response, $H_s=4.7$ ft, $T_p=8.2$ s	99
5.15	Roll vs Heave, $H_s=4.7$ ft, $T_p=8.2$ s	101
5.16	Heave vs Wave, $H_s=4.7$ ft, $T_p=8.2$ s	102
5.17	Measured and Predicted Response, $H_s=4.7$ ft, $T_p=8.2$ s	105
5.18	Measured and Predicted Response, $H_s=4.7$ ft, $T_p=8.2$ s	106
5.19	Roll Spectral Densities, $H_s=4.7$ ft, $T_p=8.2$ s	108
5.20	Heave Spectral Densities, $H_s=4.7$ ft, $T_p=8.2$ s	109
5.21	Roll Histograms, $H_s=4.7$ ft, $T_p=8.2$ s	110
5.22	Heave Histograms, $H_s=4.7$ ft, $T_p=8.2$ s	111

LIST OF FIGURES (Continued)

<u>Figure</u>		<u>Page</u>
5.23	Measured and FWN Predicted Response, $H_s=4.7$ ft, $T_p=8.2$ s	112
5.24	Roll Spectral Densities, $H_s=4.7$ ft, $T_p=8.2$ s	114
5.25	Heave Spectral Densities, $H_s=4.7$ ft, $T_p=8.2$ s	115
5.26	Wave Histograms, $H_s=4.7$ ft, $T_p=8.2$ s	116
5.27	Roll Histograms, $H_s=4.7$ ft, $T_p=8.2$ s	117
5.28	Heave Histograms, $H_s=4.7$ ft, $T_p=8.2$ s	118
6.1	Parallel Virtual Machine Setup	123
6.2	OSU's Meiko CS-2 Supercomputer	125
6.3	Time History of an Ensemble of 50 Realizations	126
6.4	Example Time History of Barge Capsize	129
6.5	Contours of Evolution of RHS Model Joint PDF Estimation for $H_s=4.7$ ft, $T_p=8.2$ s	130
6.6	3-D Surface Plots of Evolution of RHS Model Joint PDF Estimation for $H_s=4.7$ ft, $T_p=8.2$ s	131
6.7	Contours of Evolution of RHS Model Joint PDF Estimation for $H_s=14.1$ ft, $T_p=8.2$ s	132
6.8	3-D Surface Plots of Evolution of RHS Model Joint PDF Estimation for $H_s=14.1$ ft, $T_p=8.2$ s	133
6.9	Curves showing Estimates of Percentage of Capsize for RHS Model	134
6.10	Contours of Evolution of RH Model Joint PDF Estimation for $H_s=4.7$ ft, $T_p=8.2$ s	135
6.11	3-D Surface Plots of Evolution of RH Model Joint PDF Estimation for $H_s=4.7$ ft, $T_p=8.2$ s	136

LIST OF FIGURES (Continued)

<u>Figure</u>		<u>Page</u>
6.12	Curve of Estimates of Percentage of Capsize for RH Model	137
7.1	Time Series of Transient Chaotic Response	139
7.2	Roll and Roll Velocity Phase Plane	141
7.3	Time Series of Periodic Roll Response	142
7.4	Phase Plane for Periodic Roll	143
7.5	Poincare Map for Periodic Roll	144
7.6	Time Series for Chaotic Response for Roll	145
7.7	Phase Plane for Chaotic Roll	146
7.8	Poincare Map for Chaotic Roll	147
7.9	Long Time Series for Chaotic Roll	148
7.10	Time Series of Response for $KG=9.23$ ft	149
7.11	Roll Time Series for $KG=9.23$ ft	150
7.12	Phase Plane for Roll before Chaos with $KG=9.23$ ft	152
7.13	Phase Plane for Roll with Chaos, $KG=9.23$ ft	153
7.14	Time Series of Response, $KG=11.23$ ft	154
7.15	Roll Time Series for $KG=11.23$ ft	155
7.16	Phase Plane for Roll, $KG=11.23$ ft	156
7.17	Poincare Map, $KG=11.23$ ft	157

LIST OF FIGURES (Continued)

<u>Figure</u>		<u>Page</u>
7.18	Time Series for Intermittent Roll List, $KG=12.23$ ft	158
7.19	Shortened Time Series of Roll List, $KG=12.23$ ft	159
7.20	Phase Plane for Intermittent List, $KG=12.23$ ft	160
7.21	3-D Trajectory plot of Roll, Heave Sway, $KG=12.23$ ft	161
7.22	Phase Plane for $H=6.6$ ft, $T=8$ s	163
7.23	Poincare Map for $H=6.6$ ft, $T=8$ s	164
7.24	Roll Spectral Density for $H=6.6$ ft, $T=8$ s	165
7.25	3-D Phase-Plane with Heave, $H=6.6$ ft, $T=8$ s	166
7.26	Phase Plane for $H=7$ ft, $T=8$ s	167
7.27	Poincare Map for $H=7$ ft, $T=8$ s	168
7.28	Roll Spectral Density for $H=7$ ft, $T=8$ s	169
7.29	3-D Phase-Plane with Heave, $H=7$ ft, $T=8$ s	170
7.30	Phase Plane for $H=7.4$ ft, $T=8$ s	171
7.31	Poincare Map for $H=7.4$ ft, $T=8$ s	172
7.32	Roll Spectral Density for $H=7.4$ ft, $T=8$ s	173
7.33	3-D Phase-Plane with Heave, $H=7.4$ ft, $T=8$ s	174

LIST OF TABLES

<u>Table</u>		<u>Page</u>
4.1	Prototype and 1/16 Scale Barge Parameters	42
4.2	Physical Model Test Cases	42
4.3	Natural Periods from Damped Free Vibration Tests	43
4.4	System Parameters for 3-DOF Roll-Heave-Sway Model Regular Wave Cases	48
4.5	System Parameters for 2-DOF Roll-Heave Model Regular Wave Cases	65
5.1	System Parameters for 3-DOF Roll-Heave-Sway Model Random Wave Case Test SB25 with Measured Input	83
5.2	System Parameters for 3-DOF Roll-Heave-Sway Model Random Wave Case Test SB25 with Simulated Input	100
5.3	System Parameters for 2-DOF Roll-Heave Model Random Wave Case Test SB25 with Measured Input	104
5.4	System Parameters for 2-DOF Roll-Heave Model Random Wave Case Test SB25 with Simulated Input	113

LIST OF APPENDICES

- A Roll-Heave Stiffness Figures (Section 2)
- B System Identification Figures, Roll-Heave-Sway Model (Section 4.2)
- C System Identification Figures, Roll-Heave Model (Section 4.3)
- D Comparison Figures, Roll-Heave-Sway Model (Section 5.1)
- E Comparison Figures, Roll-Heave Model (Section 5.2)

LIST OF APPENDIX FIGURES

<u>Figure</u>		<u>Page</u>
A.1	Geometric States for Combined Roll-Heave	186
A.2	Four Main States for Combined Roll-Heave	187
A.3	Righting Moment Curves, $-4 \text{ ft} < \text{Heave} < 0 \text{ ft}$	188
A.4	Righting Moment Curves, $0 < \text{Heave} < 4 \text{ ft}$	189
A.5	Righting Moment Curves, $8 \text{ ft} < \text{KG} < 12 \text{ ft}$	190
A.6	Righting Moment Surface, Analytical Method	191
A.7	Righting Moment Surface, Polynomial Fit	192
A.8	Percent Error in Righting Moment Surface	193
A.9	Percent Error in Righting Moment, Roll Projection	194
A.10	Percent Error in Righting Moment, Heave Projection	195
A.11	Heave Restoring Force Surface, Analytical Method	196
A.12	Heave Restoring Force Surface, Polynomial Fit	197
A.13	Percent Error in Heave Restoring Force Surface	198
A.14	Percent Error in Heave Restoring Force, Roll Projection	199
A.15	Percent Error in Heave Restoring Force, Heave Projection	200
A.16	Righting Moment Comparison, Model vs Eureka	201
A.17	Righting Moment Comparison, Model vs Liaw et al (1993)	202
B.1	Measured and Predicted Response, $H=6 \text{ ft}$, $T=5 \text{ s}$	204
B.2	Measured and Predicted Response, $H=6 \text{ ft}$, $T=5 \text{ s}$	205
B.3	Roll vs Wave, $H=6 \text{ ft}$, $T=5 \text{ s}$	206

LIST OF APPENDIX FIGURES (Continued)

<u>Figure</u>		<u>Page</u>
B.4	Roll vs Heave, H=6 ft, T=5 s	207
B.5	Roll vs Sway, H=6 ft, T=5 s	208
B.6	Heave vs Wave, H=6 ft, T=5 s	209
B.7	Heave vs Sway, H=6 ft, T=5 s	210
B.8	Phase Plane for Roll and Roll Velocity, H=6 ft, T=5 s	211
B.9	Wave Spectral Densities, H=6 ft, T=5 s	212
B.10	Wave Spectral Densities, H=6 ft, T=5 s (semilog)	213
B.11	Roll Spectral Densities, H=6 ft, T=5 s	214
B.12	Roll Spectral Densities, H=6 ft, T=5 s (semilog)	215
B.13	Heave Spectral Densities, H=6 ft, T=5 s	216
B.14	Heave Spectral Densities, H=6 ft, T=5 s (semilog)	217
B.15	Sway Spectral Densities, H=6 ft, T=5 s	218
B.16	Sway Spectral Densities, H=6 ft, T=5 s (semilog)	219
B.17	Measured and Predicted Response, H=7 ft, T=8 s	220
B.18	Measured and Predicted Response, H=7 ft, T=8 s	221
B.19	Roll vs Wave, H=7 ft, T=8 s	222
B.20	Roll vs Heave, H=7 ft, T=8 s	223
B.21	Roll vs Sway, H=7 ft, T=8 s	224
B.22	Heave vs Wave, H=7 ft, T=8 s	225

LIST OF APPENDIX FIGURES (Continued)

<u>Figure</u>		<u>Page</u>
B.23	Heave vs Sway, H=7 ft, T=8 s	226
B.24	Phase Plane for Roll and Roll Velocity, H=7 ft, T=8 s	227
B.25	Wave Spectral Densities, H=7 ft, T=8 s	228
B.26	Wave Spectral Densities, H=7 ft, T=8 s (semilog)	229
B.27	Roll Spectral Densities, H=7 ft, T=8 s	230
B.28	Roll Spectral Densities, H=7 ft, T=8 s (semilog)	231
B.29	Heave Spectral Densities, H=7 ft, T=8 s	232
B.30	Heave Spectral Densities, H=7 ft, T=8 s (semilog)	233
B.31	Sway Spectral Densities, H=7 ft, T=8 s	234
B.32	Sway Spectral Densities, H=7 ft, T=8 s (semilog)	235
B.33	Measured and Predicted Response, H=6 ft, T=10 s	236
B.34	Measured and Predicted Response, H=6 ft, T=10 s	237
B.35	Roll vs Wave, H=6 ft, T=10 s	238
B.36	Roll vs Heave, H=6 ft, T=10 s	239
B.37	Roll vs Sway, H=6 ft, T=10 s	240
B.38	Heave vs Wave, H=6 ft, T=10 s	241
B.39	Heave vs Sway, H=6 ft, T=10 s	242
B.40	Phase Plane for Roll and Roll Velocity, H=6 ft, T=10 s	243
B.41	Wave Spectral Densities, H=6 ft, T=10 s	244
B.42	Wave Spectral Densities, H=6 ft, T=10 s (semilog)	245

LIST OF APPENDIX FIGURES (Continued)

<u>Figure</u>		<u>Page</u>
B.43	Roll Spectral Densities, H=6 ft, T=10 s	246
B.44	Roll Spectral Densities, H=6 ft, T=10 s (semilog)	247
B.45	Heave Spectral Densities, H=6 ft, T=10 s	248
B.46	Heave Spectral Densities, H=6 ft, T=10 s (semilog)	249
B.47	Sway Spectral Densities, H=6 ft, T=10 s	250
B.48	Sway Spectral Densities, H=6 ft, T=10 s (semilog)	251
C.1	Measured and Predicted Response, H=6 ft, T=5 s	253
C.2	Measured and Predicted Response, H=6 ft, T=5 s	254
C.3	Roll vs Wave, H=6 ft, T=5 s	255
C.4	Roll vs Heave, H=6 ft, T=5 s	256
C.5	Heave vs Wave, H=6 ft, T=5 s	257
C.6	Phase Plane for Roll and Roll Velocity, H=6 ft, T=5 s	258
C.7	Wave Spectral Densities, H=6 ft, T=5 s	259
C.8	Wave Spectral Densities, H=6 ft, T=5 s (semilog)	260
C.9	Roll Spectral Densities, H=6 ft, T=5 s	261
C.10	Roll Spectral Densities, H=6 ft, T=5 s (semilog)	262
C.11	Heave Spectral Densities, H=6 ft, T=5 s	263
C.12	Heave Spectral Densities, H=6 ft, T=5 s (semilog)	264
C.13	Measured and Predicted Response, H=7 ft, T=8 s	265
C.14	Measured and Predicted Response, H=7 ft, T=8 s	266

LIST OF APPENDIX FIGURES (Continued)

<u>Figure</u>		<u>Page</u>
C.15	Roll vs Wave, H=7 ft, T=8 s	267
C.16	Roll vs Heave, H=7 ft, T=8 s	268
C.17	Heave vs Wave, H=7 ft, T=8 s	269
C.18	Phase Plane for Roll and Roll Velocity, H=7 ft, T=8 s	270
C.19	Wave Spectral Densities, H=7 ft, T=8 s	271
C.20	Wave Spectral Densities, H=7 ft, T=8 s (semilog)	272
C.21	Roll Spectral Densities, H=7 ft, T=8 s	273
C.22	Roll Spectral Densities, H=7 ft, T=8 s (semilog)	274
C.23	Heave Spectral Densities, H=7 ft, T=8 s	275
C.24	Heave Spectral Densities, H=7 ft, T=8 s (semilog)	276
C.25	Measured and Predicted Response, H=6 ft, T=10 s	277
C.26	Measured and Predicted Response, H=6 ft, T=10 s	278
C.27	Roll vs Wave, H=6 ft, T=10 s	279
C.28	Roll vs Heave, H=6 ft, T=10 s	280
C.29	Heave vs Wave, H=6 ft, T=10 s	281
C.30	Phase Plane for Roll and Roll Velocity, H=6 ft, T=10 s	282
C.31	Wave Spectral Densities, H=6 ft, T=10 s	283
C.32	Wave Spectral Densities, H=6 ft, T=10 s (semilog)	284
C.33	Roll Spectral Densities, H=6 ft, T=10 s	285
C.34	Roll Spectral Densities, H=6 ft, T=10 s (semilog)	286

LIST OF APPENDIX FIGURES (Continued)

<u>Figure</u>		<u>Page</u>
C.35	Heave Spectral Densities, H=6 ft, T=10 s	287
C.36	Heave Spectral Densities, H=6 ft, T=10 s (semilog)	288
D.1	Measured and Predicted Response, Hs=4.7 ft, Tp=8.2 s	290
D.2	Measured and Predicted Response, Hs=4.7 ft, Tp=8.2 s	291
D.3	Roll vs Wave, Hs=4.7 ft, Tp=8.2 s	292
D.4	Roll vs Heave, Hs=4.7 ft, Tp=8.2 s	293
D.5	Roll vs Sway, Hs=4.7 ft, Tp=8.2 s	294
D.6	Heave vs Wave, Hs=4.7 ft, Tp=8.2 s	295
D.7	Heave vs Sway, Hs=4.7 ft, Tp=8.2 s	296
D.8	Phase Plane for Roll and Roll Velocity, Hs=4.7 ft, Tp=8.2 s	297
D.9	Wave Spectral Densities, Hs=4.7 ft, Tp=8.2 s	298
D.10	Roll Spectral Densities, Hs=4.7 ft, Tp=8.2 s	299
D.11	Heave Spectral Densities, Hs=4.7 ft, Tp=8.2 s	300
D.12	Sway Spectral Densities, Hs=4.7 ft, Tp=8.2 s	301
D.13	Wave Histograms, Hs=4.7 ft, Tp=8.2 s	302
D.14	Roll Histograms, Hs=4.7 ft, Tp=8.2 s	303
D.15	Heave Histograms, Hs=4.7 ft, Tp=8.2 s	304
D.16	Sway Histograms, Hs=4.7 ft, Tp=8.2 s	305
D.17	Measured and FWN Predicted Response, Hs=4.7 ft, Tp=8.2 s	306
D.18	Measured and FWN Predicted Response, Hs=4.7 ft, Tp=8.2 s	307

LIST OF APPENDIX FIGURES (Continued)

<u>Figure</u>		<u>Page</u>
D.19	Roll vs Wave, $H_s=4.7$ ft, $T_p=8.2$ s	308
D.20	Roll vs Heave, $H_s=4.7$ ft, $T_p=8.2$ s	309
D.21	Roll vs Sway, $H_s=4.7$ ft, $T_p=8.2$ s	310
D.22	Heave vs Wave, $H_s=4.7$ ft, $T_p=8.2$ s	311
D.23	Heave vs Sway, $H_s=4.7$ ft, $T_p=8.2$ s	312
D.24	Phase Plane for Roll and Roll Velocity, $H_s=4.7$ ft, $T_p=8.2$ s	313
D.25	Wave Spectral Densities, $H_s=4.7$ ft, $T_p=8.2$ s	314
D.26	Roll Spectral Densities, $H_s=4.7$ ft, $T_p=8.2$ s	315
D.27	Heave Spectral Densities, $H_s=4.7$ ft, $T_p=8.2$ s	316
D.28	Sway Spectral Densities, $H_s=4.7$ ft, $T_p=8.2$ s	317
D.29	Wave Histograms, $H_s=4.7$ ft, $T_p=8.2$ s	318
D.30	Roll Histograms, $H_s=4.7$ ft, $T_p=8.2$ s	319
D.31	Heave Histograms, $H_s=4.7$ ft, $T_p=8.2$ s	320
D.32	Sway Histograms, $H_s=4.7$ ft, $T_p=8.2$ s	321
E.1	Measured and Predicted Response, $H_s=4.7$ ft, $T_p=8.2$ s	323
E.2	Measured and Predicted Response, $H_s=4.7$ ft, $T_p=8.2$ s	324
E.3	Roll vs Wave, $H_s=4.7$ ft, $T_p=8.2$ s	325
E.4	Roll vs Heave, $H_s=4.7$ ft, $T_p=8.2$ s	326
E.5	Heave vs Wave, $H_s=4.7$ ft, $T_p=8.2$ s	327
E.6	Phase Plane for Roll and Roll Velocity, $H_s=4.7$ ft, $T_p=8.2$ s	328

LIST OF APPENDIX FIGURES (Continued)

<u>Figure</u>		<u>Page</u>
E.7	Wave Spectral Densities, $H_s=4.7$ ft, $T_p=8.2$ s	329
E.8	Roll Spectral Densities, $H_s=4.7$ ft, $T_p=8.2$ s	330
E.9	Heave Spectral Densities, $H_s=4.7$ ft, $T_p=8.2$ s	331
E.10	Wave Histograms, $H_s=4.7$ ft, $T_p=8.2$ s	332
E.11	Roll Histograms, $H_s=4.7$ ft, $T_p=8.2$ s	333
E.12	Heave Histograms, $H_s=4.7$ ft, $T_p=8.2$ s	334
E.13	Measured and FWN Predicted Response, $H_s=4.7$ ft, $T_p=8.2$ s	335
E.14	Measured and FWN Predicted Response, $H_s=4.7$ ft, $T_p=8.2$ s	336
E.15	Roll vs Wave, $H_s=4.7$ ft, $T_p=8.2$ s	337
E.16	Roll vs Heave, $H_s=4.7$ ft, $T_p=8.2$ s	338
E.17	Heave vs Wave, $H_s=4.7$ ft, $T_p=8.2$ s	339
E.18	Phase Plane for Roll and Roll Velocity, $H_s=4.7$ ft, $T_p=8.2$ s	340
E.19	Wave Spectral Densities, $H_s=4.7$ ft, $T_p=8.2$ s	341
E.20	Roll Spectral Densities, $H_s=4.7$ ft, $T_p=8.2$ s	342
E.21	Heave Spectral Densities, $H_s=4.7$ ft, $T_p=8.2$ s	343
E.22	Wave Histograms, $H_s=4.7$ ft, $T_p=8.2$ s	344
E.23	Roll Histograms, $H_s=4.7$ ft, $T_p=8.2$ s	345
E.24	Heave Histograms, $H_s=4.7$ ft, $T_p=8.2$ s	346

NOMENCLATURE

B	beam of barge
C_{22L}	linear hydrodynamic damping coefficient for sway
C_{22N}	nonlinear hydrodynamic damping coefficient for sway
C_{33L}	linear hydrodynamic damping coefficient for heave
C_{33N}	nonlinear hydrodynamic damping coefficient for heave
C_{44L}	linear hydrodynamic damping coefficient for roll
C_{44N}	nonlinear hydrodynamic damping coefficient for roll
D	depth of barge
f	frequency
F_1	applied force in surge direction
F_2	applied force in sway direction
F_3	applied force in heave direction
g	gravity
H	wave height
Hs	significant wave height
I	rigid body inertia
I_{44}	added inertia in roll direction
k	wave number
KG	Vertical Center of Gravity above Keel
L	length of barge
LCG	Longitudinal Center of Gravity

NOMENCLATURE (Continued)

m	mass
m_{a22}	added mass in sway direction
m_{a33}	added mass in heave direction
M_1	applied moment in roll direction
M_2	applied moment in pitch direction
M_3	applied moment in yaw direction
R_{22}	stiffness in sway direction
R_{33}	stiffness in heave direction
R_{44}	stiffness in roll direction
t	time
T_p	spectral peak period
TCG	Transverse Center of Gravity
v	wave velocity in y direction
\dot{v}	wave acceleration in y direction
VCG	Vertical Center of Gravity
w	wave velocity in z direction
\dot{w}	wave acceleration in z direction
x	surge displacement
x_g	x position of center of gravity
y	sway displacement
y_g	y position of center of gravity

NOMENCLATURE (Continued)

z	heave displacement
z_g	z position of center of gravity
β	damping coefficient for noise filter
ϵ	random phase
η	wave free surface elevation
η'	wave slope
ω	wave radian frequency
ϕ	roll angle
Φ	velocity potential
ψ	yaw angle
Θ	pitch angle
ξ	white noise
ζ	damping ratio

Modelling, Validation and Simulation of Multi-Degree-of-Freedom Nonlinear Stochastic Barge Motions

1.0 INTRODUCTION

1.1 Problem Definition

The U.S. Navy is currently in the process of designing ship-to-shore cargo barges and need a capability to determine the stability of the barges for certain operational sea conditions. They require the identification of motions and accelerations for design of connector joints and securing of cargo. Information on the seakeeping characteristics with likelihood of capsizing is of concern to them as well. The barges will operate in many different directional sea states, but the most unstable scenario is if the barge broaches and becomes broadside to the waves in the so called "beam seas" and may incur large amplitude roll, heave and sway motions with possibility of capsize. In the case of ship shapes other than barges, the most unstable scenario usually is associated with following or quartering seas. However, for following and/or quartering seas, the barge has significant restoring moments along the diagonal of the hull form and so this will not be as unstable.

At the present, the Navy uses linear frequency domain ship motion models, nonlinear time domain models, and experimental measurements for their research and development. This information is cost effective and useful under motion design situations. Their frequency domain models provide linear response characteristics for a range of wave periods. For larger motions, their nonlinear time domain ship motion

models provide a response for a specified wave input. The nonlinear time domain models are well tested but a limitation is they provide one realization of the response for a given wave case and require discretization of the barge into many finite elements. This provides more accurate response for final design purposes but requires significant computational effort.

1.2 Objective

The objective of this research is to examine the capability of a 3-DOF model (or lower order) to estimate stochastic properties of the barge response. This simpler low dimensional model may capture the important nonlinear characteristics of the response for large angle motions. With fewer degrees-of-freedom, the governing equations of motion may be solved faster and in parallel a supercomputer or network of workstations. The net result is a large ensemble of response motions to provide a statistical estimate of the predicted response. This tool will compliment their existing ship motion models for preliminary design.

1.3 Research Approach

A literature review of recent ship and barge motion modelling is conducted. As one of the main goals of this research is to provide stochastic estimates of the motions of a barge in a seaway, the focus is primarily on research by others which describes the motions as a set of nonlinear differential equations with solution in the time domain.

This approach allows stochastic estimates of the response by simulation of many responses concurrently to produce an ensemble. The plan is to extend the standard Single-Degree-of-Freedom (SDOF) roll motion model (Yim *et al*, 1995) to include coupling effects due to heave and sway motions. The thought is the model may provide improved results at large roll angles since the heave and sway are coupled into the roll through hydrostatics and rigid body kinematics. The equations of motion of a rigid body (barge) in air are obtained. Next the barge is placed in water and effects due to hydrostatics are included. Waves are applied and terms modelling the hydrodynamic properties are added. Relative motion effects of the barge with respect to the free surface are included.

Once the model is developed, identification of added inertia, added mass and damping are first estimated from potential theory and then adjusted by simulation and comparison to measured data.

Numerical pluck tests are conducted to perform preliminary response trials on the analytical model as a basis of initial computer code validation. The damped free vibration natural periods and log decrement in damping were investigated to verify agreement with the physical model test results.

The 3-DOF model is reduced to a 2-DOF model to examine the effect of sway on response prediction. Comparison of roll and heave response is performed with the measured physical model test data.

Examples of Monte Carlo simulations of these equations of motion are conducted to demonstrate the capability of estimates of barge response for small and large waves to examine likelihood of capsize.

During the identification procedure for added mass, added inertia and damping, chaotic behavior was found for regular wave cases. These are discussed with examples.

1.4 Background

In research conducted earlier at Oregon State University, a Single-Degree-of-Freedom (SDOF) system (Yim *et al*, 1995) was developed to model pure roll motion of a barge in beam seas. Nonlinearities in the righting moment and in the fluid-structure viscous effects were included in the model. The damping included a linear term plus a "Morison" type quadratic or cubic term. The righting moment included nonlinear stiffness terms to provide a more accurate restoring moment at larger roll angles. The nonlinear roll stiffness term is necessary to predict extreme roll response and the likelihood of capsize for a given sea state and duration. This type of SDOF model was beneficial in that it provided fairly good prediction of the roll motions for simple shapes, such as a barge with a reasonable amount of effort. The SDOF model was compared with measured barge motion data and was found capable of reasonable predictions in terms of statistical moments, spectral densities, and histograms.

In this study, the SDOF model is extended to the MDOF model for roll, heave and sway to include coupling effects induced by the large angle motions. For a symmetric barge in beam seas, these are the dominant transverse motions.

1.5 Related Ship Motion Studies

Liaw (1993) investigated heave excited roll of a ship in head and following seas and found the quadratic coupling effect of heave with roll should be included in dynamic stability analysis. This changes the Mathieu type of equation to Hill's equation. He explained the parametric excitations are dangerous to ship stability because it introduces a time varying component into the roll restoring moment. Thus even without direct roll excitation, the excitations in heave or pitch introduce roll motions. He investigated the effects of an extra quadratic heave term coupled into roll not used in the Mathieu equation. The results indicate changes in the instability regions by including the quadratic term, which may help stabilize the system when the heave is not too large. He found the dynamic stability regions and boundaries depend on the excitation and natural frequencies for both roll and heave. The damping and beam-draft ratios affect the stability regions as well.

In a related study by Liaw *et al* (1993), a 2-DOF heave excited roll model was investigated. The use of nonlinear dynamic analysis tools were applied to gain further insight into the behavior. They showed possibility of chaotic response. The model considered was a free floating rectangular barge subject to head or following seas. One observation is the restoring moment changes character when location of the center of gravity with respect to the free surface is varied. They demonstrated when the barge is unstable at zero roll, it has equilibrium at a steady list angle. The problem transitions from one of a single potential well to that of twin wells.

Donescu and Virgin (1993) studied the nonlinear coupled roll-heave model of a ship in beam seas. They found cases when periodic waves can lead to resonant conditions in roll with possibility of capsizing. They mapped regions of stability and instability for different initial conditions in their model. Cases of period doubling and chaotic response were found. They discovered cases which contradict linear theory, namely increasing wave steepness does not always lead to the occurrence of capsizing. Their results showed regions of capsizing after a certain amount of cycles.

Another related study of nonlinear roll response was conducted by Virgin (1987). He modelled the roll motion of a ship as a SDOF system with nonlinear damping and roll stiffness. Cases of complex behavior prior to capsizing were found for deterministic loading. He showed slight randomness in the excitation does not eliminate chaotic behavior but makes it "fuzzy". Period doubling routes to chaotic roll response were found. He studied the effects of introducing a static bias offset in roll and studying the effects for a range of wave frequencies. This bias was shown to increase the likelihood of capsizing.

Virgin and Bishop (1988) investigated nonlinear behavior in ship roll, articulated tower and semisubmersible. They modelled the ship roll as a SDOF system with nonlinear damping and a higher order polynomial for roll restoring moment. They studied the effects of a damped free vibration and showed the nonlinear damping results in limit cycles while the nonlinear righting moment leads to multiple equilibrium points. They showed sensitivity of initial conditions for a ship with steady list and demonstrate possibility of capsizing.

Paulling (1961) investigated transverse stability for head, following and overtaking swells both theoretically and experimentally. He showed the maximum righting arm is decreased by 50% for the case of a wave amidships compared to still water values and recommended that it should be considered in ship design.

Paulling and Rosenberg (1959) investigated nonlinear motions of a ship with coupling between roll, pitch and heave motions. They showed unstable motion may result if any one of the degrees of freedom is parametrically excited by the other two. Instabilities occur when the natural frequency in the unstable motion is nearly one half of that of the exciting motion (subharmonic), or when the natural frequencies are nearly equal (primary resonance).

Falzarano and Taz Ul Mulk (1994) investigated nonlinear coupled motions of a ship at large angles for various heading angles. They studied the roll, sway and yaw for a T-AGOS survey vessel. The steady-state amplitude of roll of this vessel was found to be multi-valued and highly coupled to sway and yaw. They explained multi-valuedness comes from the backbone curve and well known "jump" phenomenon in nonlinear systems. Backbone curves for their equations of motion are presented and the character of the backbone curves changed for the SDOF and MDOF cases.

Falzarano and Troesch (1990) investigated the vessel with water on deck situation and analyzed it with modern geometric methods. Modelling the roll motion of a fishing vessel with water on deck, damping effects due to bilge keels for various regular waves was analyzed. They located regions of stability for the *Patti-B* clam dredge. Initial

conditions due to transient effects were found to be crucial and may eventually determine safety.

Falzarano *et al* (1991) modelled the motion of a ship as a SDOF in roll and MDOF in roll, yaw and sway velocity. They used strip theory models to determine the frequency dependent added mass, damping and hydrodynamic force transfer functions. They were interested in studying the stability of a ship in seas using the ships heading as a bifurcation parameter. The fishing Trawler, *Patti B*, was used as the case study as this vessel capsized twice in operation resulting in the death of six seamen.

Falzarano *et al* (1992) studied transient motions of a ship subject to periodic wave excitation. Here, they used the theory of lobe dynamics (Wiggins 1988) to demonstrate unpredictability of capsize. A SDOF roll model derived from a 6-DOF model was studied. Their model used frequency dependent added mass and damping coefficients with a "Morison" type quadratic structural drag. These coefficients were identified from ideal flow theory. They used empirical techniques described in Himeno (1981) to identify the real fluid damping effect terms.

Other groups of researchers studied the roll motions of ships from a stochastic or probabilistic perspective (Roberts (1982a,b), Dahle *et al* (1988), Lin and Yim (1995a), Kwon *et al* (1993) and Cai *et al* (1993)). The work done by Dahle *et al* (1988) was in the form of a probabilistic model where probability of sea state and capsize specified and conditional probabilities were computed. Roberts (1982a) modelled the roll motion of a ship by the Fokker-Planck-Kolmogorov method to obtain the probability distribution of roll response. He proposed an averaging approximation to reduce the

FPK equation from two dimensions down to one to allow for ease of solution. This assumption requires the damping to be light so the roll response is narrow banded. Roberts (1982b) studied effects of linear and nonlinear damping and found for the linear case, there was a critical value, below which the roll becomes unstable. For nonlinear damping, the roll was stable under all conditions. Lin and Yim (1995a) modelled the roll motion of a ship by the Fokker-Planck equation and studied the effects of noise on deterministic regular wave loads. They showed the ship roll motion to be governed by two diverse dynamical regions - homoclinic and heteroclinic, where the heteroclinic region relates to capsize. They examined chaotic response behavior with noise with the aid of probability density functions. Kwon *et al* (1993) modelled the roll motion of a ship subject to an equivalent white noise model of the ocean waves. They studied mean upcrossing times for a nonlinear model of roll righting moment and nonlinear damping. Cai *et al* (1994) provided a stochastic model of nonlinear roll motion of a ship. They modelled the excitation as a stationary Gaussian random process with non-white broad band spectra. The total energy in their dynamical system is approximated as a Markov process, using modified version of quasi-conservative averaging. They treated the capsizing of the ship as a first passage problem in stochastic dynamics. Multiplicative excitation and stiffness nonlinearity were found to be important.

2. EQUATIONS OF MOTION

A mathematical model representative of the physics of the fluid structure interaction for the barge in ocean waves is derived. The motions of a rigid body in air are obtained first and then the barge will be placed in water and the effects due to hydrostatics and hydrodynamics will be included. Once the complete 3-DOF model for the barge motions in beam seas are derived, the equations of motion will be reduced to a 2-DOF model for roll-heave and finally a 1-DOF model for roll. The 3-DOF and 2-DOF models are selected for calibration and density estimations. The 1-DOF model is being investigated under a parallel research effort.

2.1 Modelling Assumptions

Before development of the equations of motion are presented, the underlying physical assumptions for model development are summarized as follow. The wave free surface is assumed linear across the beam of the barge. This means ocean wave lengths are significantly longer than the beam. Wave forces and moments act at the center of gravity and are based on momentum theory compared to instantaneous integration of pressure methods. The effect of water-on-deck is treated statically, being modelled only in the hydrostatic restoring moment. Along with this assumption is no bulwarks are present. Coefficients of added inertia, added mass and damping are assumed constant. The longitudinal center of gravity (LCG) is amidships. This is consistent with the physical model in the test data. The barge is symmetric longitudinally and laterally.

Radiation and viscous damping are modelled collectively as a linear and "Morison" type quadratic term.

Barge length, beam, displacement, draft, location of KG, specific weight of water, roll center, are considered variable input parameters. Effects due to a linear mooring stiffness may be switched on or off for sway motions.

2.2 Roll-Heave-Sway Model

2.2.1 Rigid Body Relationships

The rigid body dynamic equations of motion for the barge are based on Newton's Second Law which states the rate of change of linear momentum equals the applied forces and the rate of change of angular momentum equals the applied moments:

$$\frac{d}{dt}(mv) = F \quad \frac{d}{dt}(I\omega) = M \quad (2.1)$$

An inertial coordinate system is placed at the location of the prescribed body-fixed "roll center" of the barge under static equilibrium. Note the inertial coordinate system coincides with the body-fixed (moving) coordinate system initially. Static roll righting moments and heave buoyant restoring forces are calculated as a function of the position and rotation of the barge about the roll center. Equilibrium of forces and moments are considered about the roll center (the position of which is time dependent with respect to the inertia coordinates) with heave and sway directions respect to the inertial coordinates. The body-fixed coordinates are defined such that X=Surge,

Y=Sway, Z=Heave, ϕ =Roll, Θ =Pitch, and ψ =Yaw (Figure 2.1). If the (body-fixed) coordinate system origin (i.e. the roll center) is at the center of gravity of barge and the coordinate system axes are aligned with the principal axes of inertia, the equations become,

$$\begin{aligned}
 F_1 &= m(\ddot{x} + \dot{\theta}z - \psi\dot{y}) \\
 F_2 &= m(\ddot{y} + \psi\dot{x} - \dot{\phi}z) \\
 F_3 &= m(\ddot{z} + \dot{\phi}y - \dot{\theta}x) \\
 M_4 &= I_{44}\ddot{\phi} + (I_{66} - I_{55})\dot{\theta}\dot{\psi} \\
 M_5 &= I_{55}\ddot{\theta} + (I_{44} - I_{66})\dot{\psi}\dot{\phi} \\
 M_6 &= I_{66}\ddot{\psi} + (I_{55} - I_{44})\dot{\phi}\dot{\theta}
 \end{aligned} \tag{2.2}$$

The coupling terms represent the components of centripetal accelerations on the body arising from the moving (body-fixed) coordinate system and the inertial difference terms represent gyroscopic moments arising from the moving system (Abkowitz, 1969). We place the origin of the moving coordinate system at an assumed "center of rotation". Since this may not coincide with the center of gravity, the equations of motion are modified to become,

$$\begin{aligned}
 F_1 &= m[\ddot{x} + \dot{\theta}z - \psi\dot{y} - x_g(\dot{\theta}^2 + \dot{\psi}^2) + y_g(\dot{\phi}\dot{\theta} - \dot{\psi}) + z_g(\dot{\phi}\dot{\psi} + \ddot{\theta})] \\
 F_2 &= m[\ddot{y} + \psi\dot{x} - \dot{\phi}z - y_g(\dot{\psi}^2 + \dot{\phi}^2) + z_g(\dot{\theta}\dot{\psi} - \ddot{\phi}) + x_g(\dot{\theta}\dot{\phi} + \dot{\psi})] \\
 F_3 &= m[\ddot{z} + \dot{\phi}y - \dot{\theta}x - z_g(\dot{\phi}^2 + \dot{\theta}^2) + x_g(\dot{\psi}\dot{\phi} - \ddot{\theta}) + y_g(\dot{\psi}\dot{\theta} + \ddot{\phi})] \\
 M_4 &= I_{44}\ddot{\phi} + (I_{66} - I_{55})\dot{\theta}\dot{\psi} + m[y_g(\ddot{z} + \dot{\phi}\dot{y} - \dot{\theta}\dot{x}) - z_g(\ddot{y} + \dot{\psi}\dot{x} - \dot{\phi}\dot{z})] \\
 M_5 &= I_{55}\ddot{\theta} + (I_{44} - I_{66})\dot{\psi}\dot{\phi} + m[z_g(\ddot{x} + \dot{\theta}\dot{z} - \dot{\psi}\dot{y}) - x_g(\ddot{z} + \dot{\phi}\dot{y} - \dot{\theta}\dot{x})] \\
 M_6 &= I_{66}\ddot{\psi} + (I_{55} - I_{44})\dot{\phi}\dot{\theta} + m[x_g(\ddot{y} + \dot{\psi}\dot{x} - \dot{\phi}\dot{z}) - y_g(\ddot{x} + \dot{\theta}\dot{z} - \dot{\psi}\dot{y})]
 \end{aligned} \tag{2.3}$$

Here, the extra terms represent centrifugal forces acting at the origin due to eccentricity of center of gravity about the origin and inertial reaction forces, and moments about the origin induced by acceleration of the center of gravity relative to the origin.

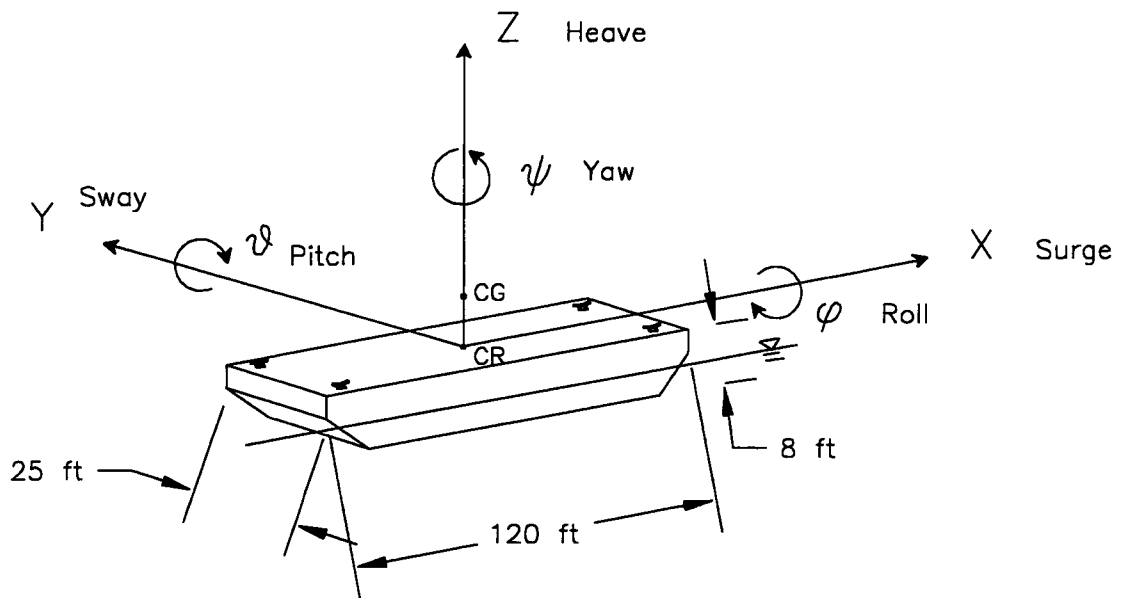


Figure 2.1

Coordinate System Definition

Up to now, we have the rigid body equations of motion for all 6-DOF without addition of the fluid forces and fluid moments. One of the main objectives in this study is to extend the equations of motion for a SDOF system in roll to a MDOF system. For a symmetric barge in beam seas, the dominant response will be in sway, heave and roll. The surge, pitch and yaw motions become negligible. Equation 2.3 now becomes,

$$\begin{aligned} F_2 &= m[\ddot{y} - \dot{\phi}\dot{z} - z_g\ddot{\phi}] \\ F_3 &= m[\ddot{z} + \dot{\phi}\dot{y} - z_g\dot{\phi}^2] \\ M_4 &= I_{44}\ddot{\phi} - m[z_g(\ddot{y} - \dot{\phi}\dot{z})] \end{aligned} \quad (2.4)$$

These equations show the kinematic coupling in the heave and sway equations with extra terms due to the vertical location of the center of gravity not coinciding with the origin of the coordinate system. The longitudinal and lateral center's of gravity coincide with the origin for the barge under study (NFESC, 1996), (i.e. x_g and y_g are zero) and so those terms do not appear in the equations.

2.2.2 Addition of Relative Motion Hydrostatic Terms

Placing the barge in water will add terms due to the hydrostatic "Archimedes" buoyant restoring forces and moments. As the barge heaves up and down, the available righting energy of the barge in roll changes. Exact expressions relating the effects of heave on the righting moment were derived from analytical geometry. The analytical geometric method for calculation of the righting moment and buoyant heave force begins with the complete arrangement of possible configurations of the barge in water shown in Figure 2.2. These cases may be subdivided into combinations of four main states

Geometric States for Combined Roll-Heave

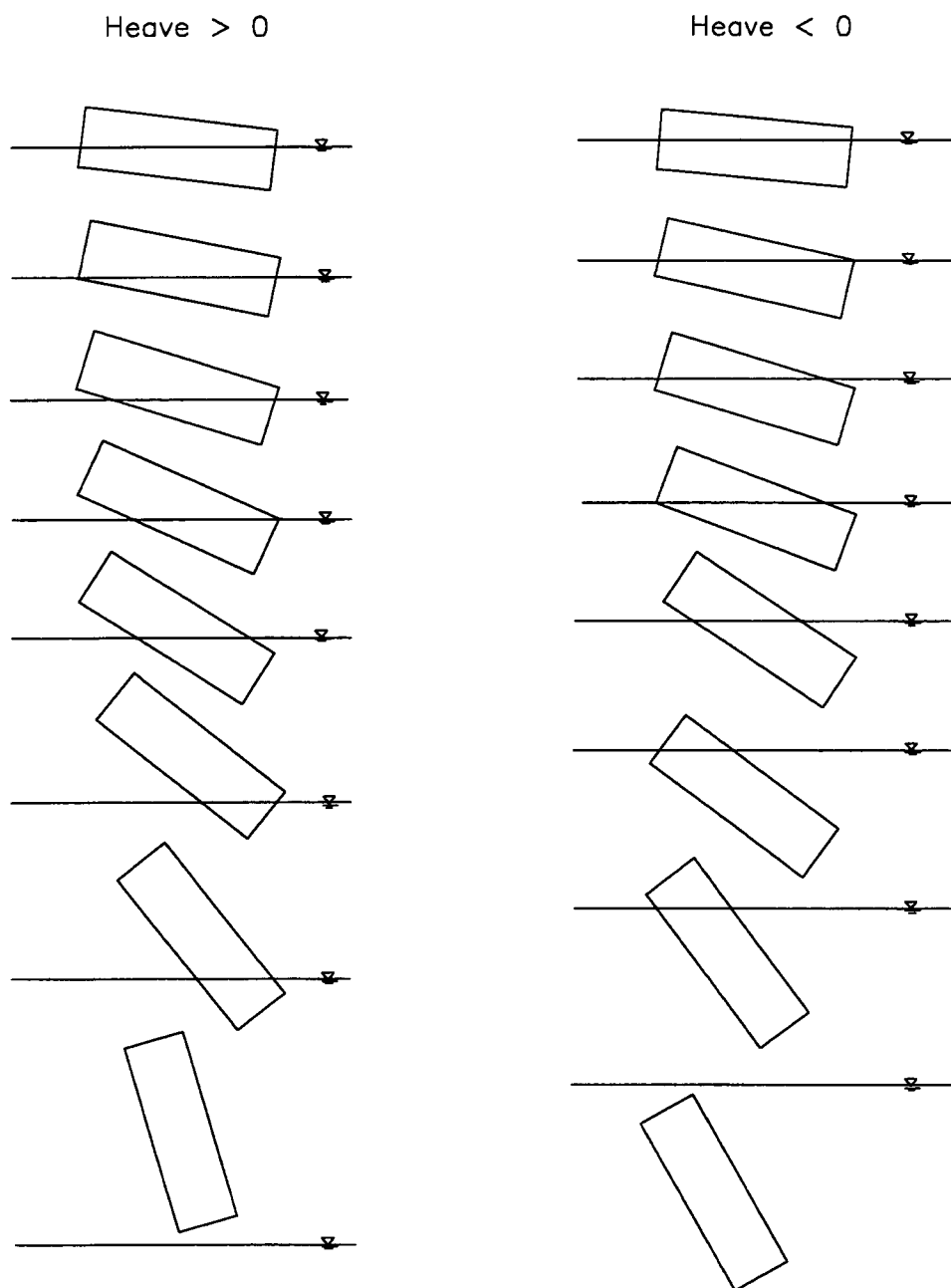


Figure 2.2

Geometric States for Combined Roll-Heave

(Figure 2.3). As the barge is rotated through the roll angles at a value of heave, the method determines which state the underwater portion falls within and subdivides it into triangular sections. From these triangles, the center of buoyancy may be obtained by averaging all the centroids of each triangle.

The initial position of the barge is prescribed by "roll center" with respect to the inertial coordinates. From here, a range of heave (with respect to the inertial coordinates) and roll (about the roll center) values are decided *a priori* and the righting moments are computed over this range. This produces a set of righting moment curves for incremental discrete values of heave. The heave range is typically set at maximum value of the barge being totally out of the water at zero roll and the minimum heave is set at total submergence at zero roll. The maximum and minimum roll values are determined by sample calculations to see what angle the righting moment becomes zero. This may be between +/-60 and +/-90 degrees. Thus a set of hydrostatic stiffness terms are derived relative to the inertial coordinate system with origin at the assumed roll center under statics. The polynomial fit for heave restoring force as a function of roll results in

$$R_{33}(z, \phi) = [A_{1_1}\phi^4 + A_{1_2}\phi^2 + A_{1_3}]z^2 + [A_{2_1}\phi^4 + A_{2_2}\phi^2 + A_{2_3}]z + [A_{3_1}\phi^4 + A_{3_2}\phi^2 + A_{3_3}] \quad (2.5)$$

Here, the coefficient A_{3_3} , is the static vertical force due to the displaced volume at Mean Water Level (MWL).

Similarly, the polynomial expression for the roll restoring moment with heave coupling becomes Equation 2.6.

Four Main States for Combined Roll-Heave

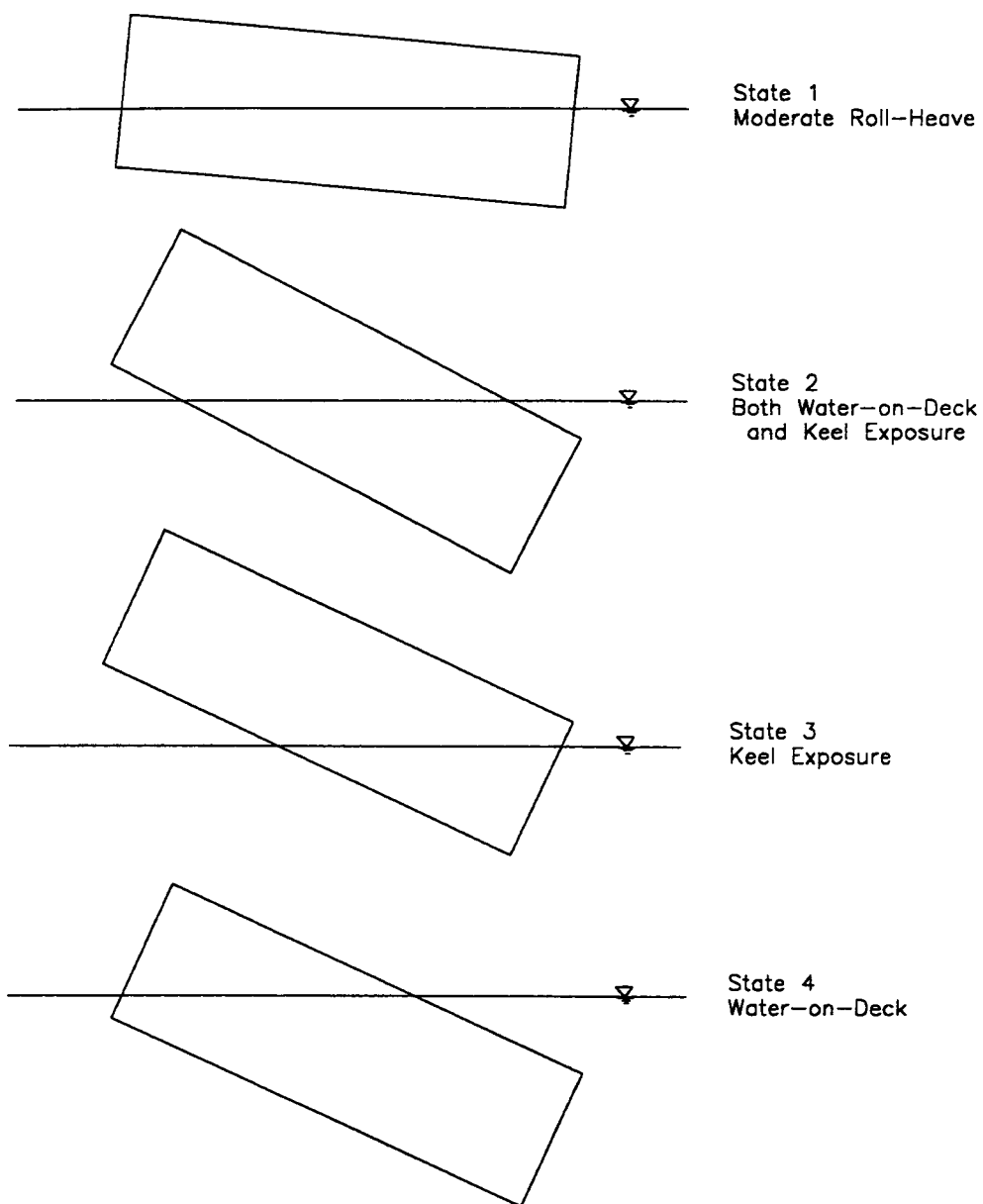


Figure 2.3

Four Main States for Combined Roll-Heave

$$\begin{aligned}
R_{44}(\phi, z) = & [B_{1_1}z^4 + B_{1_2}z^3 + B_{1_3}z^2 + B_{1_4}z + B_{1_5}] \phi^{13} \\
& [B_{3_1}z^4 + B_{3_2}z^3 + B_{3_3}z^2 + B_{3_4}z + B_{3_5}] \phi^{11} \\
& [B_{5_1}z^4 + B_{5_2}z^3 + B_{5_3}z^2 + B_{5_4}z + B_{5_5}] \phi^9 \\
& [B_{7_1}z^4 + B_{7_2}z^3 + B_{7_3}z^2 + B_{7_4}z + B_{7_5}] \phi^7 \\
& [B_{9_1}z^4 + B_{9_2}z^3 + B_{9_3}z^2 + B_{9_4}z + B_{9_5}] \phi^5 \\
& [B_{11_1}z^4 + B_{11_2}z^3 + B_{11_3}z^2 + B_{11_4}z + B_{11_5}] \phi^3 \\
& [B_{13_1}z^4 + B_{13_2}z^3 + B_{13_3}z^2 + B_{13_4}z + B_{13_5}] \phi^1
\end{aligned} \tag{2.6}$$

The ordering of the subscripts follows the convention used in the numerical model derived from the Matlab software package (The Mathworks, 1993). The results of these expressions may be shown graphically in Figures 2.4 and 2.5. These figures show righting moment curves over a range of heave values and roll angles. The curves are asymmetric in heave because they are calculated with a roll center at 7 ft above the keel. Appendix A provides additional plots of these hydrostatic relationships. The effects of changing the center of gravity on the righting moment curves is seen in Appendix A.5. It is apparent the range of stability falls as the KG increases. Surfaces of the roll and heave curves calculated from analytical geometry and least squares fit can be seen in Figures A.4 and Figure A.5.

To allow for high speed time domain simulation of the stochastic equations of motion, this matrix of roll-heave curves are fitted with sufficiently high order polynomials by least square approximation. Various high and low order polynomials were tried to find the optimum fit. A 13th order polynomial in roll and quadratic in heave was found to be sufficient to qualify the general character of the coupled roll-

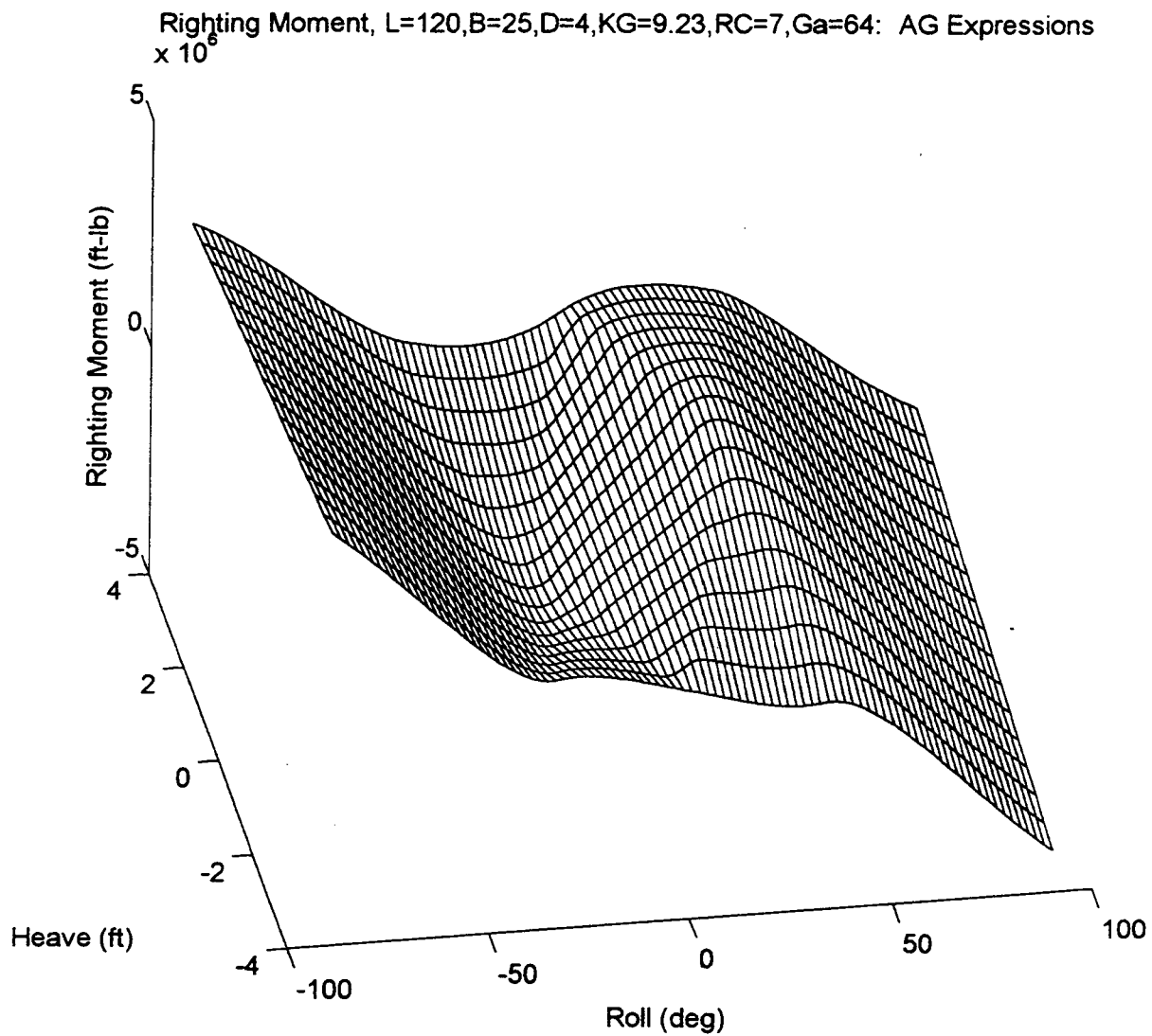


Figure 2.4

Righting Moment Surface, Analytical Method

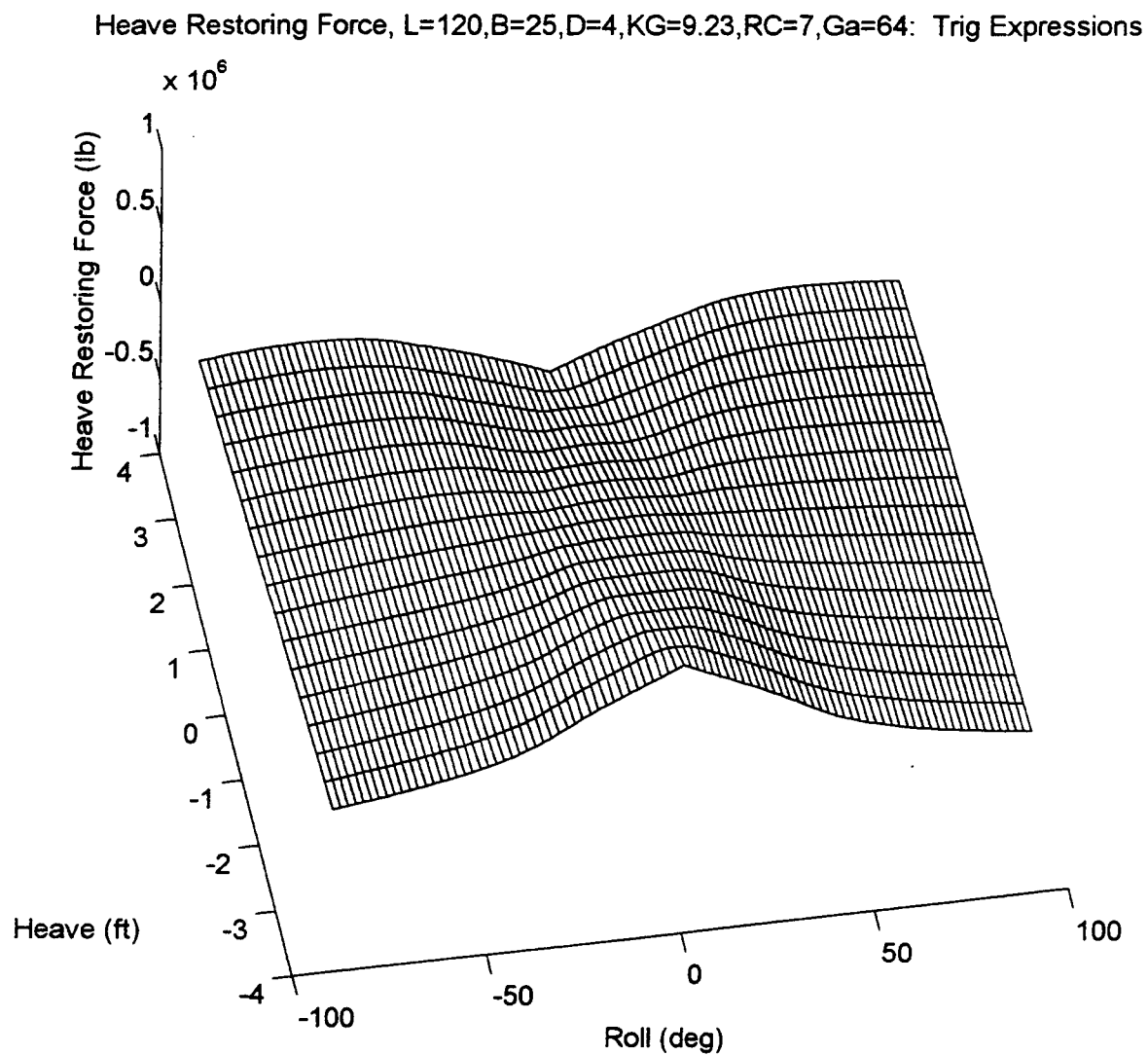


Figure 2.5

Heave Restoring Force Surface, Analytical Method

heave restoring moment-forces. The fitted righting moment and heave force surfaces are shown in Appendix A.7 and A.12. The error between the "exact" analytical expressions and the least square fit is shown in Figures A.8-A.10 and A.13-A.15 in Appendix A. The maximum error is less than 5%. Righting moment for zero heave is compared to that of (Paulling, 1995) as shown in Figure A.16 in Appendix A.

Righting moment curves from these expressions using similar parameters to those of Liaw *et al* (1993) were favorable and are provided in Figure A.17.

Modifying these stiffness terms to include relative motions between the moving barge and the wave free surface elevation and wave slope changes the restoring force for heave in Equations 2.5 to become

$$\begin{aligned}
 R_{33}(z, \phi, \frac{\partial \eta}{\partial y}) = & [A_{1_1}(\phi - \frac{\partial \eta}{\partial y})^4 + A_{1_2}(\phi - \frac{\partial \eta}{\partial y})^2 + A_{1_3}] (z - \eta)^2 \\
 & + [A_{2_1}(\phi - \frac{\partial \eta}{\partial y})^4 + A_{2_2}(\phi - \frac{\partial \eta}{\partial y})^2 + A_{2_3}] (z - \eta) \\
 & + [A_{3_1}(\phi - \frac{\partial \eta}{\partial y})^4 + A_{3_2}(\phi - \frac{\partial \eta}{\partial y})^2 + A_{3_3}]
 \end{aligned} \tag{2.7}$$

Similarly, the restoring moment in roll with relative motion effects modifies Equation 2.6 to become Equation 2.8.

$$\begin{aligned}
R_{44}(\phi, z, \eta, \frac{\partial \eta}{\partial y}) = & [B_{1_1}(z-\eta)^4 + B_{1_2}(z-\eta)^3 + B_{1_3}(z-\eta)^2 + B_{1_4}(z-\eta) + B_{1_5}] (\phi - \frac{\partial \eta}{\partial y})^{13} \\
& [B_{3_1}(z-\eta)^4 + B_{3_2}(z-\eta)^3 + B_{3_3}(z-\eta)^2 + B_{3_4}(z-\eta) + B_{3_5}] (\phi - \frac{\partial \eta}{\partial y})^{11} \\
& [B_{5_1}(z-\eta)^4 + B_{5_2}(z-\eta)^3 + B_{5_3}(z-\eta)^2 + B_{5_4}(z-\eta) + B_{5_5}] (\phi - \frac{\partial \eta}{\partial y})^9 \\
& [B_{7_1}(z-\eta)^4 + B_{7_2}(z-\eta)^3 + B_{7_3}(z-\eta)^2 + B_{7_4}(z-\eta) + B_{7_5}] (\phi - \frac{\partial \eta}{\partial y})^7 \quad (2.8) \\
& [B_{9_1}(z-\eta)^4 + B_{9_2}(z-\eta)^3 + B_{9_3}(z-\eta)^2 + B_{9_4}(z-\eta) + B_{9_5}] (\phi - \frac{\partial \eta}{\partial y})^5 \\
& [B_{11_1}(z-\eta)^4 + B_{11_2}(z-\eta)^3 + B_{11_3}(z-\eta)^2 + B_{11_4}(z-\eta) + B_{11_5}] (\phi - \frac{\partial \eta}{\partial y})^3 \\
& [B_{13_1}(z-\eta)^4 + B_{13_2}(z-\eta)^3 + B_{13_3}(z-\eta)^2 + B_{13_4}(z-\eta) + B_{13_5}] (\phi - \frac{\partial \eta}{\partial y})
\end{aligned}$$

These generalized force-displacement relationships may be seen in Figure 2.6.

Adding Equations 2.7 and Equation 2.8 to Equation 2.4 the equilibrium of force and moment equations becomes

$$\begin{aligned}
m[\ddot{y} - \dot{\phi}\dot{z} - z_g\ddot{\phi}] &= F_2 \\
m[\ddot{z} + \dot{\phi}\dot{y} - z_g\dot{\phi}^2] + R_{33}(\phi, z, \eta, \frac{\partial \eta}{\partial y}) &= F_3 \\
I_{44}\ddot{\phi} - m[z_g(\ddot{y} - \dot{\phi}\dot{z})] + R_{44}(\phi, z, \eta, \frac{\partial \eta}{\partial y}) &= M_4
\end{aligned} \quad (2.9)$$

2.2.3 Addition of Relative Motion Hydrodynamic Terms

Placing the barge in still water and adding ocean wave excitation introduces terms to represent added mass and added inertia due to relative motion accelerations of the barge and the wave. To take into account energy dissipation effects due to radiation of waves from the barge and flow separation around the hull, the hydrodynamic damping

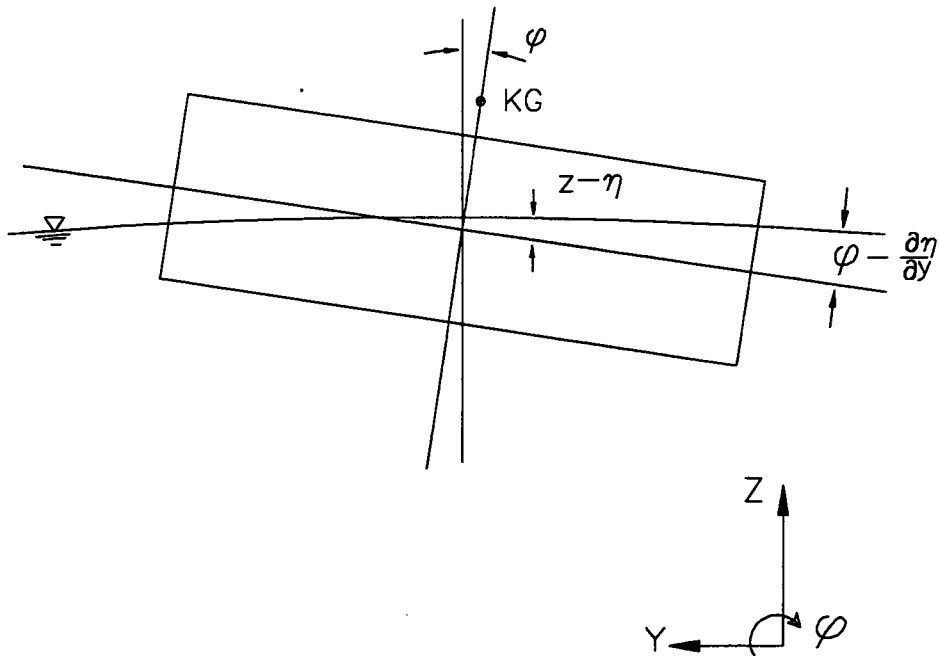


Figure 2.6

Relative Motion System

may be modelled as a relative motion linear and nonlinear term. The viscous damping for roll is relative to the time rate of change of wave slope, where the slope is in terms of the sway direction (for beam sea conditions). These additional force and moment terms are added to Equation 2.9 to become

$$\begin{aligned}
 m\ddot{y} + m_{a_{22}}(\ddot{y} - \dot{v}) + C_{22_L}(\dot{y} - v) + C_{22_N}(\dot{y} - v)|\dot{y} - v| - m\dot{\phi}\dot{z} - mz_g\ddot{\phi} &= 0 \\
 m\ddot{z} + m_{a_{33}}(\ddot{z} - \dot{w}) + C_{33_L}(\dot{z} - w) + C_{33_N}(\dot{z} - w)|\dot{z} - w| + m\dot{\phi}\dot{y} \\
 - mz_g\dot{\phi}^2 + mg + R_{33}(z, \phi, \eta, \frac{\partial\eta}{\partial y}) &= 0 \\
 I_{44}\ddot{\phi} + I_{a_{44}}(\ddot{\phi} - \frac{\partial\ddot{\eta}}{\partial y}) + C_{44_L}(\dot{\phi} - \frac{\partial\dot{\eta}}{\partial y}) + C_{44_N}(\dot{\phi} - \frac{\partial\dot{\eta}}{\partial y})|\dot{\phi} - \frac{\partial\dot{\eta}}{\partial y}| \\
 + mz_g\dot{\phi}\dot{z} - mz_g\dot{y} + R_{44}(\phi, z, \eta, \frac{\partial\eta}{\partial y}) - mgz_g\sin\phi &= 0
 \end{aligned} \tag{2.10}$$

In equation 2.10, the effects due to weight of the barge and heeling moment have been added as well.

Equation 2.10 is improved further to include directional components of added mass in heave and sway for larger wave slopes and a "synthetic linear mooring" is added in sway only for purposes of matching the experimental data. This term may be switched off in the numerical solution process for a true free floating barge. The mooring stiffness is set so the natural period in sway due to addition of the mooring lines will be very low and out of the range of first order response. The cosine and sine modifications to the restoring terms account for directional changes in buoyancy at larger wave slopes. The heeling moment due to weight of the barge is removed from the hydrostatic righting moment terms as this term remains in the inertial coordinate system. This means the term "Righting Moment" typically used by Naval Architects is

different here in the sense that the moment is due solely to the shift in the center of buoyancy only. Equation 2.10 now becomes,

$$\begin{aligned}
& m\ddot{y} + m_{a_{22}} \cos\left(\frac{\partial\eta}{\partial y}\right)(\ddot{y}-\dot{v}) + m_{a_{33}} \sin\left(\left|\frac{\partial\eta}{\partial y}\right|\right)(\ddot{y}-\dot{v}) + C_{22_L}(\dot{y}-v) \\
& \quad + C_{22_N}(\dot{y}-v)|\dot{y}-v| - m\dot{\phi}\dot{z} - m(z_g \cos\phi)\ddot{\phi} \\
& \quad + R_{33}(\phi, z, \eta, \frac{\partial\eta}{\partial y}) \sin\left(\frac{\partial\eta}{\partial y}\right) + K_{moor}y = 0 \\
\\
& m\ddot{z} + m_{a_{33}} \cos\left(\frac{\partial\eta}{\partial y}\right)(\ddot{z}-\dot{w}) + m_{a_{22}} \sin\left(\left|\frac{\partial\eta}{\partial y}\right|\right)(\ddot{z}-\dot{w}) + C_{33_L}(\dot{z}-w) \\
& \quad + C_{33_N}(\dot{z}-w)|\dot{z}-w| + m\dot{\phi}\dot{y} - m(z_g \cos\phi)\dot{\phi}^2 + mg \\
& \quad + R_{33}(z, \phi, \eta, \frac{\partial\eta}{\partial y}) \cos\left(\frac{\partial\eta}{\partial y}\right) = 0 \\
\\
& I_{44}\ddot{\phi} + I_{a_{44}}\left(\ddot{\phi} - \frac{\partial\ddot{\eta}}{\partial y}\right) + C_{44_L}\left(\dot{\phi} - \frac{\partial\dot{\eta}}{\partial y}\right) + C_{44_N}\left(\dot{\phi} - \frac{\partial\dot{\eta}}{\partial y}\right)\left|\dot{\phi} - \frac{\partial\dot{\eta}}{\partial y}\right| \\
& \quad + m(z_g \cos\phi)\dot{\phi}\dot{z} - m(z_g \cos\phi)\ddot{y} + R_{44}(\phi, z, \eta, \frac{\partial\eta}{\partial y}) \cos\left(\frac{\partial\eta}{\partial y}\right) \\
& \quad - mgz_g \sin\phi = 0
\end{aligned} \tag{2.11}$$

In process of identifying the system coefficients (Section 4), Equation 2.11 is adjusted further such that the relative motion terms in hydrodynamic damping for sway and heave are reduced to a linear and nonlinear "Morison" structural form. This form of damping improved the comparisons of roll, heave and sway with the measured data in both amplitude and phase for the coefficients identified. With these modifications, Equation 2.11 becomes Equation 2.12.

$$\begin{aligned}
& m\ddot{y} + m_{a_{22}} \cos\left(\frac{\partial\eta}{\partial y}\right) (\ddot{y} - \dot{v}) + m_{a_{33}} \sin\left(\left|\frac{\partial\eta}{\partial y}\right|\right) (\ddot{y} - \dot{v}) + C_{22_t} \dot{y} \\
& \quad + C_{22_n} \dot{y} |\dot{y}| - m\dot{\phi}\dot{z} - m(z_g \cos\phi) \ddot{\phi} \\
& \quad + R_{33}\left(\phi, z, \eta, \frac{\partial\eta}{\partial y}\right) \sin\left(\frac{\partial\eta}{\partial y}\right) + K_{moor} y = 0 \\
\\
& m\ddot{z} + m_{a_{33}} \cos\left(\frac{\partial\eta}{\partial y}\right) (\ddot{z} - \dot{w}) + m_{a_{22}} \sin\left(\left|\frac{\partial\eta}{\partial y}\right|\right) (\ddot{z} - \dot{w}) + C_{33_t} \dot{z} \\
& \quad + C_{33_n} \dot{z} |\dot{z}| + m\dot{\phi}\dot{y} - m(z_g \cos\phi) \dot{\phi}^2 + mg \\
& \quad + R_{33}\left(z, \phi, \eta, \frac{\partial\eta}{\partial y}\right) \cos\left(\frac{\partial\eta}{\partial y}\right) = 0 \\
\\
& I_{44} \ddot{\phi} + I_{a_{44}} \left(\ddot{\phi} - \frac{\partial\ddot{\eta}}{\partial y}\right) + C_{44_t} \left(\dot{\phi} - \frac{\partial\dot{\eta}}{\partial y}\right) + C_{44_n} \left(\dot{\phi} - \frac{\partial\dot{\eta}}{\partial y}\right) \left|\dot{\phi} - \frac{\partial\dot{\eta}}{\partial y}\right| \\
& \quad + m(z_g \cos\phi) \dot{\phi}\dot{z} - m(z_g \cos\phi) \ddot{y} + R_{44}\left(\phi, z, \eta, \frac{\partial\eta}{\partial y}\right) \cos\left(\frac{\partial\eta}{\partial y}\right) \\
& \quad - mgz_g \sin\phi = 0
\end{aligned} \tag{2.12}$$

A description of the ocean wave field will now be provided. For linear regular waves, let the velocity potential and associated wave profile and associate time and spatial partial derivatives be defined as

$$\begin{aligned}
\Phi &= A \frac{g \cosh k(h+z)}{\omega \cosh(kh)} \cos(ky - \omega t) \\
\eta &= \frac{1}{g} \frac{\partial\Phi}{\partial t} \Big|_{z=0} = A \sin(ky - \omega t) \\
\dot{\eta} &= \frac{\partial\eta}{\partial t} = -\omega A \cos(ky - \omega t) \\
\ddot{\eta} &= \frac{\partial\dot{\eta}}{\partial t} = -\omega^2 \eta
\end{aligned} \tag{2.13a}$$

$$\begin{aligned}
\eta' &= \frac{\partial \eta}{\partial y} = kA \cos(ky - \omega t) \\
\dot{\eta}' &= \frac{\partial \dot{\eta}}{\partial y} = \omega kA \sin(ky - \omega t) \\
\ddot{\eta}' &= \frac{\partial \ddot{\eta}}{\partial y} = -\omega^2 kA \cos(ky - \omega t) \\
v &= -\frac{\partial \Phi}{\partial y} = \frac{Agk \cosh k(h+z)}{\omega \cosh(kh)} \sin(ky - \omega t) \\
\dot{v} &= \frac{\partial u}{\partial t} = -Agk \frac{\cosh k(h+z)}{\cosh(kh)} \cos(ky - \omega t) \\
w &= -\frac{\partial \Phi}{\partial z} = \frac{Agk \sinh k(h+z)}{\omega \cosh(kh)} \cos(ky - \omega t) \\
\dot{w} &= \frac{\partial w}{\partial t} = Agk \frac{\sinh k(h+z)}{\cosh(kh)} \sin(ky - \omega t)
\end{aligned} \tag{2.13b}$$

For now assume deep water and consider water particle kinematics at Mean Water Line (MWL) with $y=0$ and $z=0$. Then the dispersion equation and linear wave expressions become,

$$\begin{aligned}
k &= \frac{\omega^2}{g}, \\
\eta &= A \sin(ky - \omega t) \\
\dot{\eta} &= -\omega A \cos(ky - \omega t) \\
\ddot{\eta} &= -\omega^2 \eta \\
v &= \omega \eta \\
\dot{v} &= \omega \dot{\eta} \\
w &= -\dot{\eta}
\end{aligned} \tag{2.14a}$$

$$\begin{aligned}
\dot{w} &= \omega^2 \eta \\
\eta' &= \frac{\partial \eta}{\partial y} = -\frac{\omega}{g} \dot{\eta} \\
\dot{\eta}' &= \frac{\partial \dot{\eta}}{\partial y} = \frac{\omega^3}{g} \eta \\
\ddot{\eta}' &= \frac{\partial \ddot{\eta}}{\partial y} = \frac{\omega^3}{g} \dot{\eta}
\end{aligned} \tag{2.14b}$$

For random waves, the wave free surface elevation may be represented as sum of regular waves (Chakrabarti, 1994) by,

$$\eta = \sum_{i=1}^N \frac{H_i}{2} \sin(k_i y - \omega_i t + \epsilon_i) \tag{2.15}$$

which adheres to an ocean wave spectral model such as that of Bretschneider (Chakrabarti, 1994) represented by,

$$S(\omega) = 0.1687 H_s^2 \frac{\omega_s^4}{\omega^5} e^{-0.675(\frac{\omega_s}{\omega})^4} \tag{2.16}$$

thus now, the simulation of the wave profile becomes,

$$\eta = \sum_{i=1}^N \frac{H_i}{2} \sin(k_i y - \omega_i t + \epsilon_i) \tag{2.17}$$

where,

$$\begin{aligned}
H_i &= 2\sqrt{2S(\omega)\Delta\omega} \\
\epsilon_i &= 2\pi R_i
\end{aligned} \tag{2.18}$$

and H_i is the wave height from the wave spectrum and ϵ is a uniformly distributed random phase angle between $(0, 2\pi)$ by a random number generator (Chakrabarti, 1994).

Equations 2.15 - 2.18 are valid means of obtaining a unidirectional random wave profile, however for this application of estimation of stochastic properties via Monte Carlo simulations, the approach becomes computationally restrictive. Another approach is to use a linear second order differential equation that possesses a transfer function consistent with the expected random wave properties. The input is merely Gaussian white noise with the output being the random wave profile. The form of this approach lends itself well to solution of the equations of motion because it simply appends two extra first order ode's in the time domain solution process. This is explained next.

Let the free surface elevation, η , be that of a random sea. Another representation of Equation 2.15 may be used in the form of a linear "random white noise" filter. The filter is produced to satisfy the statistical and spectral properties of the wave profile.

Let the filter for free surface elevation be defined as

$$m\ddot{\eta} + c\dot{\eta} + k\eta = \xi \quad (2.19)$$

where ξ is Gaussian white noise which may readily be obtained by a using a "pseudo random number generator" provided on any computer system and making the distribution Gaussian. The transfer function and the spectral density function of the output of the filtered white noise (Lin and Yim, 1995b) are

$$|H(f)| = \frac{1}{[-(2\pi f)^2 + (2\pi f_o)^2]^2 + (2\pi\beta_n)^2} \quad (2.20)$$

$$S_\eta(f) = \frac{S_o}{[-(2\pi f)^2 + (2\pi f_o)^2]^2 + (2\pi\beta_n)^2} \quad (2.21)$$

Values for m , c , and k are set to satisfy the variance and peak period of the auto spectrum for the true free surface. The best fit is provided by equating the total energy, the magnitude of the maximum spectral density, and the spectral peak frequency (Lin and Yim, 1995b).

Combining Equations 2.12, 2.14 and 2.19 produces eight coupled first order differential equations of motion which may simulated in a Monte Carlo simulation. Next, the effects due to sway and then heave are removed from the model.

2.3 Roll-Heave Model

Removal of sway coupling from Equation 2.13 reduces the 3-DOF model to a 2-DOF model in roll and heave

$$\begin{aligned} m\ddot{z} + m_{a_{33}}(\ddot{z} - \dot{w}) + C_{33_l}\dot{z} + C_{33_n}z|\dot{z}| - m(z_g \cos\phi)\dot{\phi}^2 \\ + mg + R_{33}(z, \phi, \eta, \frac{\partial\eta}{\partial y}) = 0 \\ I_{44}\ddot{\phi} + I_{a_{44}}(\ddot{\phi} - \frac{\partial\ddot{\eta}}{\partial y}) + C_{44_l}(\dot{\phi} - \frac{\partial\dot{\eta}}{\partial y}) + C_{44_n}(\phi - \frac{\partial\eta}{\partial y})|\dot{\phi} - \frac{\partial\dot{\eta}}{\partial y}| \\ + m(z_g \cos\phi)\dot{\phi}\dot{z} + R_{44}(\phi, z, \eta, \frac{\partial\eta}{\partial y}) - mgz_g \sin\phi = 0 \end{aligned} \quad (2.22)$$

2.4 Roll Model

Further uncoupling the heave response from roll, the SDOF equation in roll becomes,

$$\begin{aligned}
 I_{44}\ddot{\phi} + I_{a_{44}}\left(\ddot{\phi} - \frac{\partial \ddot{\eta}}{\partial y}\right) + C_{44_e}\left(\dot{\phi} - \frac{\partial \dot{\eta}}{\partial y}\right) + C_{44_n}\left(\dot{\phi} - \frac{\partial \dot{\eta}}{\partial y}\right) \left|\dot{\phi} - \frac{\partial \dot{\eta}}{\partial y}\right| \\
 + R_{44}\left(\phi, z, \eta, \frac{\partial \eta}{\partial y}\right) - mgz_g \sin\phi = 0
 \end{aligned}
 \tag{2.23}$$

3. NUMERICAL SOLUTION OF EQUATIONS OF MOTION

To obtain stochastic estimates of the response of the barge in random beam seas, Equation 2.11 will be solved numerically in the time domain by parallel processing to get an ensemble of motions. For this purpose, Equation 2.11 is reduced to first order Ordinary Differential Equations (ODE's) and integrated by standard numerical methods. This section provides details of the form of these ODE's and the solution method.

3.1 First Order Differential Equations

Equation 2.11 contains acceleration components for both sway and roll in each of sway and roll (second order differential) equilibrium equations. To reduce this form to one amenable for solution, these two equations are treated as a system of two equations (sway and roll) and two unknowns (sway acceleration and roll angular acceleration). The equations are reduced by Cramer's method and the determinant is checked to ensure it is not close to zero. The heave equation contains coupling in the kinematics but may be reduced to a first order ODE independently. Written in the form of two equations and two unknowns yields,

$$\begin{aligned} A_{11}\ddot{y} + A_{12}\ddot{\phi} &= C_1 \\ A_{21}\ddot{y} + A_{22}\ddot{\phi} &+ C_2 \end{aligned} \tag{3.1}$$

where

$$\begin{aligned}
A_{11} &= m + m_{a_{22}} \cos\left(\frac{\partial\eta}{\partial y}\right) \\
A_{12} &= -mz_g \cos(\phi) \\
A_{21} &= -mz_g \cos(\phi) \\
A_{22} &= I_{44} + I_{a_{44}} \\
C_1 &= m_{a_{22}} \dot{v} + C_{22_l}(v-\dot{y}) + C_{22_n}(v-\dot{y})|v-\dot{y}| - m\phi\dot{z} \\
&\quad - R_{33}\left(\phi, z, \eta, \frac{\partial\eta}{\partial y}\right) \sin\left(\frac{\partial\eta}{\partial y}\right) - K_{moor}y \\
C_2 &= I_{a_{44}} \frac{\partial\ddot{\eta}}{\partial y} + C_{44_l}\left(\frac{\partial\dot{\eta}}{\partial y} - \dot{\phi}\right) + C_{44_n}\left(\frac{\partial\dot{\eta}}{\partial y} - \dot{\phi}\right) \left|\frac{\partial\dot{\eta}}{\partial y} - \dot{\phi}\right| - mz_g\dot{\phi}\dot{z} \\
&\quad - R_{44}\left(\phi, z, \eta, \frac{\partial\eta}{\partial y}\right) + mgz_g \sin\phi
\end{aligned} \tag{3.2}$$

and

$$DET = \begin{bmatrix} A_{11} & A_{12} \\ A_{21} & A_{22} \end{bmatrix} \quad \ddot{y} = \frac{\begin{bmatrix} C_1 & A_{12} \\ C_2 & A_{22} \end{bmatrix}}{DET} \quad \ddot{\phi} = \frac{\begin{bmatrix} A_{11} & C_1 \\ A_{21} & C_2 \end{bmatrix}}{DET} \tag{3.3}$$

Introducing these expressions as part of the solution, the eight first order ODE's become that shown collectively on the next page as Equation 3.4.

$$\begin{aligned}
X_1 &= \phi \\
\dot{X}_1 &= X_2 = \dot{\phi} \\
\dot{X}_2 &= (A_{11}C_2 - A_{21}C_1) / DET \\
X_3 &= z \\
\dot{X}_3 &= X_4 = \dot{z} \\
\dot{X}_4 &= [m_{a_{33}} \cos\left(\frac{\partial \eta}{\partial X_5}\right) \dot{w} + m_{a_{22}} \sin\left(\left|\frac{\partial \eta}{\partial X_5}\right|\right) \dot{w} + C_{33_l}(w - X_4) \\
&\quad + C_{33_w}(w - X_4) |w - X_4| - mX_2X_6 + mz_g \cos(X_1)X_2^2 - mg \\
&\quad - R_{33}(X_3, X_1, \eta, \frac{\partial \eta}{\partial X_5}) \cos\left(\frac{\partial \eta}{\partial X_5}\right)] / (I_{44} + I_{a_{44}}) \\
X_5 &= y \\
\dot{X}_5 &= X_6 = \dot{y} \\
\dot{X}_6 &= (C_1A_{22} - C_2A_{12}) / DET
\end{aligned} \tag{3.4}$$

3.1.1 Deterministic Excitation Formulation

The expressions for the wave and wave properties in Equation 3.4 for deterministic regular waves may be calculated directly from Equations 2.13 and 2.14. One would simply calculate these values in the time domain at each time step and substitute these values into Equation 3.4.

3.1.2 Measured Excitation Formulation

If measured waves are input into Equation 3.4, the wave properties of Equation 2.13 and 2.14 are calculated by central difference method. The second order and fourth order accurate formulas are,

$$f'(x_i) = \frac{f(x_{i+1}) - f(x_{i-1}))}{2h}$$

$$f''(x_i) = \frac{f(x_{i+1}) - 2f(x_i) + f(x_{i-1}))}{h^2}$$
(3.5)

$$f'(x_i) = \frac{-f(x_{i+2}) + 8f(x_{i+1}) - 8f(x_{i-1}) + f(x_{i-2}))}{12h}$$

$$f''(x_i) = \frac{-f(x_{i+2}) + 16f(x_{i+1}) - 30f(x_i) + 16f(x_{i-1}) - f(x_{i-2}))}{12h^2}$$

Using these central difference expressions, the water particle kinematics may be calculated from the measured wave profile.

3.1.3 Filtered White Noise Formulation

This formulation for the excitation is used in the Monte Carlo simulations where the random normally distributed white noise is processed through a linear filter with a transfer function to match the ocean wave spectrum. The second order ODE's were presented in Section 2.2.3 as Equations 2.19 - 2.21. Using this filtered white noise excitation with Equation 3.4 forms eight first order ODE's provided as Equation 3.6.

$$\begin{aligned}
X_1 &= \phi \\
\dot{X}_1 &= X_2 = \dot{\phi} \\
\dot{X}_2 &= (A_{11}C_2 - A_{21}C_1) / DET \\
X_3 &= z \\
\dot{X}_3 &= X_4 = \dot{z} \\
\dot{X}_4 &= [m_{a_{33}} \cos(\frac{\partial \eta}{\partial X_5}) \dot{w} + m_{a_{22}} \sin(|\frac{\partial \eta}{\partial X_5}|) \dot{w} + C_{33_L} (w - X_4) \\
&\quad + C_{33_N} (w - X_4) |w - X_4| - mX_2X_6 + mz_g \cos(X_1)X_2^2 - mg \\
&\quad - R_{33}(X_3, X_1, \eta, \frac{\partial \eta}{\partial X_5}) \cos(\frac{\partial \eta}{\partial X_5})] / (I_{44} + I_{a_{44}}) \\
X_5 &= y \\
\dot{X}_5 &= X_6 = \dot{y} \\
\dot{X}_6 &= (C_1A_{22} - C_2A_{12}) / DET \\
X_7 &= \eta \\
\dot{X}_7 &= X_8 = \dot{\eta} \\
\dot{X}_8 &= [-C_{eq}X_8 - K_{eq}X_7 + \sigma\delta] / m_{eq}
\end{aligned} \tag{3.6}$$

3.2 Time Domain Solution Method

We selected a 4th order Runge-Kutta method to solve the equations of motion (Press *et al*, 1986), for which a subroutine that can handle a system of ODE's is readily available and is well tested. In addition, Press *et al* (1986) provide a Gaussian distributed random number generator for use in our filtered white noise model.

4. IDENTIFICATION OF SYSTEM COEFFICIENTS

The Naval Facilities Engineering Service Center, Port Hueneme, California, conducted several measurements of a moored and a partially constrained barge in regular and random seas (NFESC, 1995). These data sets are used to compare and calibrate the equations of motion coefficients for added inertia, added mass, linear radiation and nonlinear "Morison" oscillatory hydrodynamic damping.

Coefficients in the governing equations of motion for roll, sway and heave are identified using regular waves of heights from 6 ft - 10 ft and wave periods of 5 - 10 seconds. In the next section, these coefficients are used for comparison with the random wave test cases and in some cases, adjusted to provide a best fit.

4.1 Potential Theory Estimates and Experimental Data

Existing linear ship motion programs and experimental data are used to provide a means for identifying the added mass and damping coefficients in the equations of motion.

4.1.1 Potential Theory

Paulling (1995) furnished values of frequency dependent added mass, added inertia and radiation damping obtained from one of his linear potential theory ship motion programs for a U.S Navy barge (NFESC, 1995). These curves, shown in Figures 4.1

to Figure 4.3, provided starting estimates for use in identification of the coefficients in the equations of motion.

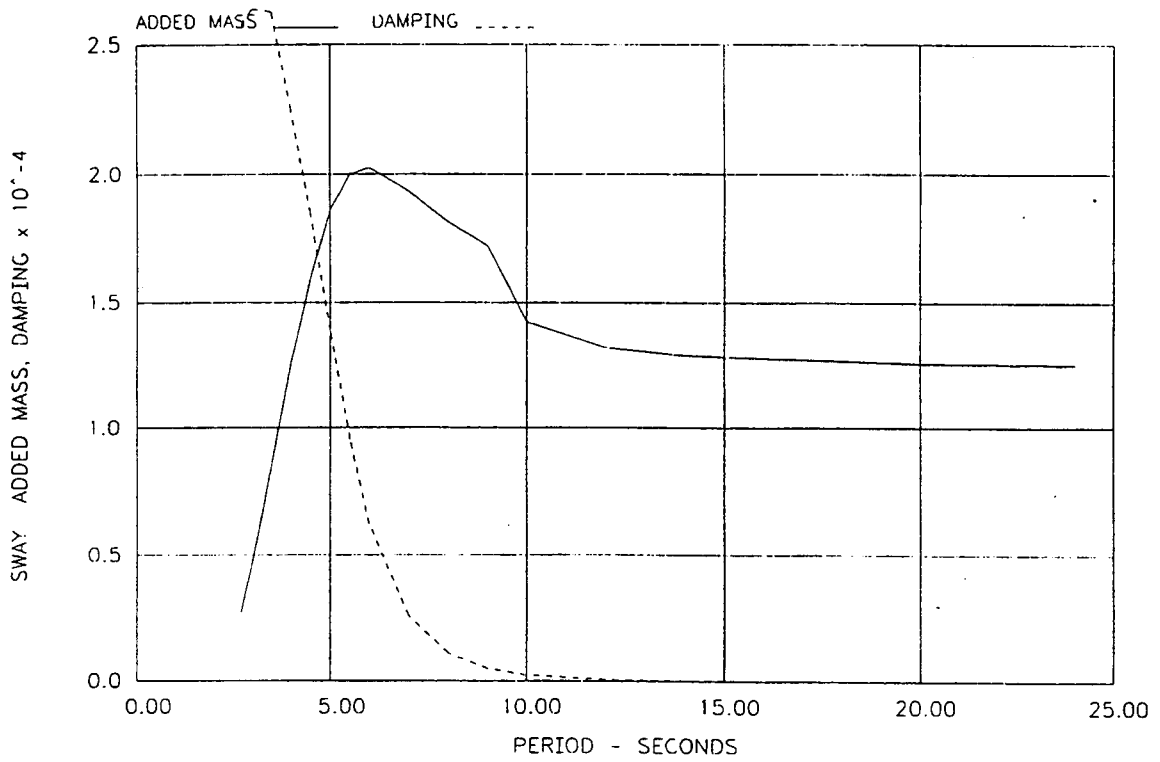
4.1.2 Physical Model Test Data

Under collaboration with the U.S Navy, we were provided with multiple data sets of measured physical model test data for two different U.S. Navy model barges (NFESC, 1995). The first data set consists of motions of a 1/16 scale barge in regular and random seas oriented at multiple headings to the waves. The second set is a different U.S Navy barge that was constrained in the pitch, surge and yaw mode but free to move in roll, heave and sway. The third set, is similar to the first set but the model was increased to 1/8 scale and experienced capsize responses. All of these data sets contain regular and random wave cases.

For the research presented, only the first measured data set is used. Parallel and future research tasks are using the other data sets. In using this data set, an additional term is provided in the equation of motion for sway to model the restraining mooring lines of the barge in the wave flume. This term is discussed in more detail later.

The particulars for the experimental data investigated in the research discussed here are shown in Tables 4.1 and 4.2. Free vibration tests of the barge in roll, heave and sway were also conducted to provide estimates of the viscous damping and linear natural periods. The results are shown in Table 4.3.

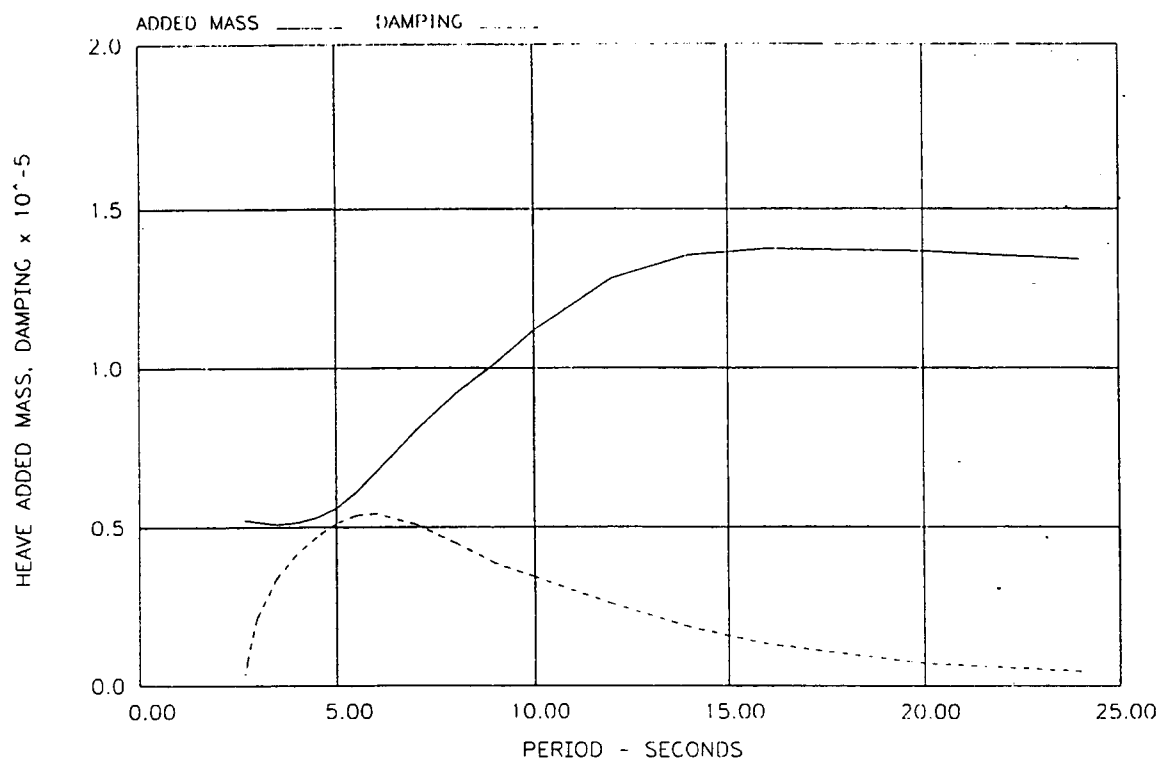
SCRCP - Vers. 1.1a : 05/31/9



NCEL BARGE - FULL SCALE - 120x25x5 ft.

Figure 4.1 Added Mass and Damping for Sway

SCRCOF - Vers. 1.1a : 05/31/91

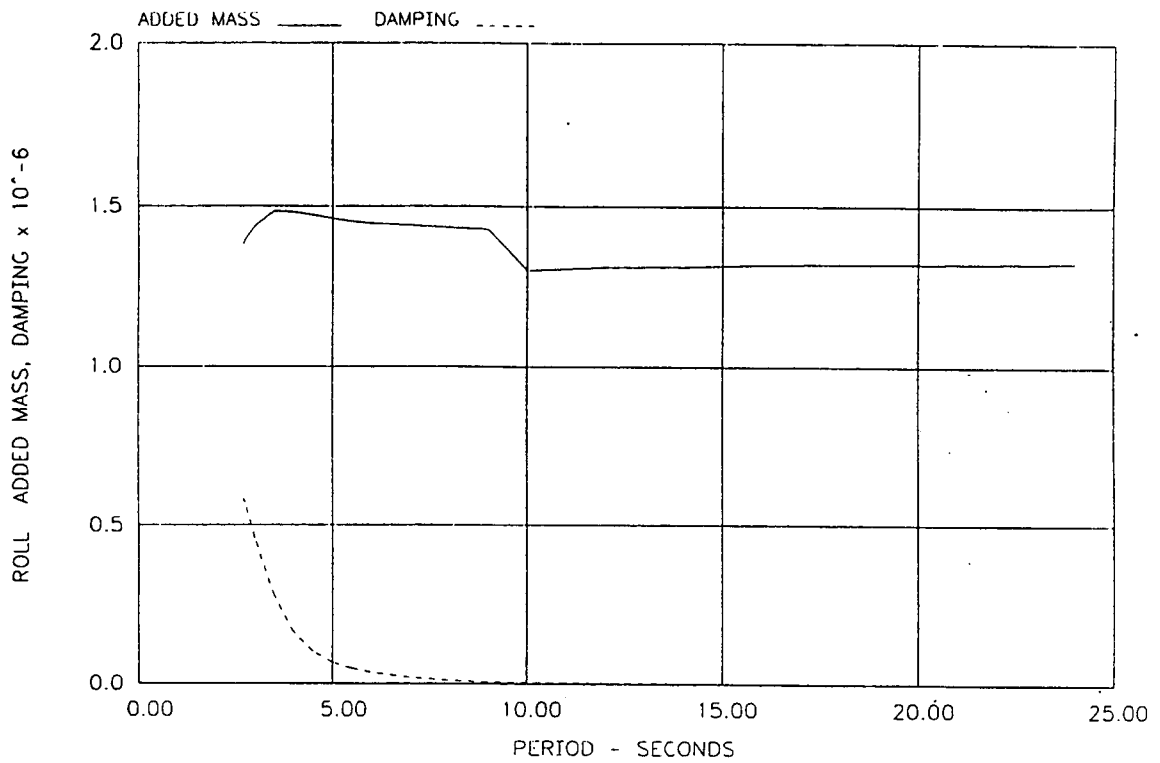


NCEL BARGE - FULL SCALE - 120x25x5 ft.

Figure 4.2

Added Mass and Damping for Heave

SCRCOF - Vers. 1.1a : 05/31/95



NCEL BARGE - FULL SCALE - 120x25x5 ft.

Figure 4.3

Added Inertia and Damping for Roll

Table 4.1 Prototype and 1/16 Scale Barge Parameters

Item	Full Scale	Model Scale
Length	120.0 ft	7.5 ft
Width	25.0 ft	1.56 ft
Height	8.0 ft	0.5 ft
Draft	4.0 ft	0.25 ft
KG	9.23 ft	0.58 ft
Weight	662.5 kips	157.7 lbs

Table 4.2 Physical Model Test Cases

Test Case	Wave Type	H (ft) or Hs (ft)	T (s) or Tp (s)
SB25	Random	4.7	8.2
SB26	Regular	6.0	5.0
SB27	Regular	6.0	6.0
SB28	Regular	6.0	7.0
SB29	Regular	7.0	8.0
SB30	Regular	6.0	10.0
SB31	Regular	10.0	10.0
SB33	Random	5.0	8.0

Table 4.3 Natural Periods from Damped Free Vibration Tests

Motion	Natural Period
Roll	5.25 s
Heave	4.00 s
Sway	27.14 s

Provided with these measurements of the natural periods, an estimate of the added inertia may be calculated using the known barge inertia and hydrostatic righting moment information. The true added inertia and damping will be different due to relative motion effects as the barge moves in the waves. The dissipation of energy takes two forms. The first, called radiation damping, is due to the resultant wave induced motion of the barge which in turn produces waves radiating away. The second takes the form of viscous effects and flow separation at the barge-wave interface. The sharp corners on the keel and sides may allow for shedding of vortices. Another form of damping, which may or may not be minimal, is due to the material damping of the mooring system and hydrodynamic damping as the mooring moves in the water. Increased drag due to vortex induced oscillations of the mooring (if any) would be negligible for this case but may be a important in ocean structures where the mooring system (or tendons) is in deep water (e.g towed bodies, tension leg platforms, drilling risers).

4.2 Identification for Roll-Heave-Sway Model

The roll-heave-sway model contains coefficients for added inertia, added mass and damping that must be evaluated. For convenience, the equations of motion are provided again as Equations 4.1-4.3.

$$\begin{aligned}
m\ddot{y} + m_{a_{22}} \cos\left(\frac{\partial\eta}{\partial y}\right)(\ddot{y}-\dot{v}) + m_{a_{33}} \sin\left(\left|\frac{\partial\eta}{\partial y}\right|\right)(\ddot{y}-\dot{v}) + C_{22_l}(\dot{y}-v) \\
+ C_{22_n}(\dot{y}-v)|\dot{y}-v| - m\dot{\phi}\dot{z} - m(z_g \cos\phi)\ddot{\phi} \\
+ R_{33}\left(\phi, z, \eta, \frac{\partial\eta}{\partial y}\right) \sin\left(\frac{\partial\eta}{\partial y}\right) + K_{moor}y = 0 \\
m\ddot{z} + m_{a_{33}} \cos\left(\frac{\partial\eta}{\partial y}\right)(\ddot{z}-\dot{w}) + m_{a_{22}} \sin\left(\left|\frac{\partial\eta}{\partial y}\right|\right)(\ddot{z}-\dot{w}) + C_{33_l}(\dot{z}-w) \\
+ C_{33_n}(\dot{z}-w)|\dot{z}-w| + m\dot{\phi}\dot{y} - m(z_g \cos\phi)\dot{\phi}^2 + mg \\
+ R_{33}\left(z, \phi, \eta, \frac{\partial\eta}{\partial y}\right) \cos\left(\frac{\partial\eta}{\partial y}\right) = 0 \\
I_{44}\ddot{\phi} + I_{a_{44}}\left(\ddot{\phi} - \frac{\partial\ddot{\eta}}{\partial y}\right) + C_{44_l}\left(\dot{\phi} - \frac{\partial\dot{\eta}}{\partial y}\right) + C_{44_n}\left(\dot{\phi} - \frac{\partial\dot{\eta}}{\partial y}\right)\left|\dot{\phi} - \frac{\partial\dot{\eta}}{\partial y}\right| \\
+ m(z_g \cos\phi)\dot{\phi}\dot{z} - m(z_g \cos\phi)\ddot{y} + R_{44}\left(\phi, z, \eta, \frac{\partial\eta}{\partial y}\right) \cos\left(\frac{\partial\eta}{\partial y}\right) \\
- mgz_g \sin\phi = 0
\end{aligned} \tag{4.1}$$

$$\begin{aligned}
R_{33}\left(z, \phi, \frac{\partial\eta}{\partial y}\right) &= [A_{1_1}\left(\phi - \frac{\partial\eta}{\partial y}\right)^4 + A_{1_2}\left(\phi - \frac{\partial\eta}{\partial y}\right)^2 + A_{1_3}] (z-\eta)^2 \\
&+ [A_{2_1}\left(\phi - \frac{\partial\eta}{\partial y}\right)^4 + A_{2_2}\left(\phi - \frac{\partial\eta}{\partial y}\right)^2 + A_{2_3}] (z-\eta) \\
&+ [A_{3_1}\left(\phi - \frac{\partial\eta}{\partial y}\right)^4 + A_{3_2}\left(\phi - \frac{\partial\eta}{\partial y}\right)^2 + A_{3_3}]
\end{aligned} \tag{4.2}$$

$$\begin{aligned}
R_{44}(\phi, z, \eta, \frac{\partial \eta}{\partial y}) = & [B_{1_1}(z-\eta)^4 + B_{1_2}(z-\eta)^3 + B_{1_3}(z-\eta)^2 + B_{1_4}(z-\eta) + B_{1_5}] (\phi - \frac{\partial \eta}{\partial y})^{13} \\
& [B_{3_1}(z-\eta)^4 + B_{3_2}(z-\eta)^3 + B_{3_3}(z-\eta)^2 + B_{3_4}(z-\eta) + B_{3_5}] (\phi - \frac{\partial \eta}{\partial y})^{11} \\
& [B_{5_1}(z-\eta)^4 + B_{5_2}(z-\eta)^3 + B_{5_3}(z-\eta)^2 + B_{5_4}(z-\eta) + B_{5_5}] (\phi - \frac{\partial \eta}{\partial y})^9 \\
& [B_{7_1}(z-\eta)^4 + B_{7_2}(z-\eta)^3 + B_{7_3}(z-\eta)^2 + B_{7_4}(z-\eta) + B_{7_5}] (\phi - \frac{\partial \eta}{\partial y})^7 \quad (4.3) \\
& [B_{9_1}(z-\eta)^4 + B_{9_2}(z-\eta)^3 + B_{9_3}(z-\eta)^2 + B_{9_4}(z-\eta) + B_{9_5}] (\phi - \frac{\partial \eta}{\partial y})^5 \\
& [B_{11_1}(z-\eta)^4 + B_{11_2}(z-\eta)^3 + B_{11_3}(z-\eta)^2 + B_{11_4}(z-\eta) + B_{11_5}] (\phi - \frac{\partial \eta}{\partial y})^3 \\
& [B_{13_1}(z-\eta)^4 + B_{13_2}(z-\eta)^3 + B_{13_3}(z-\eta)^2 + B_{13_4}(z-\eta) + B_{13_5}] (\phi - \frac{\partial \eta}{\partial y})
\end{aligned}$$

First, estimates of the coefficients from potential theory, damped free vibration tests and previous studies using system identification techniques (Yim and Bartel, 1995) provide preliminary starting values. These values were then adjusted until the predicted response compared well with the measured response. This was performed for all regular wave cases listed in Table 4.2. For purposes of brevity, we selected three regular wave test cases to present the results of identification. These are Test SB26, Test SB29 and Test SB30. These cases were selected since SB26 and SB30 bounded the wave periods and SB29 has a wave period closest to the random wave peak period in Test SB25. The random wave case is shown in the next Section. Test SB25 will be the precursor comparison before final production of the ensemble from Monte Carlo Simulation.

4.2.1 Test SB26, Regular Waves, H=6 ft, T=5 s

This measured data set has waves that are the steepest of those measured and happen to have a wave period at the linear natural period in roll. The identification yielded higher than expected damping ratios for roll but about the same for the preliminary estimates in sway and heave. The "best fit" results for all three tests are shown in Table 4.4.

The high damping ratio of 40% in roll was needed to obtain agreeable comparisons between the predicted response and the measured response for the steeper waves of Test SB26. This damping drops off substantially for longer period waves as seen in the table. The added mass and damping for sway is fairly close to the potential theory estimates for these frequencies. Interestingly, the heave damping was low for the steeper waves but high for the longer period waves.

The time histories of the measured and predicted are shown together in Figures 4.4. Both the amplitude and phase compare fairly well for roll. For this wave case, the magnitude of heave and sway are slightly underpredicted. One may note the damping in heave and sway are also low for this case (Table 4.3). Apparently, the roll-heave-sway coupling here makes the high damping in roll influence the response in heave and sway.

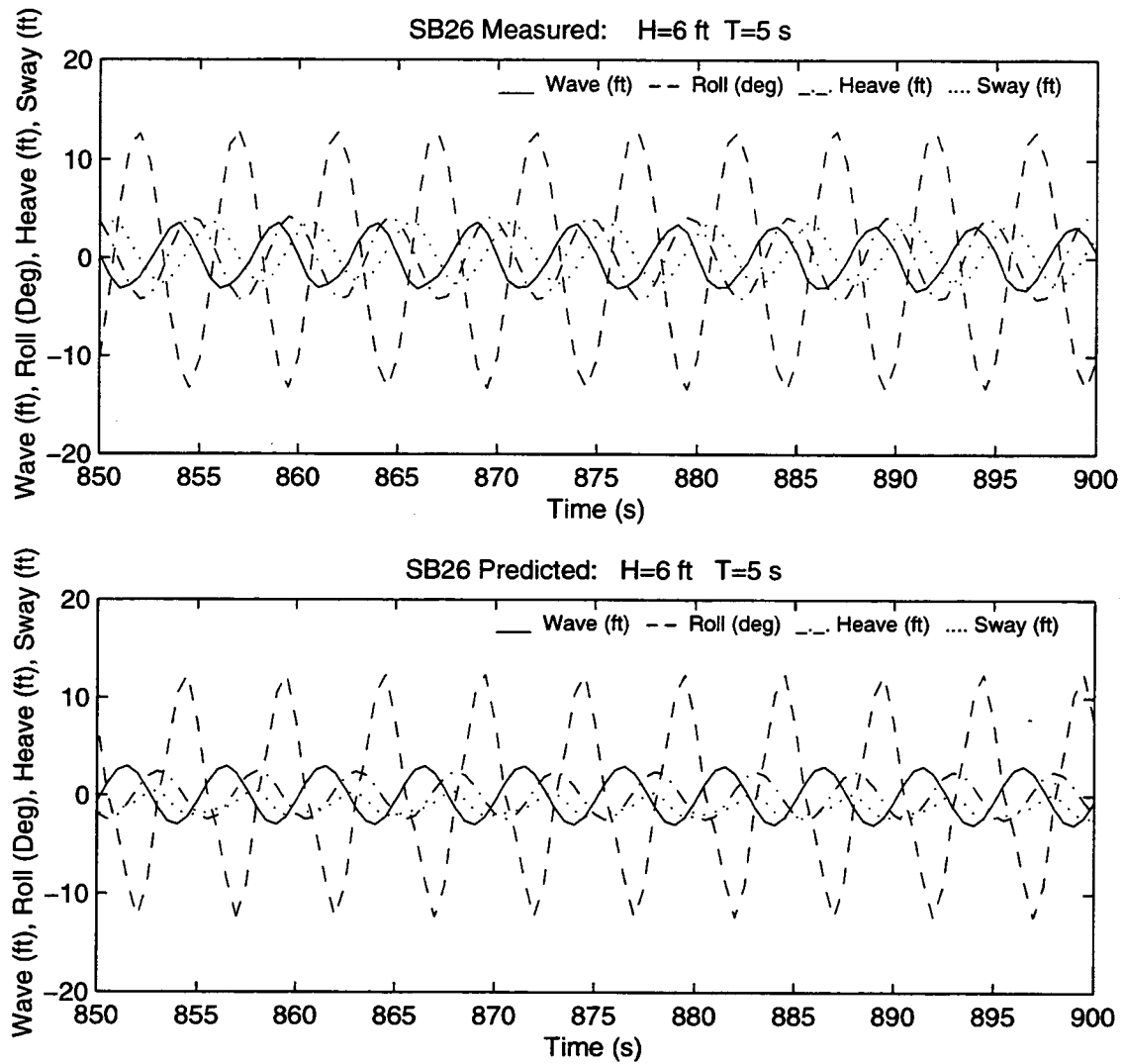


Figure 4.4

Measured and Predicted Response, H=6 ft, T=5 s

Table 4.4 System Parameters for 3-DOF Roll-Heave-Sway Model Regular Wave Cases

Parameter	SB26	SB29	SB30
M_{22} (slugs)	2.325E04	2.325E04	2.325E04
M_{a22} (slugs)	5E02	5E02	5E02
ζ_{L22}	0.025	0.005	0.015
ζ_{N22}	0.025	0.005	0.015
M_{33} (slugs)	2.325E04	2.325E04	2.325E04
M_{a33} (slugs)	1.0E05	1.0E05	1.0E05
ζ_{L33}	0.015	0.10	0.20
ζ_{N33}	0.015	0.10	0.20
I_{44} (slugs-ft ²)	2.161046E6	2.161046E6	2.161046E6
I_{a44} (slugs-ft ²)	5.49232E05	5.49232E05	5.49232E05
ζ_{L44}	0.40	0.25	0.025
ζ_{N44}	0.40	0.25	0.025

The phase plane for roll is found to differ from the measured (Figure 4.5). The predicted response has increased nonlinearity not present in the measured data. The roll spectral densities agree well with superharmonics appearing in each (Figure 4.6). The reader may refer to Appendix B for additional comparisons.

4.2.2 Test SB29, Regular Waves, H=7 ft, T=8 s

In this case, the wave period is closest to the peak period of the random wave spectrum. Time histories of the measured and predicted are shown together in

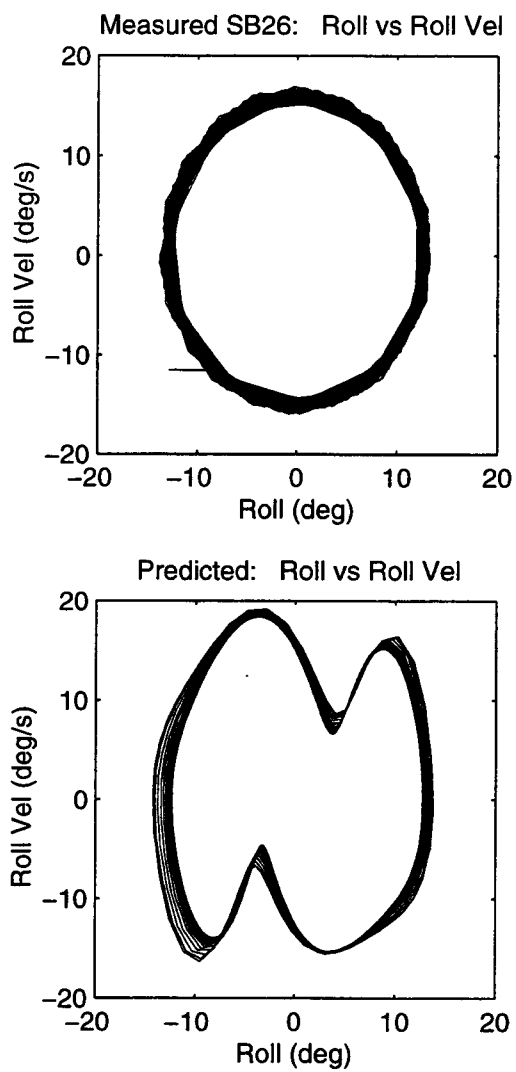


Figure 4.5

Phase Plane for Roll and Roll Velocity, $H=6$ ft, $T=5$ s

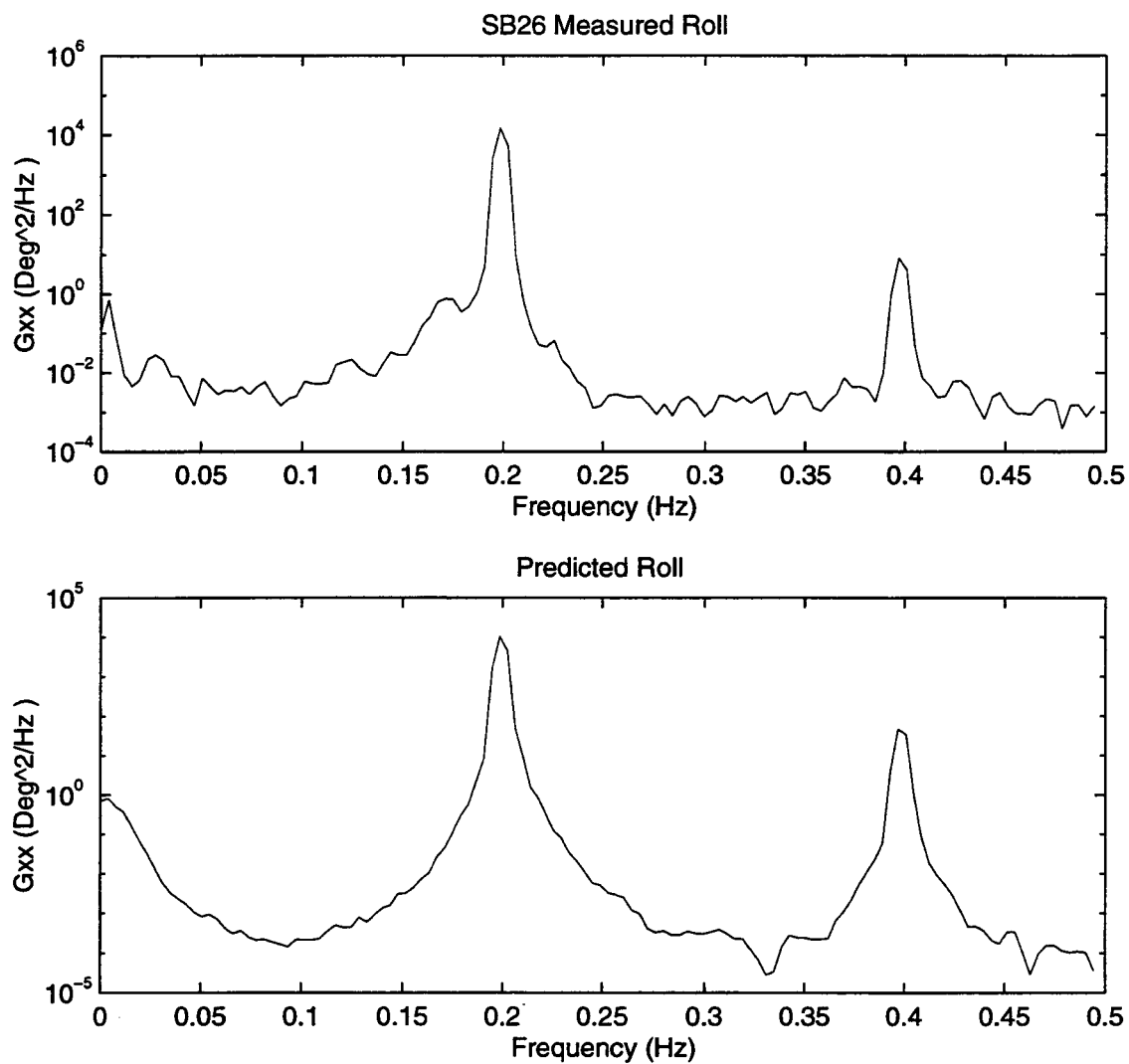


Figure 4.6

Roll Spectral Densities, $H=6$ ft, $T=5$ s (semilog)

Figure 4.7. The percent of critical damping in roll is still high at 25% but the heave is more reasonable at 10% (Table 4.4). Phase plots of the roll versus heave, roll versus wave and heave versus wave compare favorable (Figures 4.8 - 4.10). The phase diagram for roll in the predicted has a slight nonlinearity not obvious in the measured (Figure 4.11). Spectral density for both measured and predicted roll are similar with energy occurring at subharmonic frequencies (Figure 4.12). Additional figures of response are available in Appendix B for further information.

4.2.3 Test SB30, Regular Waves, H=6 ft, T=10 s

This measured case is one of the unique cases that demonstrate a superharmonic response in roll. For the predicted responses in roll, heave and sway to match the measured response, the roll damping was dropped down to 2.5% of critical while the heave was increased to 20% (Table 4.4). The sway damping remained low at 1.5%.

Time histories of the measured and predicted are shown together in Figure 4.13. The predicted roll contains the superharmonic response as the wave period is 10 seconds and the linear natural period in roll is near 5 seconds. A phase plot of the roll-sway response compares favorably as well (Figure 4.14). The measured heave-wave phase plot shows more of a "peanut" shape the prediction could not capture (Figure 4.15). The phase plane for roll also shows the presence of the superharmonic response (Figure 4.16). Distribution of energy versus frequency for roll is favorable as well as shown in Figure 4.17.

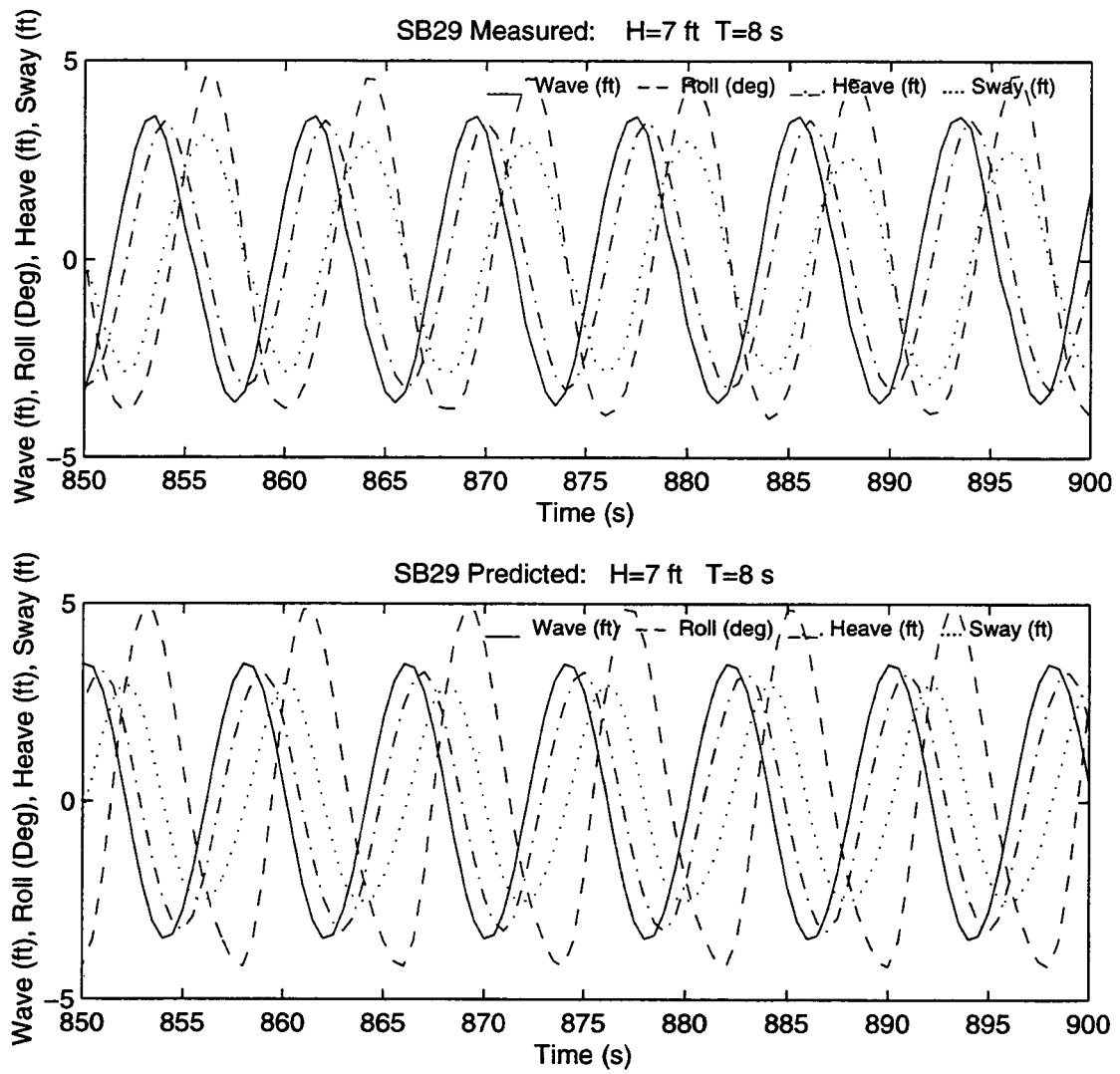


Figure 4.7

Measured and Predicted Response, H=7 ft, T=8 s

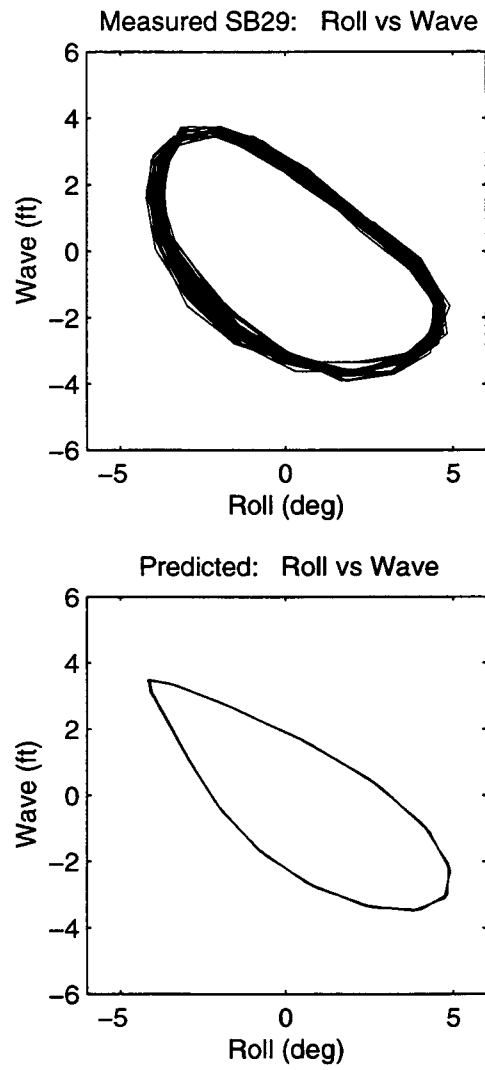


Figure 4.8

Roll vs Wave, $H=7$ ft, $T=8$ s

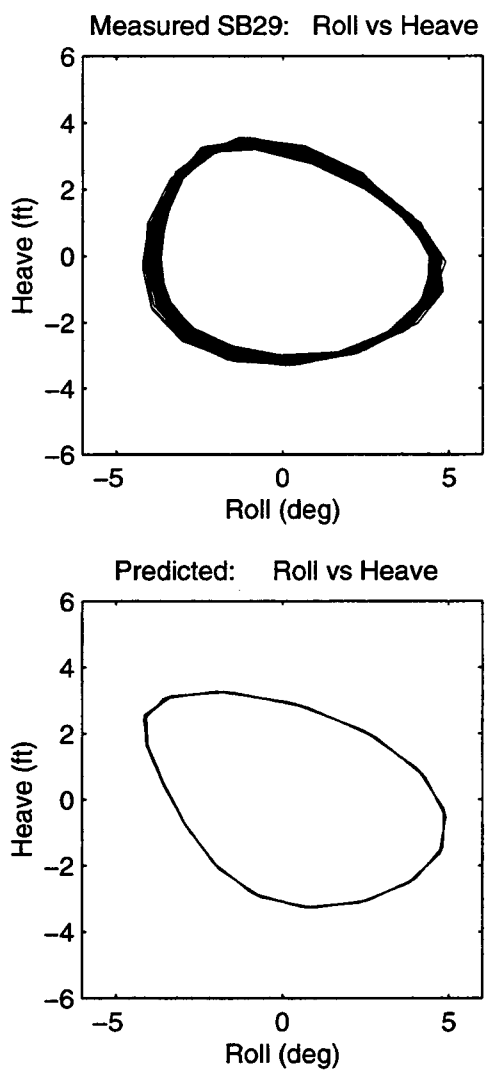


Figure 4.9

Roll vs Heave, $H=7$ ft, $T=8$ s

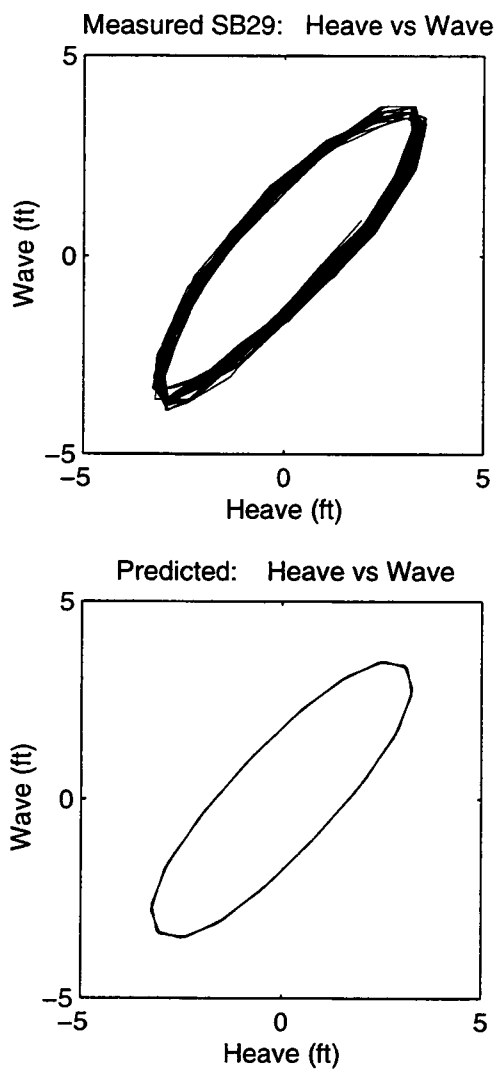


Figure 4.10

Heave vs Wave, $H=7$ ft, $T=8$ s

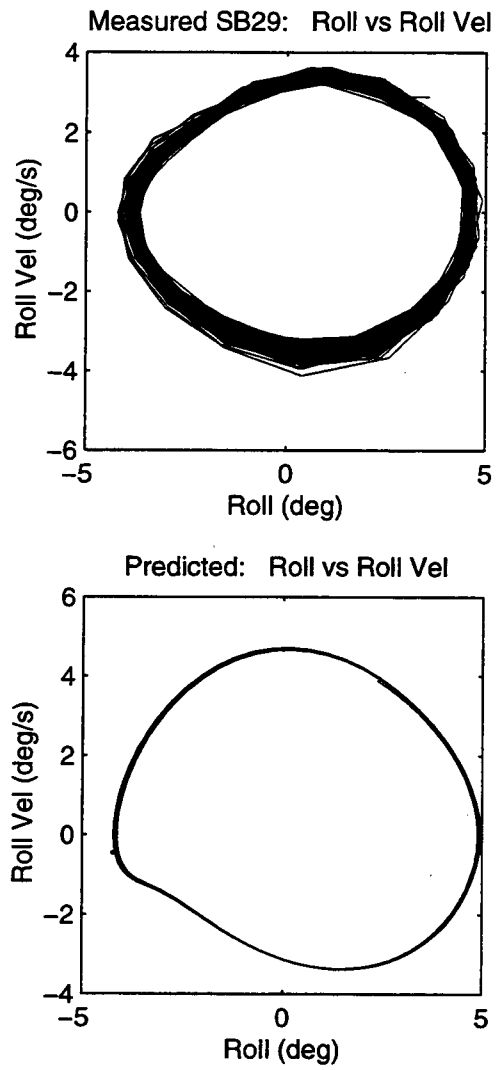


Figure 4.11

Phase Plane for Roll and Roll Velocity, $H=7$ ft, $T=8$ s

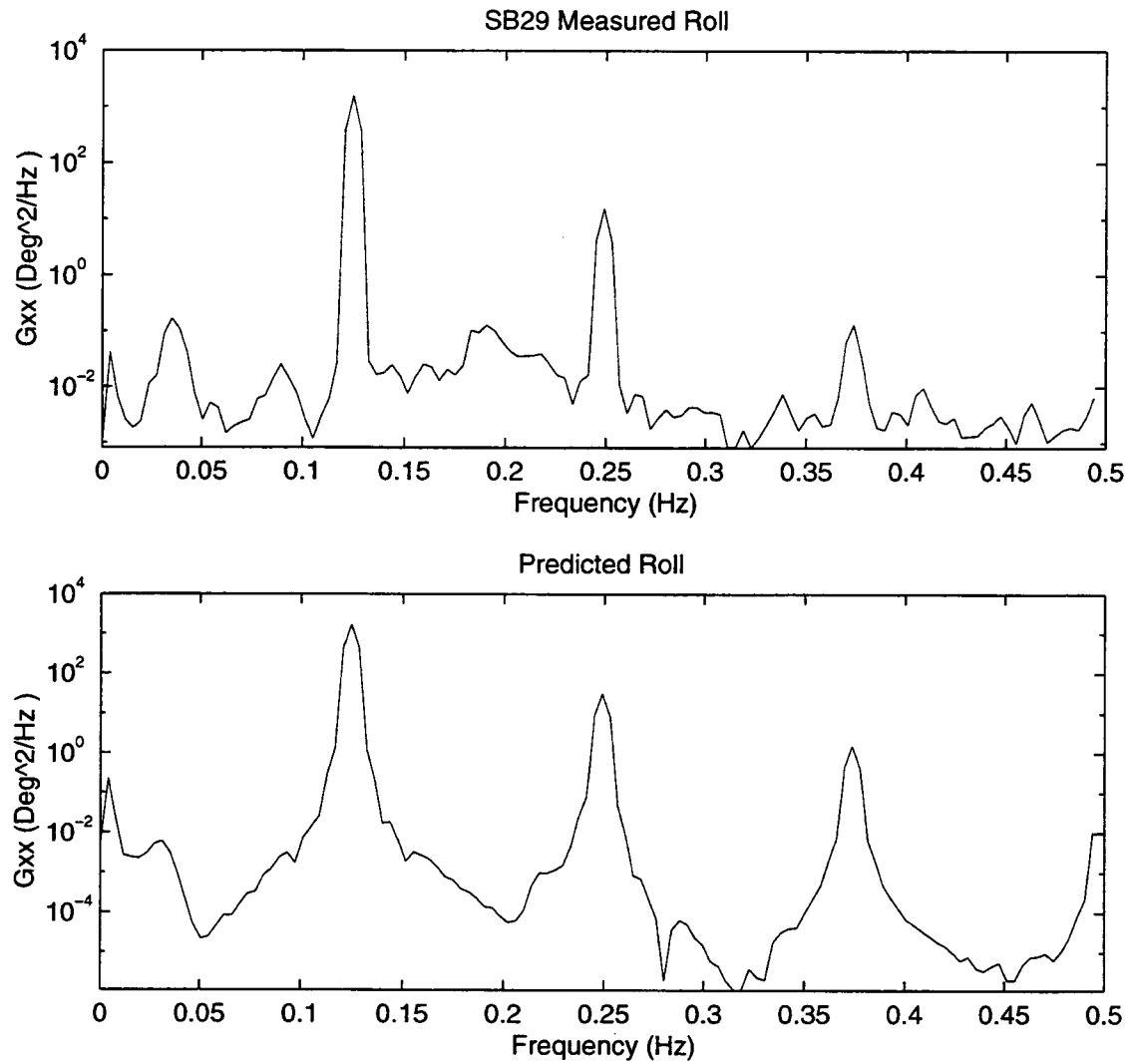


Figure 4.12 Roll Spectral Densities, H=7 ft, T=8 s (semilog)

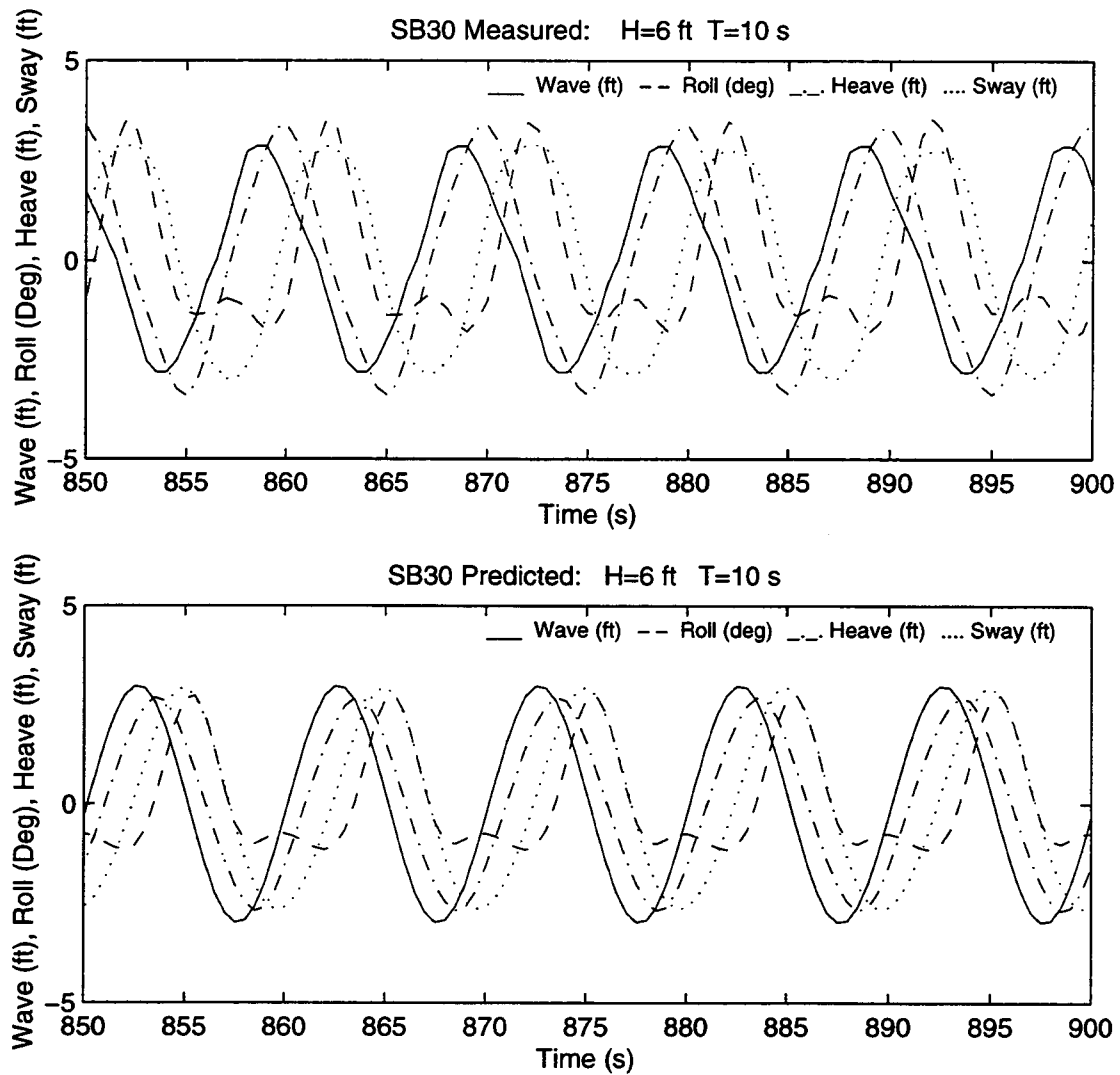


Figure 4.13

Measured and Predicted Response, H=6 ft, T=10 s

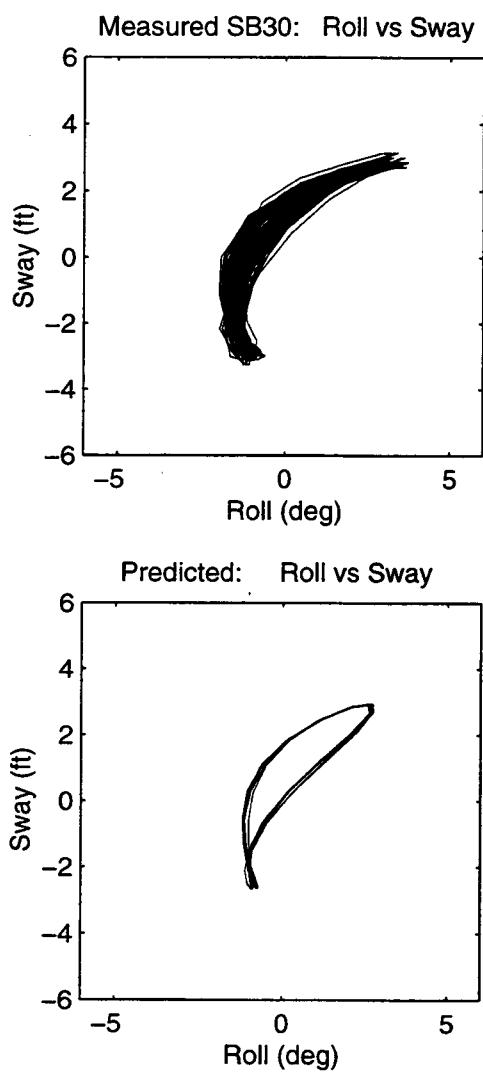


Figure 4.14

Roll vs Sway, $H=6$ ft, $T=10$ s

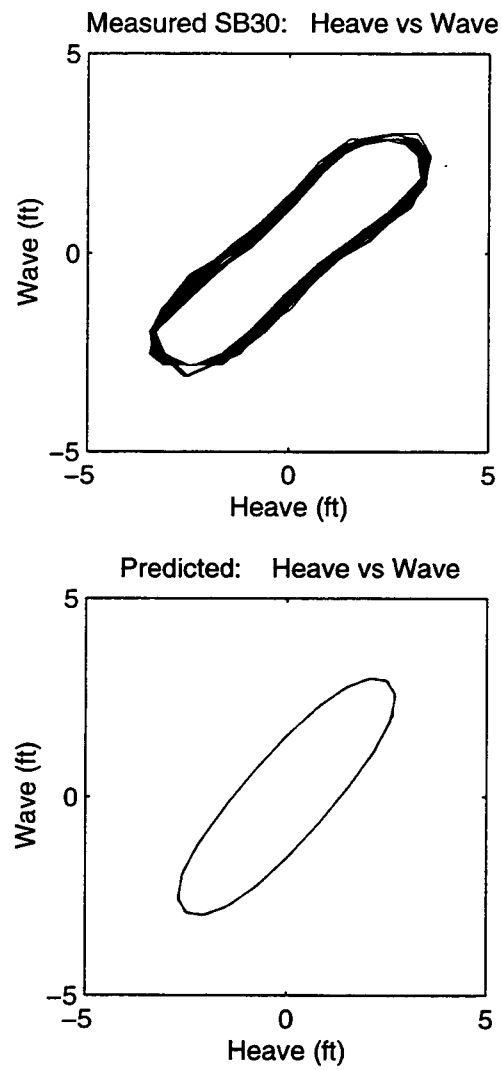


Figure 4.15

Heave vs Wave, $H=6$ ft, $T=10$ s

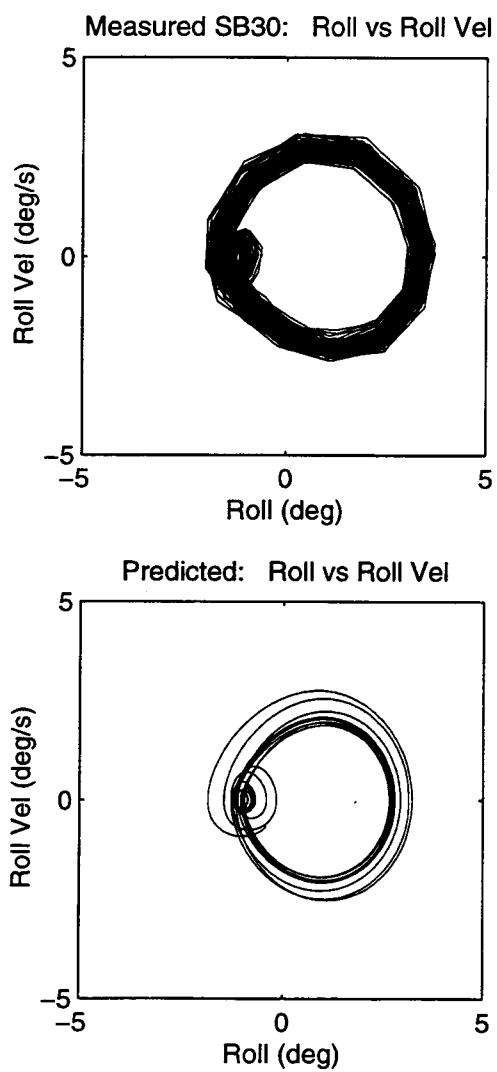


Figure 4.16

Phase Plane for Roll and Roll Velocity, $H=6$ ft, $T=10$ s

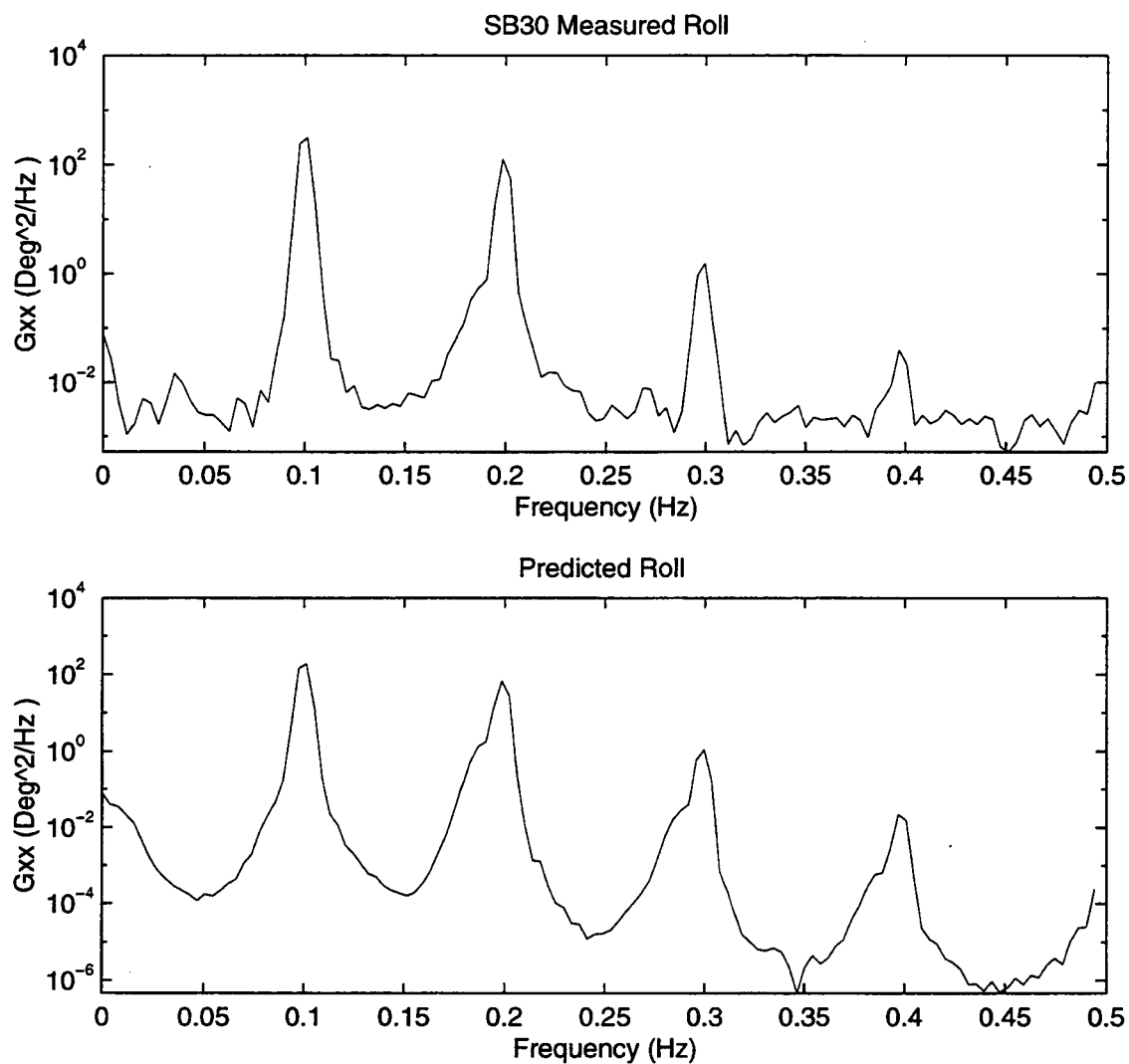


Figure 4.17

Roll Spectral Densities, $H=6$ ft, $T=10$ s (semilog)

In summary, the 3-DOF roll-heave-sway model was able to predict the measured response reasonably well for these three tests shown, however the extreme large and small values of damping in roll may not be physically correct. The main reason a higher damping is needed for the shorter period waves lies in the wave steepness. The primary form of excitation in this model is introduced as functions of wave height and slope (in stiffness terms), and time rates of change in wave slope for the damping and added inertia. For longer period waves, the barge tends to follow the waves. For case SB26, the wave period is near the natural period in roll and becomes almost resonant (assuming linearity). On the longer wave period case, the model appears to require a low damping to match the nonlinearity of the superharmonic excitation. The added mass and inertia were mostly set to match the natural periods from the damped free vibration tests (Table 4.3) and so were not altered much for this study.

4.3 Identification for Roll-Heave Model

Recognizing the benefit of simpler models, we examined how well a 2-DOF model of the barge in beam seas could predict the response compared to the 3-DOF model of the previous section. We chose the 2-DOF roll-heave model opposed to the roll-sway or heave-sway since the roll-heave would be the most natural extension from the SDOF model in roll. The reason is the hydrostatic restoring force would be more accurate taking into account the reserved buoyancy changes due to heave and roll as the barge moves in the wave. The influences of sway are of secondary nature for this symmetric barge in beam seas; especially if it is in a free floating condition. This may

not be the case for breaking waves where sway motions are crucial but that is beyond the present capabilities of this model.

For the 2-DOF roll and heave system, Equation 2.11 becomes,

$$\begin{aligned}
m\ddot{z} + m_{a_{33}} \cos\left(\frac{\partial\eta}{\partial y}\right)(\ddot{z}-\dot{w}) + m_{a_{22}} \sin\left(\left|\frac{\partial\eta}{\partial y}\right|\right)(\ddot{z}-\dot{w}) + C_{33_z}(\dot{z}-w) \\
+ C_{33_v}(\dot{z}-w)|\dot{z}-w| - m(z_g \cos\phi)\dot{\phi}^2 + mg \\
+ R_{33}\left(z, \phi, \eta, \frac{\partial\eta}{\partial y}\right) \cos\left(\frac{\partial\eta}{\partial y}\right) = 0
\end{aligned} \tag{4.4}$$

$$\begin{aligned}
I_{44}\ddot{\phi} + I_{a_{44}}\left(\ddot{\phi} - \frac{\partial\ddot{\eta}}{\partial y}\right) + C_{44_l}\left(\dot{\phi} - \frac{\partial\dot{\eta}}{\partial y}\right) + C_{44_n}\left(\dot{\phi} - \frac{\partial\dot{\eta}}{\partial y}\right)\left|\dot{\phi} - \frac{\partial\dot{\eta}}{\partial y}\right| \\
+ m(z_g \cos\phi)\dot{\phi}\dot{z} + R_{44}\left(\phi, z, \eta, \frac{\partial\eta}{\partial y}\right) \cos\left(\frac{\partial\eta}{\partial y}\right) \\
- mgz_g \sin\phi = 0
\end{aligned}$$

One may notice there remains an added mass term due to sway which we will keep at first. At first, this term was thought to be necessary for larger wave slope conditions to model the fluid-structure directional accelerations more accurately. It turns out the added mass in sway is found to be an order of magnitude lower than that of heave for this case and so this term is eventually dropped. The roll-heave stiffness terms of Equations 2.8-2.9 and the ocean wave properties are defined by Equations 2.13 and 2.14 are retained in Equation 4.4 above.

We have chosen the same measured wave and response cases used in the 3-DOF system coefficient identification study. The results for this case (similar to Table 4.4) are shown next in Table 4.5.

Table 4.5 System Parameters for 2-DOF Roll-Heave Model Regular Wave Cases

Parameter	SB26	SB29	SB30
M_{22} (slugs)	N/A	N/A	N/A
M_{a22} (slugs)	N/A	N/A	N/A
ζ_{L22}	N/A	N/A	N/A
ζ_{N22}	N/A	N/A	N/A
M_{33} (slugs)	2.325E04	2.325E04	2.325E04
M_{a33} (slugs)	7.6750E04	7.6750E04	7.6750E04
ζ_{L33}	0.025	0.15	0.05
ζ_{N33}	0.025	0.15	0.05
I_{44} (slugs-ft ²)	2.161046E6	2.161046E6	2.161046E6
I_{a44} (slugs-ft ²)	5.49232E05	5.49232E05	5.49232E05
ζ_{L44}	0.32	0.55	0.015
ζ_{N44}	0.32	0.55	0.010

4.3.1 Test SB26, Regular Waves, H=6 ft, T=5 s

As was the case for the roll-heave-sway model, the roll damping had to be increased for these steeper waves. However, now the damping is 32% of critical instead of 40%. The heave damping ratio increased to 2.5% from 1.5%. An added mass in heave of 7.7E04 slugs worked better than that used in the 3-DOF model of 1.0E05. The reason is in preserving the magnitude and phase for heave in this simpler model. Surprisingly, the results appear to be better for this model than that of the 3-DOF model (Figure 4.18). The heave versus wave response (Figure 4.19) is very agreeable. The

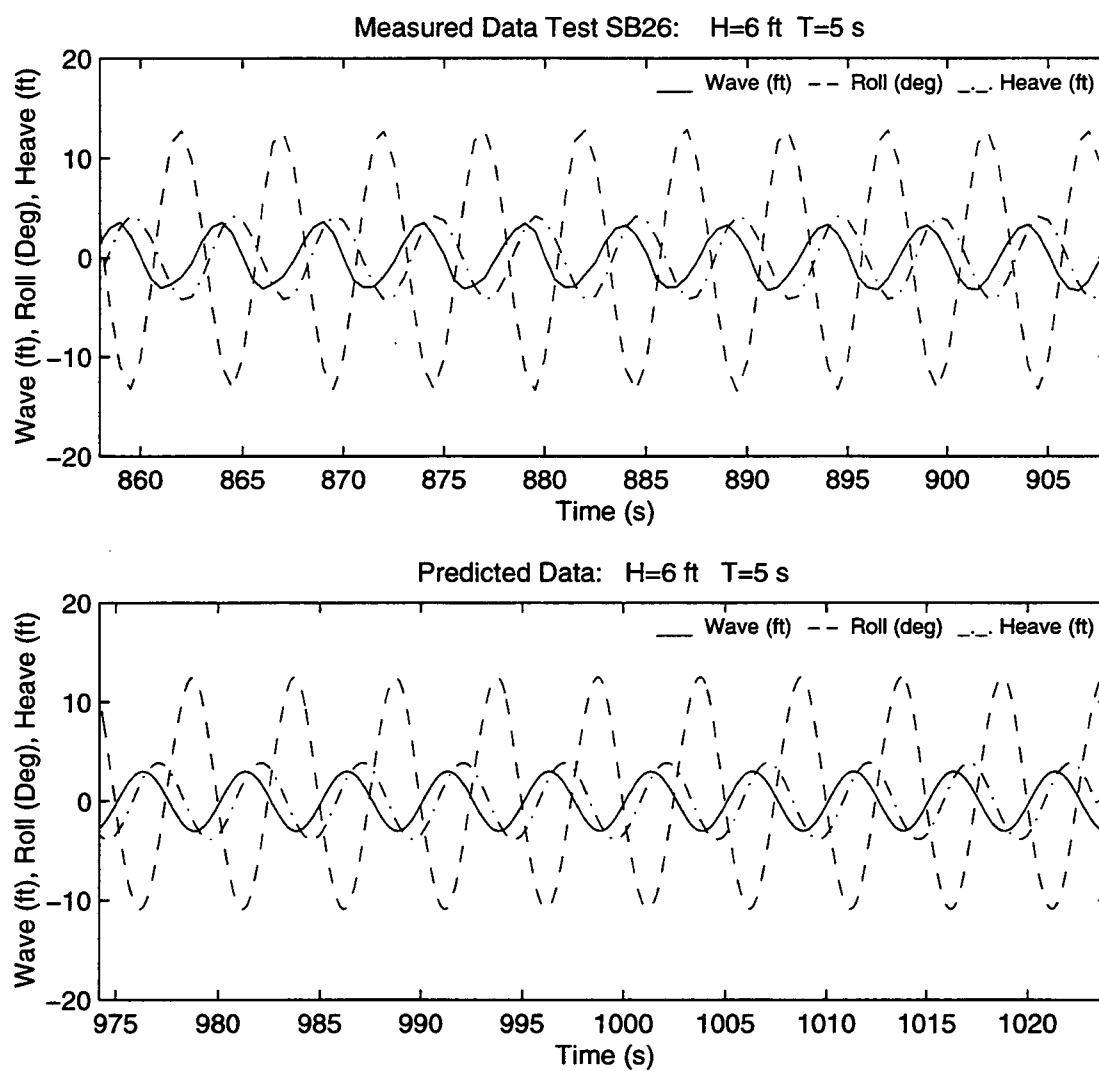


Figure 4.18

Measured and Predicted Response, H=6 ft, T=5 s

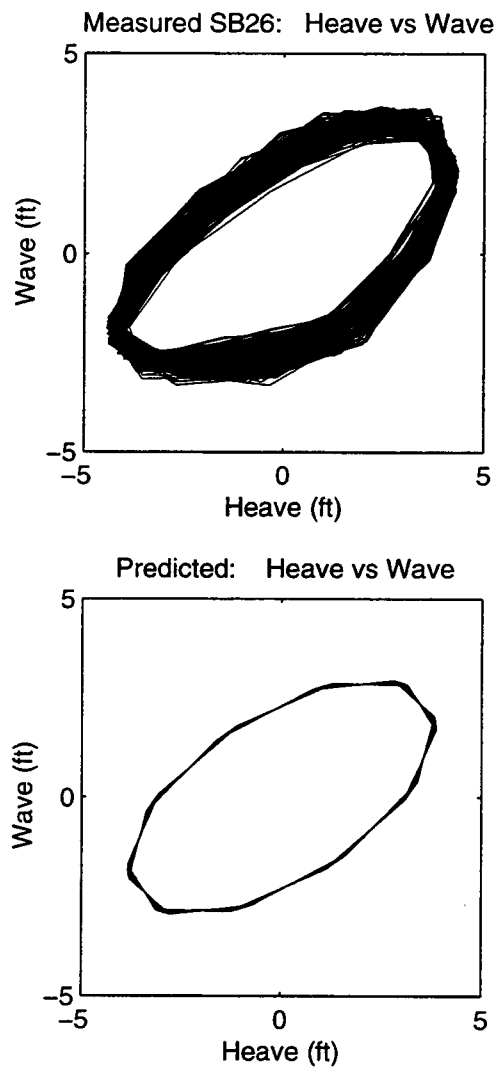


Figure 4.19

Heave vs Wave, $H=6$ ft, $T=5$ s

phase plane for roll is slightly more elliptical for the predicted response (Figure 4.20). One difference in the prediction may be due to slight nonlinearity in the measured wave profile not present in the simulated deterministic simple harmonic wave profile shown in Figure 4.21.

4.3.2 Test SB29, Regular Waves, H=7 ft, T=8 s

Time series for this test is shown in Figure 4.22 with favorable comparisons for roll and heave in both magnitude and phase. The damping ratios for roll and heave were increased to 15% and 55%, respectively (Table 4.5), which are unusually large, especially for roll. This barge has sharp edges along the keel which induce flow separation but intuition would suggest this contribution to be much less than 55% of critical. The reason probably lies in physical modeling inadequacies of this simple 2-DOF model with much of the approximation being account for in fewer "global" constant coefficients. Nevertheless, the response is predicted quite well for this case.

Predicted roll versus wave response compares well with measured data (Figure 4.23) though the measured phase is more like a "flattened oval" while the predicted is purely elliptical. One explanation for this discrepancy is in the uncertainty of the position of the measured wave relative to the barge in the wave tank. This presents some difficulties in the system identification process and possibly this information should be neglected as it may be unreliable. The relative motions between measured roll and heave and predicted roll and heave are, however, reliable and these compare well (Figure 4.24). The relative phase for the heave and the wave is also agreeable (Figure 4.25).

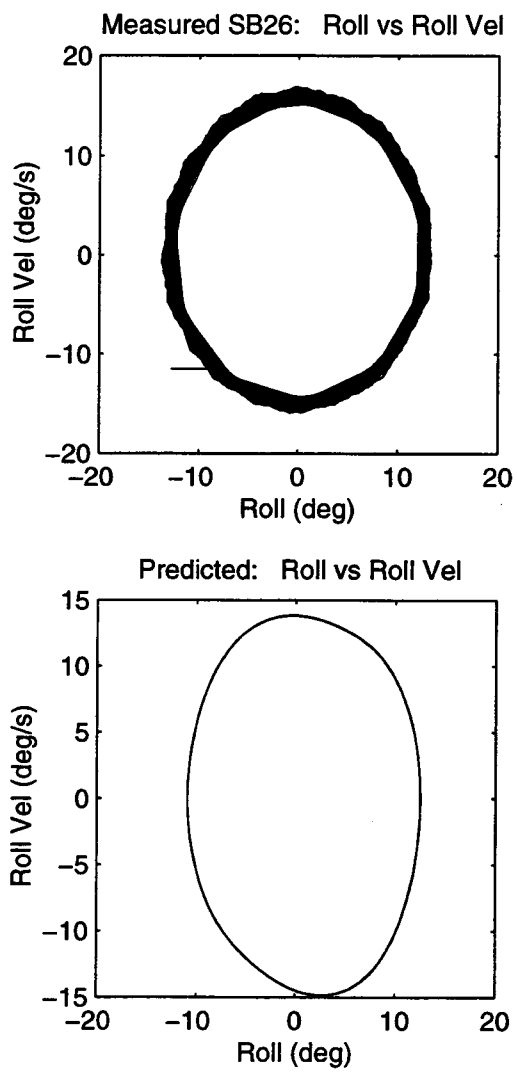


Figure 4.20

Phase Plane for Roll and Roll Velocity, $H=6$ ft, $T=5$ s

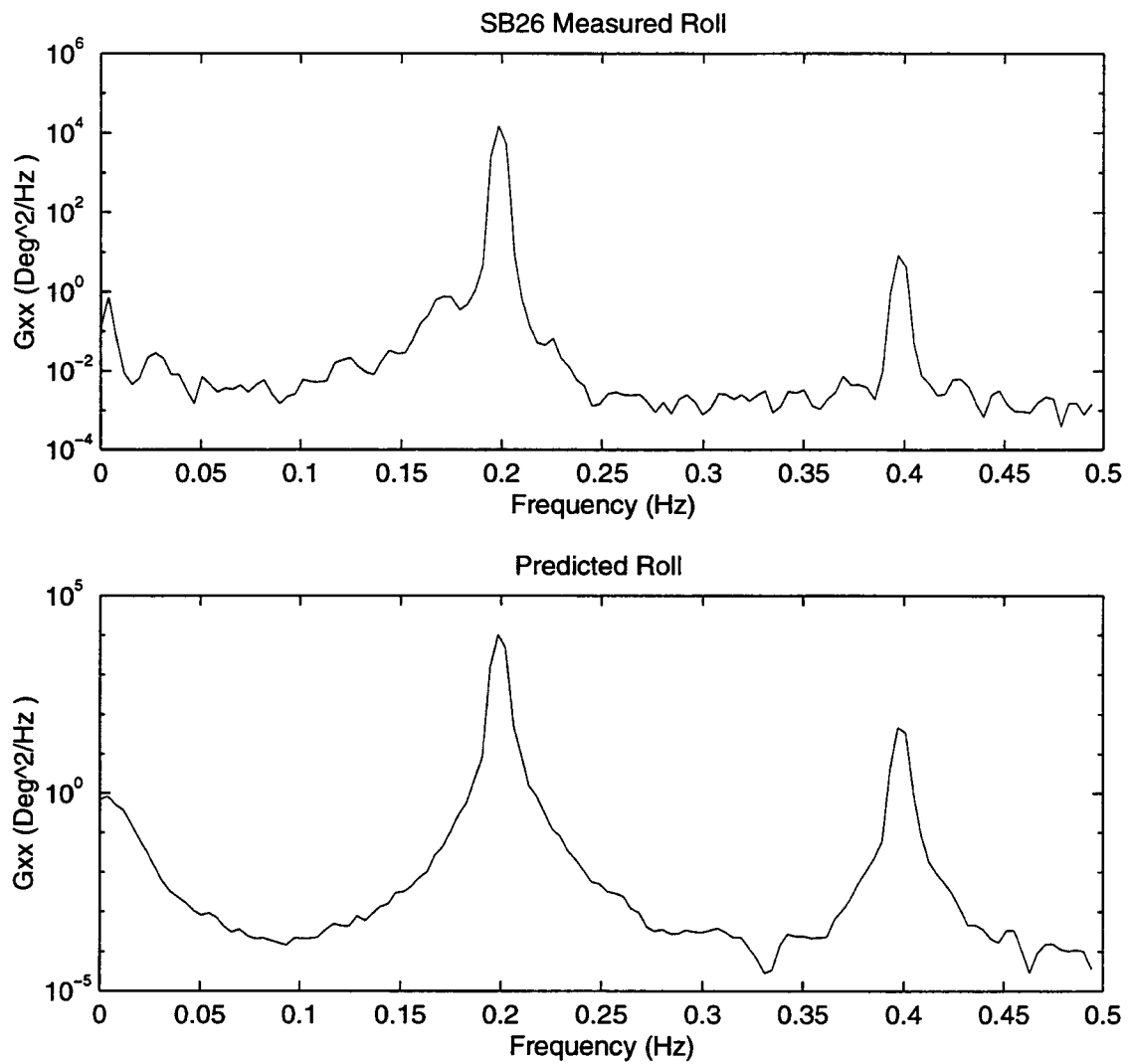


Figure 4.21 Roll Spectral Densities, H=6 ft, T=5 s

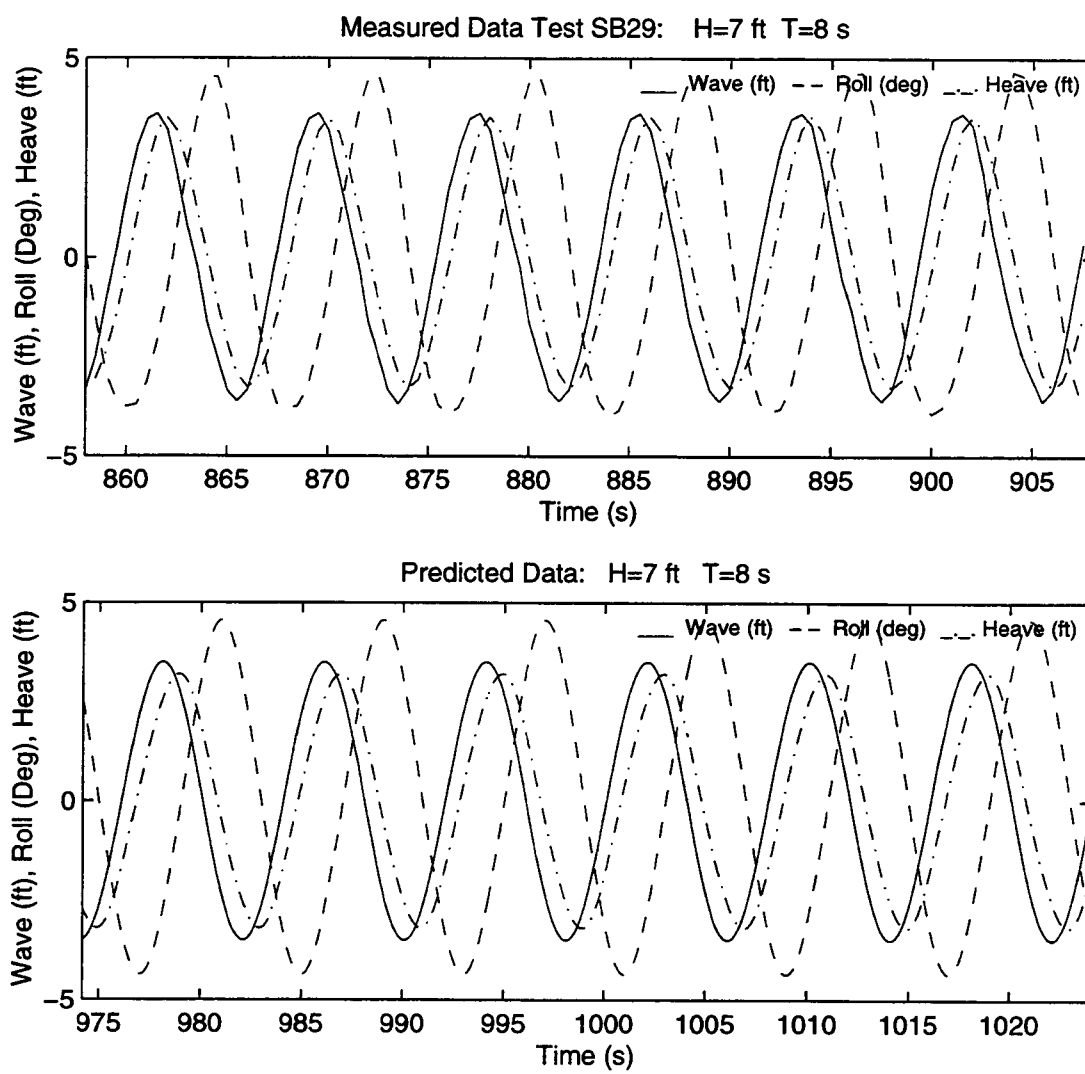


Figure 4.22

Measured and Predicted Response, H=7 ft, T=8 s

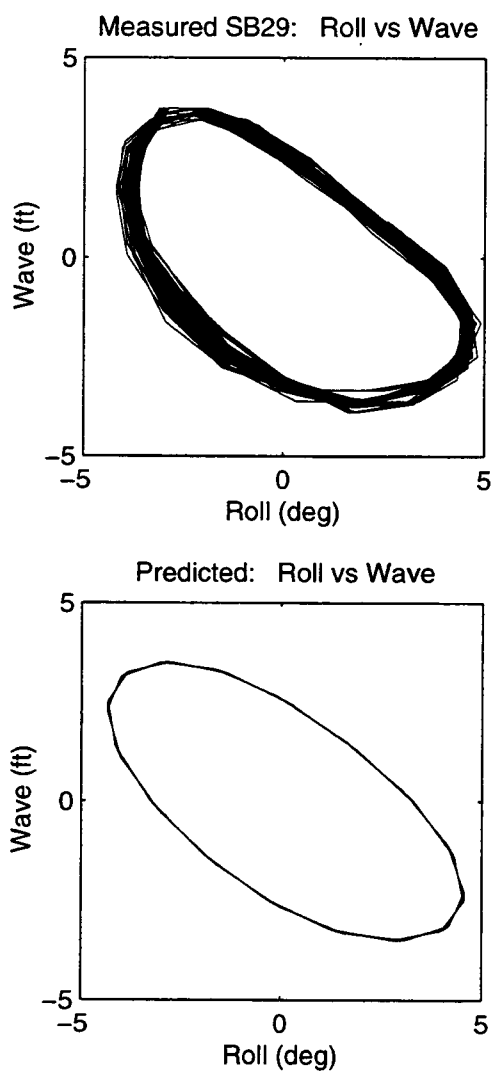


Figure 4.23

Roll vs Wave, $H=7$ ft, $T=8$ s

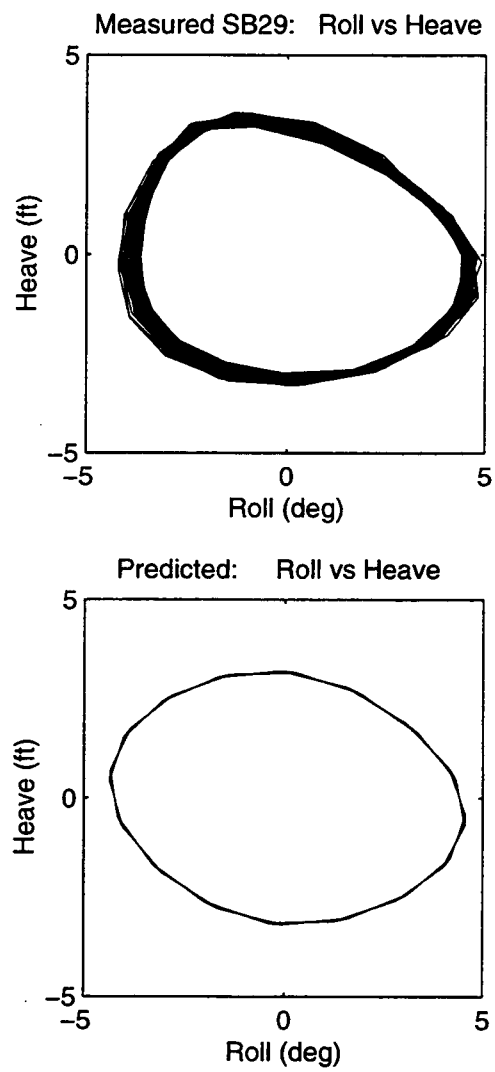


Figure 4.24

Roll vs Heave, $H=7$ ft, $T=8$ s

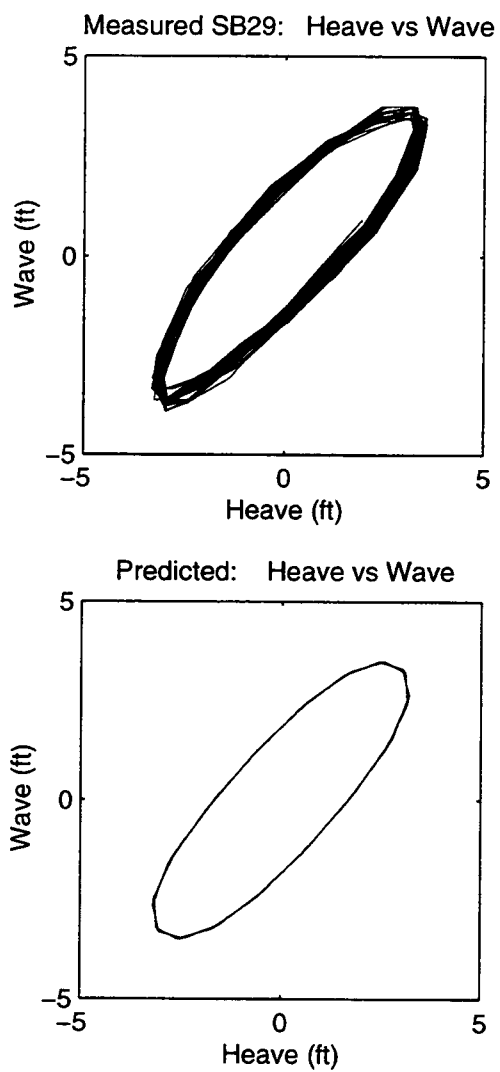


Figure 4.25

Wave vs Heave, $H=7$ ft, $T=8$ s

At this point, it is not clear whether this is coincidental or real. The phase plane for roll agrees reasonable well (Figure 4.26).

4.3.3 Test SB30, Regular Waves, H=6 ft, T=10 s

This is the case with the superharmonic response in measured roll. In this case we will show the full length of the time series (Figure 4.27) exhibiting both the measured and the predicted response side by side. (More data plots are presented in Appendix C for those interested in further details). Figure 4.27 measured and predicted roll have the apparent superharmonic roll response. The measured roll has an additional subharmonic response not present in the predicted but this, we believe, is attributed to the pure simple harmonic excitation we used which is void of any noise and nonlinearity present in the measured case. This effect is being studied under parallel investigation in a separate research task.

The predicted and measured roll versus heave phase plots match very well (Figure 4.28). Superharmonic roll response is clearly visible in Figure 4.29. The measured roll has more randomness not present in the predicted for reasons just discussed. The auto-spectral density for the roll (semilog) clearly shows the superharmonics both in measured and predicted. This prediction appears to be better than that of the 3-DOF model.

In summary, the 2-DOF model appears to predict the overall response in roll and heave comparable to those of the 3-DOF model except that the damping must be appreciably higher.

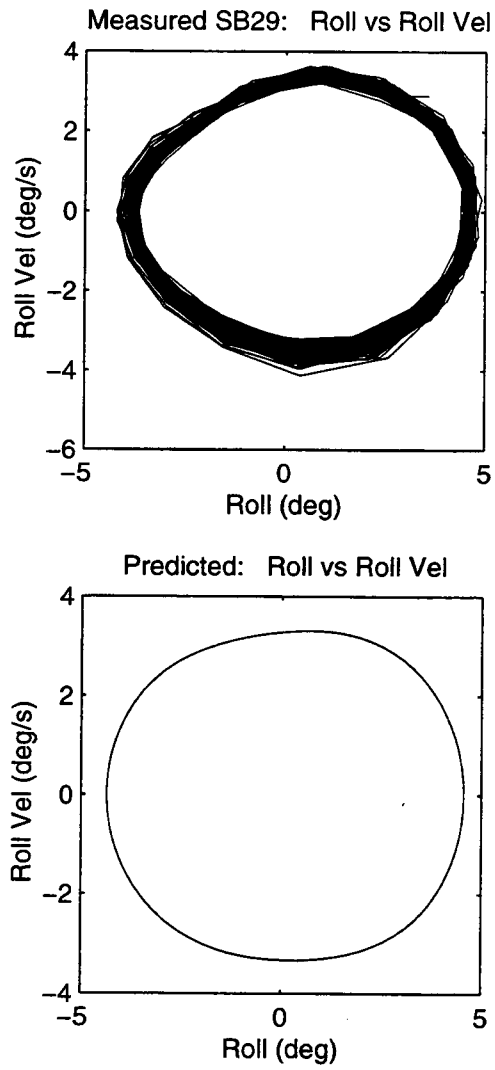


Figure 4.26

Phase Plane for Roll and Roll Velocity, $H=7$ ft, $T=8$ s

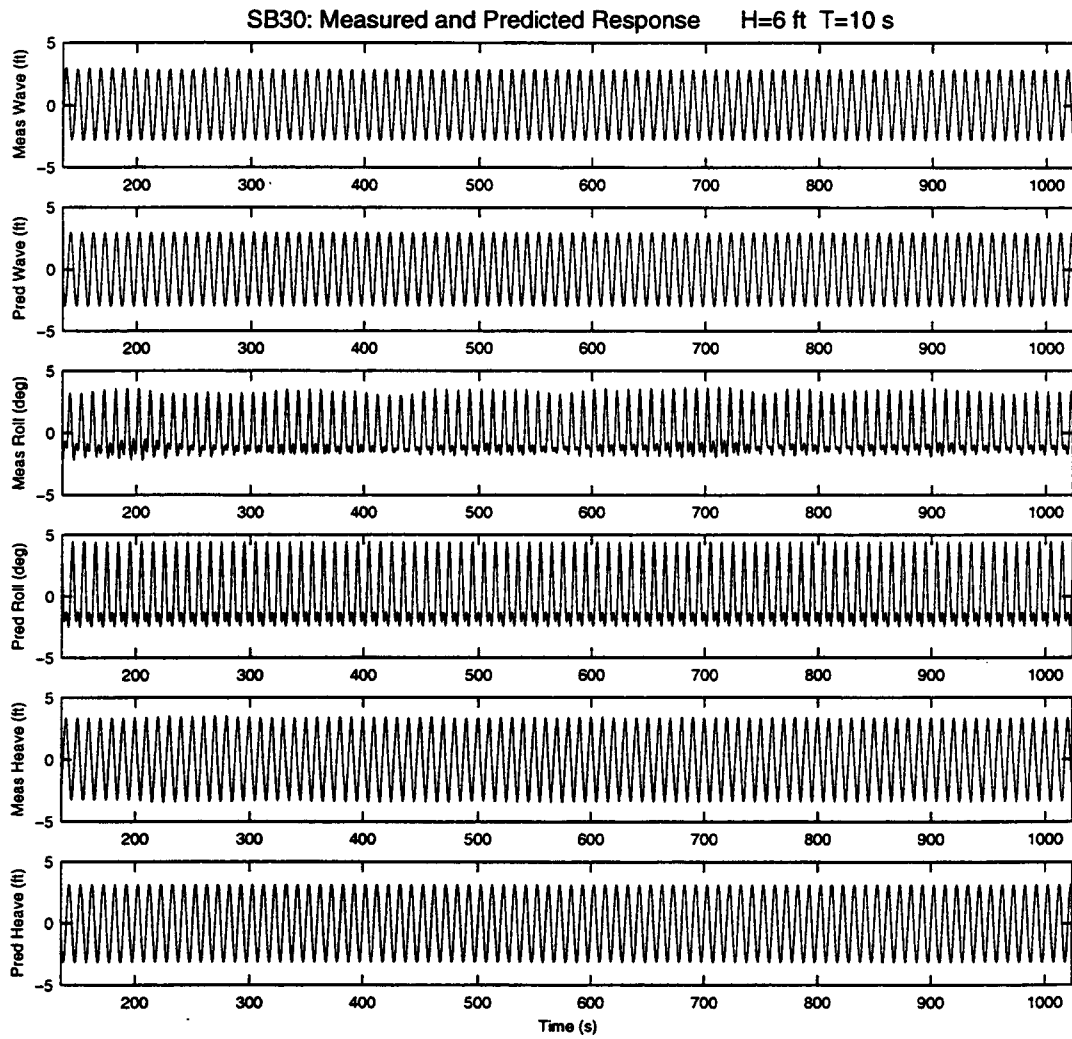


Figure 4.27

Measured and Predicted Response, $H=6$ ft, $T=10$ s

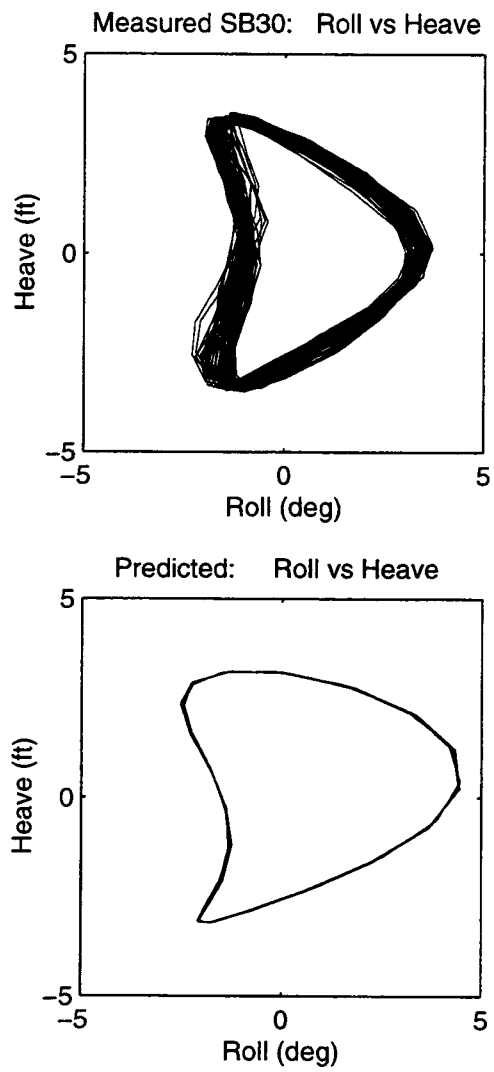


Figure 4.28

Roll vs Heave, $H=6$ ft, $T=10$ s

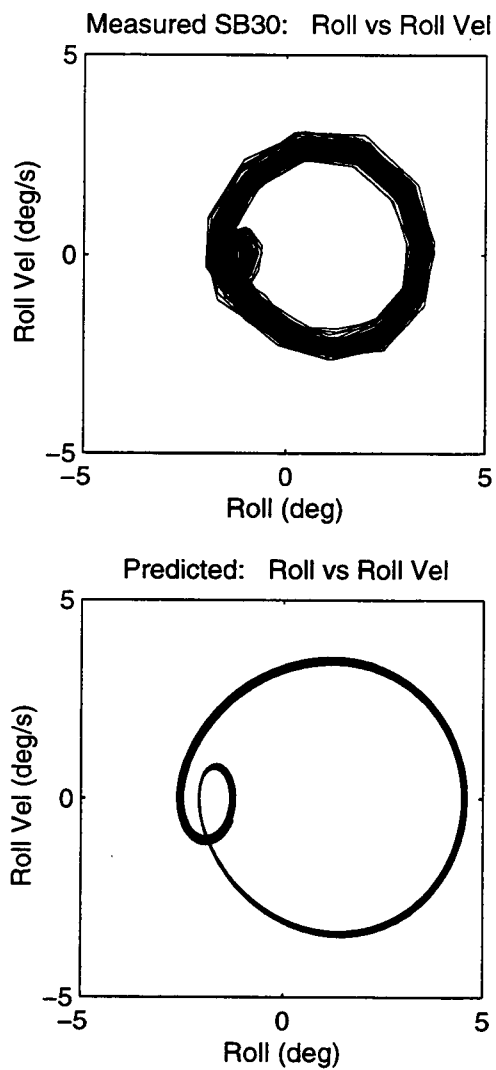


Figure 4.29

Phase Plane for Roll and Roll Velocity, $H=6$ ft, $T=10$ s

4.4 Summary of Results

Both models are able to predict these select measured response test cases by adjustment of the added mass, added inertia and damping coefficients. The values of these coefficients are however higher than expected with damping ratios as low as 1.5% or as high as 55% of critical. But with these coefficients, the models seem to be fairly accurate at predicting the given measured response. We have not discussed uncertainty in accuracy of the measured data and this is definitely a consideration. For now, we are "assuming" this information is as close to the actual test results including effects due to scaling and measurement and data acquisition uncertainties. One obvious discrepancy we are not sure about is possible "switching" of wave staff channels #1 and #6 for Test SB26. The phase of the wave channel #6 relative to the response is questionable where Channel #1 is physically more reasonable. Channel #6 was used in all other cases as this is the wave gauge directly aside the barge in the wave flume (not accounting for first or second order sway drift).

Overall, it appears the roll-heave model provided comparable results with that of the 3-DOF model for this measured data set. It may however be that we found a "best" set of coefficients and, in fact, this is the next phase in this research task to provide a more detailed systematic parametric sensitivity study and ultimately produce a set of curves for the coefficients and identify regions of nonlinear response. Most interesting nonlinear responses were found in the course of this identification and these are presented in Section 7.0.

5. COMPARISON OF NUMERICAL PREDICTIONS WITH MEASURED DATA

Identification of the added mass, added inertia and damping coefficients were obtained in Section 4 for the case of regular wave excitation. Those tests provided values of coefficients for different wave frequencies. Potential theory shows the added mass and damping vary with frequency and we found values to yield a "best fit" (statistically and visually) by time domain simulation of the equations of motion.

We now turn our attention to the case of comparing model predictions with waves more representative of nature. The measured random waves were generated to follow a distribution of energy with frequency following that of a Bretschneider spectrum (see Equation 2.16) and with a free surface that is normally (Gaussian) distributed. This model of ocean waves is one of several models available for a fully developed sea state. It assumes the spectrum to be narrow-banded and the wave heights to be Rayleigh distributed (Chakrabarti, 1994). Input to the Bretschneider model may be significant wave height and period.

Both the 3-DOF roll-heave-sway model and the 2-DOF roll-heave model will be compared with the measured response for these random waves. Unlike the system coefficient identification procedure of Section 4, the measured wave and associated wave properties (water particle kinematics) will be used for input into the models. Next, the waves will be generated by simulation of filtered white noise. The filtered white noise method is the method to be used in the Monte Carlo simulations to obtain the probability densities of response (Section 6).

5.1 Roll-Heave-Sway Model with Random Waves

5.1.1 Measured Input, $H_s=4.7$ ft, $T_p=8.2$ s

We used the measured random wave profile with a significant wave height of $H_s=4.669$ ft and peak period of $T_p=8.2$ s and numerically derived the wave properties for the model (Equation 3.5). The measured wave was filtered with a low pass tangent Butterworth filter (The Mathworks, 1993) to remove all high frequency waves above 0.25 Hz. The reason was to minimize the numerical error in obtaining derivatives and to adhere to the assumptions of the model that the wave slope is linear across the beam of the barge.

The equations of motion (2.12) were simulated in the time domain using a 4th order Runge-Kutta method (Press *et al*, 1986) with a time step of 0.1 s for 10,240 time steps per realization. The measured data was collected at 2.0 Hz (0.5 s) sample rate so we decimated the data to 0.5 Hz for spectral density comparisons but left it at 10 Hz for the time domain comparisons.

Initially we started with the coefficients obtained in Section 4.2.2 for the regular waves with 8 second period since this wave period is closest to the peak period of the measured wave spectrum. The before and after change in parameters are shown below in Table 5.1 where the SB29 column is for the regular wave at $H=6$ ft, $T=8$ s and the SB25 column is for the random waves, $H_s=4.7$ ft, $T_p=8.2$ s.

Table 5.1 System Parameters for 3-DOF Roll-Heave-Sway Model Random Wave Case Test SB25 with Measured Input

Parameter	SB29	SB25
M_{22} (slugs)	2.325E04	2.325E04
M_{a22} (slugs)	5E02	5E02
ζ_{L22}	0.005	0.02
ζ_{N22}	0.005	0.02
M_{33} (slugs)	2.325E04	2.325E04
M_{a33} (slugs)	1.0E05	1.0E05
ζ_{L33}	0.010	0.35
ζ_{N33}	0.010	0.35
I_{44} (slugs-ft ²)	2.161046E6	2.161046E6
I_{a44} (slugs-ft ²)	5.49232E05	5.49232E05
ζ_{L44}	0.25	0.05
ζ_{N44}	0.25	0.05

Observation of the damping ratios show the roll damping to be decreased while the heave and sway damping are increased. The mooring system used to restrain the barge in the wave flume was approximated by a linear spring in the sway direction. The stiffness for this spring was adjusted so the natural period in sway was much longer than the range of wave periods so it would not influence the first order response in roll and heave. We tested sway periods of 100 seconds, 50 seconds, 33 seconds and without a mooring noting the measured natural period in sway is 27.14 seconds (Table 4.2). The free floating condition caused numerical drift in sway sometimes on the order of tens of feet and sometimes tens of feet depending on the parameters and simulation duration.

For the free floating condition, the sway drift may be filtered leaving only the first order response. Since the physical model used in Test SB25 used a mooring, we modelled this with a linear mooring and then filtered the sway with a high pass filter at 0.05 Hz for comparison to the measured sway.

The time domain comparisons for the measured data and numerical predications (Figures 5.1 - 5.2) show fairly close agreement in roll but better agreement in heave. The low frequency drift in the sway motions are different because of uncertainty in the measured mooring stiffness.

Sample phase plots of the wave versus roll and heave versus wave (Figures 5.3 and 5.4) show reasonably good agreement. Additional phase plots are provided in Appendix D.

The phase plane of the roll and roll angular velocity are generally circular as seen in Figure 5.5. Note the predicted response contains additional nonlinearity due to an additional attractor at about -12 degrees. This attractor or equipotential "well" appears in detail in Section 7.0 as part of observed nonlinear behavior. It is not observed in the particular measured response. However, as discussed in Section 2.1.2 (and Appendix A, Figure A.17) on derivation of hydrostatic stiffness terms, there is a possibility of roll list (loll) angle. Barge model test results show that such a list is experienced.

Spectral densities for the wave, roll, heave and sway compare favorably between the measured and numerical prediction. The waves used in the numerical prediction show the removed energy above 0.25 Hz (Figures 5.6 - 5.9).

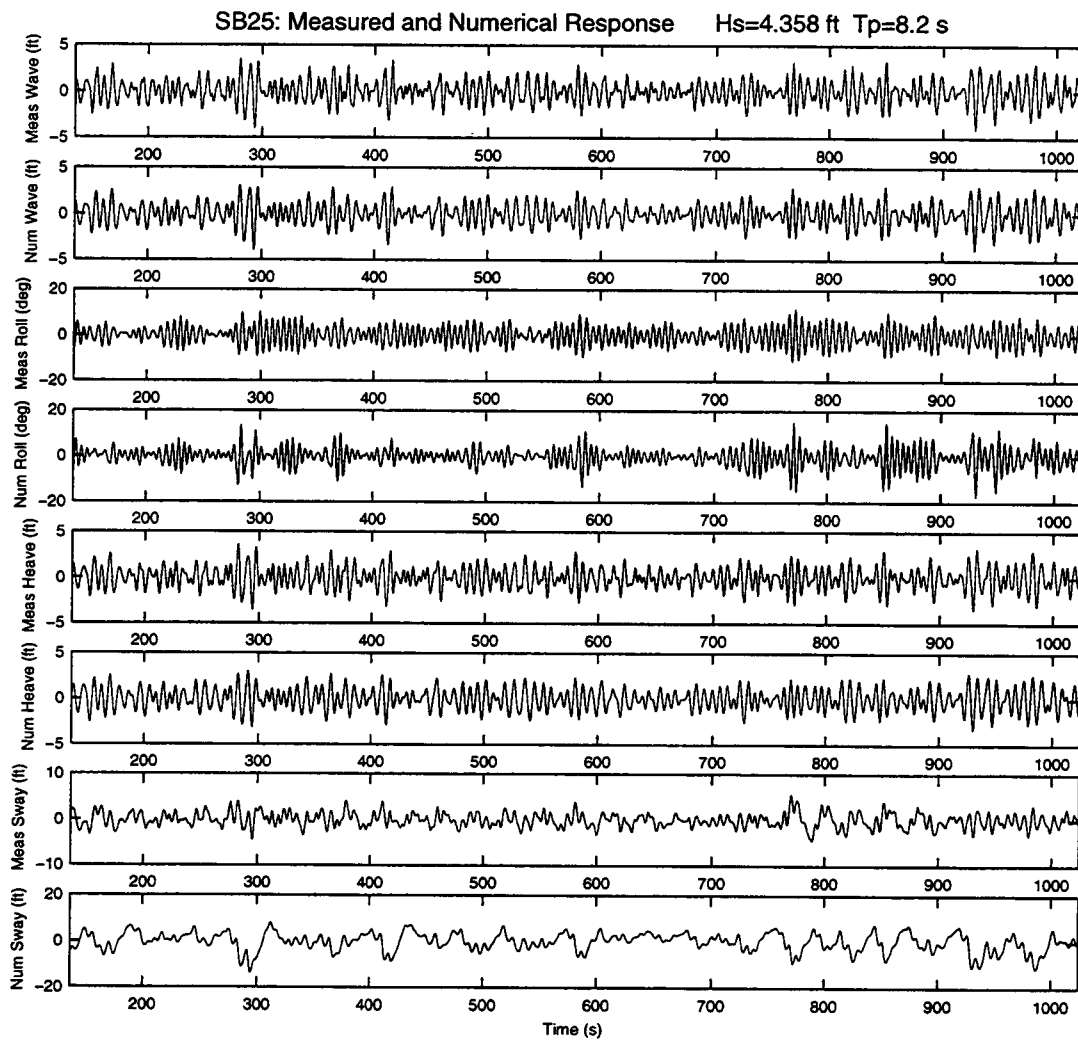


Figure 5.1

Measured and Predicted Response, Hs=4.7 ft, Tp=8.2 s

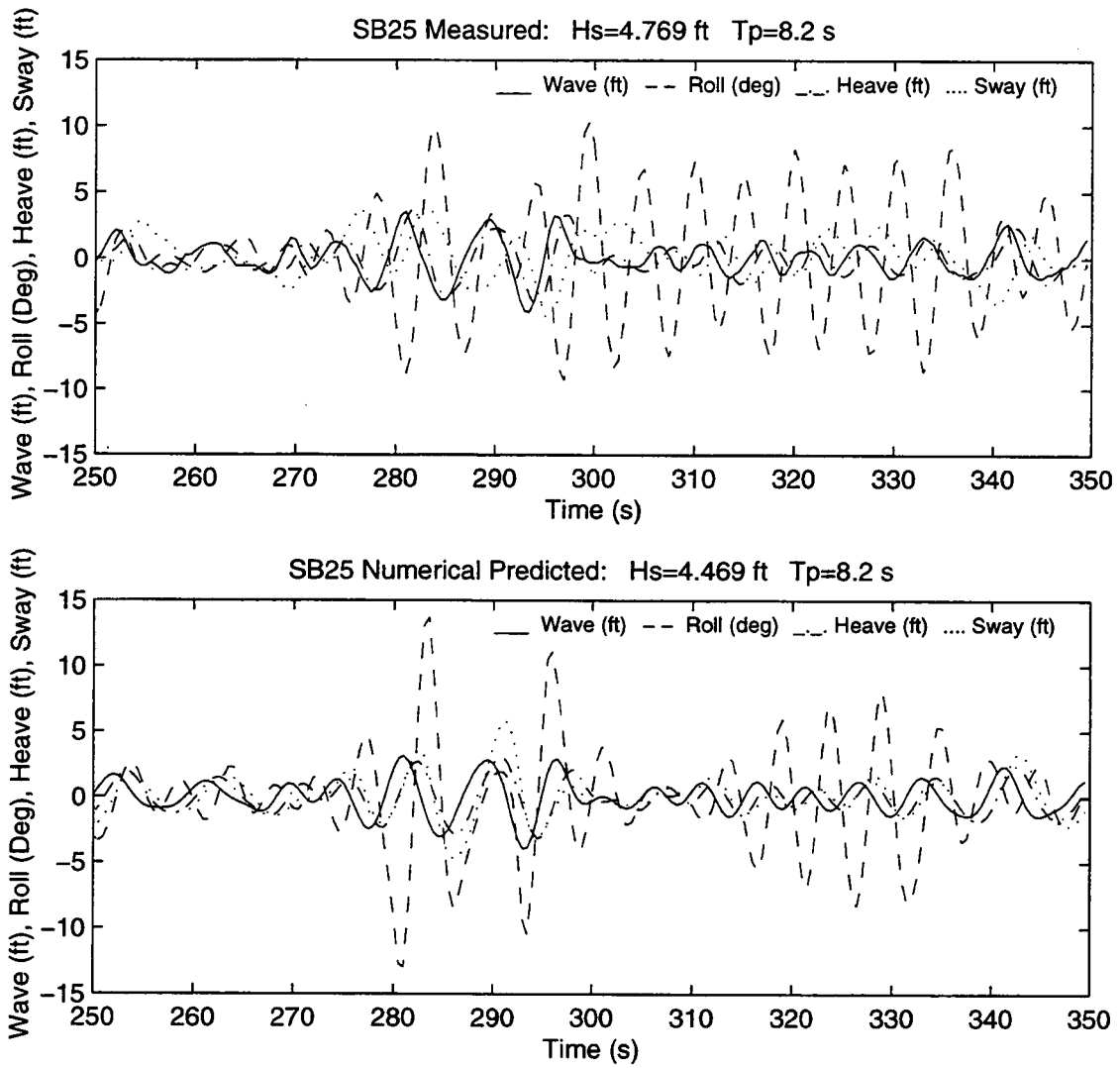


Figure 5.2

Measured and Predicted Response, Hs=4.7 ft, Tp=8.2 s

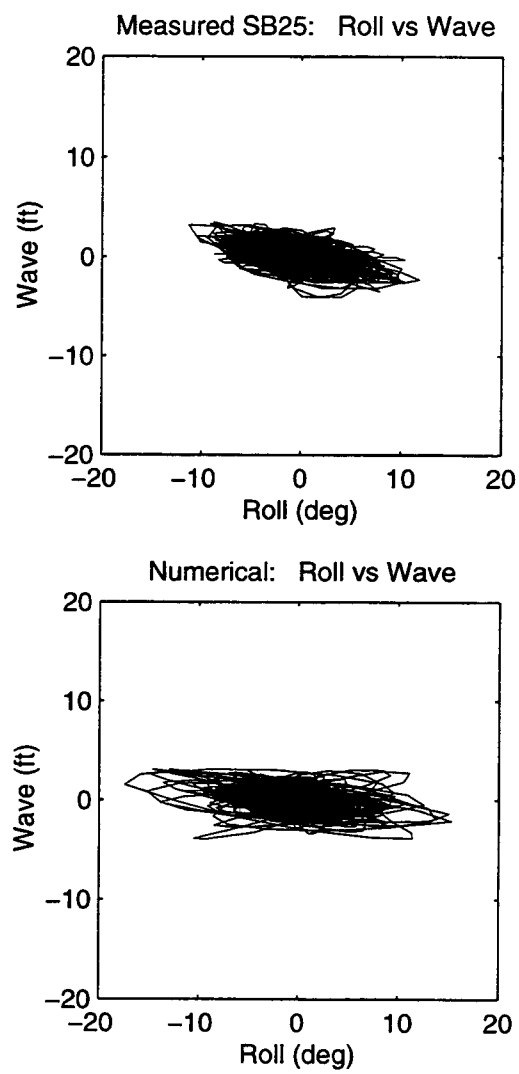


Figure 5.3

Roll vs Wave, $H_s=4.7$ ft, $T_p=8.2$ s

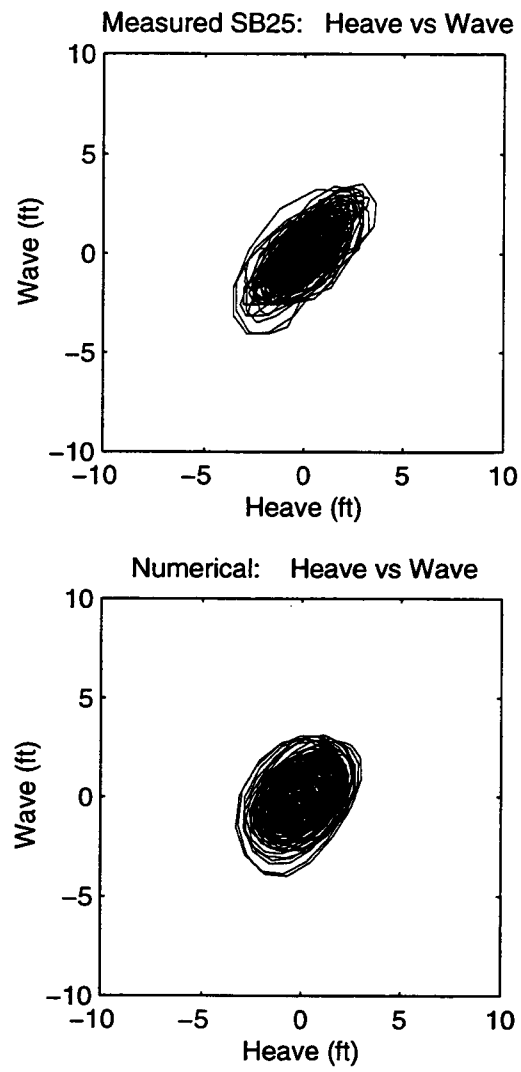


Figure 5.4

Heave vs Wave, $H_s=4.7$ ft, $T_p=8.2$ s

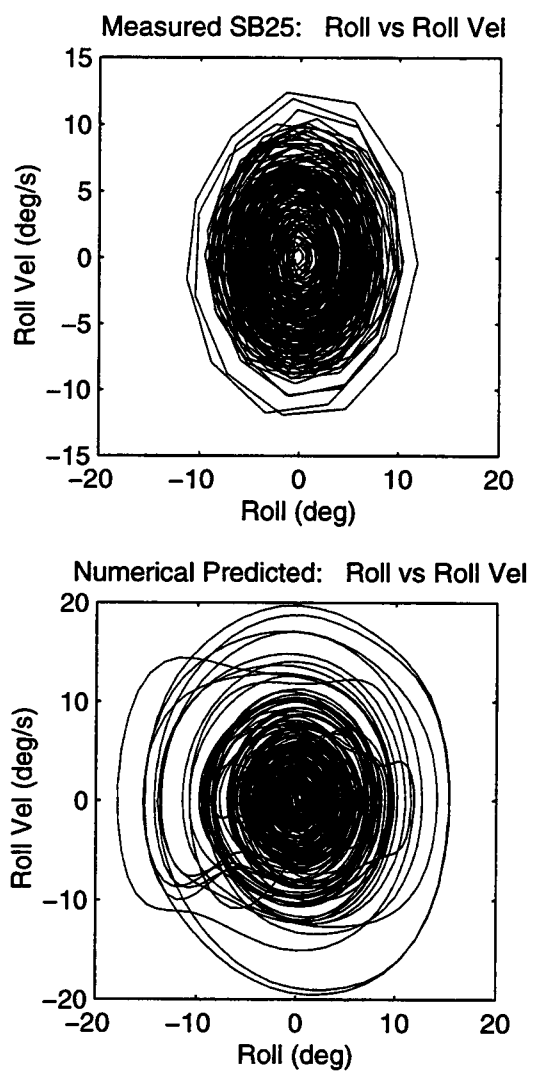


Figure 5.5

Phase Plane for Roll and Roll Velocity, $H_s=4.7$ ft, $T_p=8.2$ s

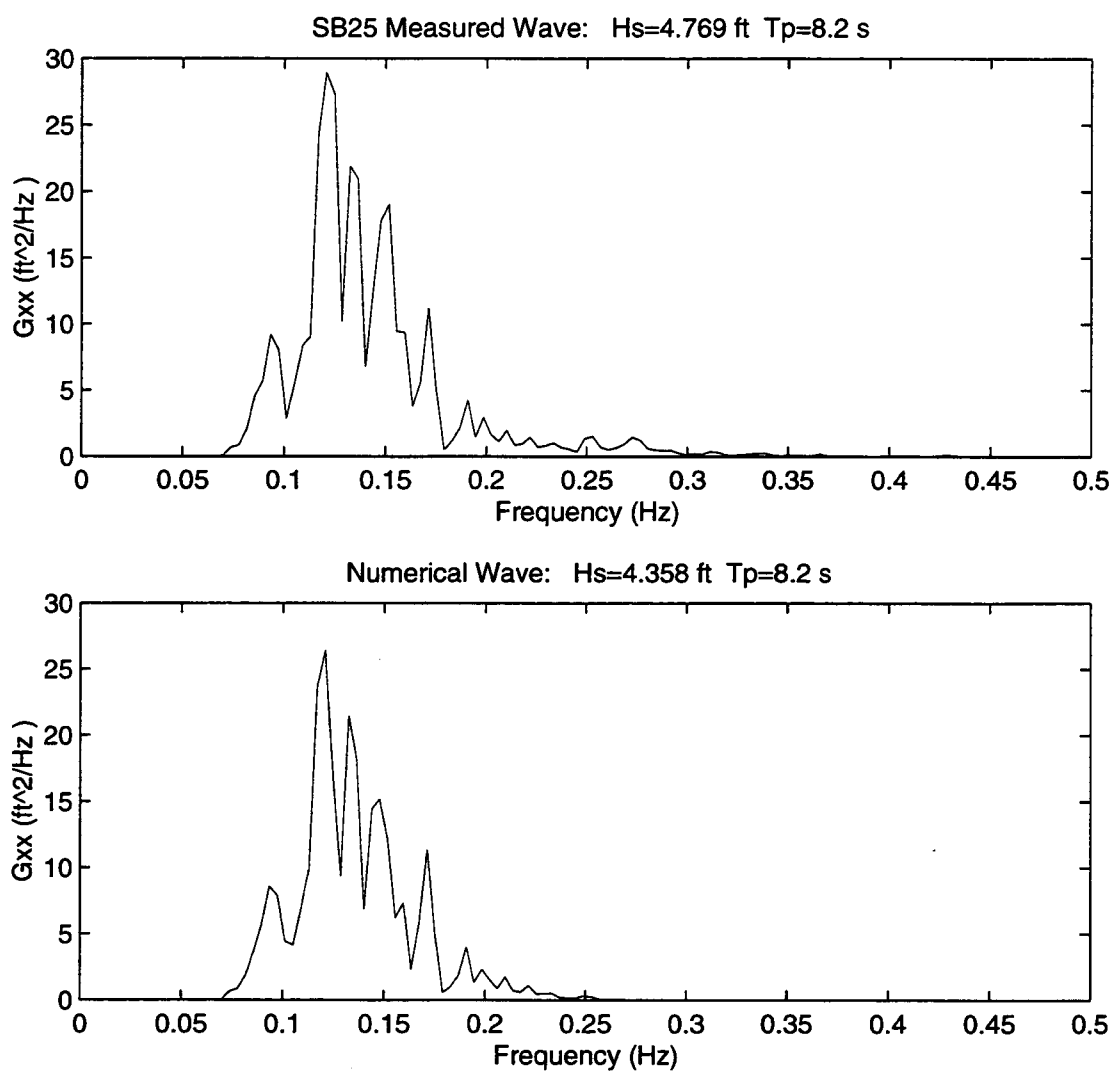


Figure 5.6

Wave Spectral Densities, $H_s=4.7$ ft, $T_p=8.2$ s

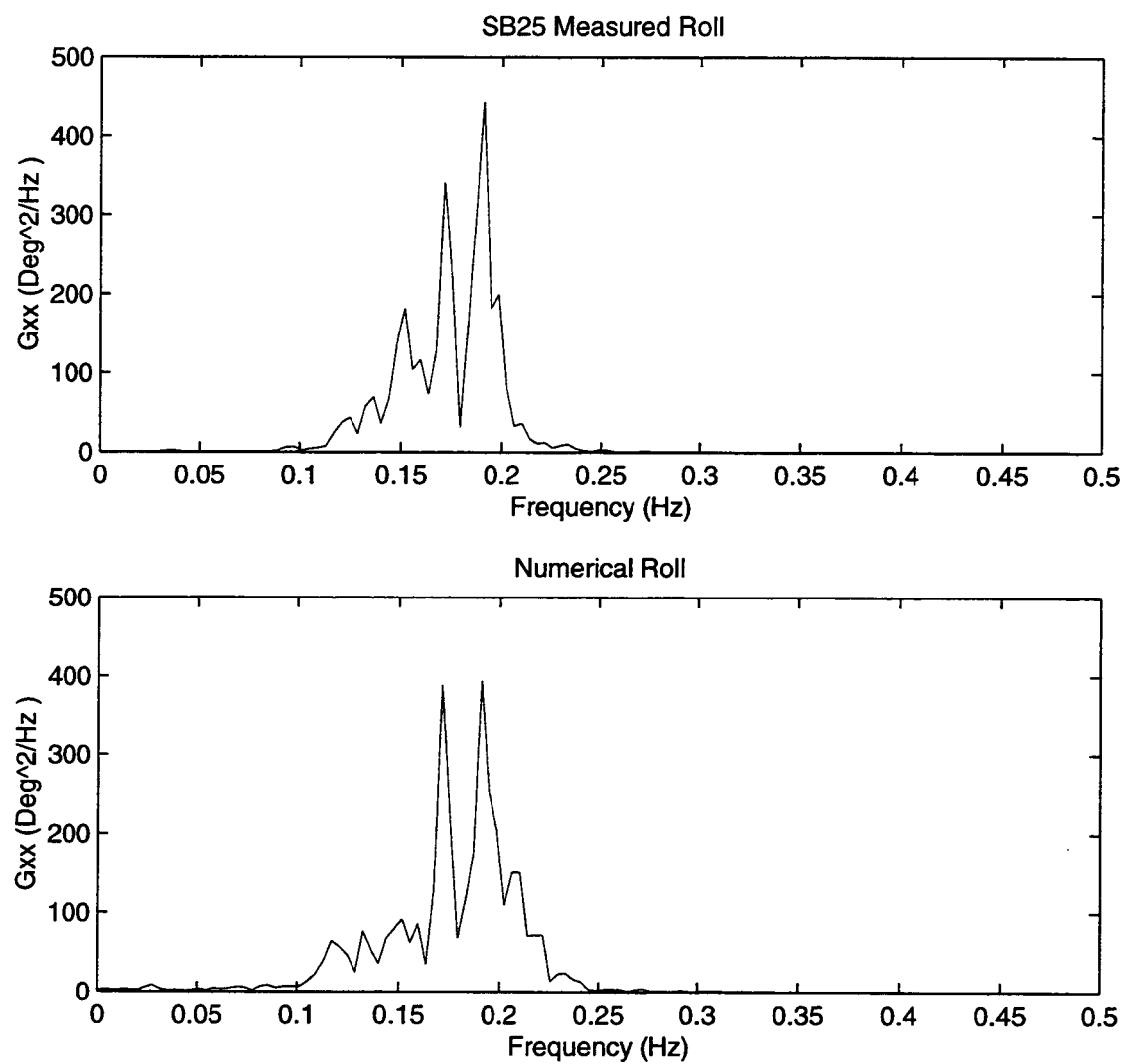


Figure 5.7

Roll Spectral Densities, $H_s=4.7$ ft, $T_p=8.2$ s

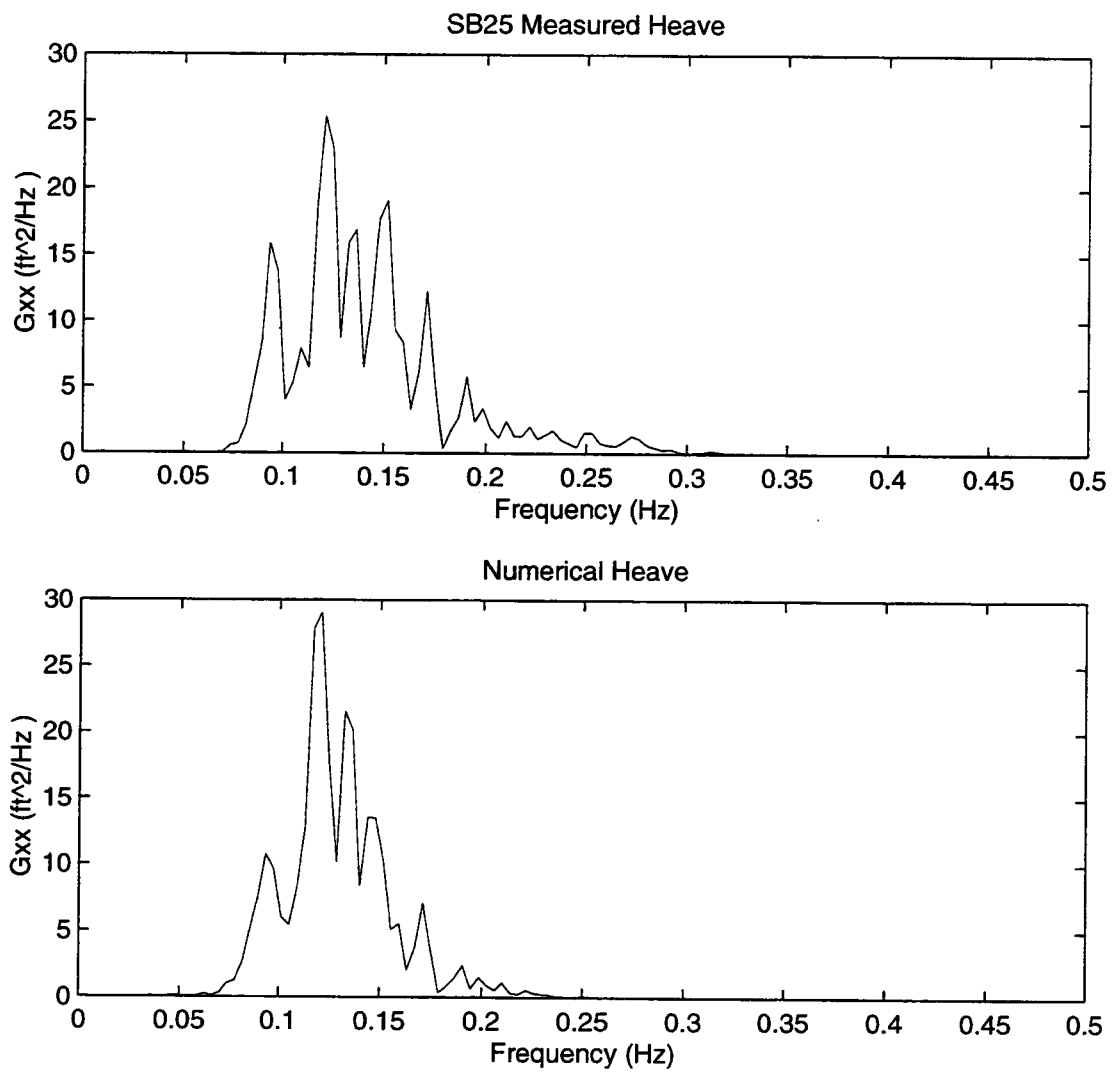


Figure 5.8 Heave Spectral Densities, $H_s=4.7$ ft, $T_p=8.2$ s

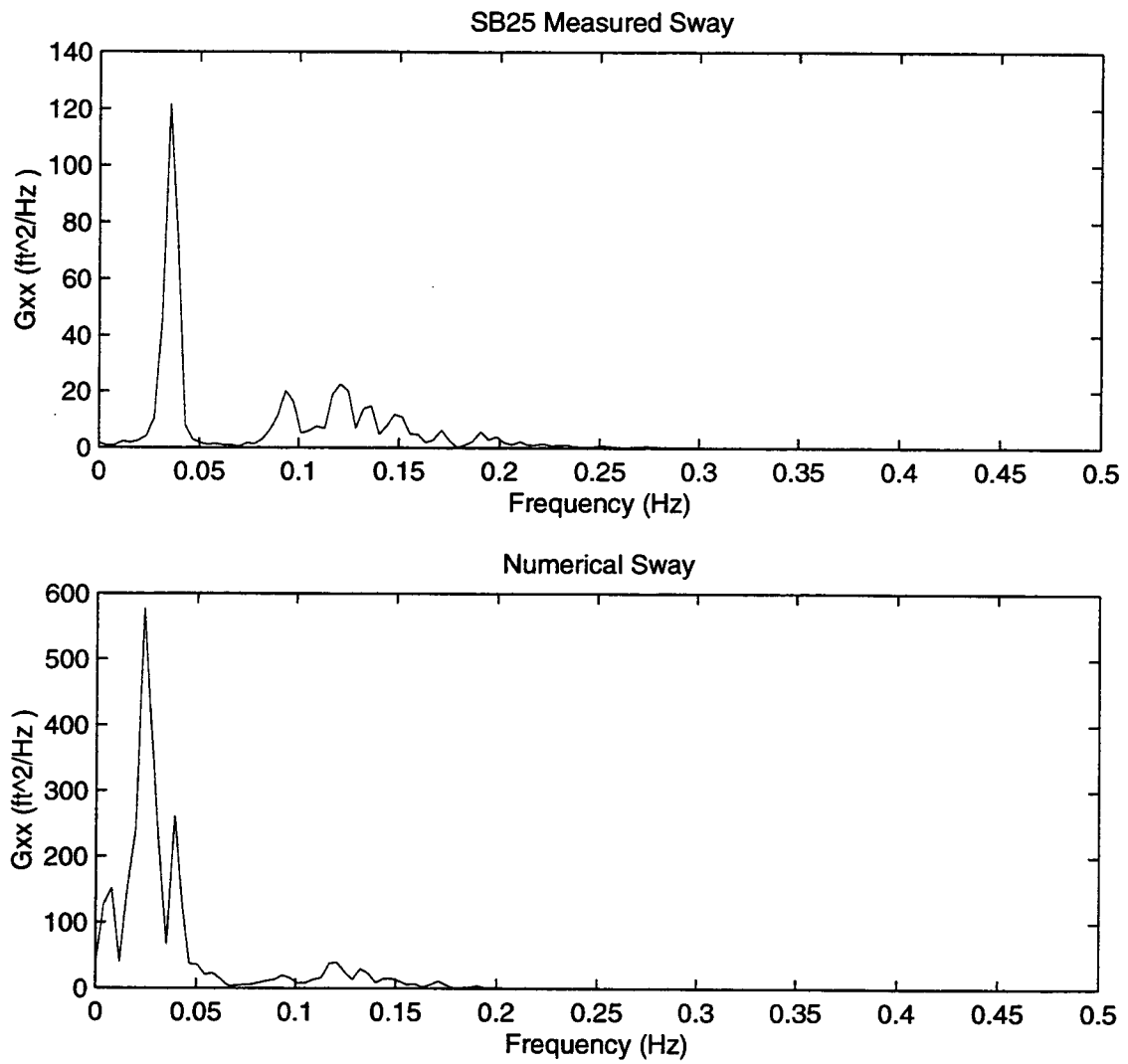


Figure 5.9 Sway Spectral Densities, $H_s=4.7$ ft, $T_p=8.2$ s

Distribution of waves and response are not as favorable (Figures 5.10 - 5.12) except for the heave. The numerical prediction of roll has more kurtosis than the measured roll. Maximum and minimum response is higher while the variance is lower. The sway distribution differs slightly with the prediction showing more skewness due to the second order drift response.

5.1.2 Filtered Noise Input, $H_s=4.7$ ft, $T_p=8.2$ s

A linear filter was used to generate Gaussian white noise for the wave profile and wave properties as input into the simulation model (Equations 2.19-2.21). Results of the coefficient adjustments from the regular waves to the random waves are shown in Table 5.2.

Observation of the damping ratios show the roll damping to be decreased while that of heave and sway increased. This differs from the measured input case in that the damping decreased for roll and heave.

Complete figures of these results are provided in Appendix D but some of the results will be presented here.

Time domain comparisons for the measured data and numerical predications (Figures 5.13 - 5.14) show close agreement in roll, heave and sway. Figure 5.14 shows the general nature of the roll and heave response to be similar to the measured which is pretty good considering the initial conditions are different for these nonlinear models. Interestingly, this comparison is better than that of the measured input (Figure 5.2) for the same time sequence presented.

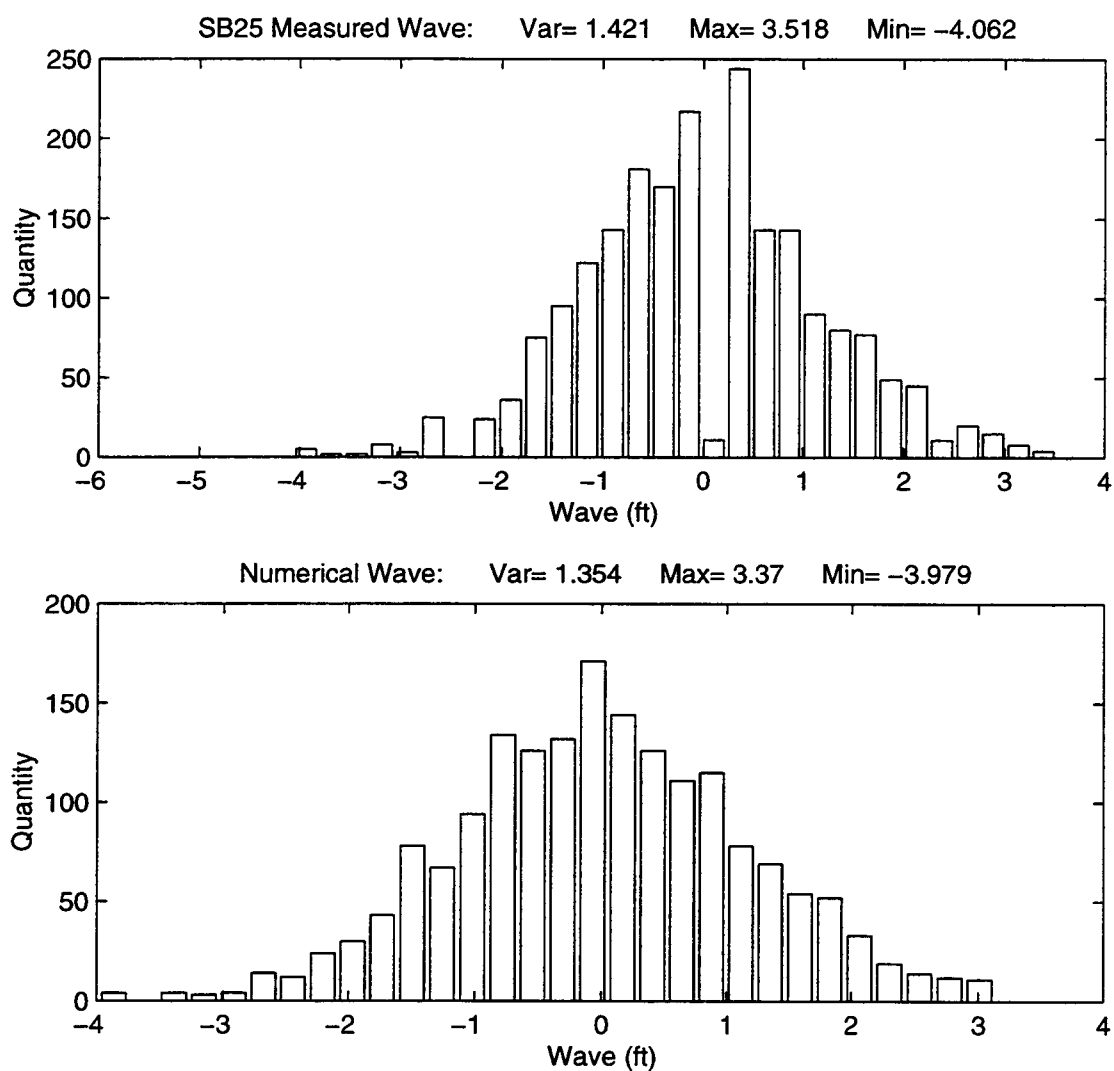


Figure 5.10

Wave Histograms, $H_s=4.7$ ft, $T_p=8.2$ s

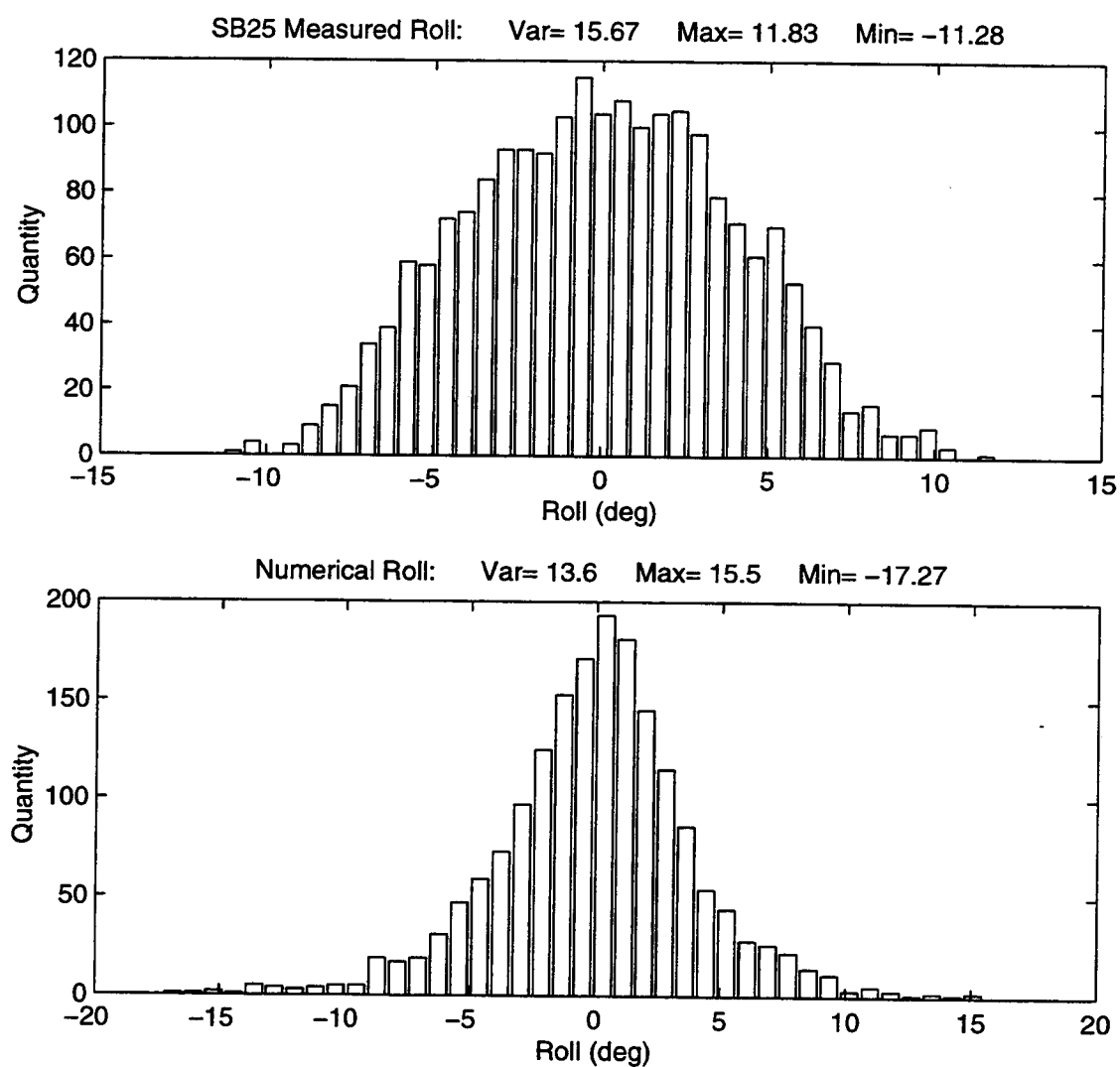


Figure 5.11

Roll Histograms, $H_s=4.7$ ft, $T_p=8.2$ s

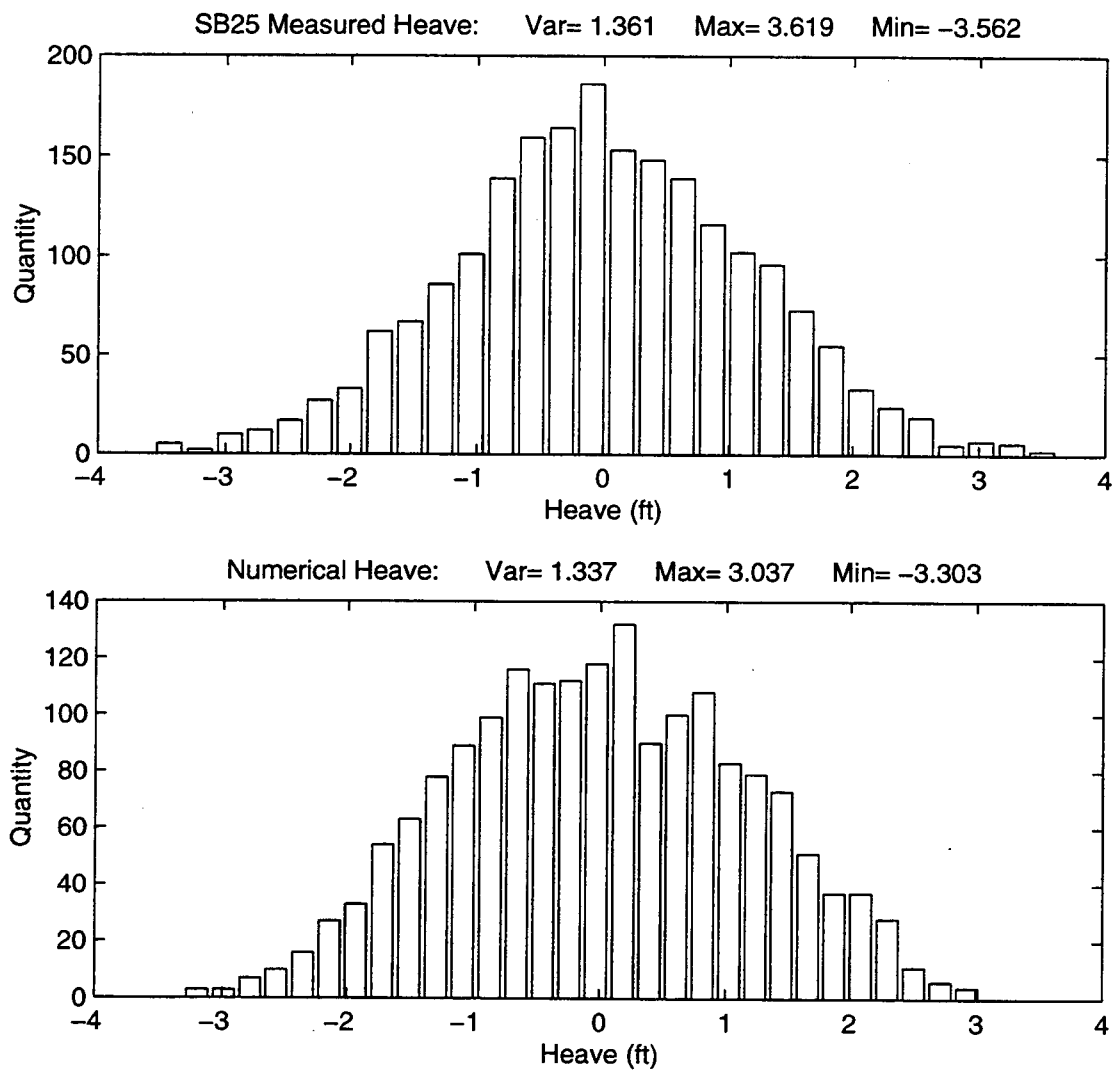


Figure 5.12

Heave Histograms, $H_s=4.7$ ft, $T_p=8.2$ s

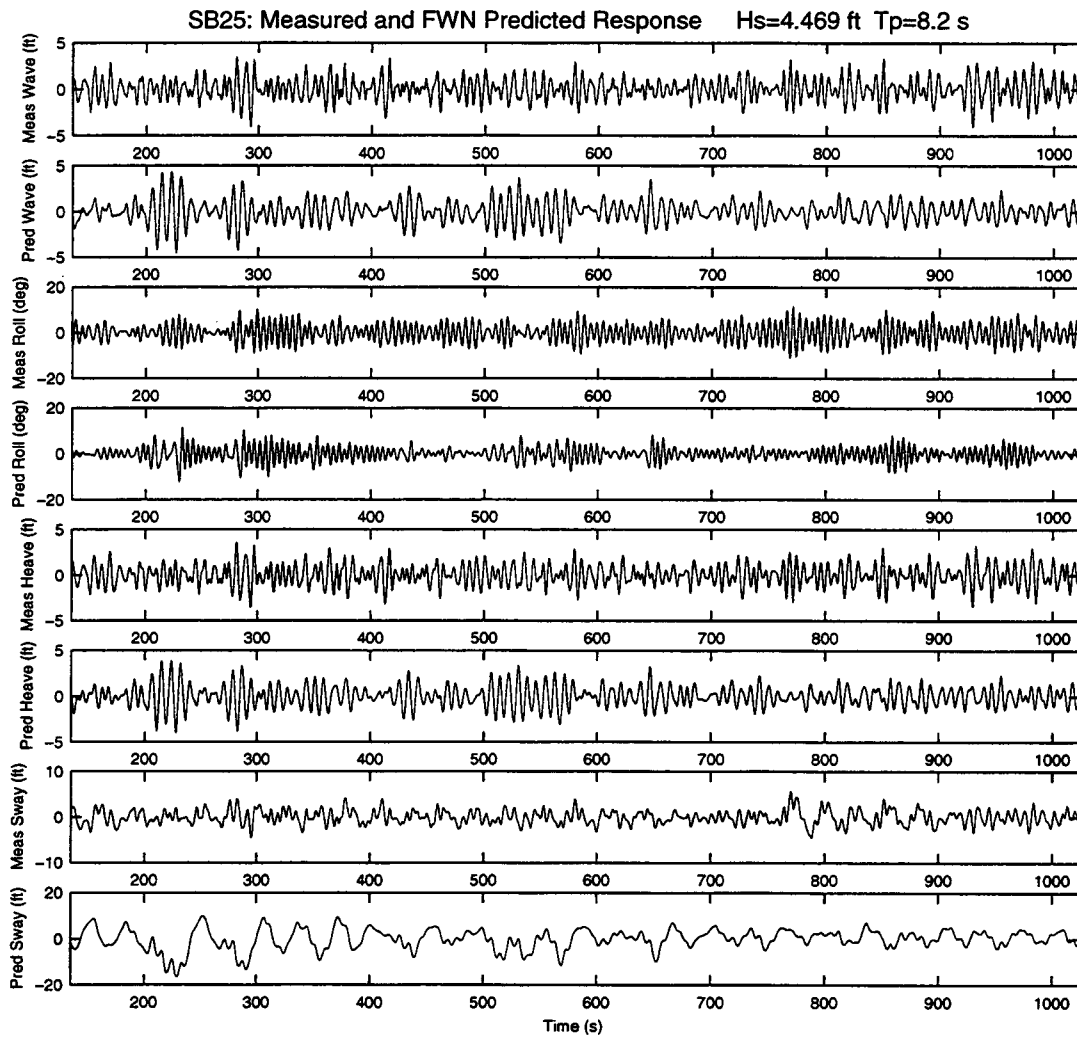


Figure 5.13

Measured and FWN Predicted Response, Hs=4.7 ft, Tp=8.2 s

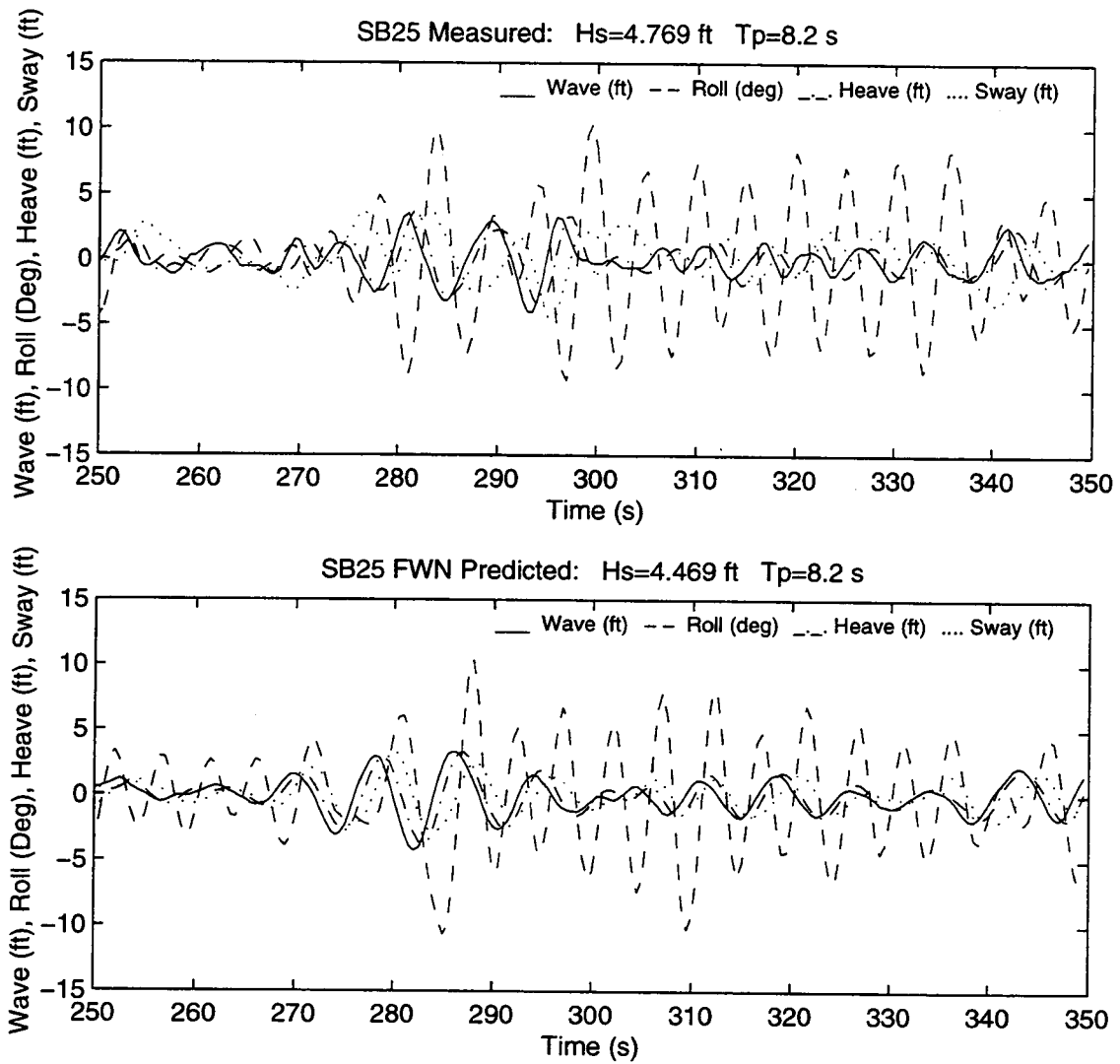


Figure 5.14

Measured and FWN Predicted Response, Hs=4.7 ft, Tp=8.2 s

Table 5.2 System Parameters for 3-DOF Roll-Heave-Sway Model Random Wave Case Test SB25 with Simulated Input

Parameter	SB29	SB25
M_{22} (slugs)	2.325E04	2.325E04
M_{a22} (slugs)	5E02	5E02
ζ_{L22}	0.005	0.01
ζ_{N22}	0.005	0.01
M_{33} (slugs)	2.325E04	2.325E04
M_{a33} (slugs)	1.0E05	1.0E05
ζ_{L33}	0.010	0.10
ζ_{N33}	0.010	0.10
I_{44} (slugs-ft ²)	2.161046E6	2.161046E6
I_{a44} (slugs-ft ²)	5.49232E05	5.49232E05
ζ_{L44}	0.25	0.015
ζ_{N44}	0.25	0.015

The phase plots of the predicted and measured roll versus heave and heave versus wave shown in Figure 5.15 and 5.16 are very similar for this case. Additional phase plots may be seen in Appendix D.

Spectral densities and probability distributions of the results are favorable and the reader is referred to Appendix D for these results.

In summary, the 3-DOF roll-heave-sway model is capable of prediction of the barge response for the presented measured case with adjustment of the damping ratios. The predicted model contains additional nonlinearity not seen in the measured response for this wave case as was observed in the phase plane for roll. The likelihood of this

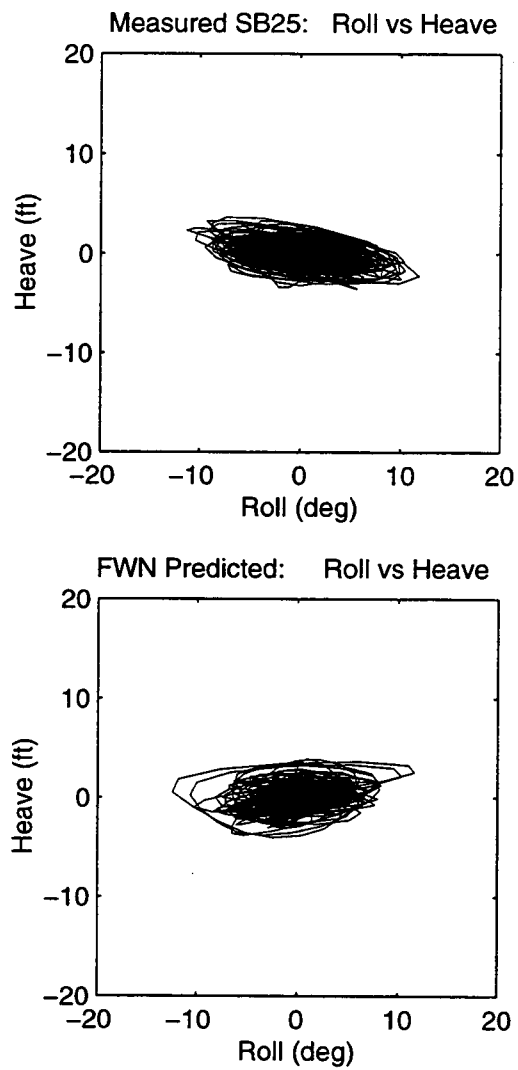


Figure 5.15

Roll vs Heave, $H_s=4.7$ ft, $T_p=8.2$ s

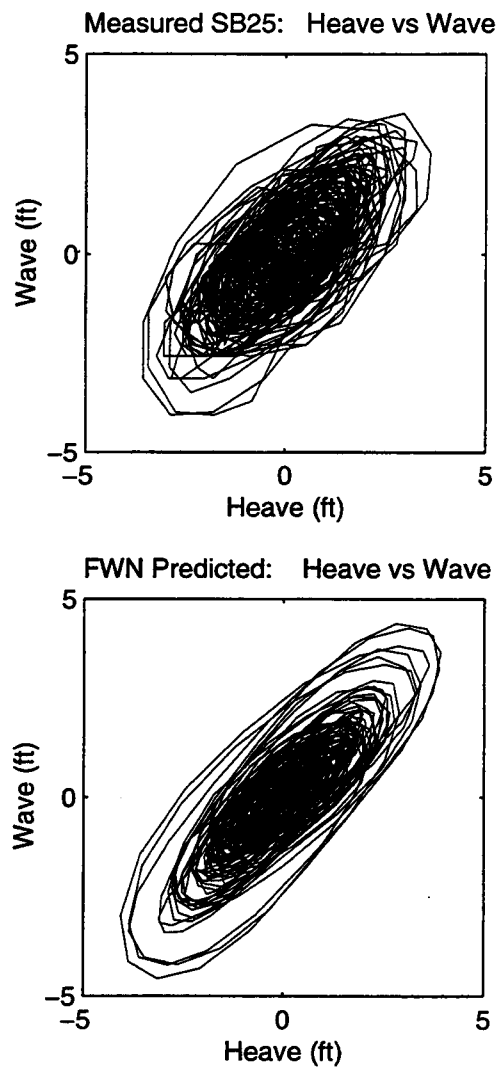


Figure 5.16

Heave vs Wave, $H_s=4.7$ ft, $T_p=8.2$ s

nonlinearity is questionable but appears in analytical forms for coupling the roll-heave hydrostatic restoring terms (both this model and Liaw *et al* (1993)). The simulated wave model appears to predict the roll response better (comparing Figure 5.14 to 5.2) but the spectral densities are more narrow banded. The histograms are however better than the case of measured input. As will be seen next, this behavior changes in the 2-DOF roll-heave model.

5.2 Roll-Heave Model with Random Waves

In this case, the same comparisons are made as was the case for the 3-DOF roll-heave-sway model with the simpler expressions for coupled roll-heave only.

5.2.1 Measured Input, $H_s=4.7$ ft, $T_p=8.2$ s

The measured wave input used in Section 5.1.1 for the 3-DOF roll-heave-sway model is used here for the 2-DOF roll-heave model. The coefficients in added mass, added inertia and damping were adjusted from those of the regular wave cases of the 2-DOF model (Section 4.3) and are presented in Table 5.3.

Table 5.3 System Parameters for 2-DOF Roll-Heave Model Random Wave Case Test SB25 with Measured Input

Parameter	SB29	SB25
M_{22} (slugs)	N/A	N/A
M_{a22} (slugs)	N/A	N/A
ζ_{L22}	N/A	N/A
ζ_{N22}	N/A	N/A
M_{33} (slugs)	2.325E04	2.325E04
M_{a33} (slugs)	7.6750E04	7.6750E04
ζ_{L33}	0.15	0.35
ζ_{N33}	0.15	0.35
I_{44} (slugs-ft ²)	2.161046E6	2.161046E6
I_{a44} (slugs-ft ²)	5.49232E05	5.49232E05
ζ_{L44}	0.55	0.08
ζ_{N44}	0.55	0.08

Notice the heave damping has increased over the regular wave case and the roll damping decreased substantially to 8% of critical. Added mass and inertia remain the same.

Time domain comparisons for the measured data and numerical predications (Figures 5.17 - 5.18) show very close agreement in the response as was the case for the simulated 3-DOF model of the previous section. This appears to be most assuring for this 2-DOF model given the initial conditions are different for the measured data and predicted.

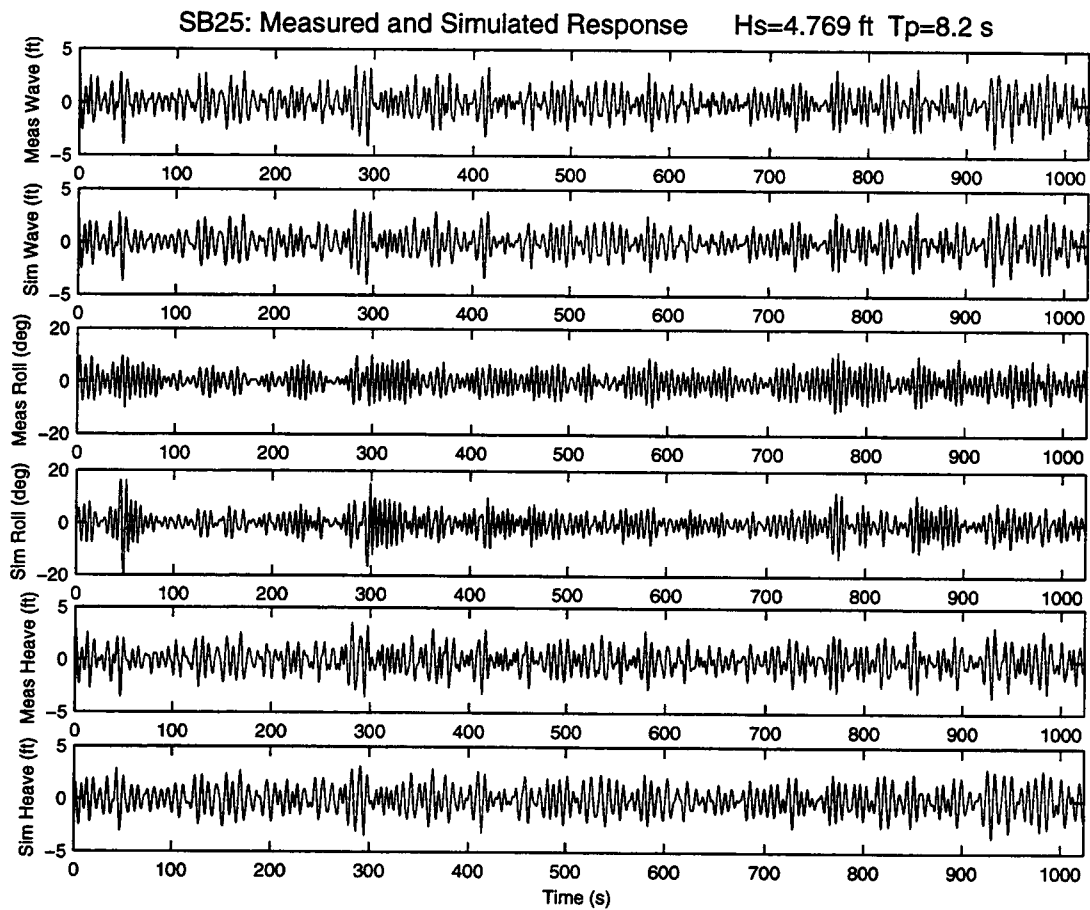


Figure 5.17

Measured and Predicted Response, $H_s=4.7$ ft, $T_p=8.2$ s

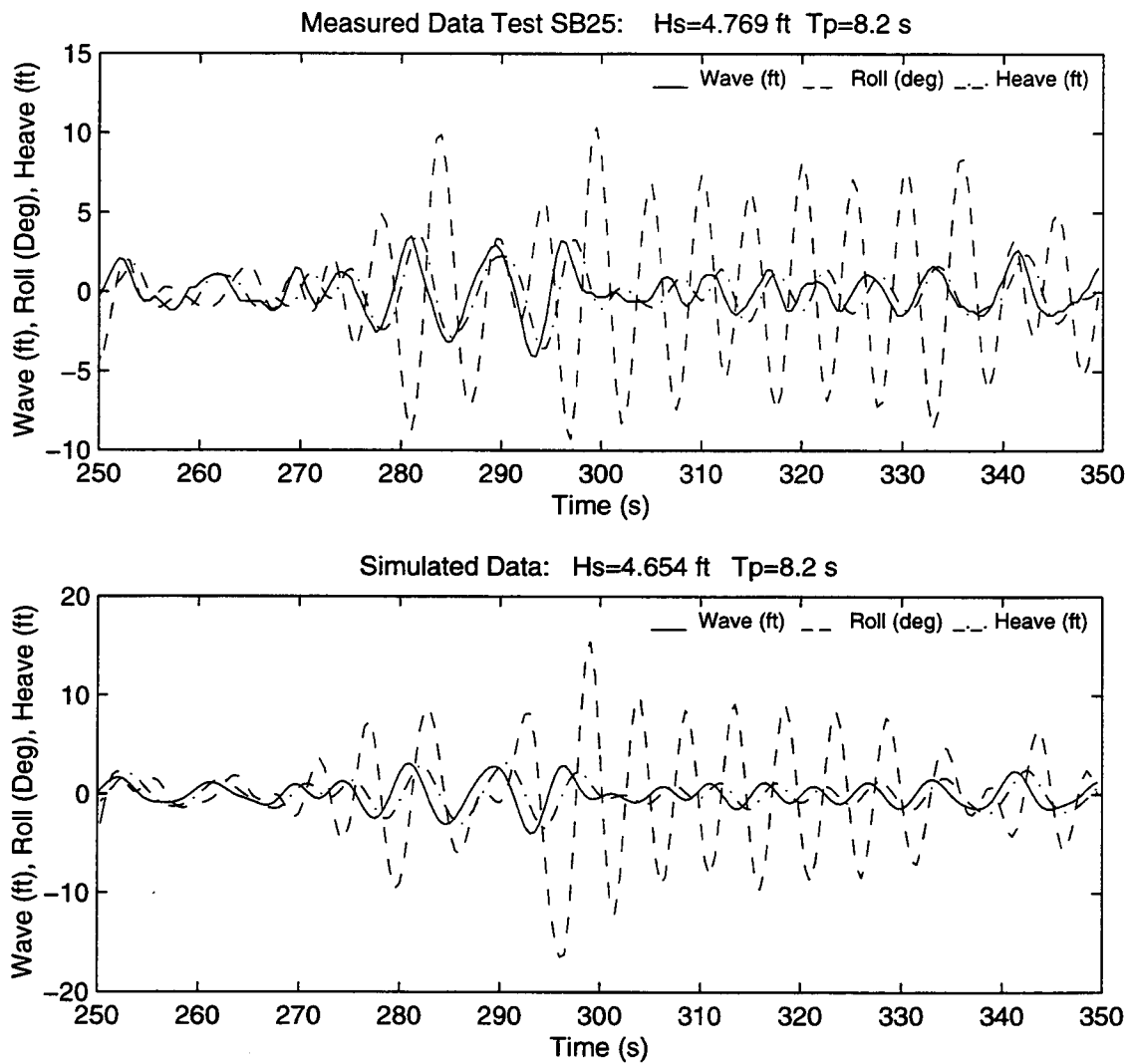


Figure 5.18 Measured and Predicted Response, $H_s=4.7$ ft, $T_p=8.2$ s

Phase plots of the wave versus roll, wave versus heave, and heave versus roll all compare favorably (see Appendix E). Better results for the spectral densities are shown in Figures 5.19 and 5.20. The energy is spread over similar frequency ranges and is comparable in magnitude. Histograms for the roll and heave are however different as seen in Figures 5.21 and 5.22.

5.2.2 Filtered Noise Input, $H_s=4.7$ ft, $T_p=8.2$ s

This model of the input excitation uses the random number generator from the computer and processes it first to become Gaussian and next through a linear 2nd order filter to produce the wave free surface elevation. The free surface elevation adheres to statistical and spectral properties of ocean waves. This is the same wave model used in the 3-DOF situation of Section 5.1.2. The system coefficients used in the regular wave identification are compared to those used here in Table 5.4.

Notice the heave damping is the same as the regular wave case and the roll damping decreased substantially to 1.5% of critical. Added mass and inertia remained the same.

Comparisons of the measured and the predicted responses in the time domain are presented in Figure 5.23. For the same time span, the roll response differs from that of Figure 5.18

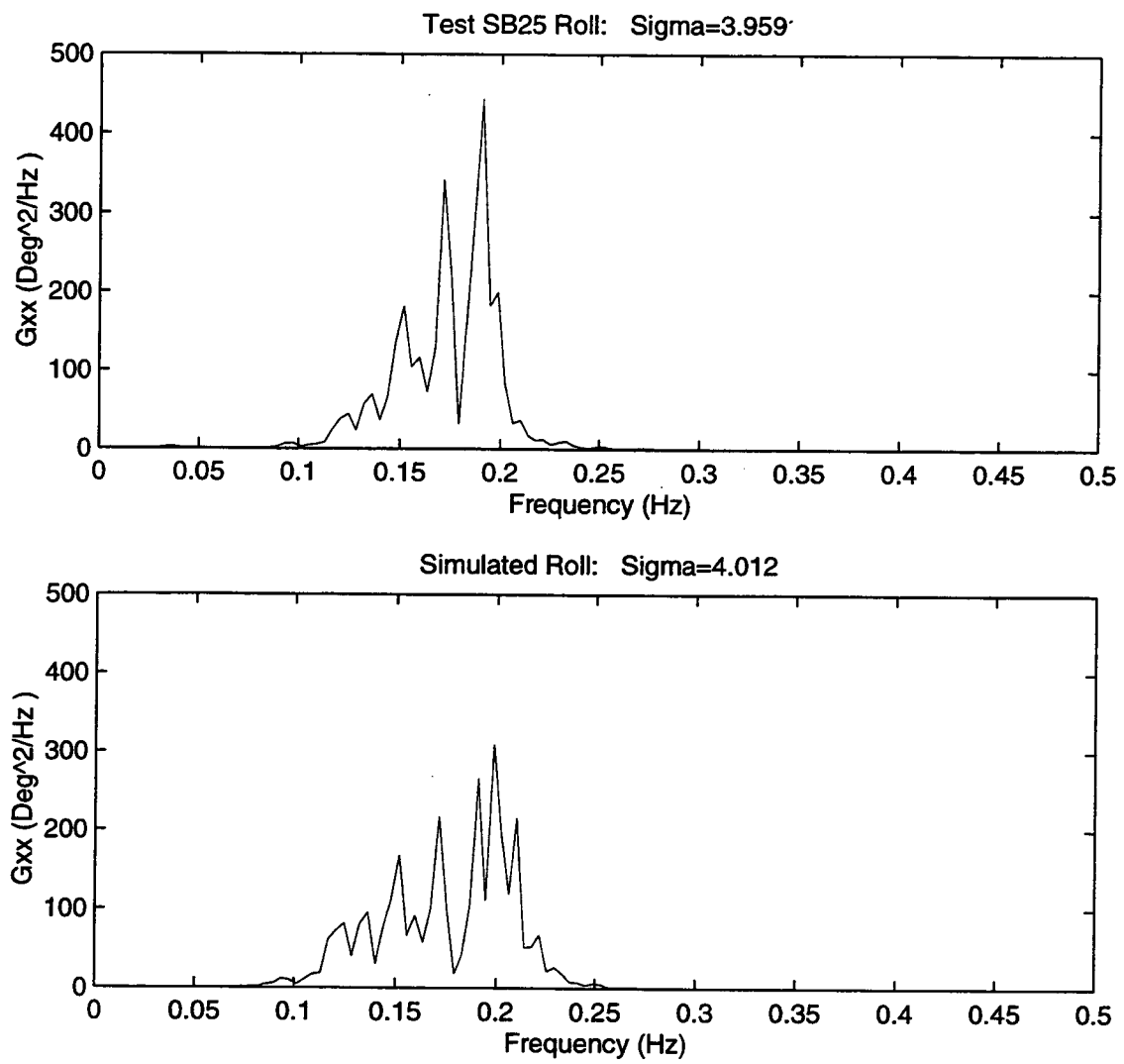


Figure 5.19

Roll Spectral Densities, $H_s=4.7$ ft, $T_p=8.2$ s

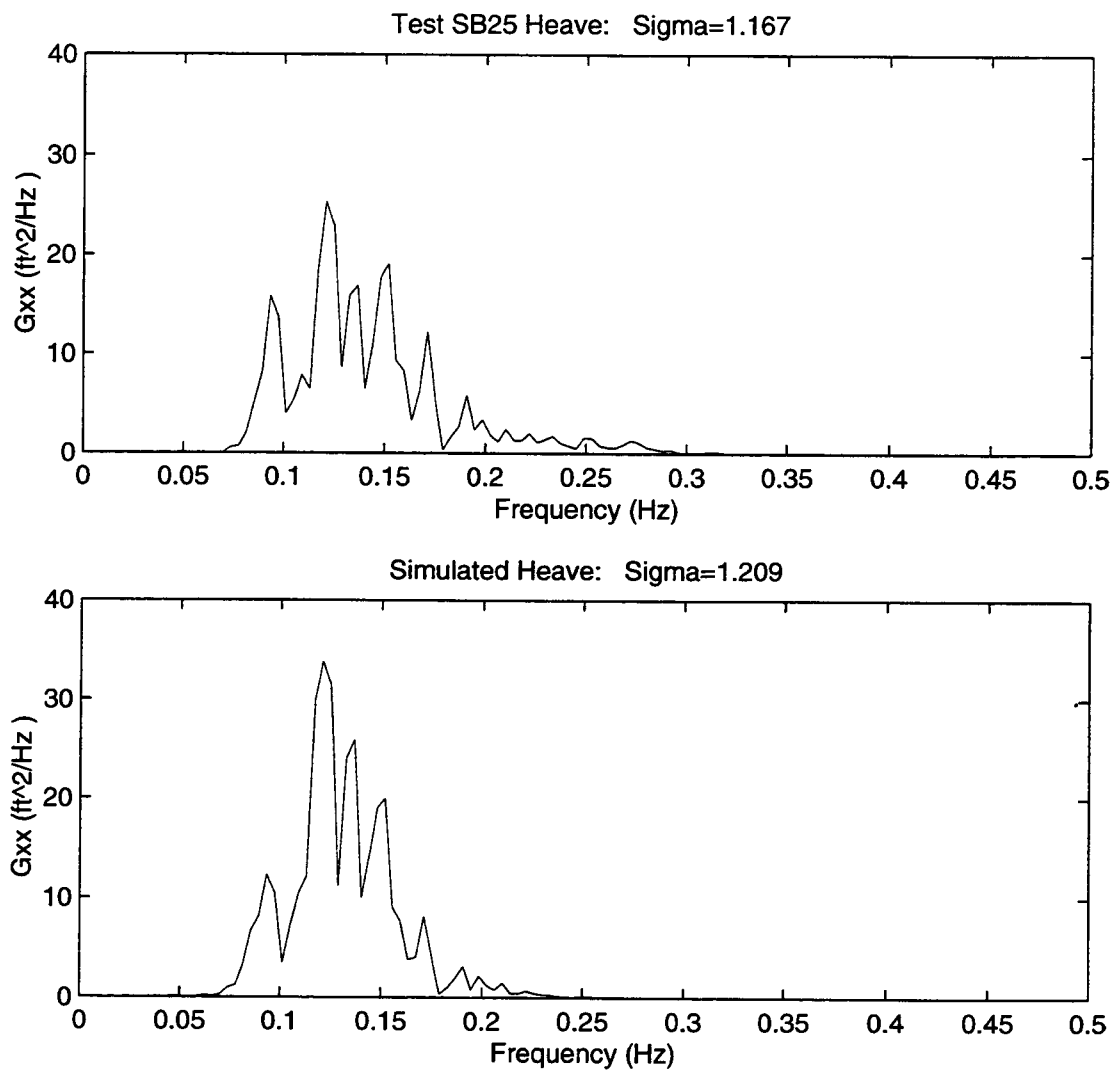


Figure 5.20

Heave Spectral Densities, $H_s=4.7$ ft, $T_p=8.2$ s

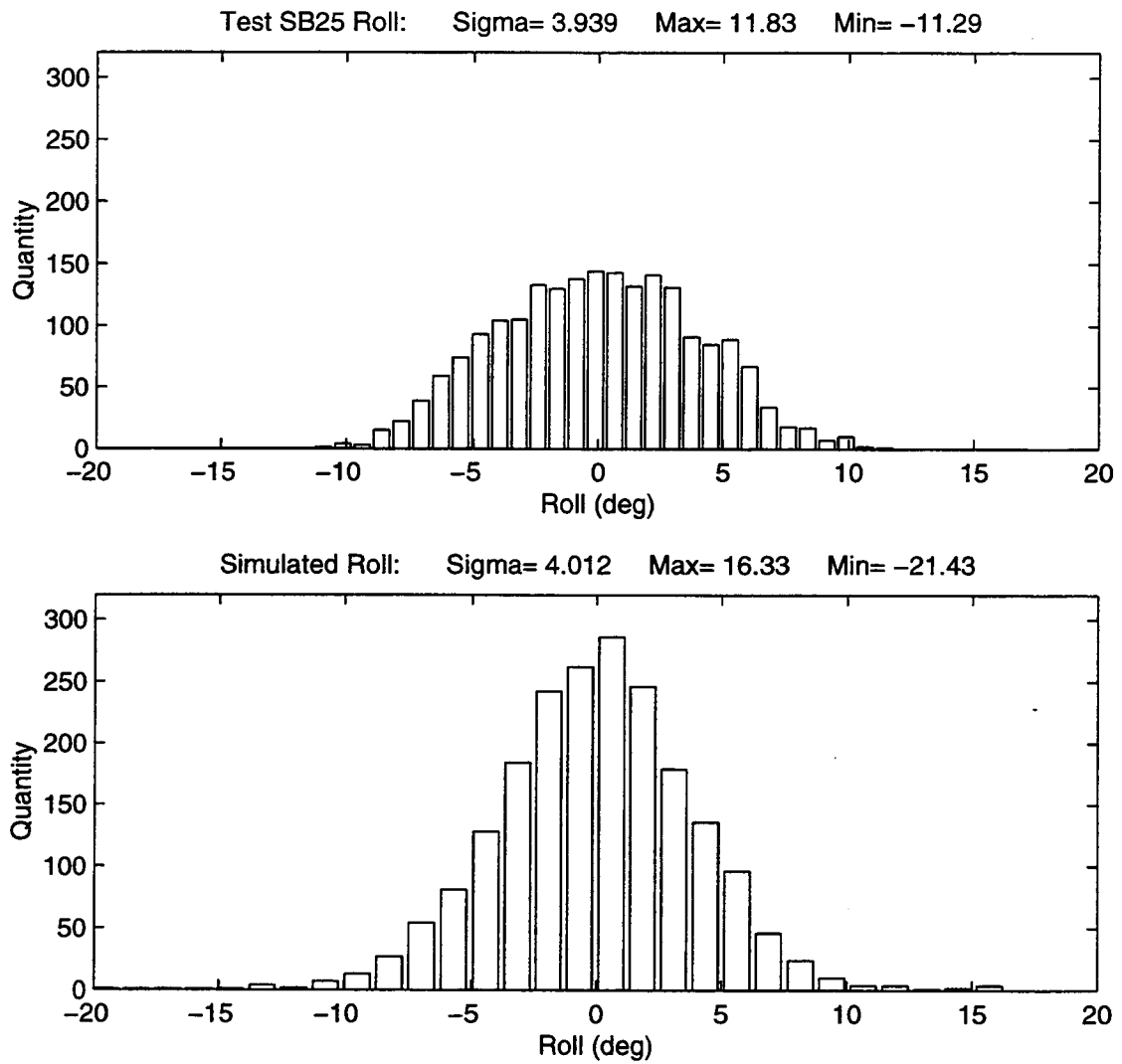


Figure 5.21

Roll Histograms, $H_s=4.7$ ft, $T_p=8.2$ s

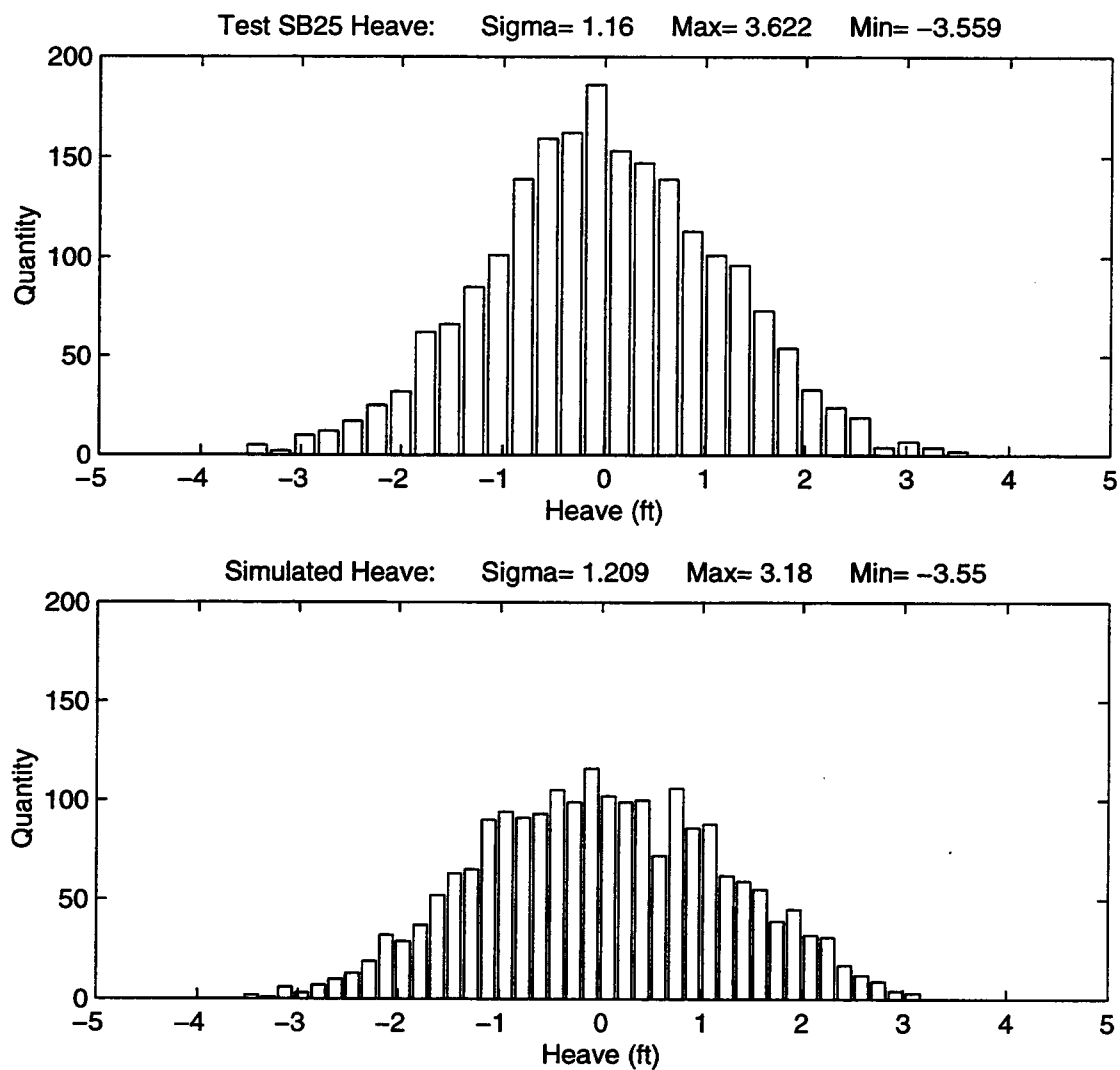


Figure 5.22

Heave Histograms, $H_s=4.7$ ft, $T_p=8.2$ s

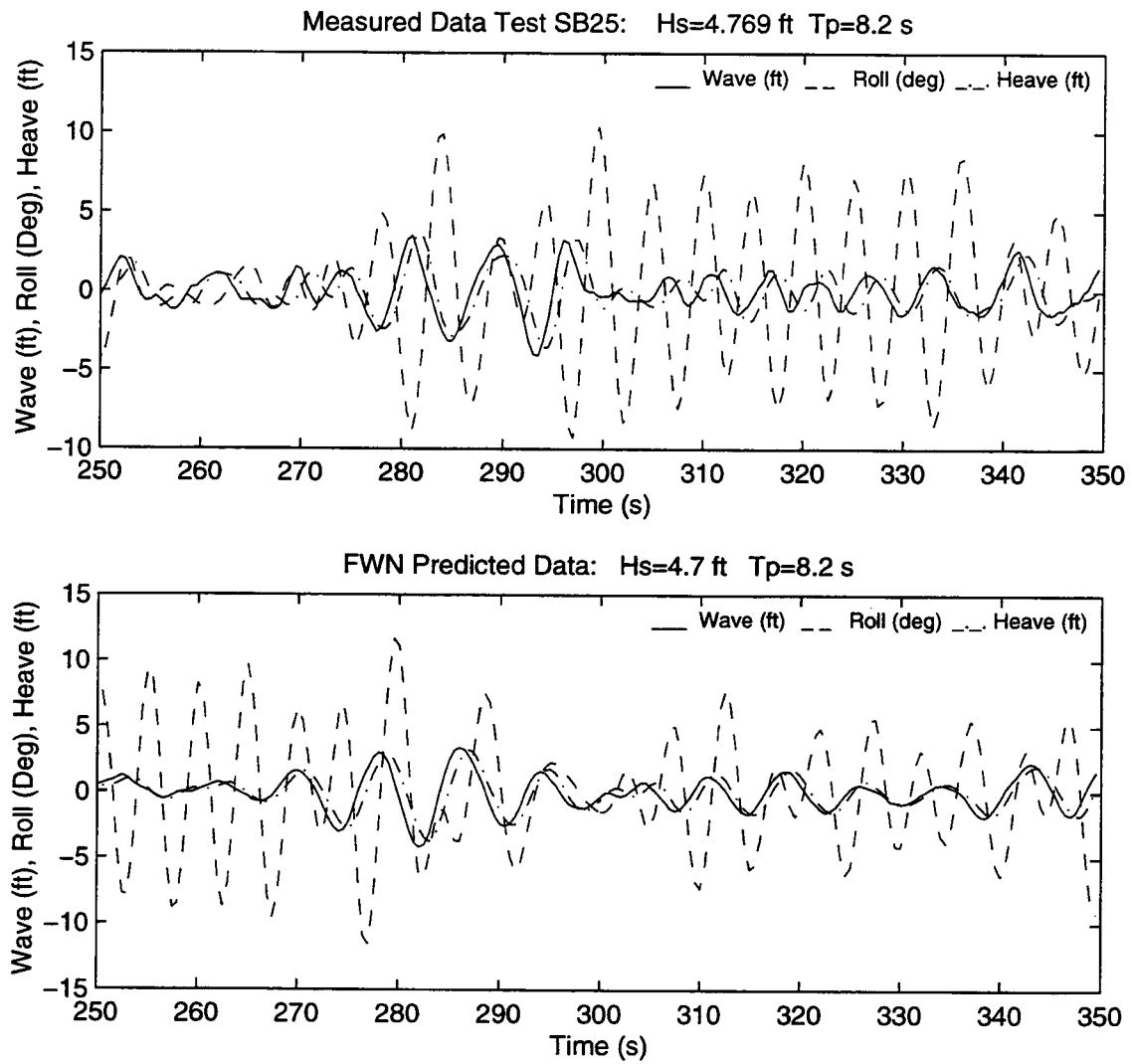


Figure 5.23

Measured and FWN Predicted Response, Hs=4.7 ft, Tp=8.2 s

Table 5.4 System Parameters for 2-DOF Roll-Heave Model Random Wave Case Test SB25 with Simulated Input

Parameter	SB29	SB25
M_{22} (slugs)	N/A	N/A
M_{a22} (slugs)	N/A	N/A
ζ_{L22}	N/A	N/A
ζ_{N22}	N/A	N/A
M_{33} (slugs)	2.325E04	2.325E04
M_{a33} (slugs)	7.6750E04	7.6750E04
ζ_{L33}	0.15	0.15
ζ_{N33}	0.15	0.15
I_{44} (slugs-ft ²)	2.161046E6	2.161046E6
I_{a44} (slugs-ft ²)	5.49232E05	5.49232E05
ζ_{L44}	0.55	0.015
ζ_{N44}	0.55	0.015

Phase plots and phase diagram of roll are very similar and the reader is referred to Appendix E for those details. Spectral densities are different as seen in Figures 5.24 and 5.25. The response is more narrow banded than the measured with more low frequency energy and less high frequency energy. This is a side effect of the filter but does not affect the first order response in heave or roll.

Distributions of wave height, roll amplitude and heave response as seen in Figures 5.26 to 5.28, compare remarkably well for this case.

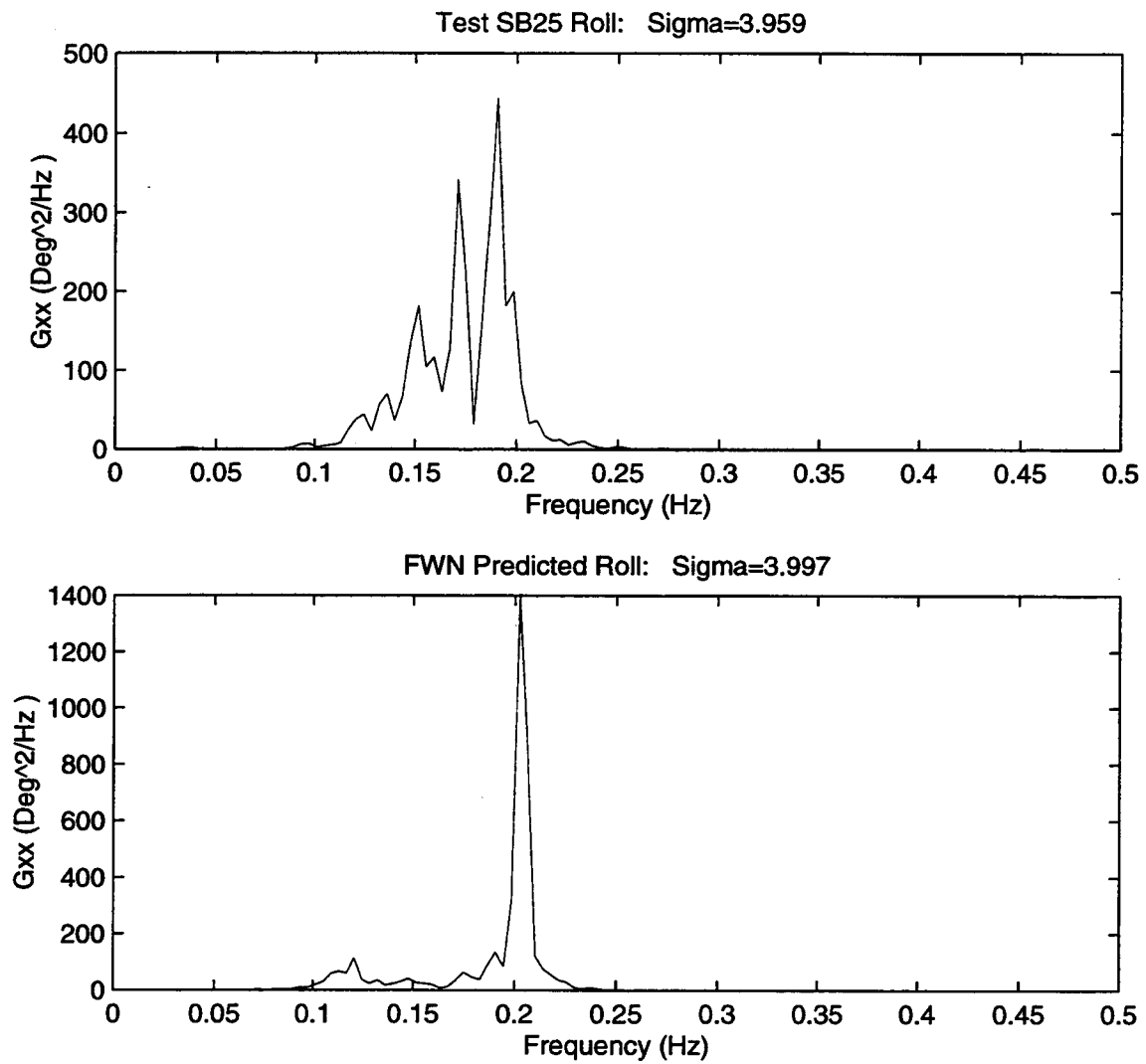


Figure 5.24

Roll Spectral Densities, $H_s=4.7$ ft, $T_p=8.2$ s

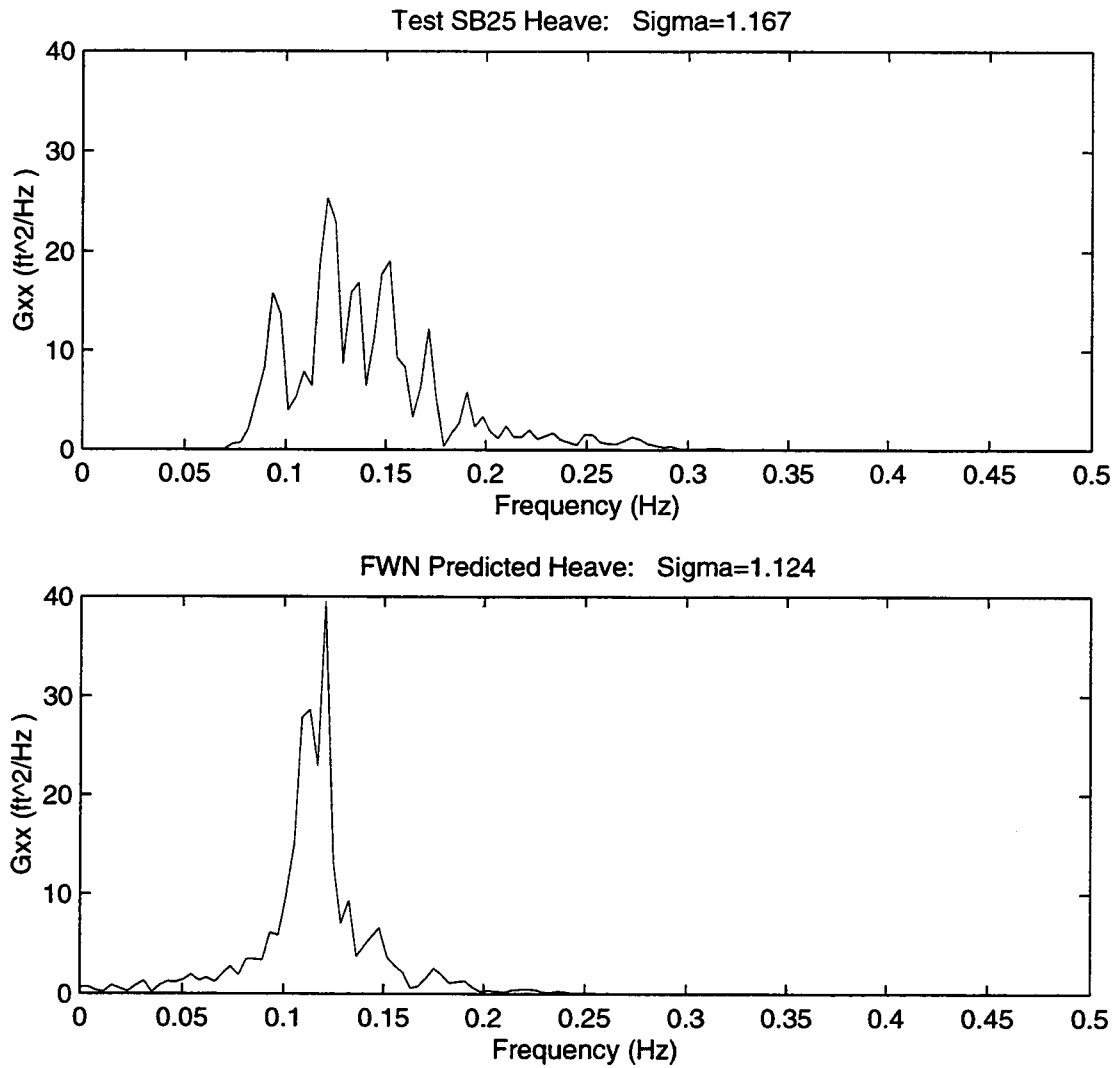


Figure 5.25 Heave Spectral Densities, $H_s=4.7$ ft, $T_p=8.2$ s

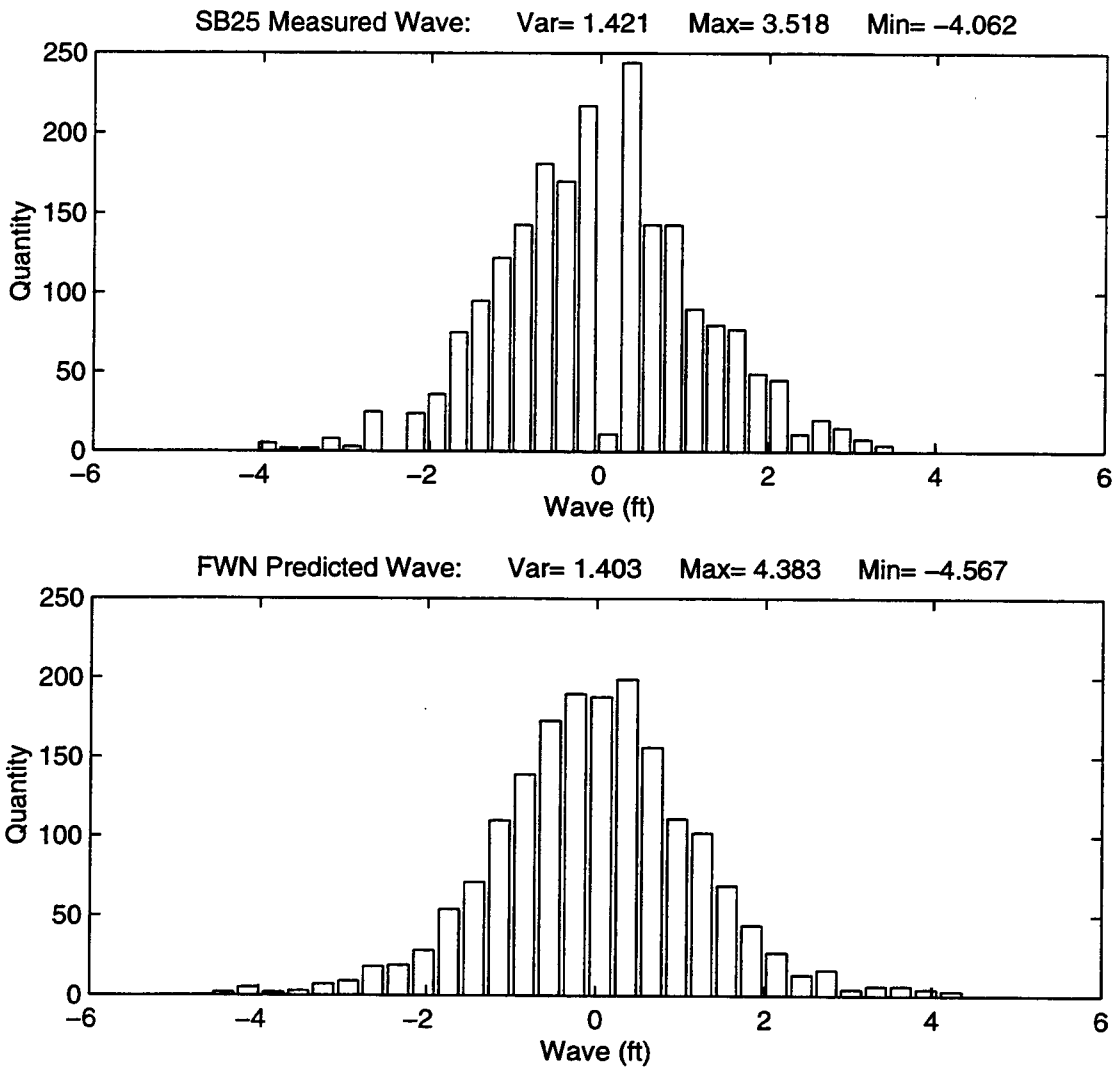


Figure 5.26 Wave Histograms, $H_s=4.7$ ft, $T_p=8.2$ s

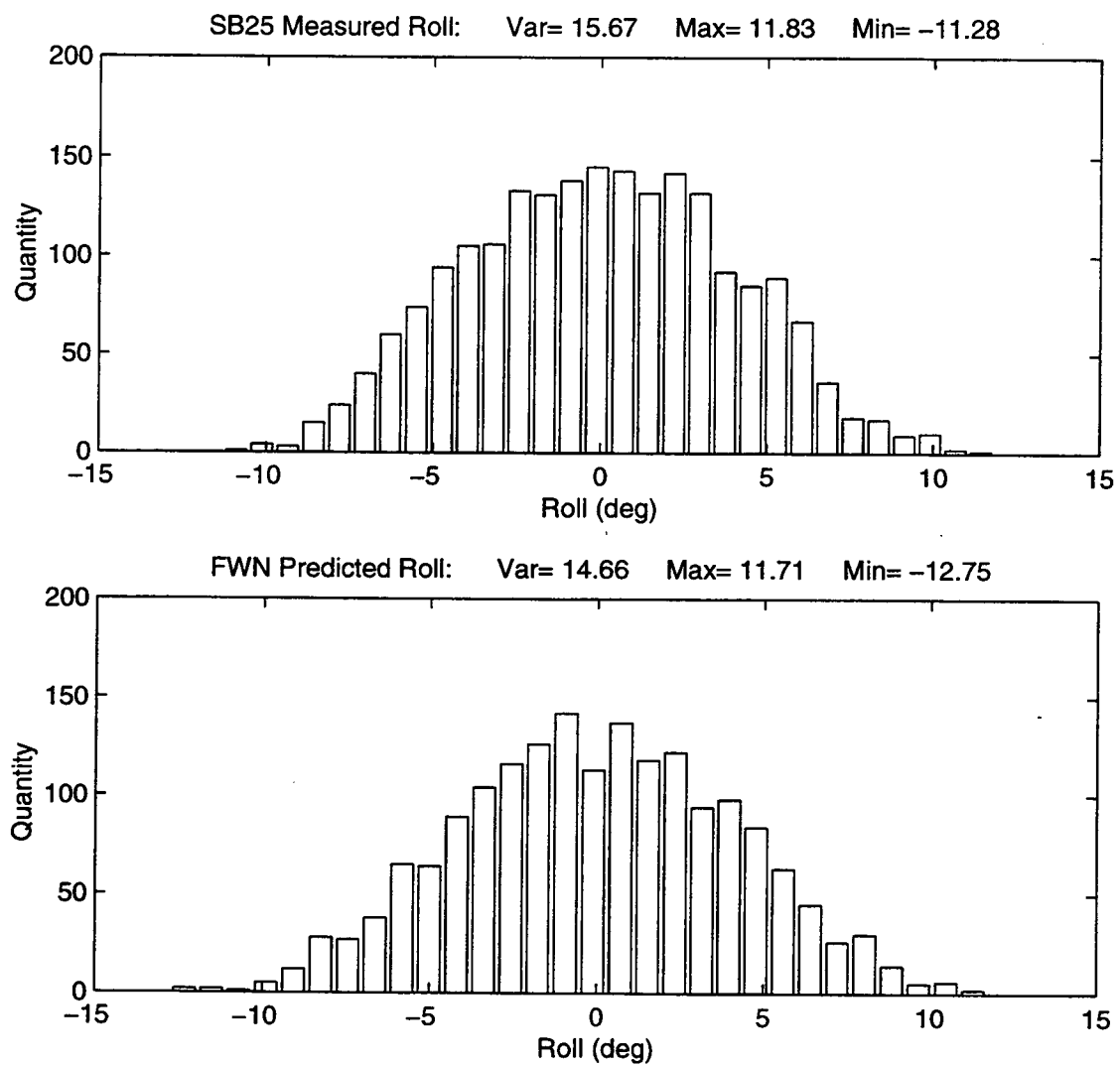


Figure 5.27

Roll Histograms, $H_s=4.7$ ft, $T_p=8.2$ s

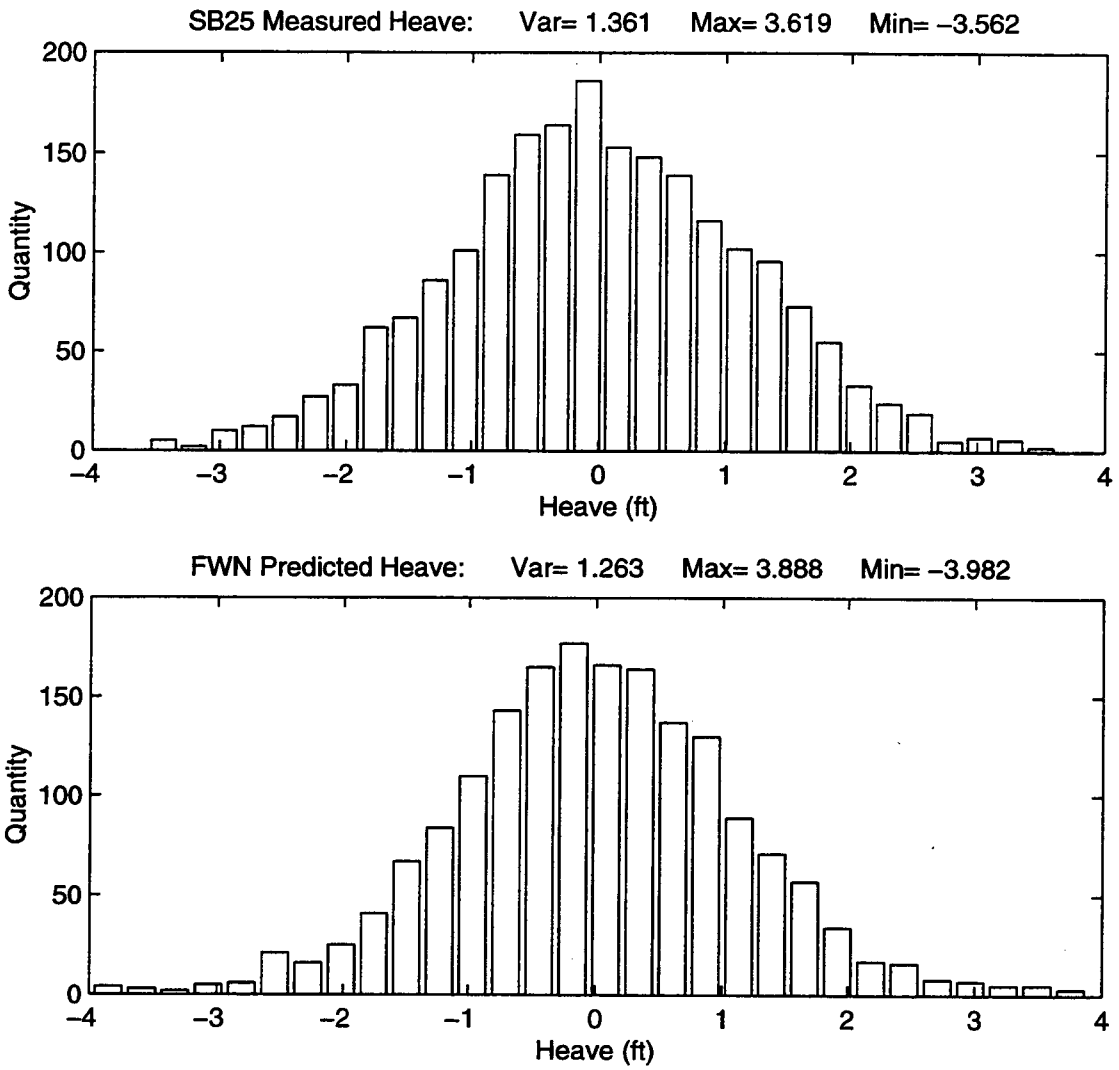


Figure 5.28 Heave Histograms, $H_s=4.7$ ft, $T_p=8.2$ s

5.3 Summary of Results

Based on the above preliminary study, both the 3-DOF and 2-DOF models seem to have some strengths and weaknesses. In some cases, one model predicts spectral densities more favorably than the other and in other cases the histograms compare better. The time series of the response were compared for a sequence of time and compared remarkably well for each model. The 3-DOF model compared more favorably in matching time histories for the simulated input while the 2-DOF model compared better for the measured waves. The 2-DOF model predicts the distributions better than the 3-DOF model, at least for roll and heave. The damping coefficients required adjustments for both models to bring the predicted response in line with the measured case.

6. STOCHASTIC RESPONSE ESTIMATIONS BY MONTE CARLO METHOD

The Monte Carlo method is a statistical sampling technique used for many years in scientific research. Cited in (Cooper, 1990), by G.D. Doolen and J. Hendricks, "the method is presently used for design of nuclear reactors, nuclear safeguard systems, oil well logging, health-physics problems, determinations of radiological doses, spacecraft radiation modeling". Collaboration with researchers (Miller and Goodlett, 1995) here at Oregon State University Oceanography Department initiated our pursuit of use of the Monte Carlo method to study stochastic ship roll response.

This marks the 50th year anniversary of the first uses of the Monte Carlo method on a computer by Enrico Fermi, Stanislaw Ulam, John von Neumann and N. Metropolis for studying statistical physics of atomic particles. The first electronic computer, the Electronic Numerical Integrator and Computer (ENIAC), was created to provide ballistic information for the U.S. Army in 1942 and provoked thoughts of Monte Carlo method. After this computer, the FERMIAC and MANIAC were created for studies in thermonuclear reactions. Today, we continue in the spirit of the Monte Carlo method for estimates of the motions of a barge in the ocean.

6.1 Algorithm Description

6.1.1 Stochastic Differential Equation Model

The form of the stochastic differential equation for this study assumes use of Equation 2.11 and 2.18 with randomness entered in the random wave excitation via filtered white noise. This results in eight first order ODE's to represent each particle with it's own randomness (Equation 3.6). To estimate the densities, we solve these eight first order ODE's for thousands or millions of realizations at each time step for a set duration. The size of the ensemble may be determined by increasing the size until there is little change in the density characteristics.

6.1.2 Pseudo Random Number Generation

The randomness in the wave excitation for each realization is provided by a "pseudo" random number generator (Price *et al*, 1986). The algorithm is based on the Box-Muller method for generating random deviates with normal distribution. In addition, the random numbers are modified to become normally distributed (Price *et al*, 1986) since real ocean free surface elevations follow this Gaussian distribution. The random numbers are generated starting with a seed and are different for each realization.

6.1.3 Parallel Program Algorithm

One of the main reasons for selecting the analytical model to represent the barge as a particle by coupled nonlinear differential equations is that the time domain solution process may be parallelized straightforwardly. We have chosen the Parallel Virtual Machine (Geist *et al*, 1994) language running on both a Meiko CS-2 Parallel Supercomputer and a network of distributed Sun Microsystems workstations.

The parallel algorithm is designed such that a so-called "master" program passes information to nodes on the parallel processors or other workstations and starts "slave" processes (Figure 6.1). The slaves solve a subset of the total ensemble and pass their results back to the master process. Once the master receives all the results from the slaves, it prints the results to a file.

Another advantage of the process is that it may provide intermediate results if one were interested in the evolution of the densities. This provides a means of checking for steady state as well.

Having the ensemble, a probability density kernel (Silverman, 1986) may be applied to assist in estimation of the probability distributions. We have implemented a Gaussian kernel and compare the results to that of raw data.

To handle capsizing, the algorithm contains conditional statements to check if the barge has exceeded a 90 degree roll angle or angular velocity. At this point, the barge is past the point of no return (see righting moment curves) and the value of roll or roll velocity is maintained at 90 degrees and 90 degree/second, respectively. Once the slaves have returned all their sub-ensembles, capsizing cases included, and the master

Parallel Virtual Machine Setup

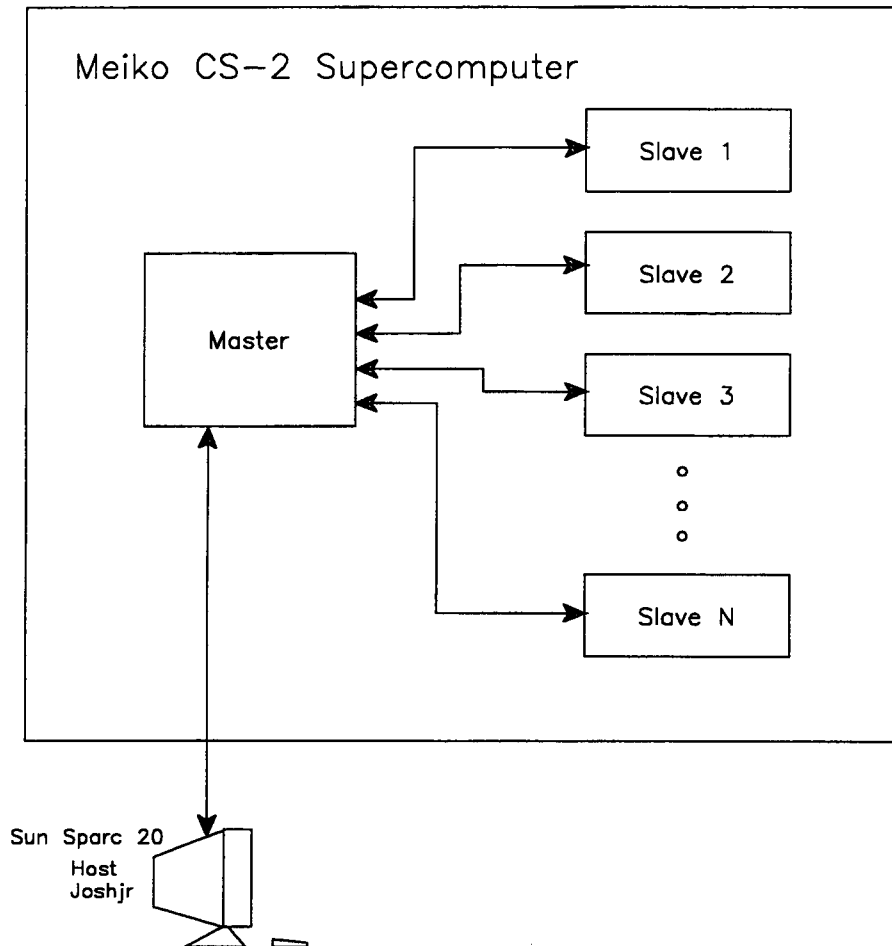


Figure 6.1

Parallel Virtual Machine (PVM) Setup

dumps the information to a file, it is simply a matter of counting the number of roll angles at 90 degrees to estimate the probability of capsize. This shows up in the densities as well as the density escapes out of the domain.

6.1.4 Simulation Parameters

The estimation of the probability densities may require thousands or millions of realizations to create a reasonably accurate density estimation. If eight parallel processors are selected, the total ensemble is divided by eight. Thus each slave handles 1/8 of the work. The time step size depends on the problem but was 0.1 second for the cases studied here. The duration of the time domain simulation varies from a few minutes to up to 20 minutes if a steady state case is needed.

6.2 3-DOF Roll-Heave-Sway Model Monte Carlo Simulations

Parallel Virtual Machine language was added to the 3-DOF numerical model to allow simulation of an ensemble of responses. An ensemble of 10,000 points was tested on the Meiko CS-2 computer (Figure 6.2) using 8 parallel processors. We ran the simulations for 12,000 time steps ($dt=0.05$ s) for printing intermediate ensembles every 50 seconds. This provides information on the evolution of the probabilistic estimate of the response for a given mission duration time (exposure time). Though the time histories of all 10,000 trajectories are not normally saved in the computation, a sample time history of 50 trajectories is provided in Figure 6.3. Both the roll and roll angular

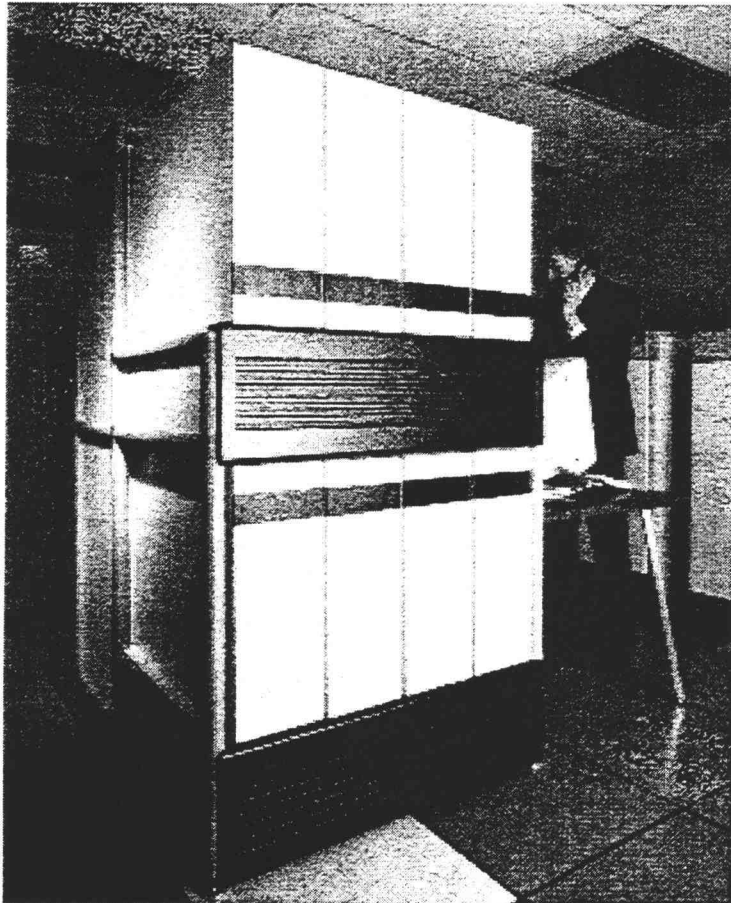


Figure 6.2

OSU's Meiko CS-2 Supercomputer

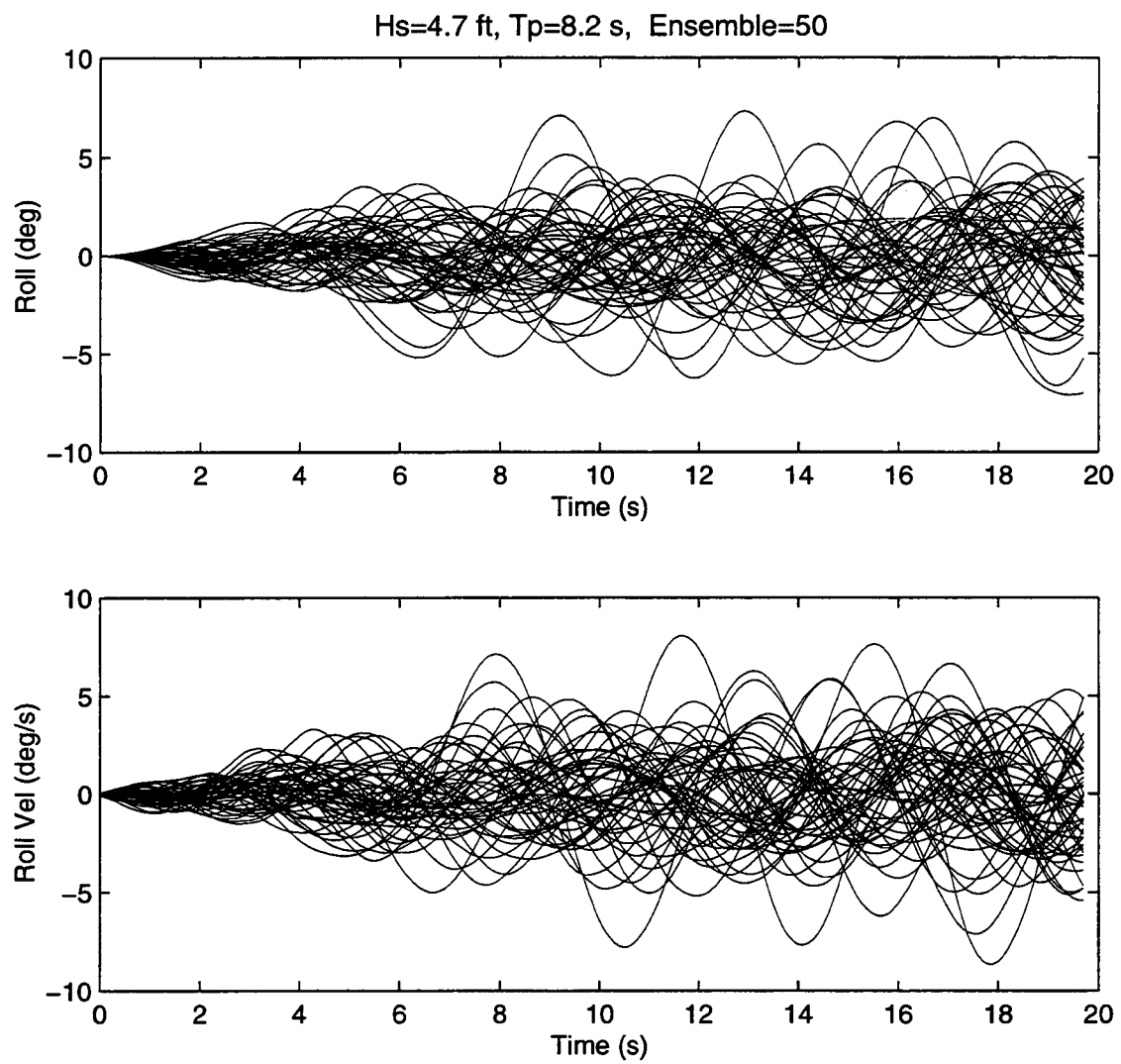


Figure 6.3

Time History of an Ensemble of 50 Realizations

velocity are shown with initial conditions of (0,0) and randomness in the responses entered at each time step via the white noise filter. Another test was run with only an ensemble of 5 realizations and one capsizes after 1 minute (Figure 6.4). After the roll response reaches 90 degrees, there is no chance of the barge righting itself and so we set the response to be a constant ± 90 degrees to indicate capsizing.

Estimates of probability of capsize for the barge were tested in two sea states with waves of $H_s=4.7$ ft, $T_p=8.2$ s and $H_s=14.1$ ft, $T_p=8.2$ s. Evolutions of the joint probability estimates are shown as contours and 3-D surface plots in Figures 6.5 - 6.8. The first wave case with $H_s=4.7$ ft, $T_p=8.2$ s, produced zero probability of capsize for 10 minutes exposure in these waves. The larger wave case produced a capsized rate of up to 3.5% shown in Figure 6.9. The next phase of this research will be to perform extensive parametric analysis of the equations of motion and check the probability estimates with some recent physical model test data with capsize cases (Yim, 1996). Here the intent is to demonstrate that the probability of capsize may be computed straightforwardly with little effort.

6.3 2-DOF Roll-Heave Model Monte Carlo Simulations

Next we examine the differences in prediction capabilities if the model is reduced to pure roll-heave. The benefit being two less first order differential equations to solve for, resulting in significant savings in computing time. The same ensemble size of 10,000 realizations were simulated with results shown in Figures 6.10 - 6.12. Figure 6.12 shows this model predicts an increased likelihood of capsizing over the roll-heave-

sway model with about 13% likelihood after 10 minutes exposure to random ocean waves compared to only 3.5% for the roll-heave-sway model. This demonstrates the need to perform further parametric evaluation of the nonlinearities in each model and compare with large amplitude seas and response motions. At this point, the idea is being presented with hopes of accurate and reliable estimates in the near future.

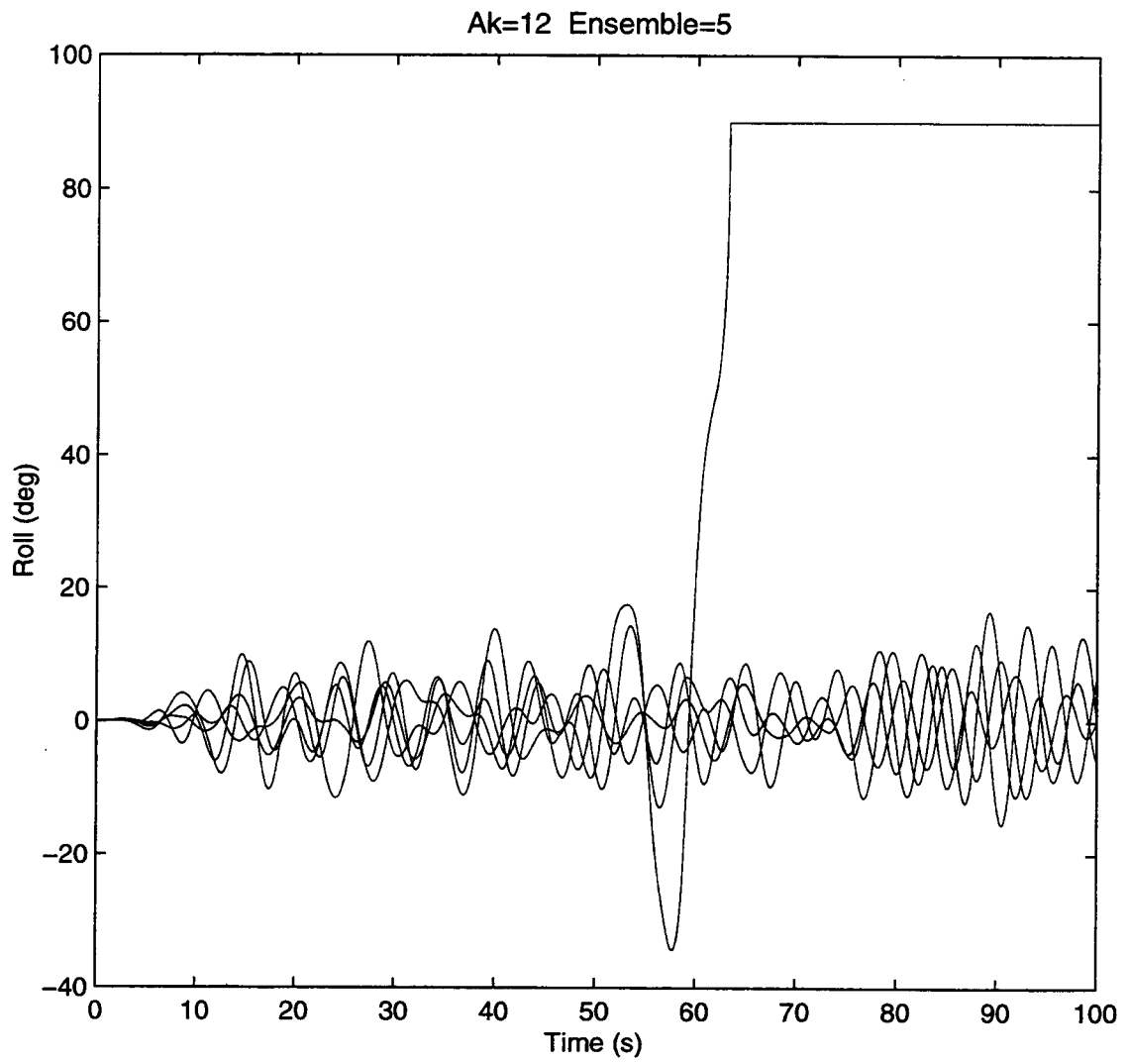


Figure 6.4

Example Time History of Barge Capsize

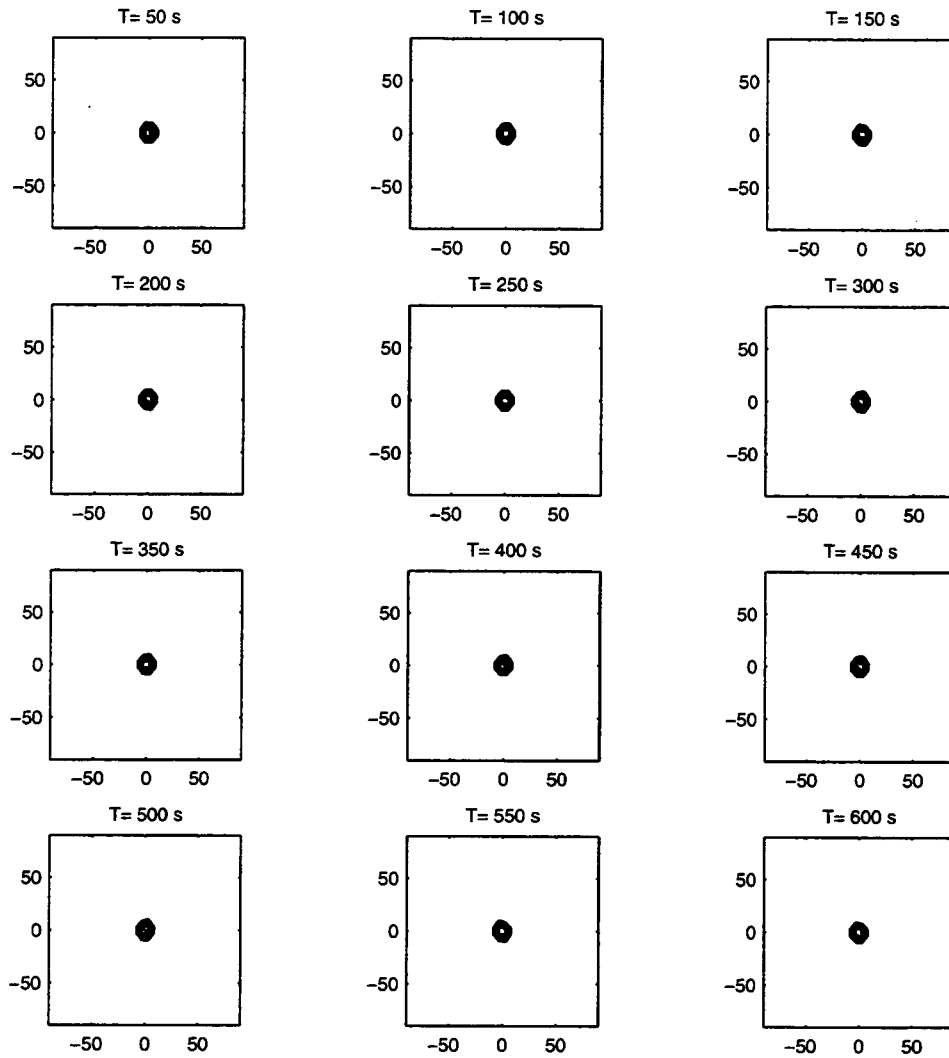


Figure 6.5 Contours of Evolution of RHS Model Joint PDF Estimation for $H_s=4.7$ ft, $T_p=8.2$ s

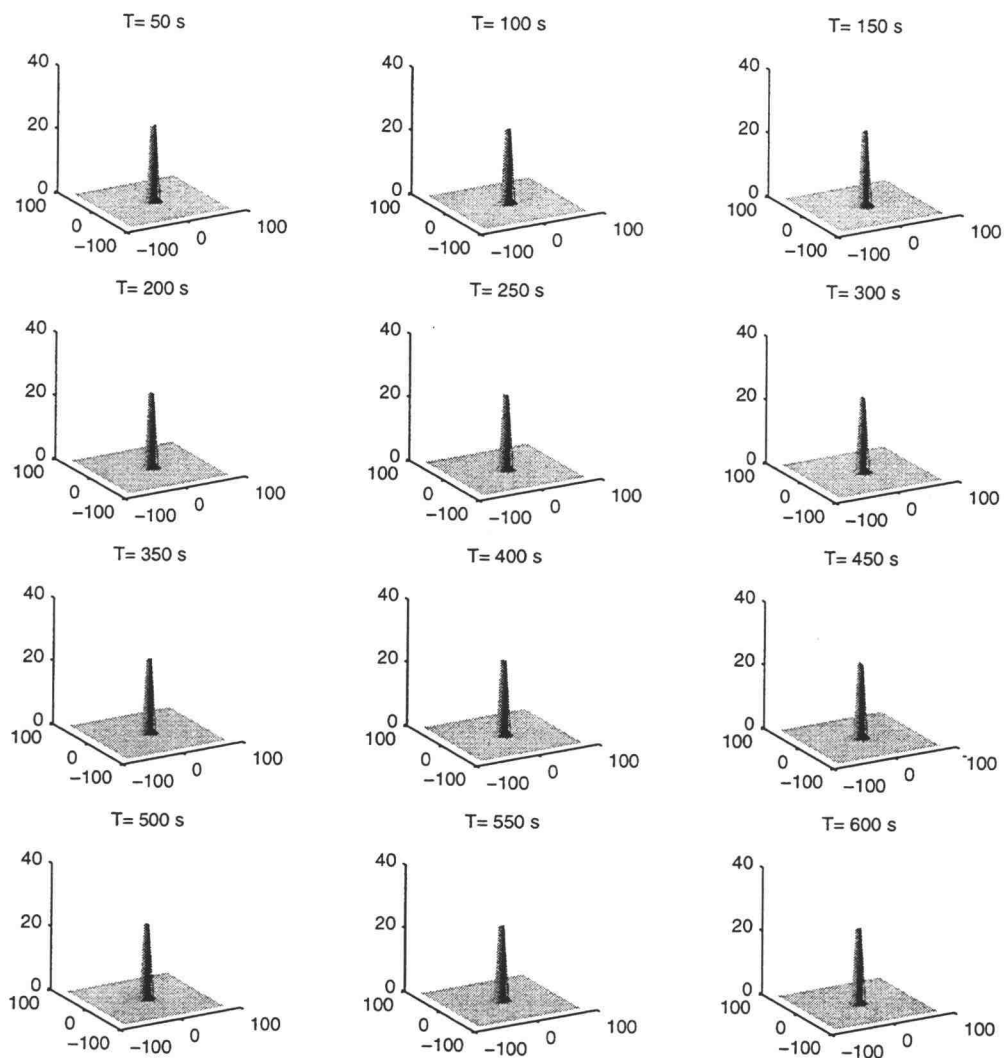


Figure 6.6

3-D Surface Plots of Evolution of RHS Model Joint PDF Estimation for $H_s=4.7$ ft, $T_p=8.2$ s

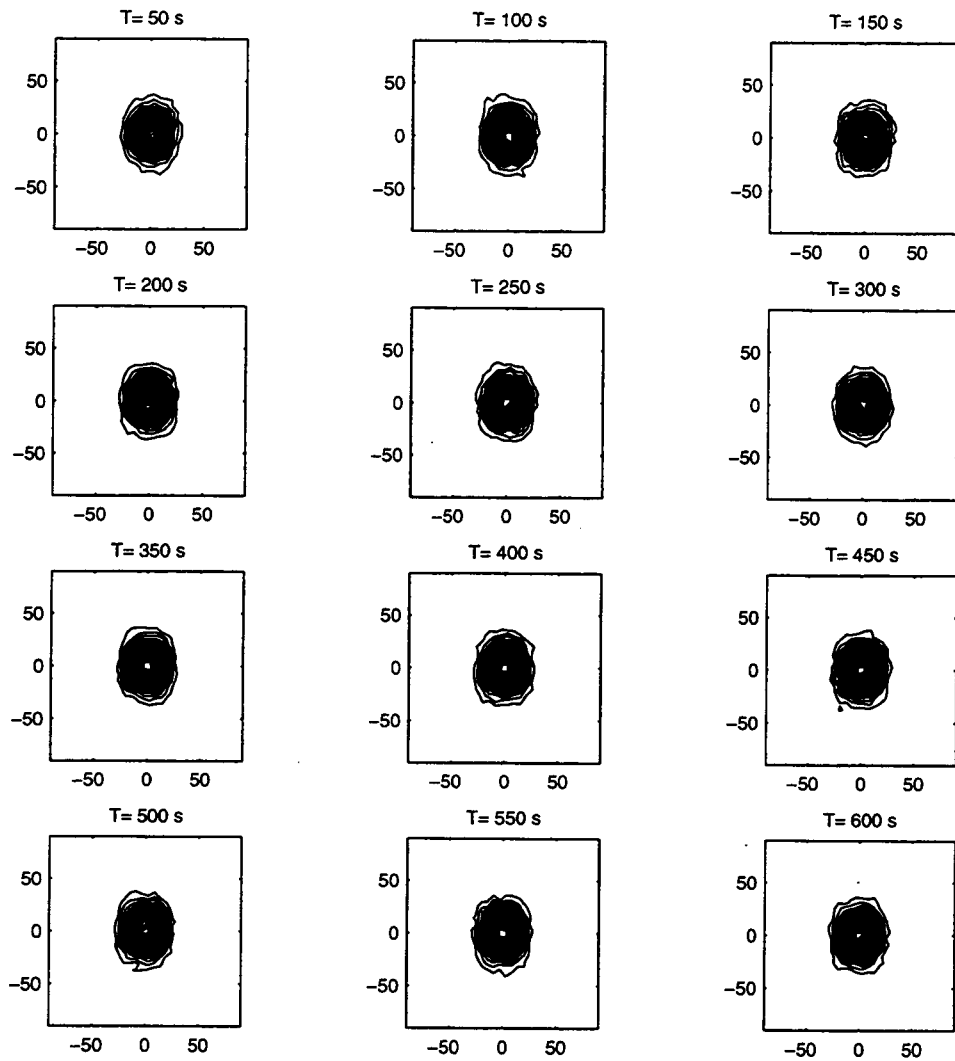


Figure 6.7 Contours of Evolution of RHS Model Joint PDF Estimation for $H_s = 14.1$ ft, $T_p = 8.2$ s

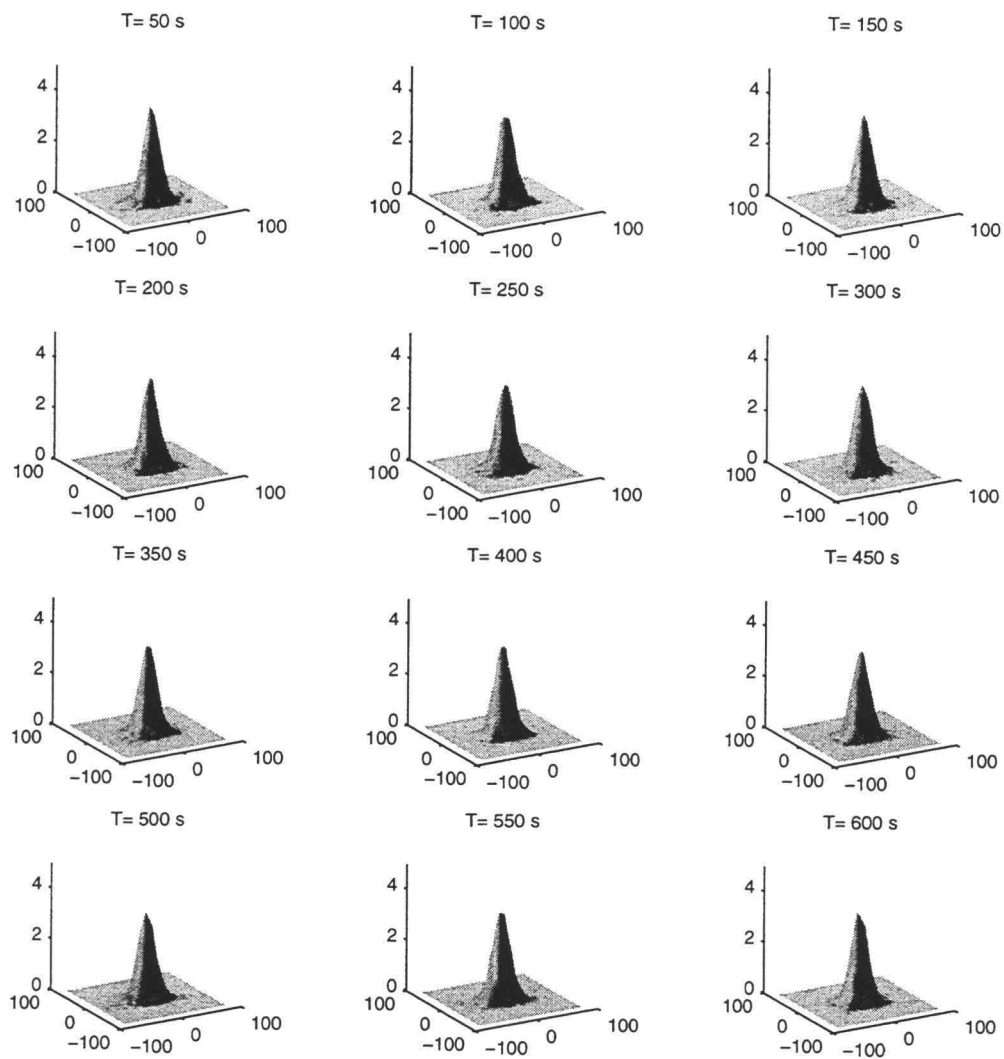


Figure 6.8

3-D Surface Plots of Evolution of RHS Model Joint PDF Estimation for $H_s=14.1$ ft, $T_p=8.2$ s

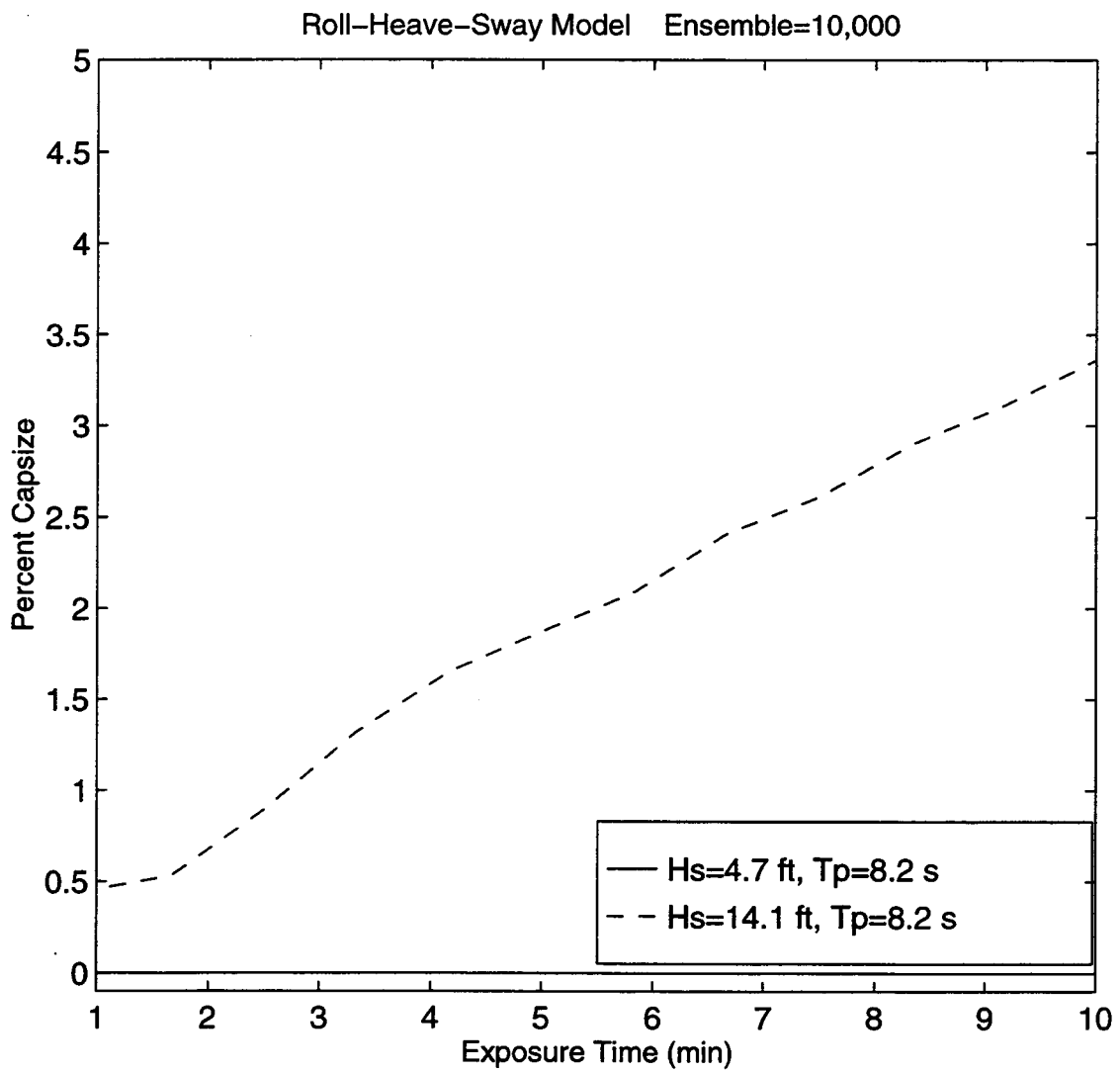


Figure 6.9

Curves showing Estimates of Percentage of Capsize
for RHS Model

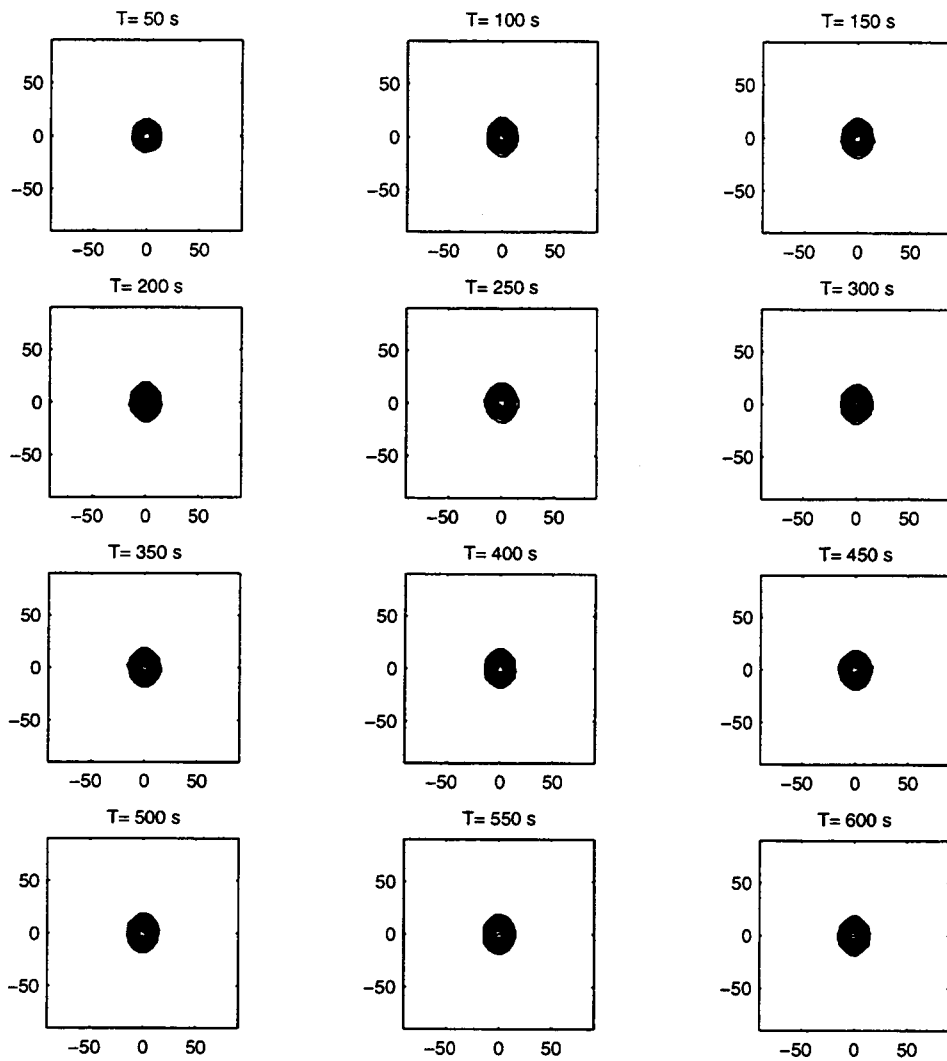


Figure 6.10

Contours of Evolution of RH Model Joint PDF Estimation
for $H_s=4.7$ ft, $T_p=8.2$ s

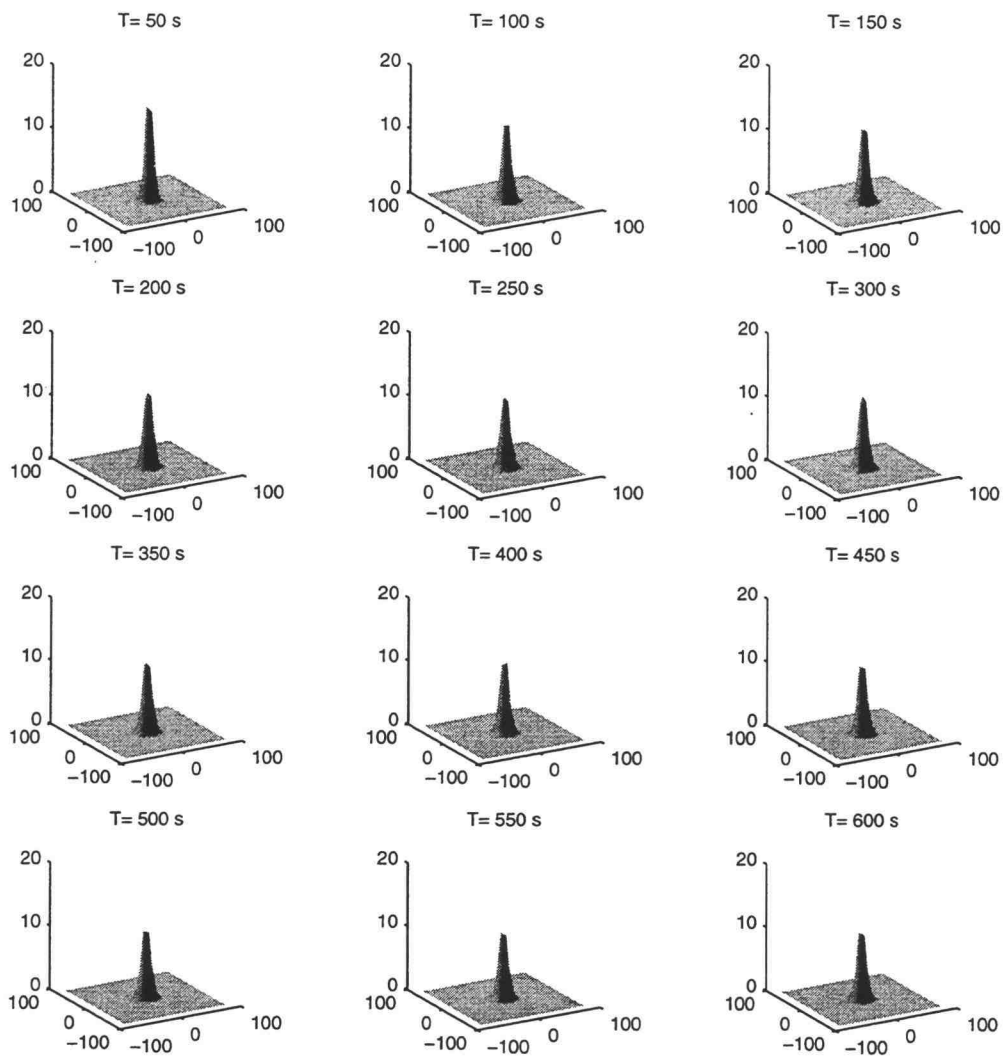


Figure 6.11 3-D Surface Plots of Evolution of RH Model Joint PDF Estimation for $H_s=4.7$ ft, $T_p=8.2$ s

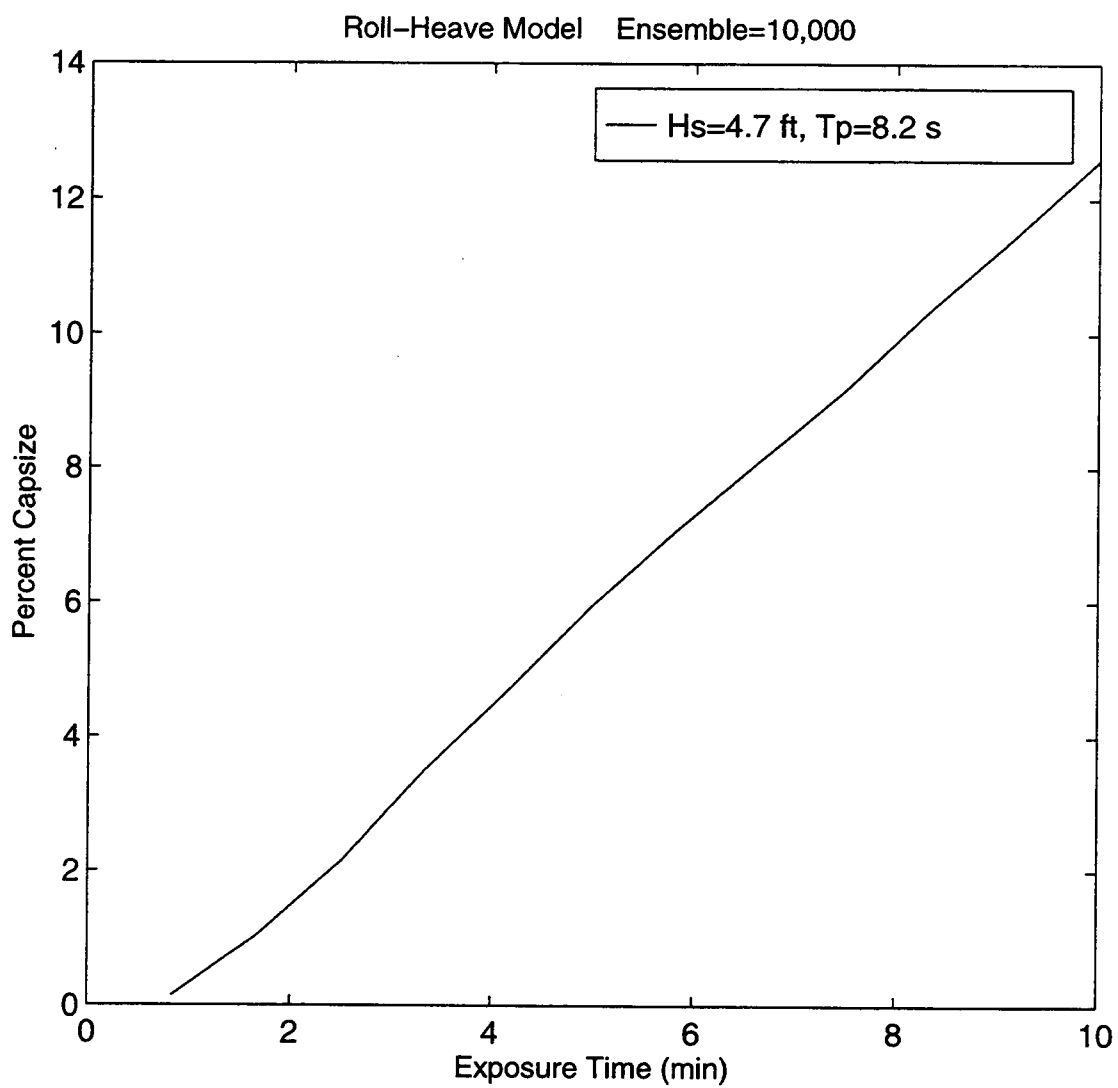


Figure 6.12

Curve of Estimates of Percentage of Capsize for RH Model

7. OBSERVED SENSITIVE NONLINEAR BEHAVIOR

Upon identifying the added inertia, added mass and damping coefficients in the equations of motion in Section 4, we found some new and interesting cases where the barge motions became irregular or "chaotic" (Moon, 1992) by slight changes in the system parameters. Sometimes the transient response becomes longer and chaotic in the sense there are no periodicities even with a period deterministic input wave load and wave moment. Other times, the response may become steady state and then diverge into chaotic response. Finally, we show an example where the barge takes on a positive and negative heel list angle (loll angle) and travels back and forth between these "double wells" from the wave excitation. All these cases are for deterministic input waves and may appear for a short time in the random wave input but is not so obvious because it is mixed in with the random response.

7.1 Transient Chaotic Response

For the case of regular wave ($H=6$ ft, $T=5$ s) excitation, the predicted compared best with the measured data for damping ratios of 32% for roll, 2.5% for heave and 1.5% for sway. These results were presented in Section 4.2 (with more details in Appendix B). If the damping ratios are changed to 2.5% for roll, 20% for heave and 1.5% for sway, the response has a transient lasting about 720 seconds and finally becomes periodic (Figure 7.1). The transient appears chaotic by the irregularity in the transient. The long transient occurs in the heave and sway as well. This is not the case

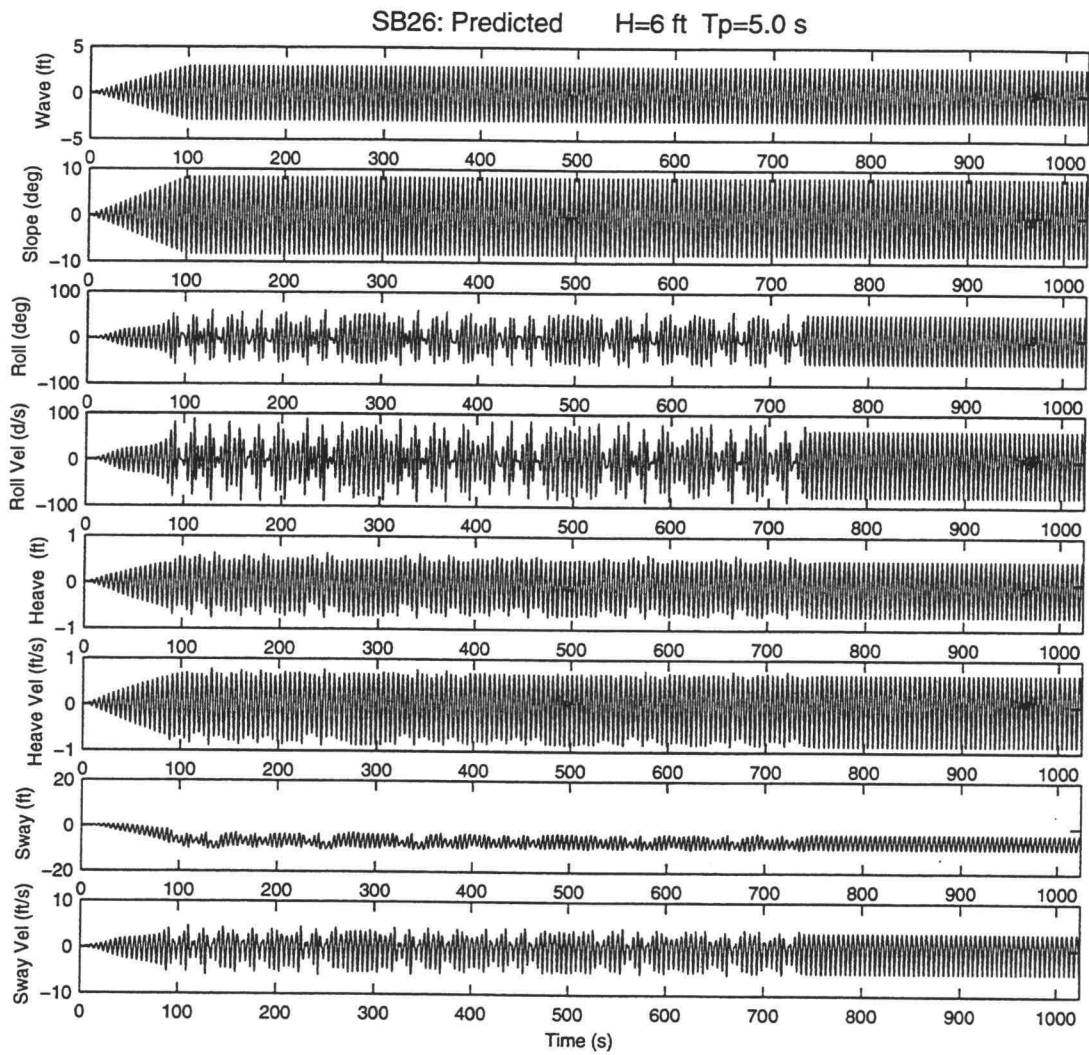


Figure 7.1

Time Series of Transient Chaotic Response

for behavior explained in Section 7.2 or 7.3. A phase plane plot of the roll vs roll angular velocity is provided in Figure 7.2. The dark line is the eventual steady state limit cycle.

7.2 Intermittent and Complete Chaotic Response

In this case, the sensitivity to coefficients occurred for regular waves, $H=7$ ft, $T=8$ s. If the predicted values for roll linear and nonlinear damping ratios of 5%, heave 20% and sway 1.5%, then regular periodic response occurs. The predicted time domain response is shown in Figure 7.3 as well. The corresponding phase plane and Poincaré map are shown in Figure 7.4 and 7.5.

If the damping ratios for roll are set to 2.5%, 20% for heave and 1.5% for sway, then the roll response becomes chaotic (Figure 7.6). The phase plane shows the transient chaos (Figure 7.7) and the Poincaré map (Figure 7.8) shows some order in the "randomness" of the response. The simulation was run for 10,000 seconds and the chaotic response never becomes periodic (Figure 7.9).

7.3 Roll List Response

This sensitivity study shows some effects of raising the vertical center of gravity of the barge. The KG was initially set at 1.23 ft above the deck of the barge as this closely approximates a U.S. Navy mission case (NFESC, 1995). The response in roll is shown in Figure 7.10 and 7.11. Here the response slowly moves from a steady state

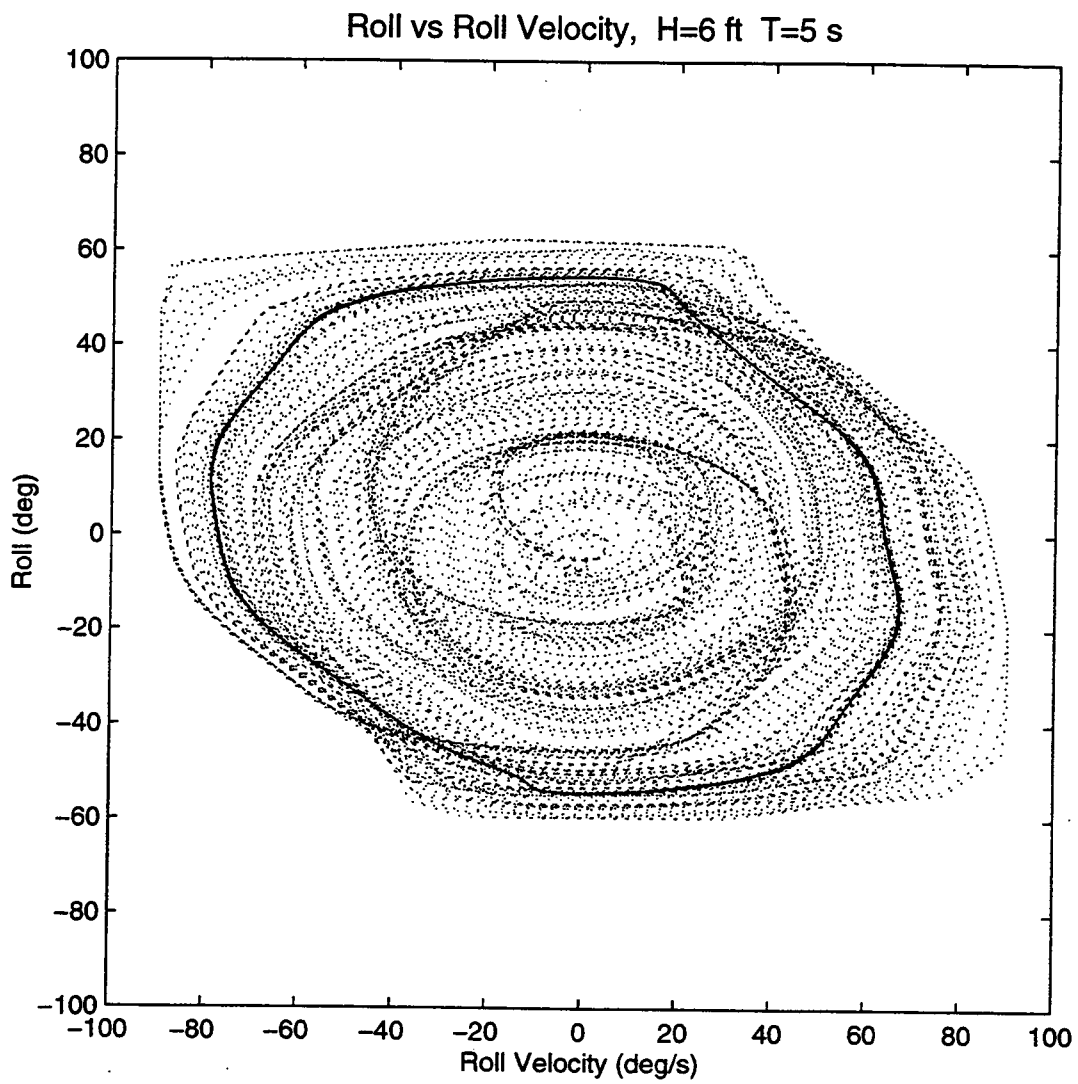


Figure 7.2

Roll and Roll Velocity Phase Plane

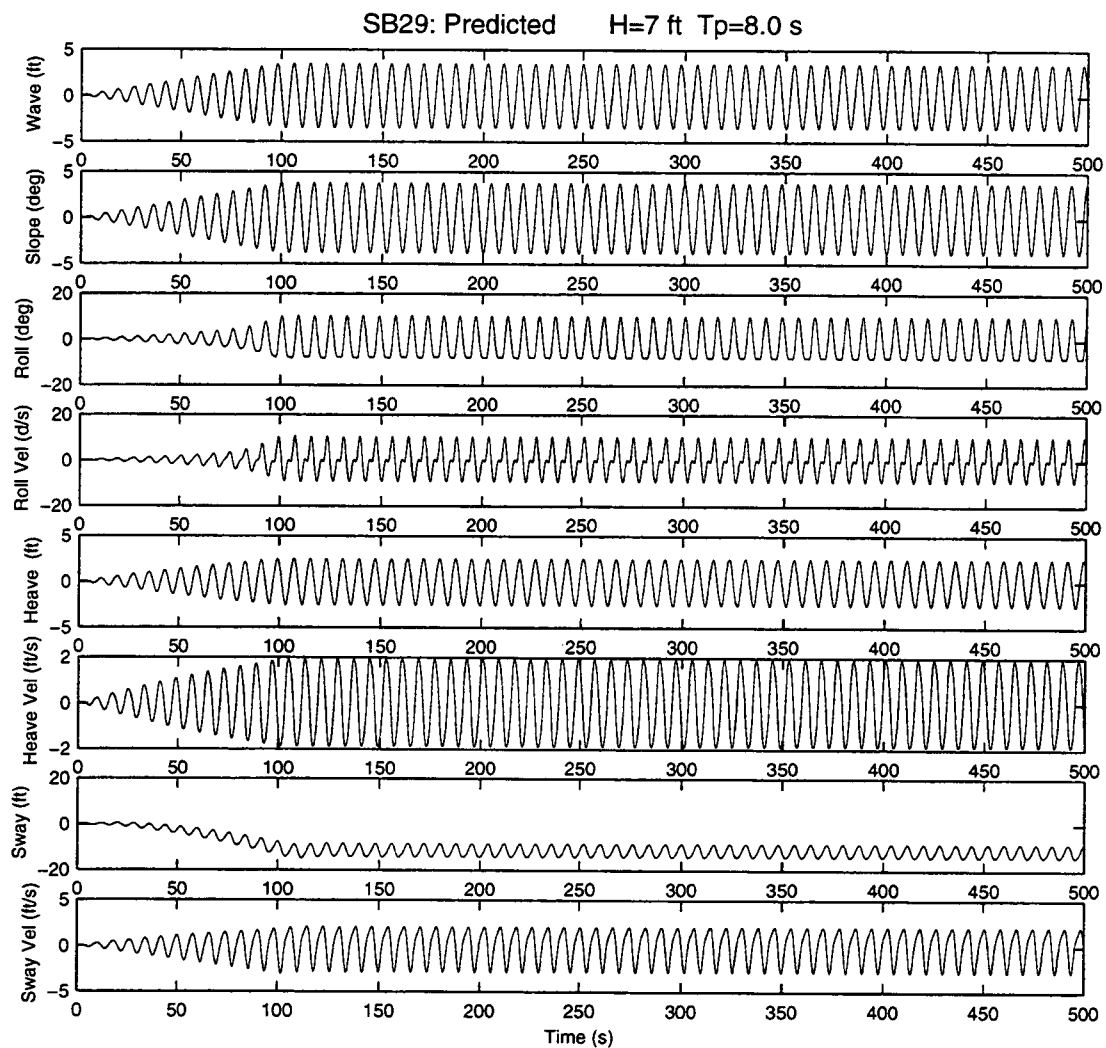


Figure 7.3

Time Series of Periodic Roll Response

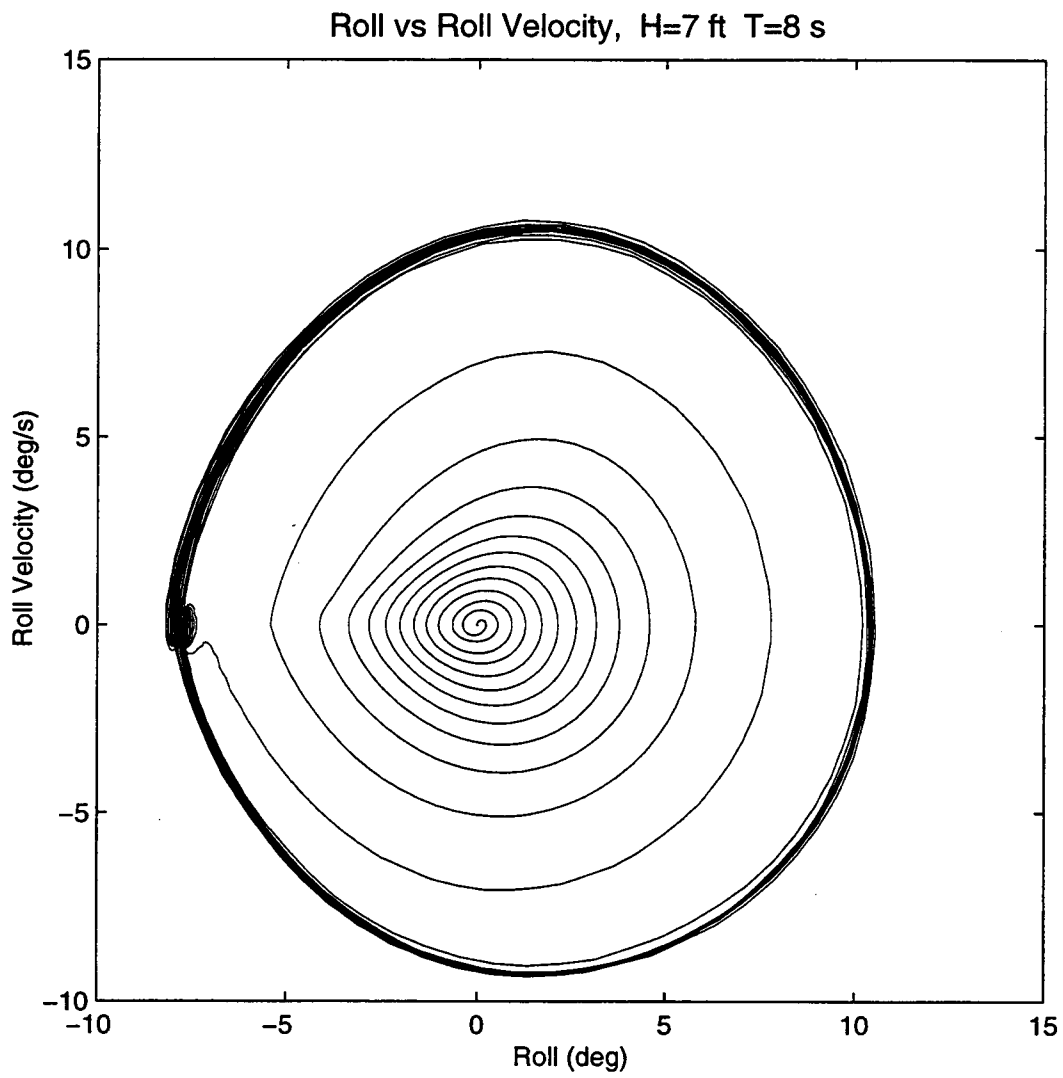


Figure 7.4

Phase Plane for Periodic Roll

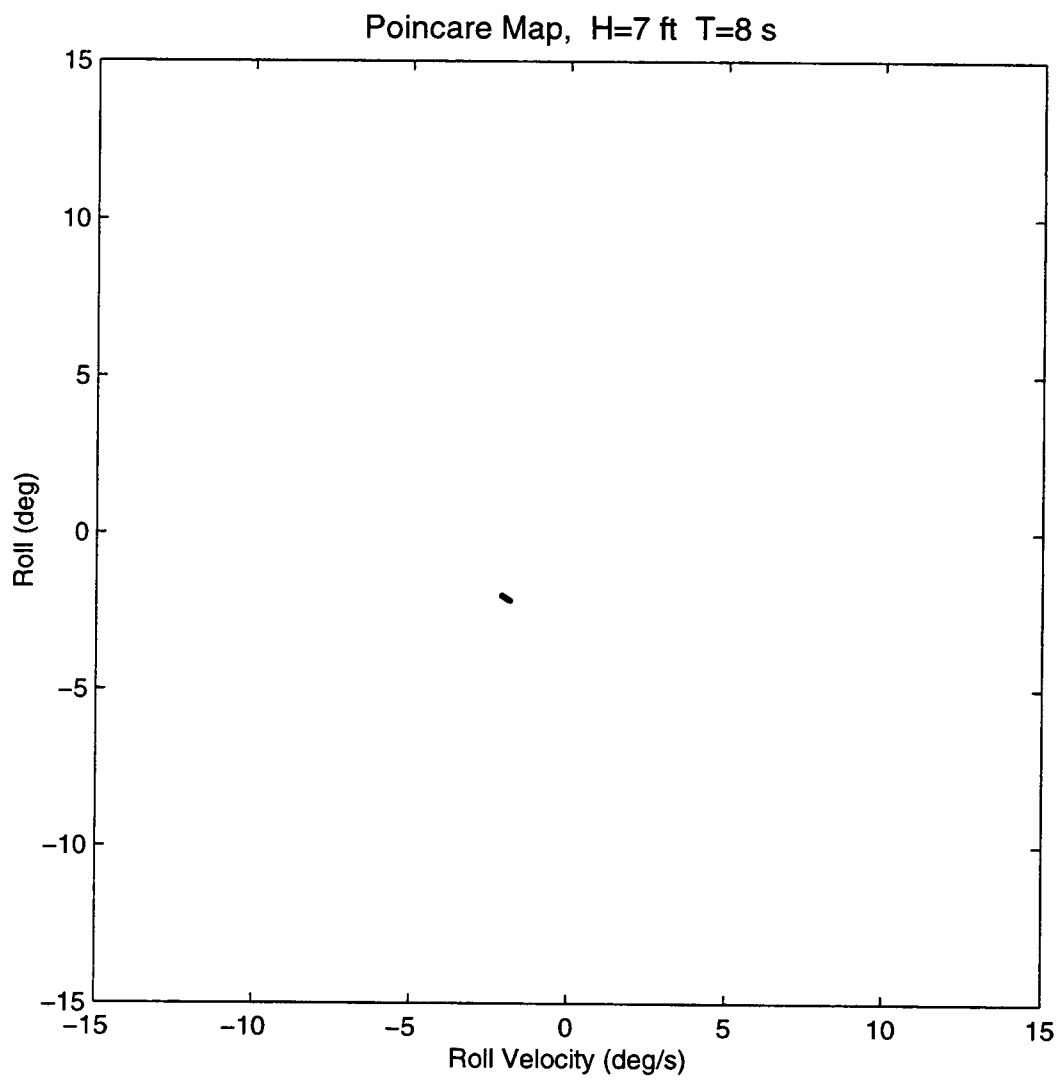


Figure 7.5

Poincare Map for Periodic Roll

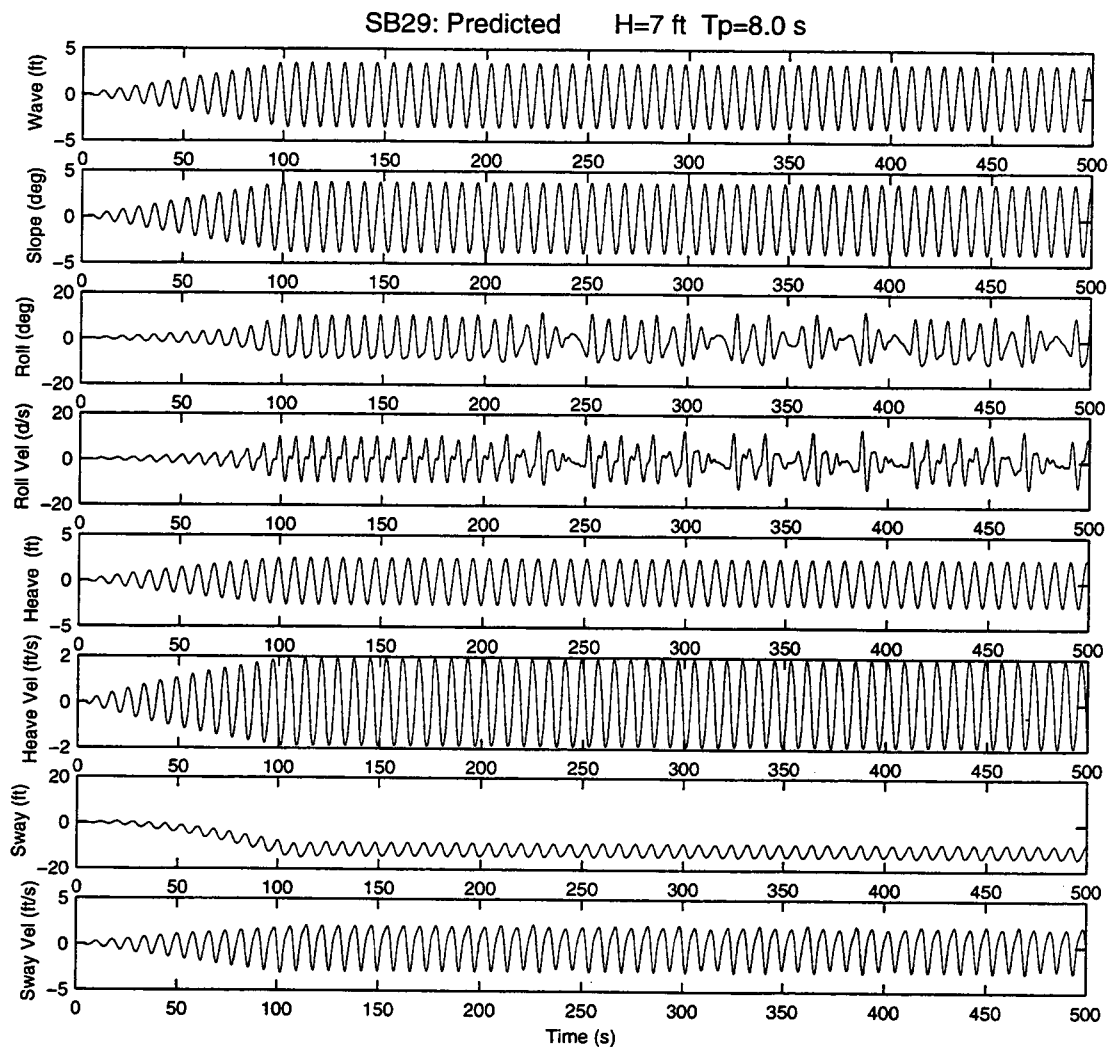


Figure 7.6

Time Series for Chaotic Response for Roll

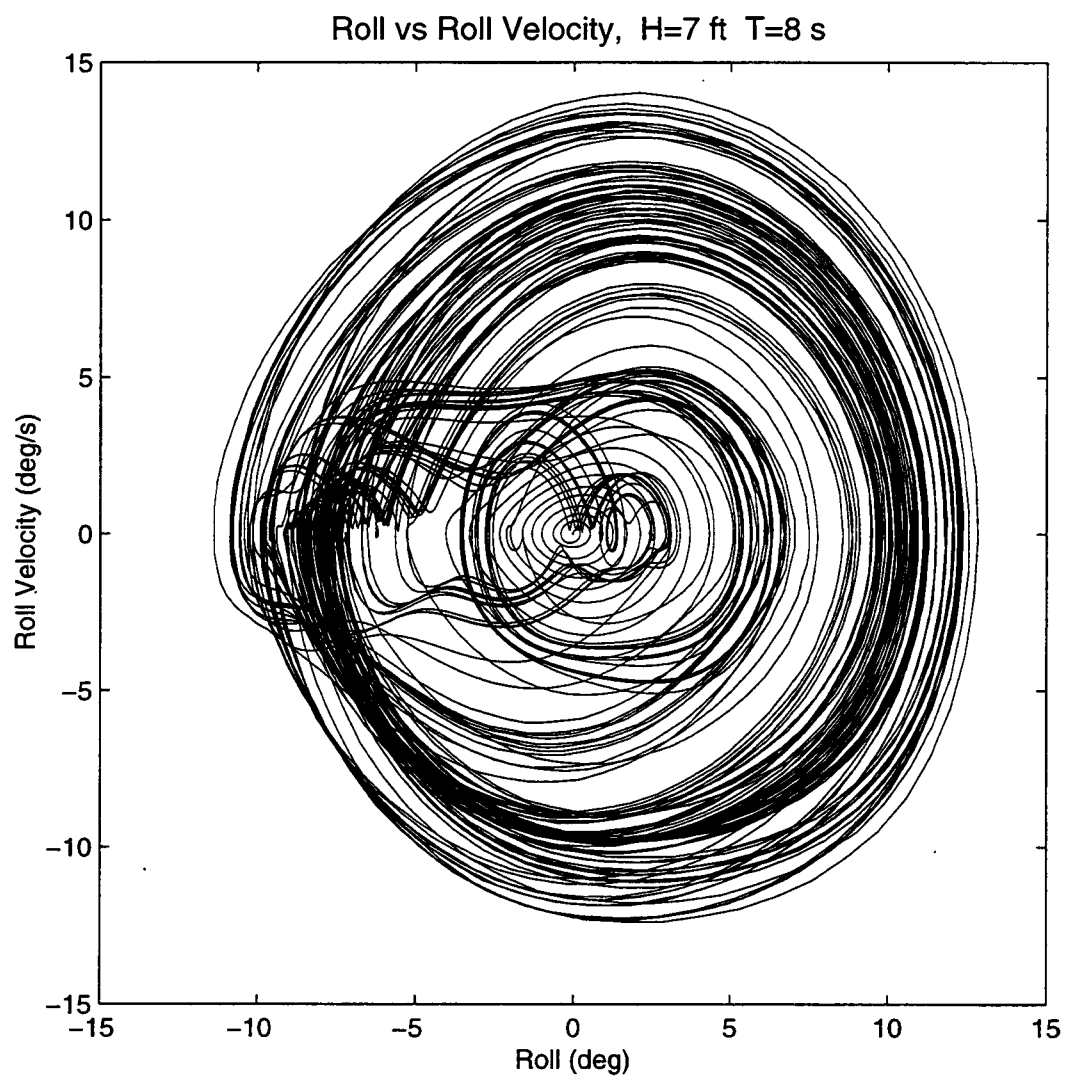


Figure 7.7

Phase Plane for Chaotic Roll

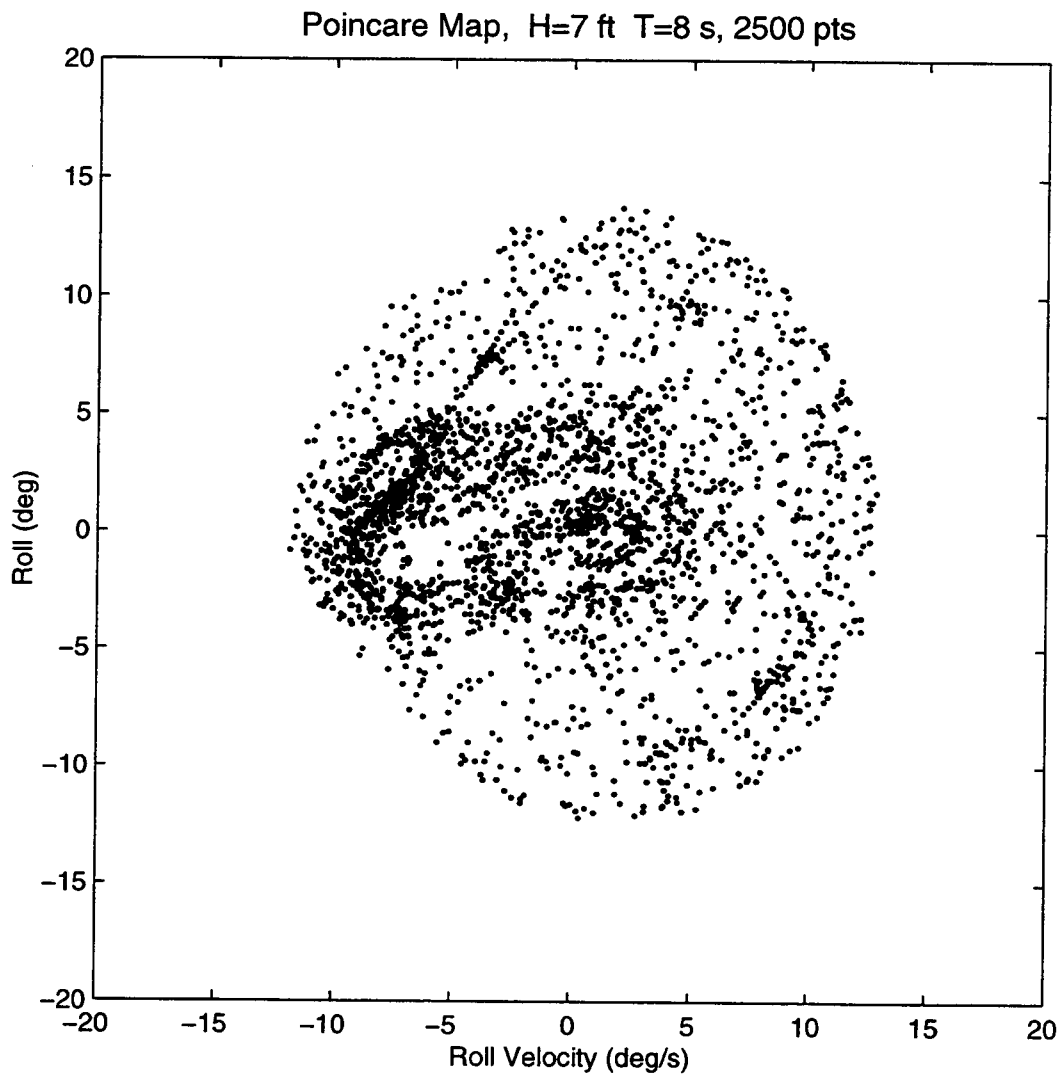


Figure 7.8

Poincare Map for Chaotic Roll

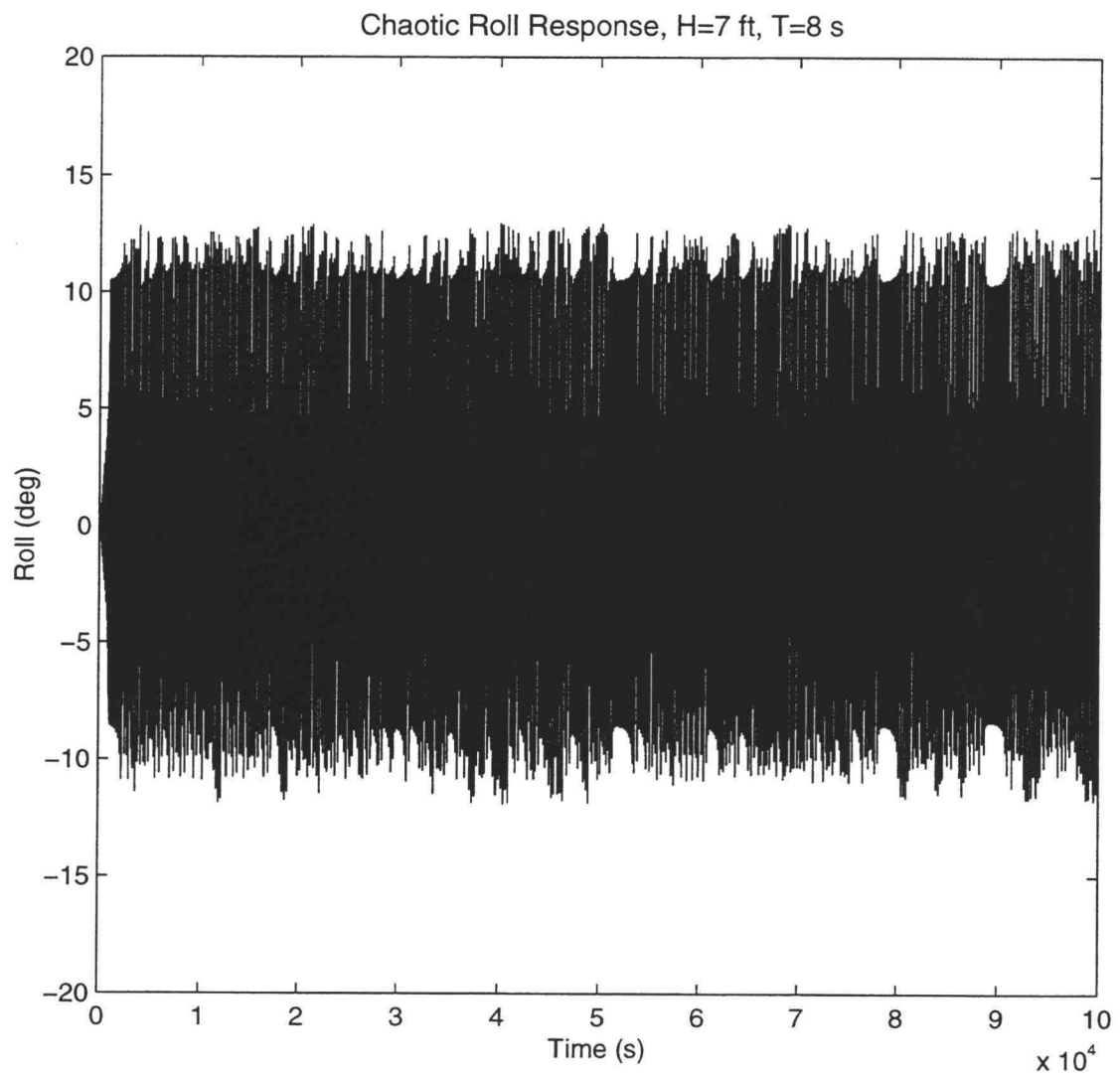


Figure 7.9

Long Time Series for Chaotic Roll

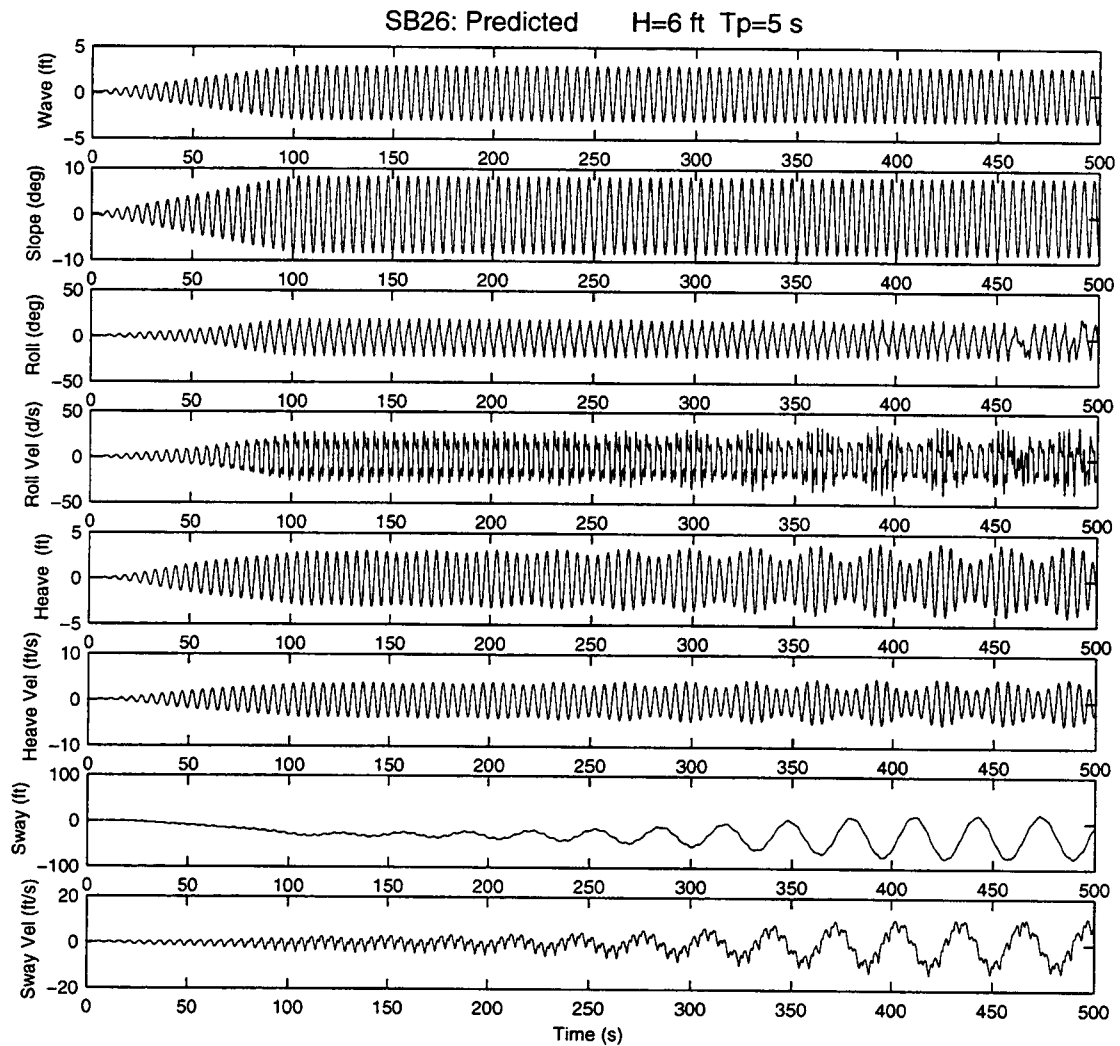


Figure 7.10

Time Series of Response for KG=9.23 ft

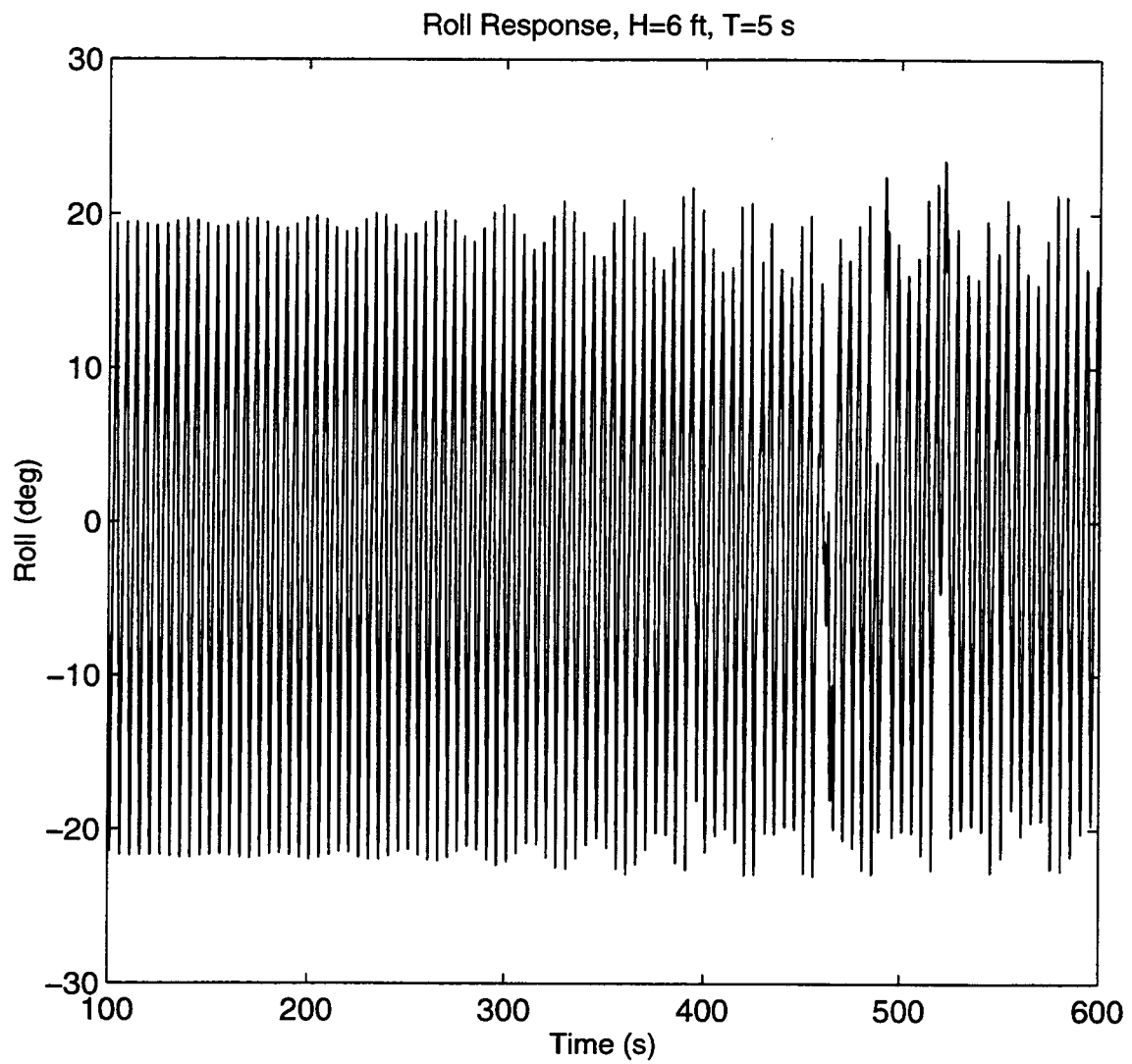


Figure 7.11

Roll Time Series for $KG=9.23$ ft

situation into intermittent chaos. The phase plane for the initial steady state response is shown in Figure 7.12 and then at a later time is shown in Figure 7.13. Figure 7.12 shows the initial transient spiraling outward to the limit cycle whereas Figure 7.13 shows the chaotic response near the limit cycle.

Now if the center of gravity is raised two more feet, from $KG=9.23$ ft to 11.23 ft, the behavior changes again to that shown in Figure 7.14 and 7.15. The roll finds equilibrium wells at about ± 12 degrees and oscillates between these roll list angles. The phase plane and Poincaré Map are shown in Figure 7.16 and 7.17, respectively. The phase plane begins to take on the appearance of a double well system.

If the center of gravity is shifted vertically up another foot, the roll list angle becomes less frequent (Figure 7.18). A shortened time segment for the roll list is shown in Figure 7.19. The corresponding phase plane shows less time spent in one well as shown by the lighter and darker lines in Figure 7.20. A 3-D trajectory plot of roll, heave and sway is seen in Figure 7.21.

One possible consequence of this sensitive nonlinear behavior is that the roll response may become attracted to equilibrium points right before capsize and may even prevent capsize. These sensitivities may be difficult to identify for the barge in random waves.

7.4 Wave Height Sensitivity

Some interesting results were obtained for the regular wave case of $H=6$ ft, $T=8$ s, when the wave height was decreased or increased by about 0.5 ft. Figures

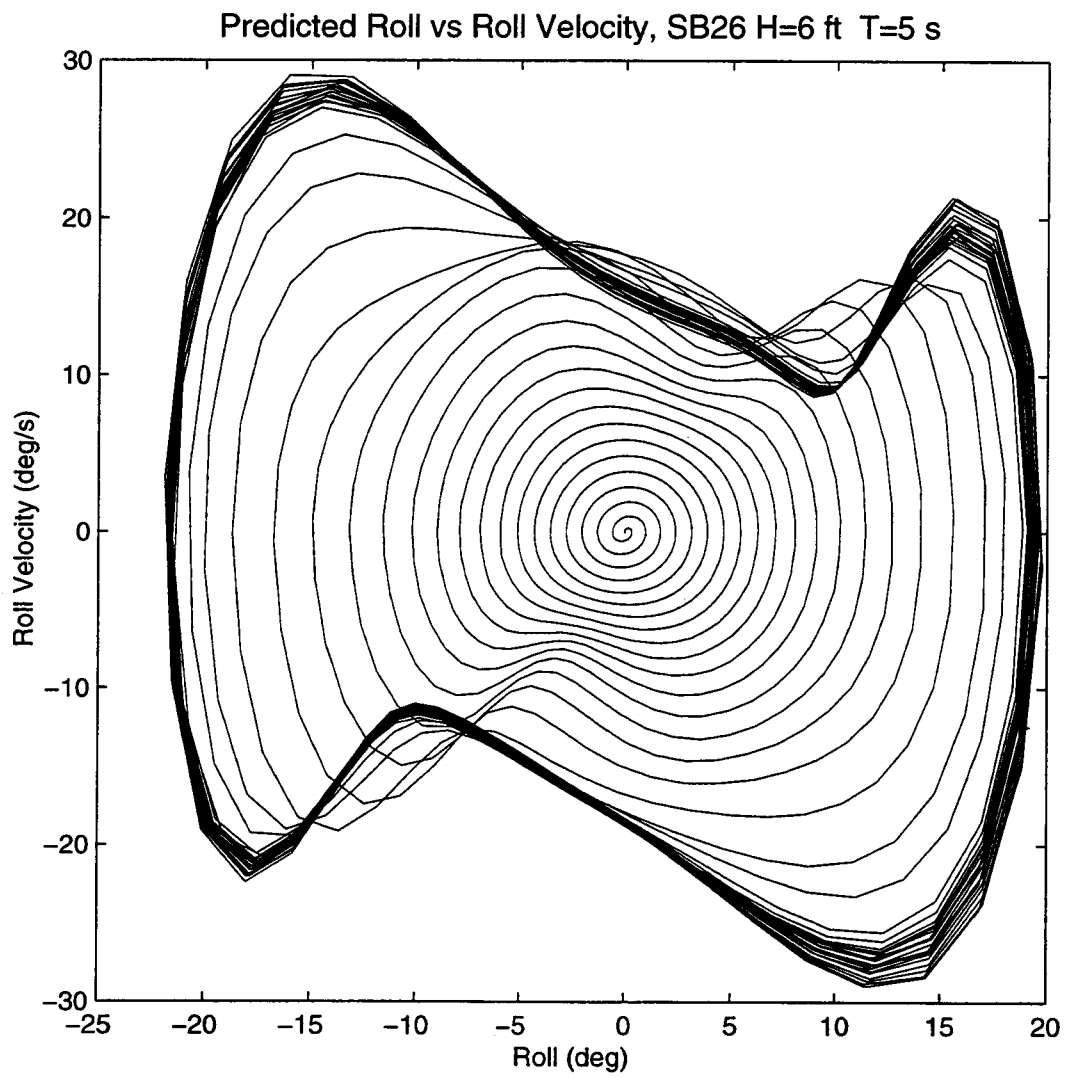


Figure 7.12

Phase Plane for Roll before Chaos with $KG=9.23$ ft

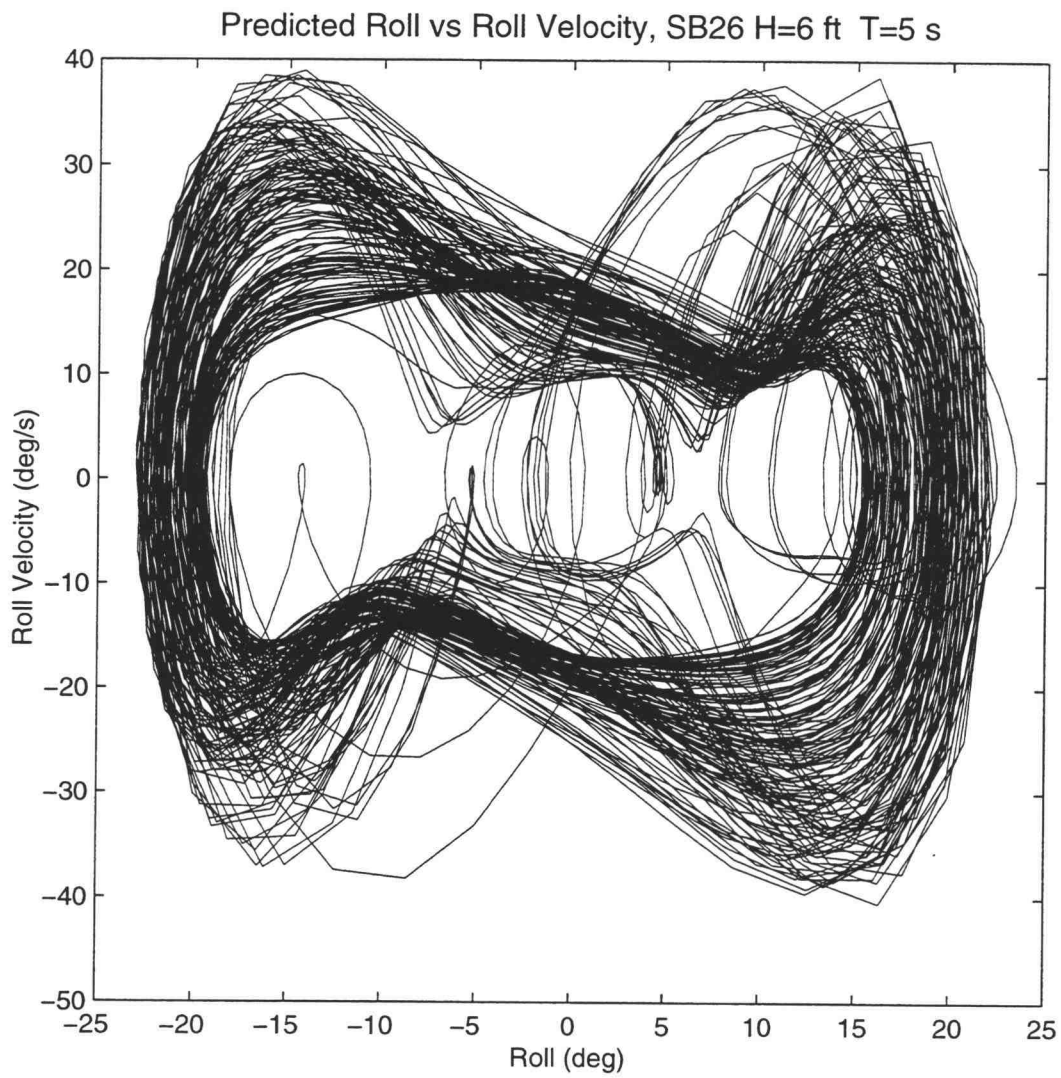


Figure 7.13

Phase Plane for Roll with Chaos, KG=9.23 ft

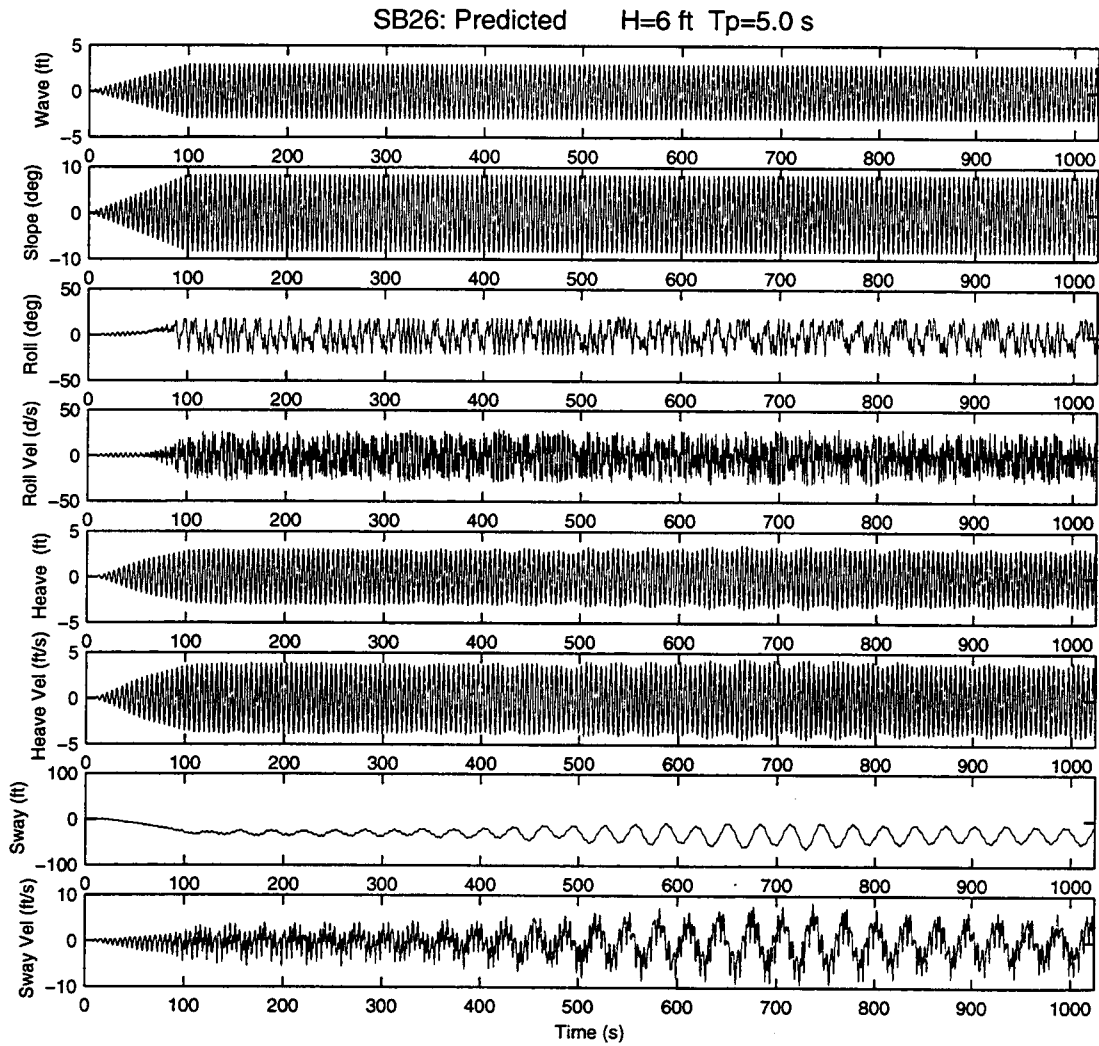


Figure 7.14

Time Series of Response, $KG=11.23$ ft

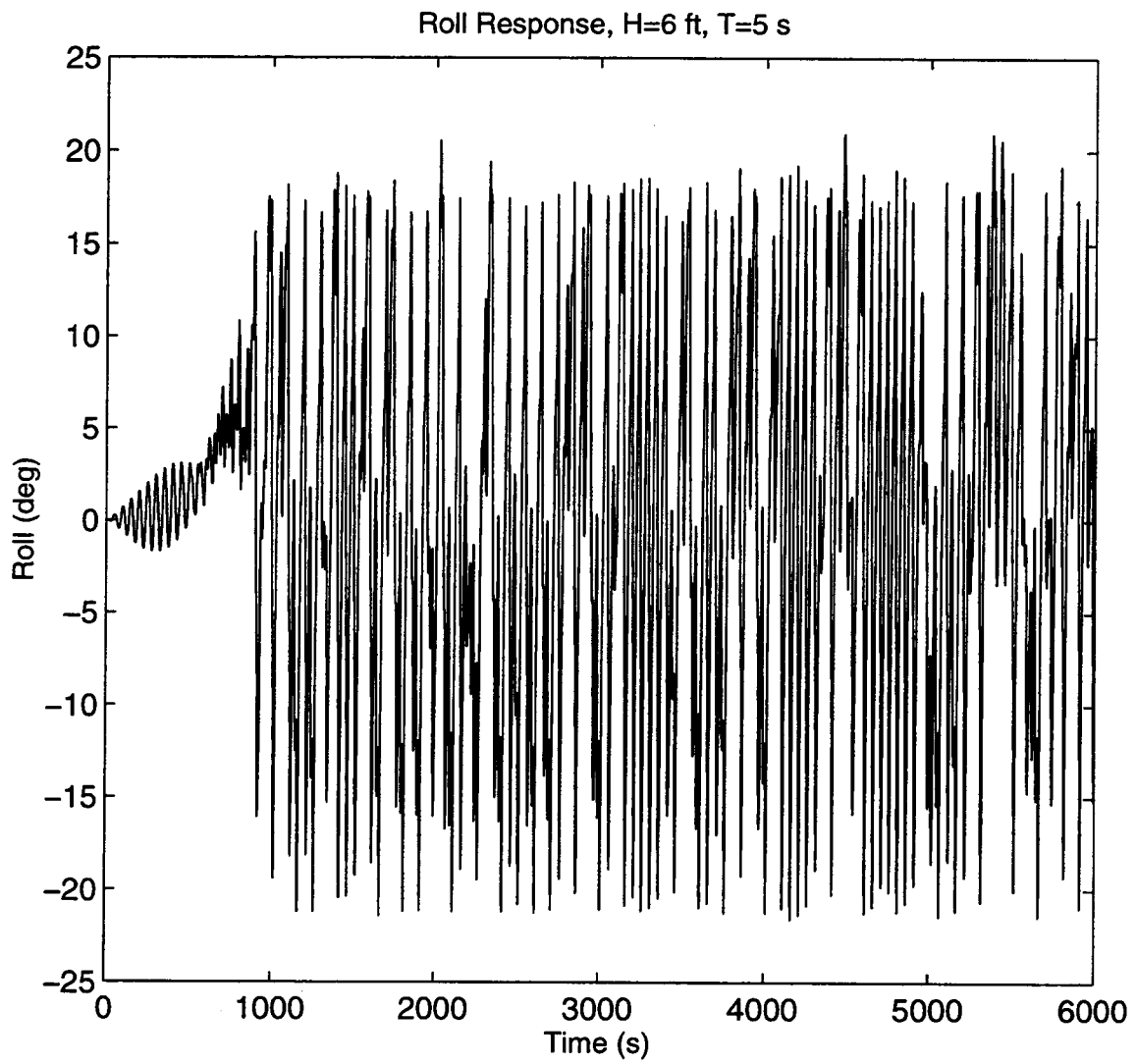


Figure 7.15

Roll Time Series for $KG=11.23$ ft

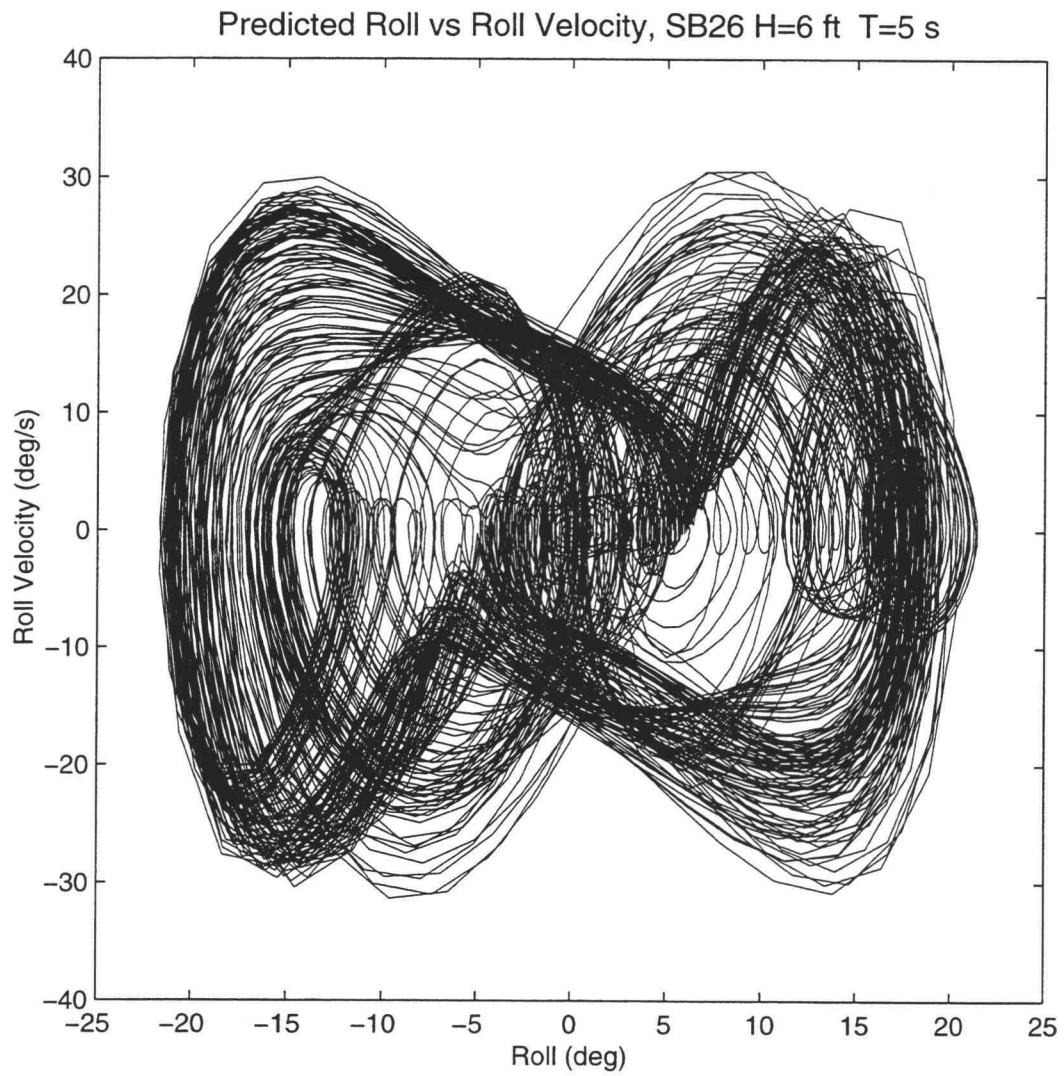


Figure 7.16

Phase Plane for Roll, KG=11.23 ft

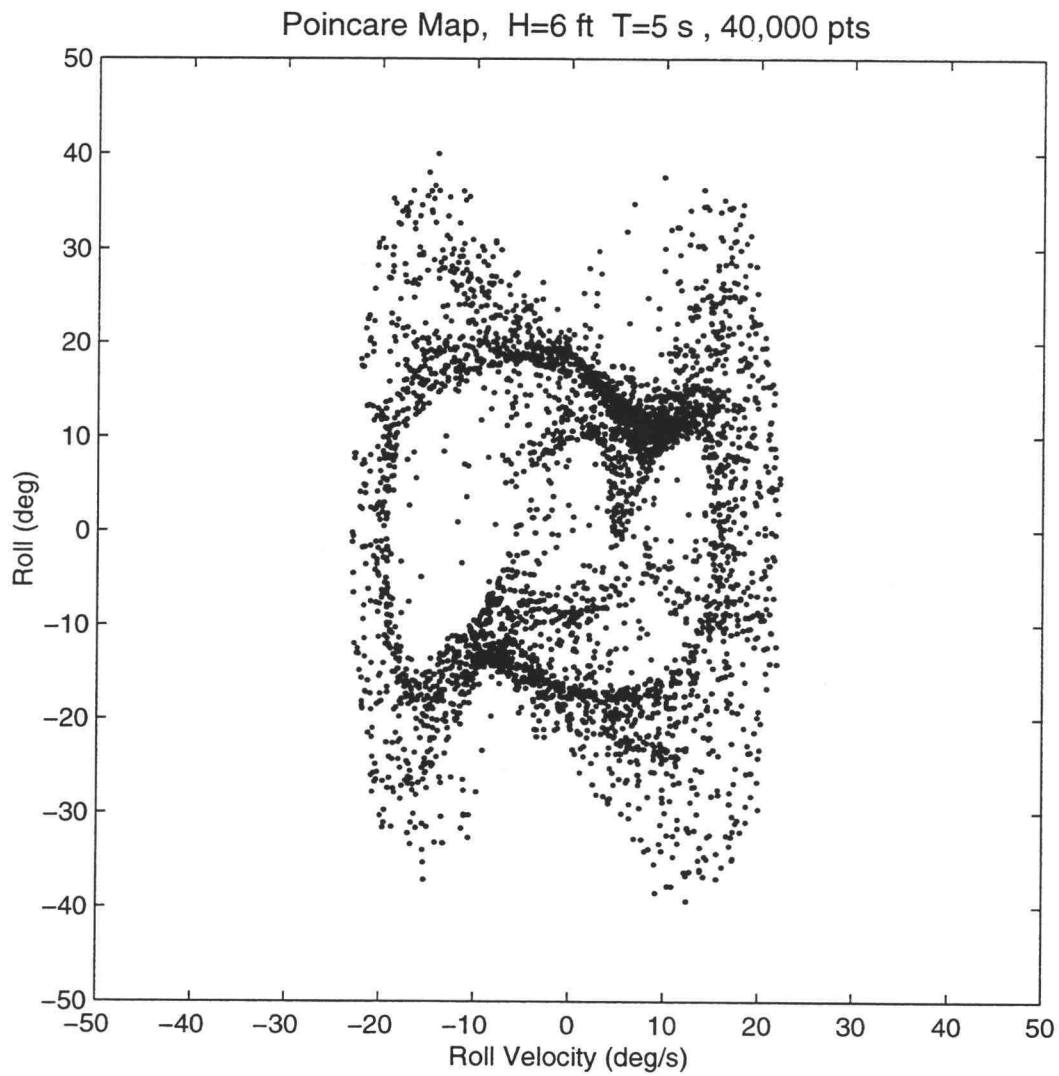


Figure 7.17

Poincare Map, KG=11.23 ft

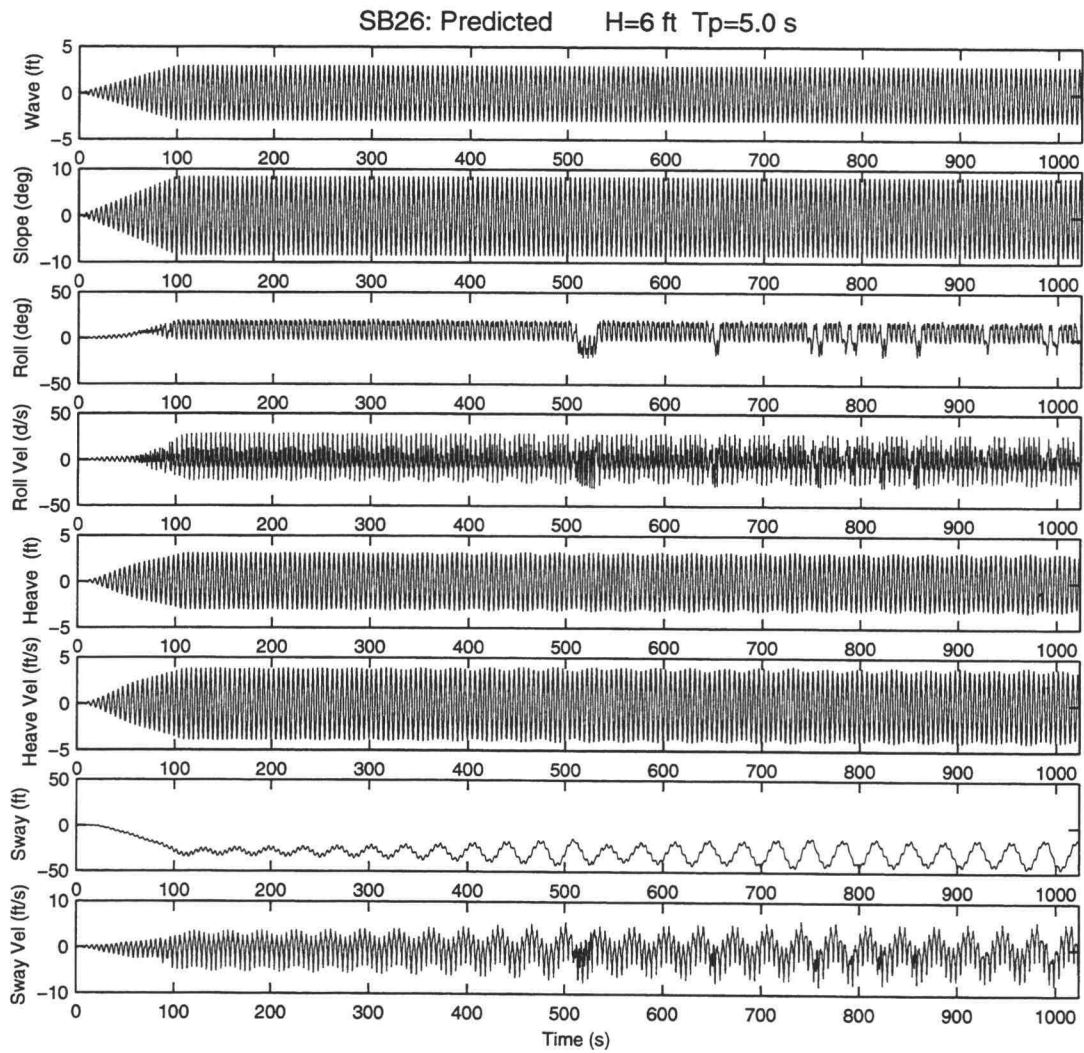


Figure 7.18

Time Series for Intermittent Roll List, KG=12.23 ft

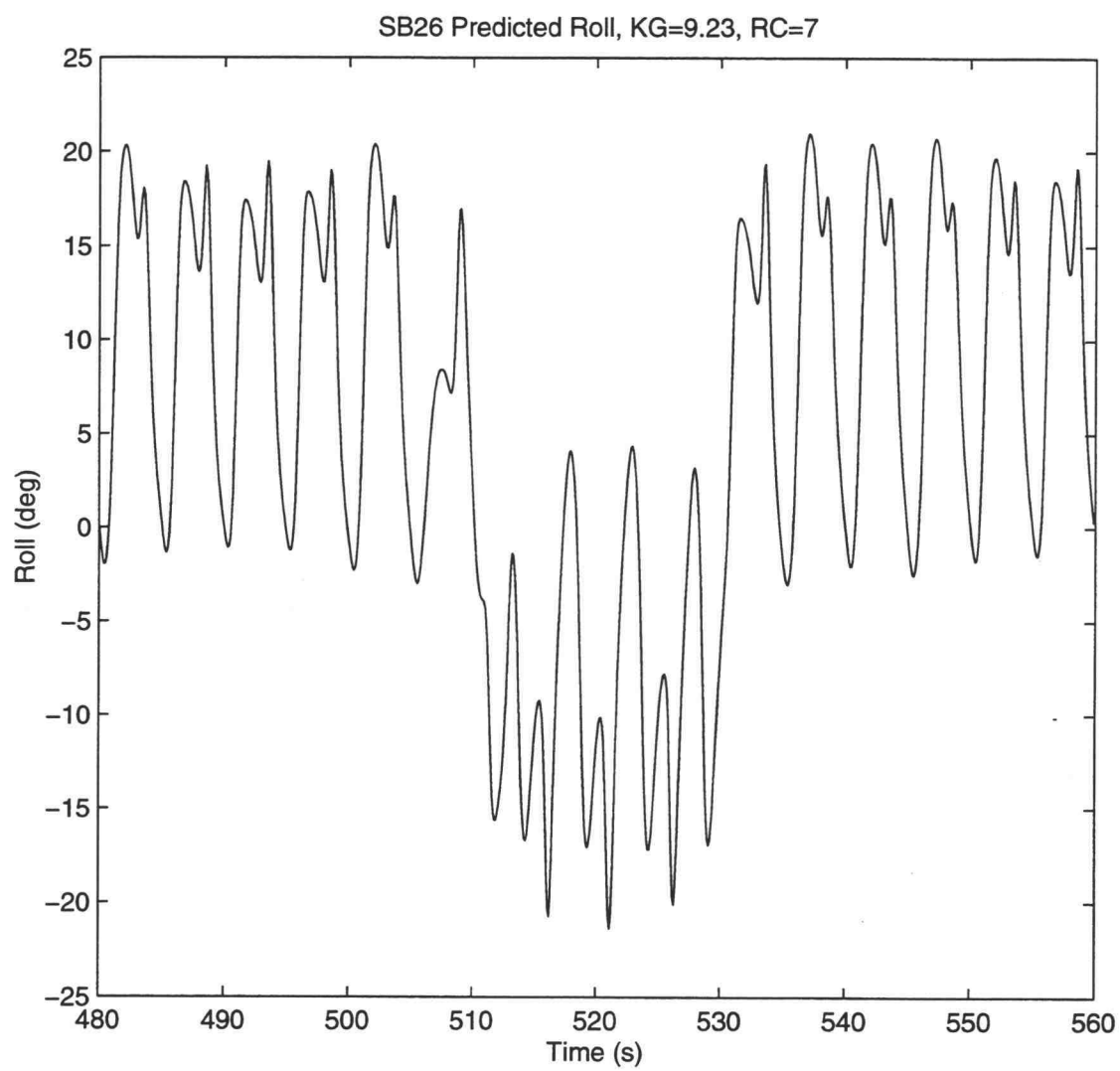


Figure 7.19

Shortened Time Series of Roll List, KG=12.23 ft

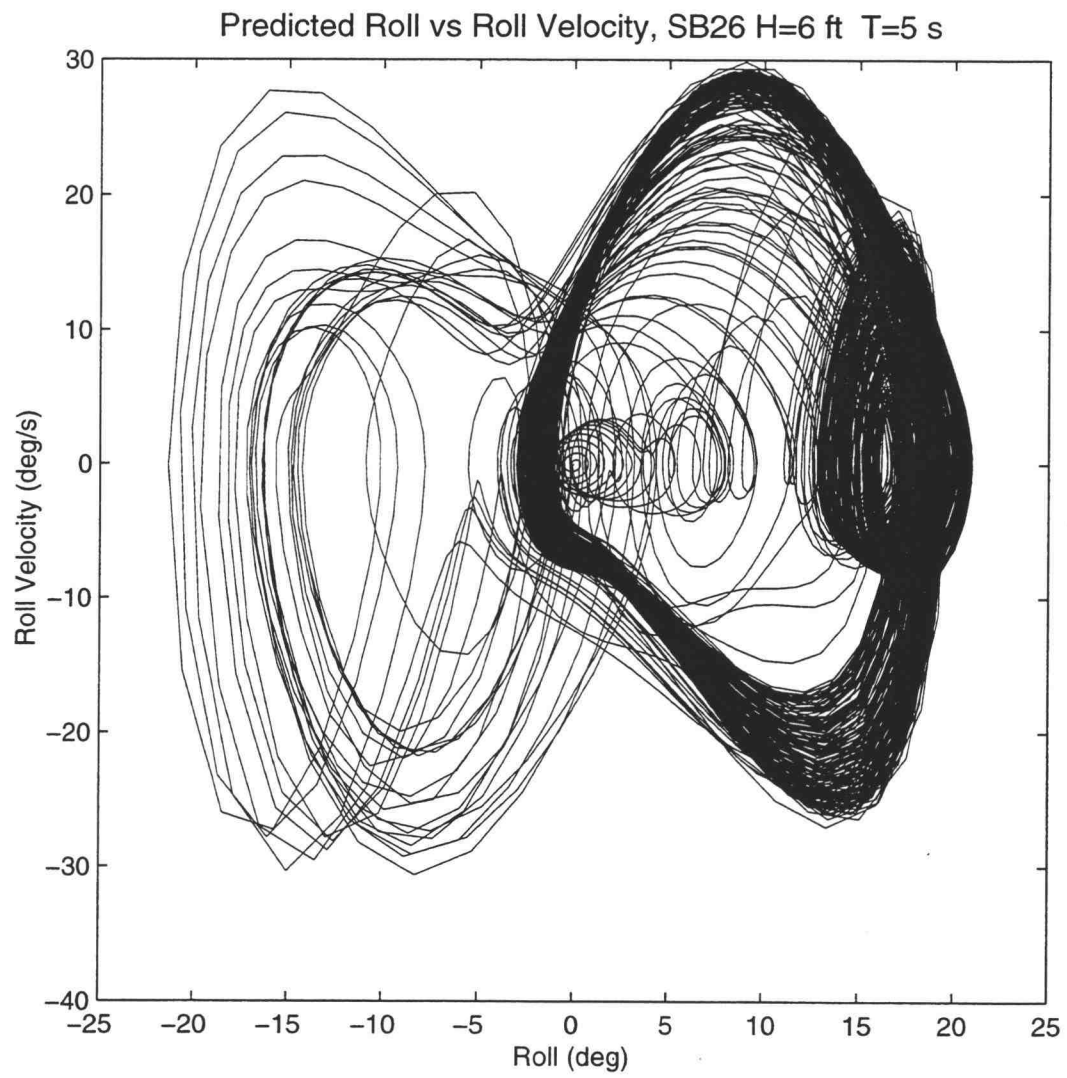


Figure 7.20

Phase Plane for Intermittent List, $KG=12.23$ ft.

Predicted Sway, Heave and Roll, SB26 H=6 ft T=5 s

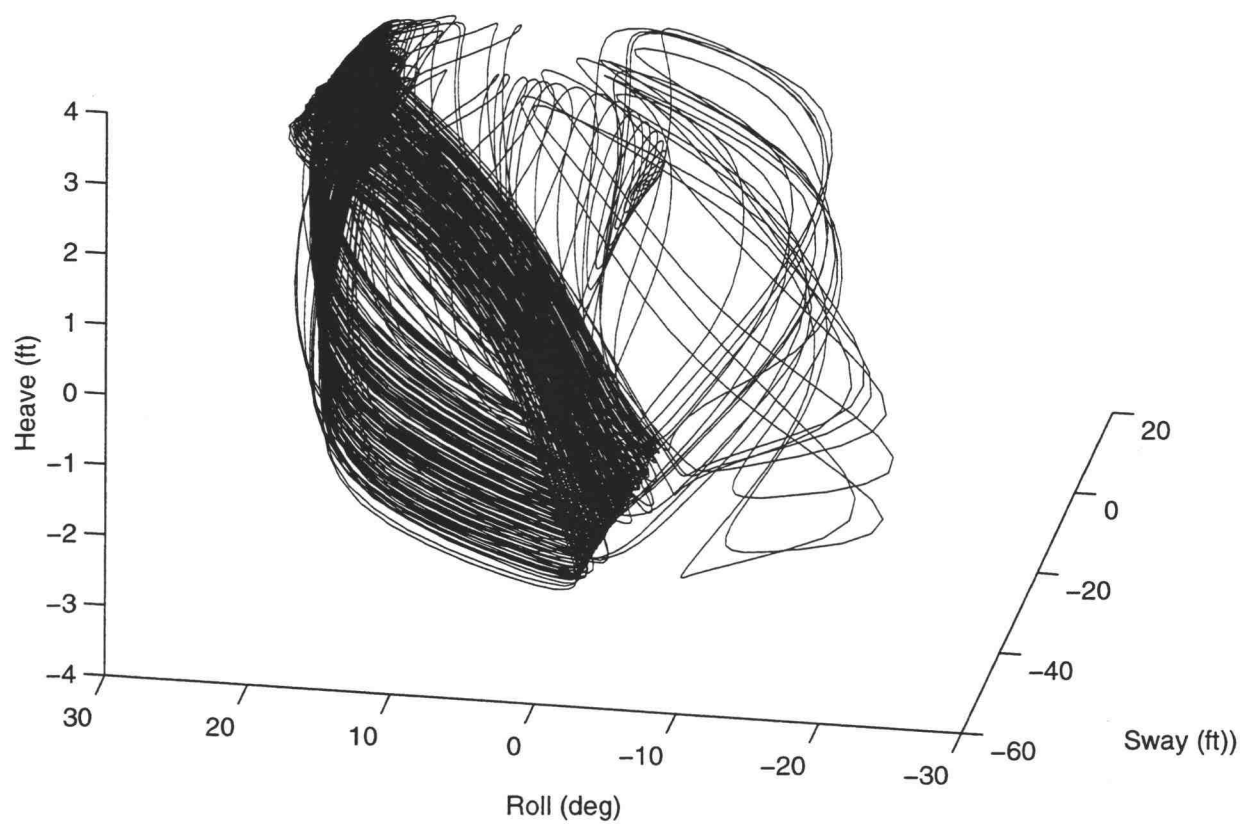


Figure 7.21

3-D Trajectory plot of Roll, Heave Sway, KG=12.23 ft

7.22 and 7.23 show the phase plane and Poincaré map for the roll at $H=6.6$ ft, $T=8$ s. The Poincaré map has a strange appearance in that it seems incomplete. The response was simulated for a much longer duration and the same pattern emerged. Figure 7.24 shows the roll energy being concentrated at three peaks. The 3-D phase plot of roll-roll angular velocity-heave is shown in Figure 7.25.

If the wave height is increased to $H=7.0$ ft with $T=8$ s, the behavior becomes noticeably different as seen in Figure 7.26 to Figure 7.29. Figure 7.27 shows an obvious period two Poincaré map.

If the wave height is again increased to $H=7.4$ ft with $T=8$ s, the character of the response changes again (Figures 7.30 - 7.33). The limit cycle shown in Figure 7.30 is much different than the other two cases. The Poincaré map also changes character as seen in Figure 7.31.

In summary, comparing these series of figures shows the response is in a sensitive nonlinear regime with significant changes in behavior for slight changes in wave height.

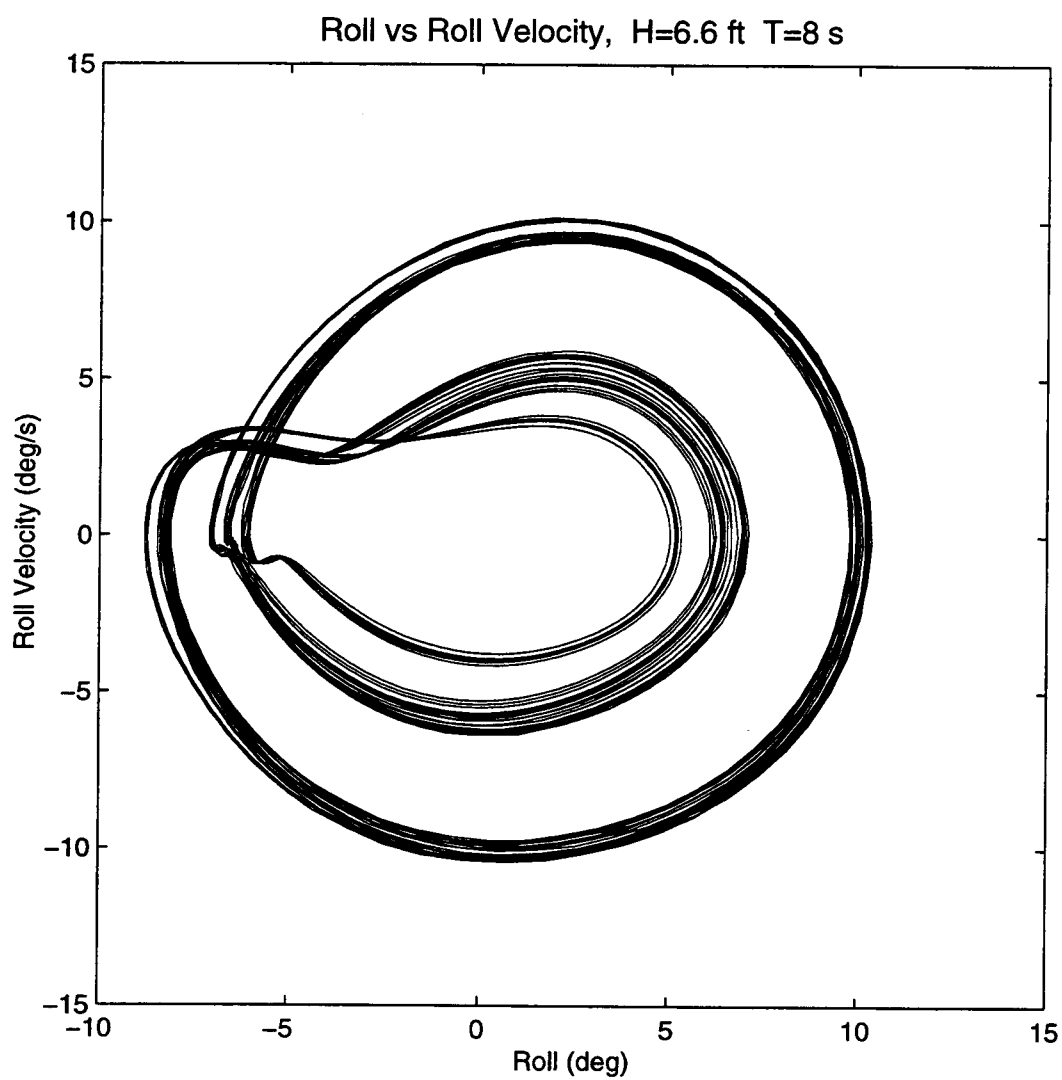


Figure 7.22

Phase Plane for H=6.6 ft, T=8 s

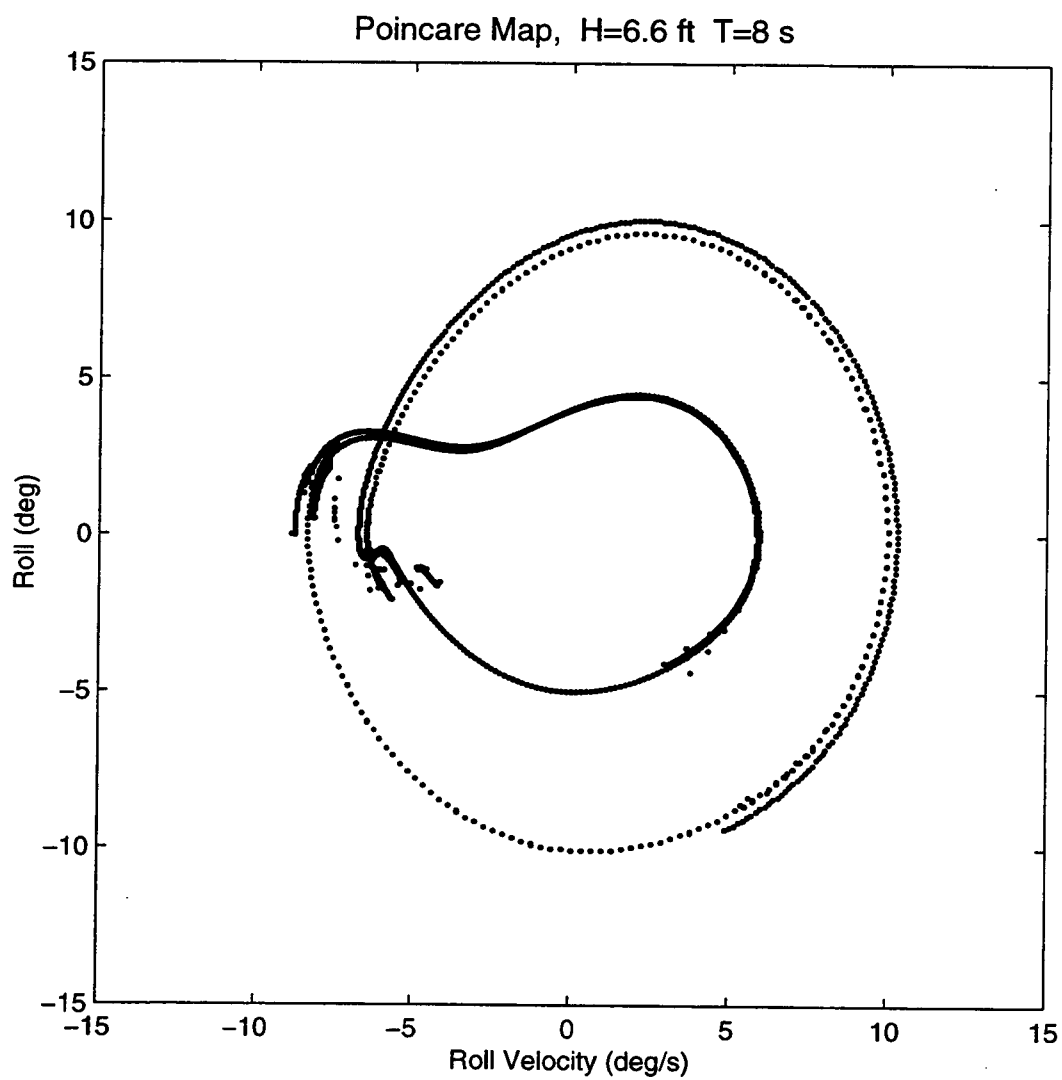


Figure 7.23

Poincare Map for $H=6.6$ ft, $T=8$ s

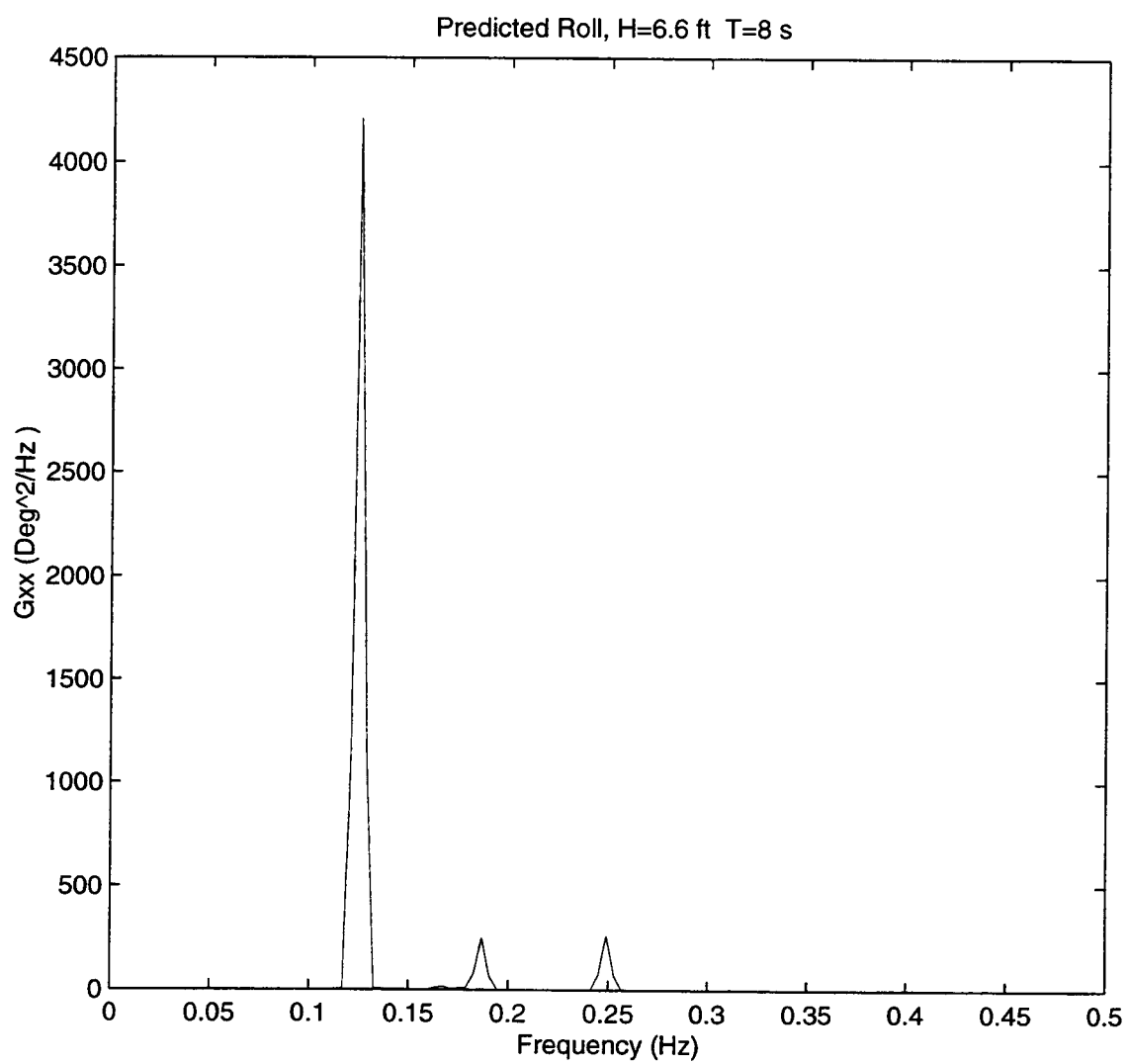


Figure 7.24

Roll Spectral Density for H=6.6 ft, T=8 s

Predicted Roll Vel, Roll and Heave $H=6.6$ ft $T=8$ s

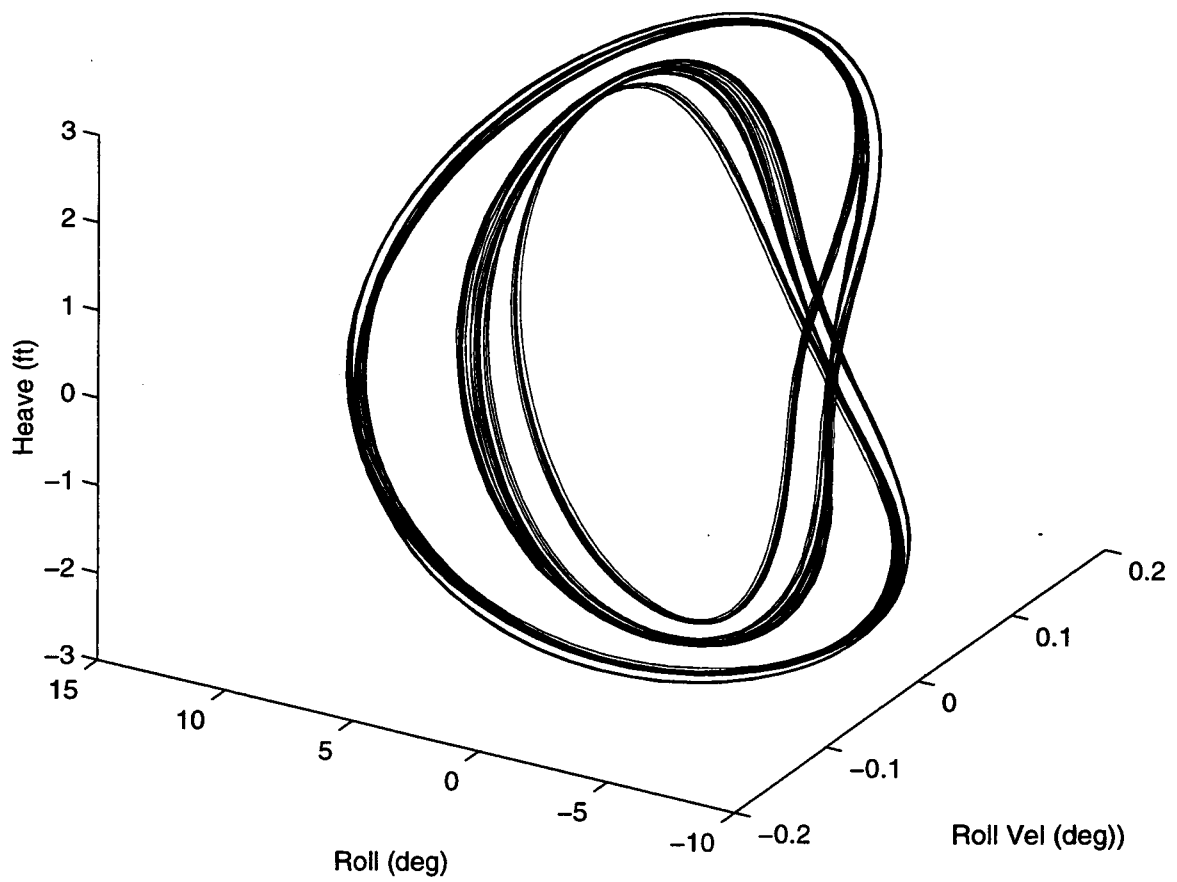


Figure 7.25

3-D Phase-Plane with Heave, $H=6.6$ ft, $T=8$ s

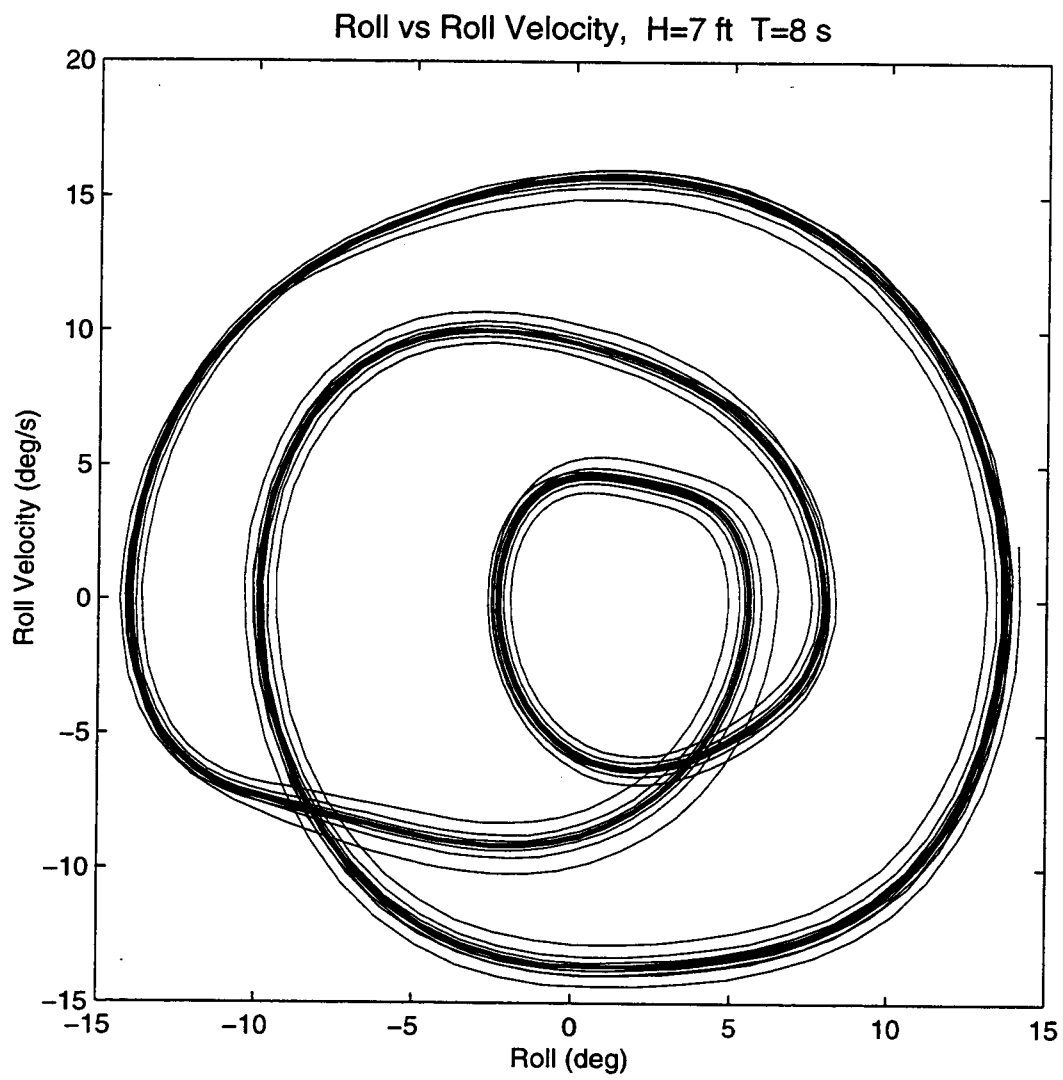


Figure 7.26

Phase Plane for H=7 ft, T=8 s

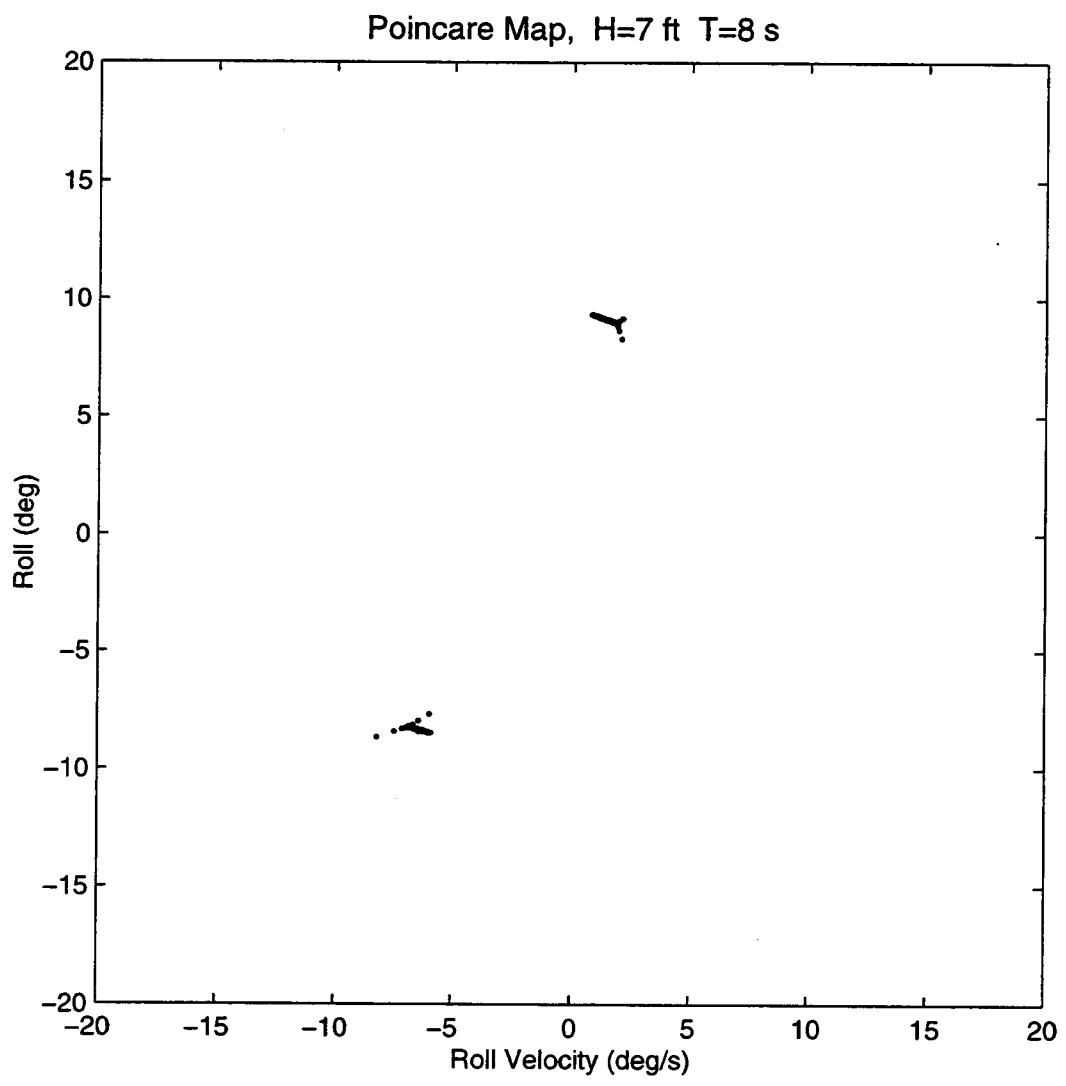


Figure 7.27 Poincare Map for H=7 ft, T=8 s

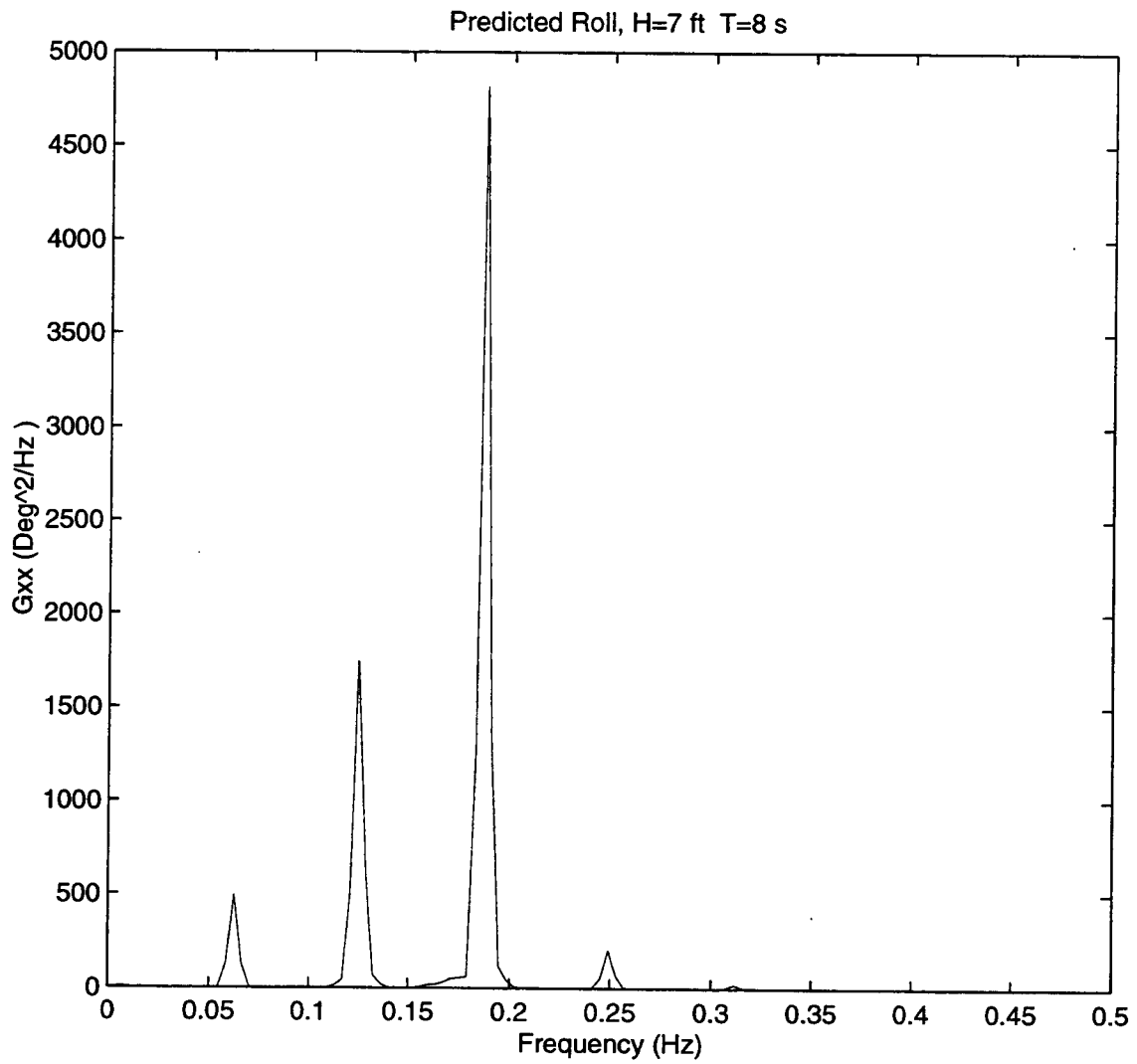


Figure 7.28

Roll Spectral Density for H=7 ft, T=8 s

Predicted Roll Vel, Roll and Heave $H=7.0$ ft $T=8$ s

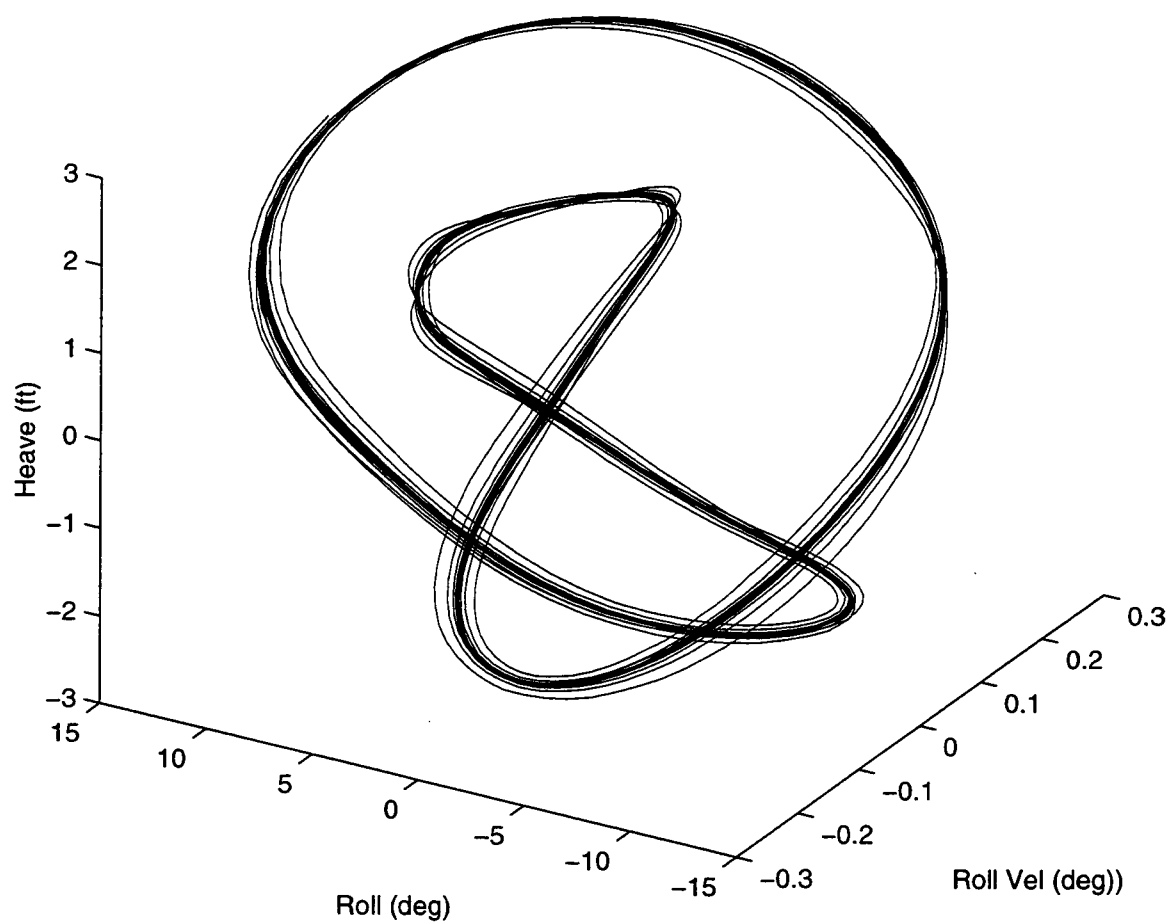


Figure 7.29

3-D Phase-Plane with Heave, $H=7$ ft, $T=8$ s

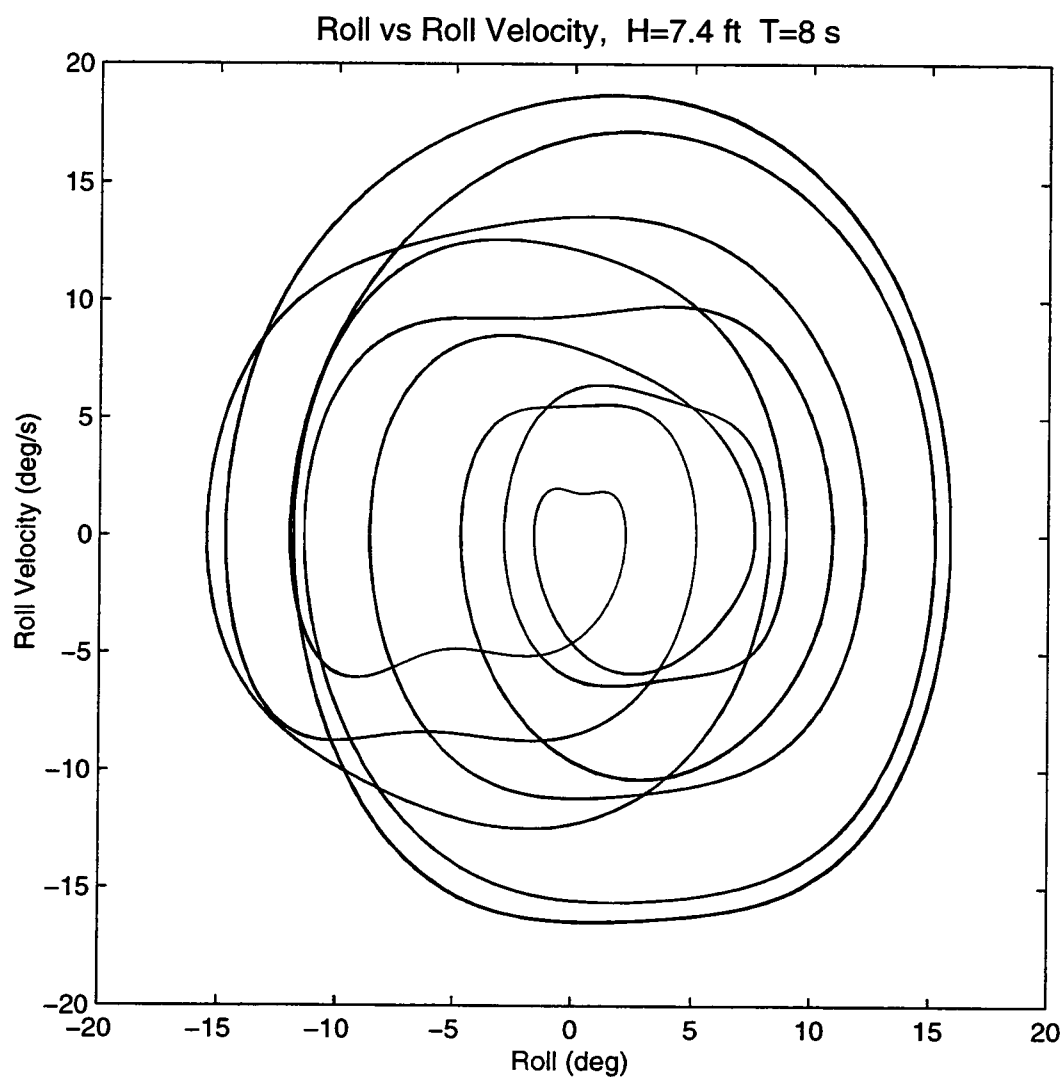


Figure 7.30

Phase Plane for H=7.4 ft, T=8 s

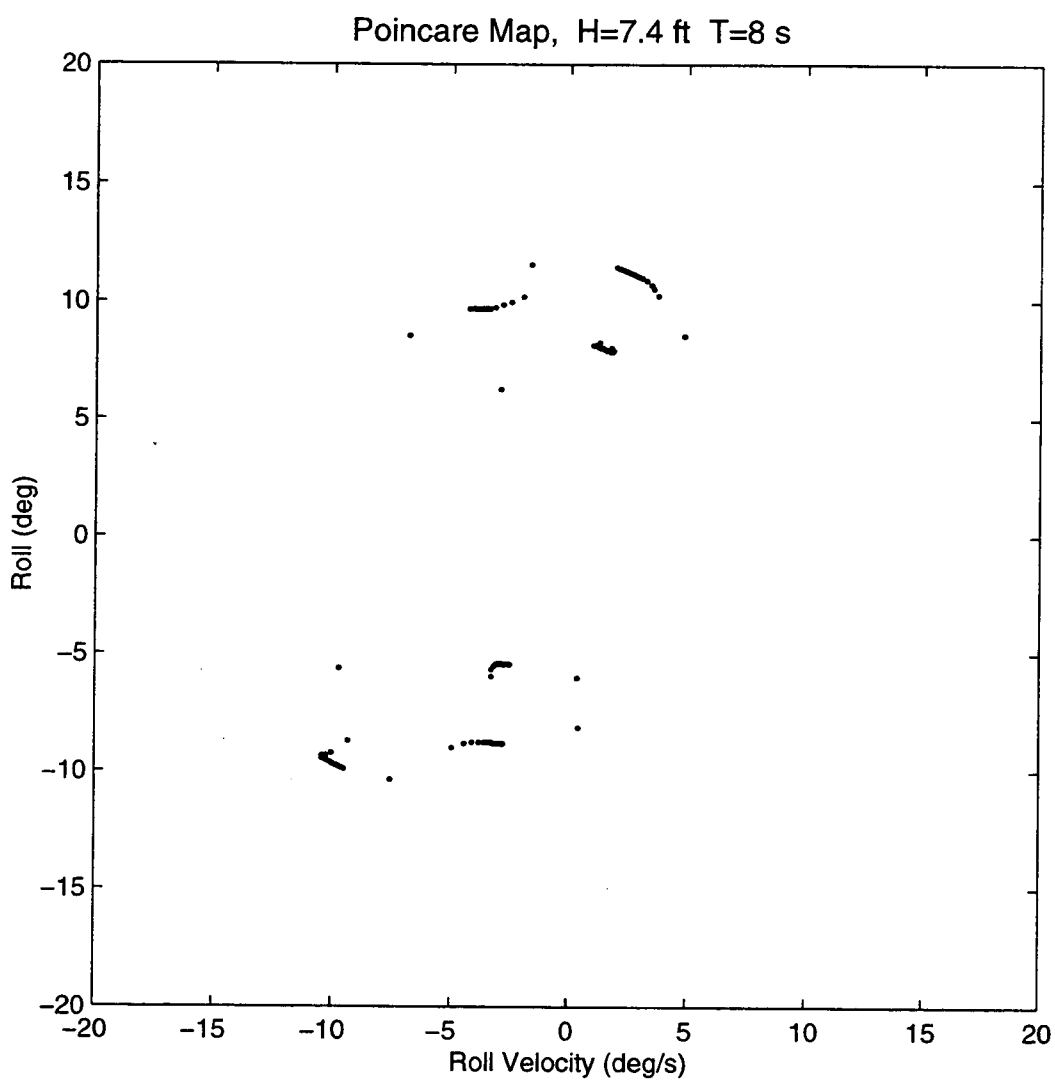


Figure 7.31

Poincare Map for H=7.4 ft, T=8 s

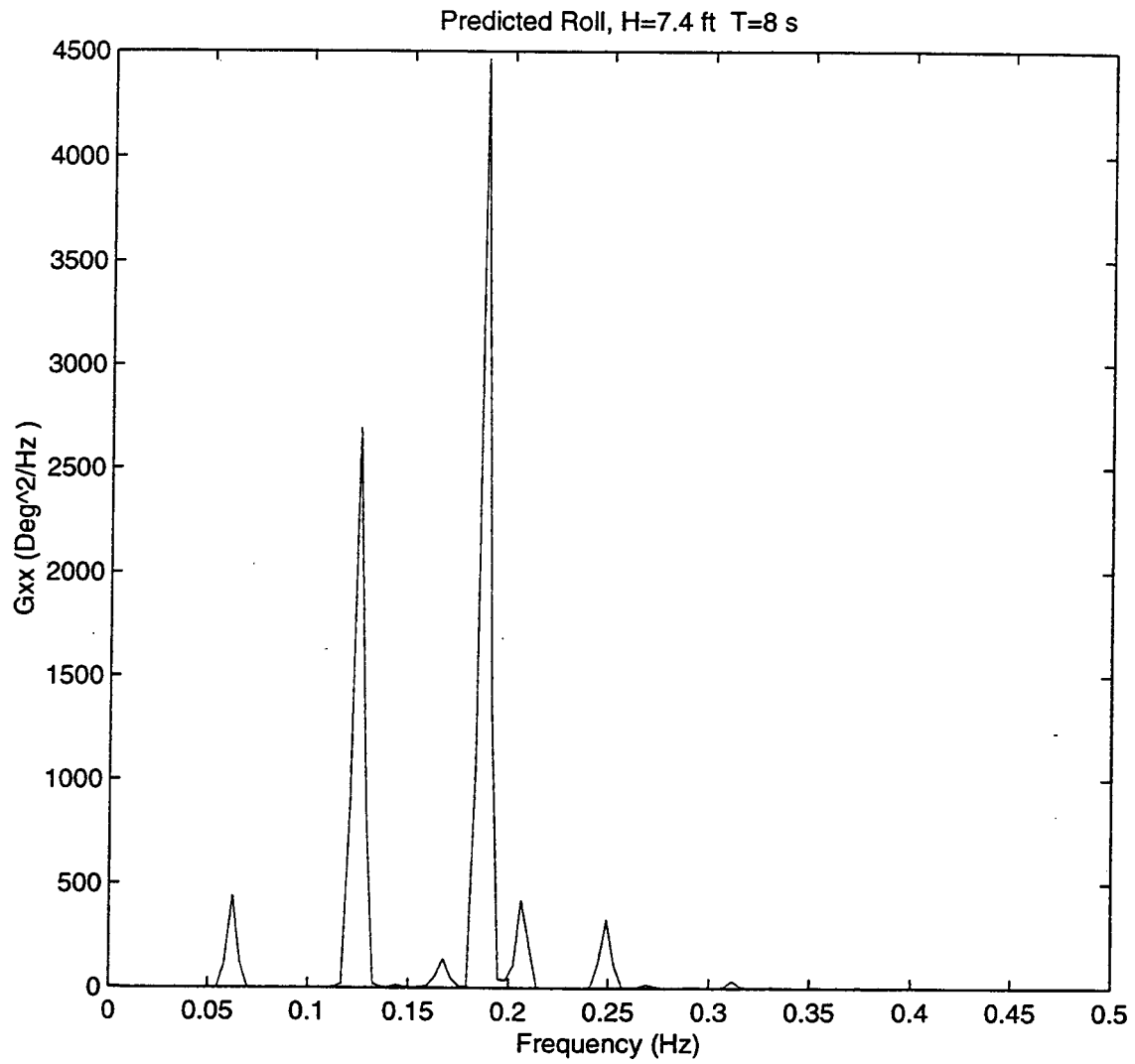


Figure 7.32

Roll Spectral Density for H=7.4 ft, T=8 s

Predicted Roll Vel, Roll and Heave $H=7.4$ ft $T=8$ s

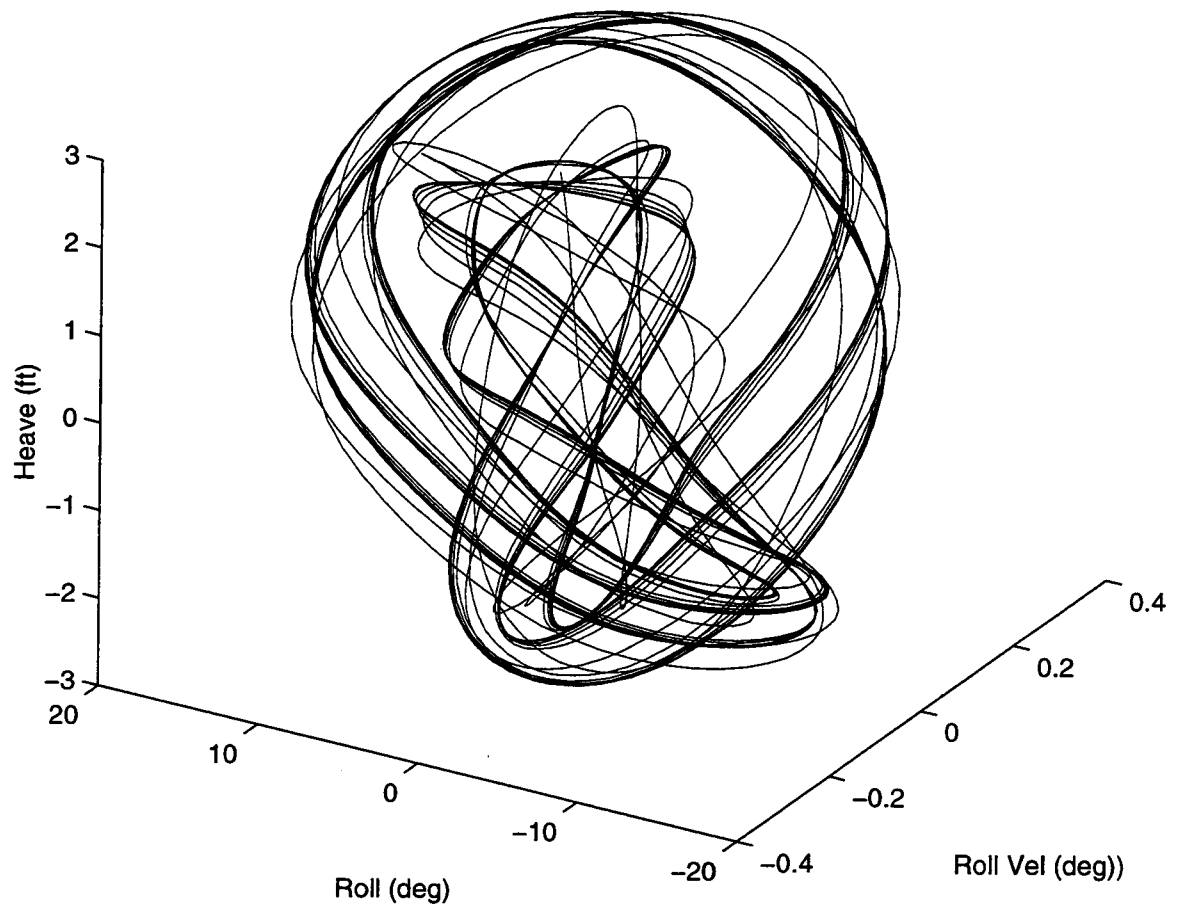


Figure 7.33

3-D Phase-Plane with Heave, $H=7.4$ ft, $T=8$ s

8. CONCLUDING REMARKS

8.1 Summary

MDOF modelling of motions of a barge subject to random beam seas was performed. Identification of the system coefficients using measured physical model test data was performed for both the 3-DOF and 2-DOF models. Comparisons of the model predictions with measured random response data were performed. Barge responses were simulated by Monte Carlo method to obtain ensembles of barge response showing the evolution of the estimated probability distribution. Examples of estimates of the likelihood of capsize were provided. Finally, some observed sensitive nonlinear behavior of the response were demonstrated.

The MDOF equations of motion for roll, heave and sway motions of a barge in random beam seas were derived based on the modelling assumptions presented. The 3-DOF model of roll-heave-sway was reduced to a 2-DOF model for roll-heave and later to a 1-DOF nonlinear model for roll.

Identification of system coefficients for both the 3-DOF and 2-DOF models was conducted using measured physical model test data for a barge in regular waves. Three regular wave cases were studied: two representing long and shorter period wave cases and the third, with a wave period near the spectral peak period for the random wave cases. The results showed both the 3-DOF and 2-DOF models were capable of accurate predictions in the time domain comparisons, phase plots, and spectral densities.

The results show the overall damping ranged from 0.5% to 40% of critical. The roll damping required the 40% damping at shorter period waves because of the increase in wave slope and being near the natural period. The roll damping was then reduced to about 1% for the ten second period waves in order to match the superharmonic shown in the measured data. The heave damping varied from 1.5% to 20% to match the amplitude and phase of the measured response. No obvious trend was observed. The sway damping remained low throughout all cases at about 1.5%. This agrees with potential theory estimates for longer wave periods.

A very small added mass for sway was found to work best for all cases. This value was 500 slugs which compared well with potential theory. For heave, the added mass values that worked best coincided with potential theory added mass values at 8 second waves. For roll, the added inertia was lowered from potential theory to help approximate the linear damped natural period. Potential theory showed values of about three times larger for longer period waves. One reason is the potential theory estimates are for a barge with slightly different shape and a draft of 5 ft versus the physical model test data with a prototype draft of 4 ft.

The system coefficients for added mass, added inertia and damping provided preliminary estimates for comparisons of the 3-DOF and 2-DOF model predictions for the case of random waves. Two random wave cases were studied. In the first case, the measured random wave data was used as input to the numerical models with wave properties derived. In the second case, a white noise filter was used to simulate the wave properties. Results from both of these cases were compared. They showed both

the 3-DOF and 2-DOF models predict the response favorably in many instances. Time series comparisons using the measured random wave as input were better for the 2-DOF model than the 3-DOF model whereas the 3-DOF model predicted the time series better the case of filtered white noise input. Both the 3-DOF and 2-DOF models were capable of capturing the global behavior of the measured data demonstrated in the figures presented. Preliminary observations suggest the 2-DOF model may be sufficiently accurate for the comparisons conducted with these lower waves. However, Chapter 7 showed the apparent sensitive nonlinear behavior of the 3-DOF model, which has yet to be detected from the 2-DOF model.

Monte Carlo simulations were performed for both the 3-DOF and 2-DOF models to demonstrate the ease of estimating the probability of response for a particular sea state and mission duration. The model allows large angle response so estimates of chance of capsize may be obtained. Evolutions of the estimates of the joint probability densities were presented with estimates of likelihood of capsize.

Finally, examples of chaotic behavior were shown for regular wave inputs. Slight differences in the selected coefficients altered the response dramatically yielding totally different behavior. This suggests the complex nonlinear response behavior requires a more precise parametric study and analysis.

One of the reasons the MDOF model was developed was to examine how the performance compares to a SDOF model. The SDOF model is being investigated in a parallel research effort and has many beneficial features over the MDOF models proposed in this study for preliminary estimates in that it may provide fairly accurate

results and requiring only the selection of a few coefficients (e.g added inertia, damping, stiffness). The 1-DOF model may be implemented easily and is the model of choice for many researchers. It is often selected because analytical analysis of nonlinear response may be performed. For a higher order model, the analytic evaluation may become intractable with present analysis capabilities. The user must resort to numerical solution procedures with qualitative analysis methods. Once the results of 1-DOF system study are provided, then a comparison between the 3-DOF, 2-DOF and 1-DOF models can be made.

8.2 Recommendations for Future Research

This thesis represents initial development of the model with comparison studies between measured physical model test data and predicted response. Some examples of stochastic estimations were provided along with demonstrations of sensitive nonlinear behavior.

Recommendations for future research are:

8.2.1 Modelling and Analysis

- Perform an extensive parametric identification of the coefficients in the models
- Identify regions of periodic and chaotic responses
- Assess the influence of the nonlinear terms for a range of sea states

- Compare estimates of capsize to recently obtained physical model test data which includes capsize cases
- Provide a matrix of values of coefficients for different barge parameters (e.g. Location of KG, displacement, length, width, draft)
- Compare results to other time domain ship motion models
- Incorporate importance sampling techniques to the Monte Carlo Model
- Study static effects due to wind, ice or shift in cargo in the model
- Improve mooring stiffness to model nonlinearities and material damping
- Develop higher order, yet efficient, models of filtered white noise to eliminate low frequency information
- Include modelling capabilities for trapped-water-on-deck due to bulwarks
- Include modelling capabilities for momentum transfer of wave slam or motions of water-on-deck as it slams against cargo
- Analyze effects of adding bilge keels or other damping mechanisms and/or motion stabilizers

8.2.2 Computational Efficiency Studies

- Investigate alternate ways of improving computational efficiency to further improve performance
- Test the parallel program version of the model on a network of workstations and compare execution times with that of a supercomputer

- Perform benchmark studies to identify what sufficient ensemble sizes need to be for accurate statistical sampling

8.2.3 Analysis Tools

- Add animation graphics to show the motions of the barge in real time for faster interpretation of results
- Incorporate latest chaotic dynamics analysis tools into a post processor to provide additional information in analysis efforts

8.2.4 User Friendliness

- Make the program more "user friendly" with window based "pop up" or "pull down" menus
- Prepare a "User Manual" with introduction of the PVM language for new users and portability of computer model

8.2.5 Naval Architect and Mariner Guidance

- Provide new stability criteria for engineers and/or ship operators
- Investigate concept of implementing a real time shipboard model which reads motions of the ship or barge directly from instrumentation and computing near real time stability estimates for ship Captains

BIBLIOGRAPHY

Abkowitz, M.A. 1969. *Stability and Motion Control of Ocean Vehicles*. MIT Press, Cambridge, MA.

Cai, G.Q., Yu, S.J. and Lin, Y.K. 1994. Ship Rolling in Random Sea. *Stochastic Dynamics and Reliability of Nonlinear Ocean Systems*, DE-Vol. 77, ASME.

Chakrabarti, S.K. 1994. *Hydrodynamics of Offshore Structures*, Computational Mechanics Publications, Southampton Boston.

Cooper, N.G. 1990. *From Cardinals to Chaos*. Cambridge University Press.

Dahle, E. AA., Myhaug, D. and Dahl, S.J. 1988. Probability of Capsizing in Steep and High Waves from the Side in Open Sea and Coastal Waters. *Ocean Engineering*, 15:2:139-151.

Donescu, P. and Virgin, L.N. 1993. Nonlinear Coupled Heave and Roll Oscillations of a Ship in Beam Seas Nonlinear Dynamics of Marine Vehicles, *ASME*.

Falzarano, J. and Taz Ul Mulk, M. 1994. Large Amplitude Rolling Motion of an Ocean Survey Vessel. *Marine Technology* 31:4:278-285.

Falzarano, J.M., Shaw, S.W. and Troesch, A.W. 1992. Application of Global Methods for Analyzing Dynamical Systems to Ship Rolling Motion and Capsizing. *International Journal of Bifurcation and Chaos*. 2:1:101-115.

Falzarano, J., and Troesch, A. 1990. Application of Modern Geometric Methods for Dynamical Systems to the Problem of Vessel Capsizing with Water-on-deck. *STAB '90, Fourth International Conference on Stability of Ships and Ocean Vehicles*, Naples, Italy.

Falzarano, J., Steindl, A., Troesch, A. and Troger, H. 1991. Rolling Motion of Ships Treated as Bifurcation Problem. *International Series of Numerical Mathematics*

Geist A., Beguelin, A., Dongarra, J., Jiang, W., Manchek, R. and Sunderam, V. 1994. *PVM: Parallel Virtual Machine A Users Guide and Tutorial for Networked Parallel Computing*, The MIT Press, Cambridge, MA.

Kwon, S.H., Kim, D.W. and McGregor, R.C. 1993. A Stochastic Roll Response Analysis of Ships in Irregular Waves. *International Journal of Offshore and Polar Engineering*, 3:1.

Liaw, C.Y. 1993. Dynamic Instability of a Parametrically Excited Ship Rolling Model. *Proc. of the Third International Offshore and Polar Engineering Conference*, Singapore.

Liaw, C.Y., Bishop, S.R. and Thompson, J.M.T. 1993. Heave-Excited Rolling Motion of a Rectangular Vessel in Head Seas. *International Journal of Offshore and Polar Engineering*, 3:1.

Lin, H. and Yim, S.C.S. 1995a. Chaotic Roll Motion and Capsizing of Ships Under Periodic Excitation with Random Noise. *Journal of Applied Research*

Lin, H. and Yim, S.C.S. 1995b. Stochastic Analysis of a Nonlinear Ocean Structural System. Oregon State University Report No. OE-95-04.

MathWorks, The, Inc. 1993. *Matlab Reference Guide*. Natick, MA.

Miller, R.N. and Goodlett, S.T. 1995. Personal communication and computer modelling.

Moon, F.C. 1992. *Chaotic and Fractal Dynamics*, John-Wiley & Sons, Inc., New York, N.Y.

NFESC. 1995. Physical Model Test Data. Naval Facilities Engineering Service Center, Port Hueneme, CA.

Paulling, J.R. 1961. The Transverse Stability of a Ship in a Longitudinal Seaway. *Journal of Ship Research*. March:37-49.

Paulling, J.R. and Rosenberg, R.M. 1959. On Unstable Ship Motions Resulting From Nonlinear Coupling. *Journal of Ship Research*. June.

Paulling, J.R. 1995. Hydrostatic Curves from Computer Model "Eureka".

Press W.H., Flannery, B.P, Teukolsky, S.A. and Vetterling, W.T. 1986. *Numerical Recipes*, Cambridge University Press.

Roberts, J.B. 1982a. A Stochastic Theory for Nonlinear Ship Rolling in Irregular Seas. *Journal of Ship Research*. 26:4:229-245.

Roberts, J.B. 1982b. Effect of Parametric Excitation on Ship Rolling Motion in Random Waves. *Journal of Ship Research*. 26:4:246-253.

Silverman, B. W. 1986. *Density Estimation for Statistics and Data Analysis*. Chapman and Hall Ltd, New York.

Virgin, L.N. 1987. The Nonlinear Rolling Response of a Vessel including Chaotic Motions leading to Capsize in Regular Seas. *Applied Ocean Research*. 9:2:89-95.

Virgin, L.N. and Bishop, S.R. 1988. Catchment Regions of Multiple Dynamic Responses in Nonlinear Problems of Offshore Mechanics. *Proceedings at 7th International Conference on Offshore Mechanics and Arctic Engineering*, Houston, TX. 15-22.

Virgin, L.N. and Erickson, B.K. 1994. A New Approach to the Overturning Stability of Floating Structures. *Ocean Engineering*. 21:1:67-80.

Yim, S.C.S., Bartel, W.A., Lin, H. and Huang, E. 1995. Nonlinear Roll Motion and Capsizing of Vessels in Random Seas. Naval Facilities Engineering Service Center, Port Hueneme, CA.

APPENDICES

APPENDIX A

Roll-Heave Stiffness Figures (Section 2)

Geometric States for Combined Roll-Heave

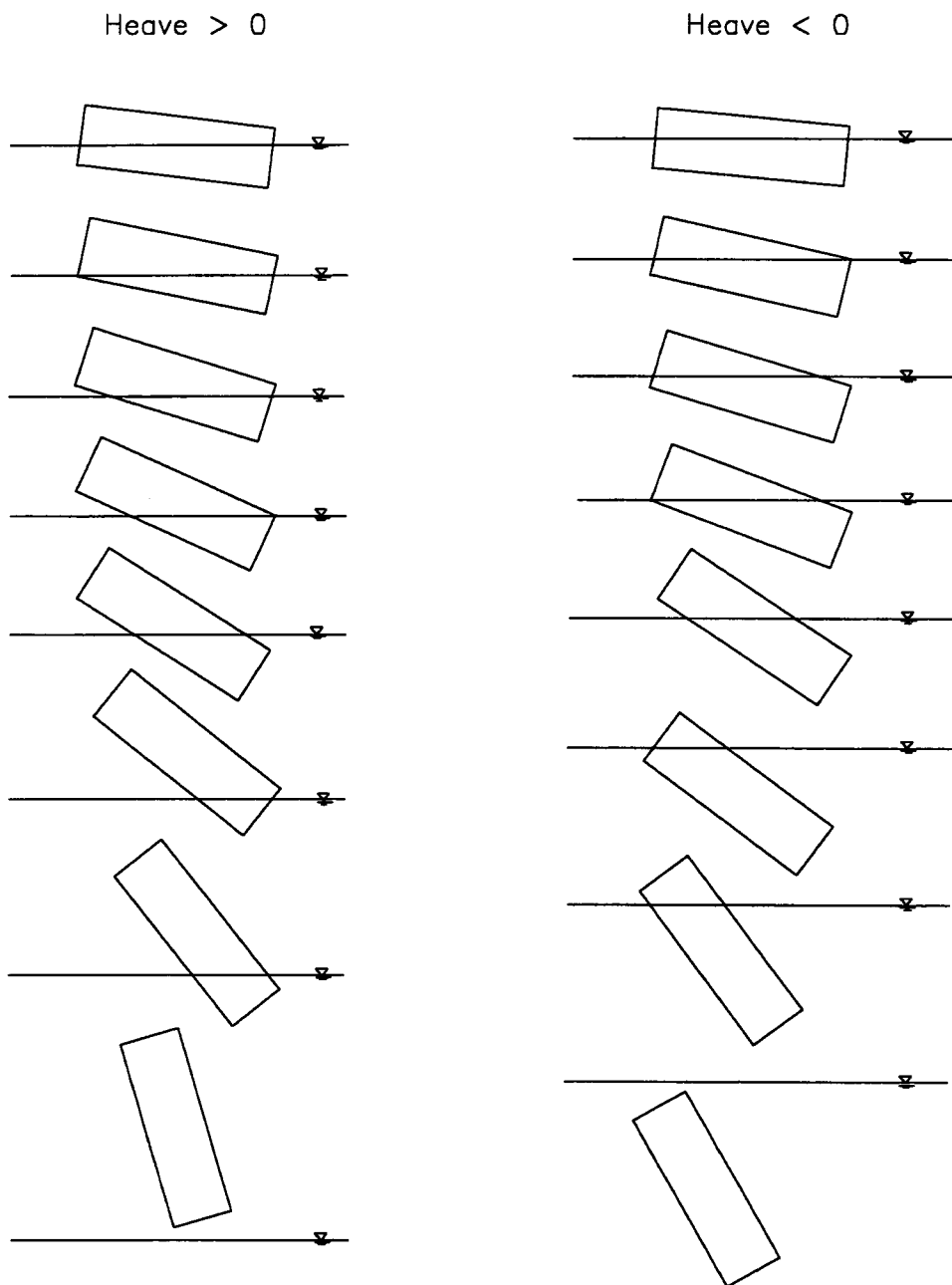


Figure A.1 Geometric States for Combined Roll-Heave

Four Main States for Combined Roll-Heave

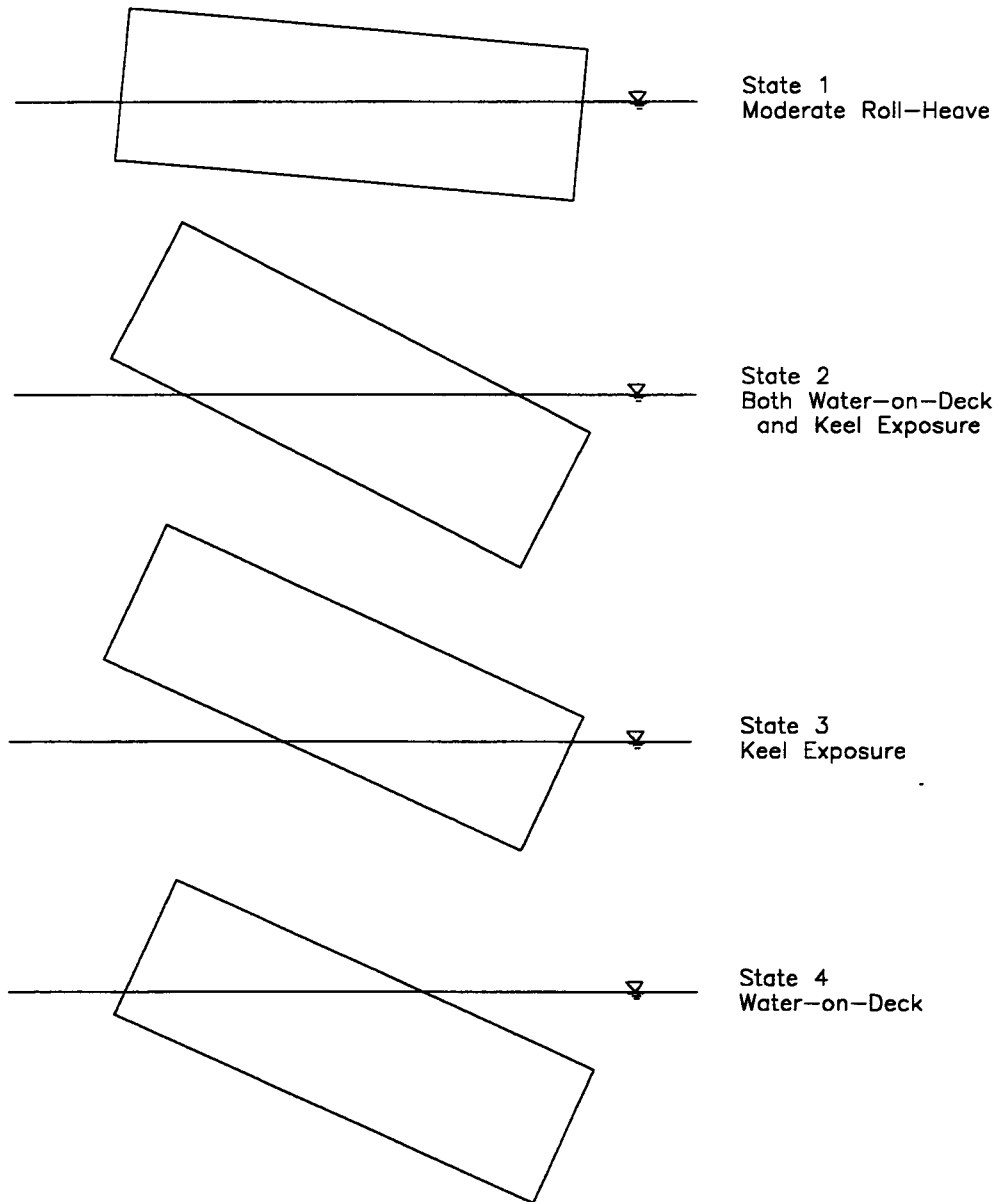


Figure A.2

Four Main States for Combined Roll-Heave

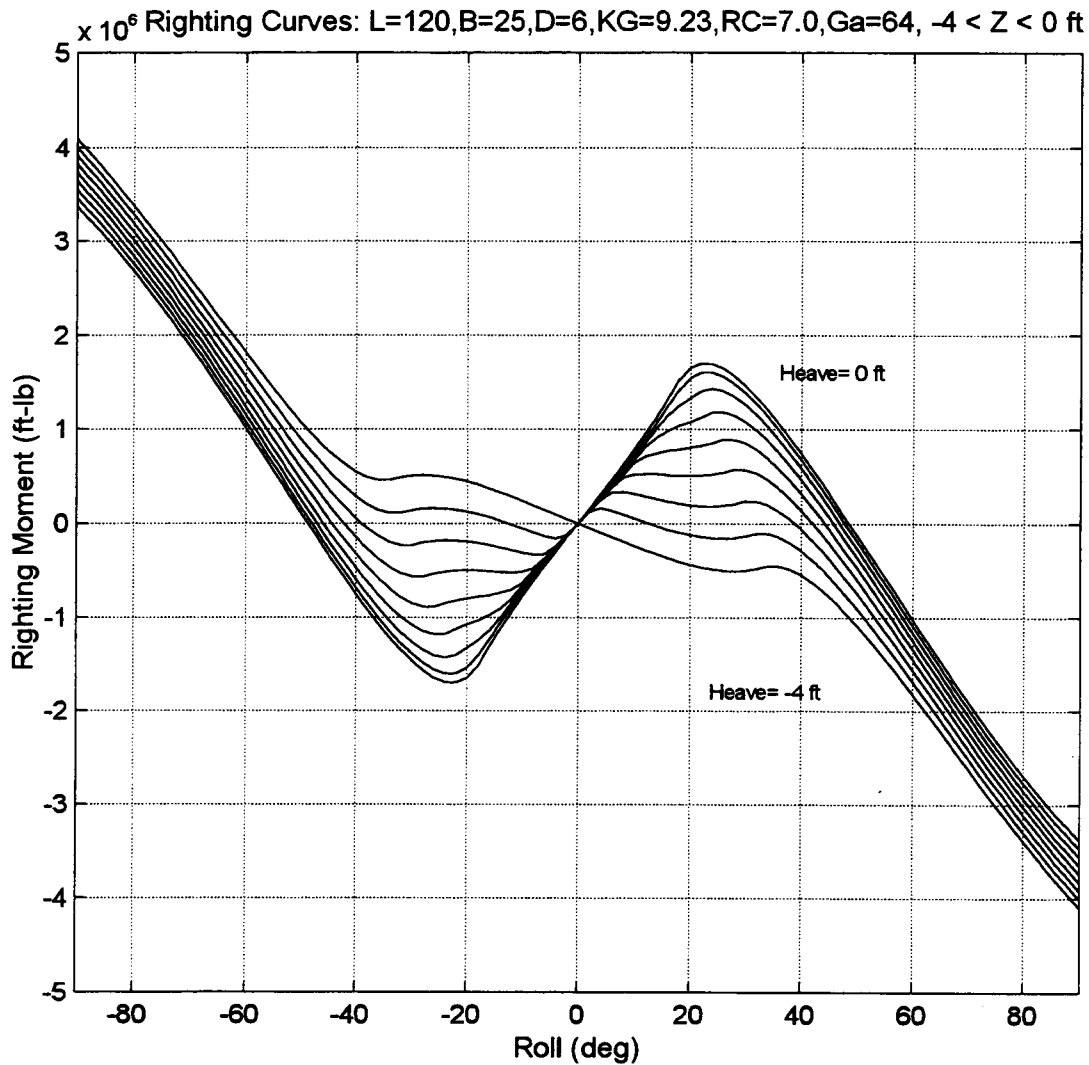


Figure A.3 Righting Moment Curves, $-4 \text{ ft} < \text{Heave} < 0 \text{ ft}$

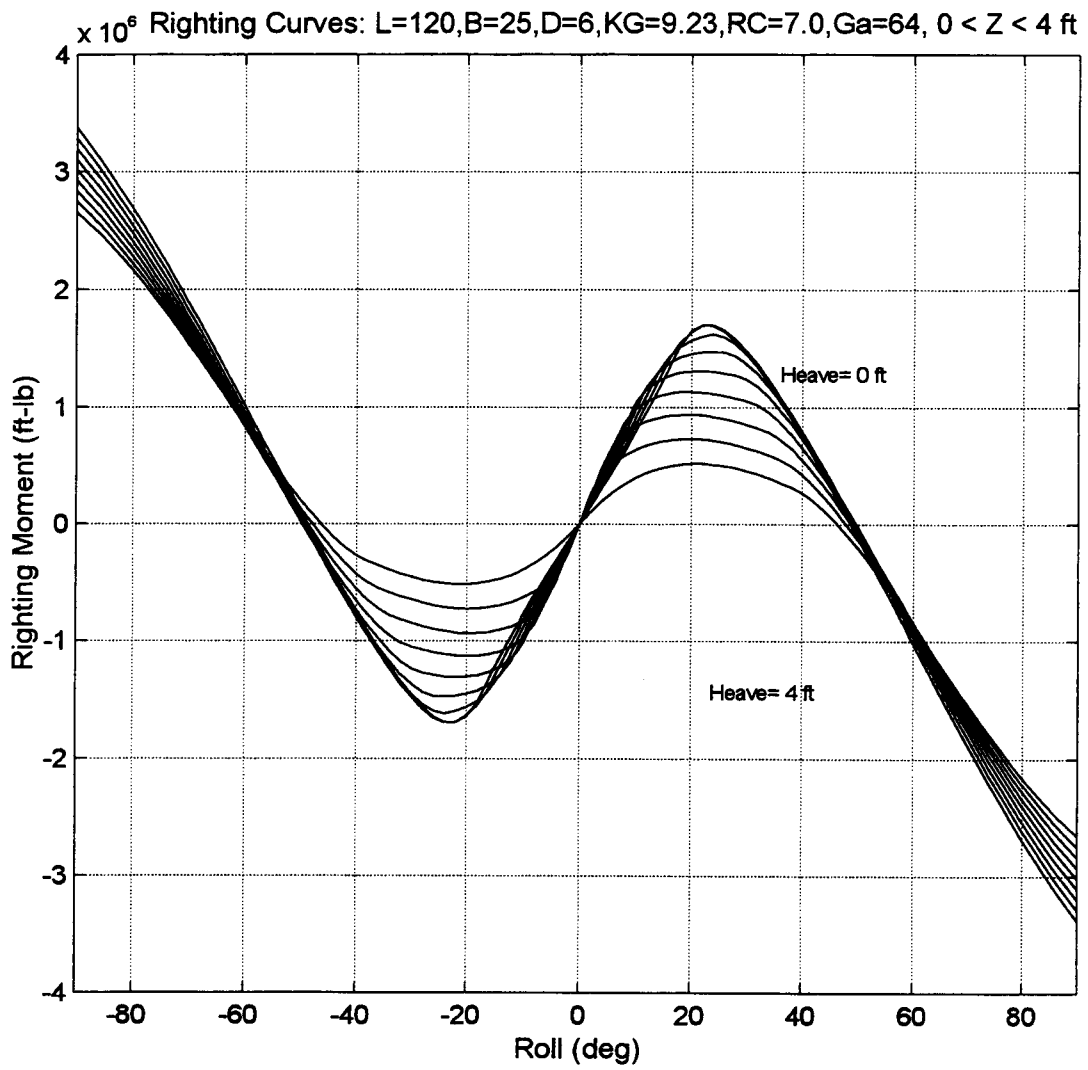


Figure A.4

Righting Moment Curves, $0 < \text{Heave} < 4$ ft

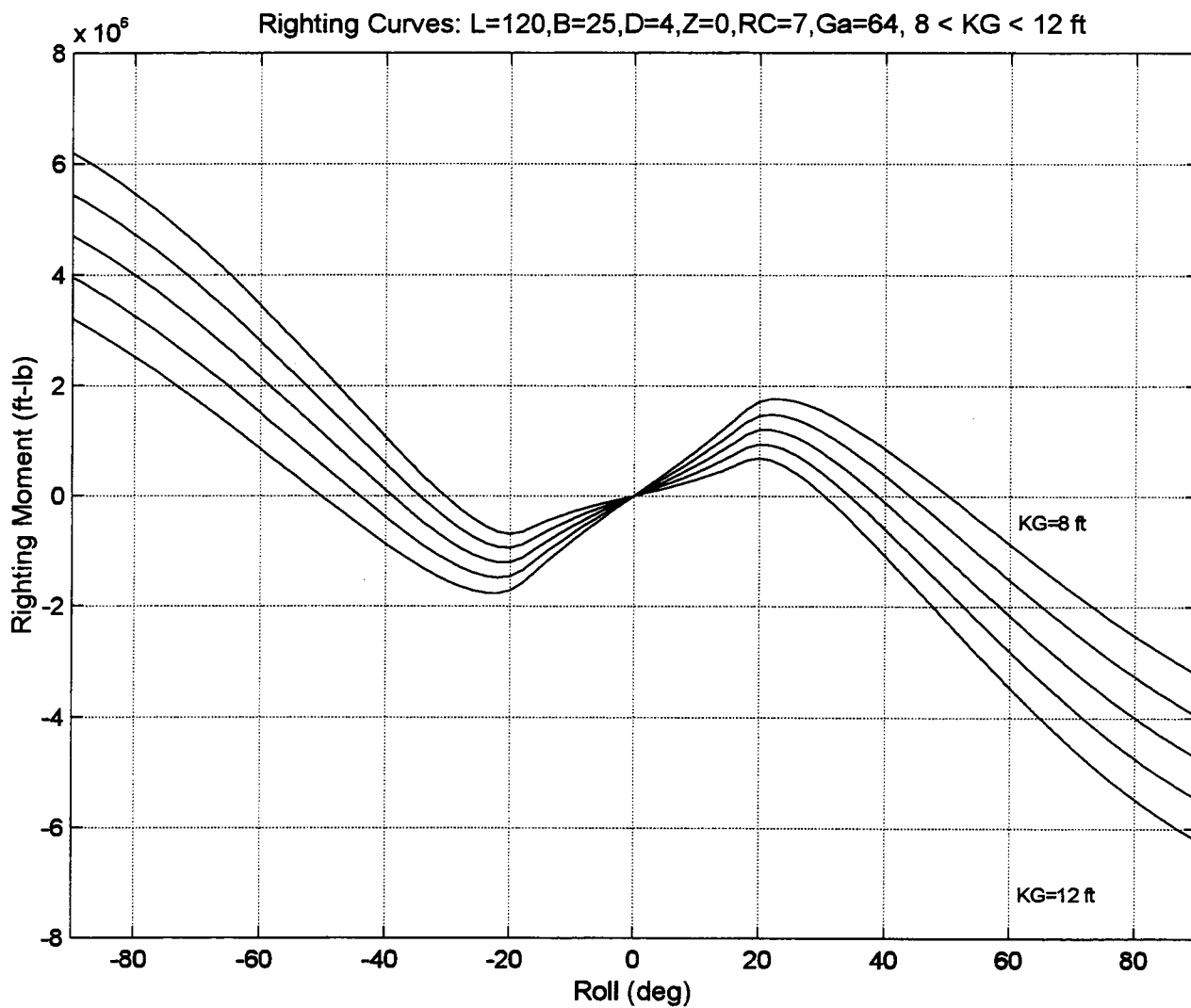


Figure A.5 Righting Moment Curves, 8 ft < KG < 12 ft

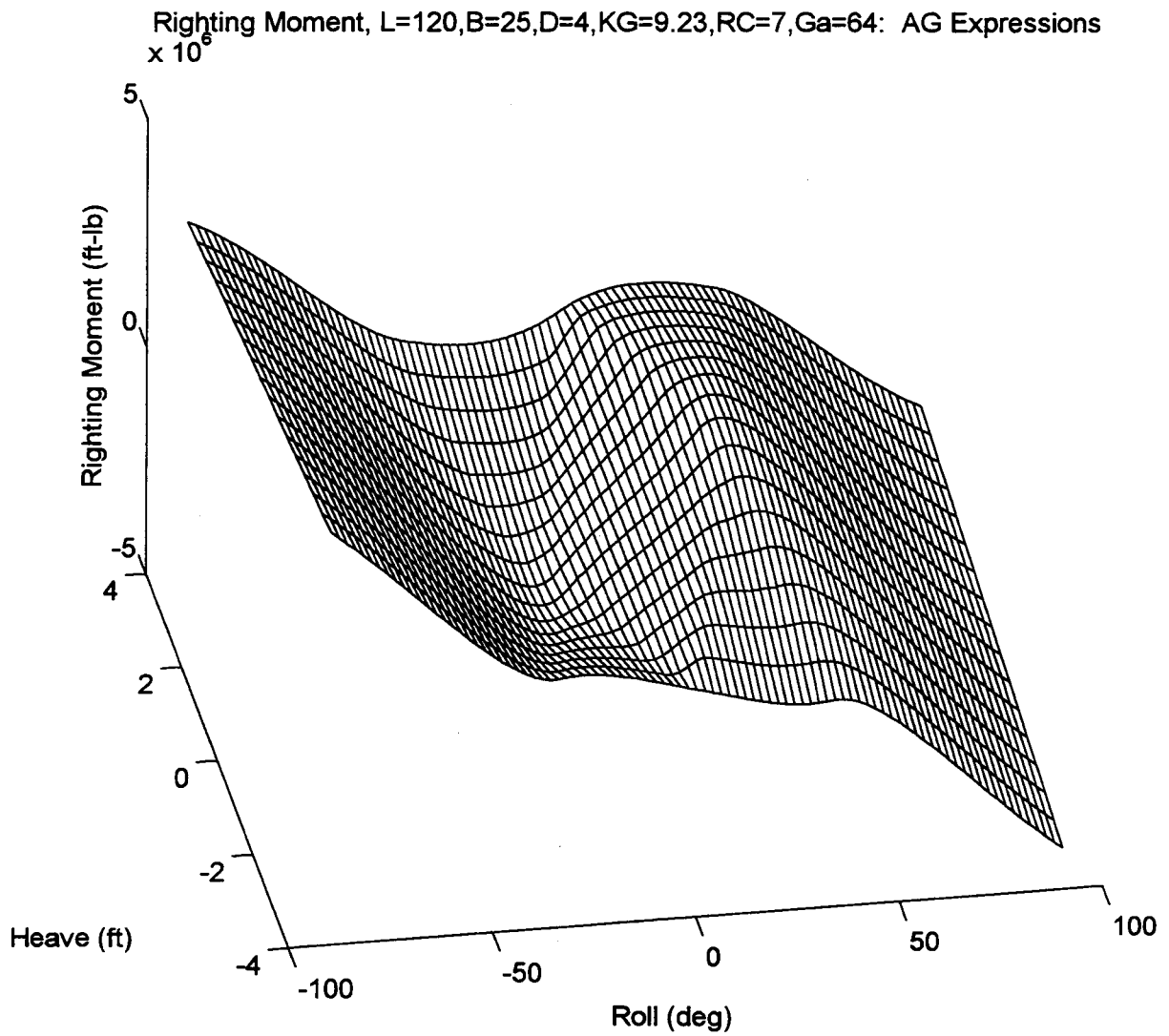


Figure A.6

Righting Moment Surface, Analytical Method

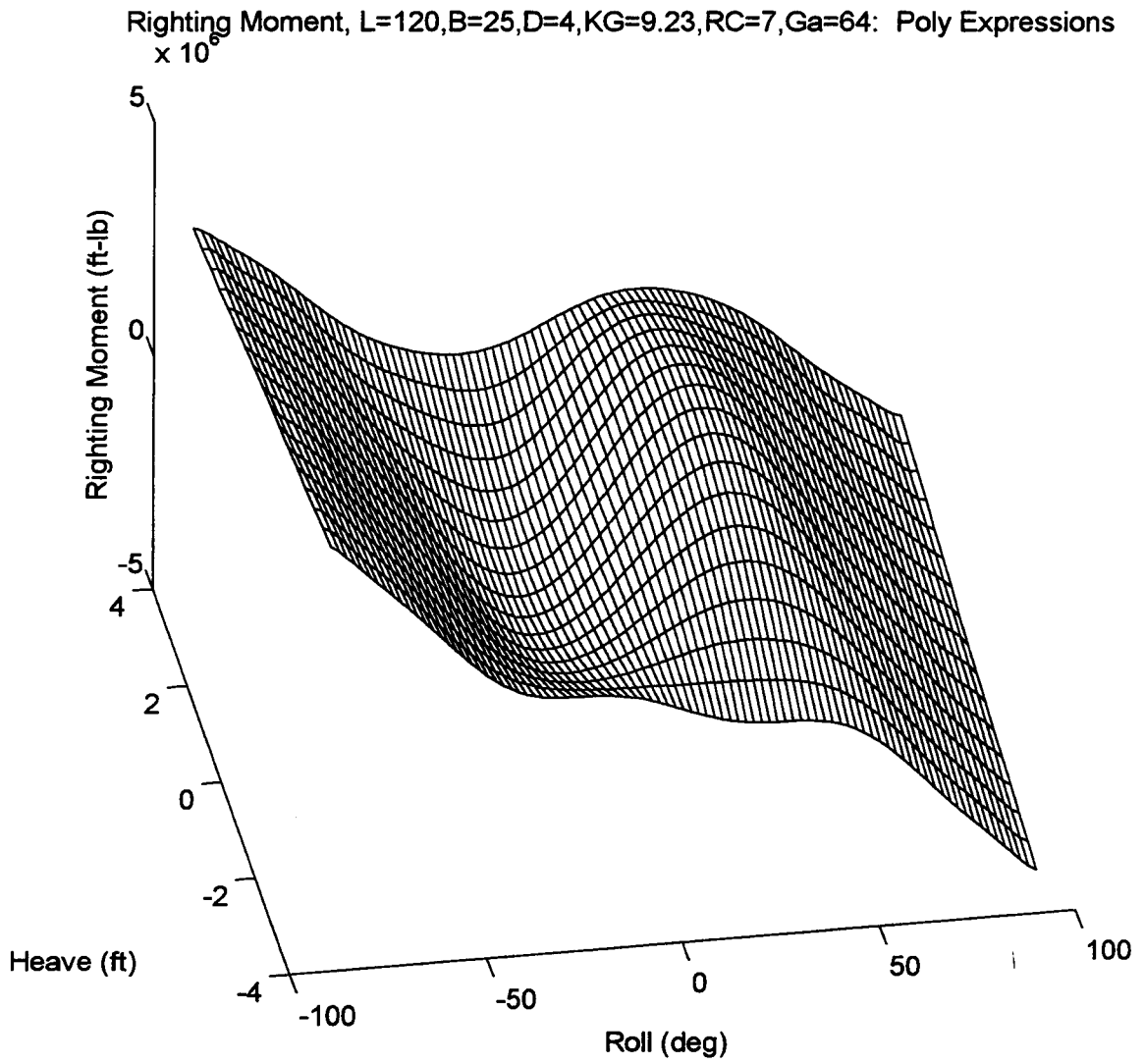


Figure A.7 Righting Moment Surface, Polynomial Fit

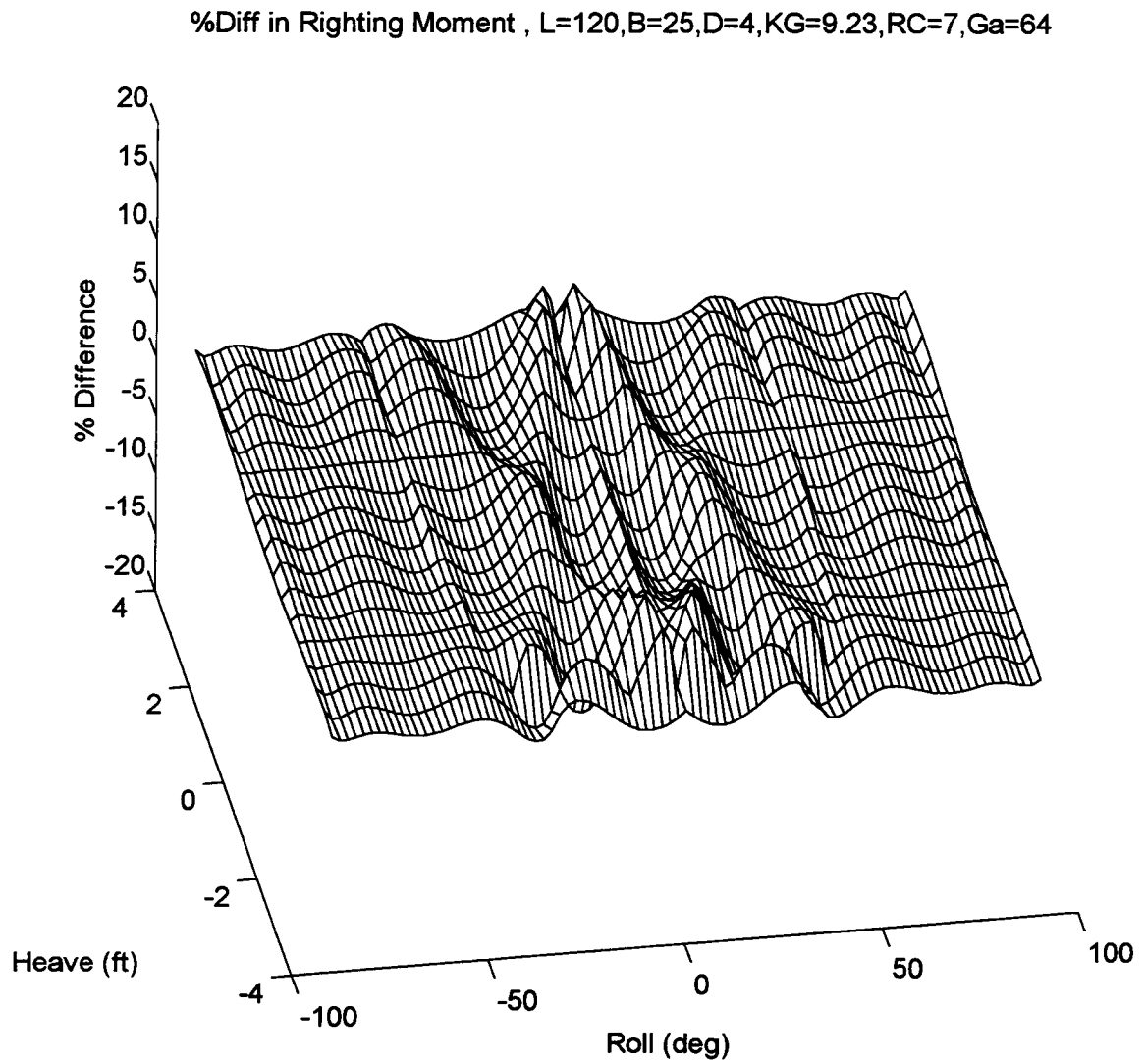


Figure A.8

Percent Error in Righting Moment Surface

A.8

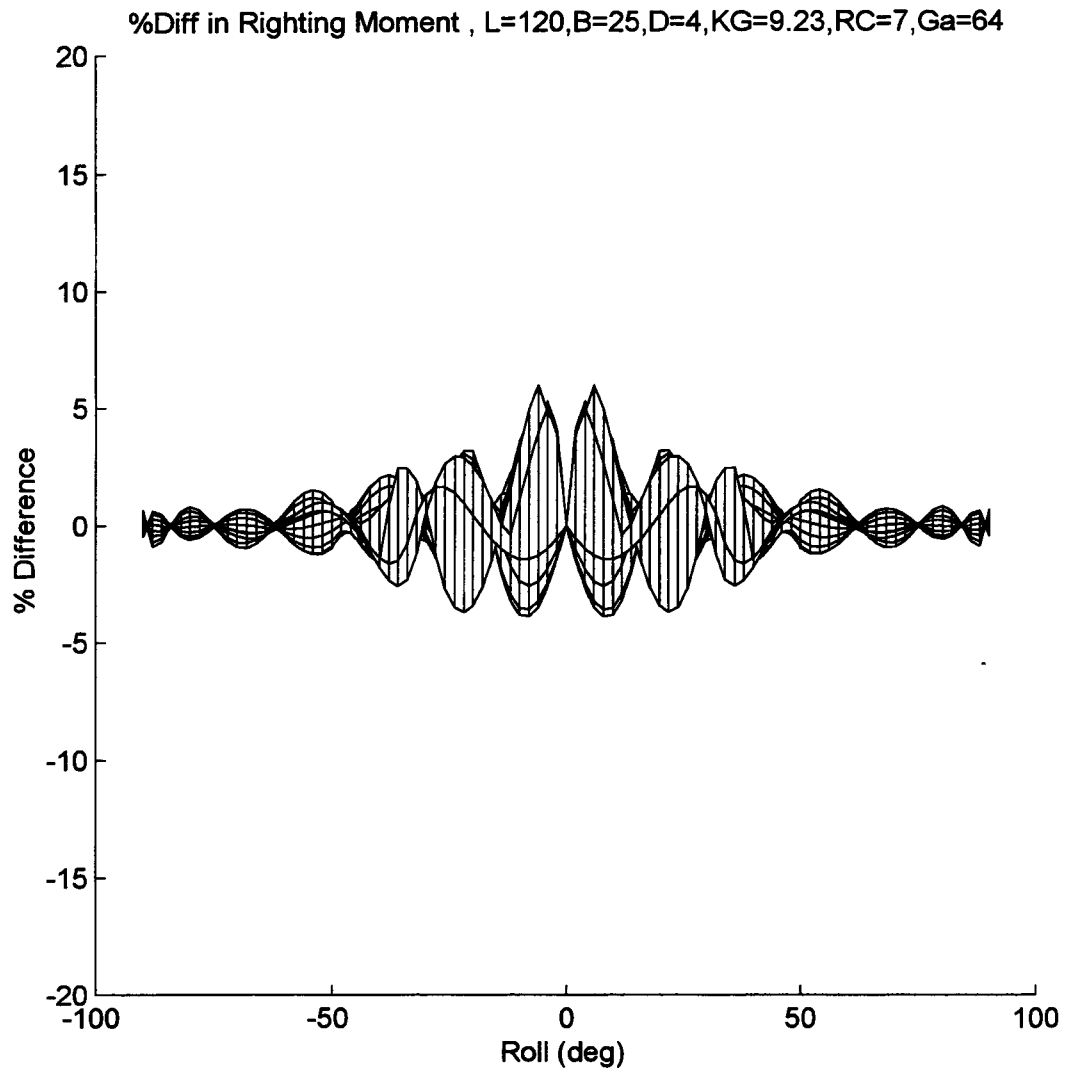


Figure A.9

Percent Error in Righting Moment, Roll Projection

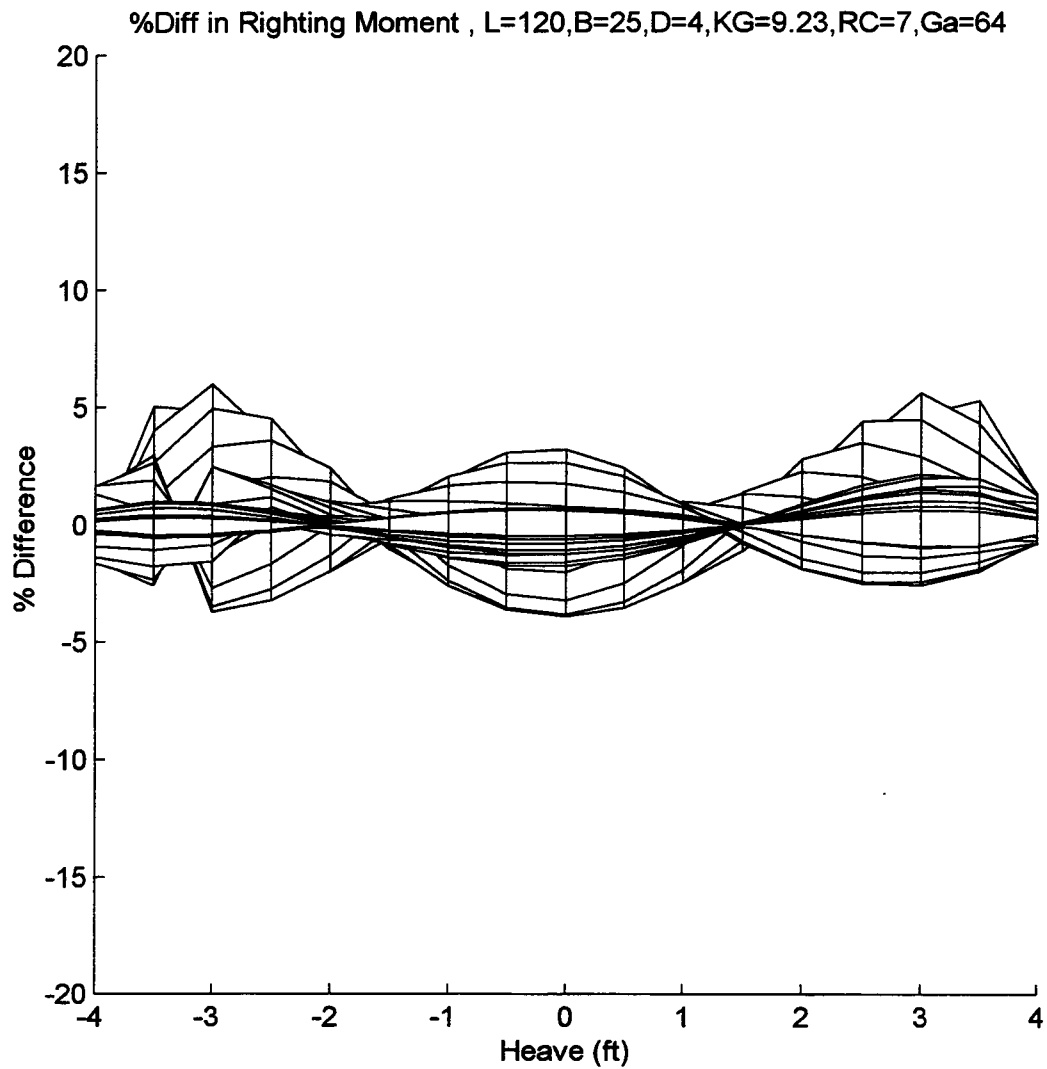


Figure A.10

Percent Error in Righting Moment, Heave Projection

A.10

Heave Restoring Force, L=120,B=25,D=4,KG=9.23,RC=7,Ga=64: Trig Expressions

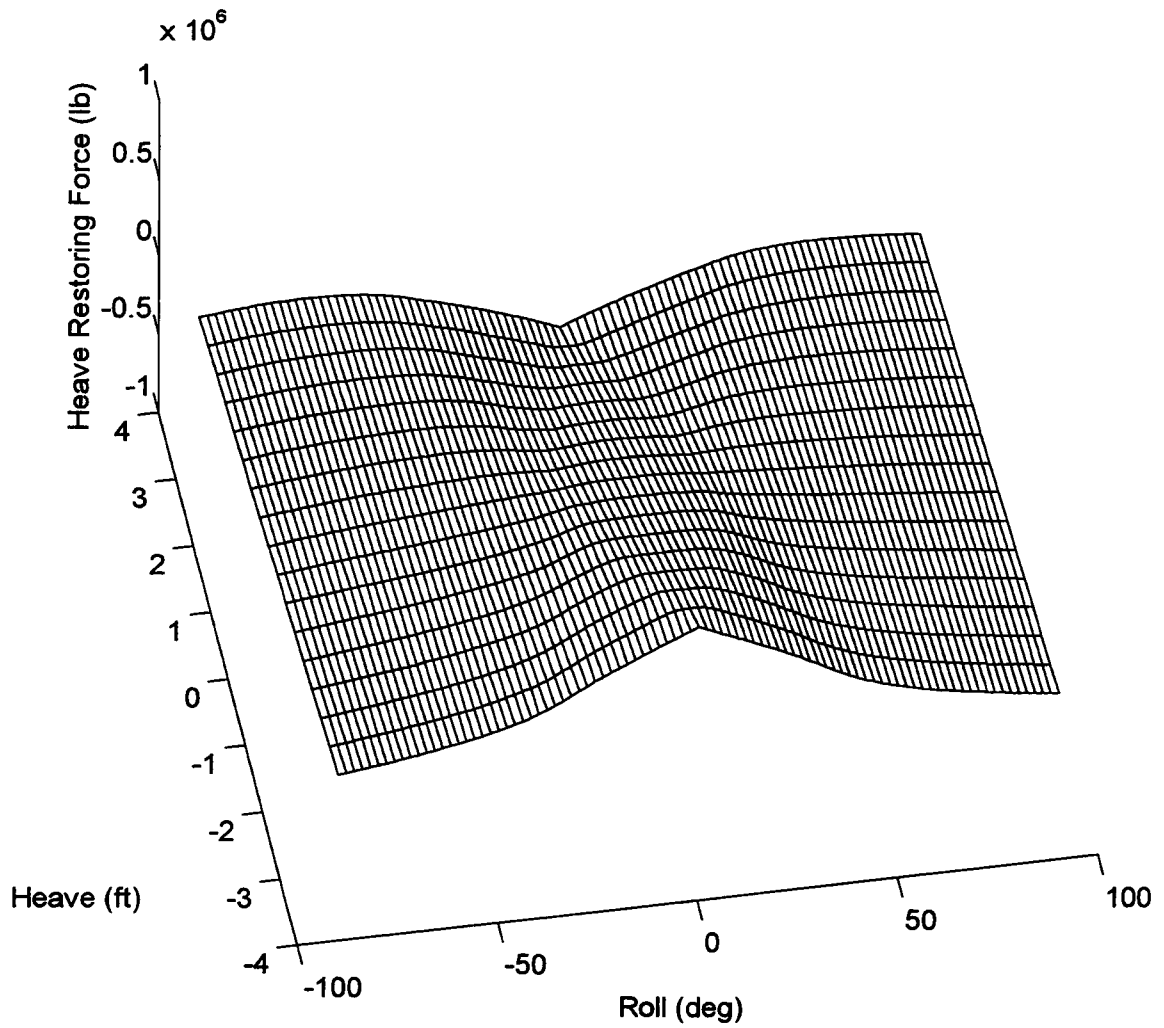


Figure A.11

Heave Restoring Force Surface, Analytical Method

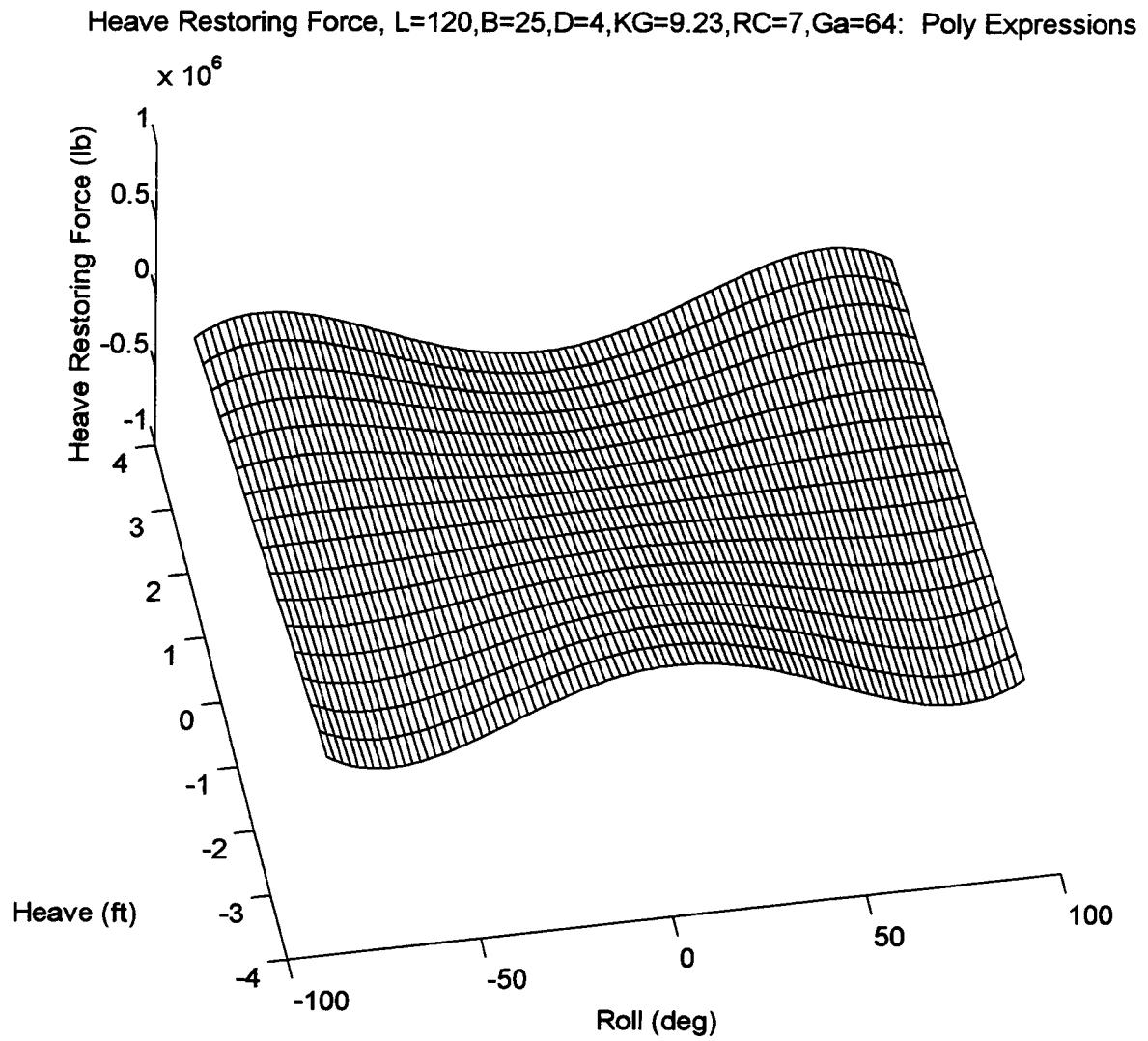


Figure A.12

Heave Restoring Force Surface, Polynomial Fit

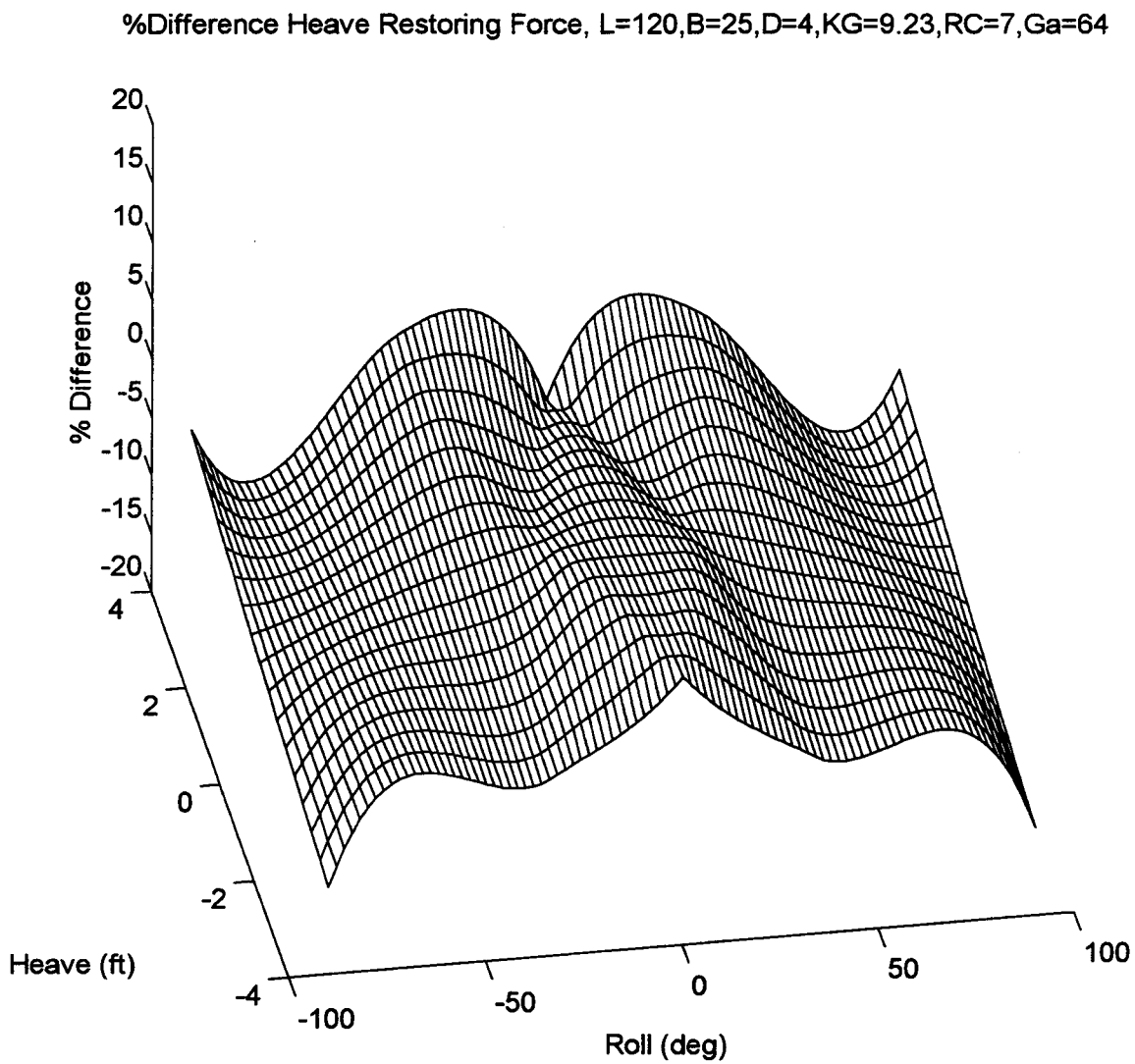


Figure A.13

Percent Error in Heave Restoring Force Surface

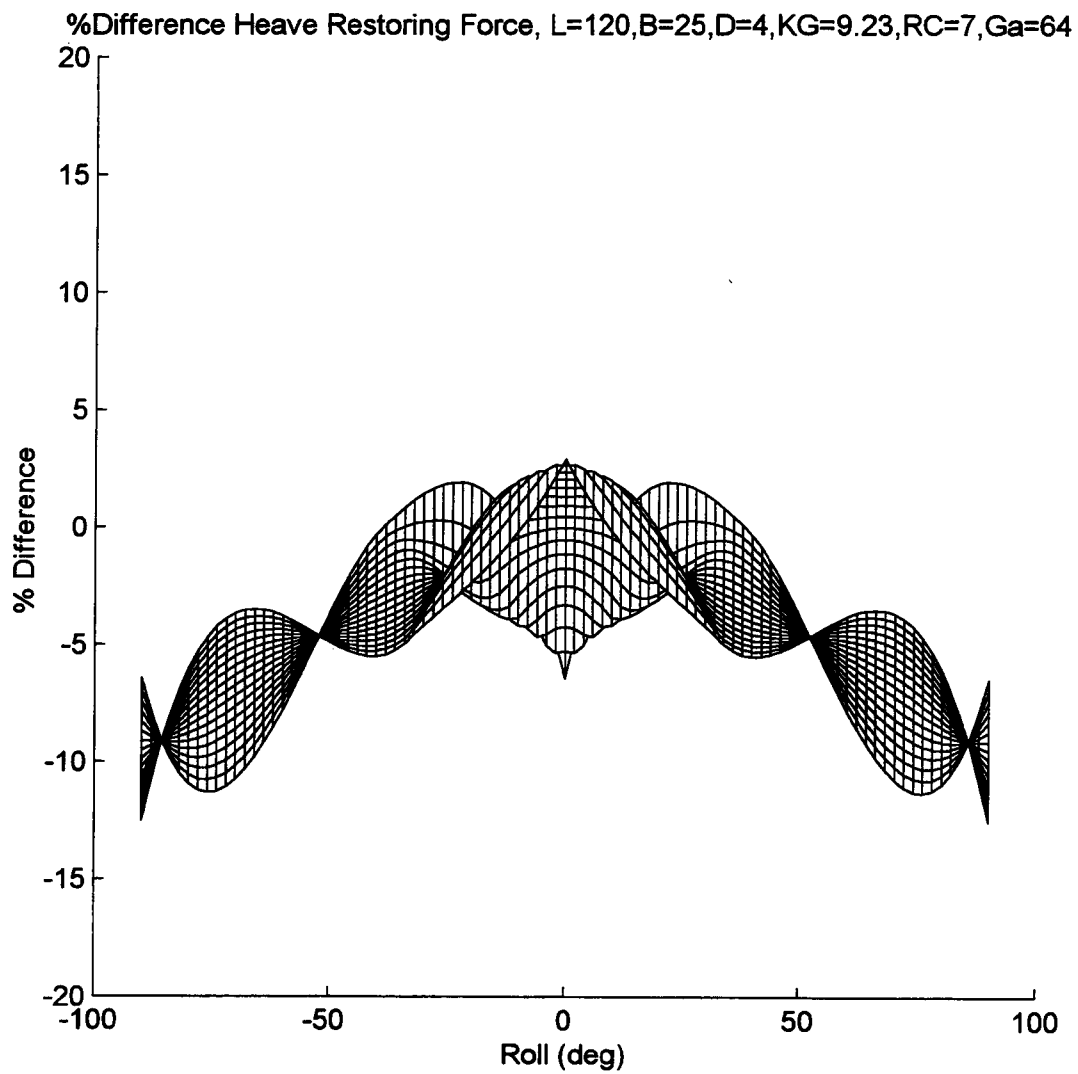


Figure A.14

Percent Error in Heave Restoring Force, Roll Projection

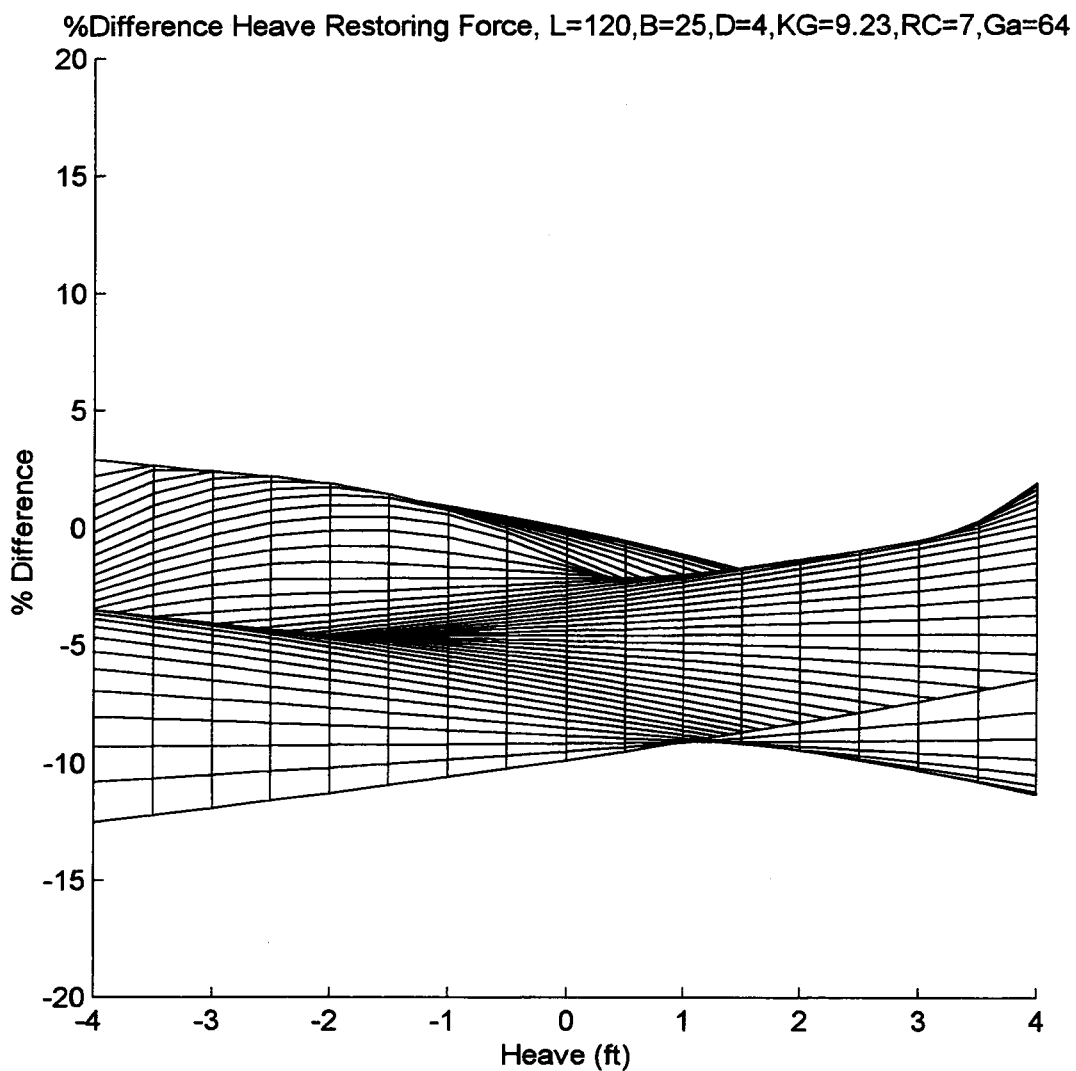


Figure A.15

Percent Error in Heave Restoring Force, Heave Projection

A.15

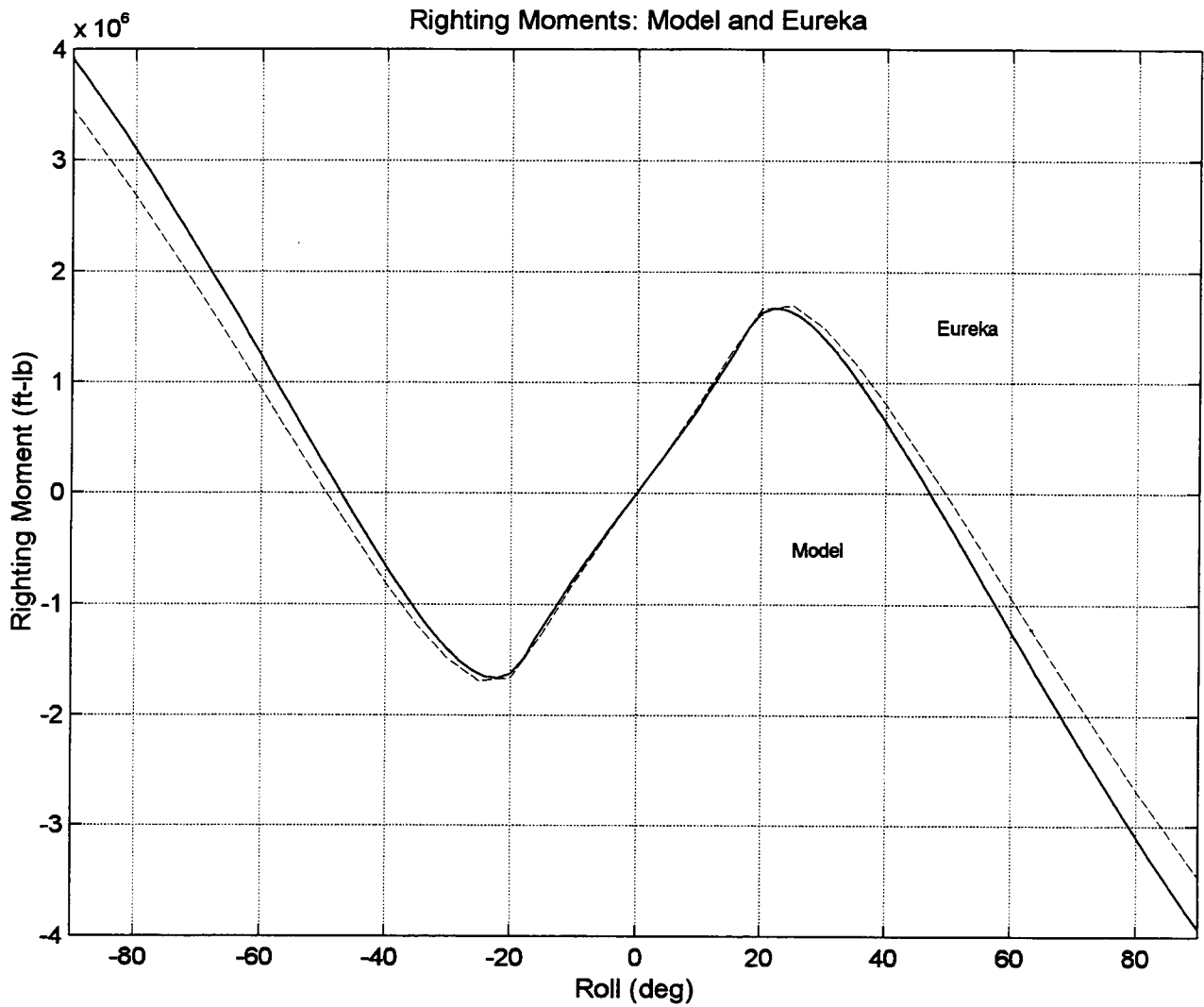


Figure A.16

Righting Moment Comparison, Model vs Eureka

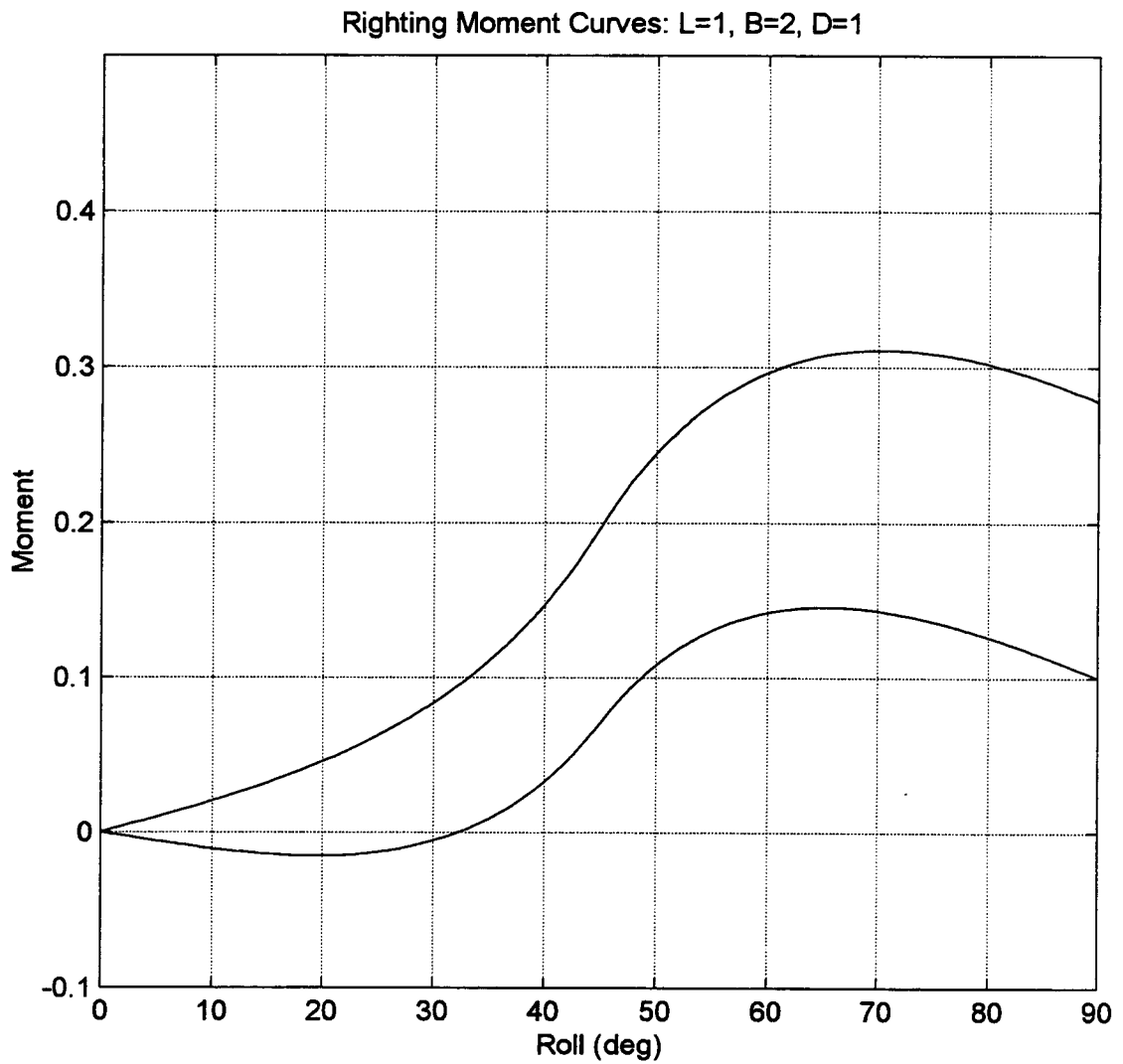


Figure A.17 Righting Moments for values of Liaw et al (1993)

APPENDIX B**System Identification Figures
Roll-Heave-Sway Model (Section 4.2)**

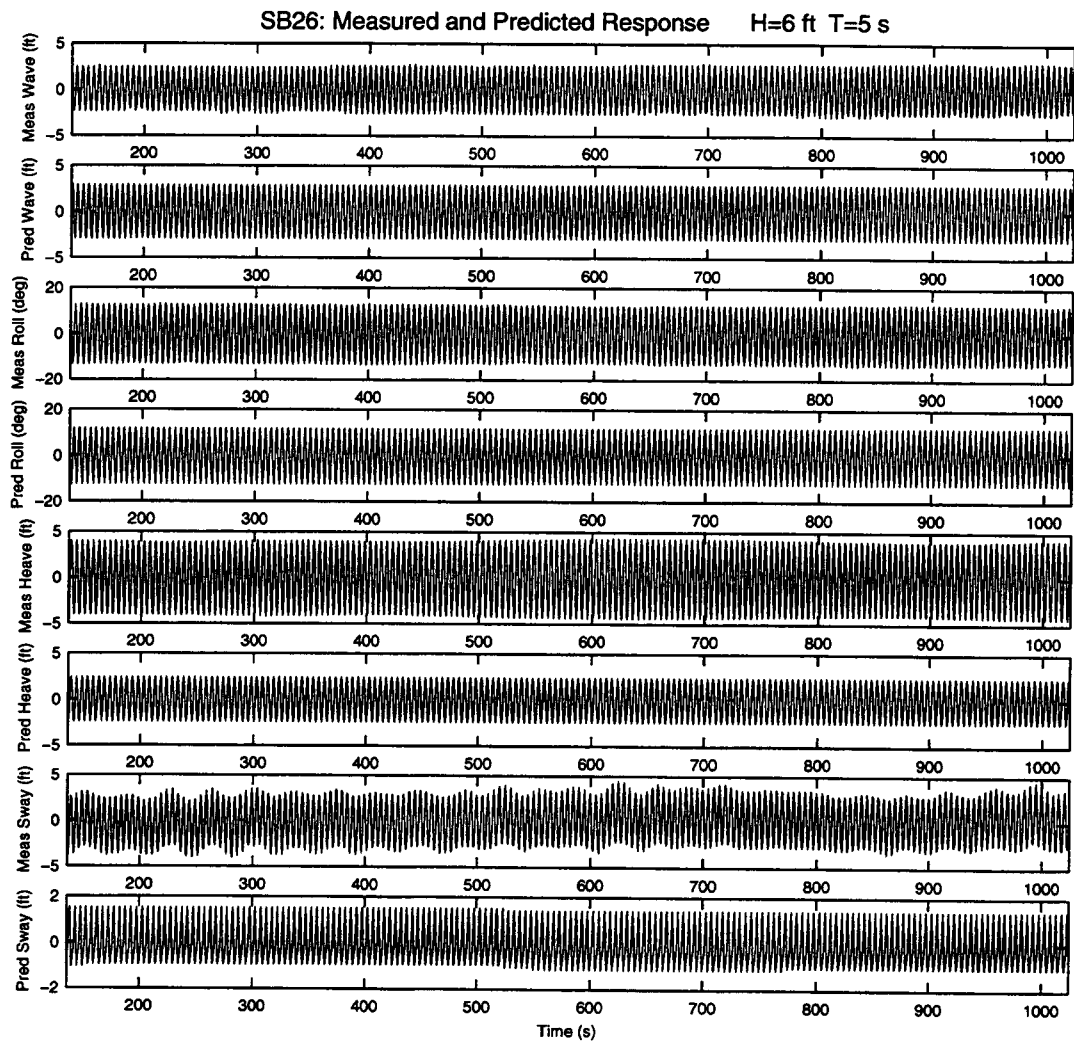


Figure B.1 Measured and Predicted Response, H=6 ft, T=5 s

B.1

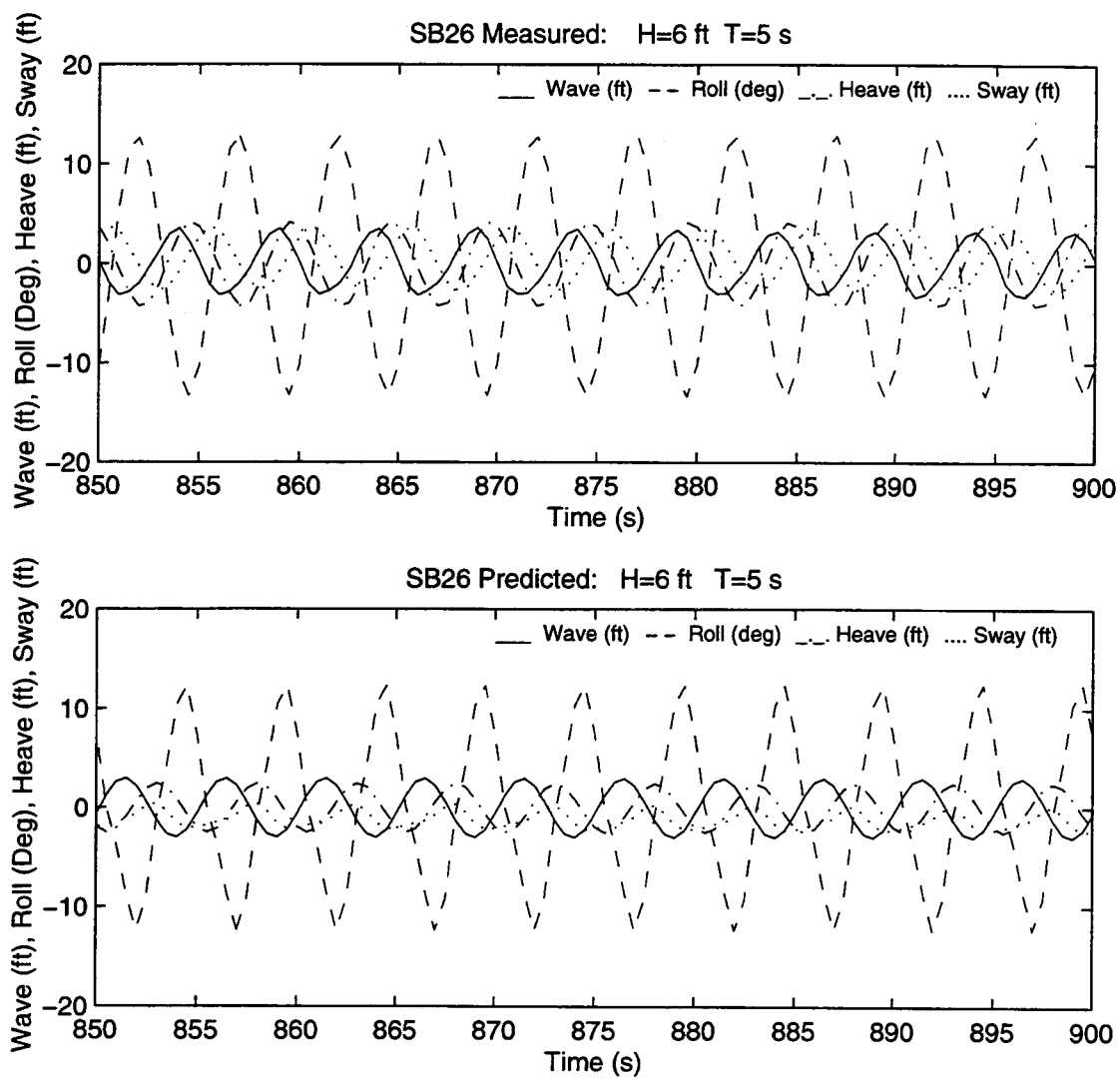


Figure B.2

Measured and Predicted Response, H=6 ft, T=5 s

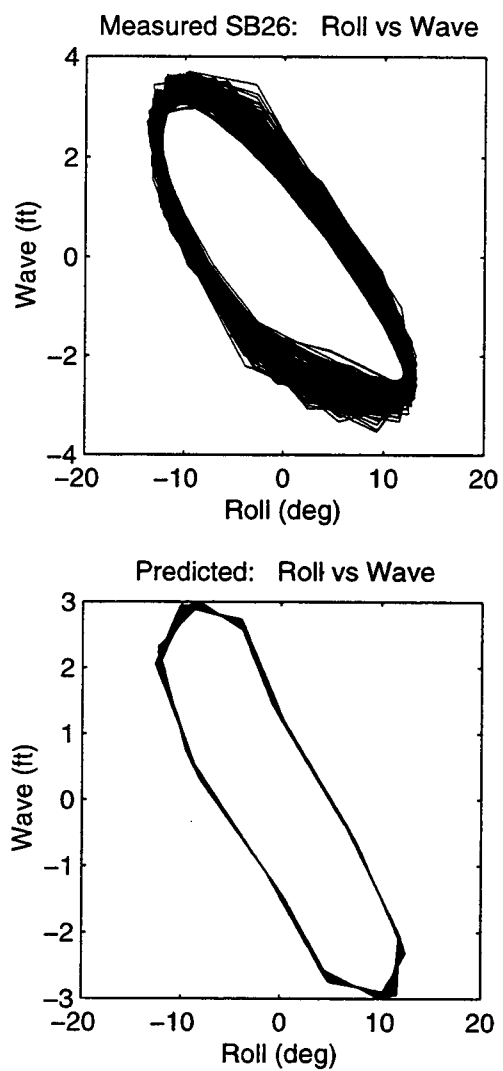


Figure B.3

Roll vs Wave, $H=6$ ft, $T=5$ s

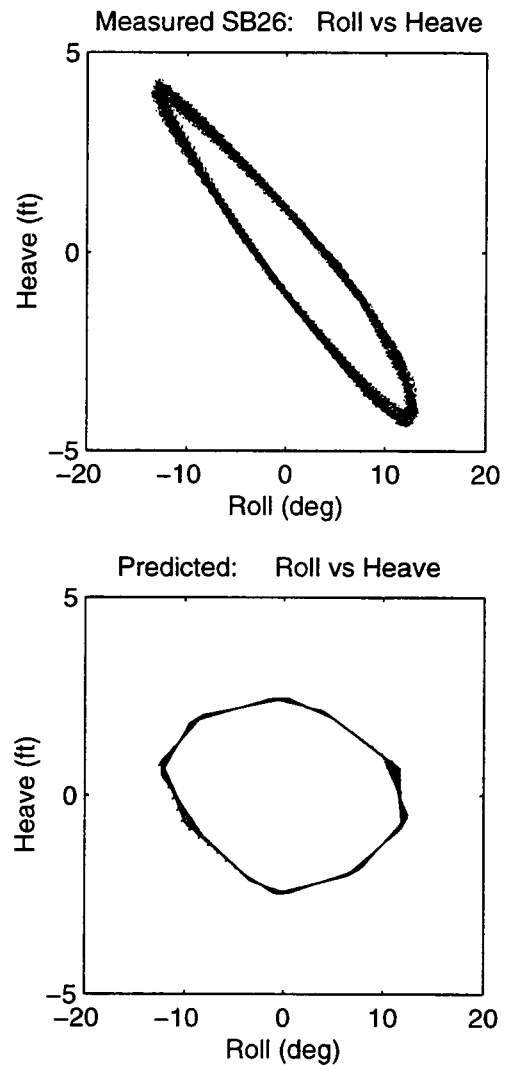


Figure B.4

Roll vs Heave, $H=6$ ft, $T=5$ s

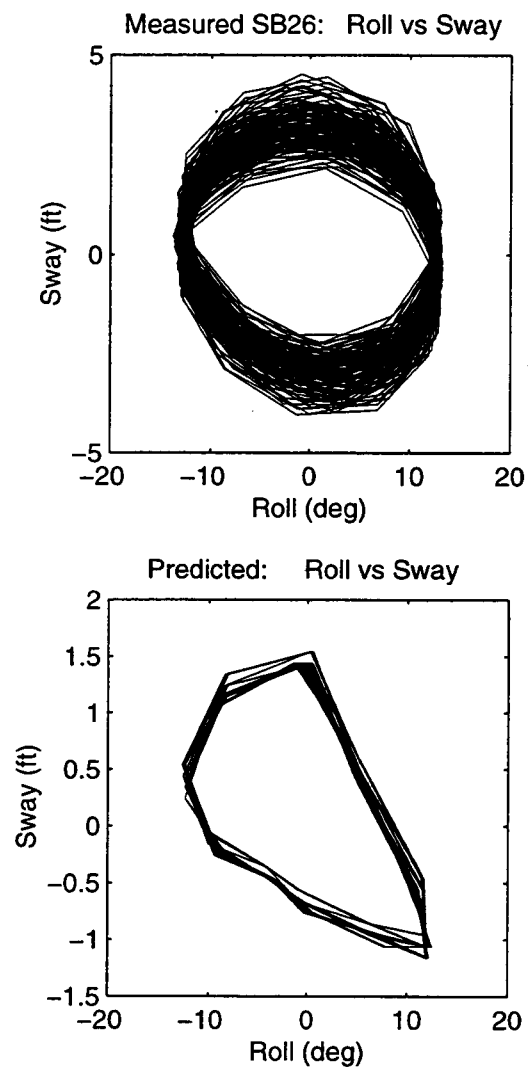


Figure B.5

Roll vs Sway, $H=6$ ft, $T=5$ s

B.5

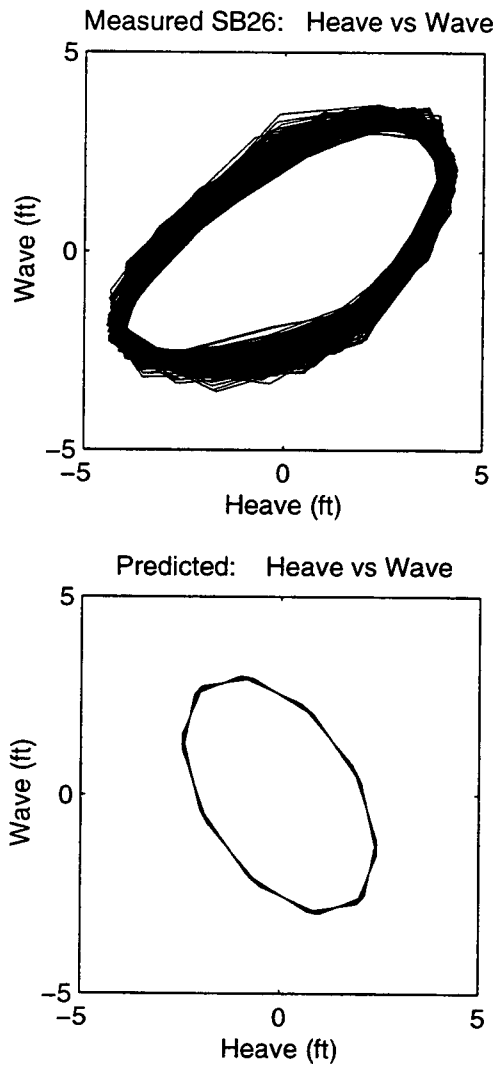


Figure B.6

Heave vs Wave, $H=6$ ft, $T=5$ s

B.6

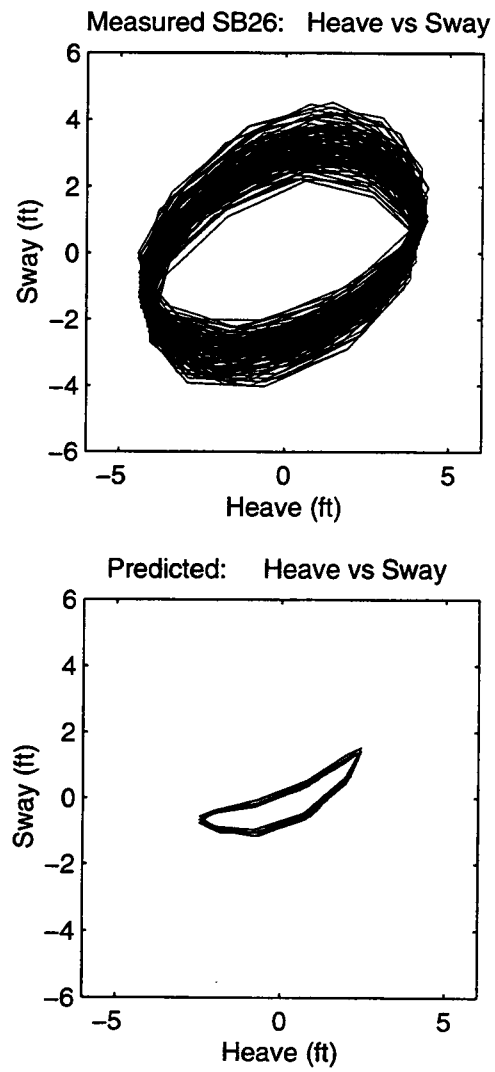


Figure B.7

Heave vs Sway, $H=6$ ft, $T=5$ s

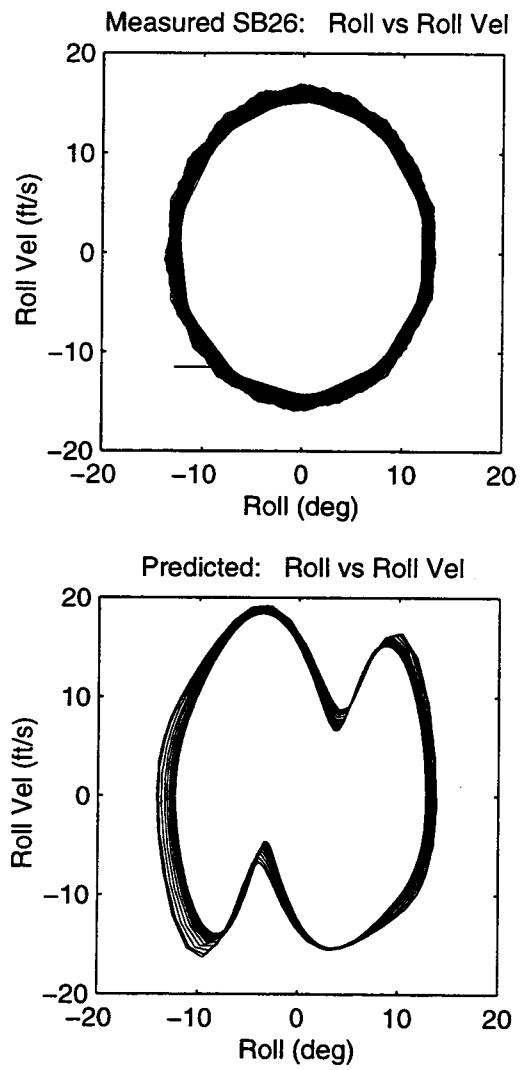


Figure B.8

Phase Plane for Roll and Roll Velocity, $H=6$ ft, $T=5$ s

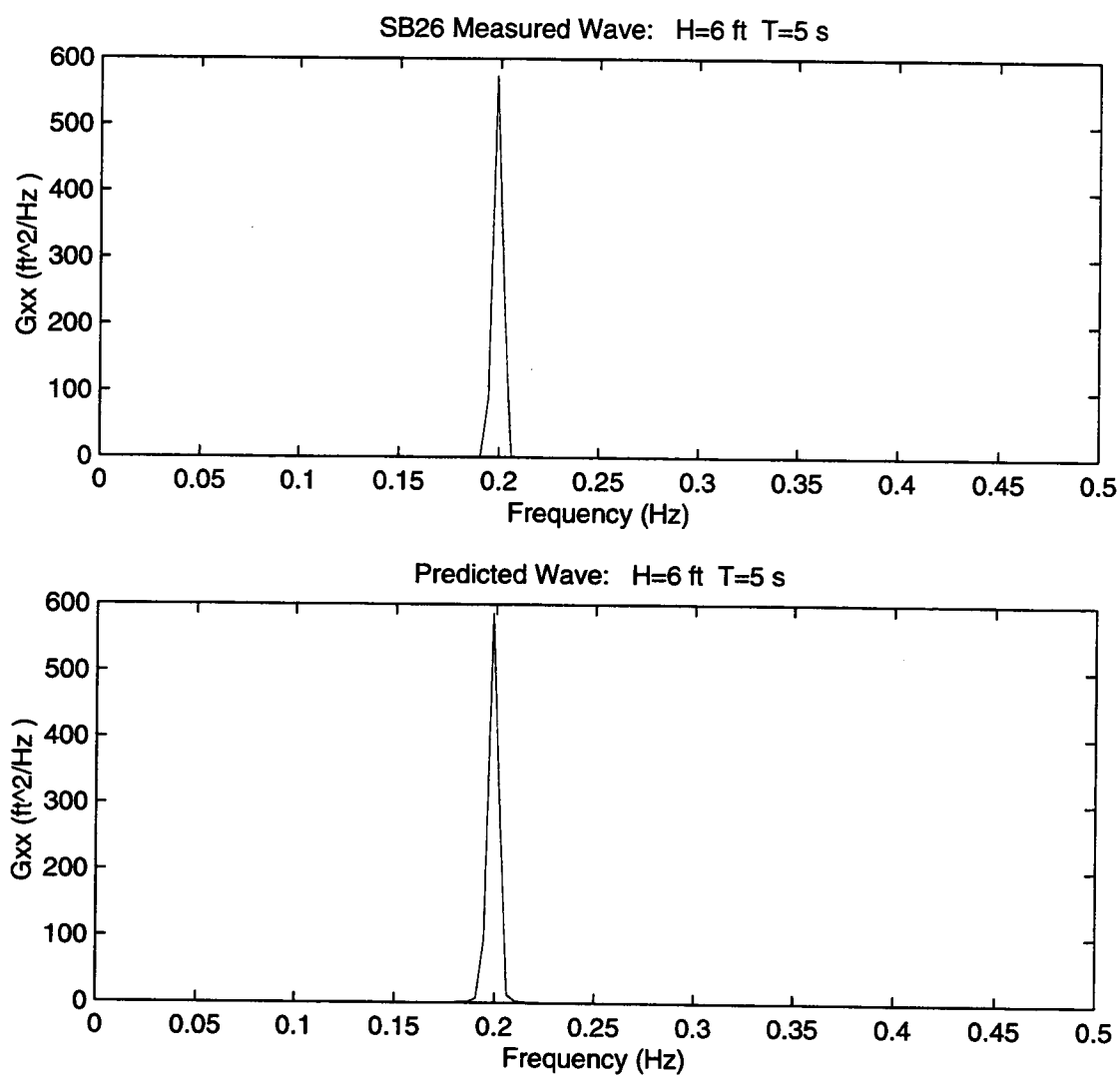


Figure B.9

Wave Spectral Densities, H=6 ft, T=5 s

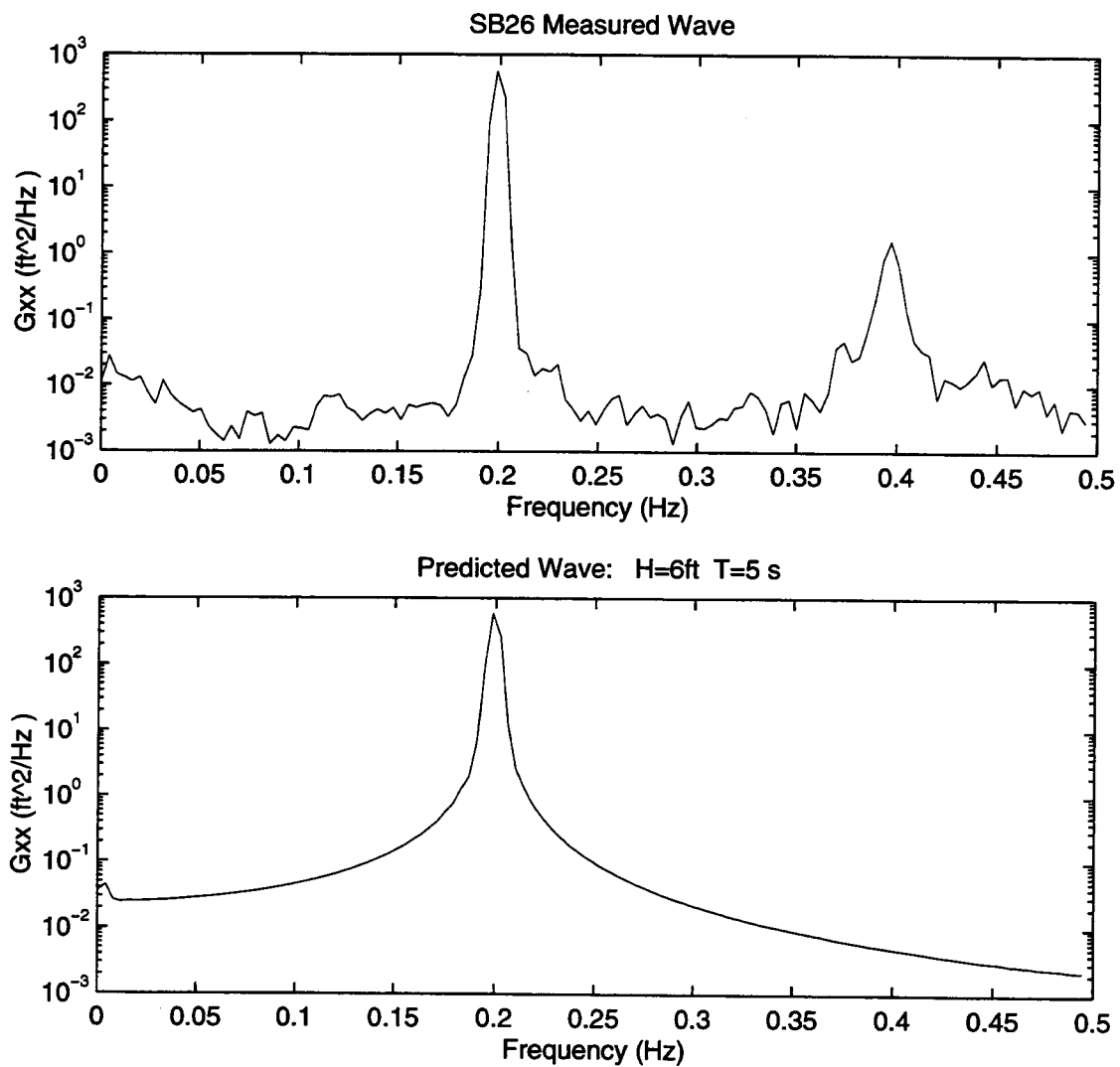


Figure B.10 Wave Spectral Densities, H=6 ft, T=5 s (semilog)

B.10

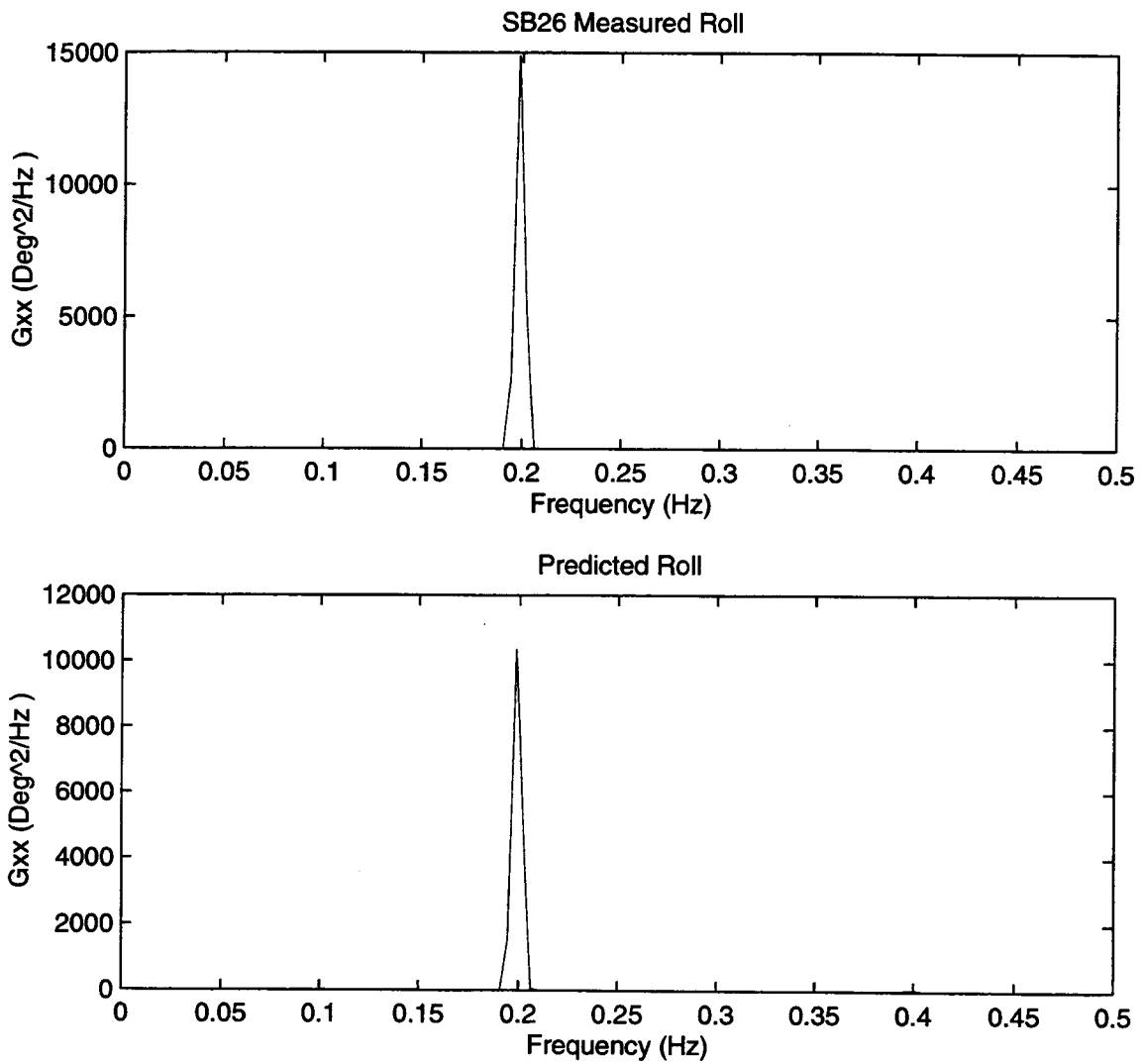


Figure B.11 Roll Spectral Densities, $H=6$ ft, $T=5$ s

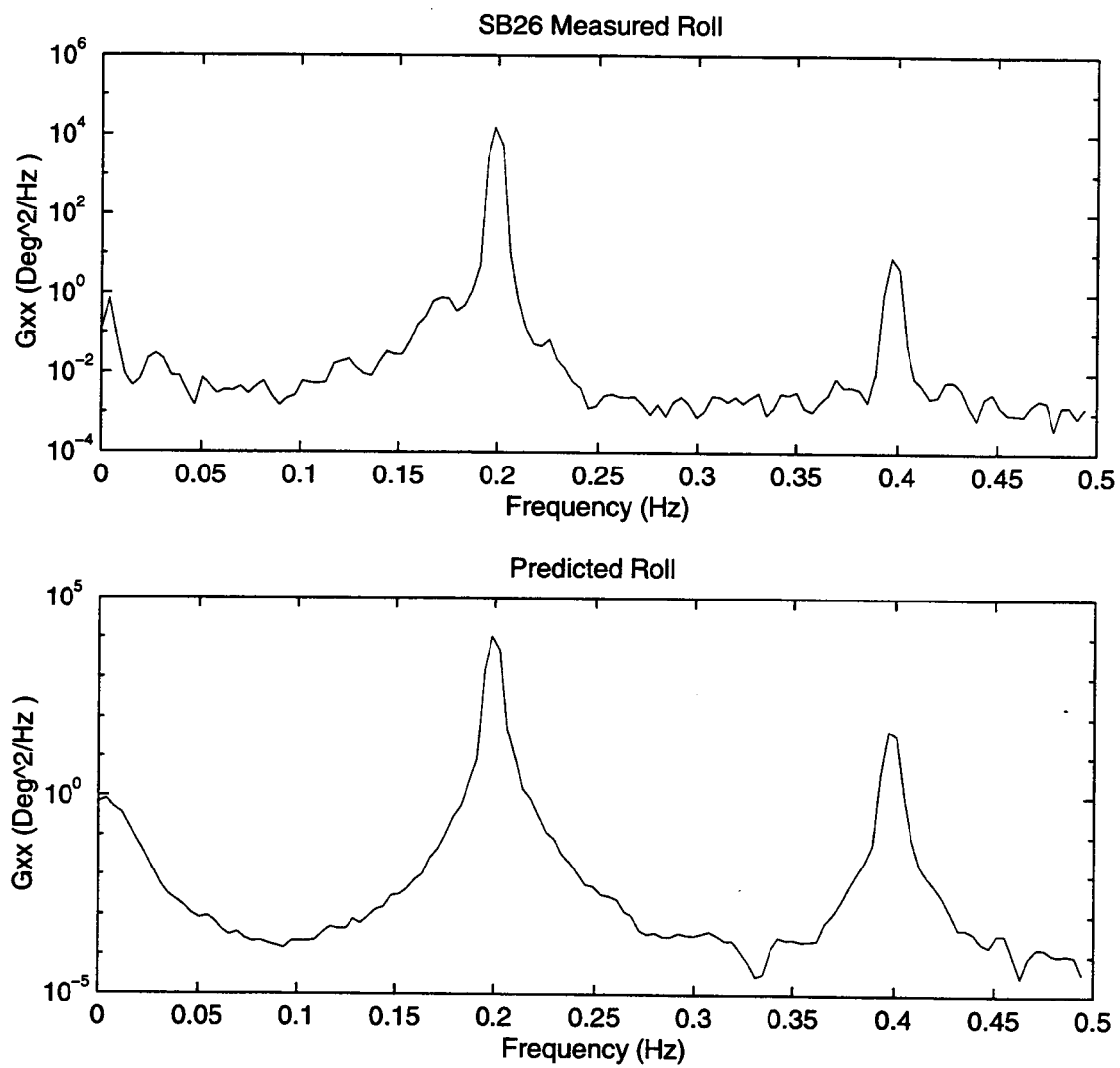


Figure B.12 Roll Spectral Densities, $H=6$ ft, $T=5$ s (semilog)

B.12

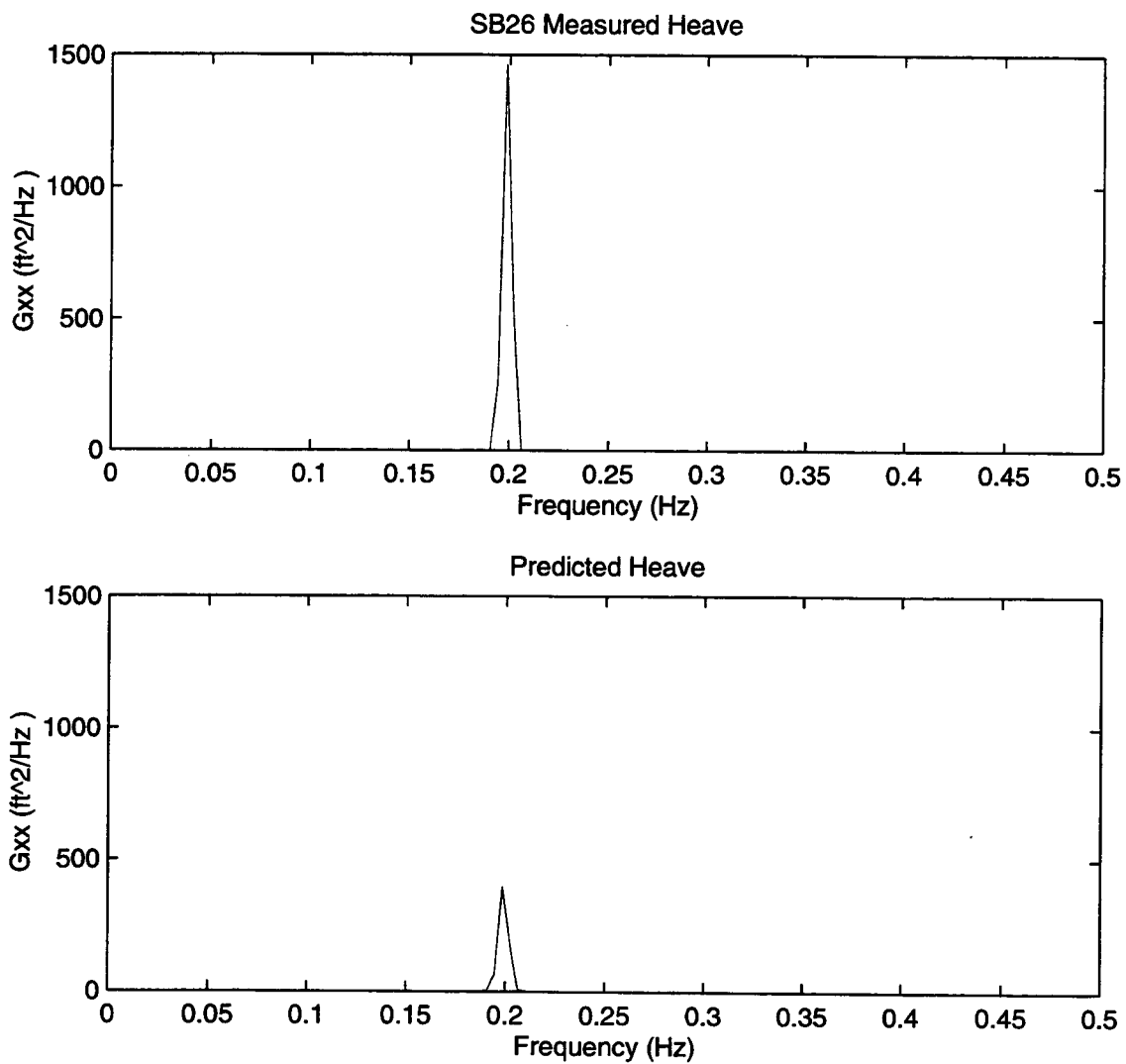


Figure B.13 Heave Spectral Densities, $H=6$ ft, $T=5$ s

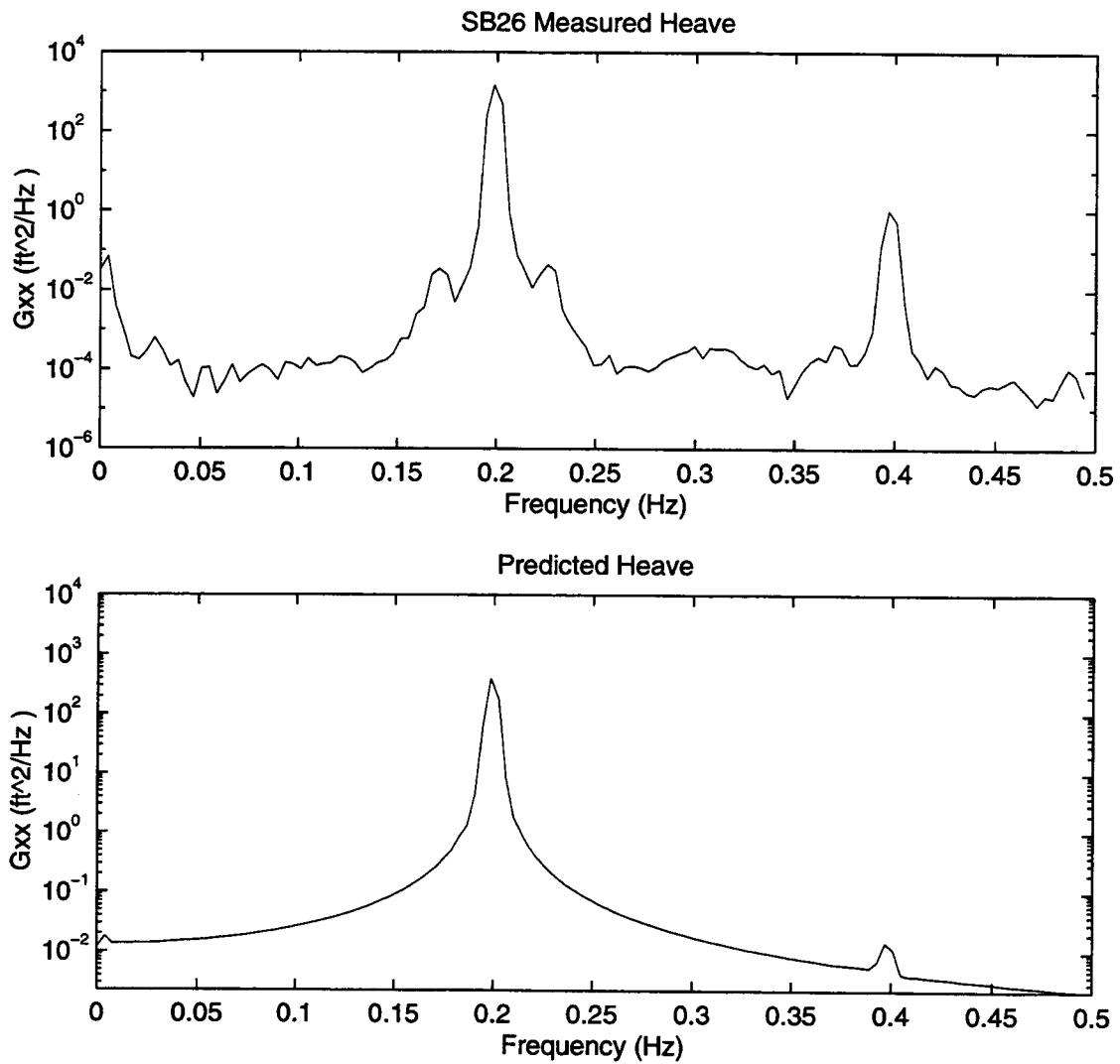


Figure B.14 Heave Spectral Densities, H=6 ft, T=5 s (semilog)

B.14

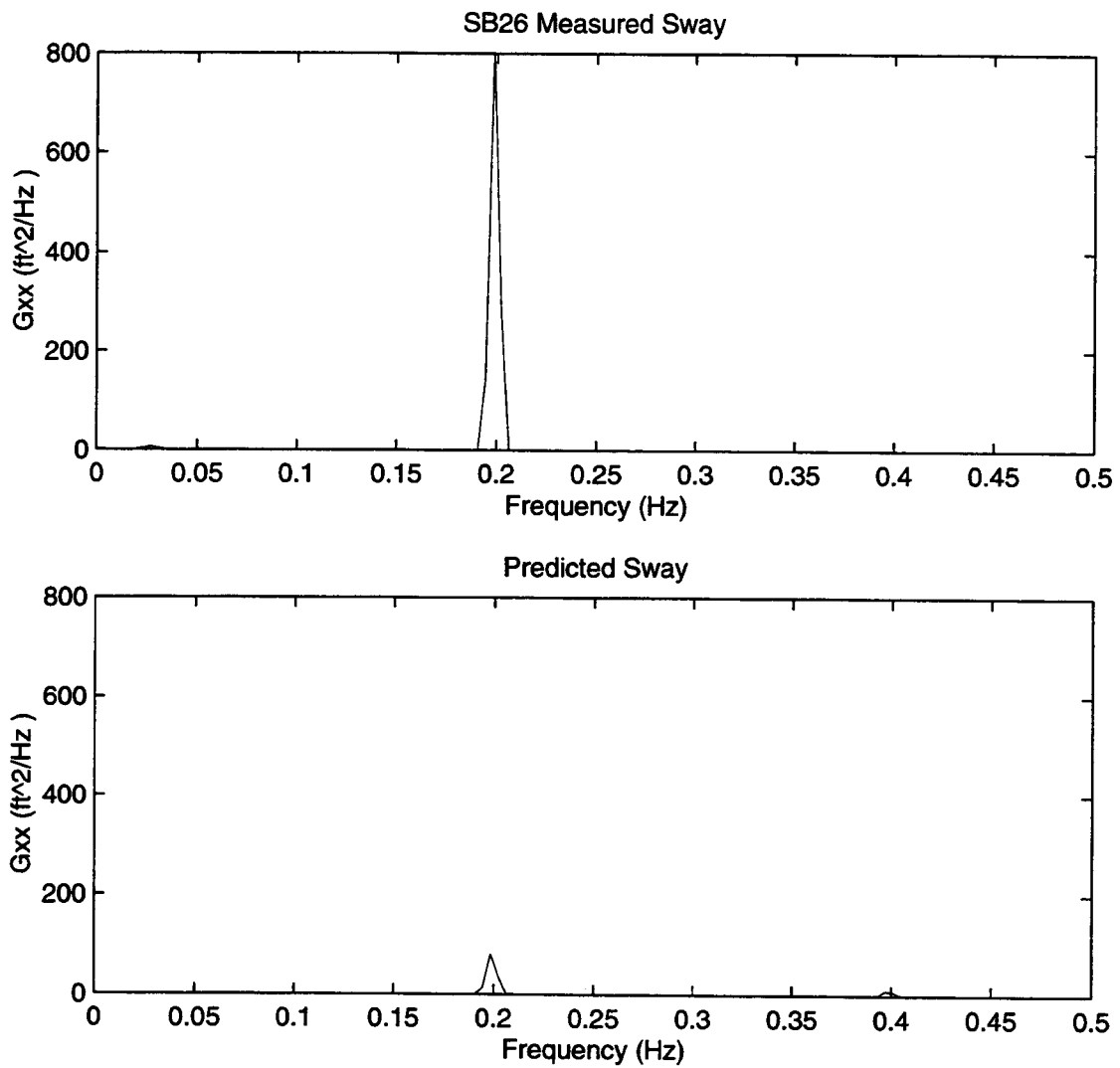


Figure B.15 Sway Spectral Densities, H=6 ft, T=5 s

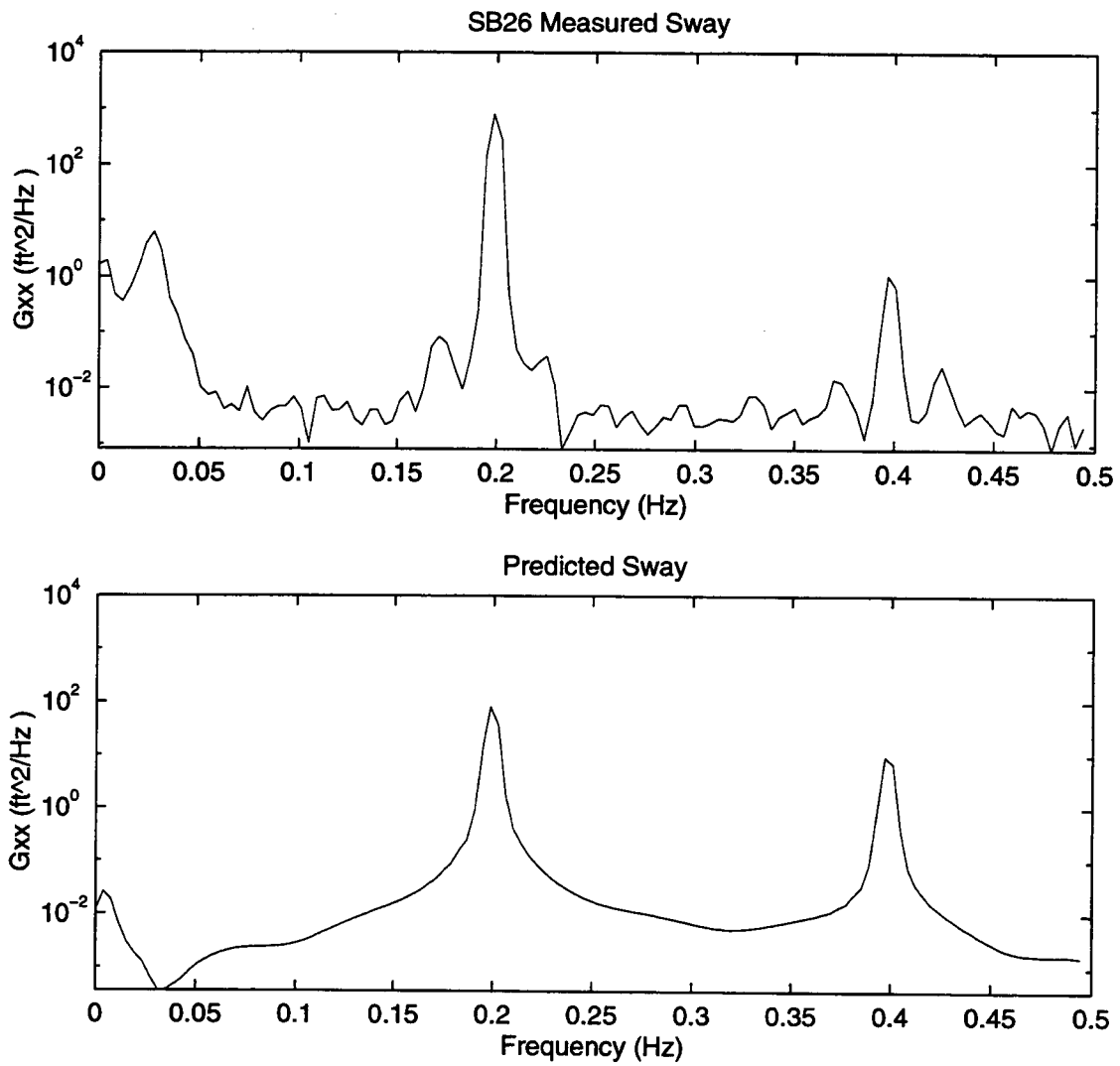


Figure B.16 Sway Spectral Densities, $H=6$ ft, $T=5$ s (semilog)

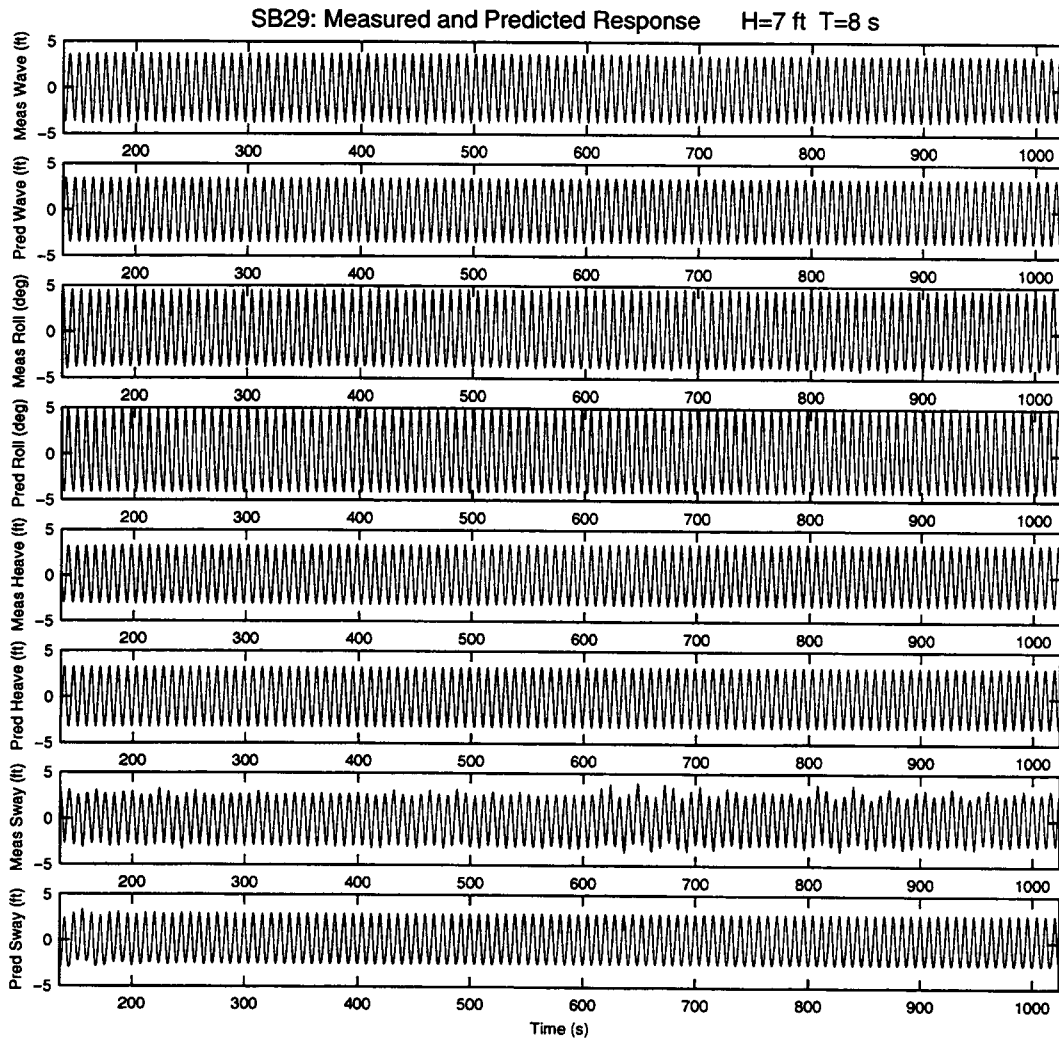


Figure B.17

Measured and Predicted Response, H=7 ft, T=8 s

B.17

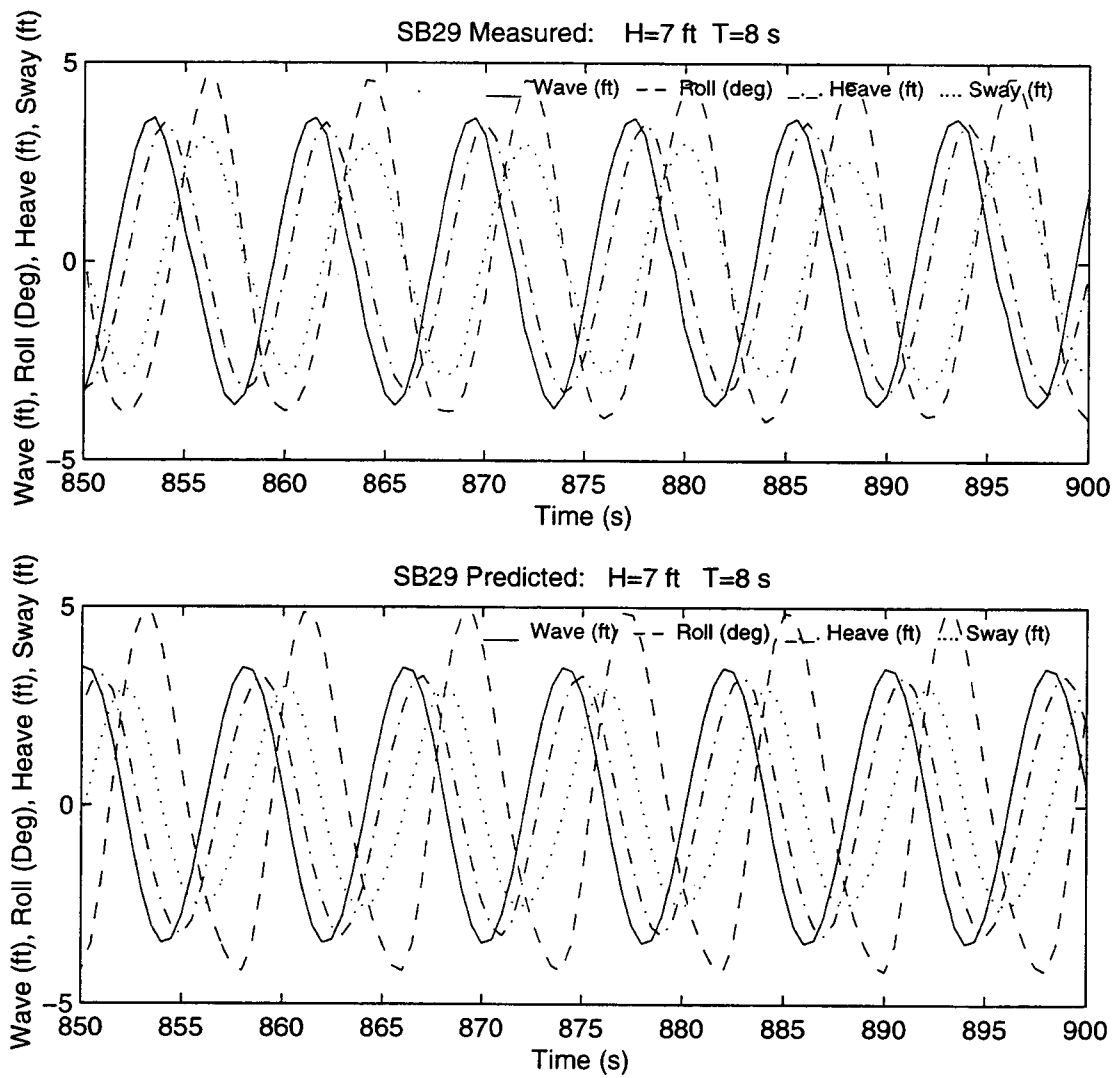


Figure B.18

Measured and Predicted Response, H=7 ft, T=8 s

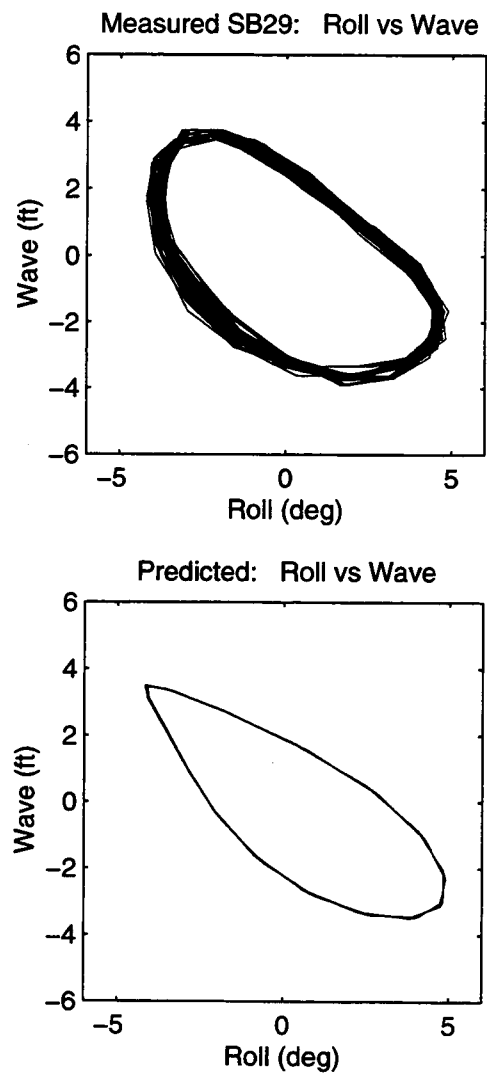


Figure B.19

Roll vs Wave, $H=7$ ft, $T=8$ s

B.19

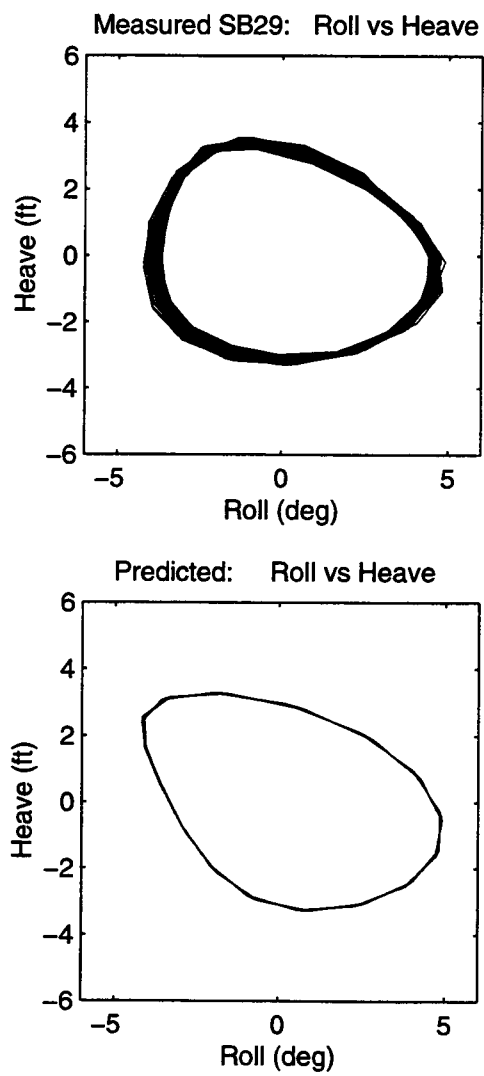


Figure B.20

Roll vs Heave, $H=7$ ft, $T=8$ s

B.20

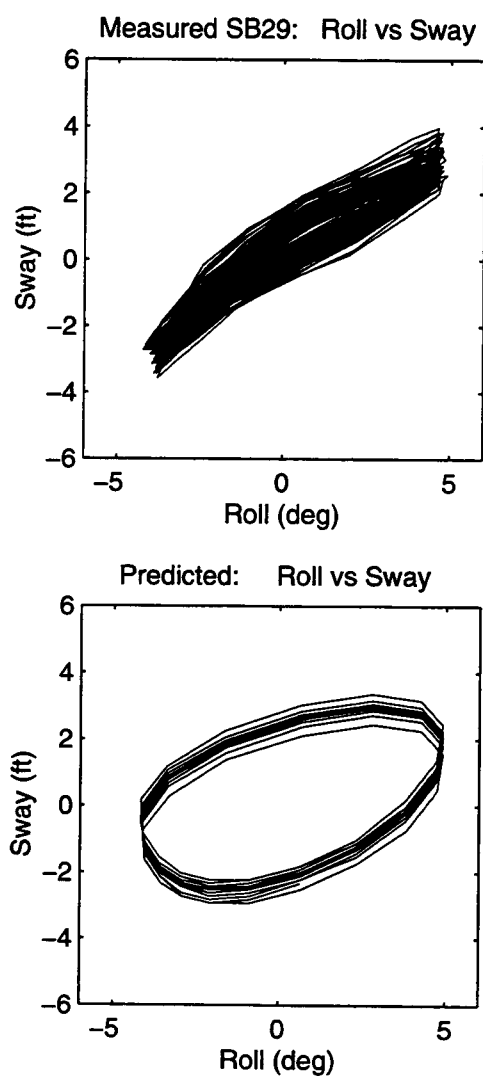


Figure B.21

Roll vs Sway, $H=7$ ft, $T=8$ s

B.21

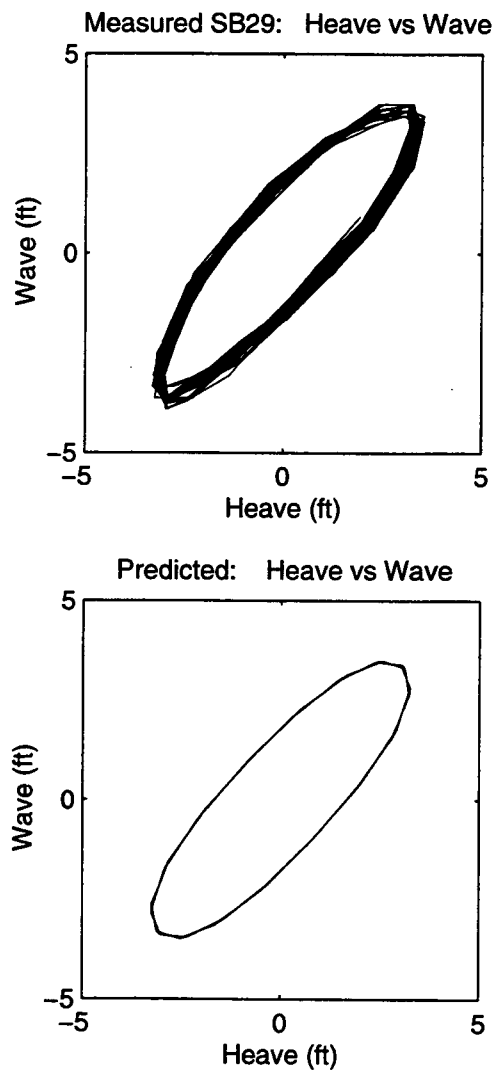


Figure B.22

Heave vs Wave, $H=7$ ft, $T=8$ s

B.22

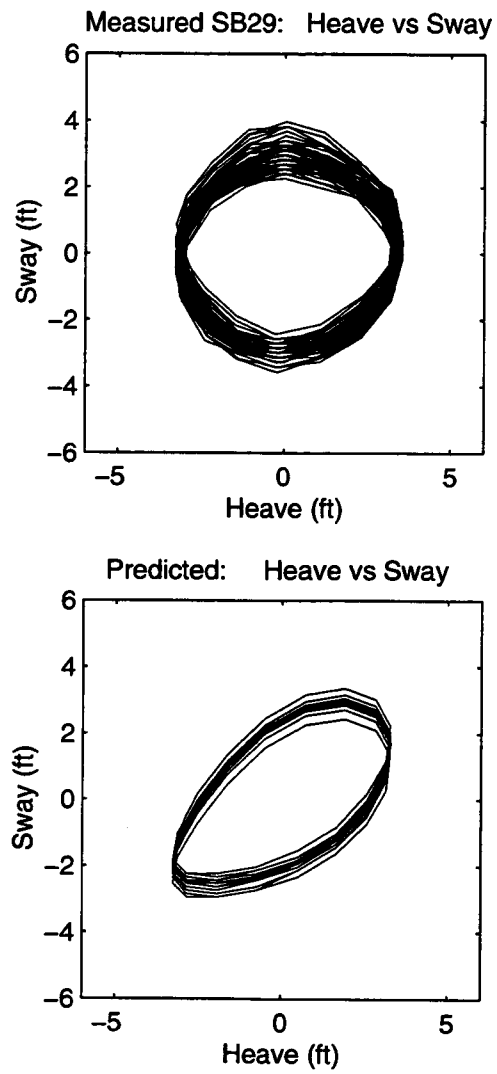


Figure B.23

Heave vs Sway, $H=7$ ft, $T=8$ s

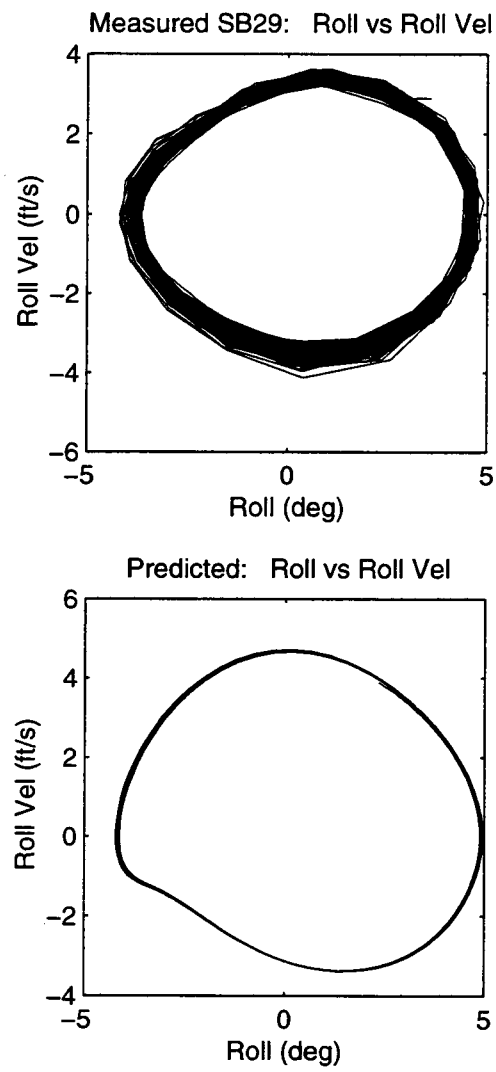


Figure B.24

Phase Plane for Roll and Roll Velocity, $H=7$ ft, $T=8$ s

B.24

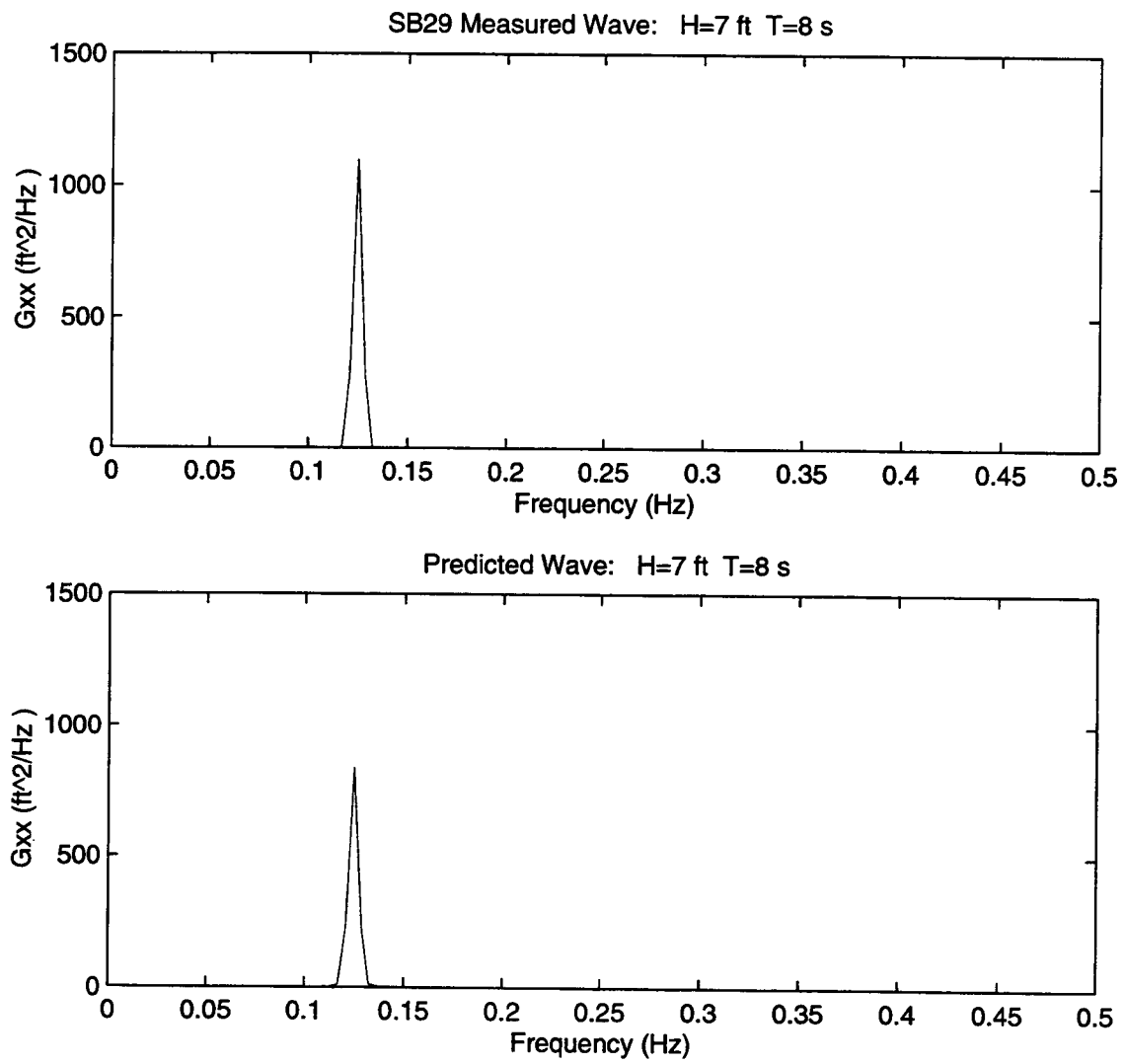


Figure B.25 Wave Spectral Densities, H=7 ft, T=8 s

B.25

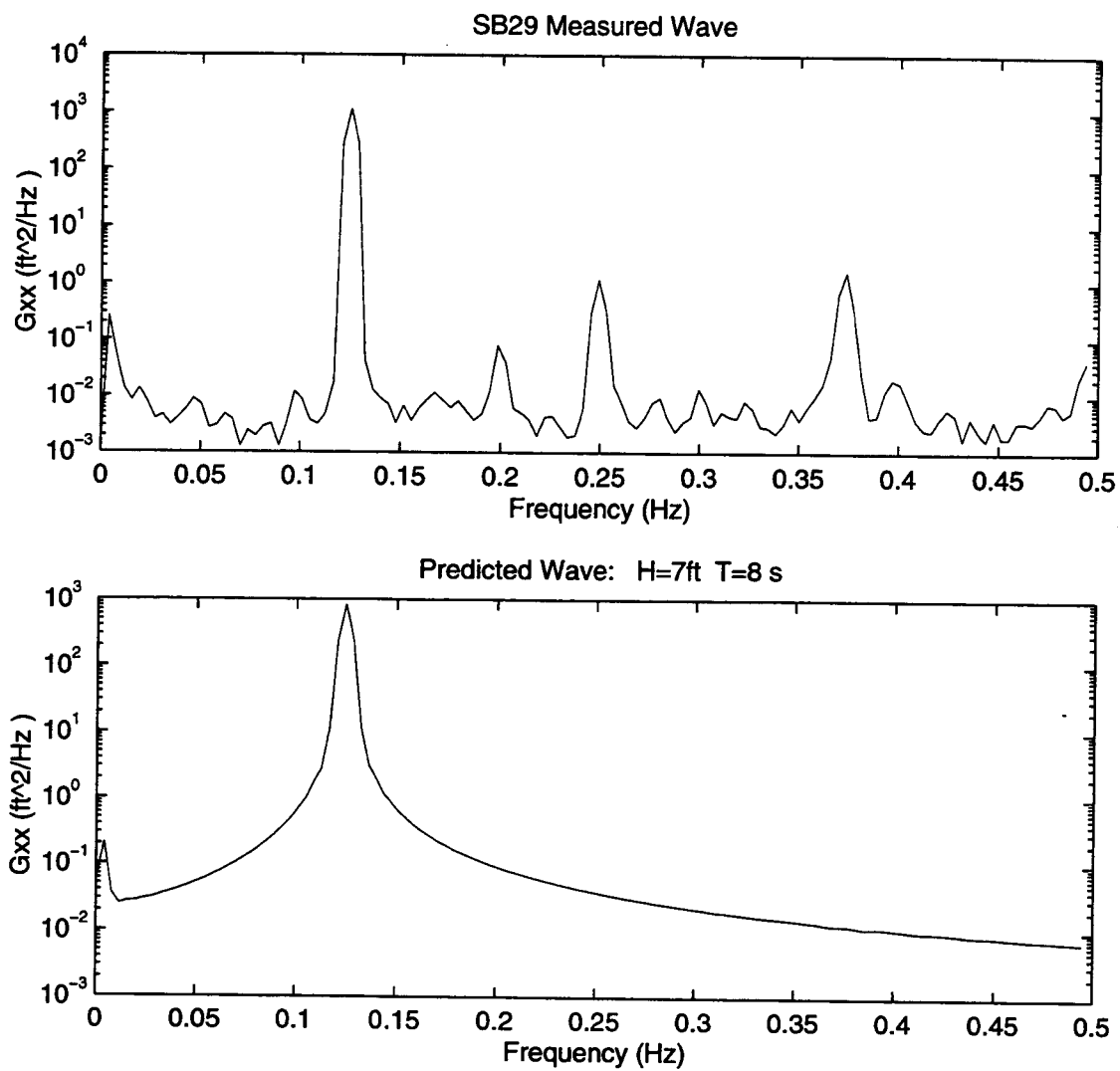


Figure B.26 Wave Spectral Densities, H=7 ft, T=8 s (semilog)

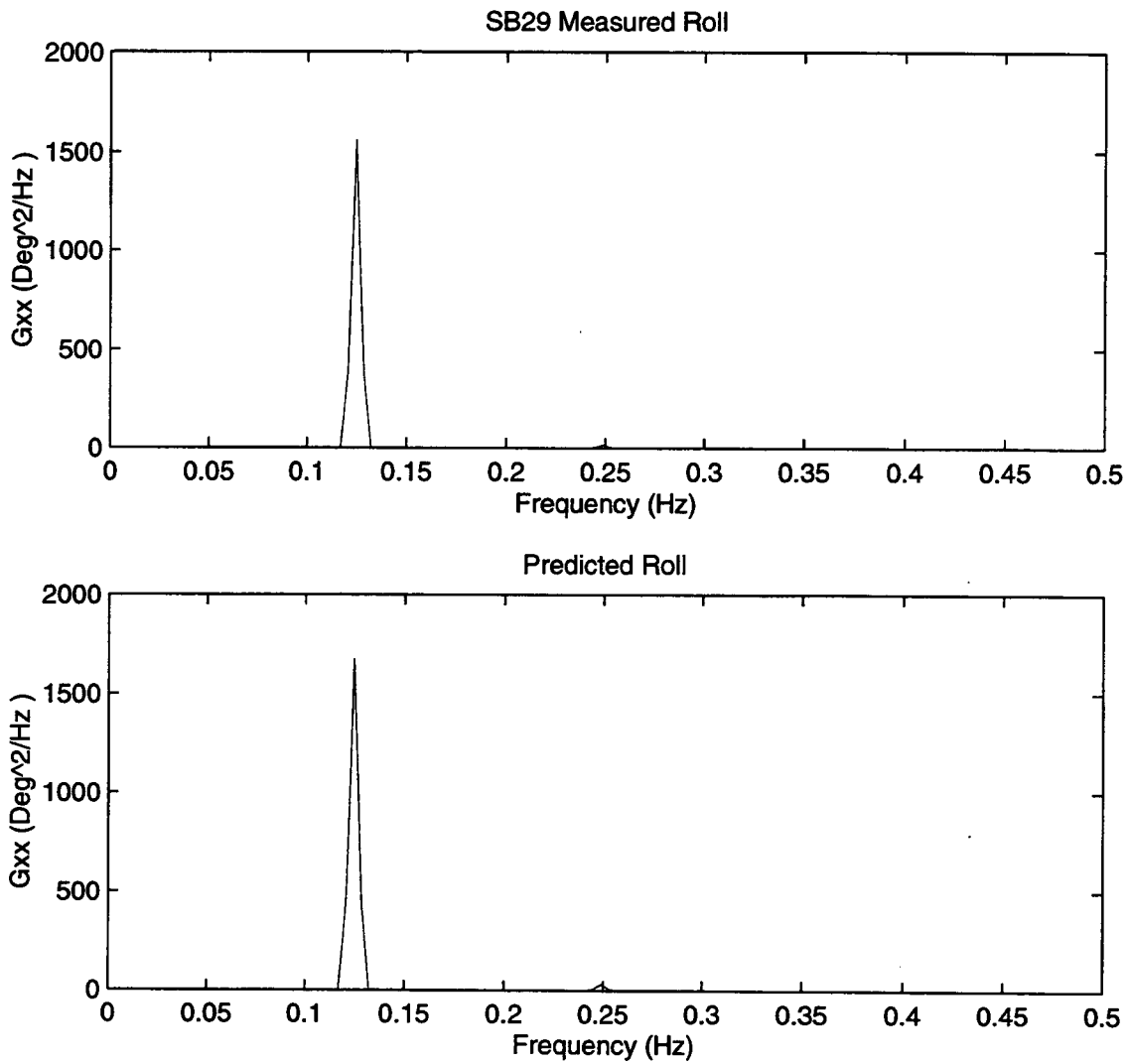


Figure B.27 Roll Spectral Densities, $H=7$ ft, $T=8$ s

B.27

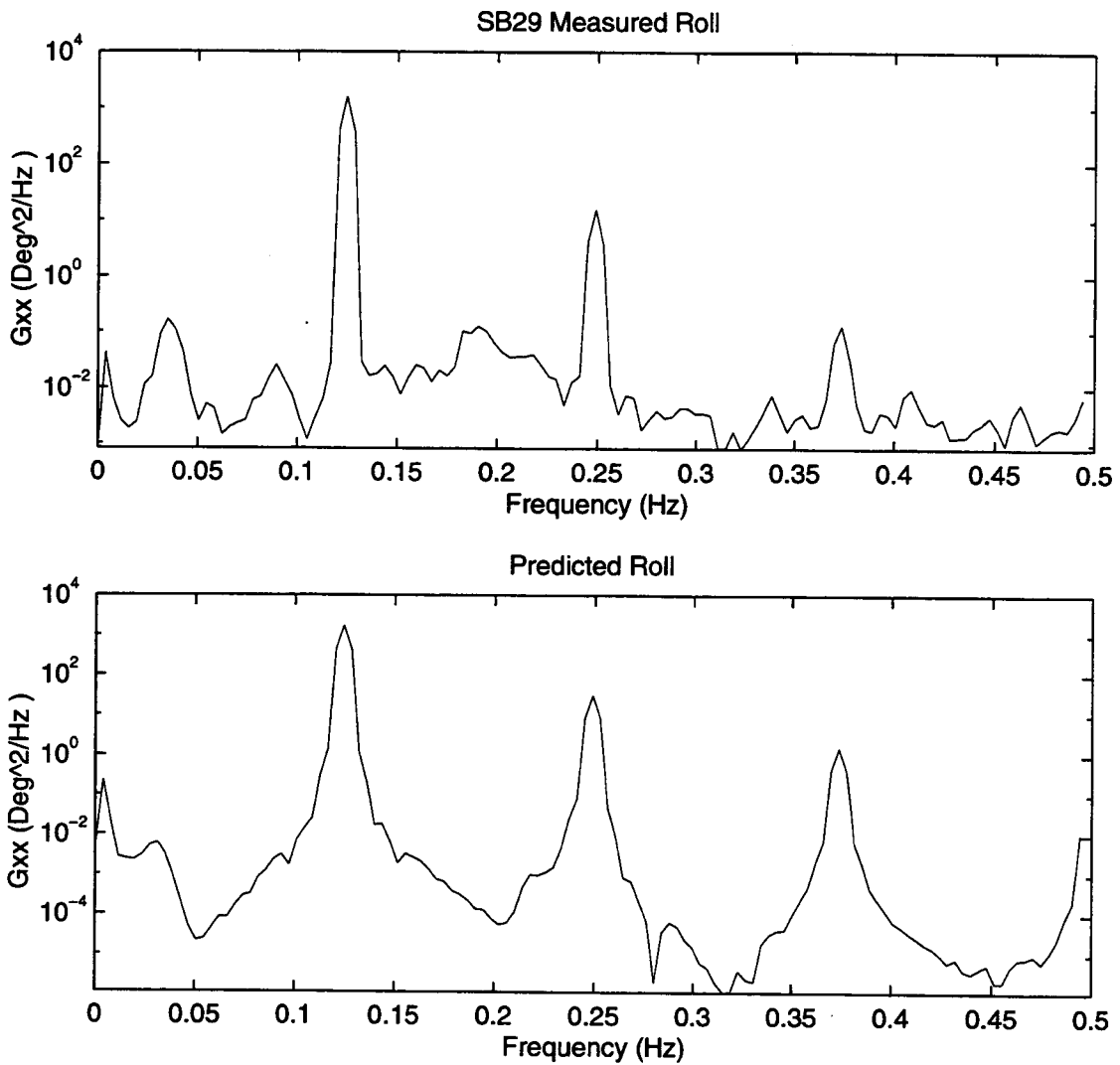


Figure B.28 Roll Spectral Densities, $H=7$ ft, $T=8$ s (semilog)

B.28

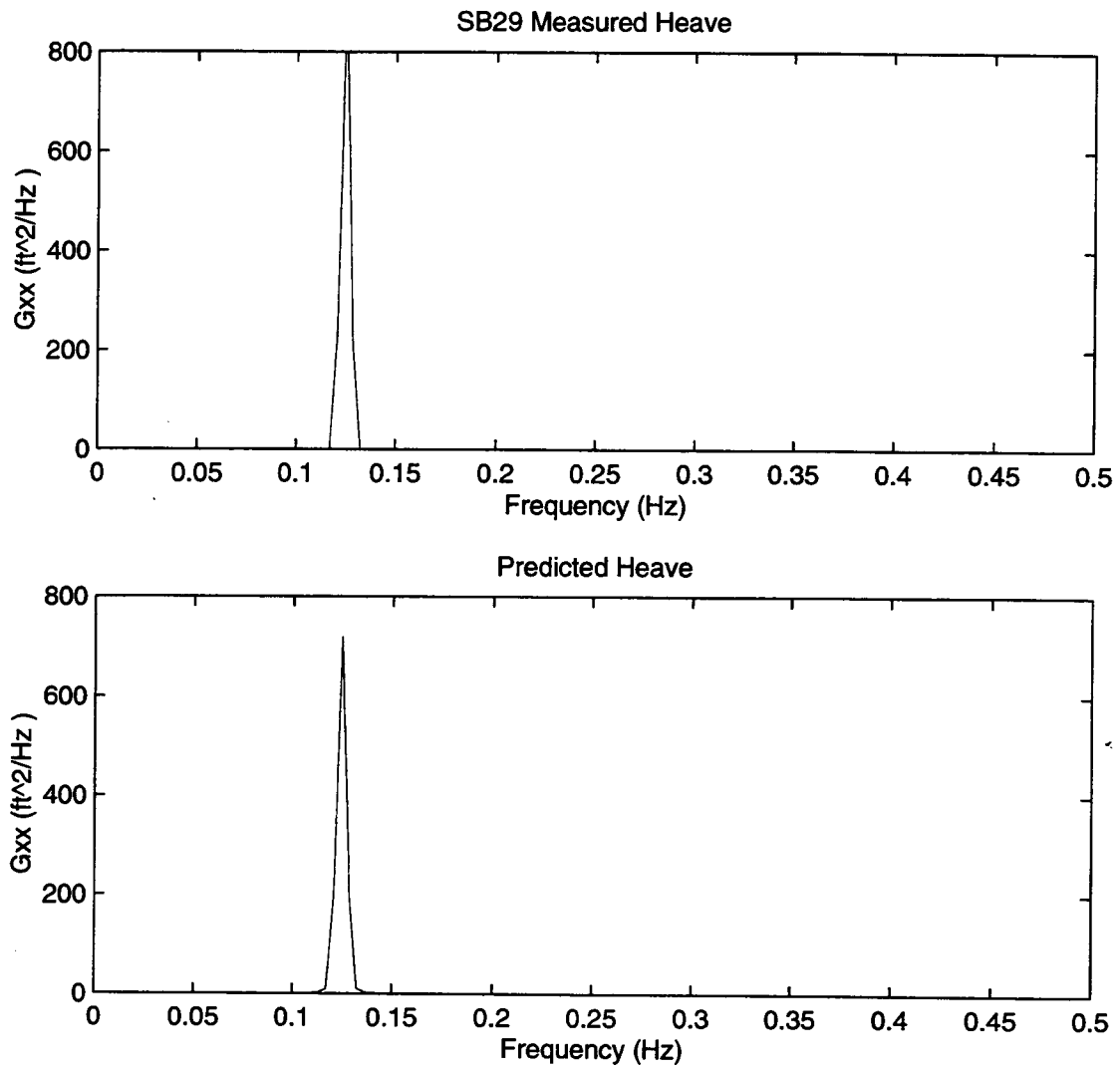


Figure B.29 Heave Spectral Densities, H=7 ft, T=8 s

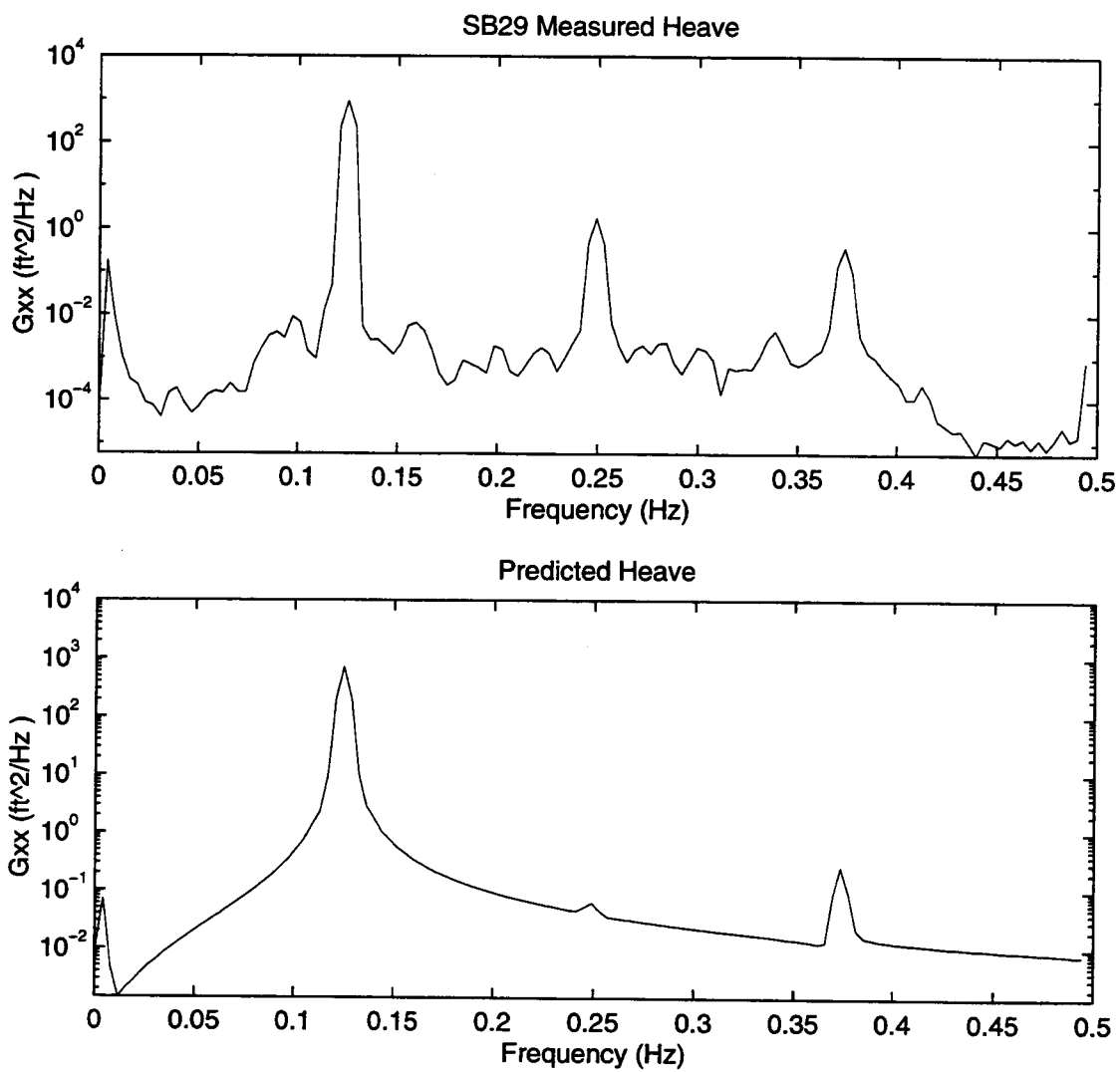


Figure B.30 Heave Spectral Densities, $H=7$ ft, $T=8$ s (semilog)

B.30

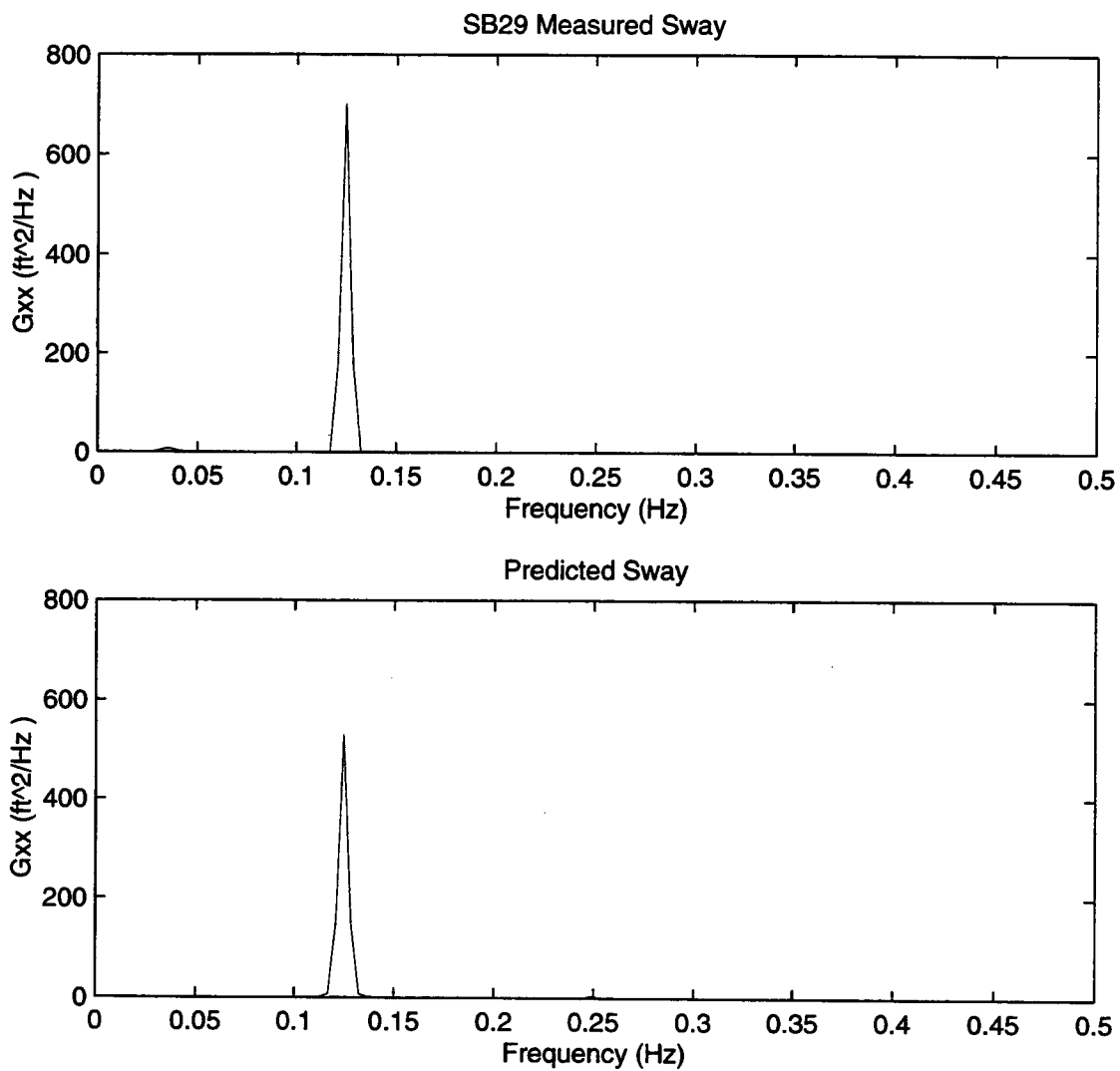


Figure B.31 Sway Spectral Densities, $H=7$ ft, $T=8$ s

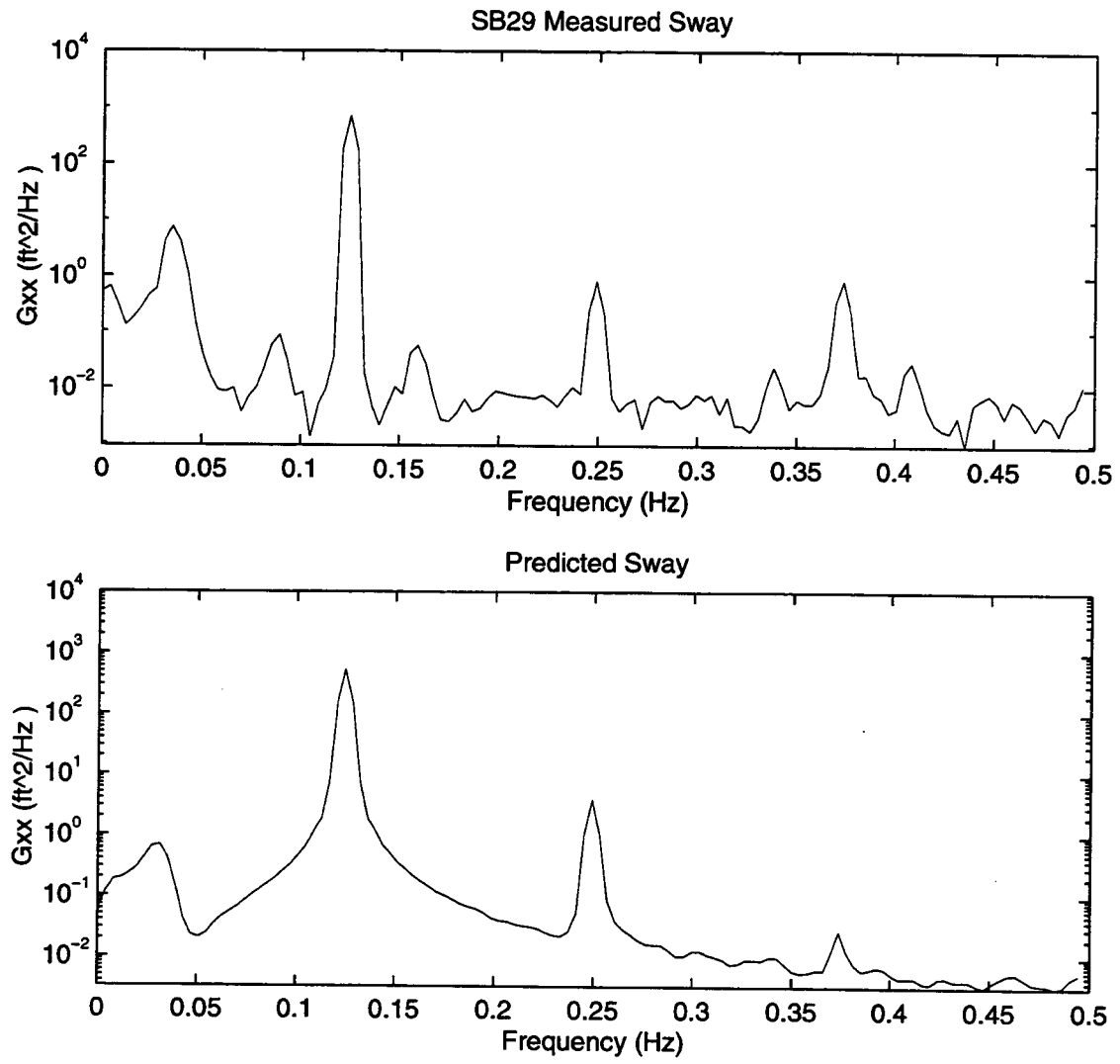


Figure B.32 Sway Spectral Densities, H=7 ft, T=8 s (semilog)

B.32

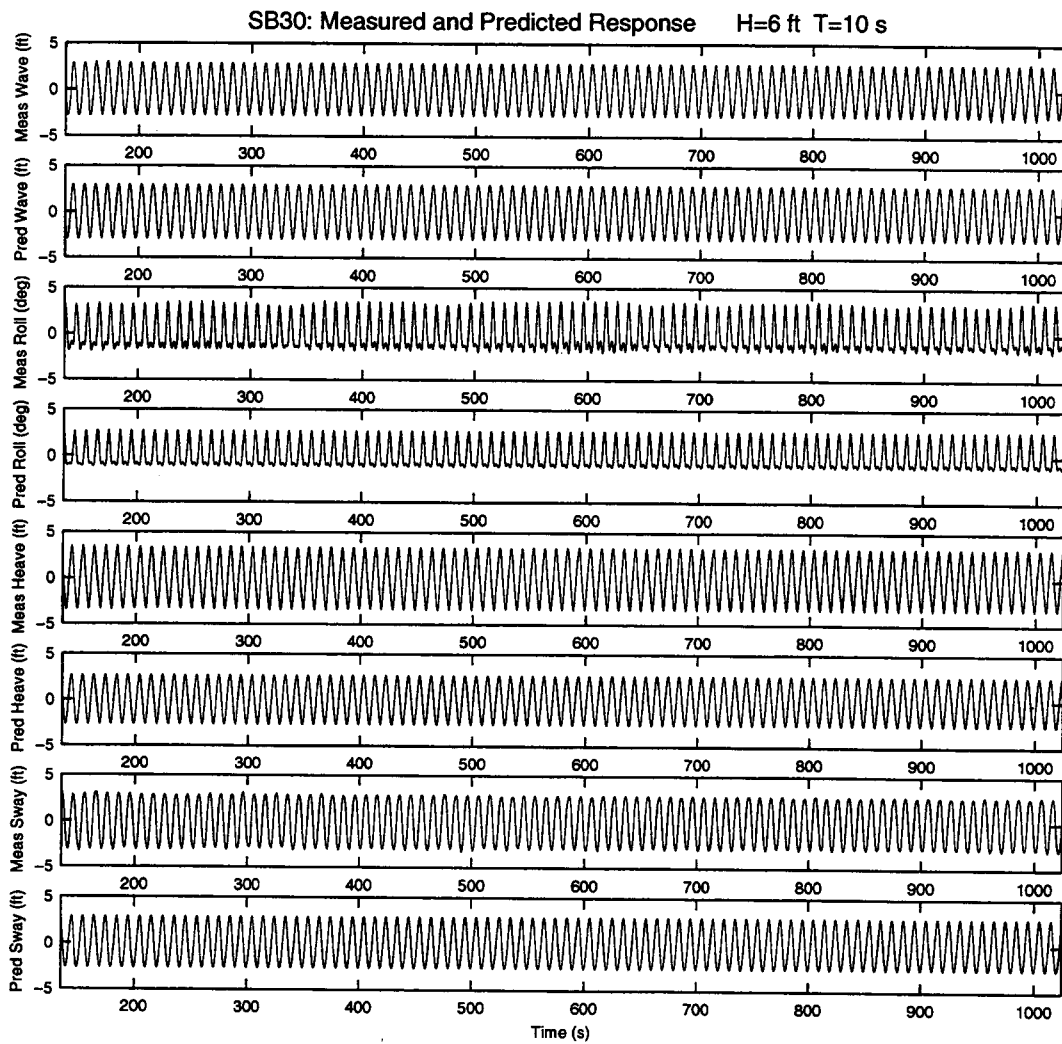


Figure B.33

Measured and Predicted Response, H=6 ft, T=10 s

B.33

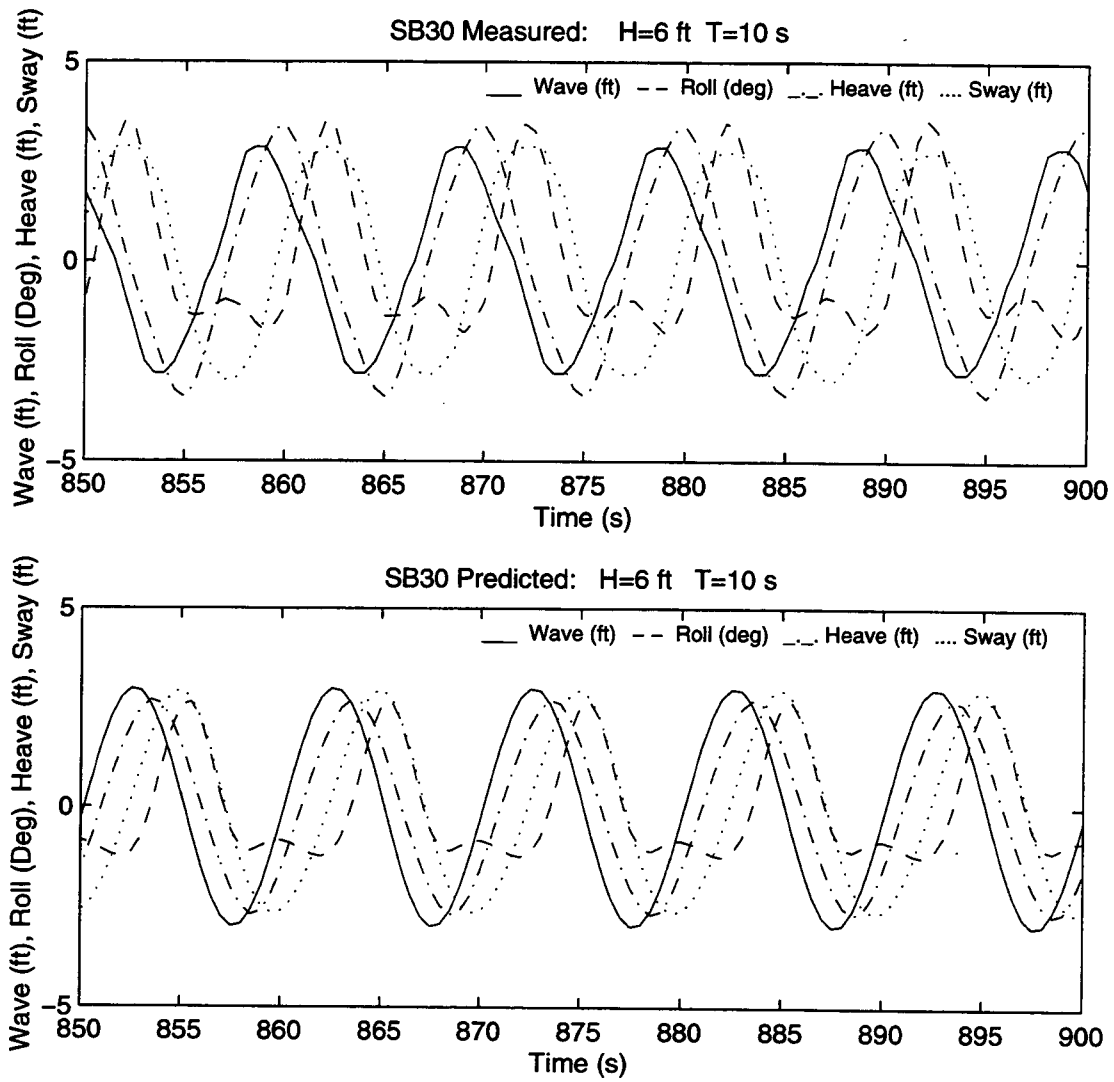


Figure B.34

Measured and Predicted Response, H=6 ft, T=10 s

B.34

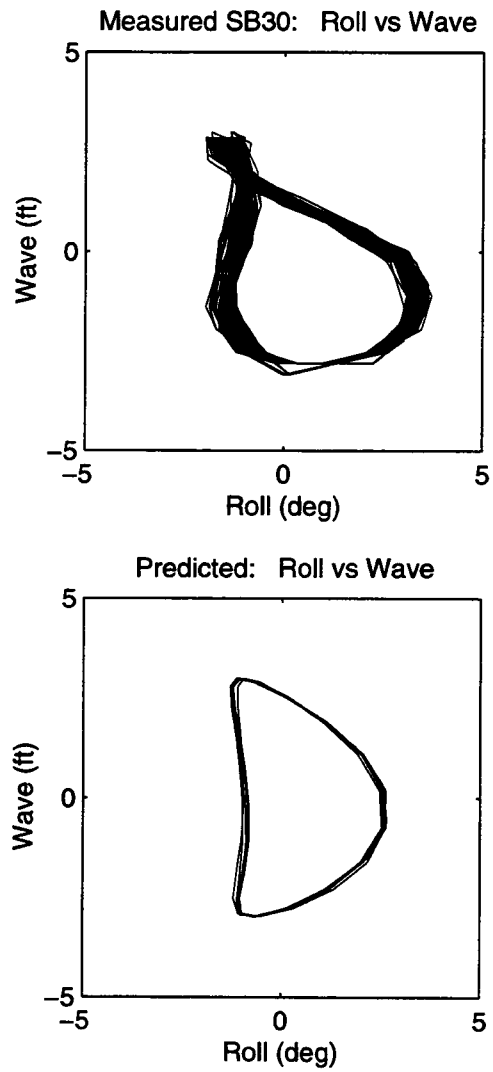


Figure B.35

Roll vs Wave, $H=6$ ft, $T=10$ s

B.35

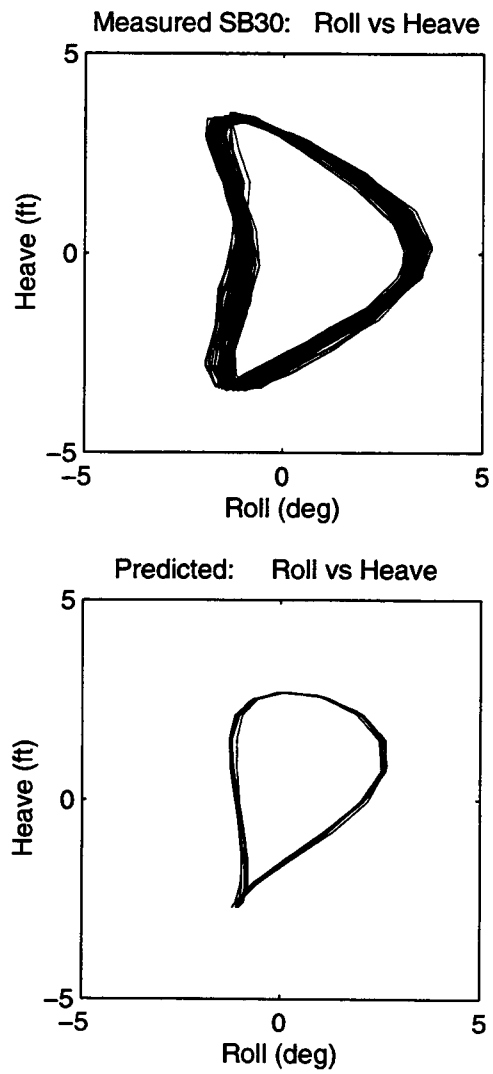


Figure B.36

Roll vs Heave, $H=6$ ft, $T=10$ s

B.36

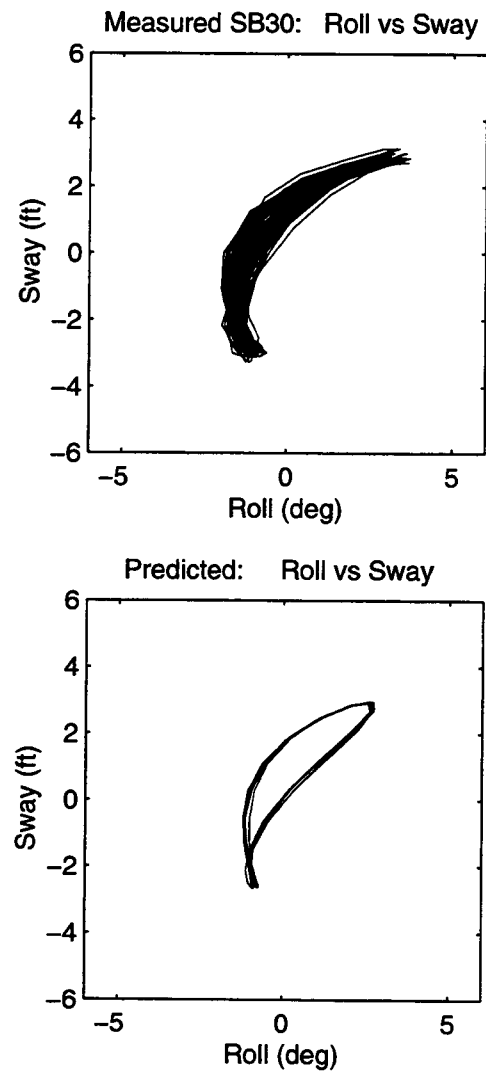


Figure B.37

Roll vs Sway, $H=6$ ft, $T=10$ s

B.37

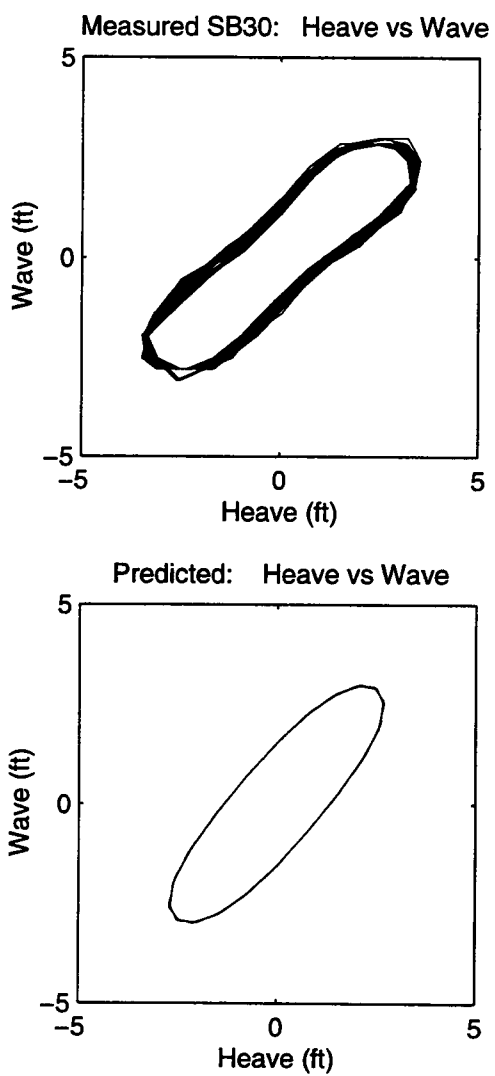


Figure B.38

Heave vs Wave, $H=6$ ft, $T=10$ s

B.38

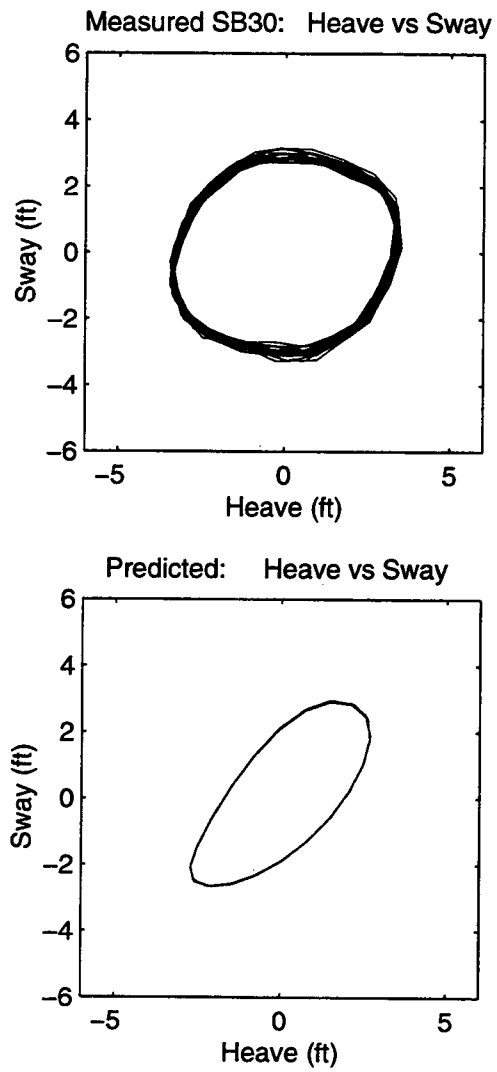


Figure B.39

Heave vs Sway, $H=6$ ft, $T=10$ s

B.39

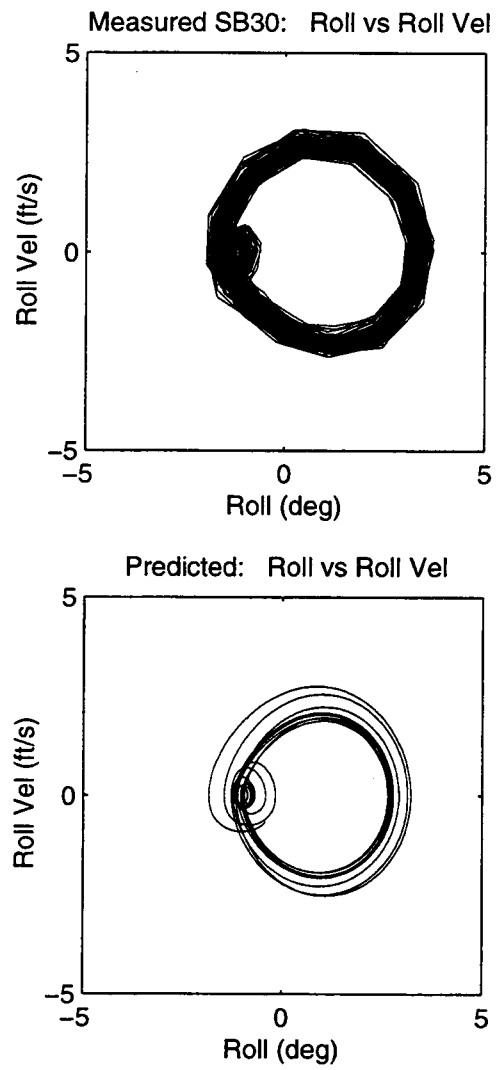


Figure B.40

Phase Plane for Roll and Roll Velocity, $H=6$ ft, $T=10$ s

B.40

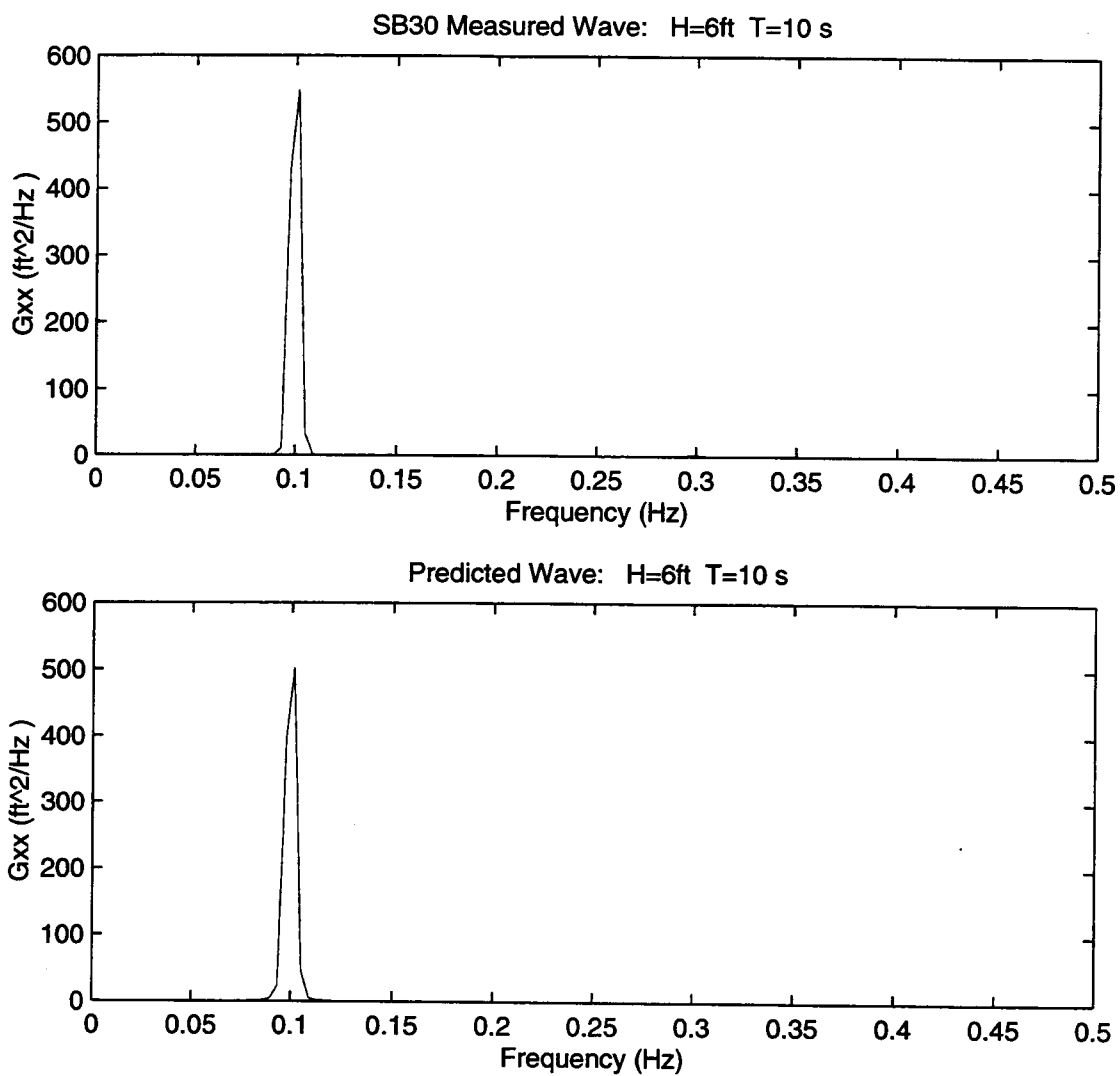


Figure B.41 Wave Spectral Densities, H=6 ft, T=10 s

B.41

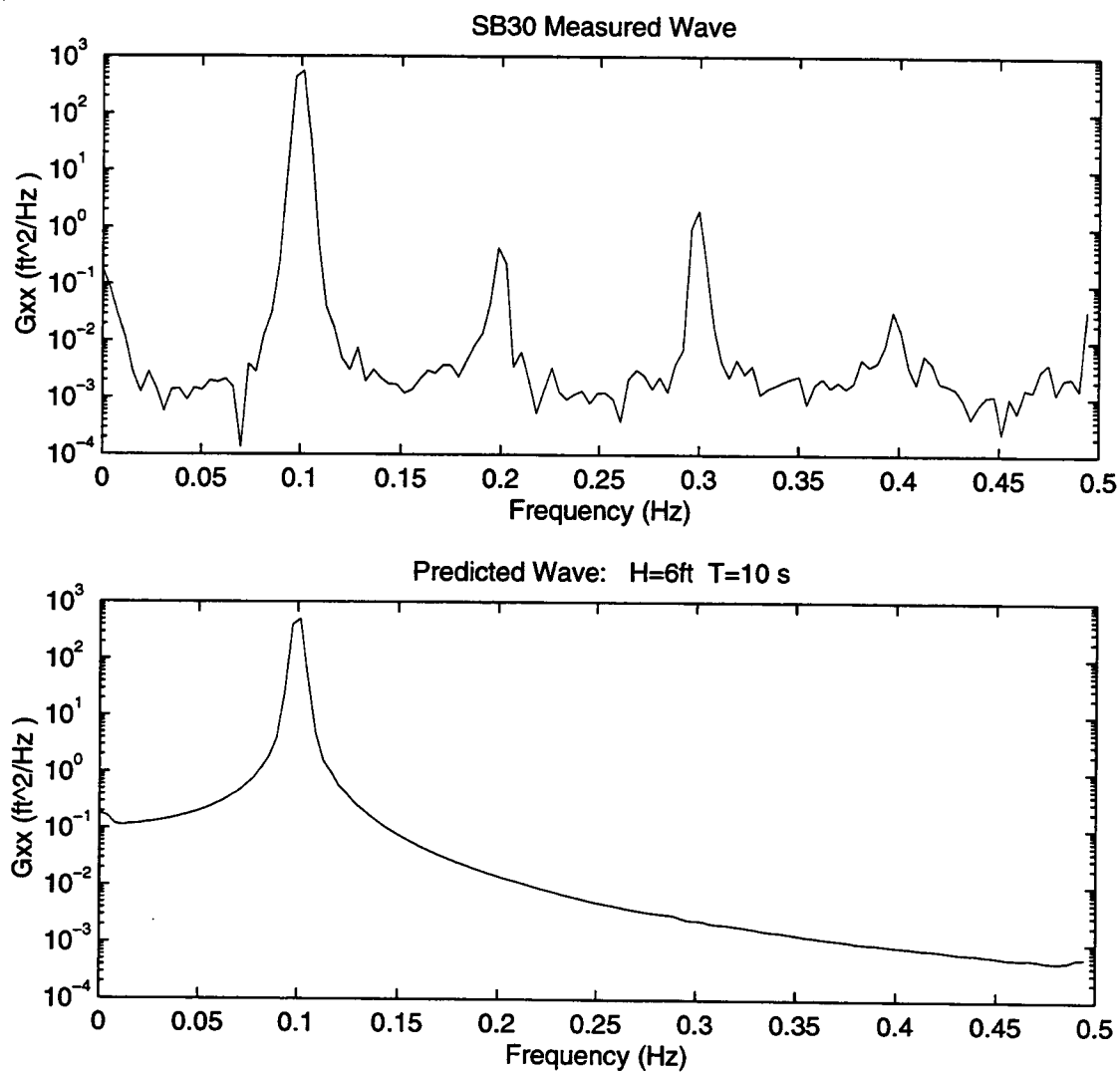


Figure B.42 Wave Spectral Densities, H=6 ft, T=10 s (semilog)

B.42

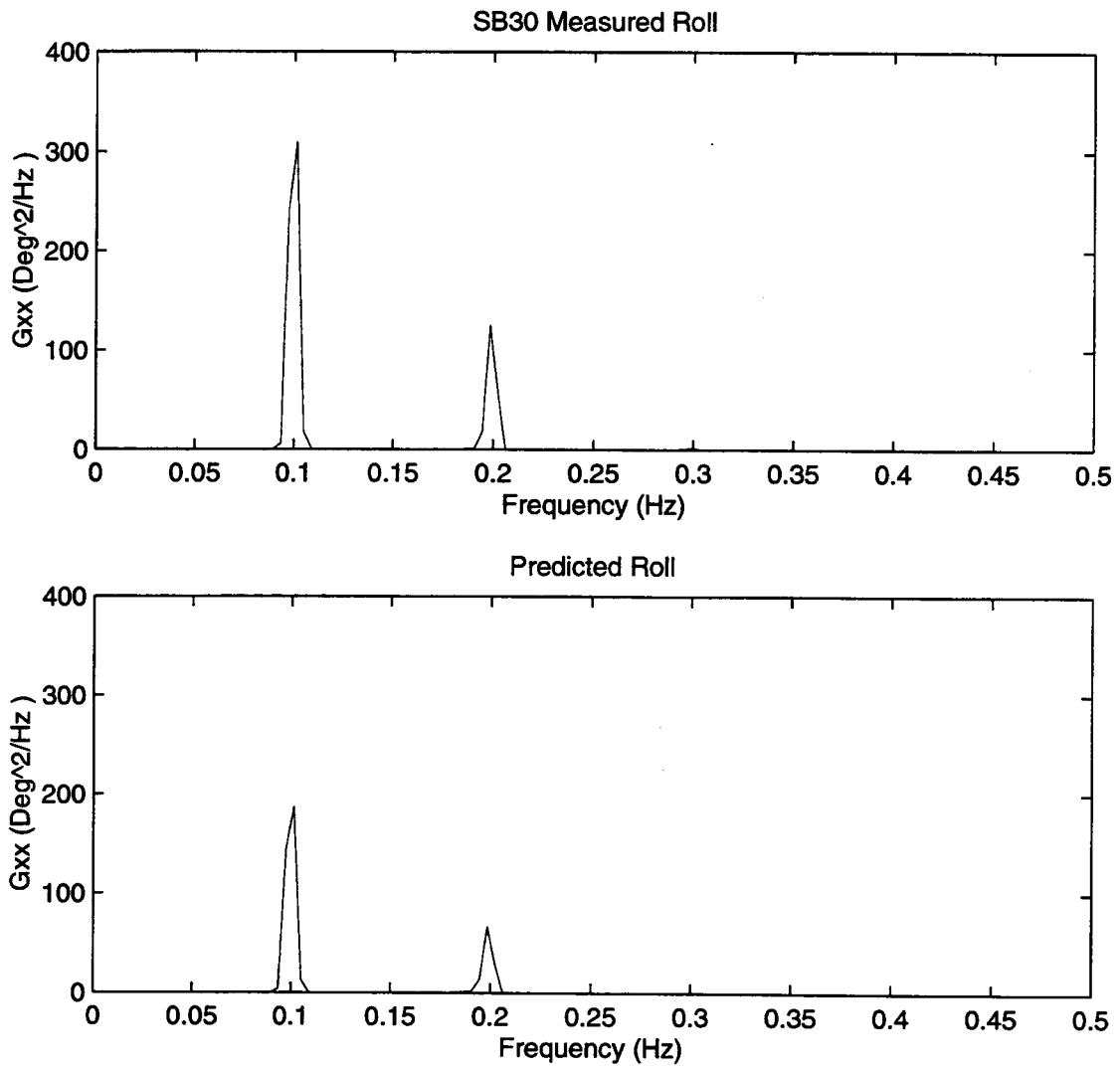


Figure B.43 Roll Spectral Densities, $H=6$ ft, $T=10$ s

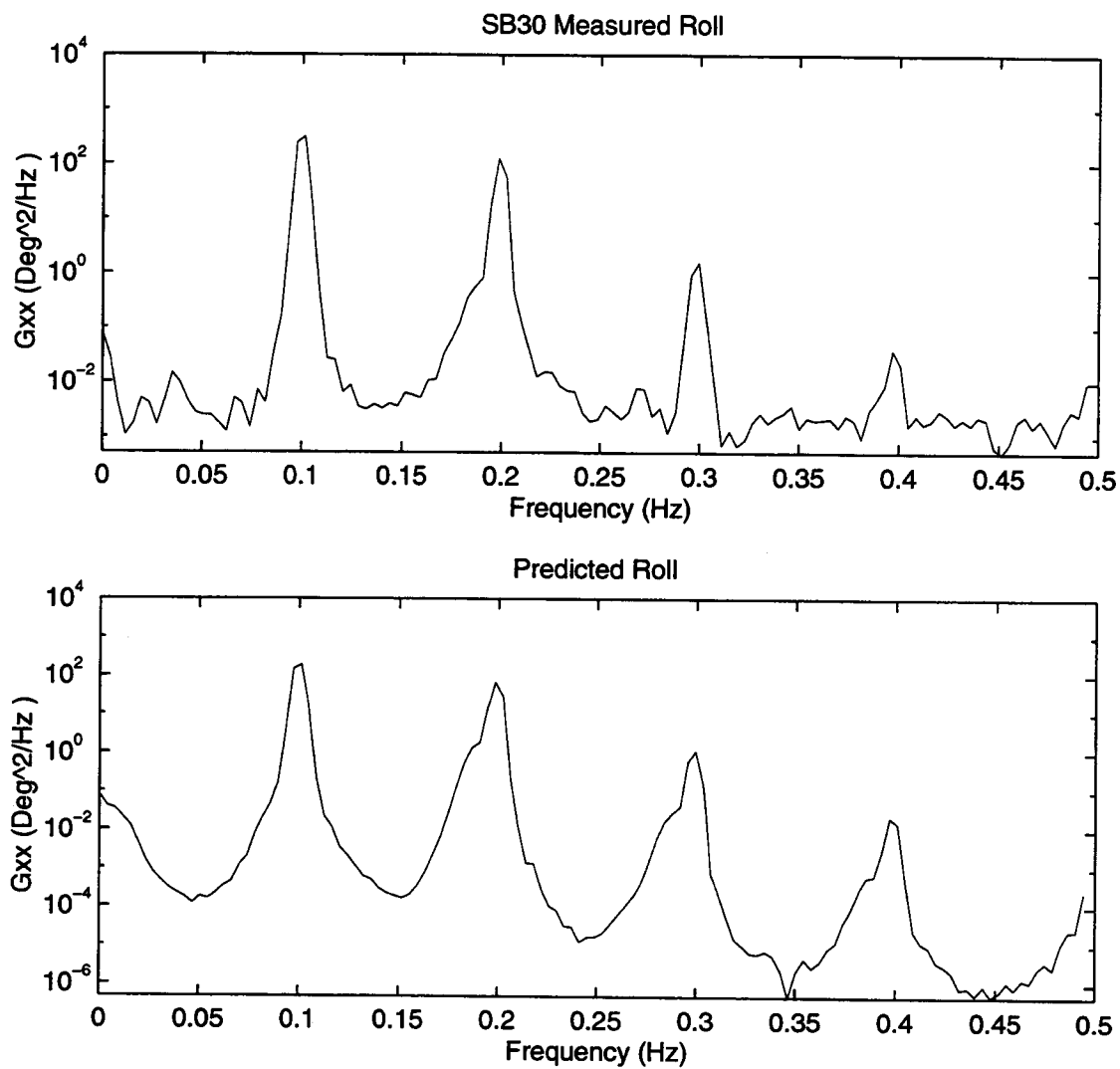


Figure B.44 Roll Spectral Densities, $H=6$ ft, $T=10$ s (semilog)

B.44

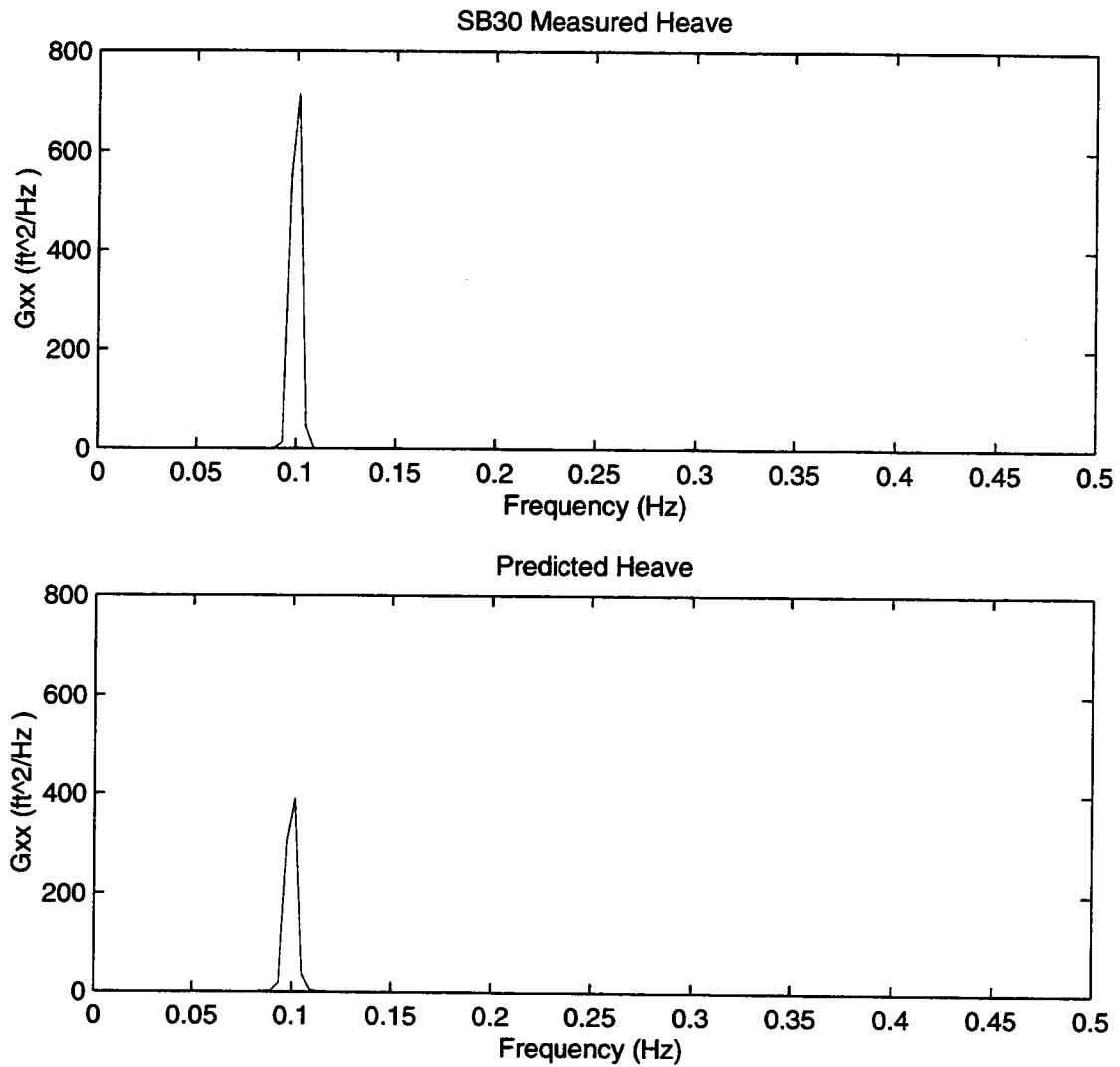


Figure B.45 Heave Spectral Densities, H=6 ft, T=10 s

B.45

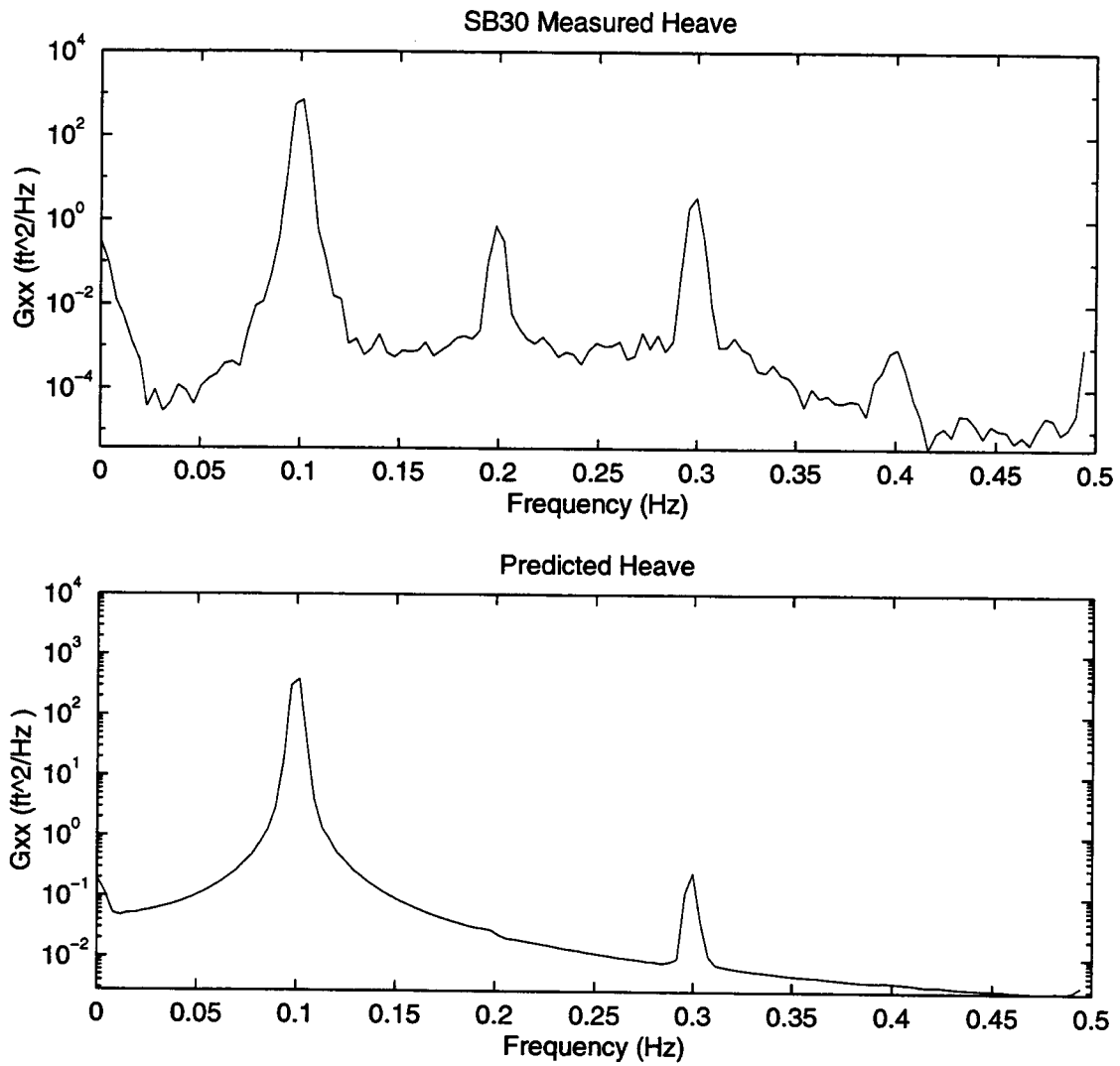


Figure B.46 Heave Spectral Densities, $H=6$ ft, $T=10$ s (semilog)

B.46

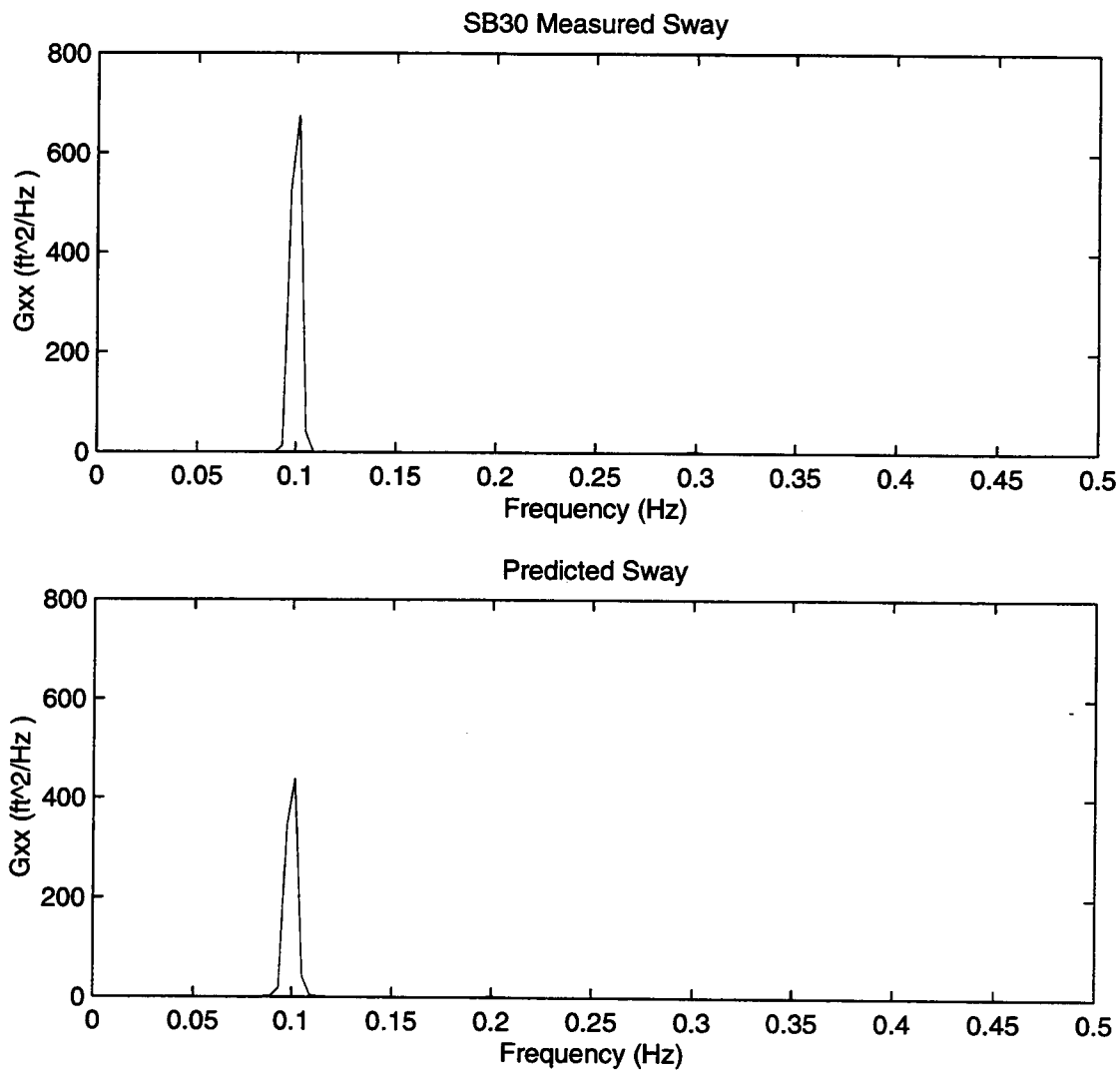


Figure B.47 Sway Spectral Densities, H=6 ft, T=10 s

B.47

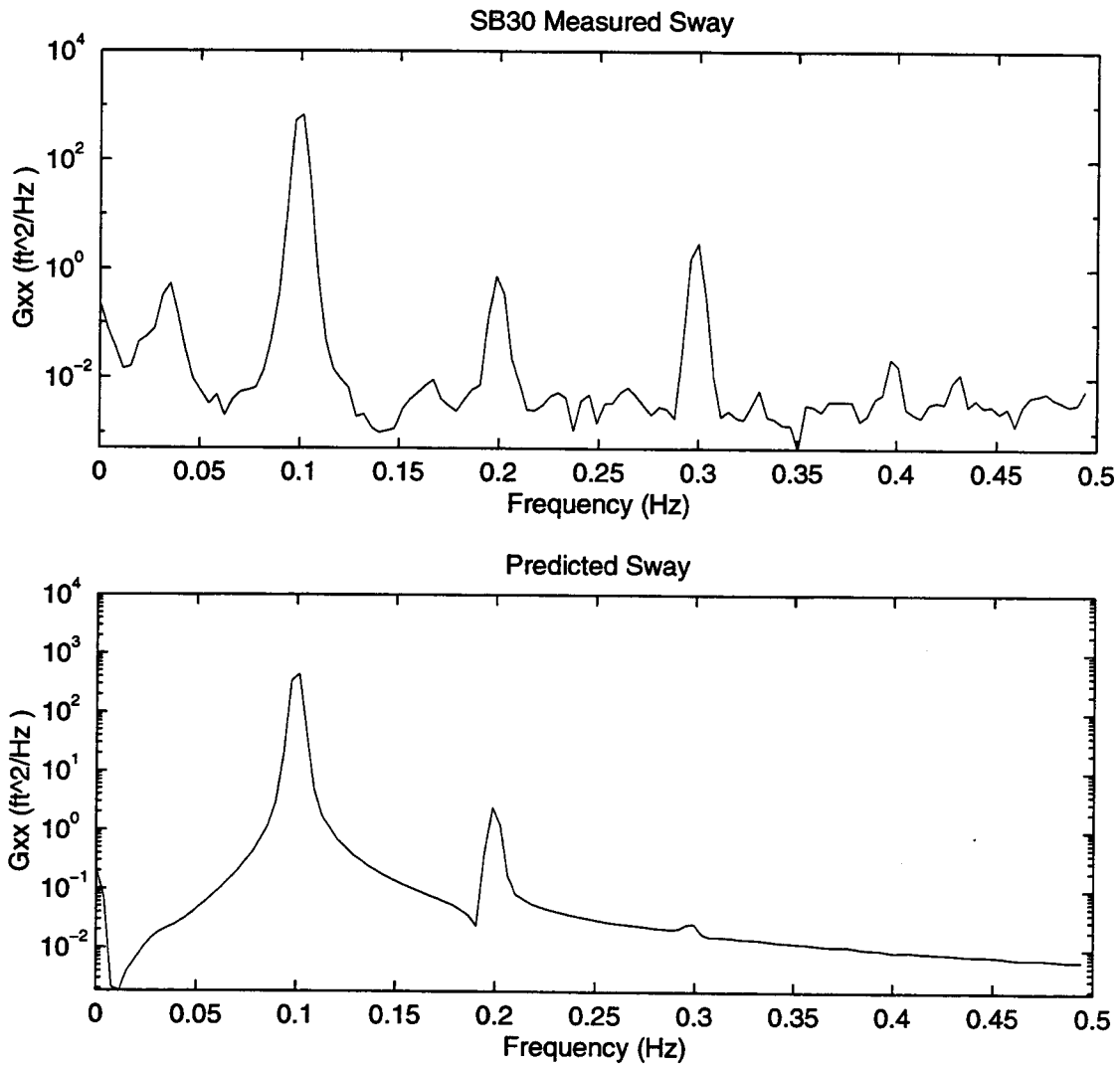


Figure B.48 Sway Spectral Densities, H=6 ft, T=10 s (semilog)

APPENDIX C**System Identification Figures
Roll-Heave Model (Section 4.3)**

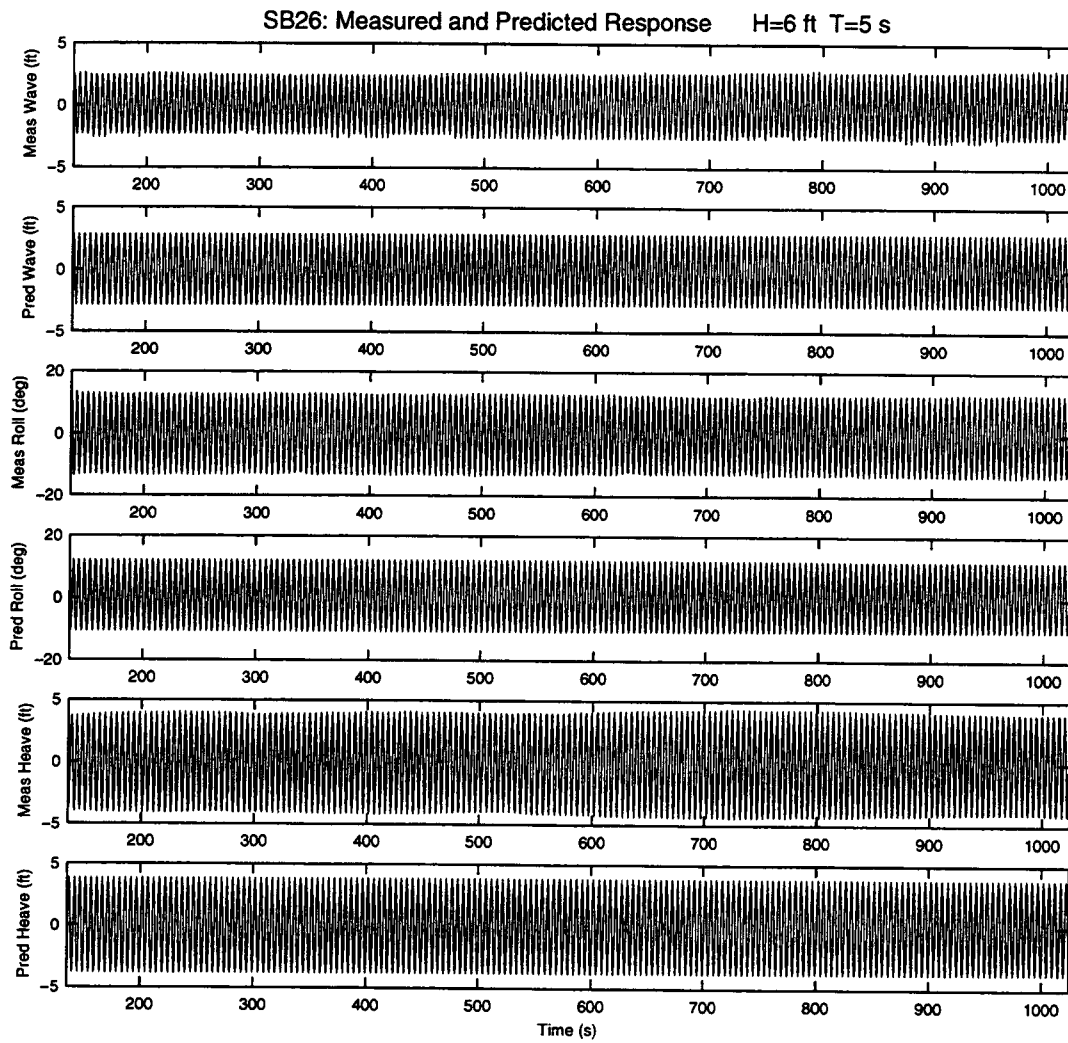


Figure C.1 Measured and Predicted Response, H=6 ft, T=5 s

C.1

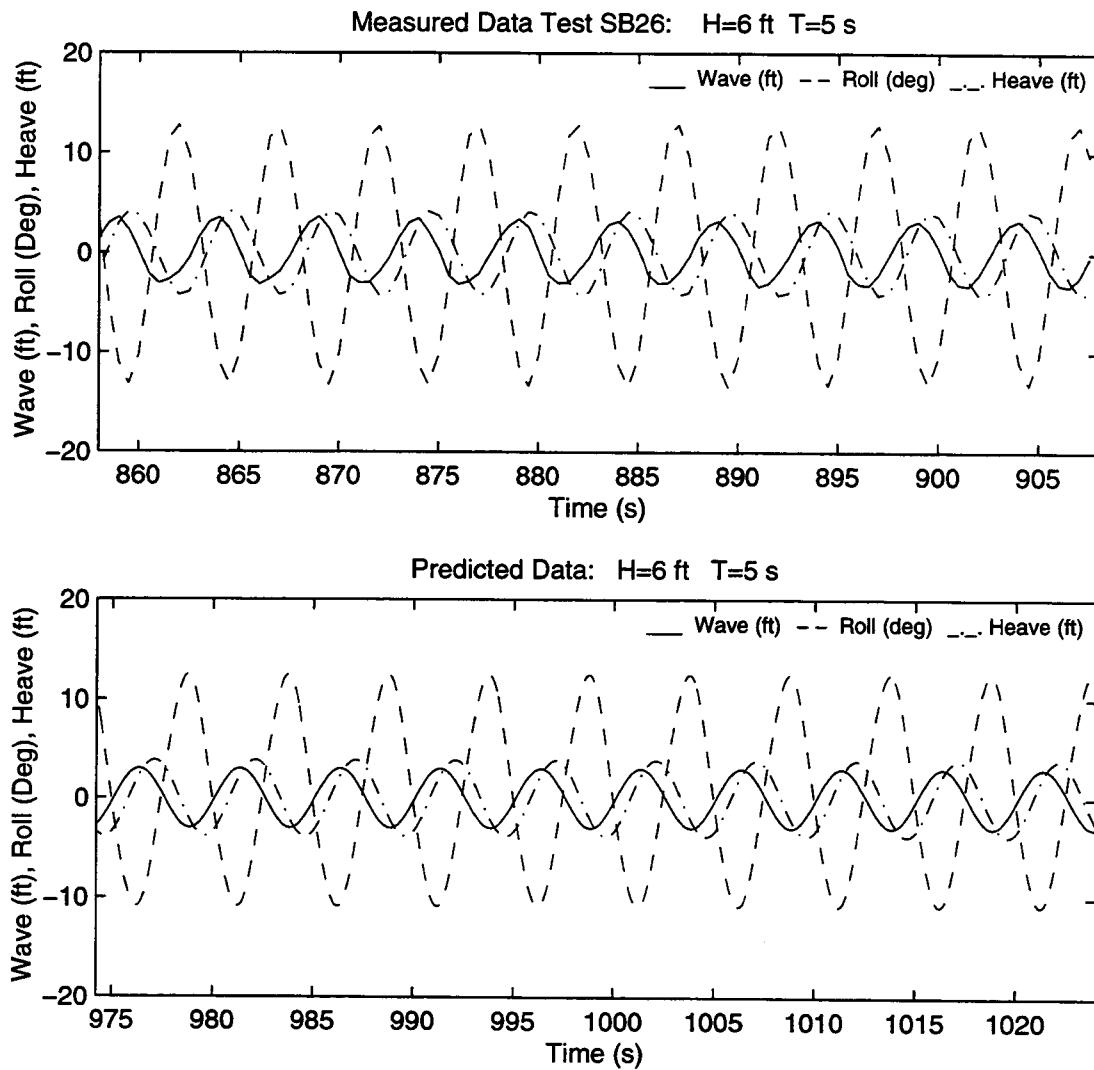


Figure C.2 Measured and Predicted Response, H=6 ft, T=5 s

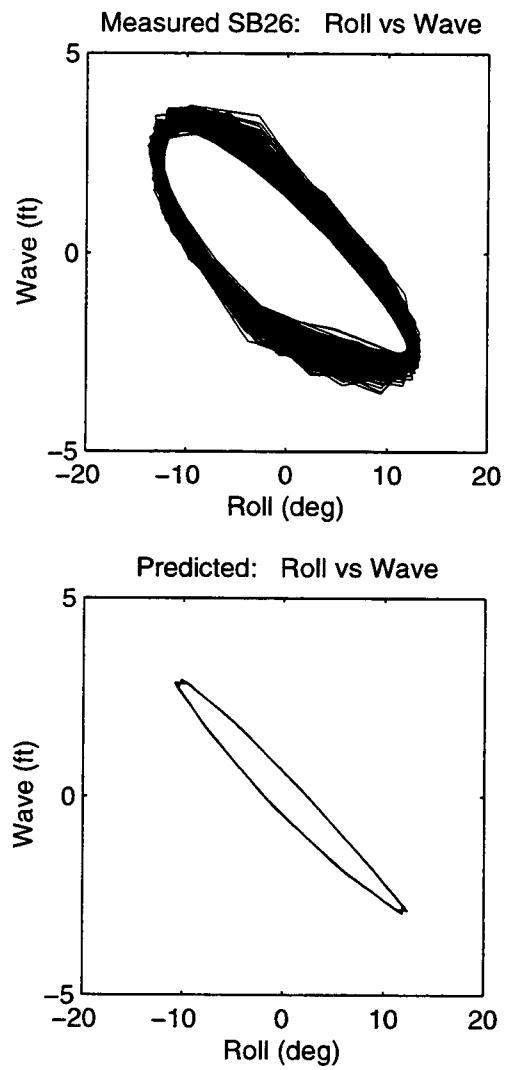


Figure C.3

Roll vs Wave, $H=6$ ft, $T=5$ s

C.3

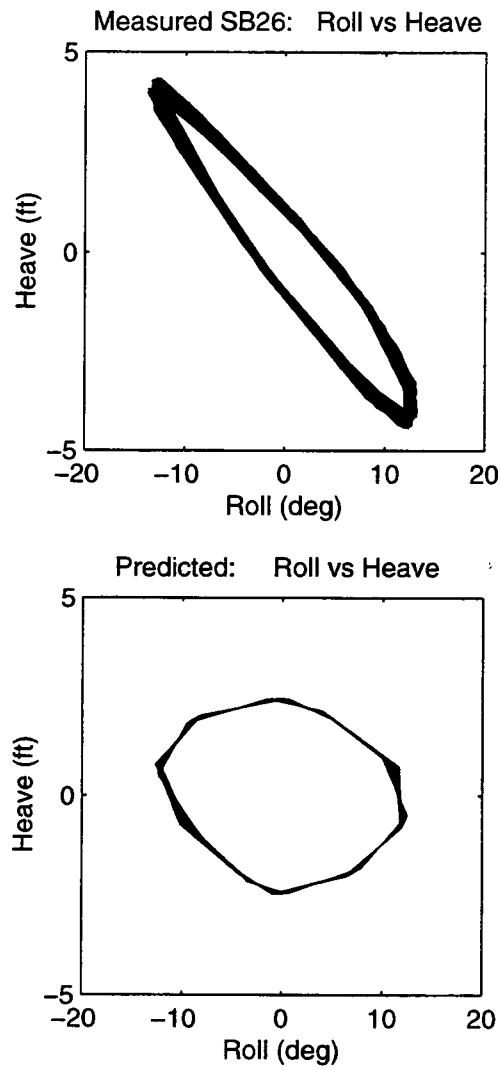


Figure C.4

Roll vs Heave, $H=6$ ft, $T=5$ s

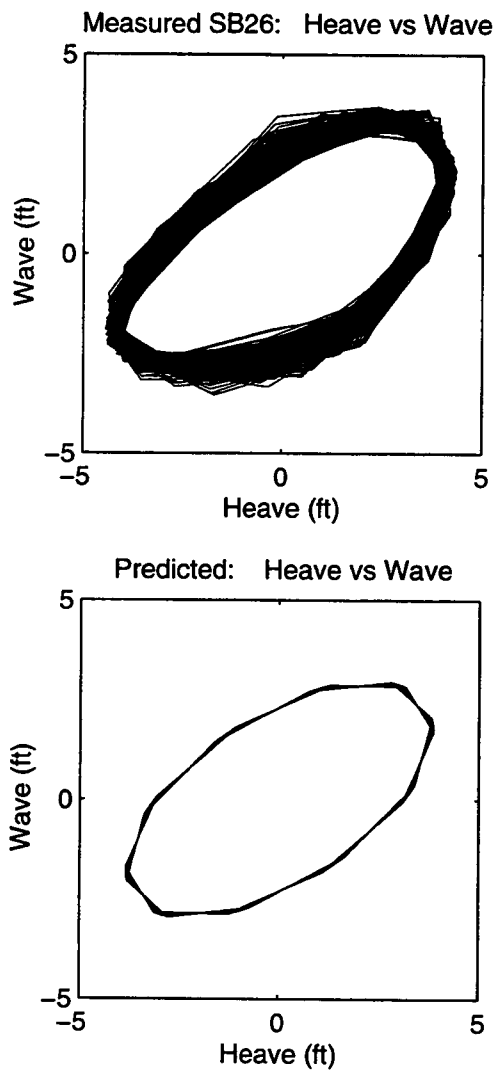


Figure C.5

Heave vs Wave, $H=6$ ft, $T=5$ s

C.5

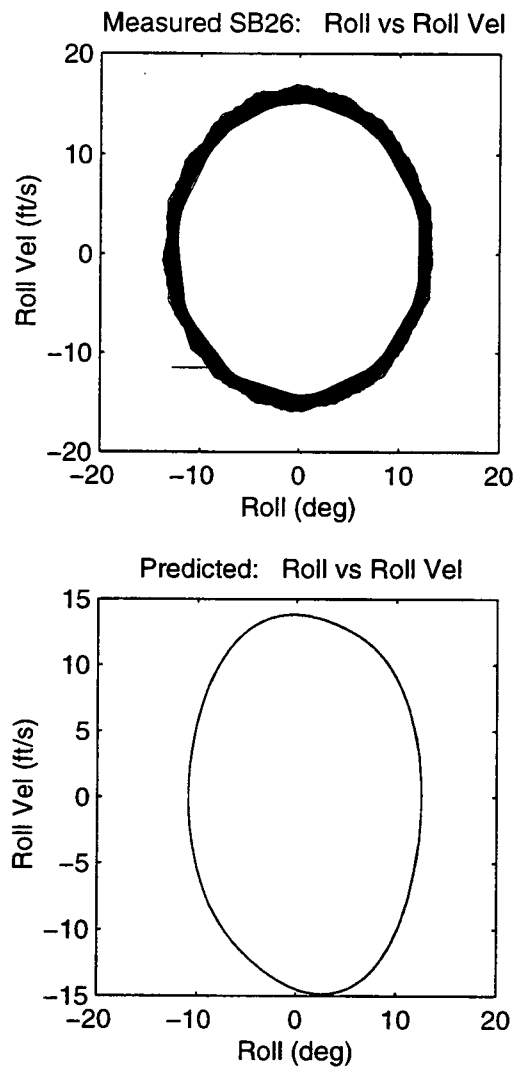


Figure C.6

Phase Plane for Roll and Roll Velocity, $H=6$ ft, $T=5$ s

C.6

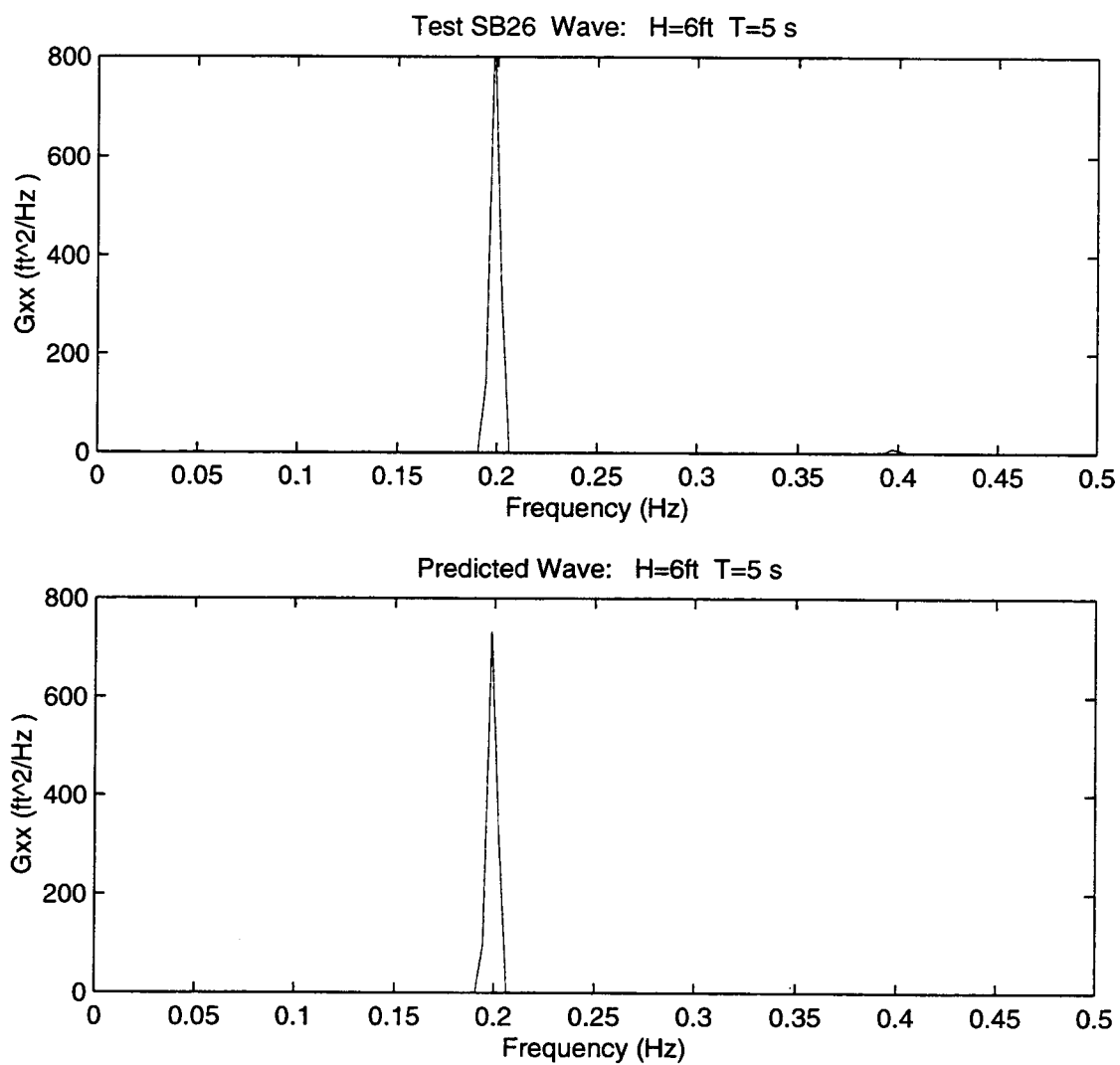


Figure C.7 Wave Spectral Densities, H=6 ft, T=5 s

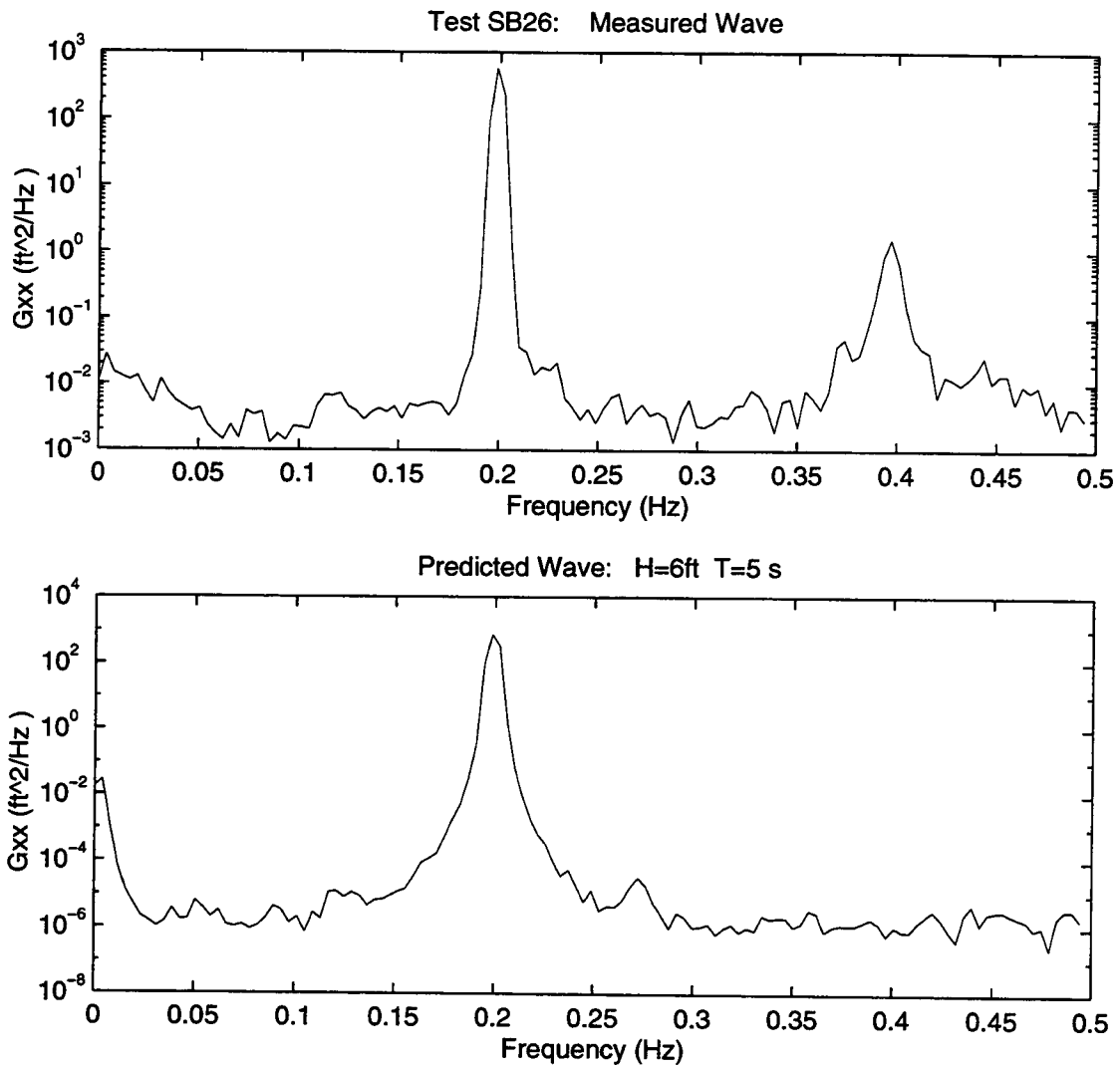


Figure C.8 Wave Spectral Densities, H=6 ft, T=5 s (semilog)

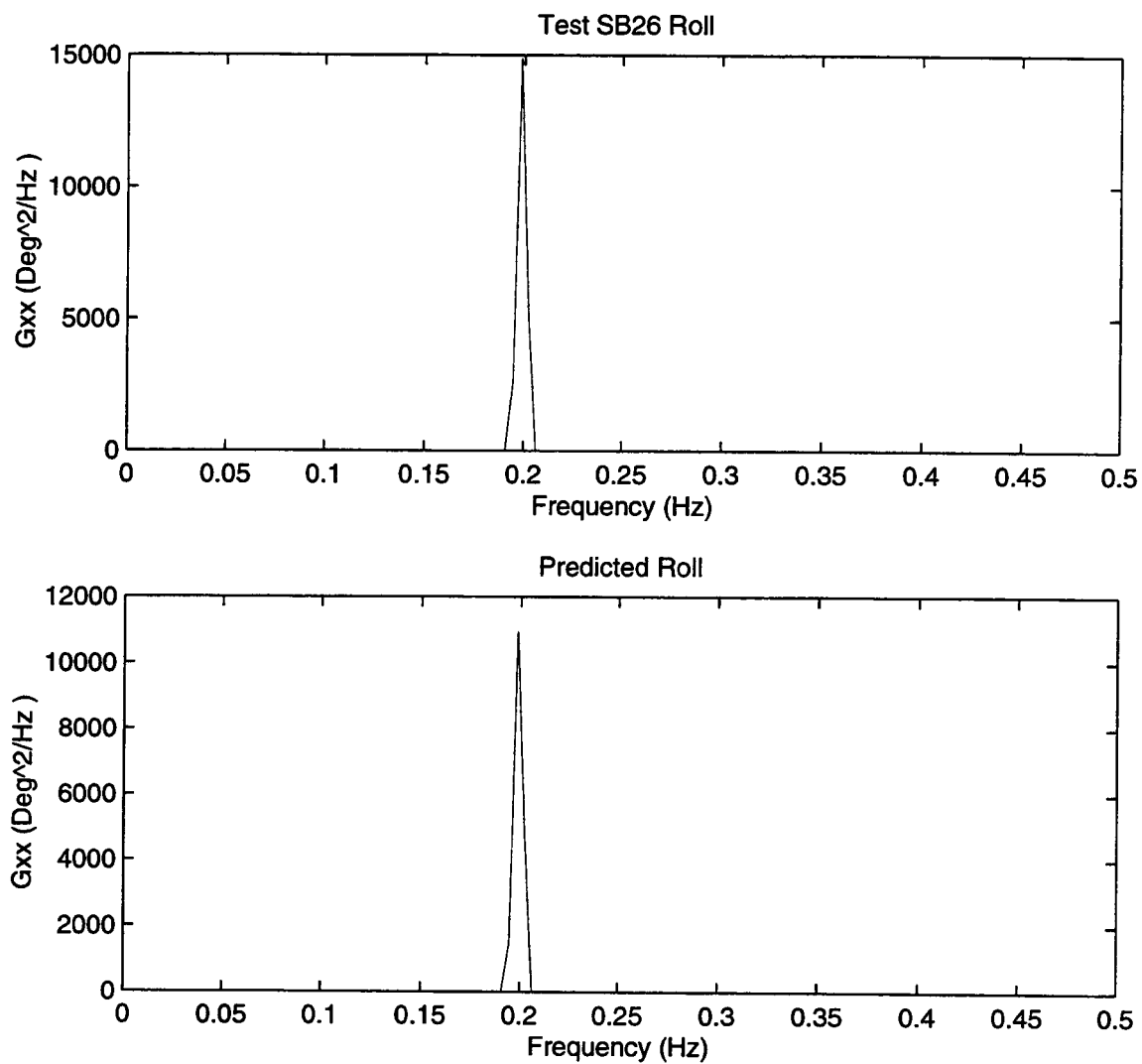


Figure C.9 Roll Spectral Densities, $H=6$ ft, $T=5$ s

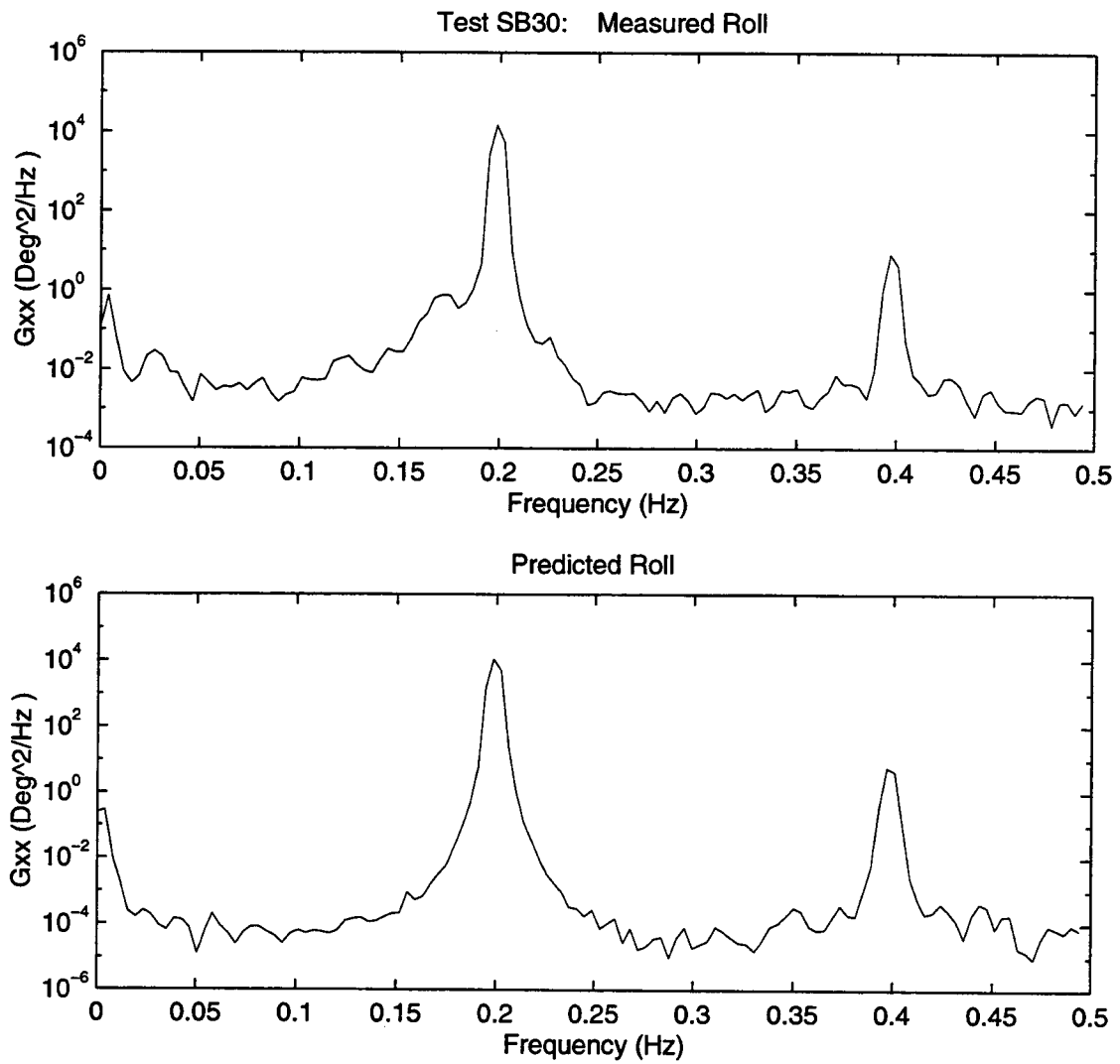


Figure C.10 Roll Spectral Densities, $H=6$ ft, $T=5$ s (semilog)

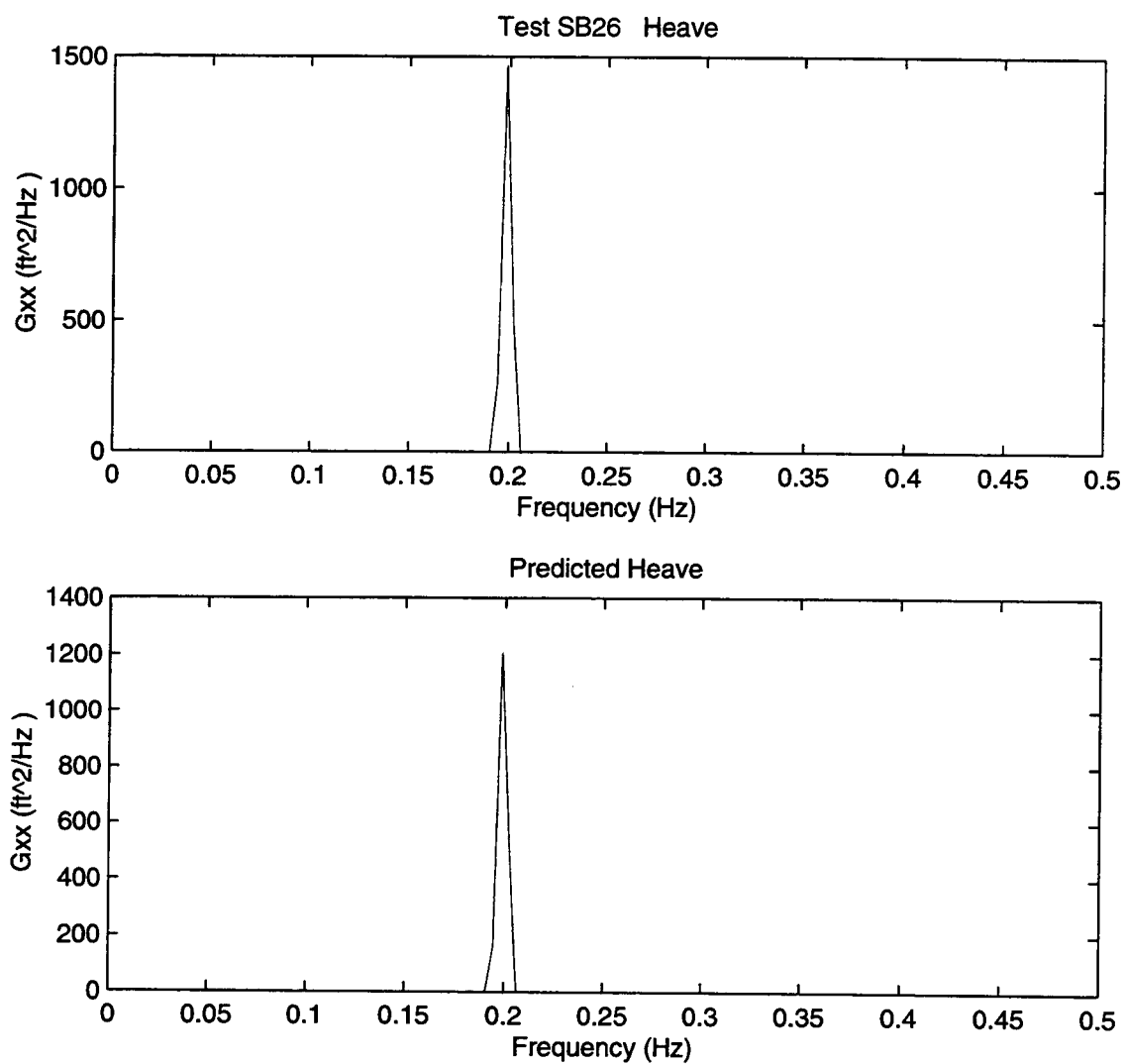


Figure C.11 Heave Spectral Densities, $H=6$ ft, $T=5$ s

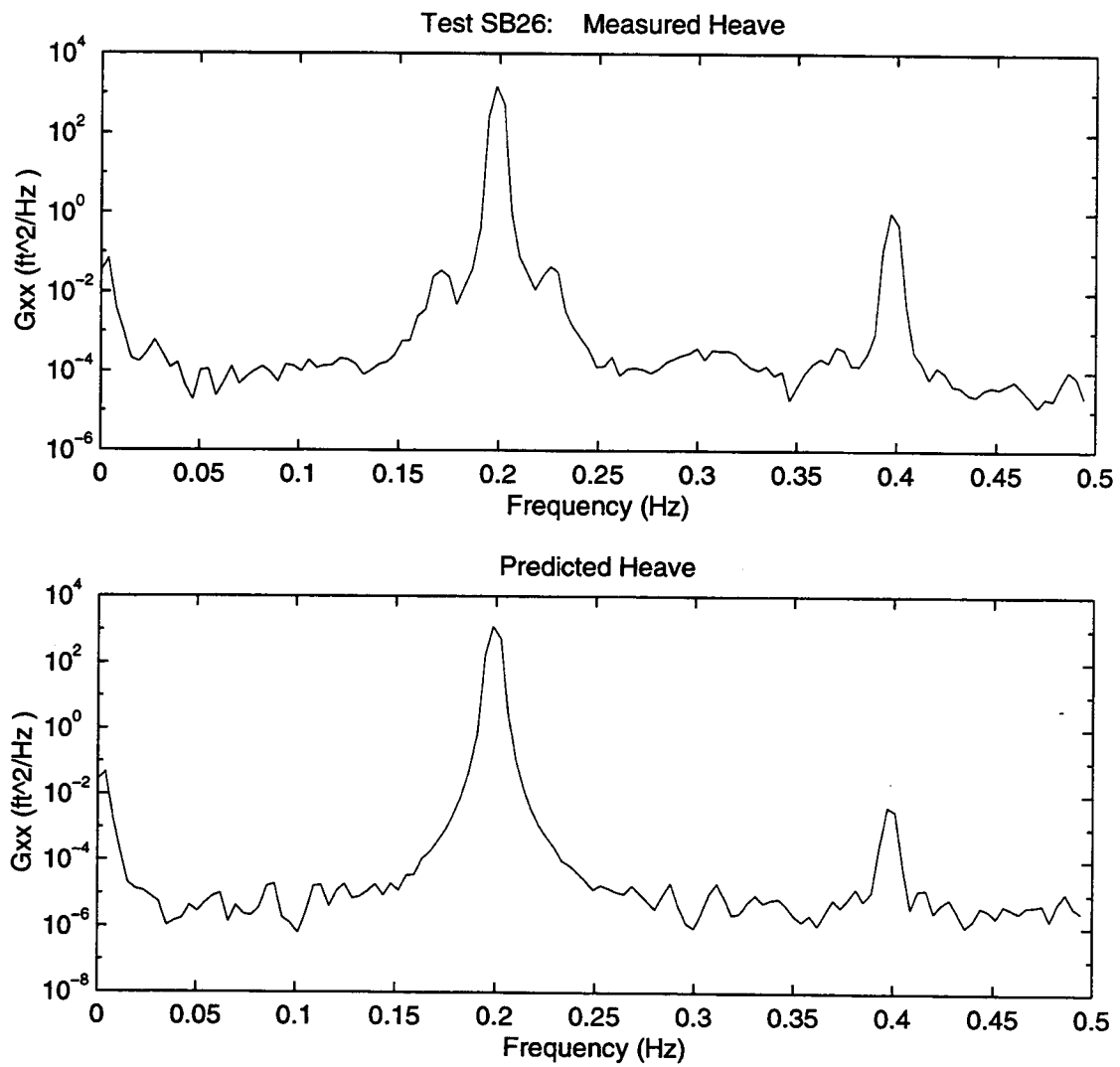


Figure C.12 Heave Spectral Densities, $H=6$ ft, $T=5$ s (semilog)

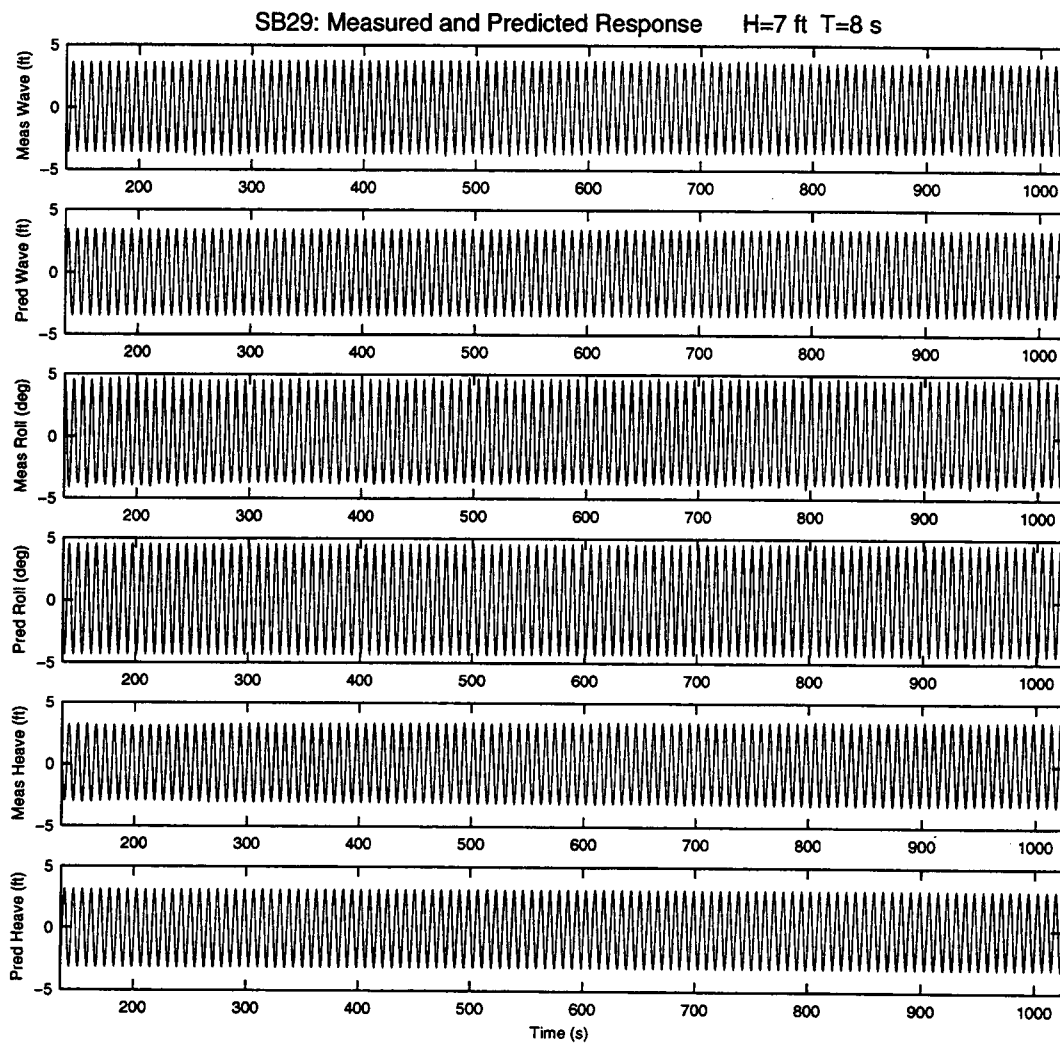


Figure C.13

Measured and Predicted Response, H=7 ft, T=8 s

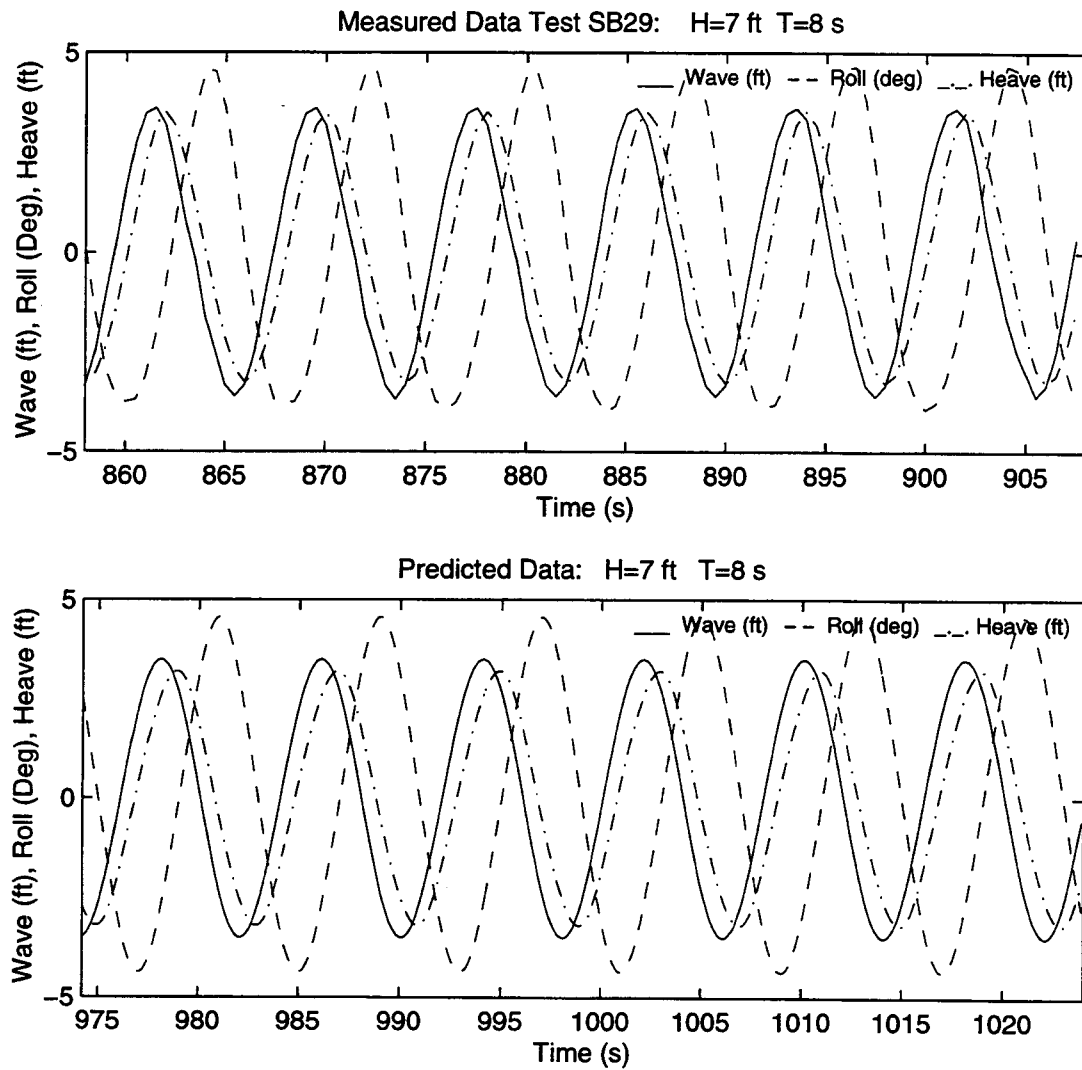


Figure C.14 Measured and Predicted Response, H=7 ft, T=8 s

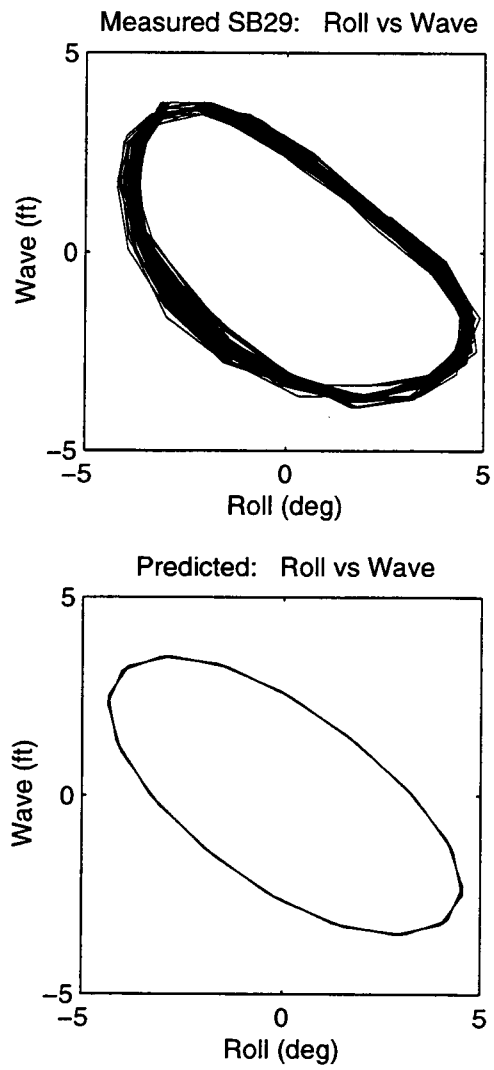


Figure C.15

Roll vs Wave, $H=7$ ft, $T=8$ s

C.15

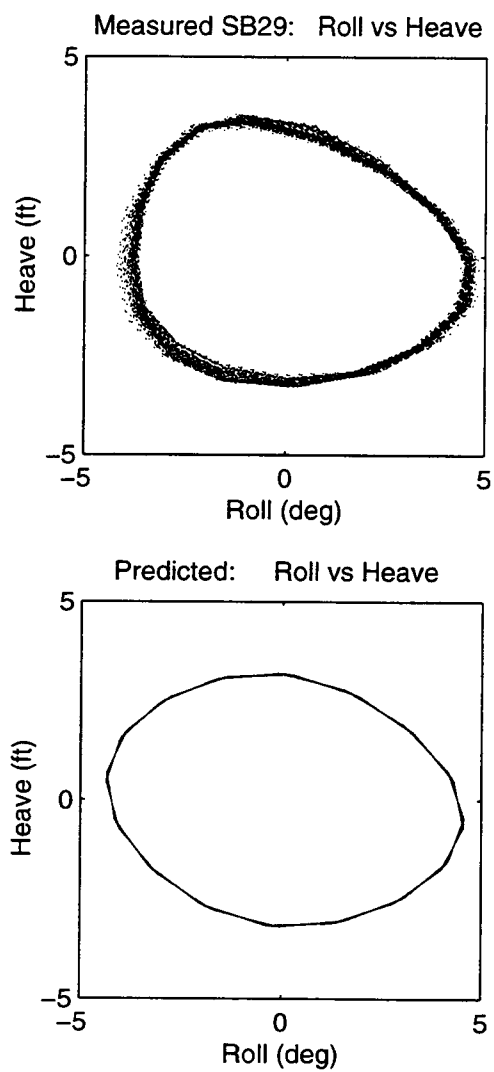


Figure C.16

Roll vs Heave, $H=7$ ft, $T=8$ s

C.16

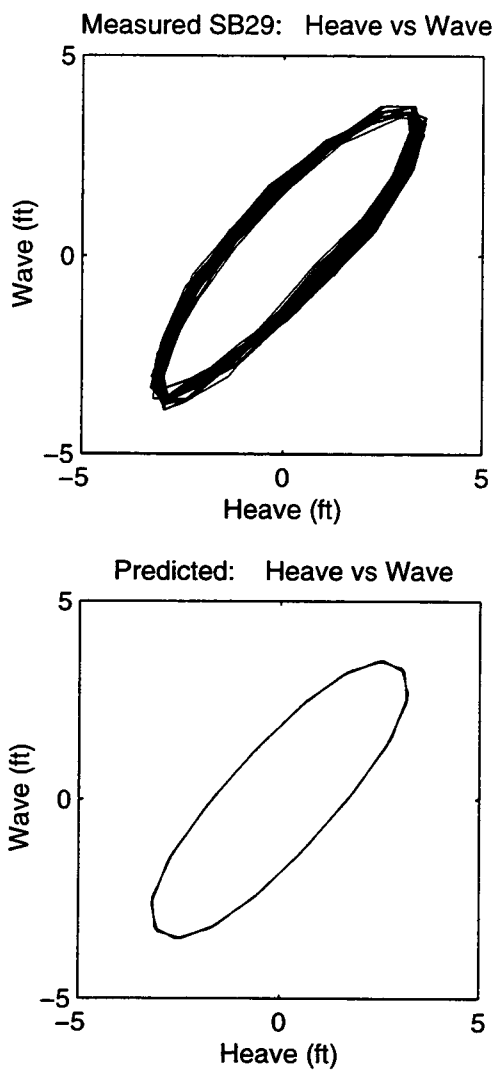


Figure C.17

Heave vs Wave, $H=7$ ft, $T=8$ s

C.17

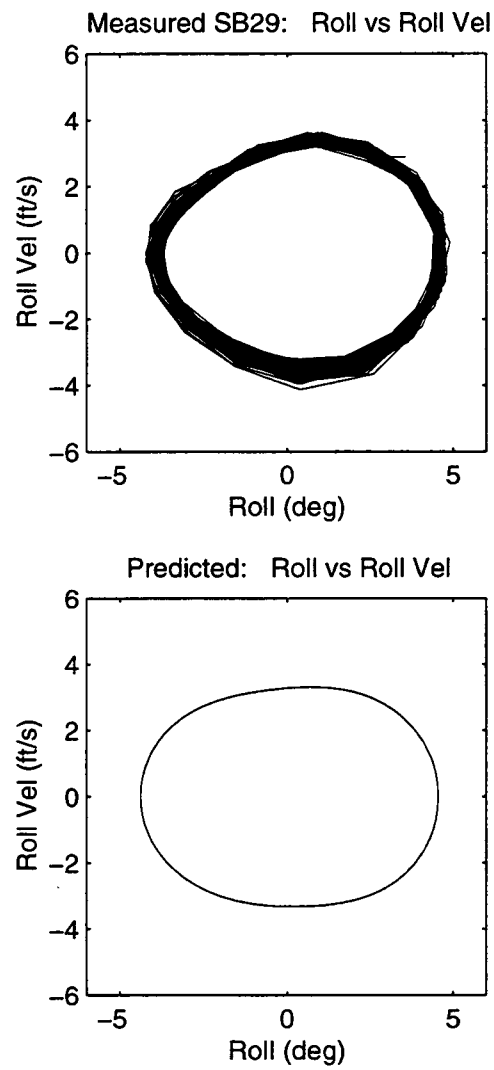


Figure C.18

Phase Plane for Roll and Roll Velocity, $H=7$ ft, $T=8$ s

C.18

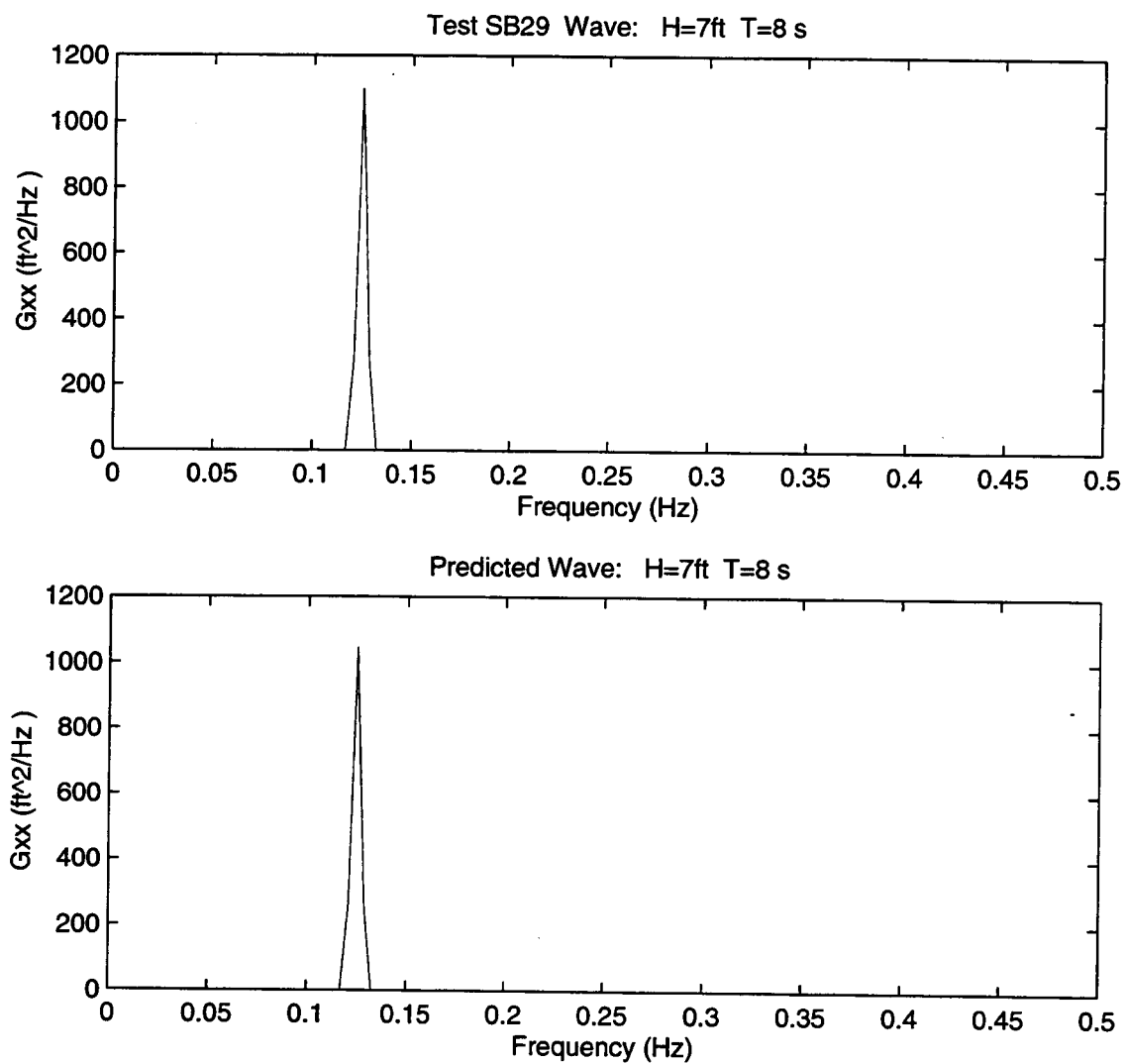


Figure C.19 Wave Spectral Densities, H=7 ft, T=8 s

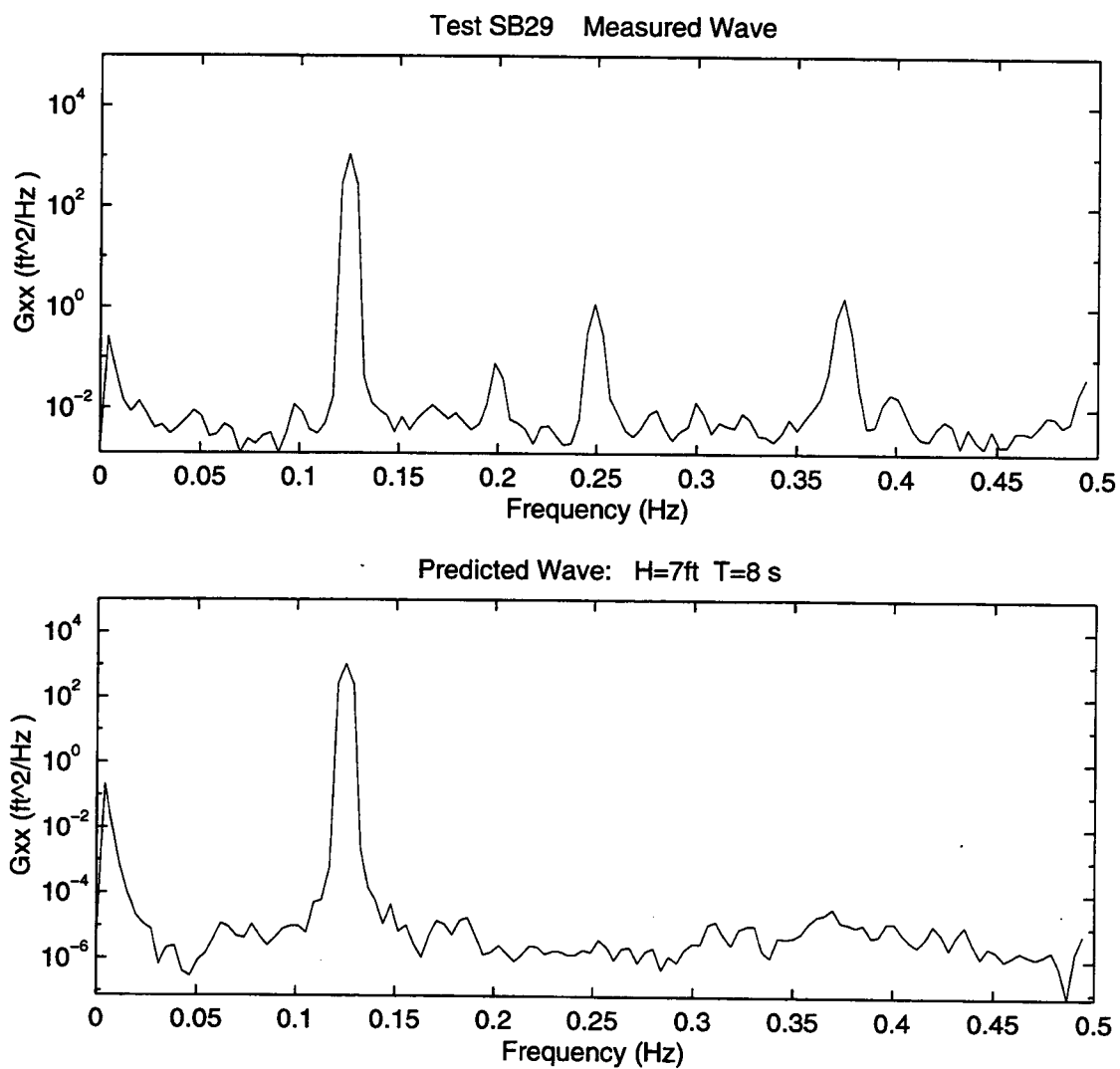


Figure C.20 Wave Spectral Densities, H=7 ft, T=8 s (semilog)

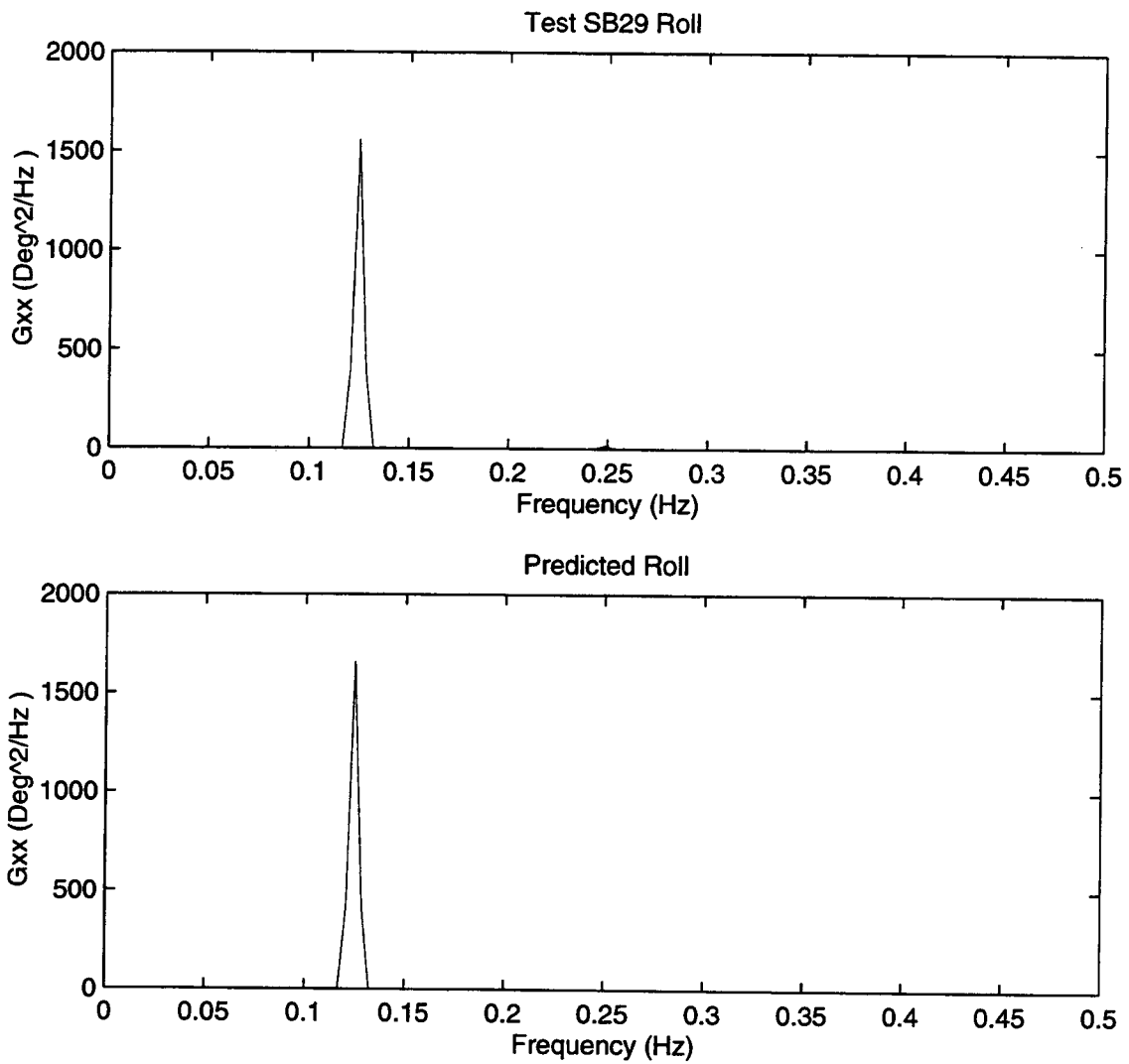


Figure C.21 Roll Spectral Densities, $H=7$ ft, $T=8$ s

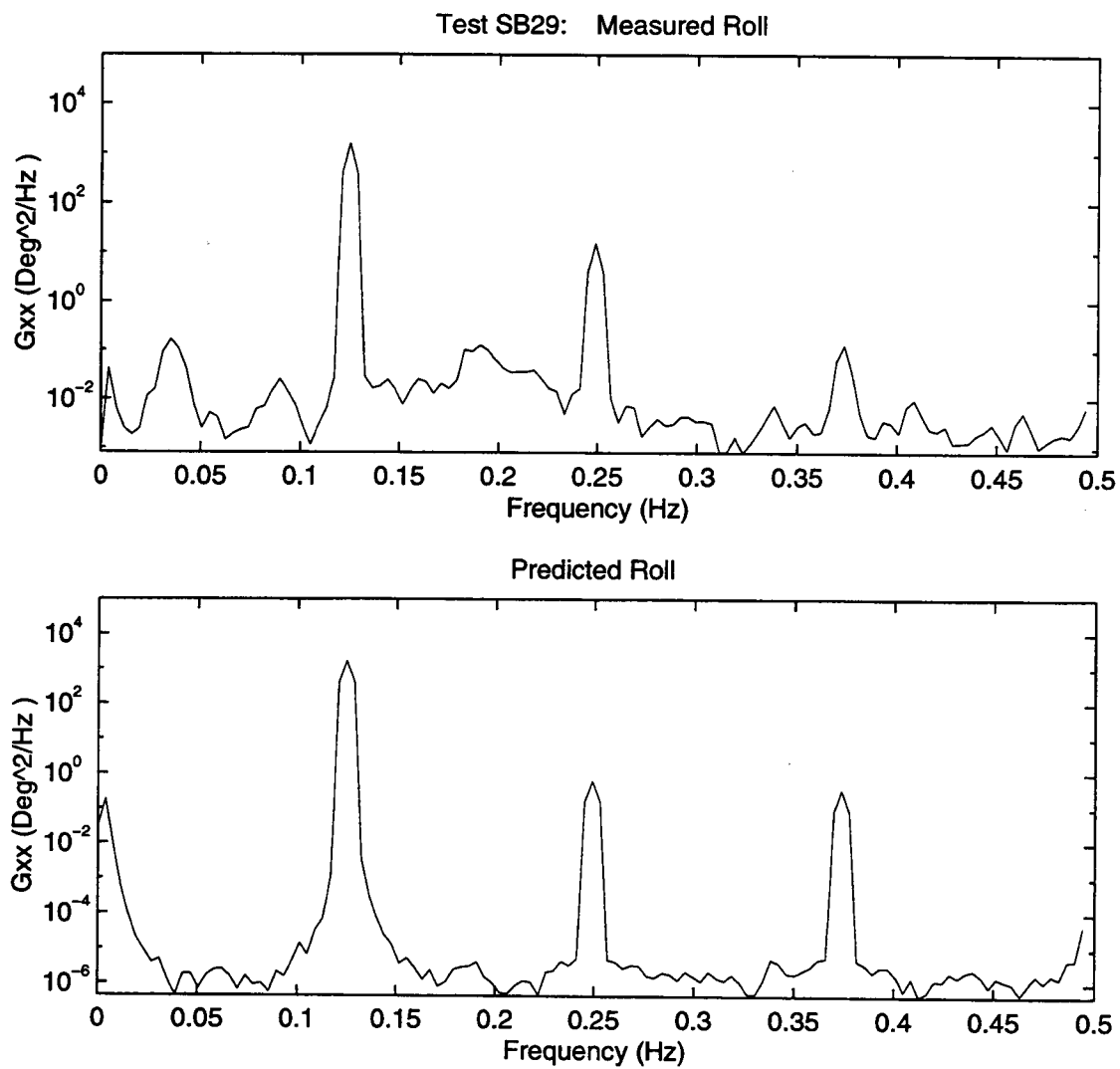


Figure C.22 Roll Spectral Densities, $H=7$ ft, $T=8$ s (semilog)

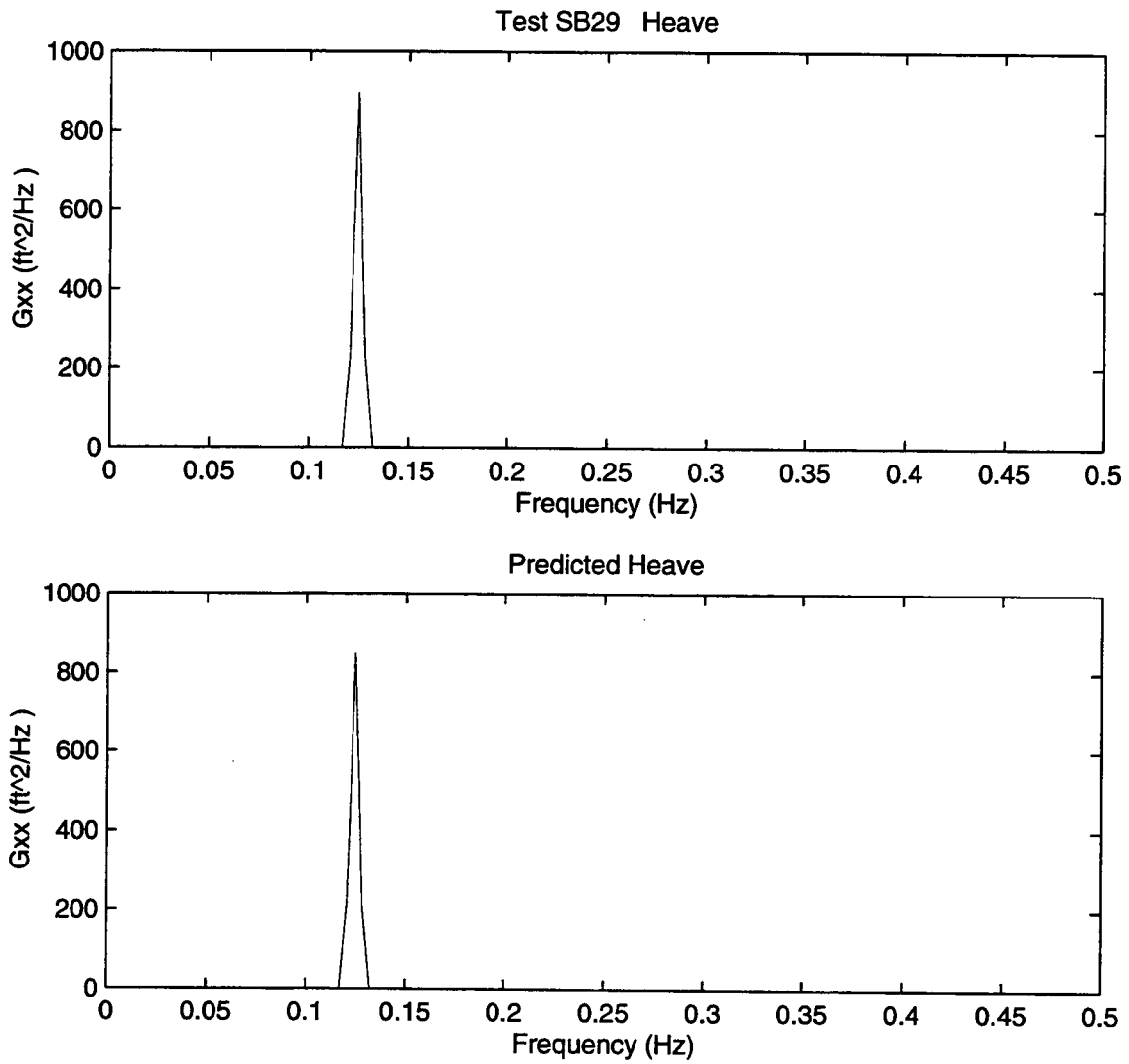


Figure C.23 Heave Spectral Densities, $H=7$ ft, $T=8$ s

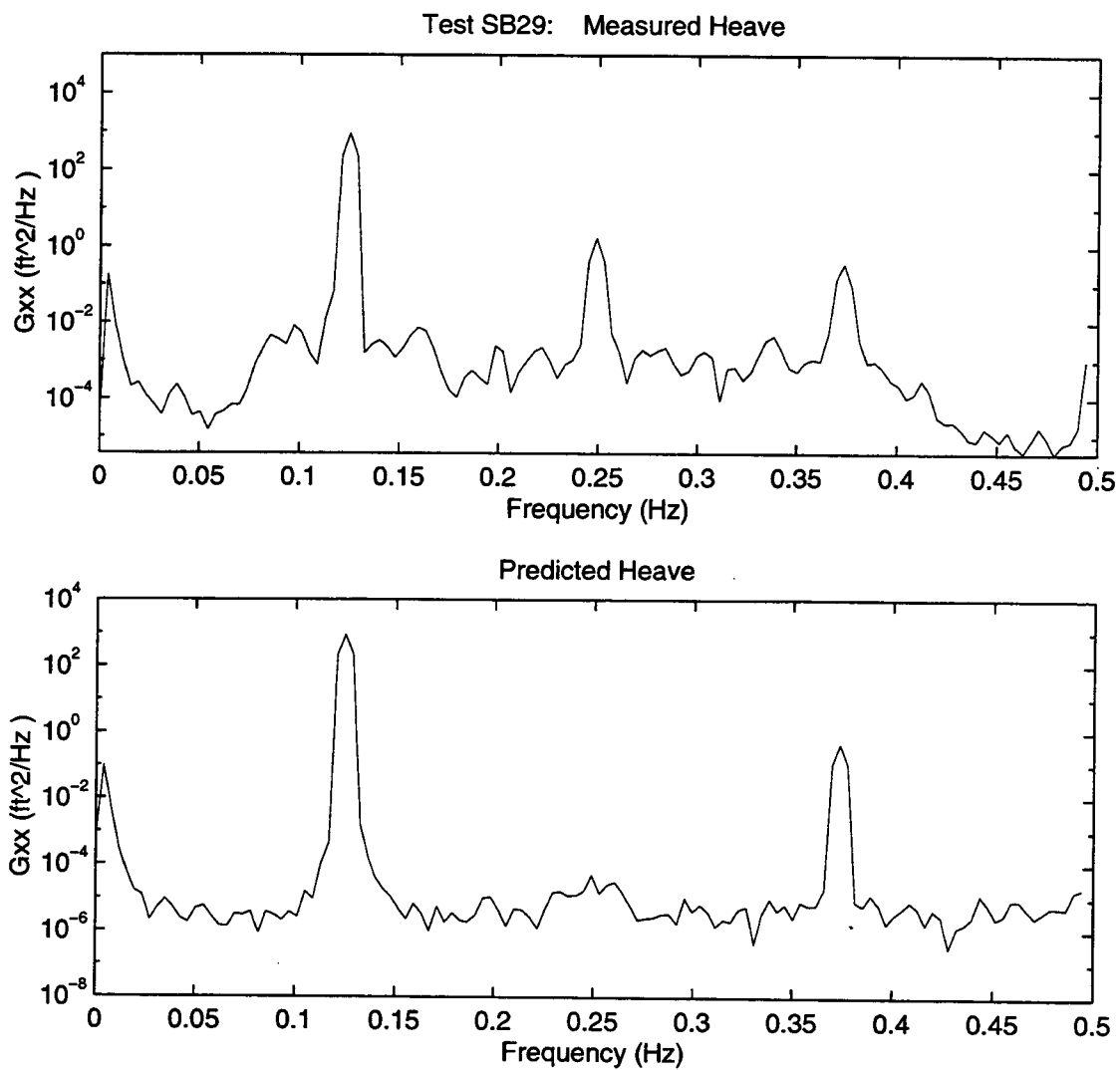


Figure C.24 Heave Spectral Densities, $H=7$ ft, $T=8$ s (semilog)

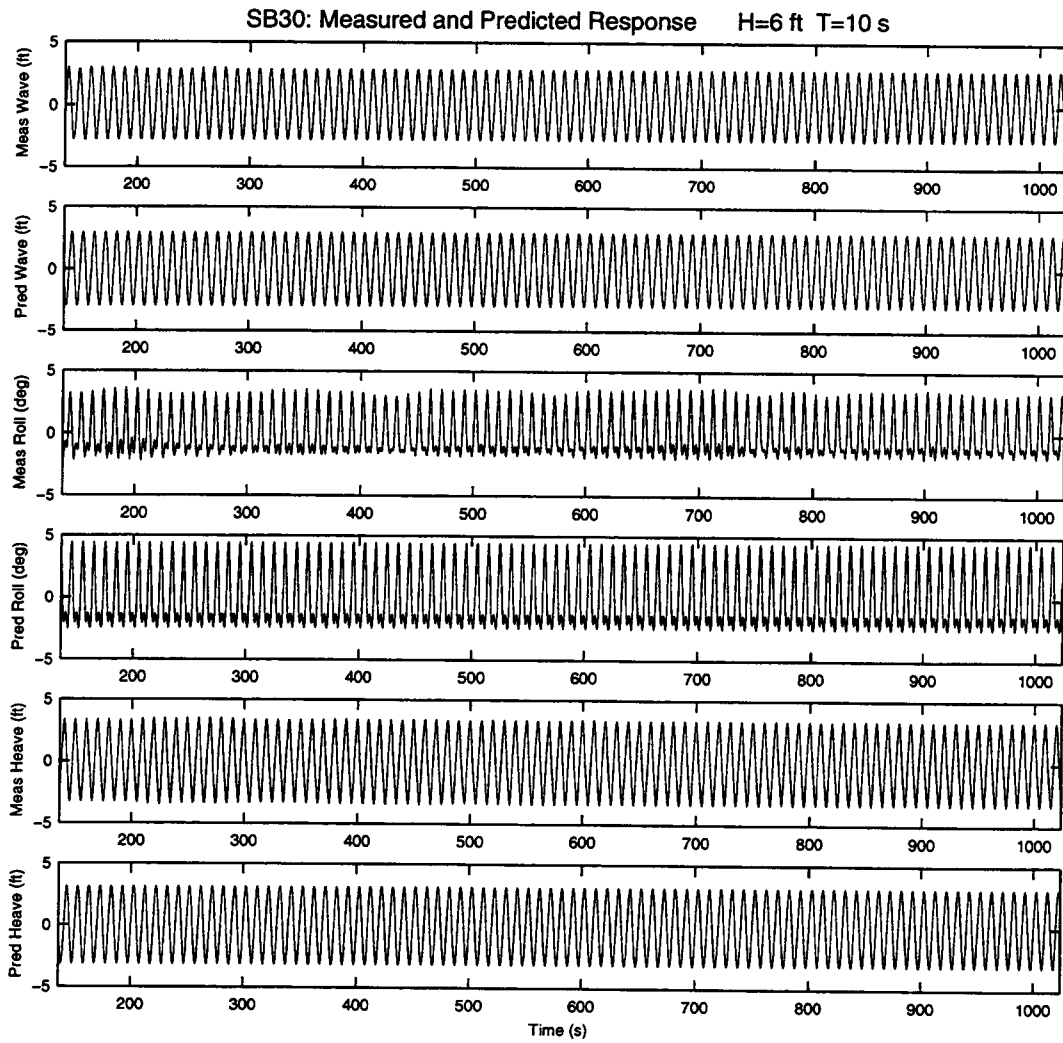


Figure C.25

Measured and Predicted Response, H=6 ft, T=10 s

C.25

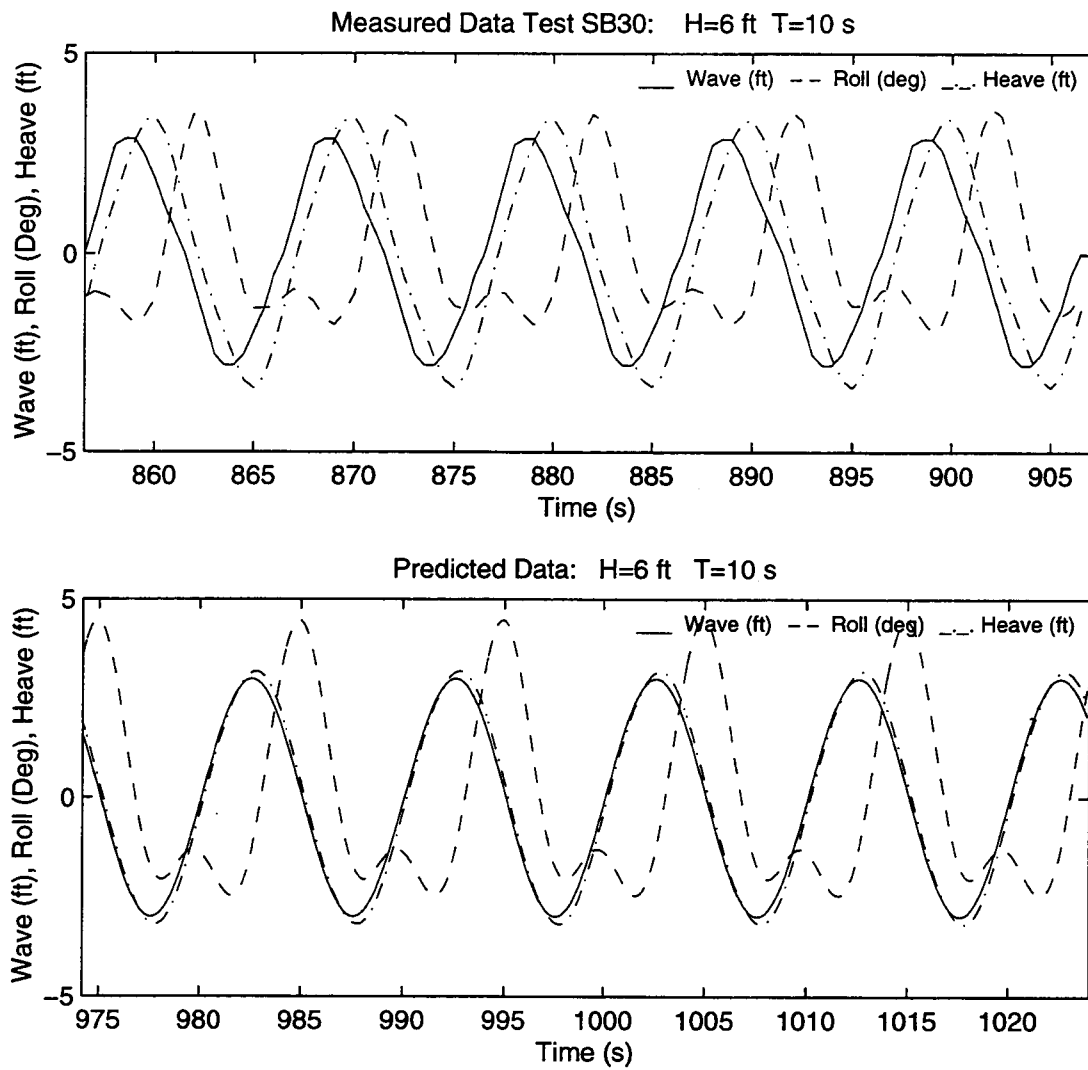


Figure C.26

Measured and Predicted Response, H=6 ft, T=10 s

C.26

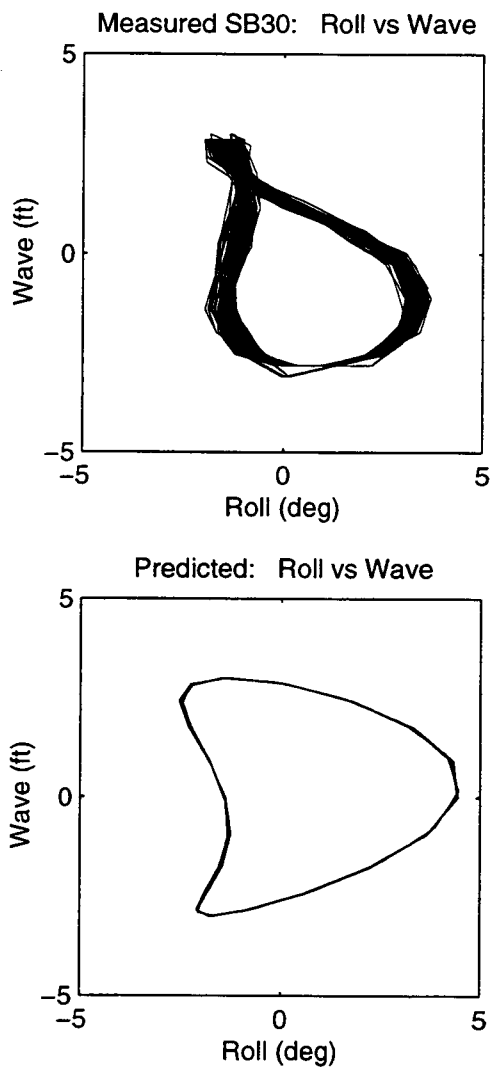


Figure C.27

Roll vs Wave, $H=6$ ft, $T=10$ s

C.27

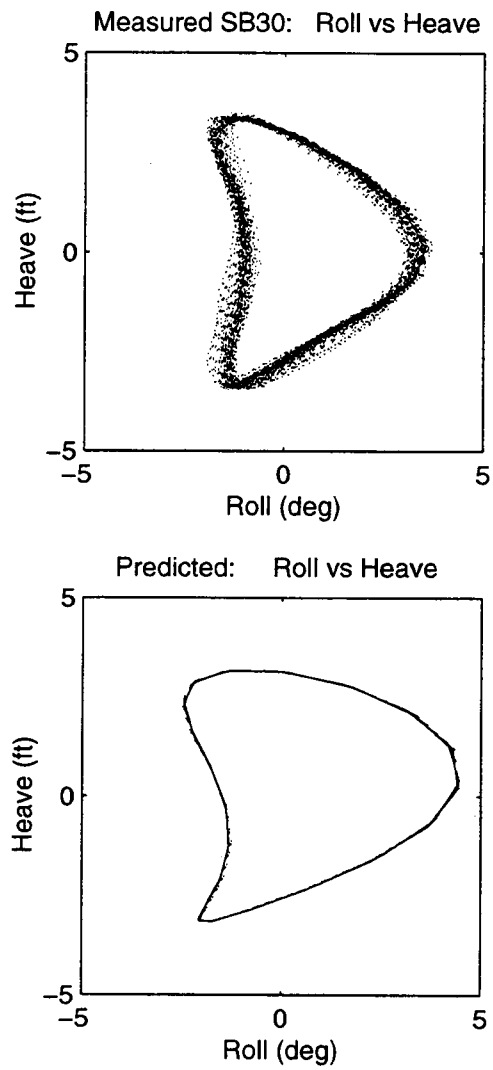


Figure C.28

Roll vs Heave, $H=6$ ft, $T=10$ s

C.28

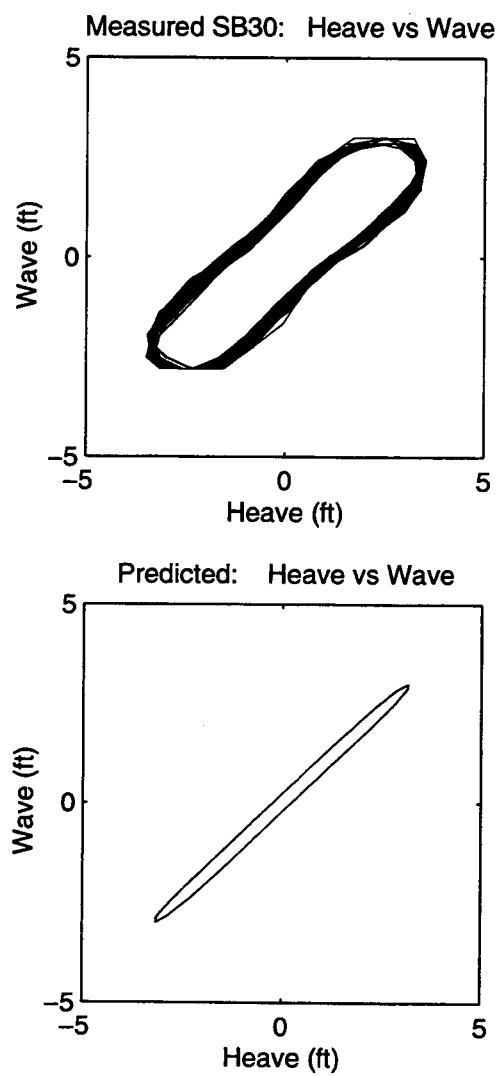


Figure C.29

Heave vs Wave, $H=6$ ft, $T=10$ s

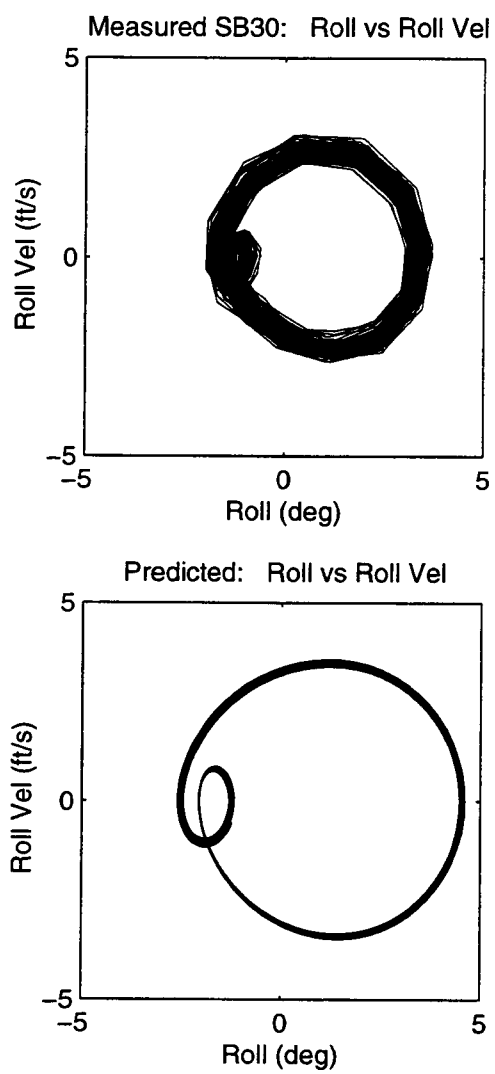


Figure C.30

Phase Plane for Roll and Roll Velocity, $H=6$ ft, $T=10$ s

C.30

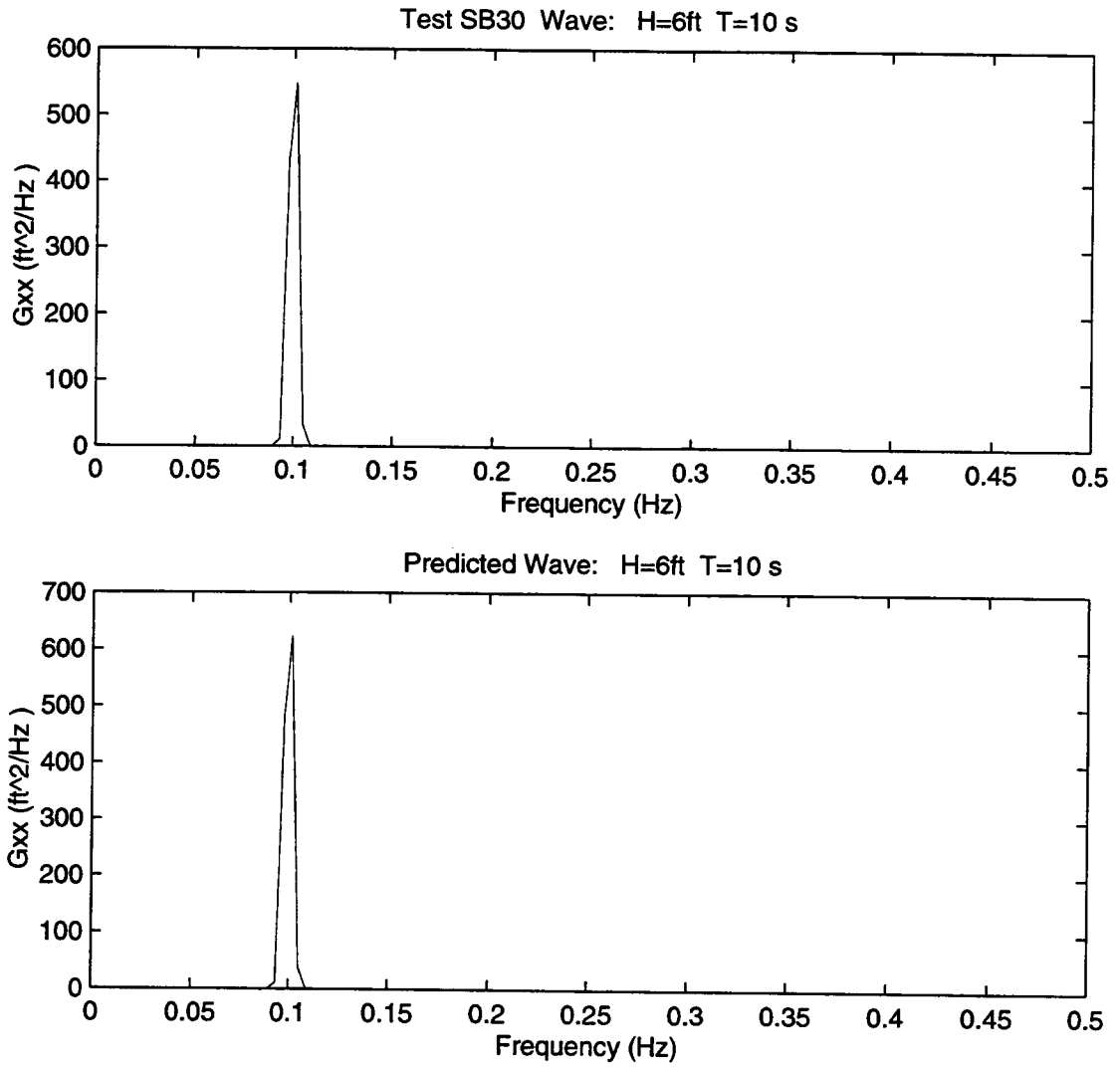


Figure C.31 Wave Spectral Densities, H=6 ft, T=10 s

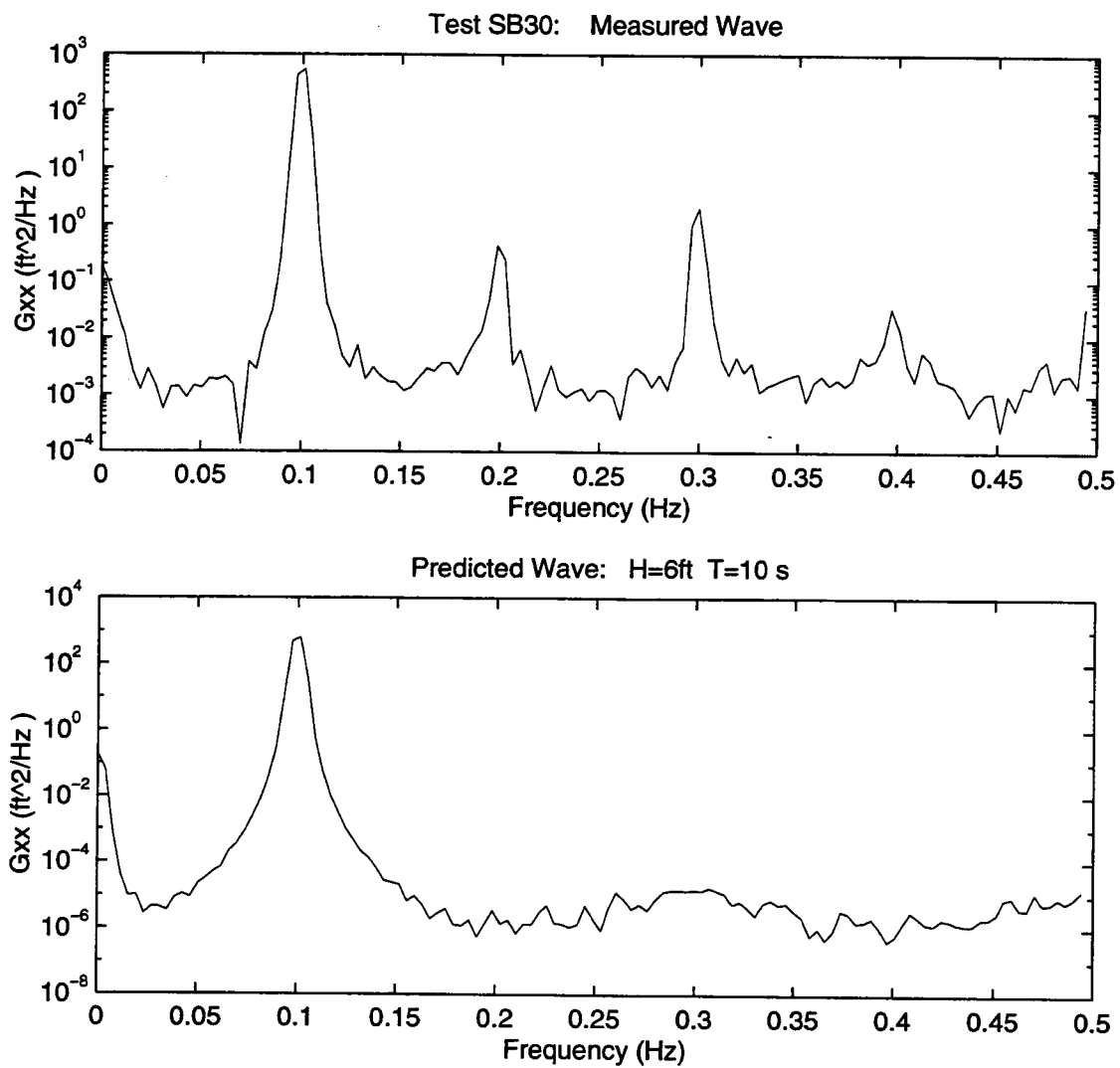


Figure C.32 Wave Spectral Densities, H=6 ft, T=10 s (semilog)

C.32

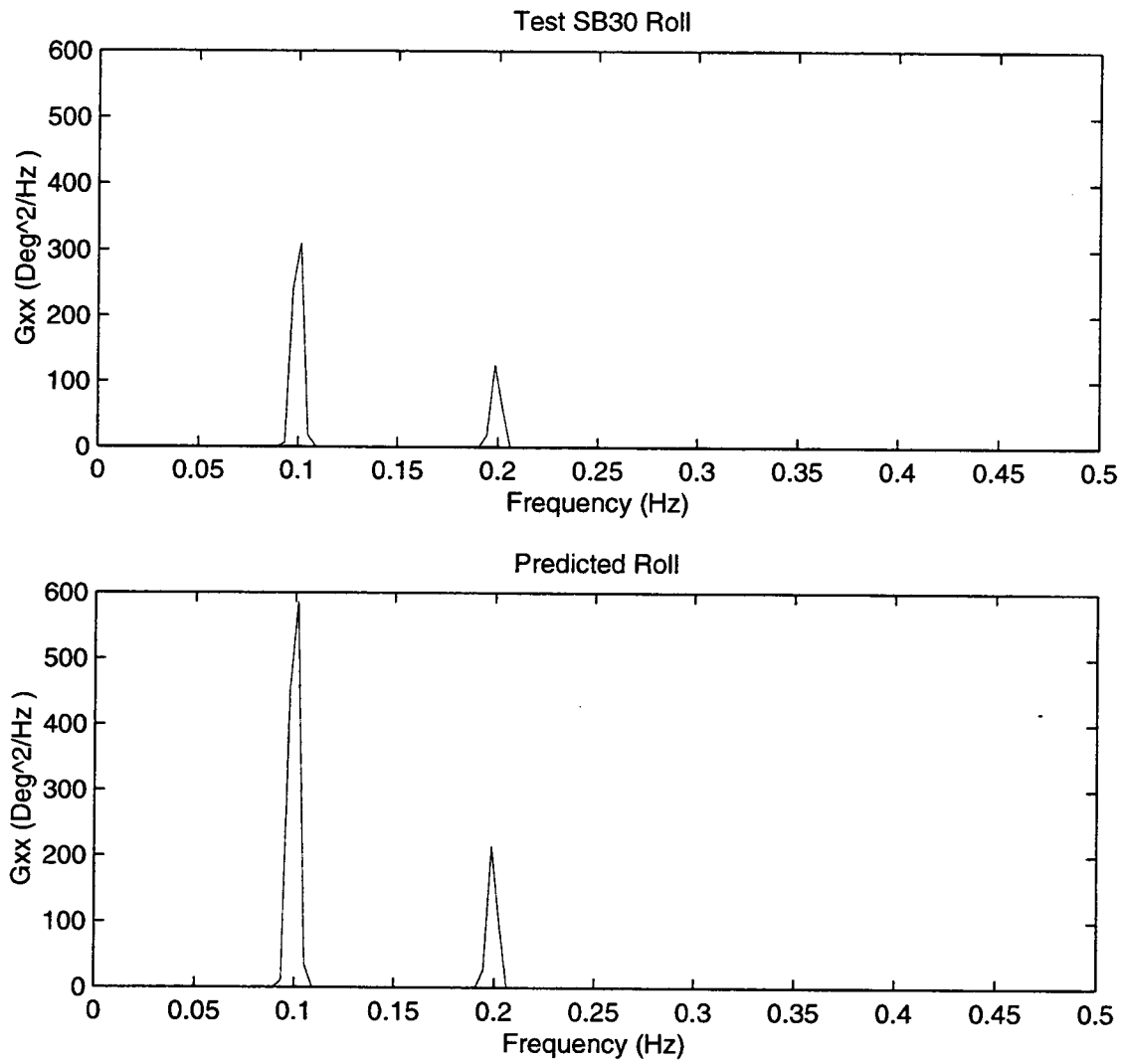


Figure C.33 Roll Spectral Densities, H=6 ft, T=10 s

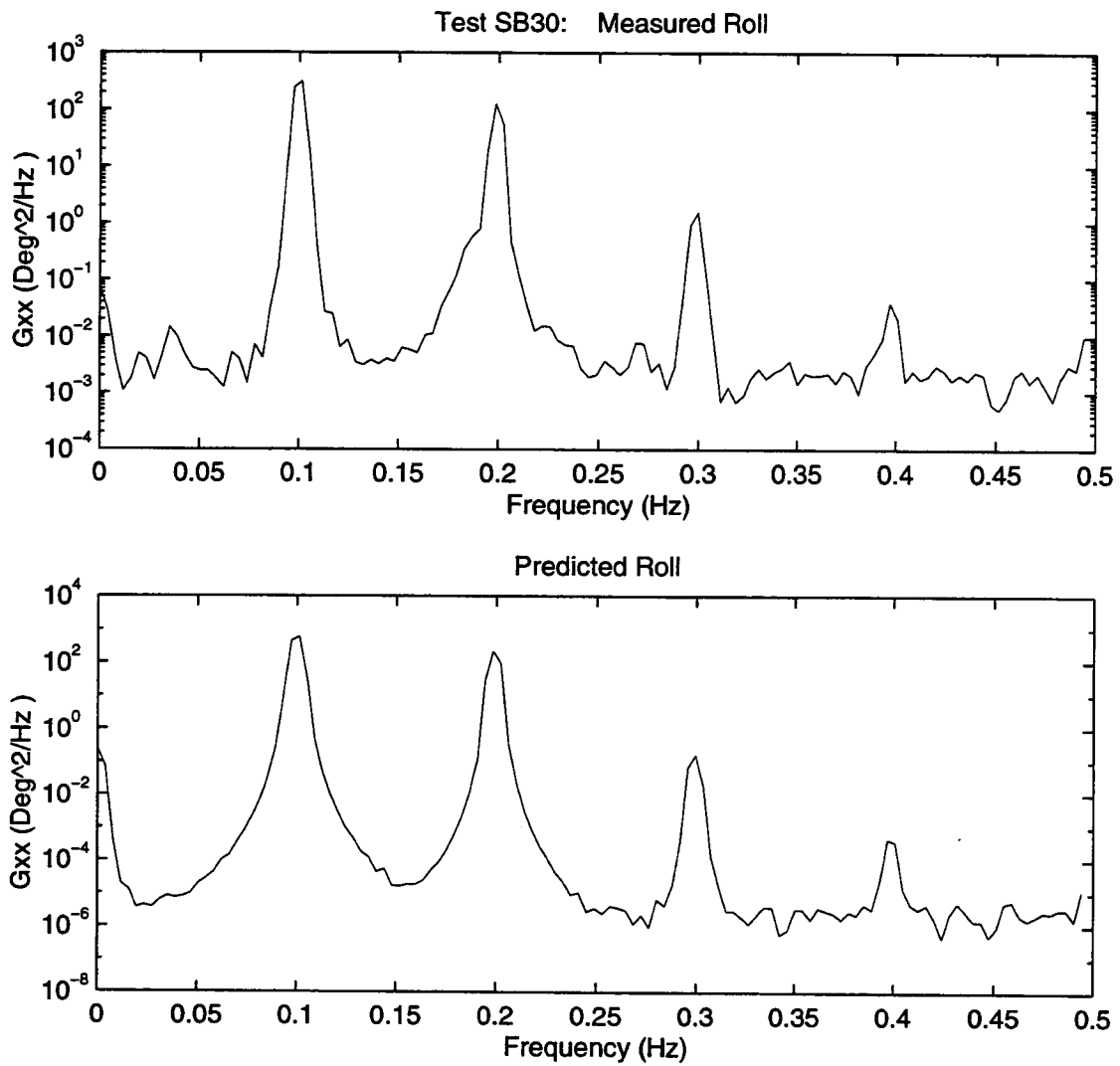


Figure C.34 Roll Spectral Densities, $H=6$ ft, $T=10$ s (semilog)

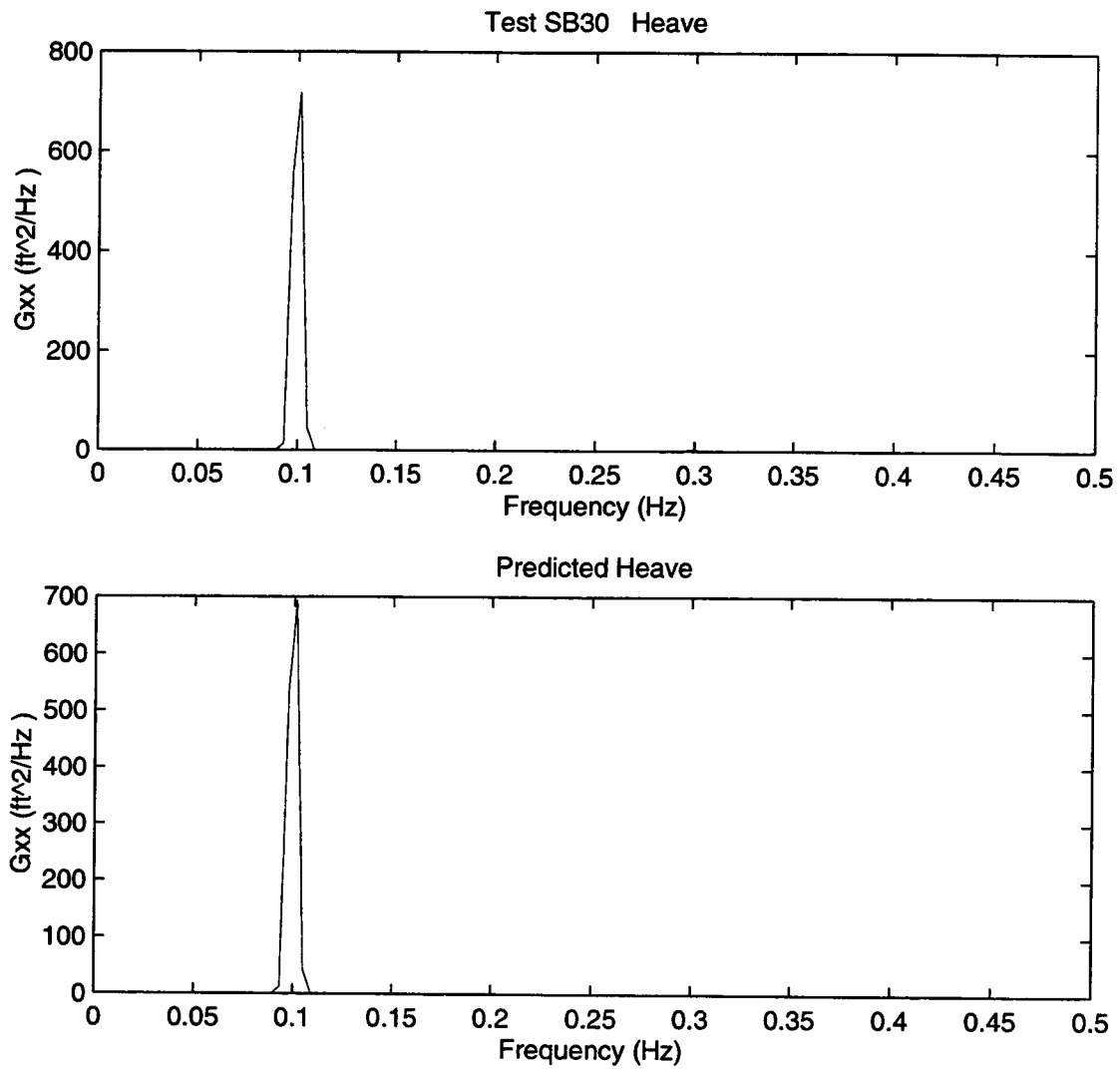


Figure C.35 Heave Spectral Densities, $H=6$ ft, $T=10$ s

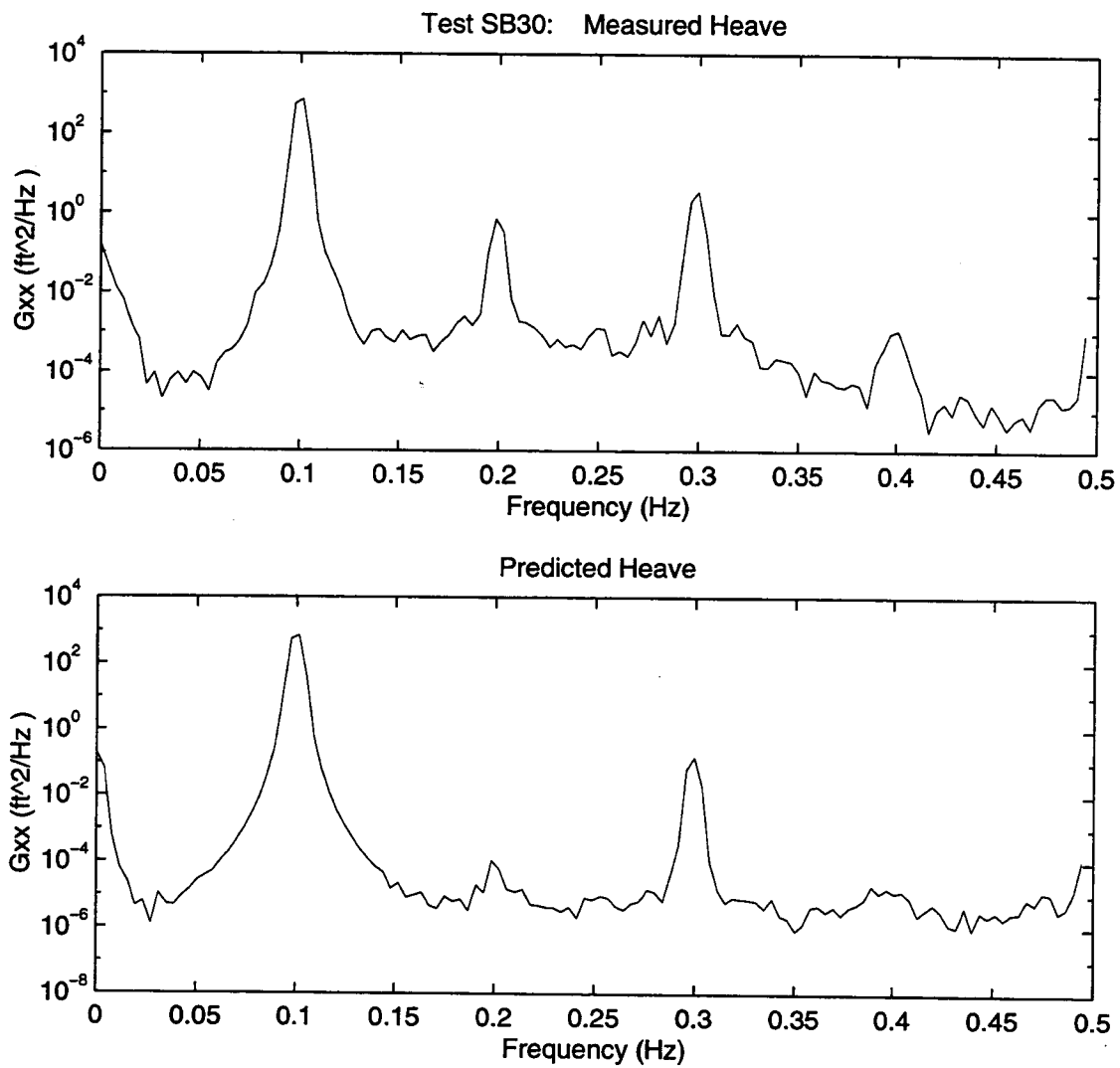


Figure C.36 Heave Spectral Densities, $H=6$ ft, $T=10$ s (semilog)

C.36

APPENDIX D**Comparison Figures
Roll-Heave-Sway Model (Section 5.1)**

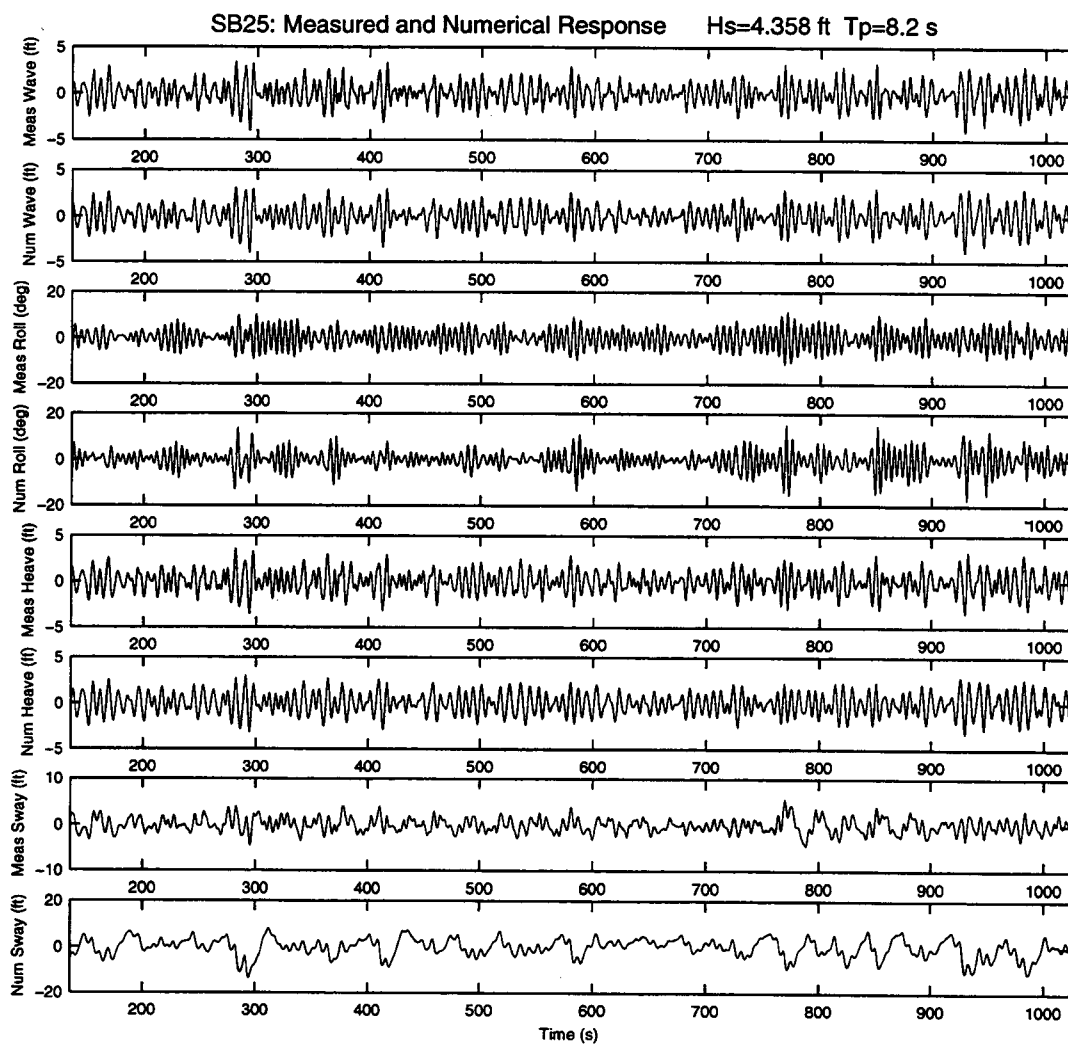


Figure D.1 Measured and Predicted Response, $H_s=4.7$ ft, $T_p=8.2$ s

D.1

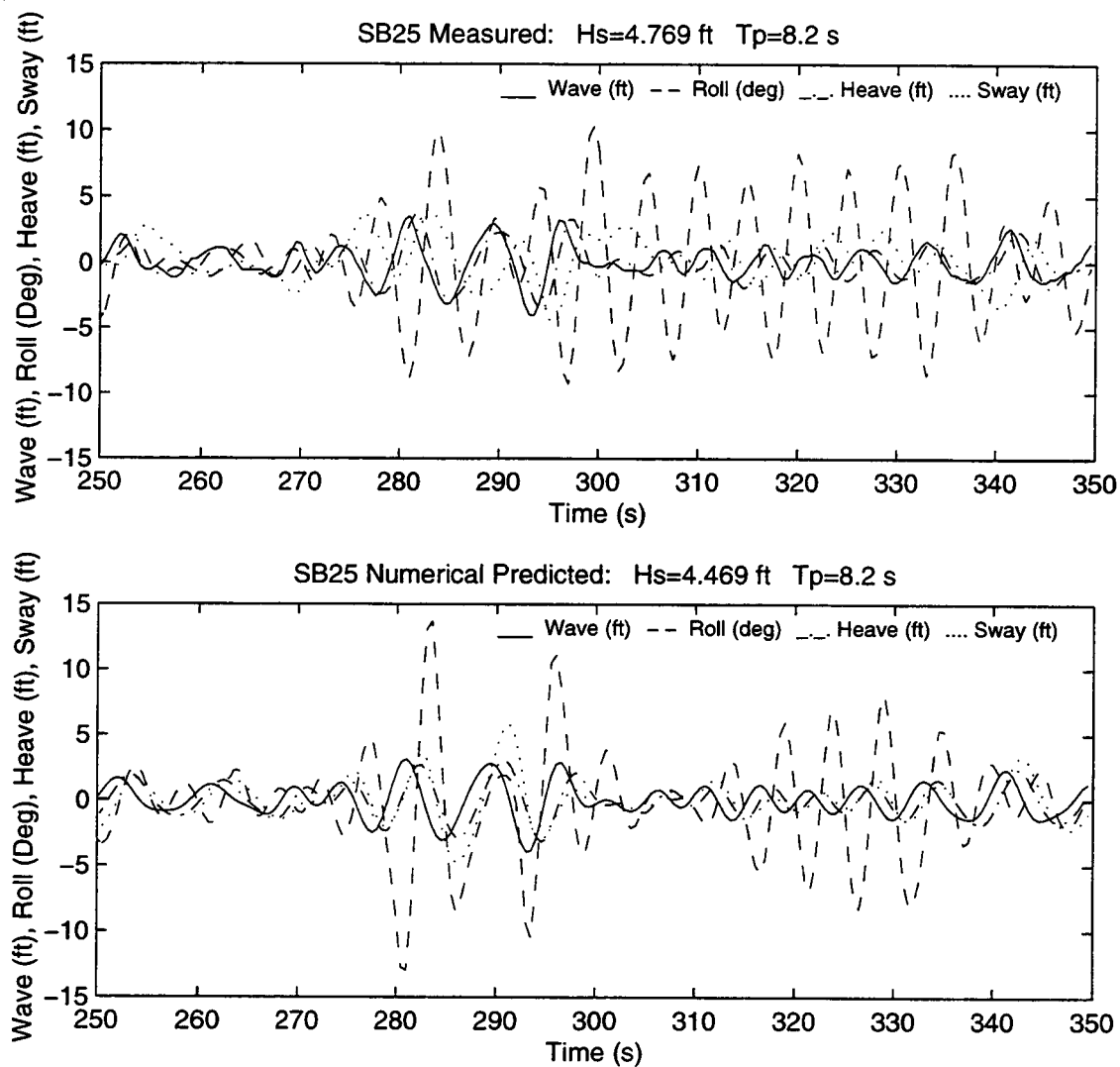


Figure D.2

Measured and Predicted Response, Hs=4.7 ft, Tp=8.2 s

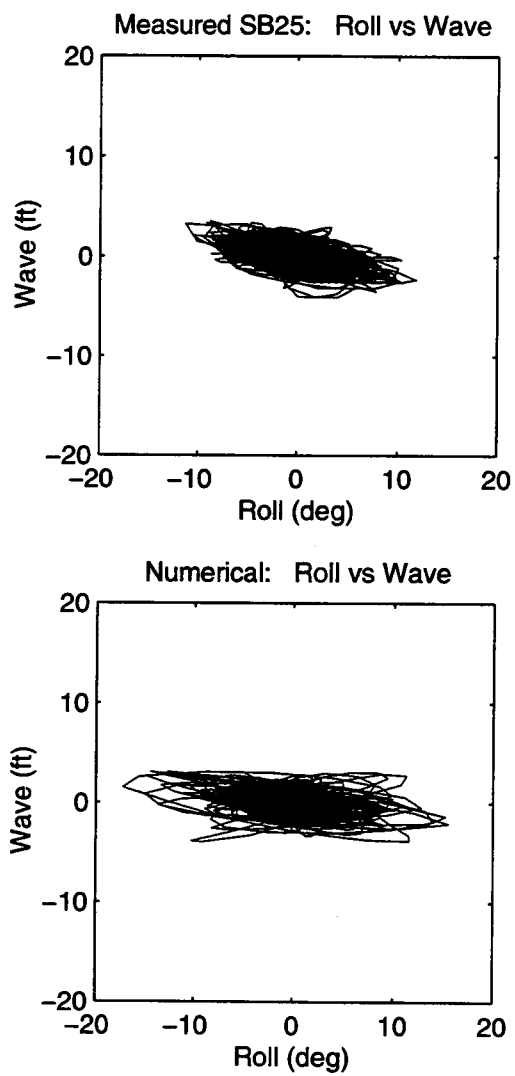


Figure D.3

Roll vs Wave, $H_s=4.7$ ft, $T_p=8.2$ s

D.3

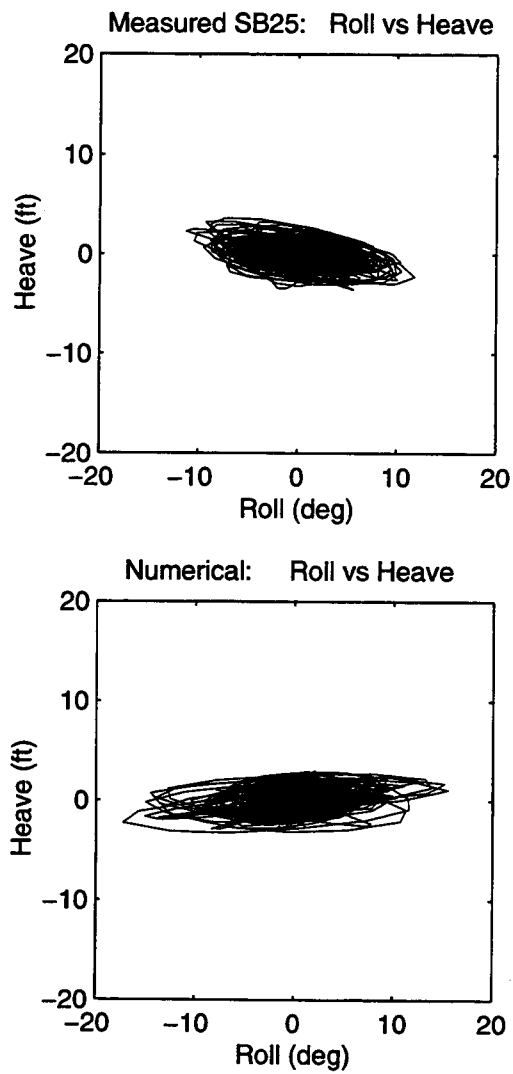


Figure D.4

Roll vs Heave, $H_s=4.7$ ft, $T_p=8.2$ s

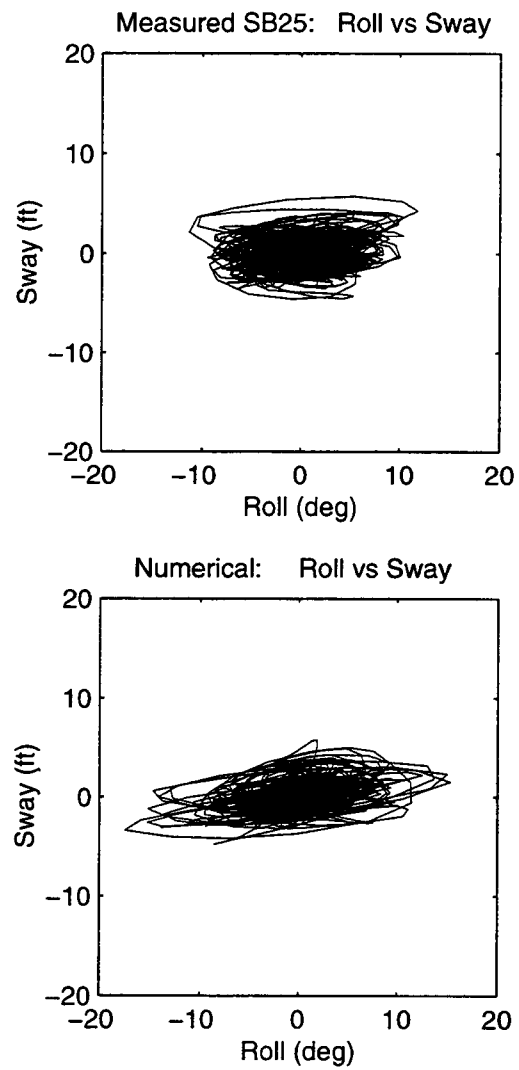


Figure D.5

Roll vs Sway, $H_s=4.7$ ft, $T_p=8.2$ s

D.5

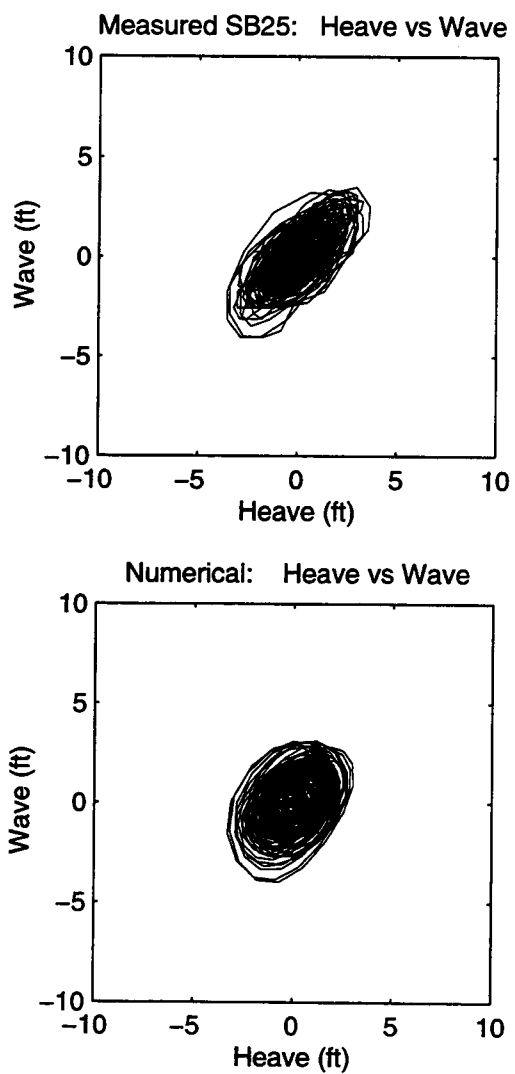


Figure D.6

Heave vs Wave, $H_s=4.7$ ft, $T_p=8.2$ s

D.6

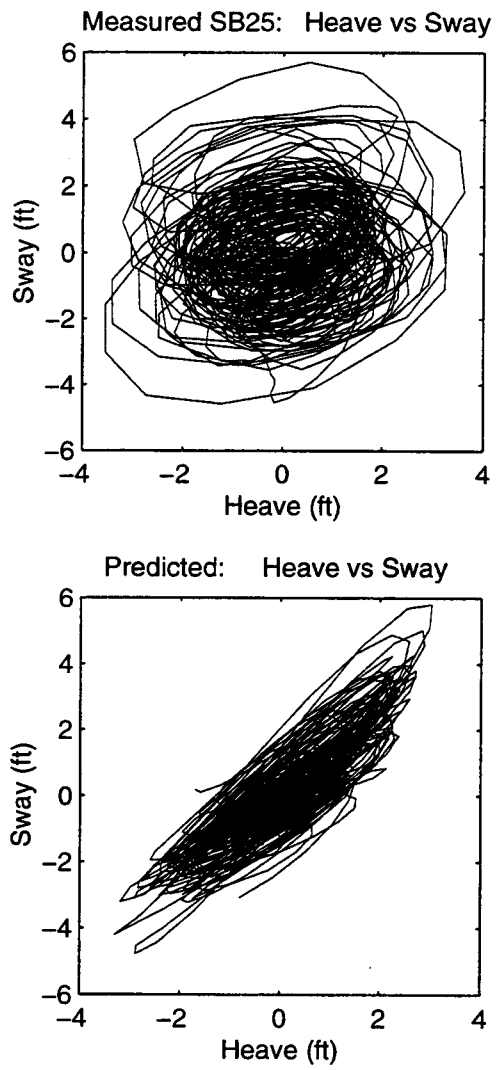


Figure D.7

Heave vs Sway, $H_s=4.7$ ft, $T_p=8.2$ s

D.7

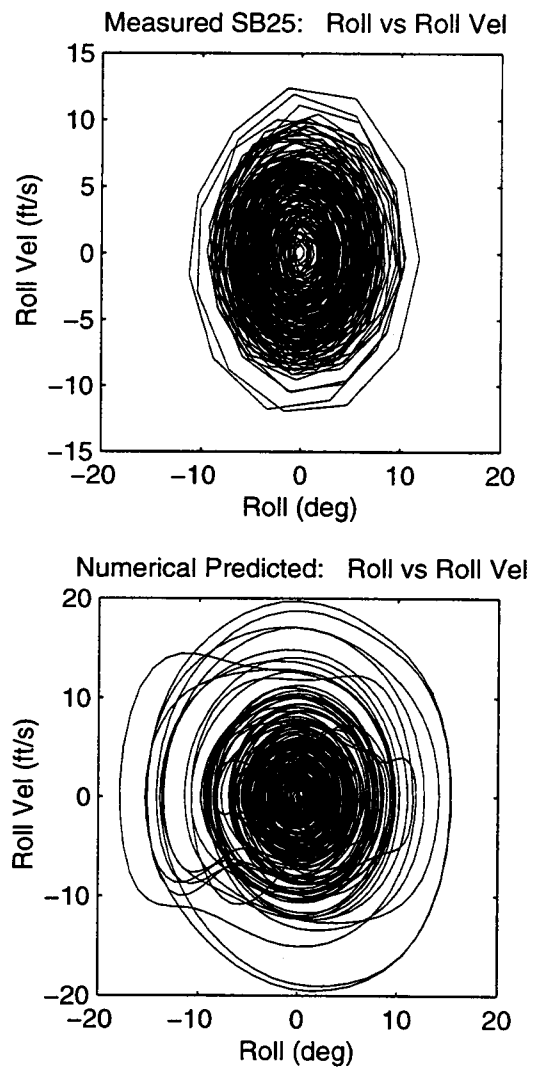


Figure D.8

Phase Plane for Roll and Roll Velocity, $H_s=4.7$ ft, $T_p=8.2$ s

D.8

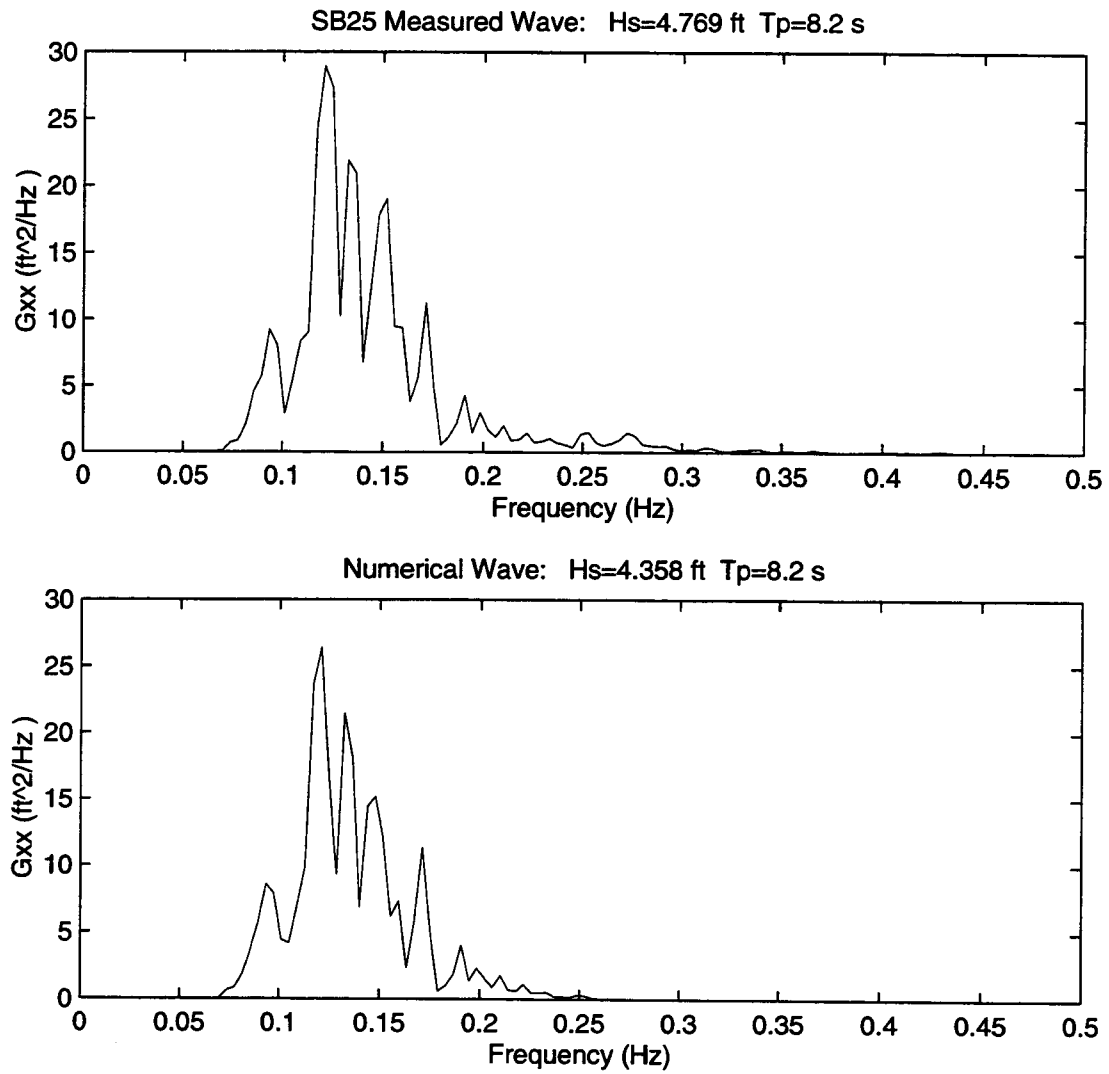


Figure D.9 Wave Spectral Densities, $H_s=4.7$ ft, $T_p=8.2$ s

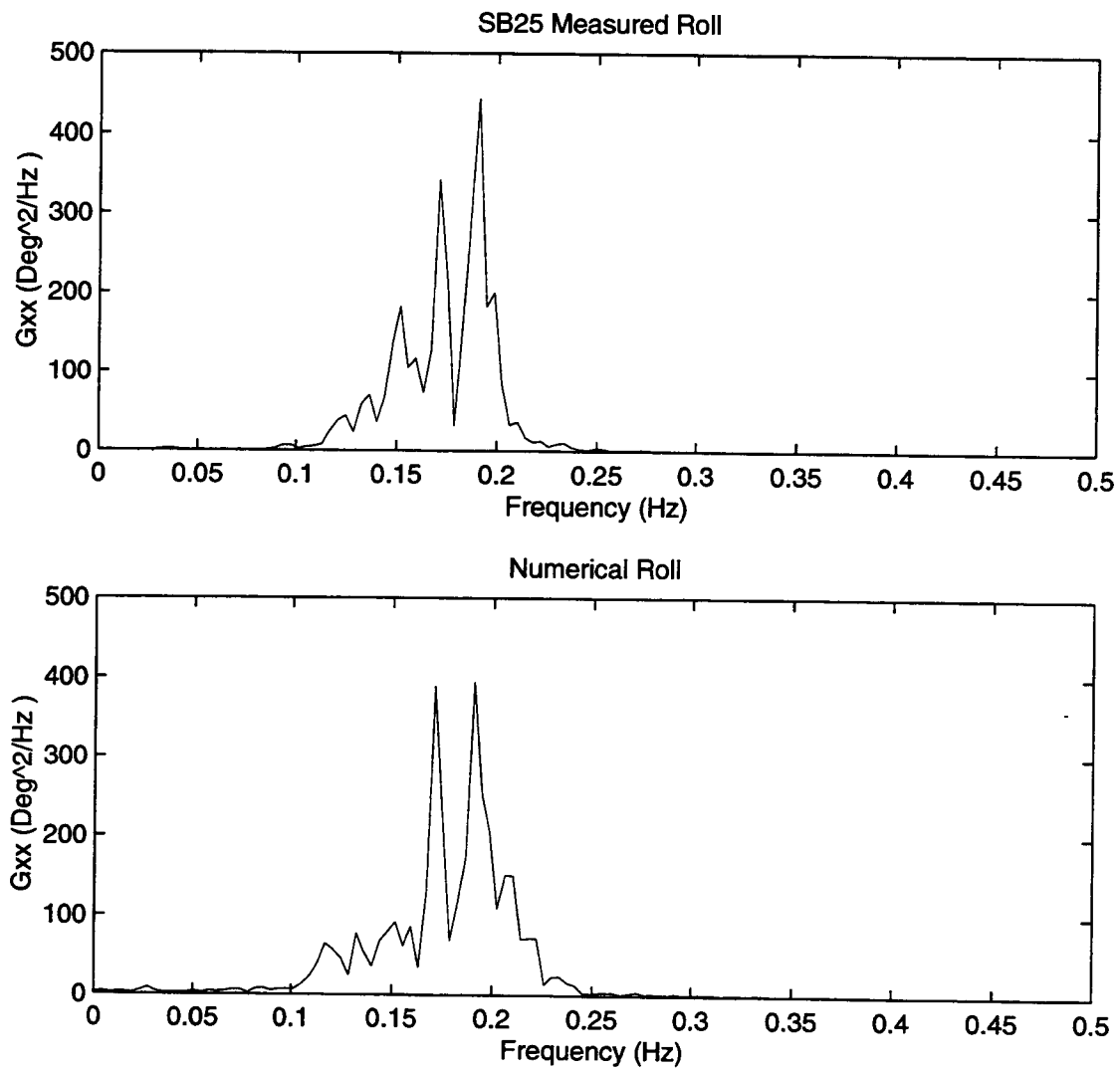


Figure D.10 Roll Spectral Densities, Hs=4.7 ft, Tp=8.2 s

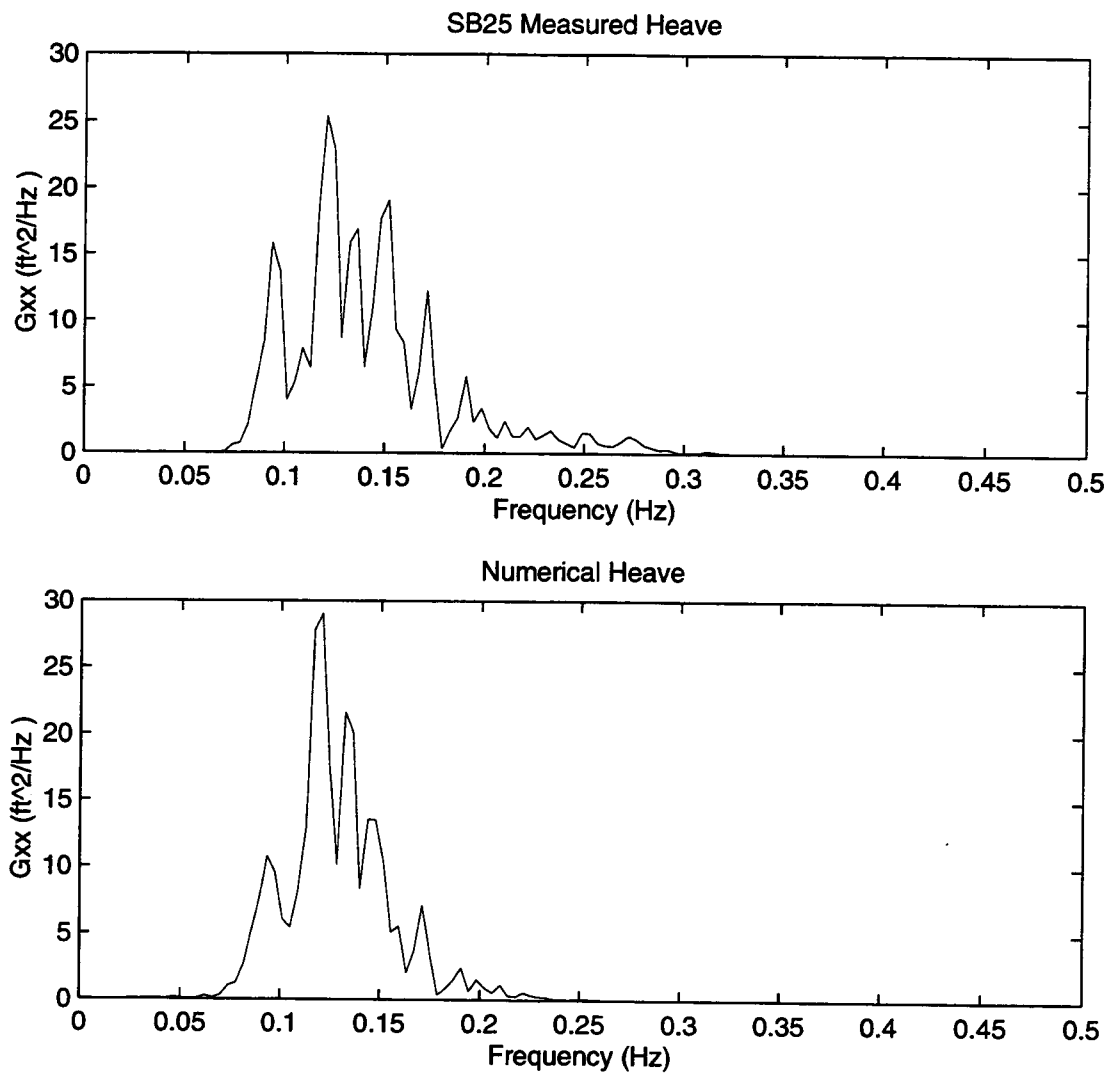


Figure D.11 Heave Spectral Densities, $H_s=4.7$ ft, $T_p=8.2$ s

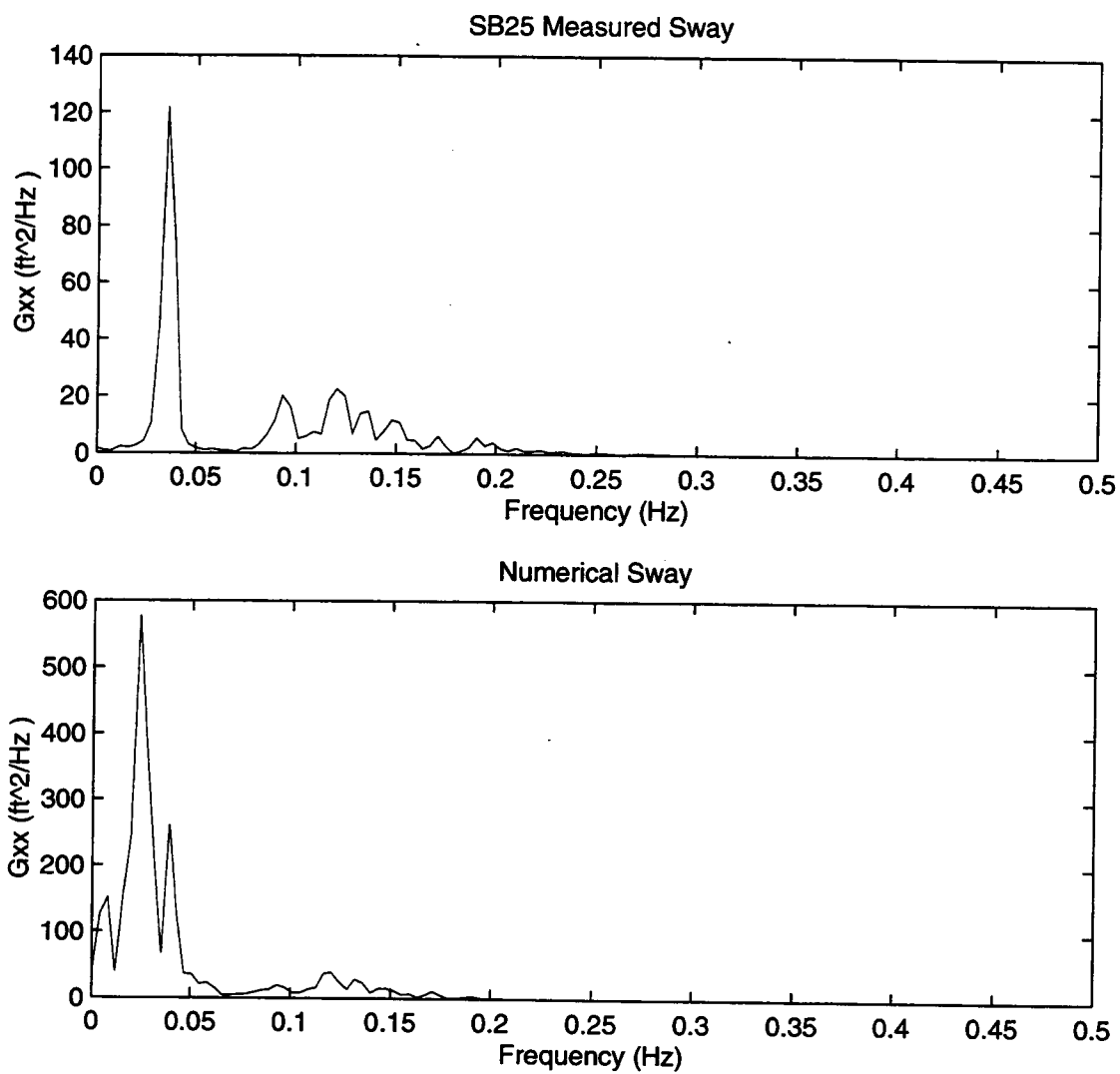


Figure D.12 Sway Spectral Densities, $H_s=4.7$ ft, $T_p=8.2$ s

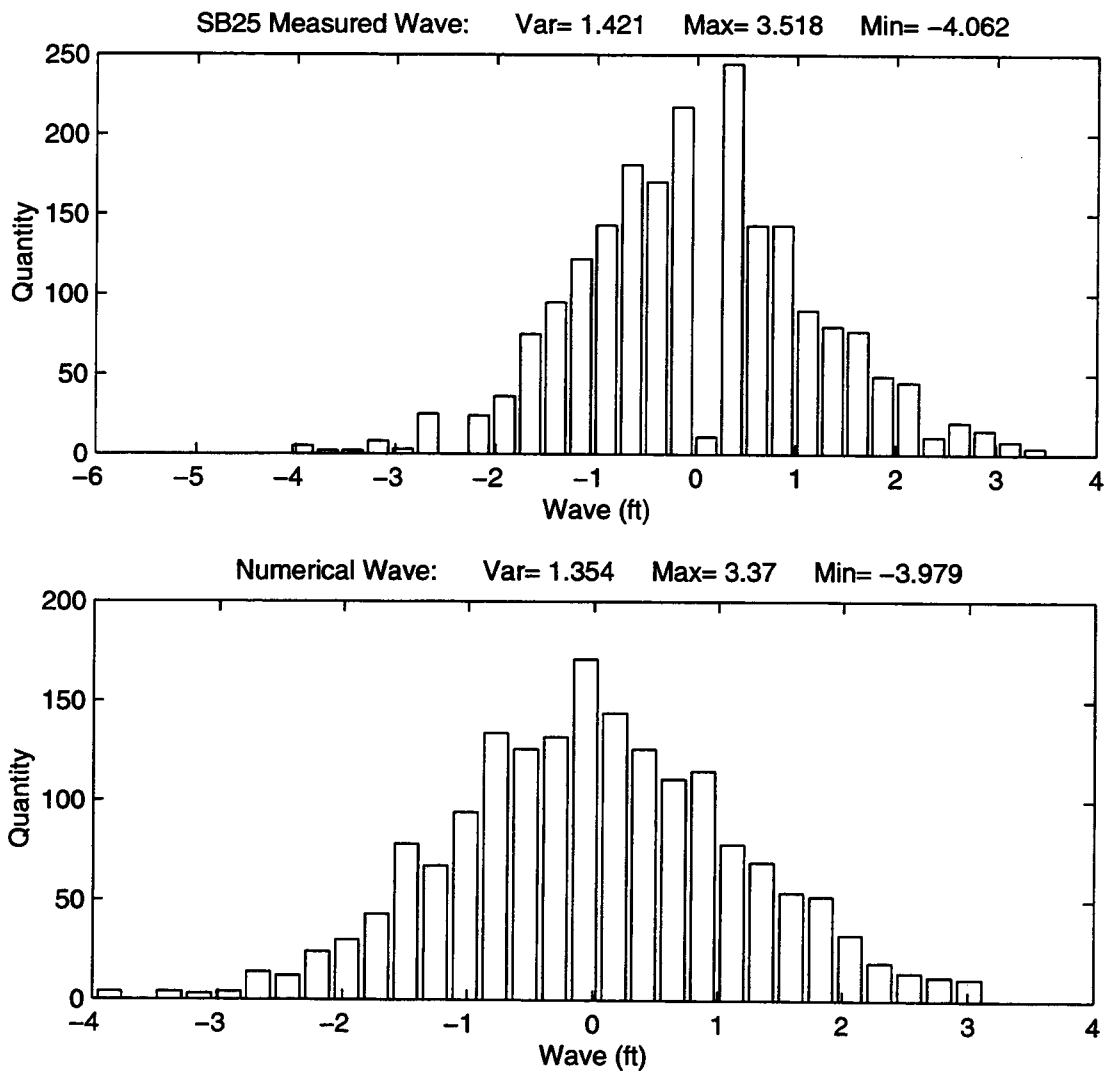


Figure D.13 Wave Histograms, Hs=4.7 ft, Tp=8.2 s

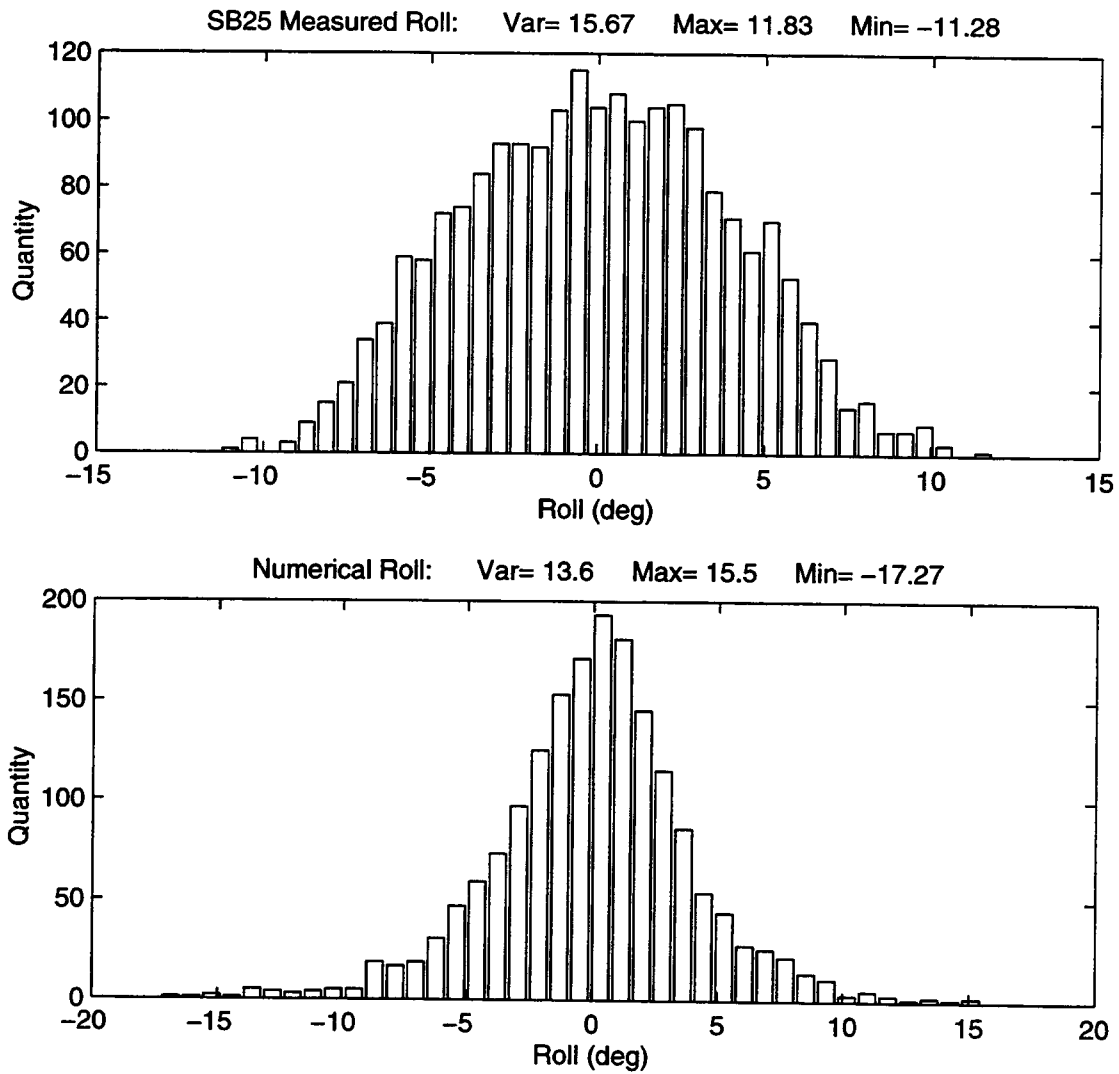


Figure D.14 Roll Histograms, $H_s=4.7$ ft, $T_p=8.2$ s

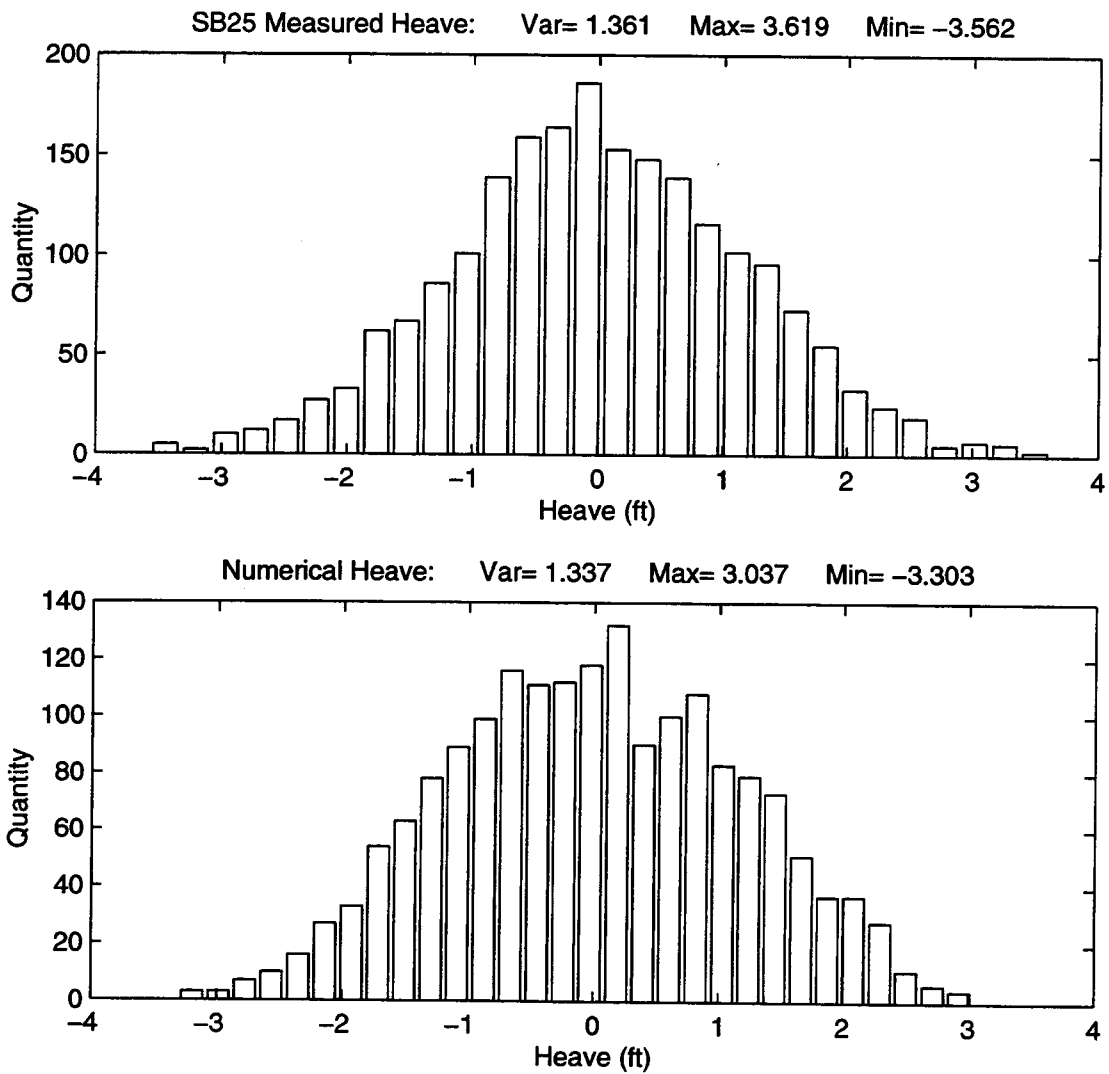


Figure D.15

Heave Histograms, $H_s=4.7$ ft, $T_p=8.2$ s

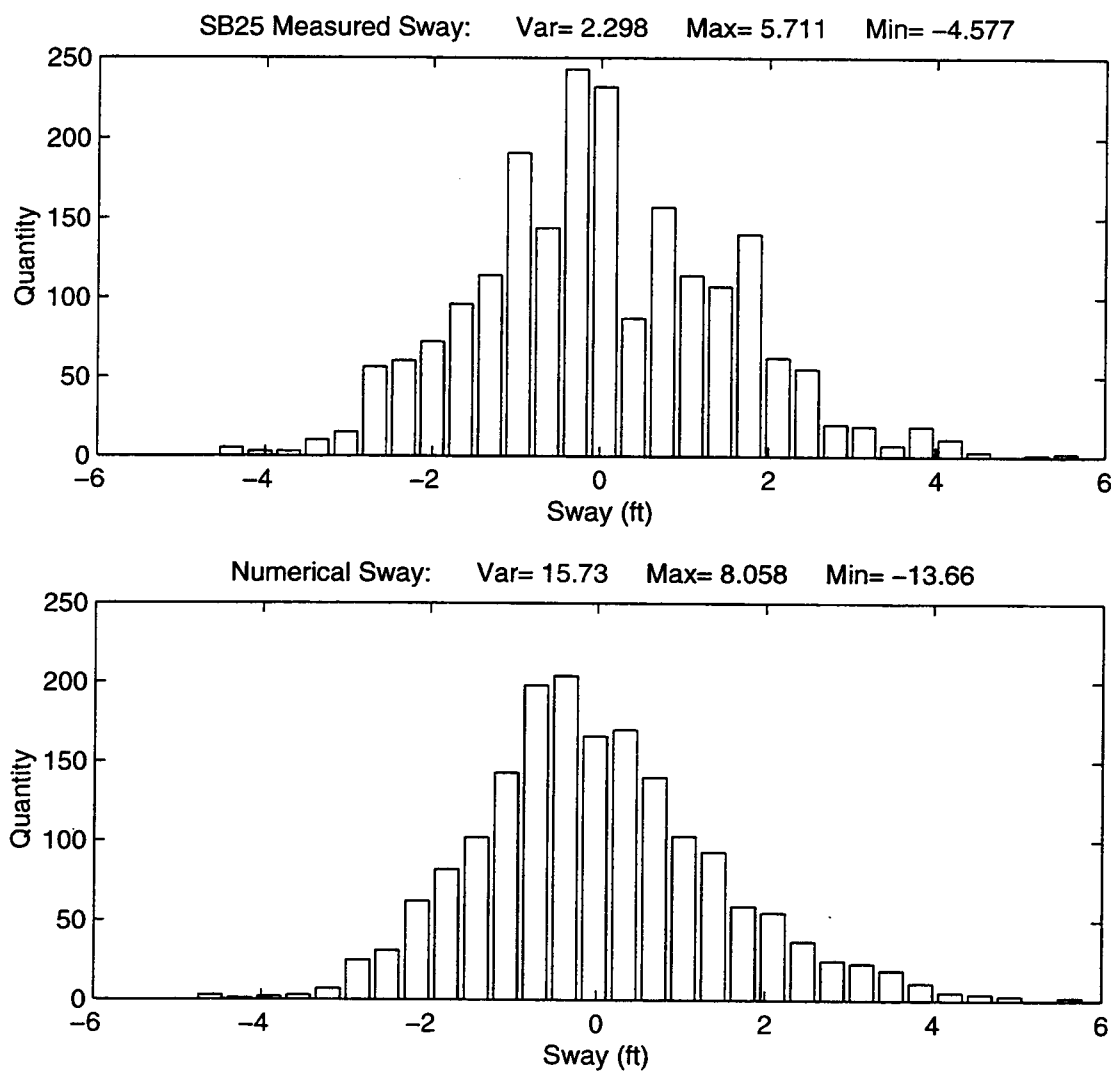


Figure D.16 Sway Histograms, $H_s=4.7$ ft, $T_p=8.2$ s

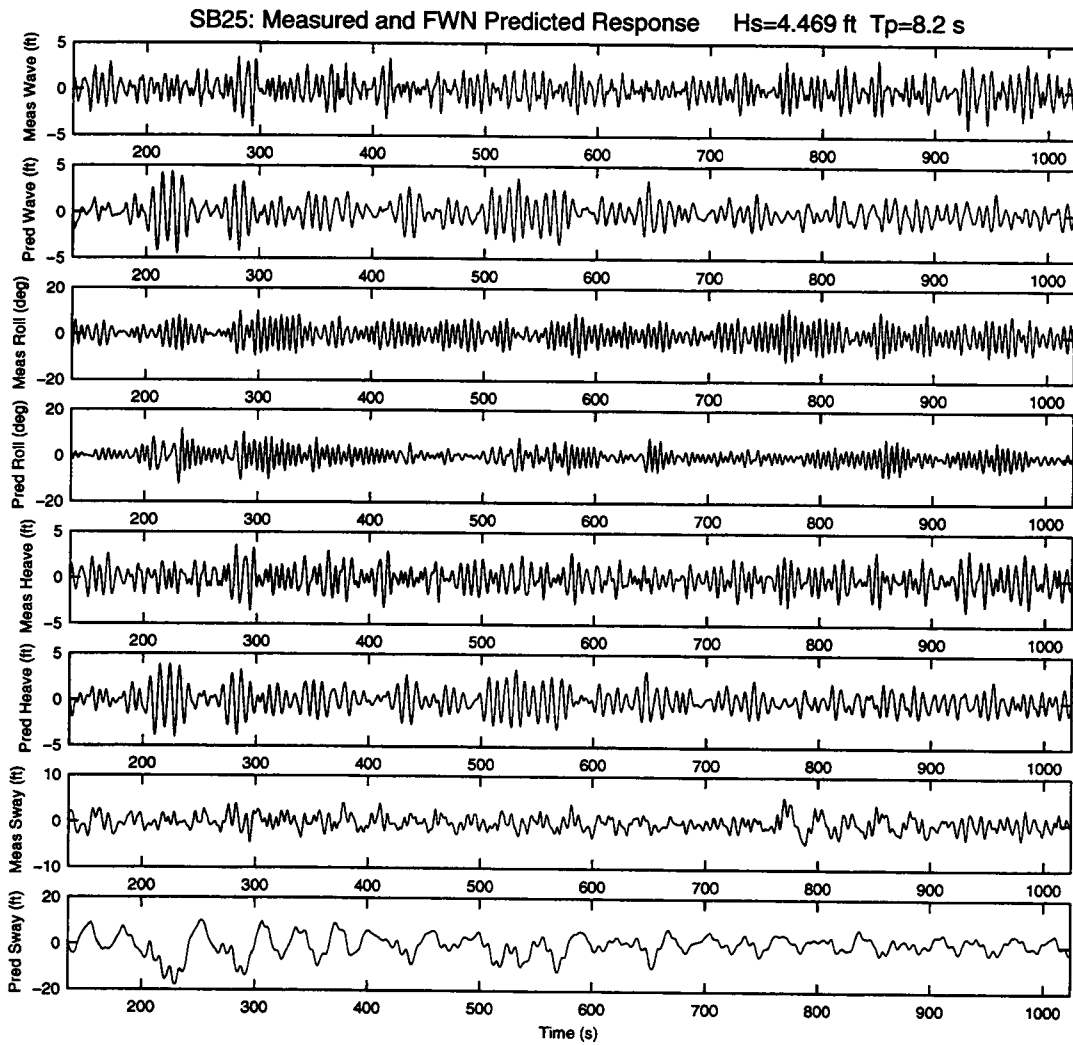


Figure D.17

Measured and FWN Predicted Response, Hs=4.7 ft, Tp=8.2 s

D.17

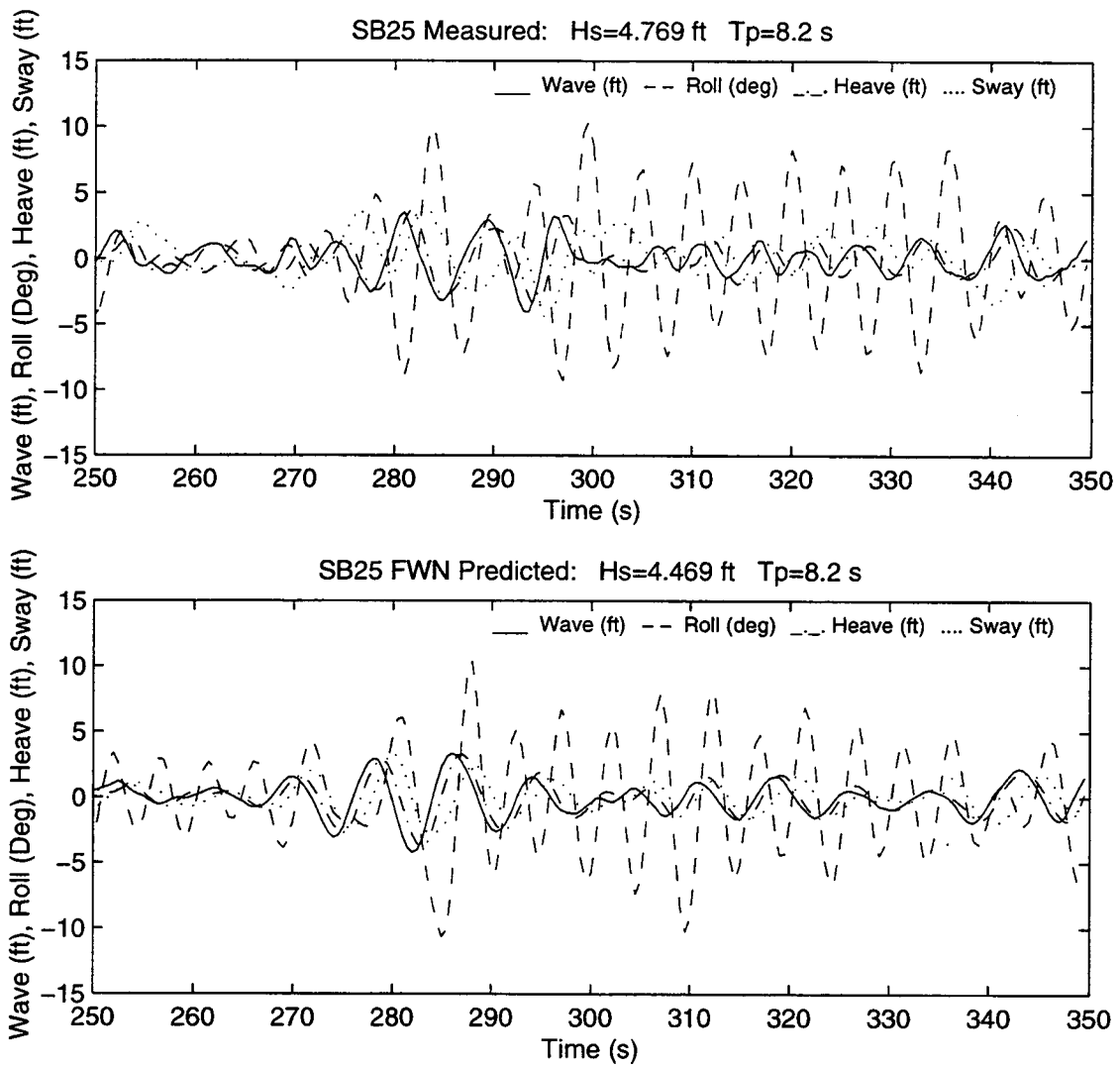


Figure D.18 Measured and FWN Predicted Response, Hs=4.7 ft, Tp=8.2 s

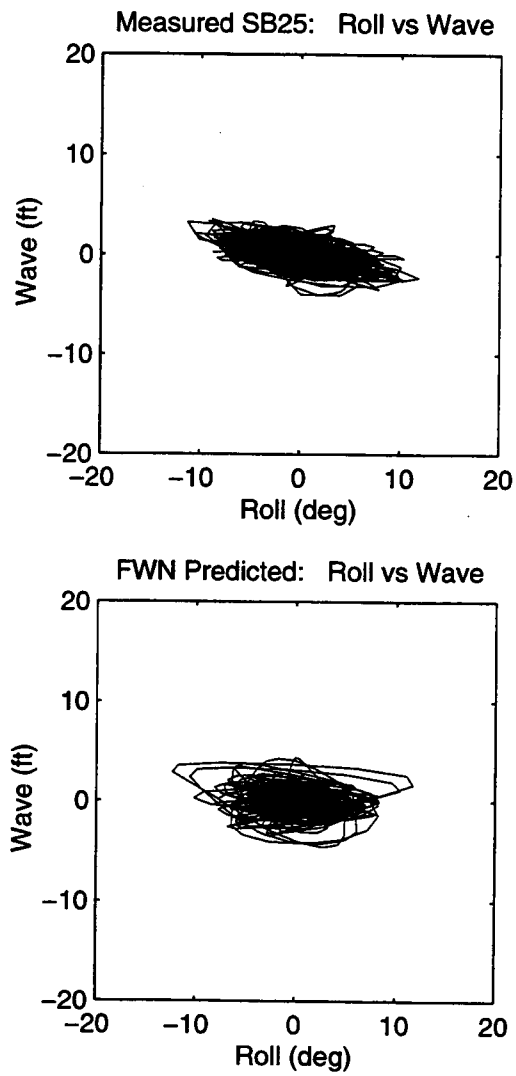


Figure D.19

Roll vs Wave, $H_s=4.7$ ft, $T_p=8.2$ s

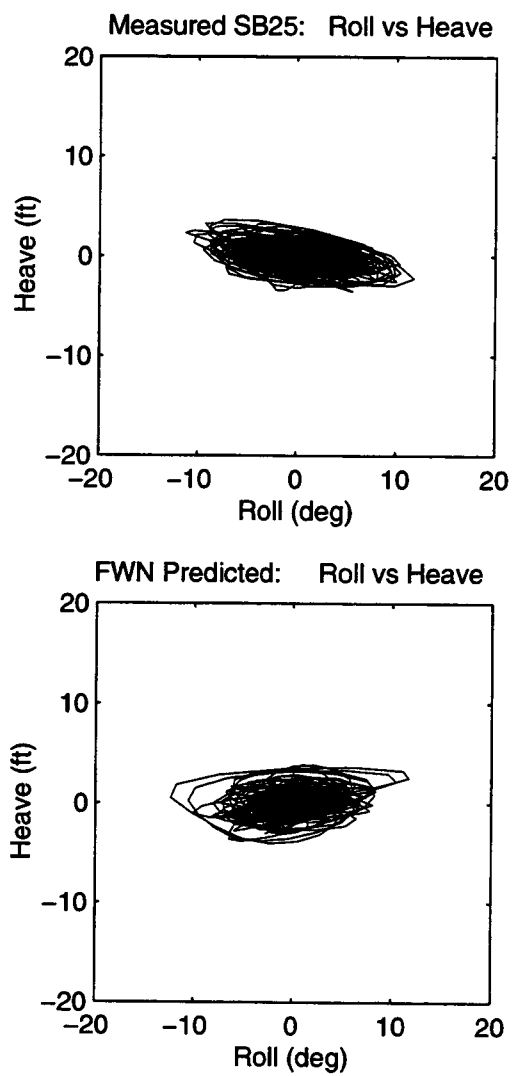


Figure D.20

Roll vs Heave, $H_s=4.7$ ft, $T_p=8.2$ s

D.20

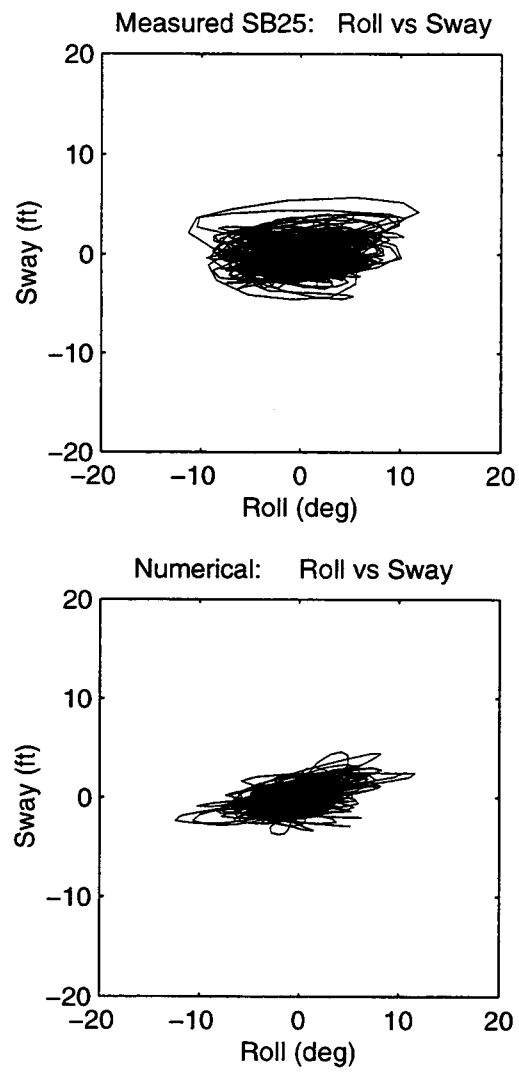


Figure D.21

Roll vs Sway, $H_s=4.7$ ft, $T_p=8.2$ s

D.21

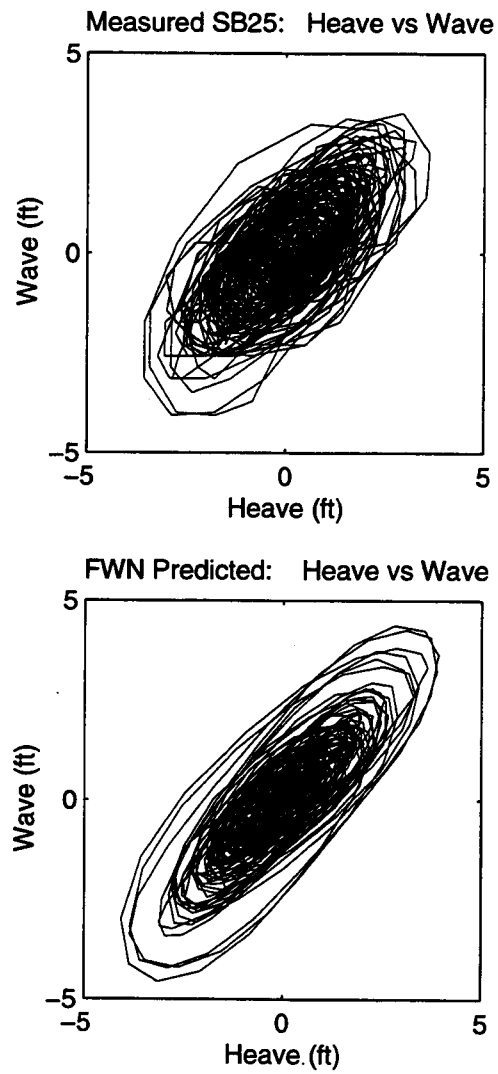


Figure D.22

Heave vs Wave, $H_s=4.7$ ft, $T_p=8.2$ s

D.22

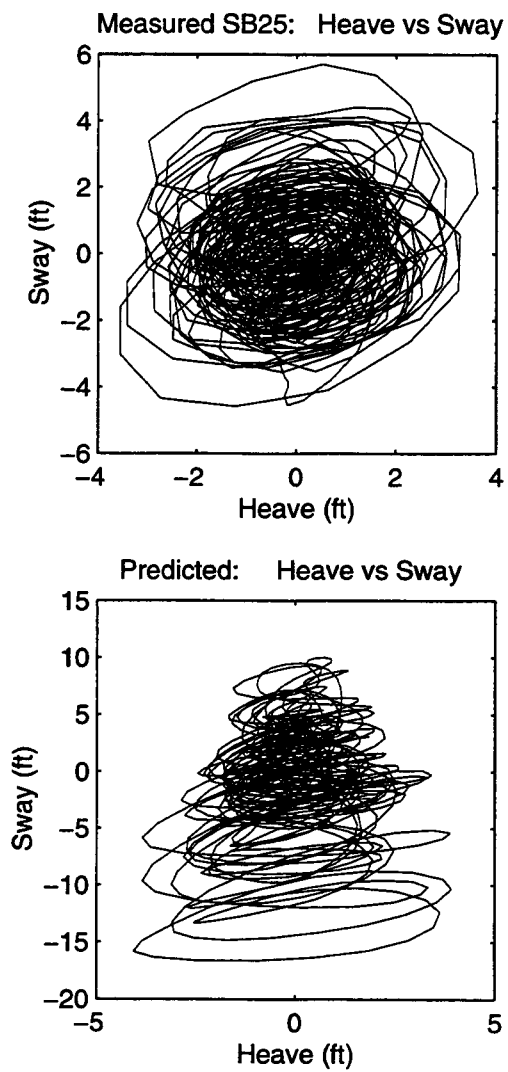


Figure D.23

Heave vs Sway, $H_s=4.7$ ft, $T_p=8.2$ s

D.23

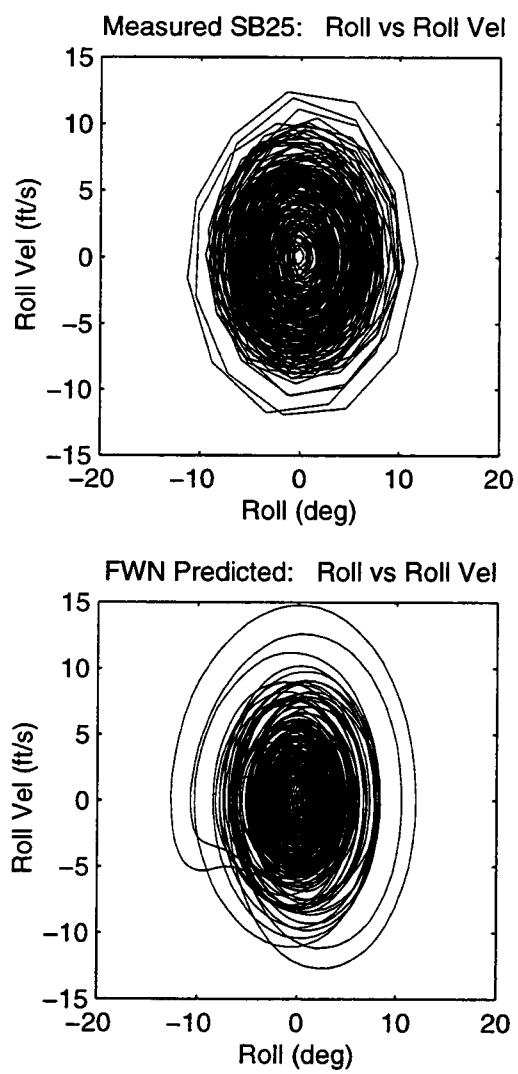


Figure D.24

Phase Plane for Roll and Roll Velocity, $H_s=4.7$ ft, $T_p=8.2$ s

D.24

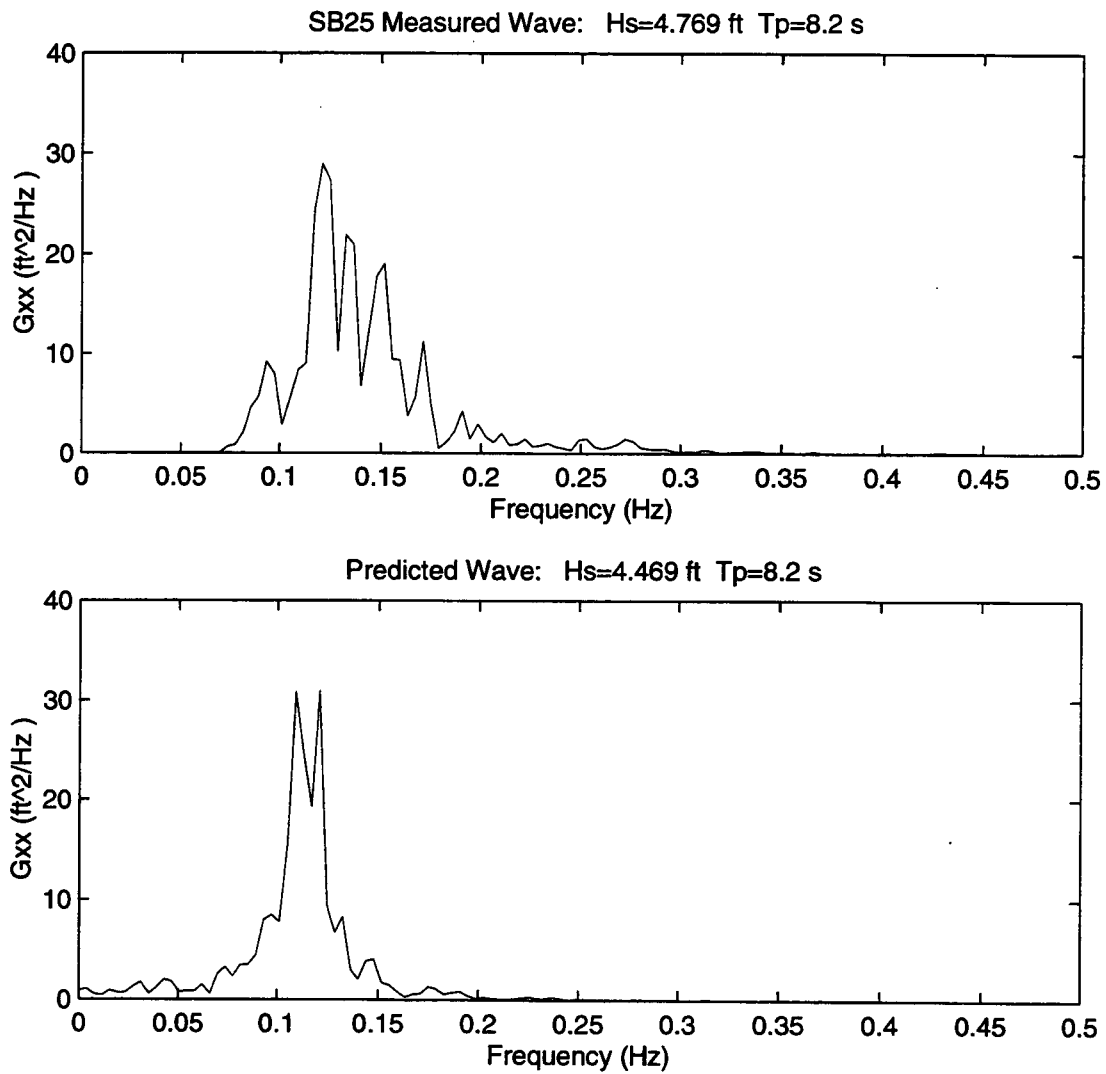


Figure D.25 Wave Spectral Densities, $H_s=4.7$ ft, $T_p=8.2$ s

D.25

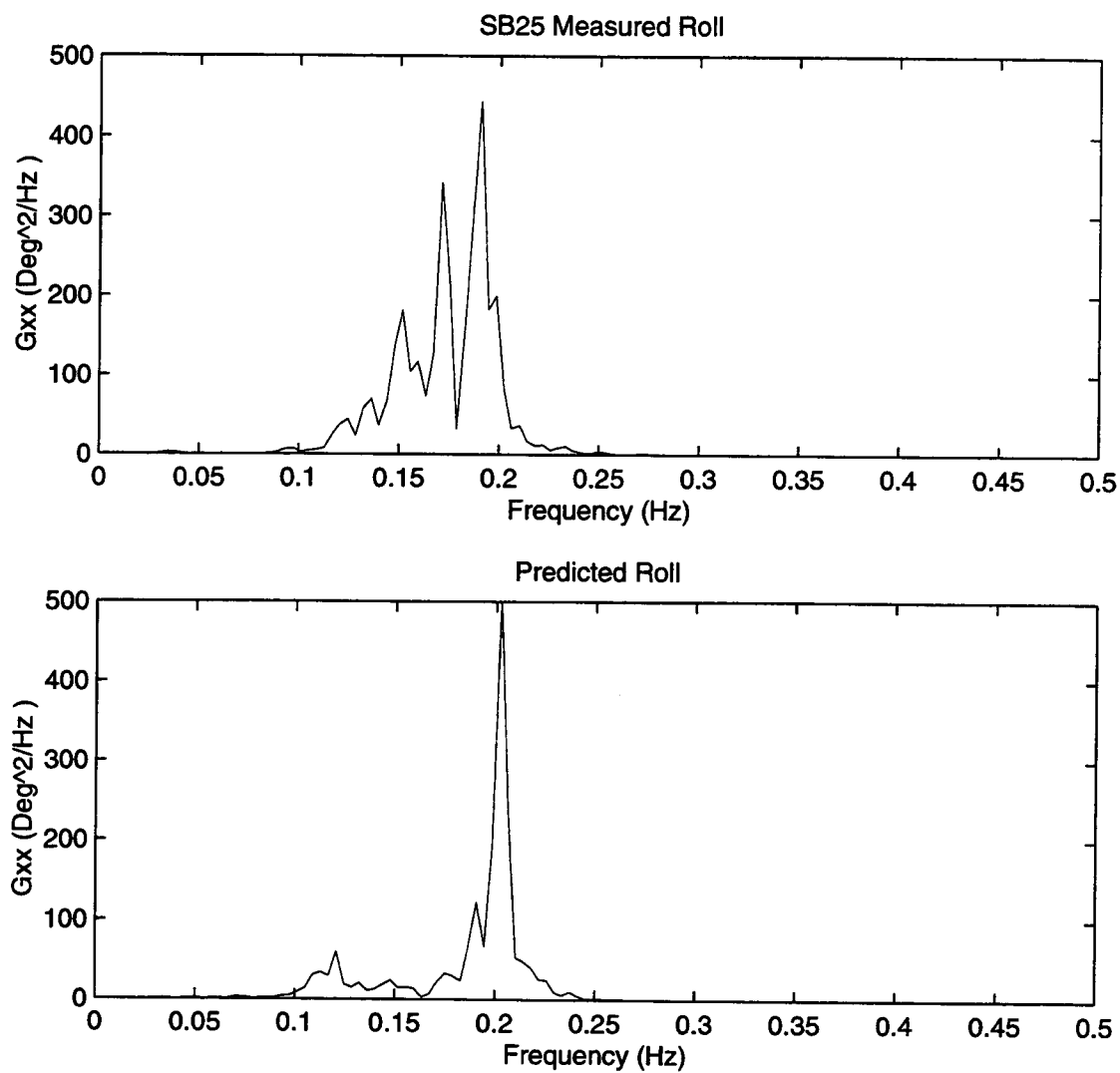


Figure D.26 Roll Spectral Densities, $H_s=4.7$ ft, $T_p=8.2$ s

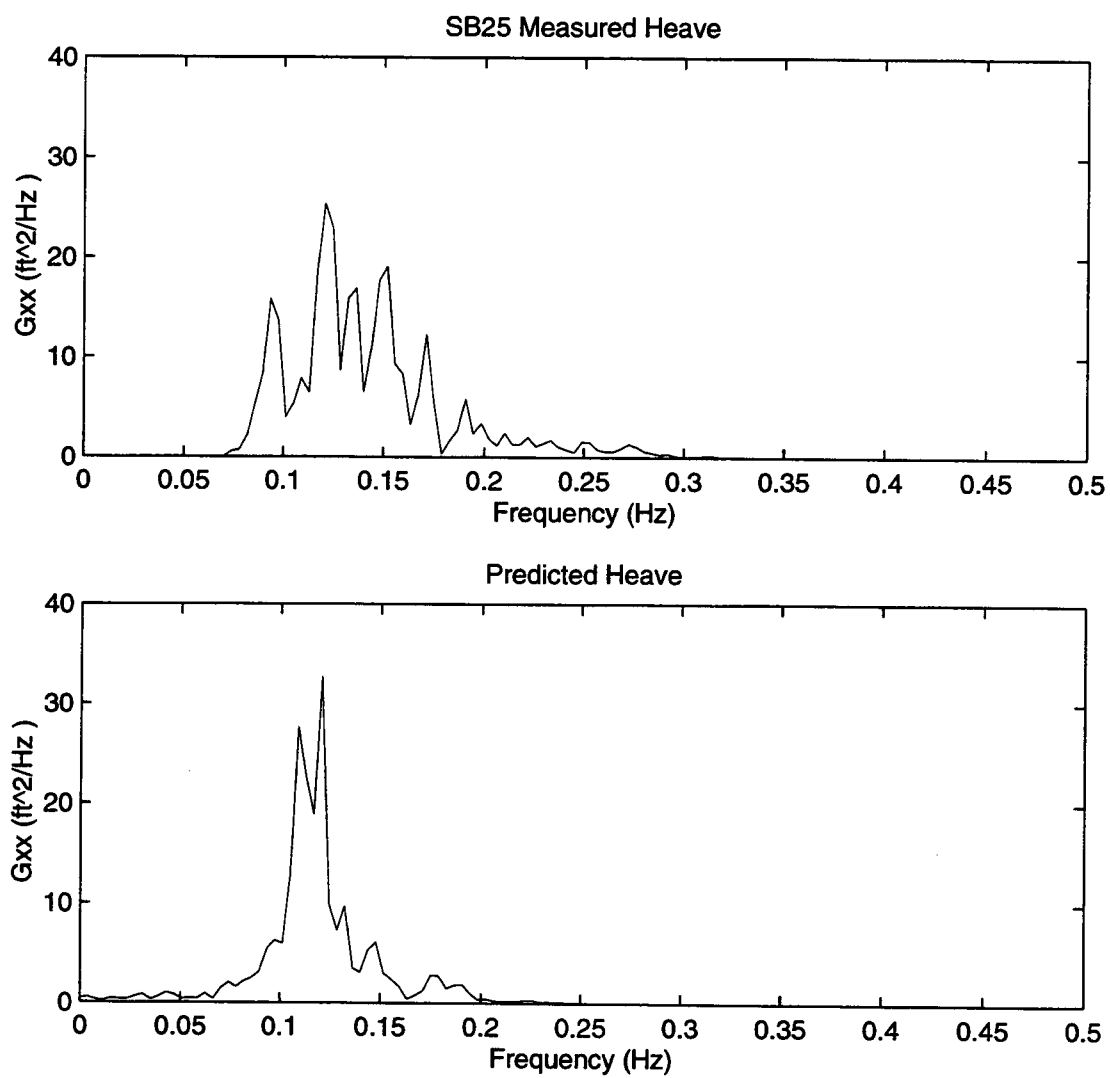


Figure D.27 Heave Spectral Densities, $H_s=4.7$ ft, $T_p=8.2$ s

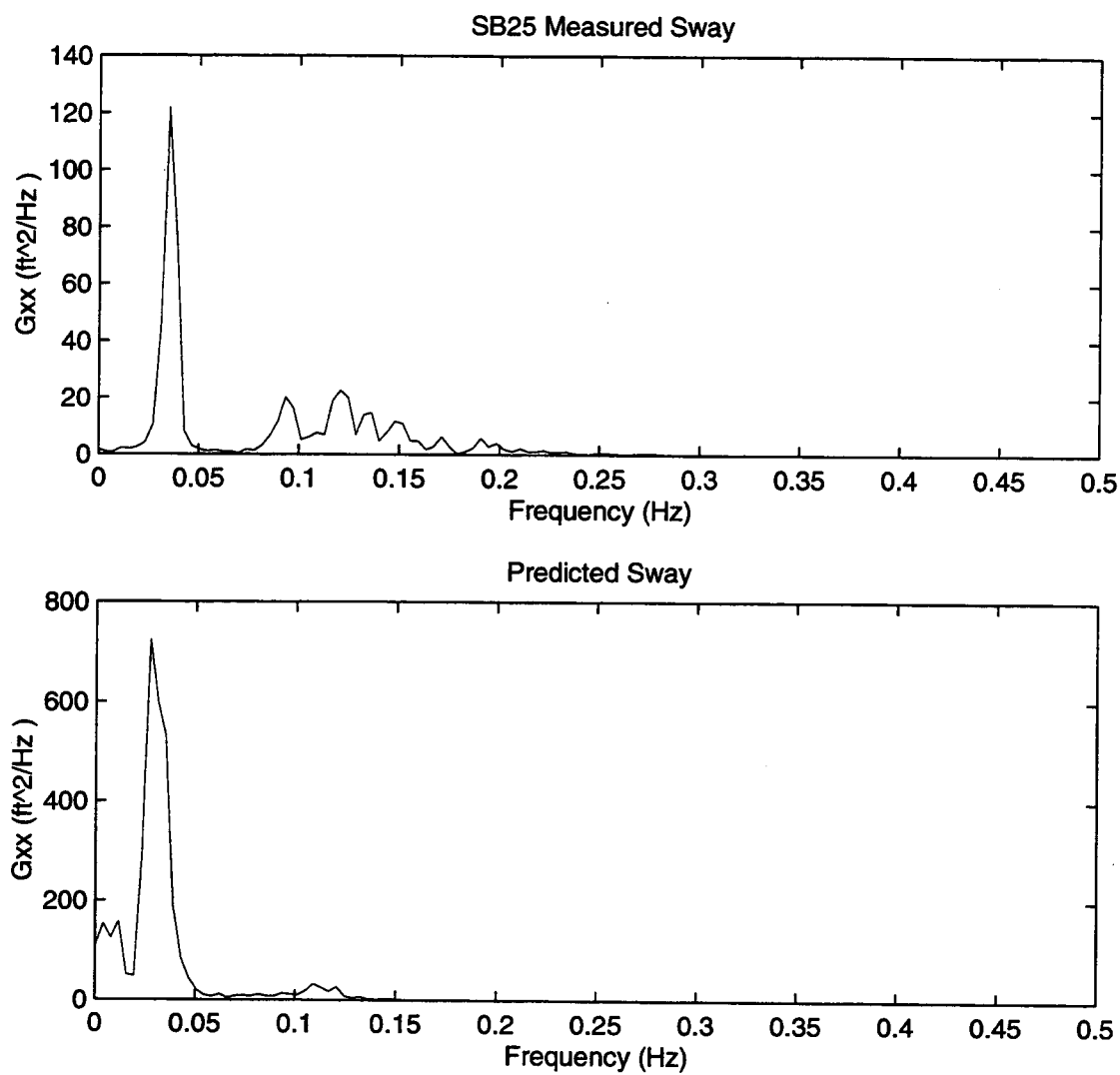


Figure D.28 Sway Spectral Densities, $H_s=4.7$ ft, $T_p=8.2$ s

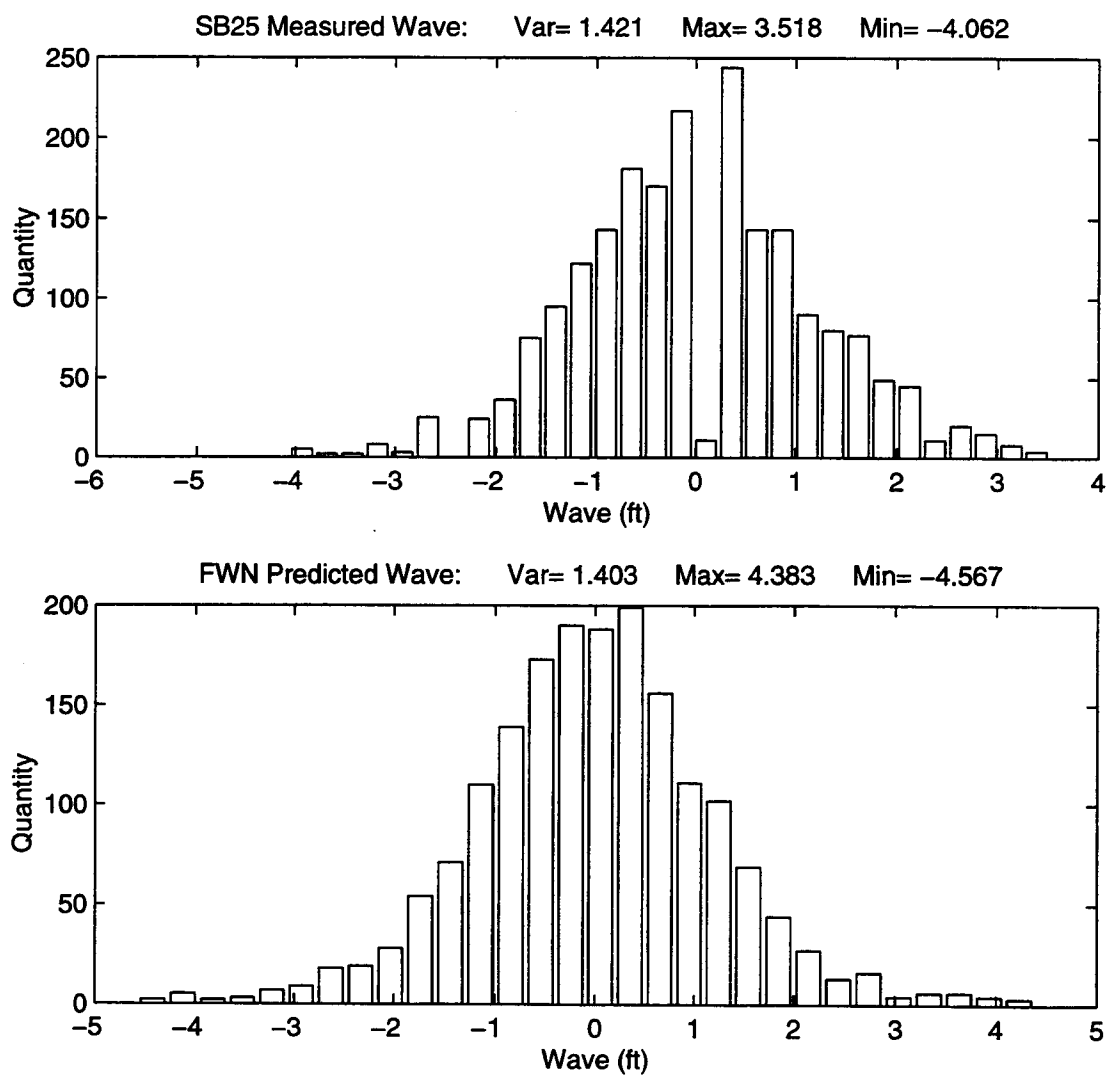


Figure D.29 Wave Histograms, $H_s=4.7$ ft, $T_p=8.2$ s

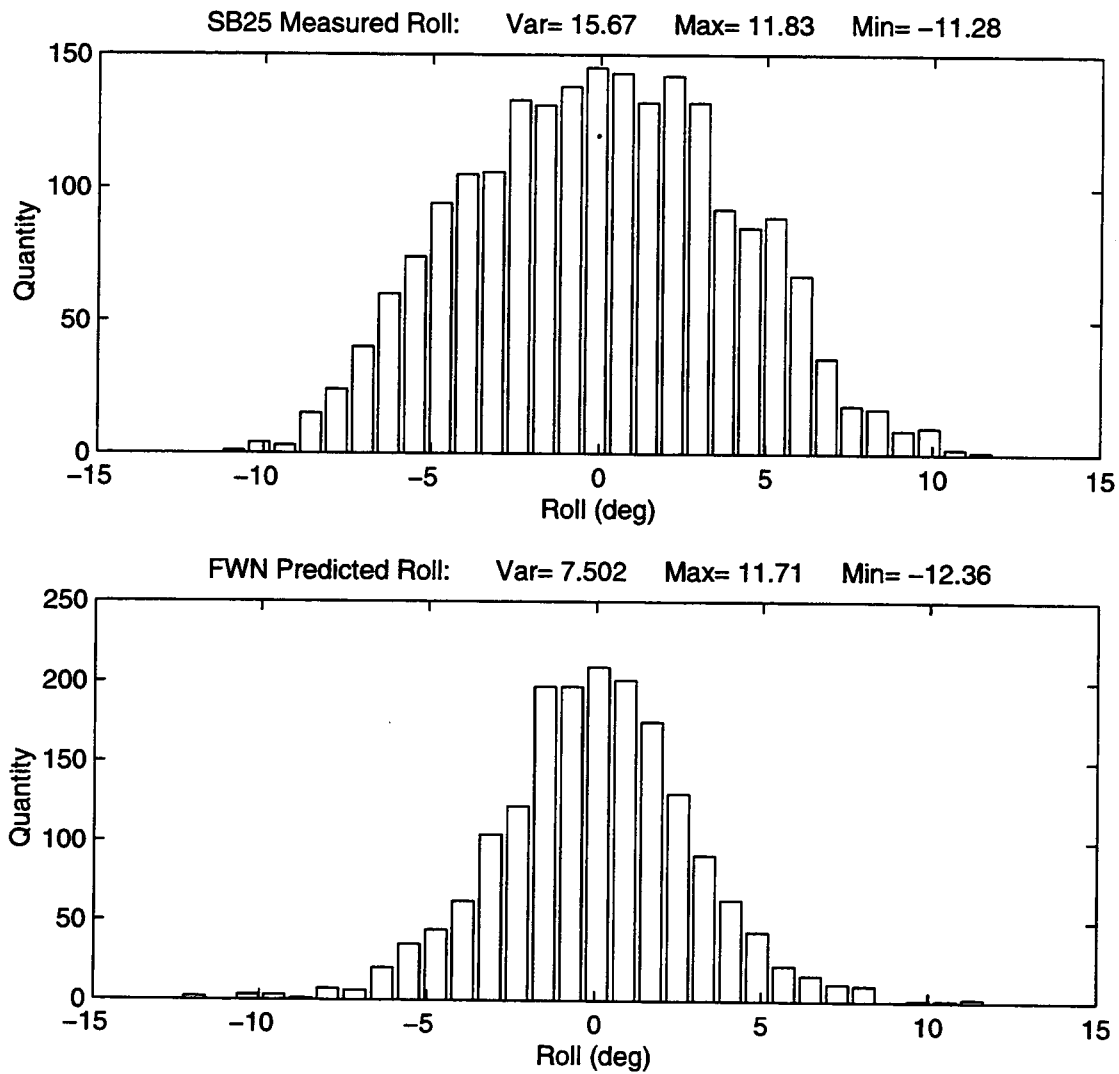


Figure D.30 Roll Histograms, $H_s=4.7$ ft, $T_p=8.2$ s

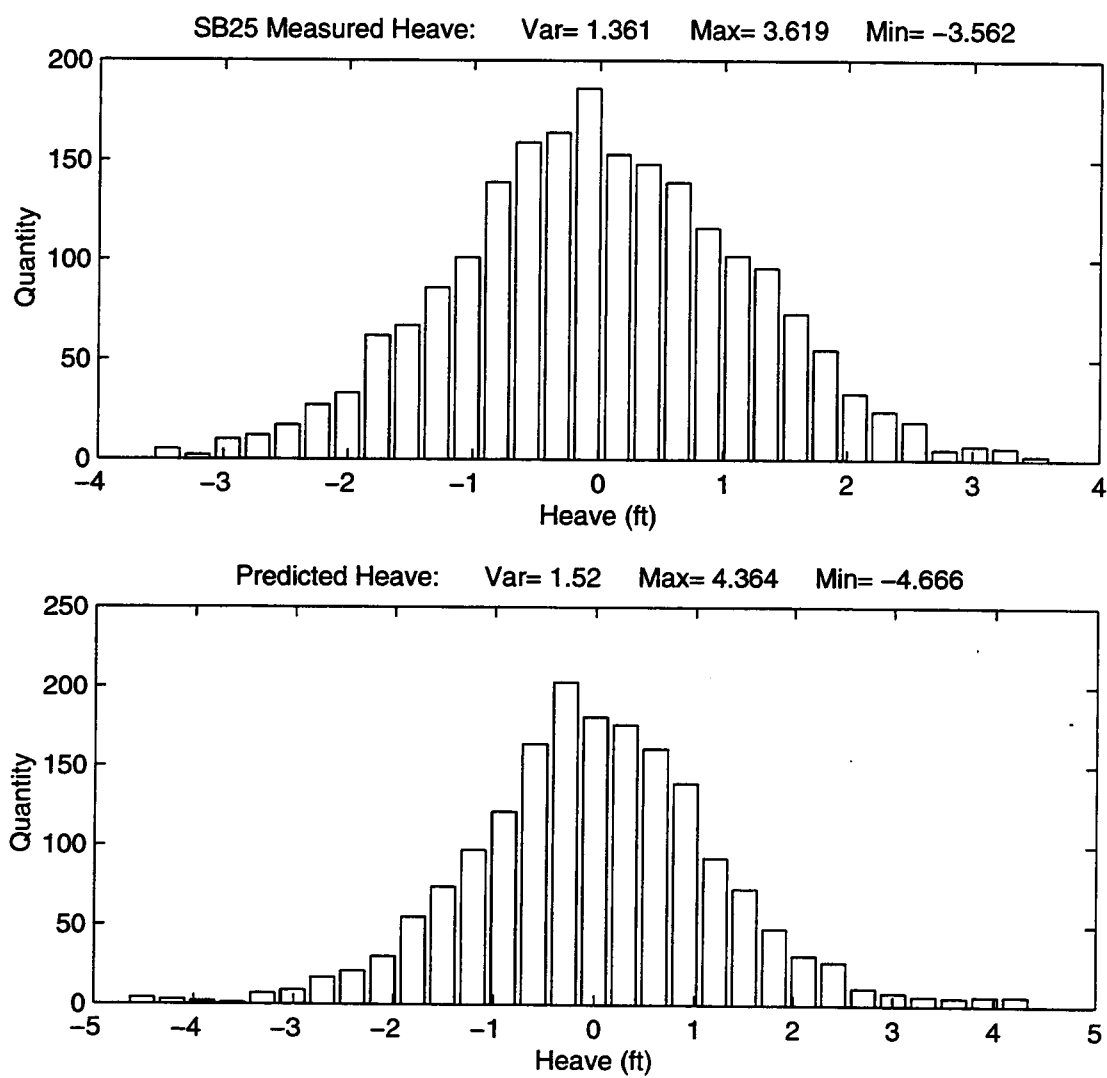


Figure D.31 Heave Histograms, $H_s=4.7$ ft, $T_p=8.2$ s

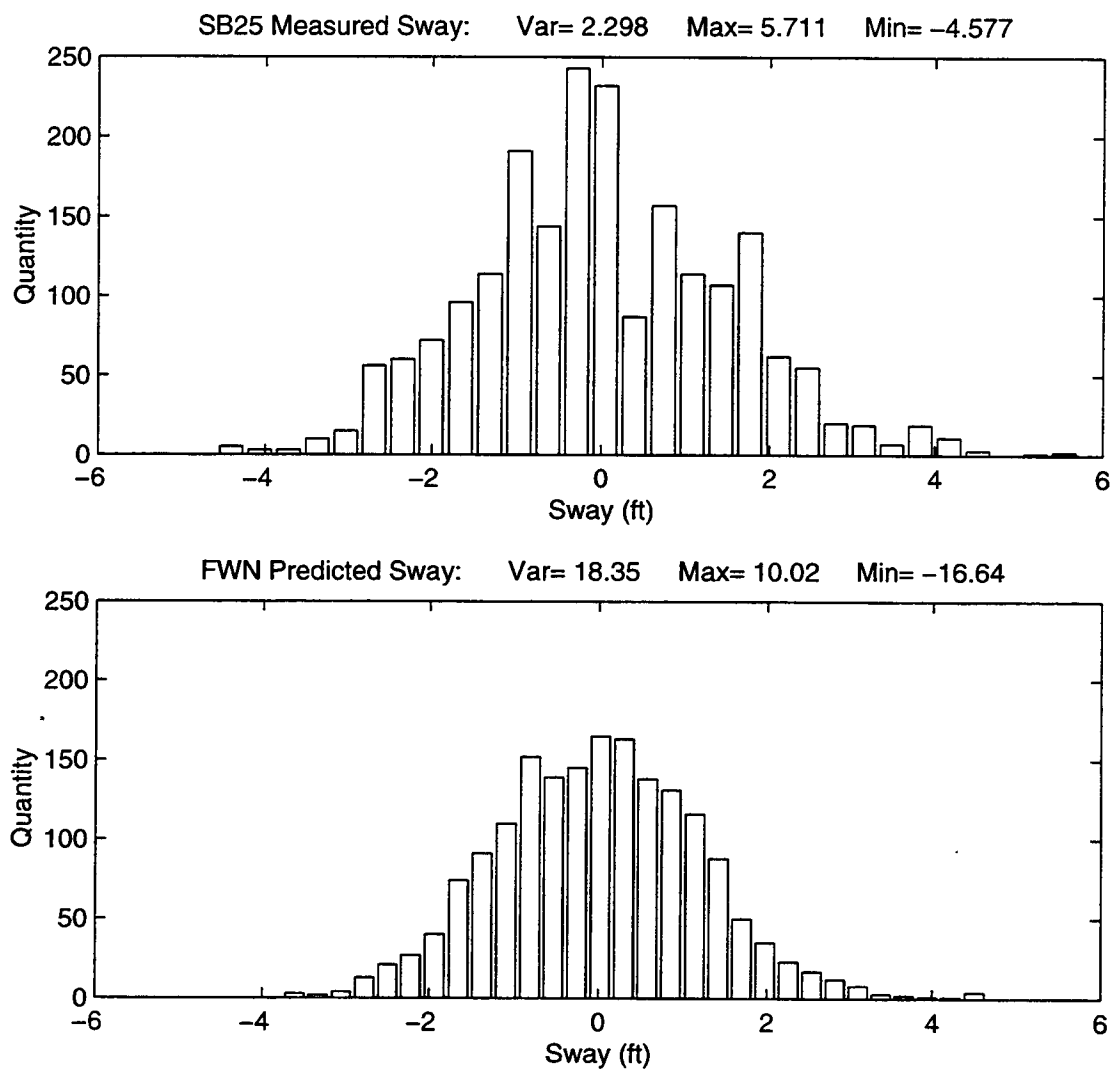


Figure D.32 Sway Histograms, $H_s=4.7$ ft, $T_p=8.2$ s

APPENDIX E**Comparison Figures
Roll-Heave Model (Section 5.2)**

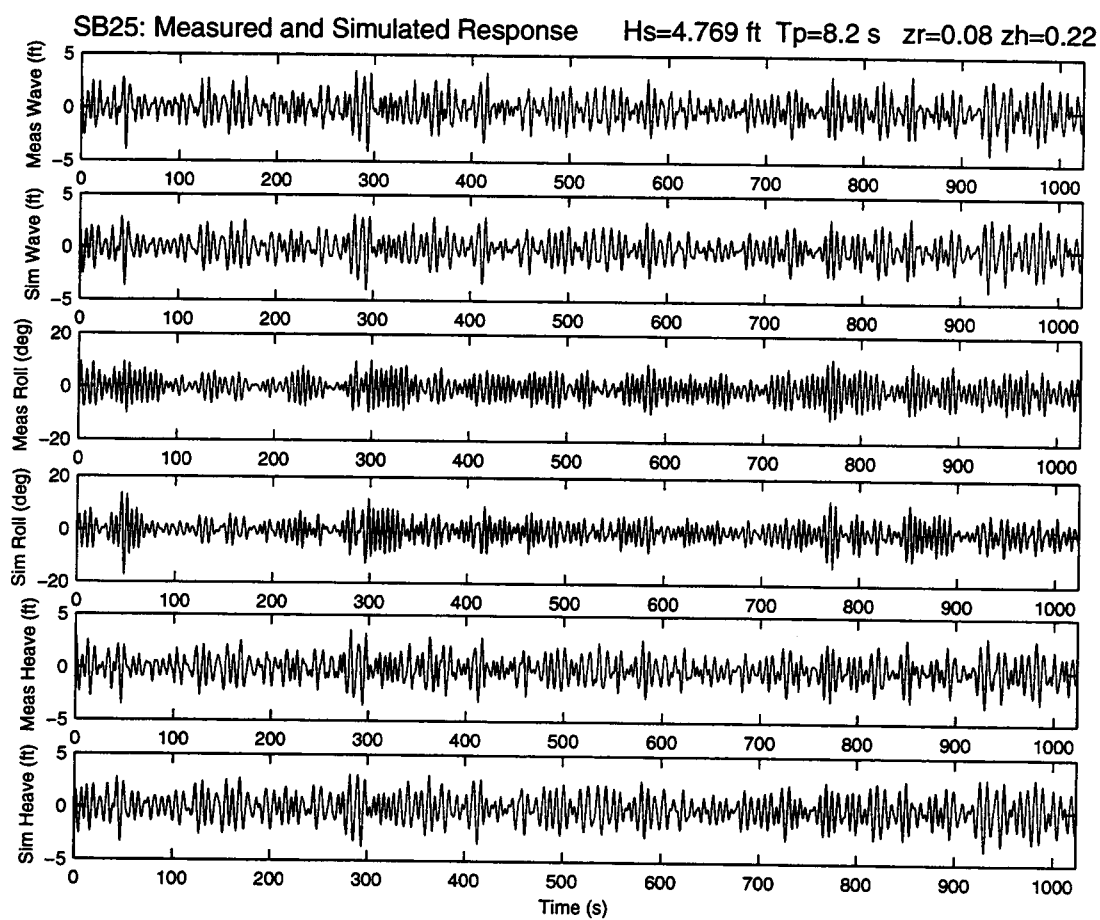


Figure E.1

Measured and Predicted Response, $H_s=4.7$ ft, $T_p=8.2$ s

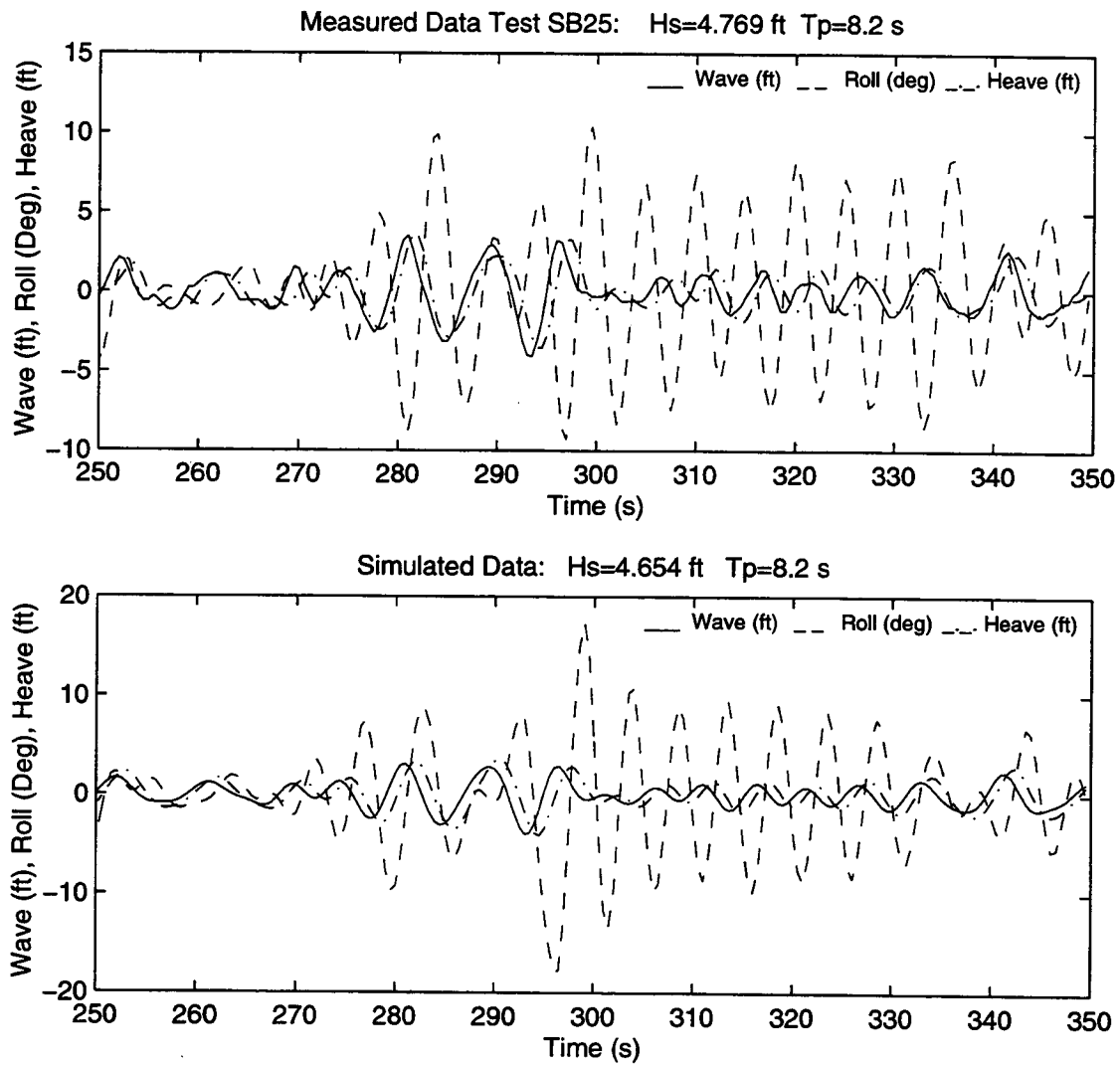


Figure E.2 Measured and Predicted Response, $H_s=4.7$ ft, $T_p=8.2$ s

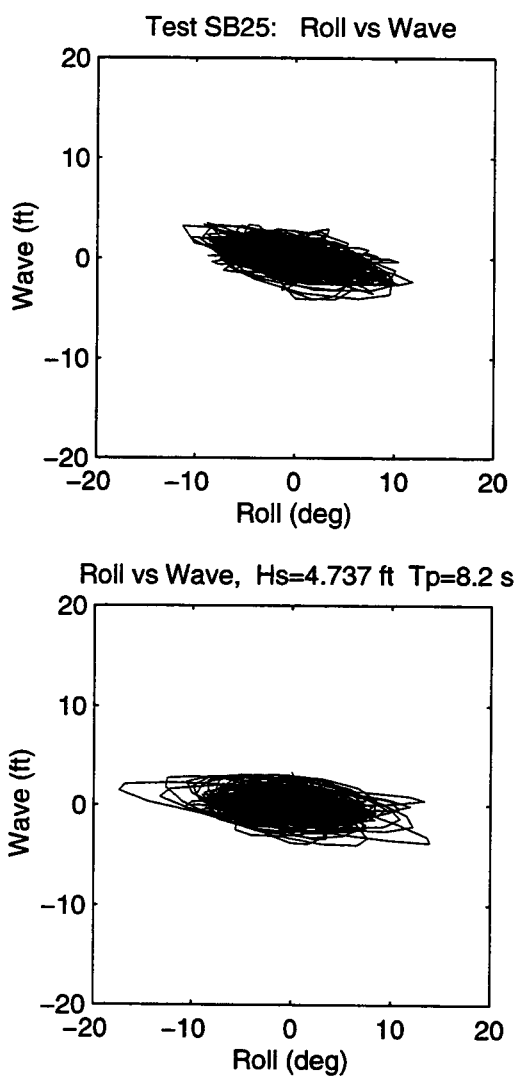


Figure E.3

Roll vs Wave, $H_s=4.7$ ft, $T_p=8.2$ s

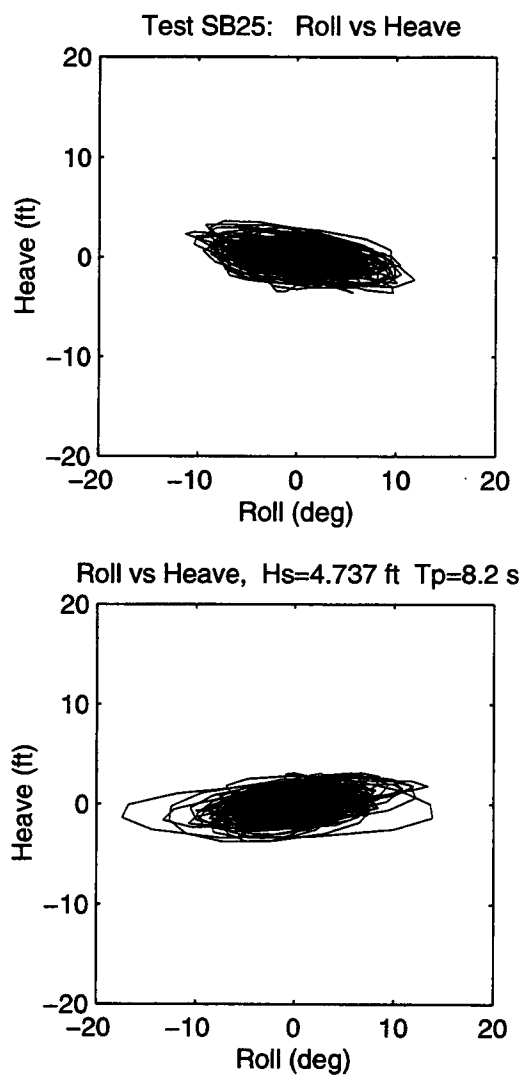


Figure E.4

Roll vs Heave, $H_s=4.7$ ft, $T_p=8.2$ s

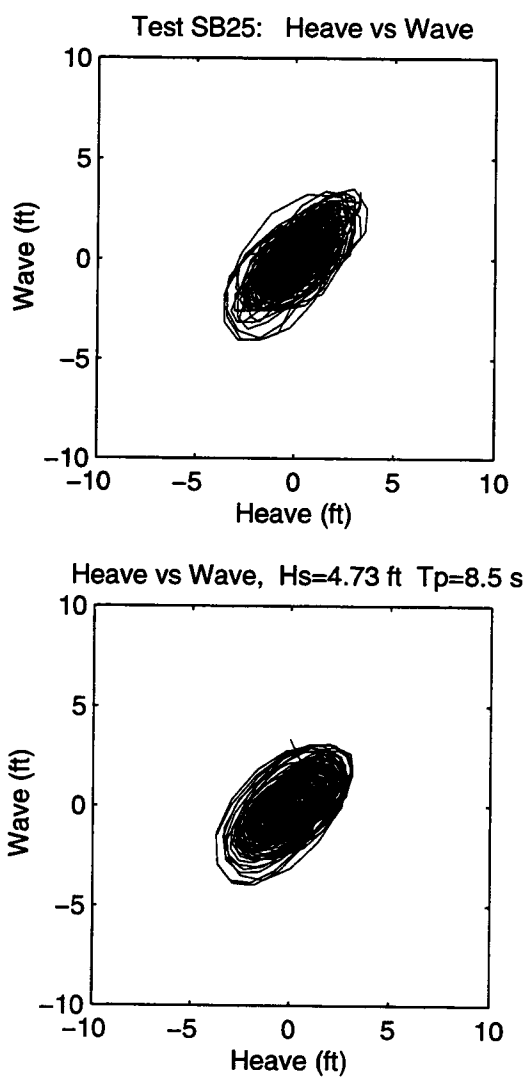


Figure E.5

Heave vs Wave, $H_s=4.7$ ft, $T_p=8.2$ s

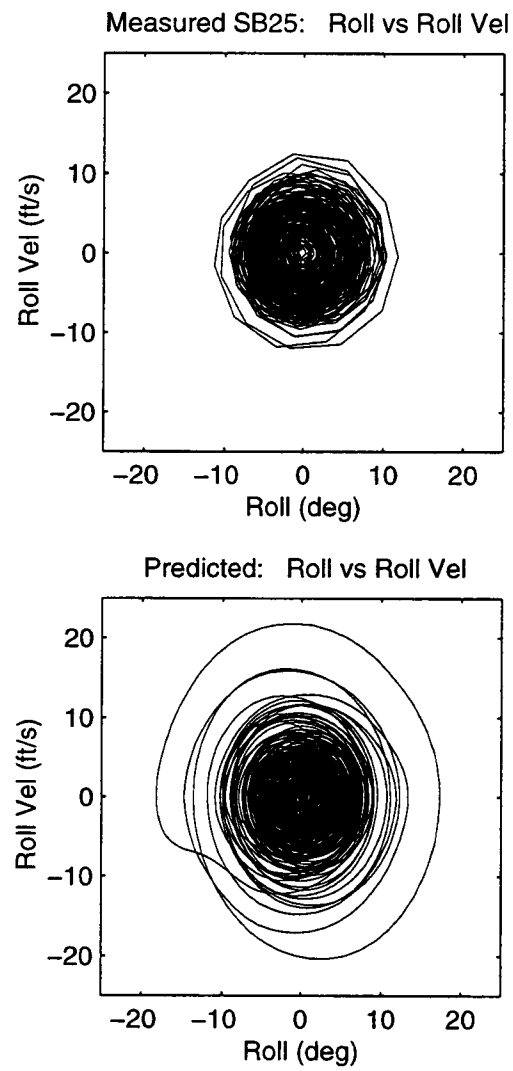


Figure E.6

Phase Plane for Roll and Roll Velocity, $H_s=4.7$ ft, $T_p=8.2$ s

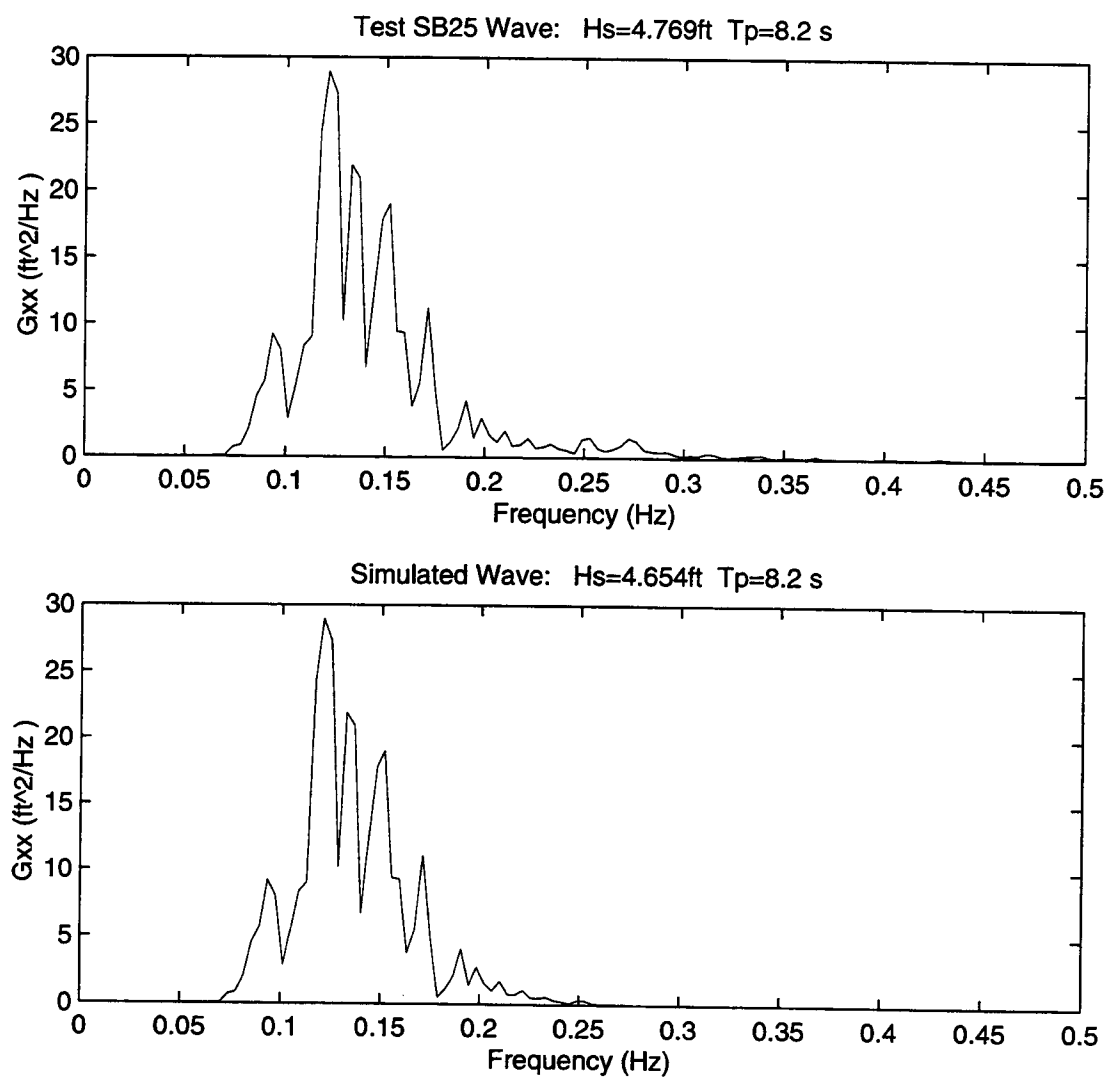


Figure E.7 Wave Spectral Densities, $H_s=4.7\text{ ft}$, $T_p=8.2\text{ s}$

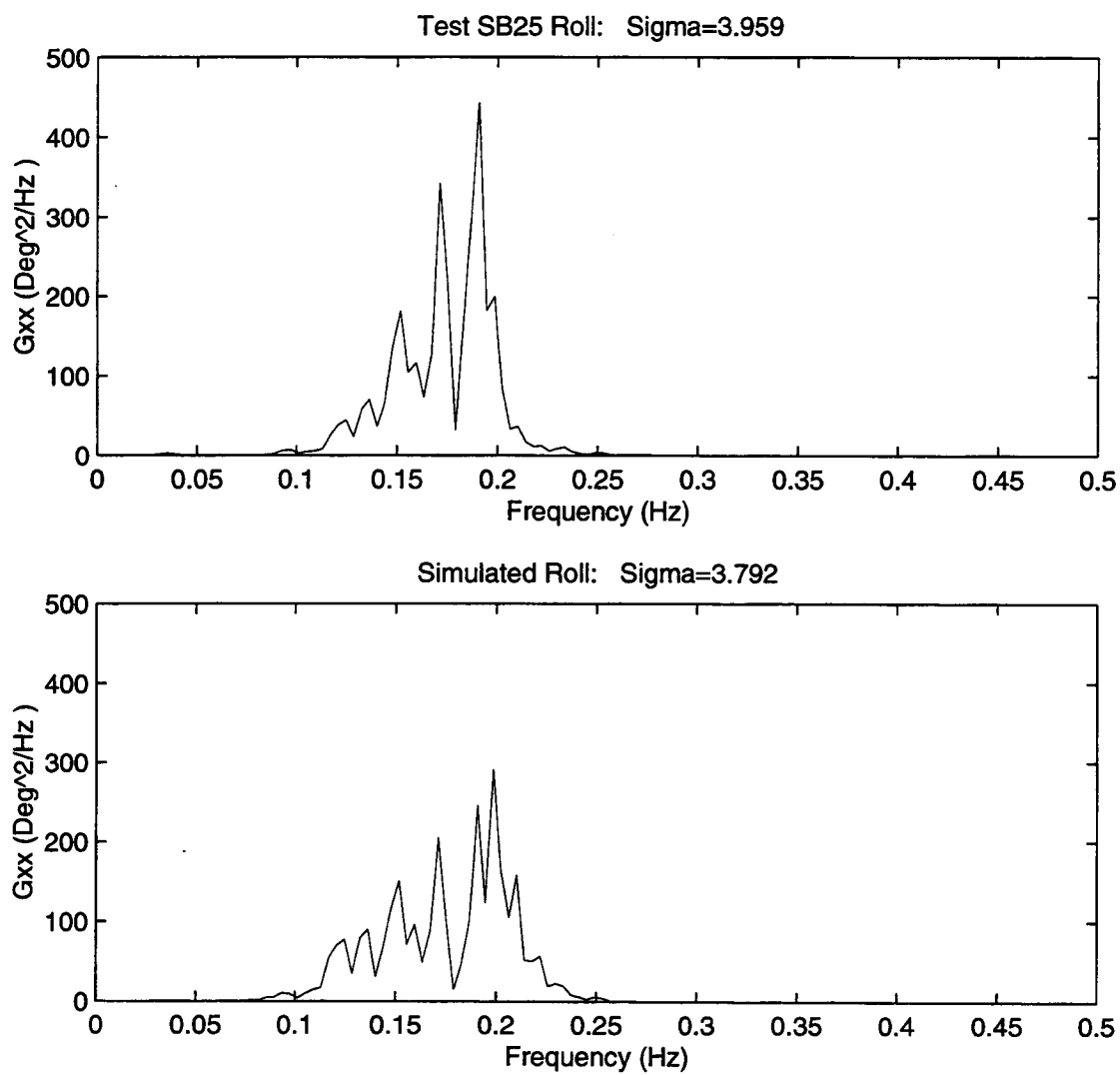


Figure E.8 Roll Spectral Densities, $H_s=4.7$ ft, $T_p=8.2$ s

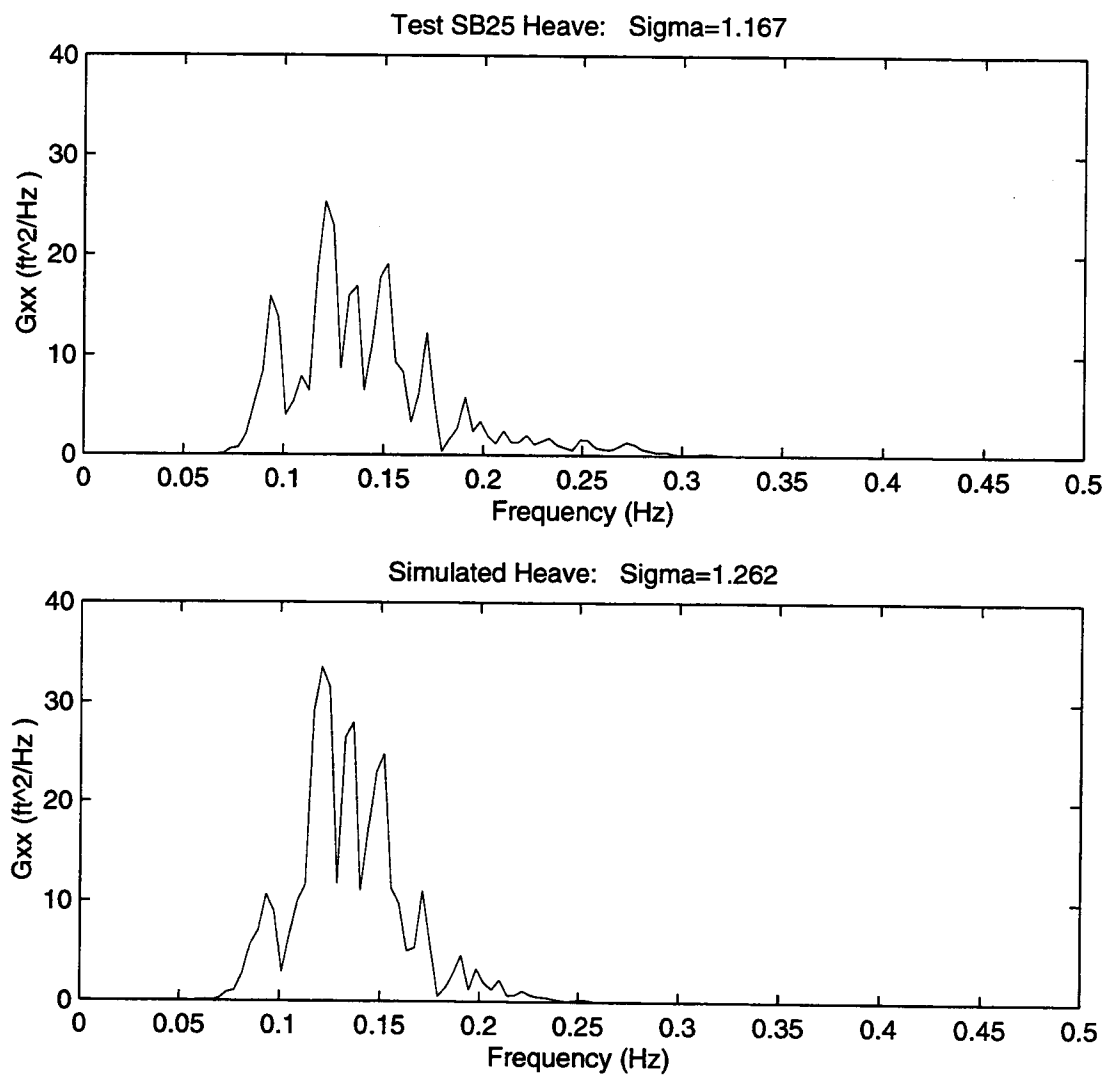


Figure E.9 Heave Spectral Densities, $H_s=4.7$ ft, $T_p=8.2$ s

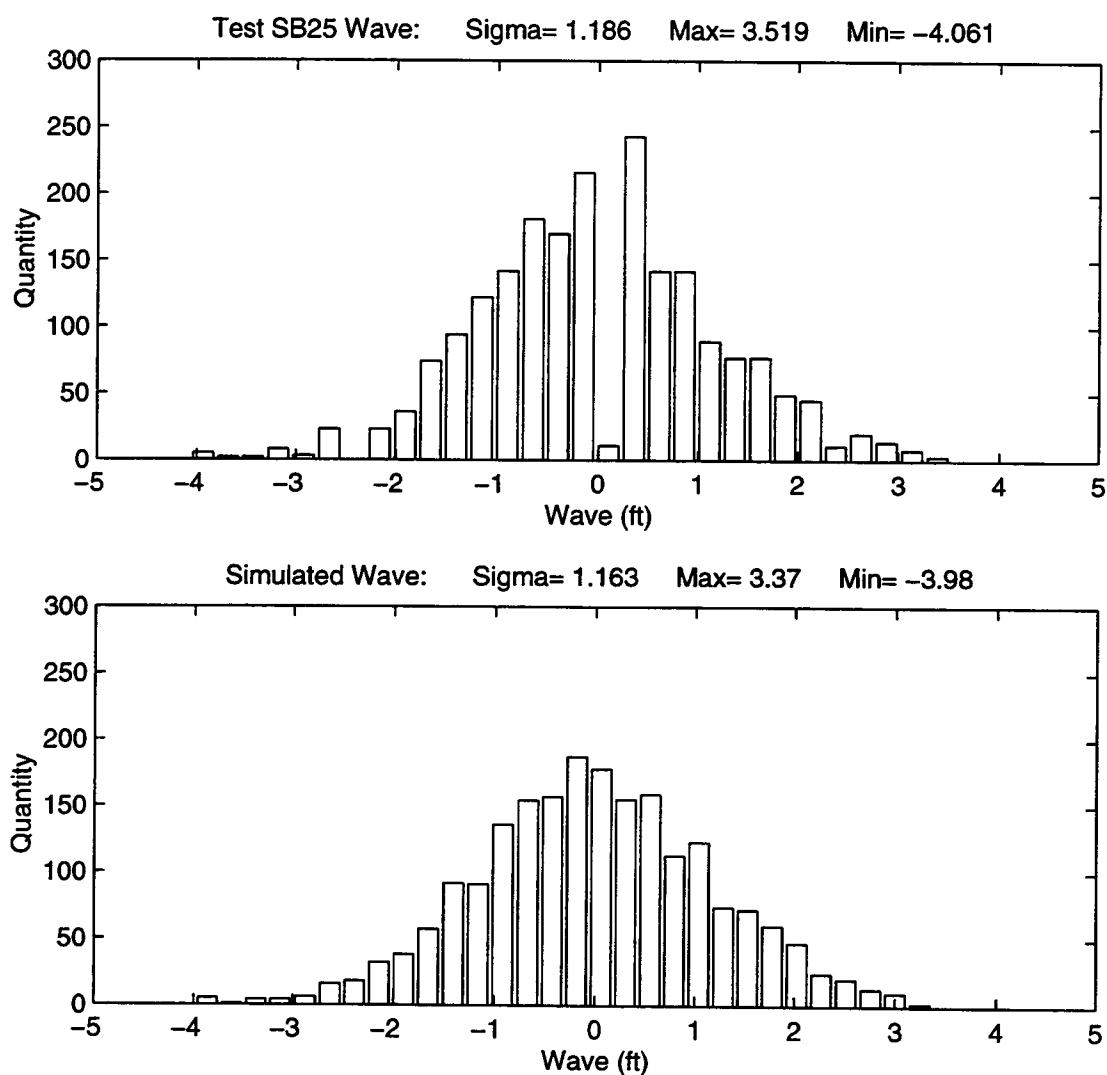


Figure E.10 Wave Histograms, $H_s=4.7$ ft, $T_p=8.2$ s

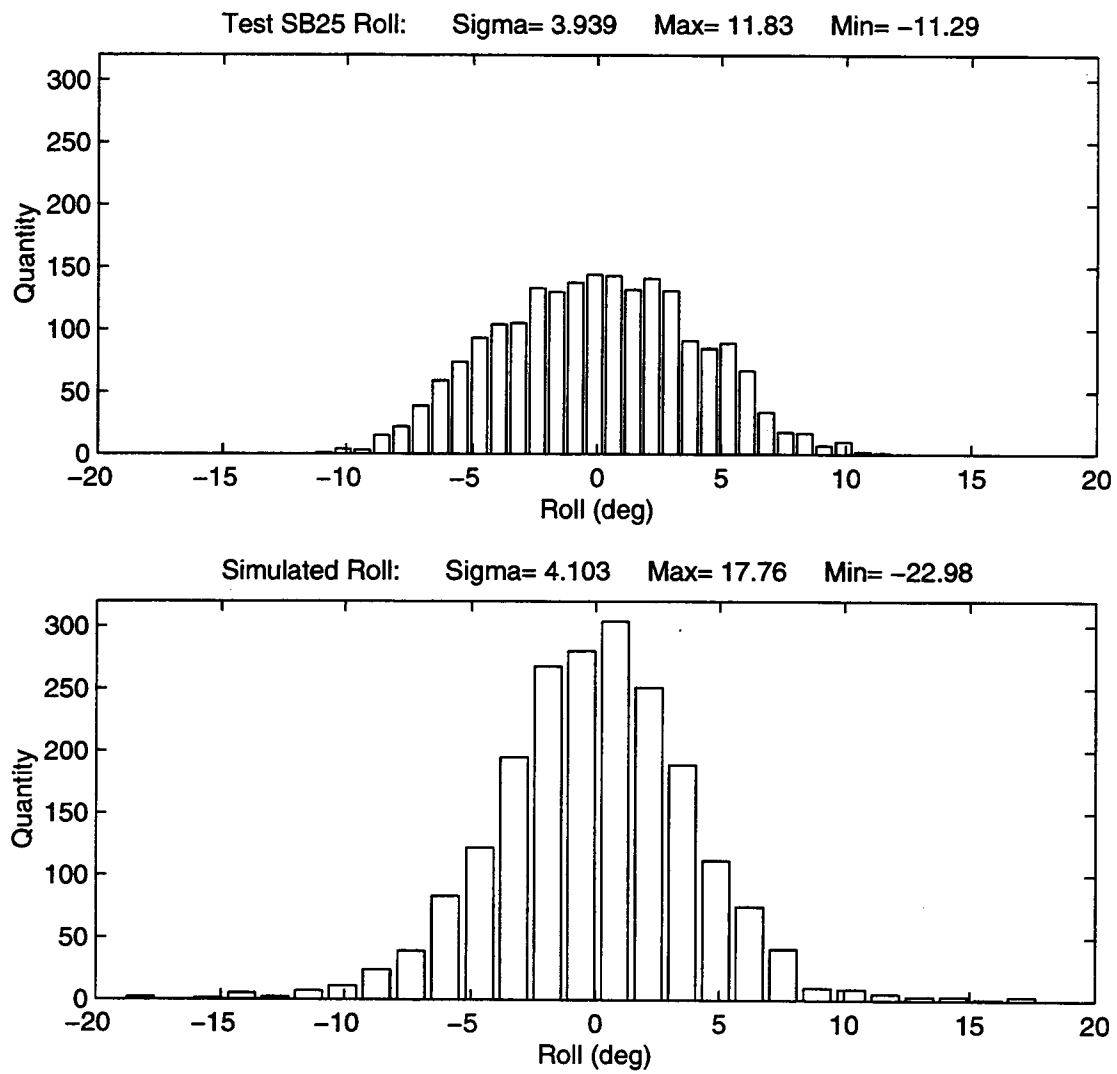


Figure E.11 Roll Histograms, $H_s=4.7$ ft, $T_p=8.2$ s

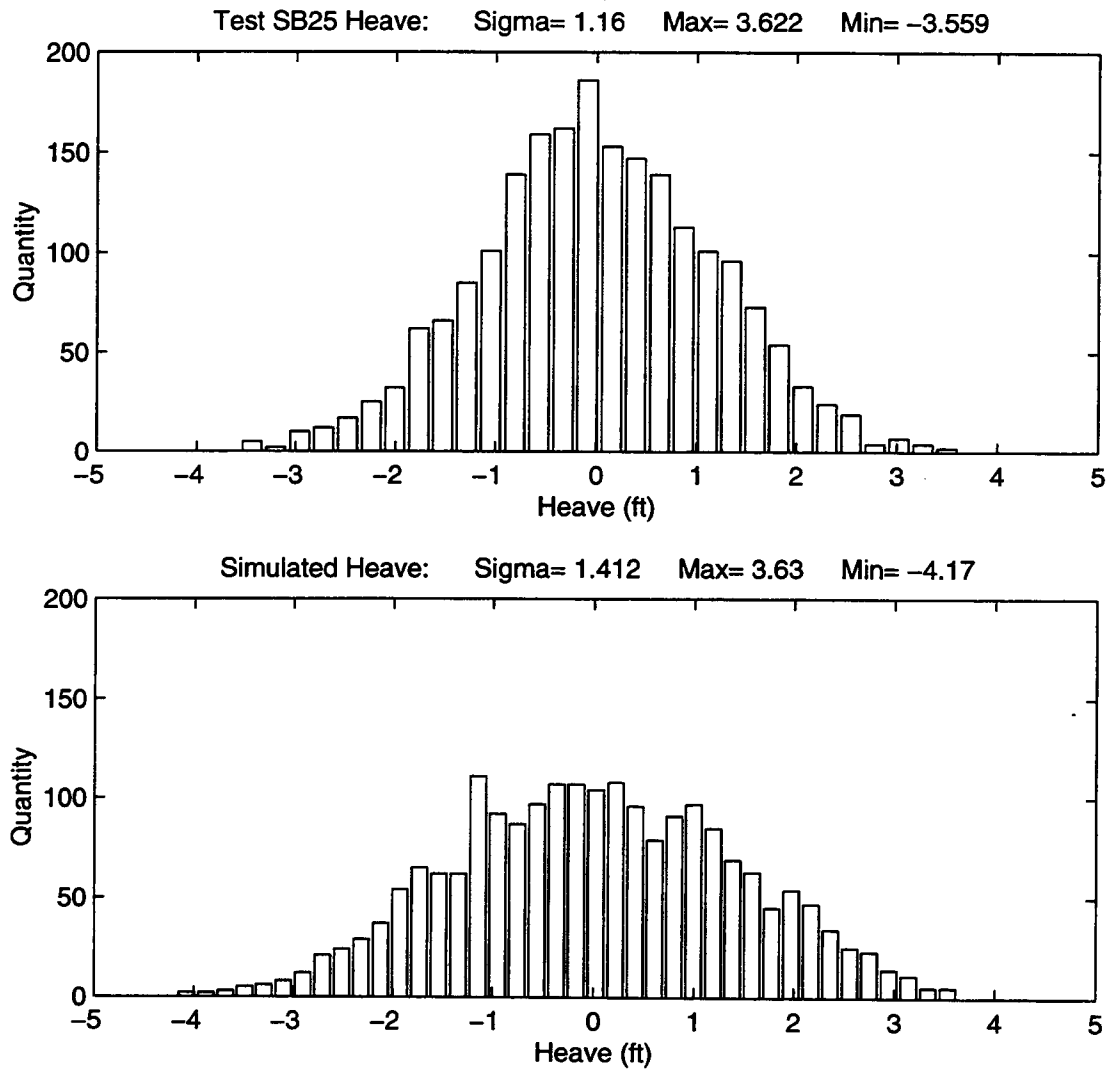


Figure E.12

Heave Histograms, $H_s=4.7$ ft, $T_p=8.2$ s

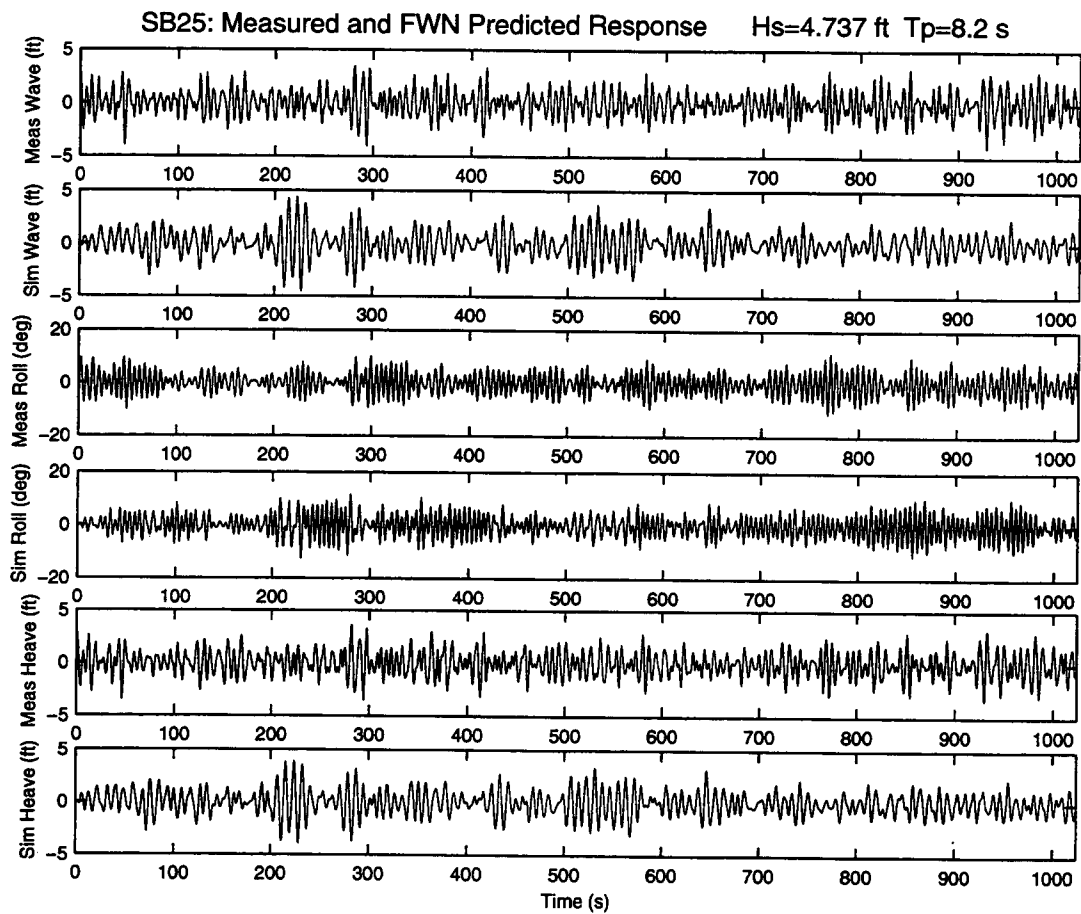


Figure E.13

Measured and FWN Predicted Response, $H_s=4.7$ ft, $T_p=8.2$ s

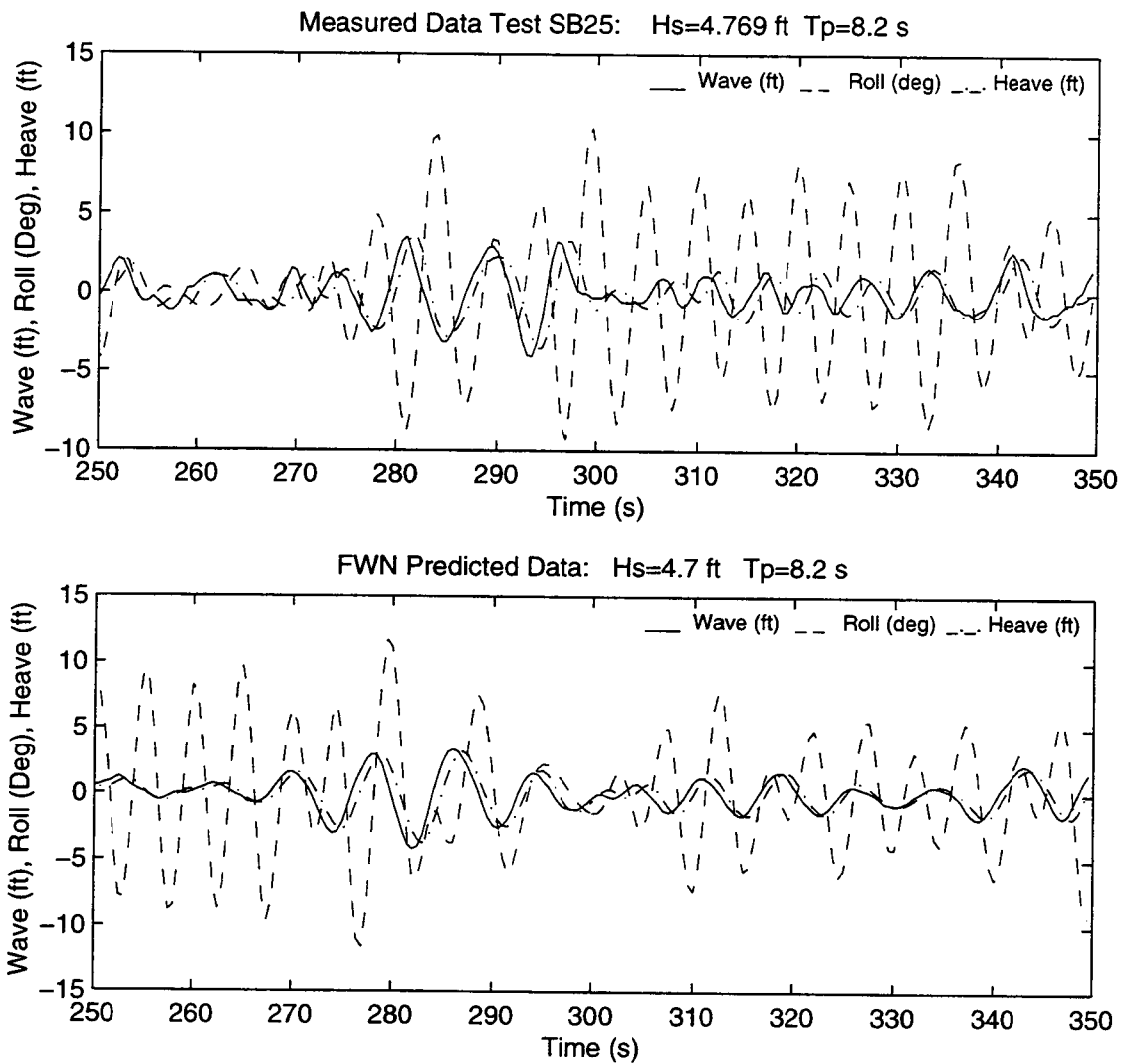


Figure E.14 Measured and FWN Predicted Response, Hs=4.7 ft, Tp=8.2 s

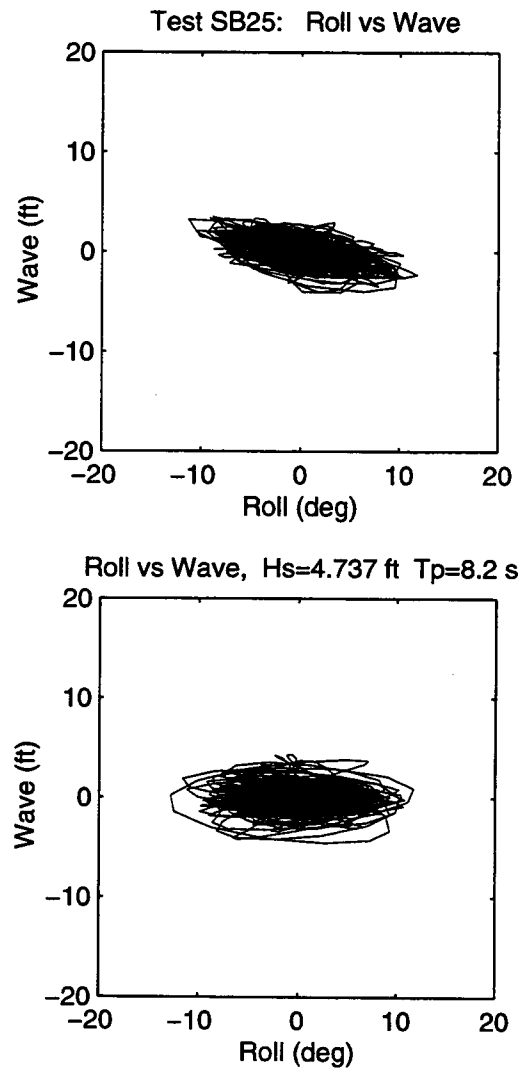


Figure E.15

Roll vs Wave, Hs=4.7 ft, Tp=8.2 s

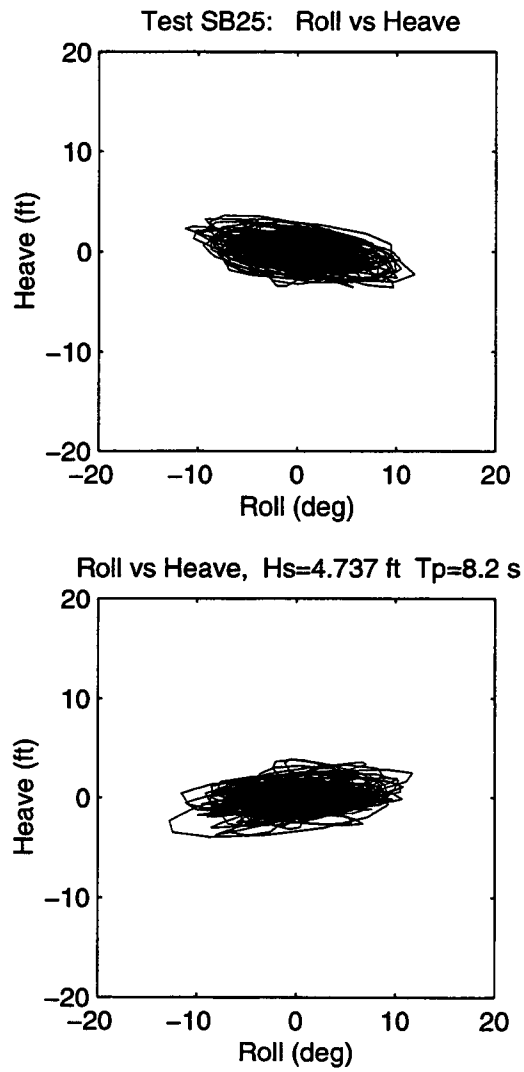


Figure E.16

Roll vs Heave, $H_s=4.7$ ft, $T_p=8.2$ s

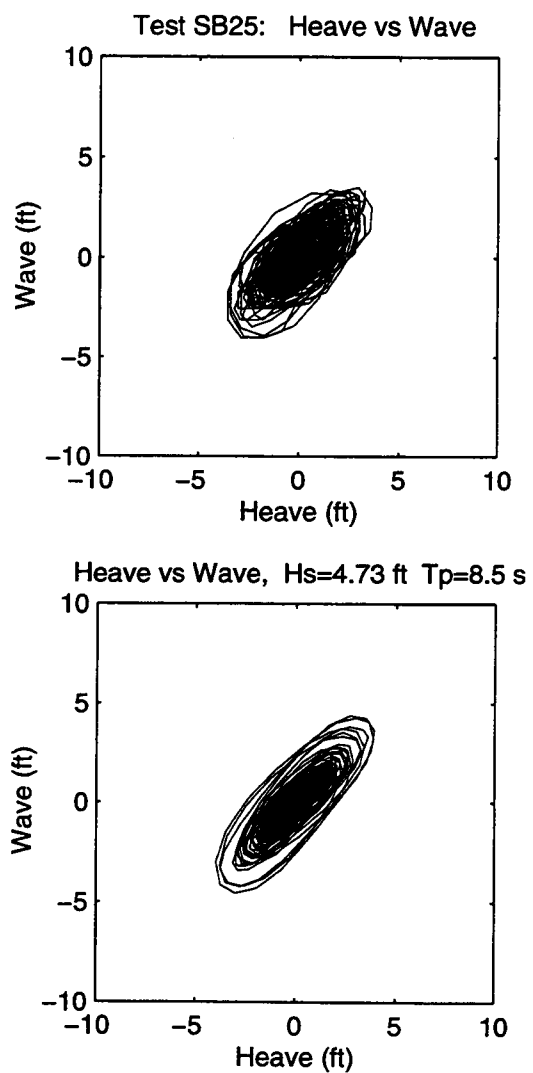


Figure E.17

Heave vs Wave, $H_s=4.7$ ft, $T_p=8.2$ s

E.17

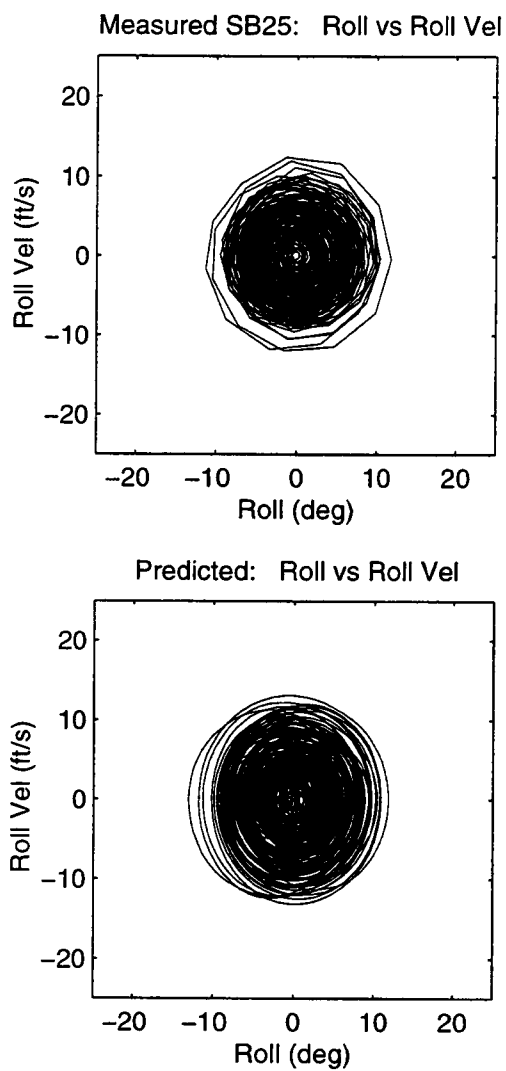


Figure E.18

Phase Plane for Roll and Roll Velocity, $H_s=4.7$ ft, $T_p=8.2$ s

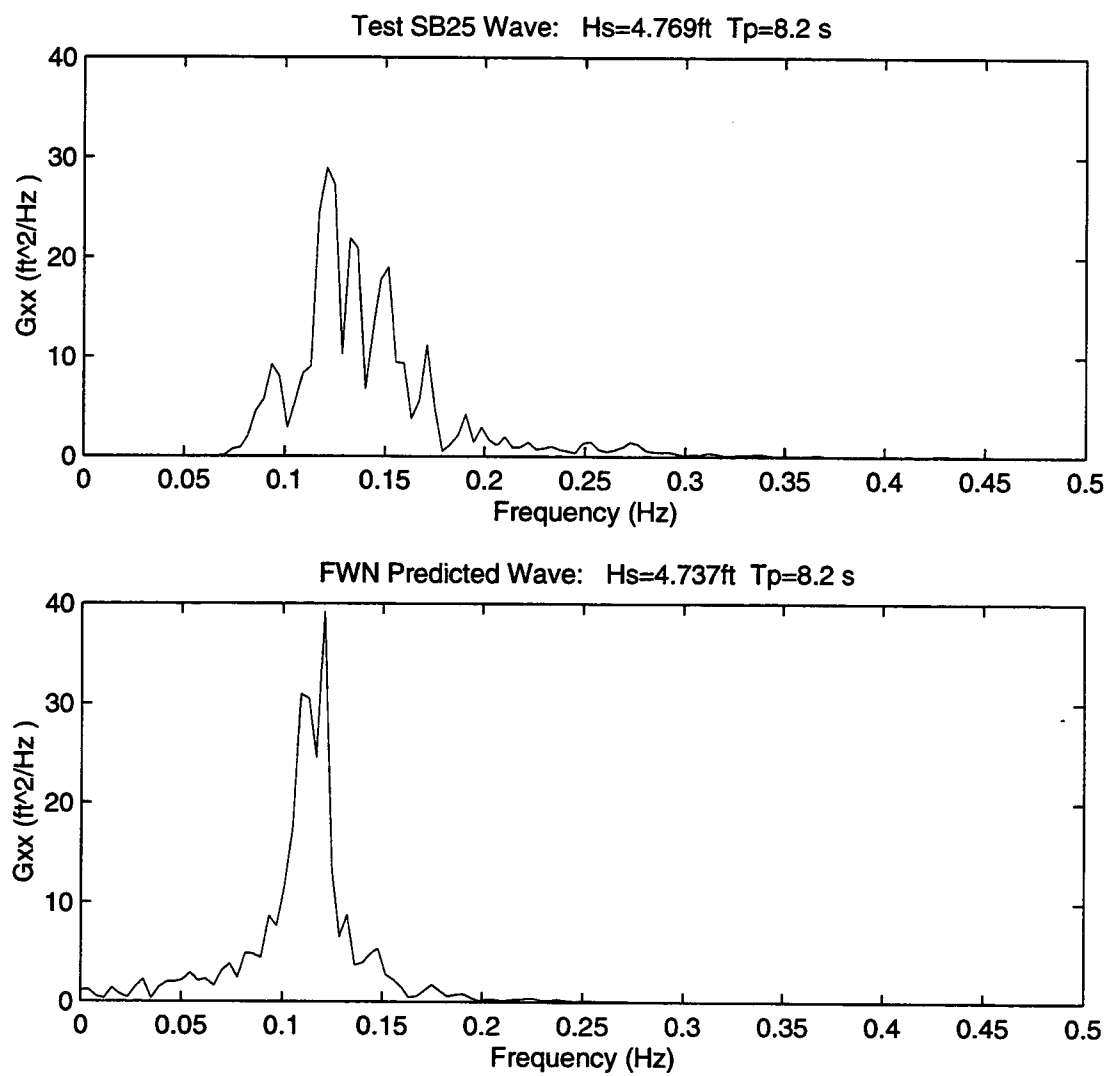


Figure E.19 Wave Spectral Densities, $H_s=4.7\text{ ft}$, $T_p=8.2\text{ s}$

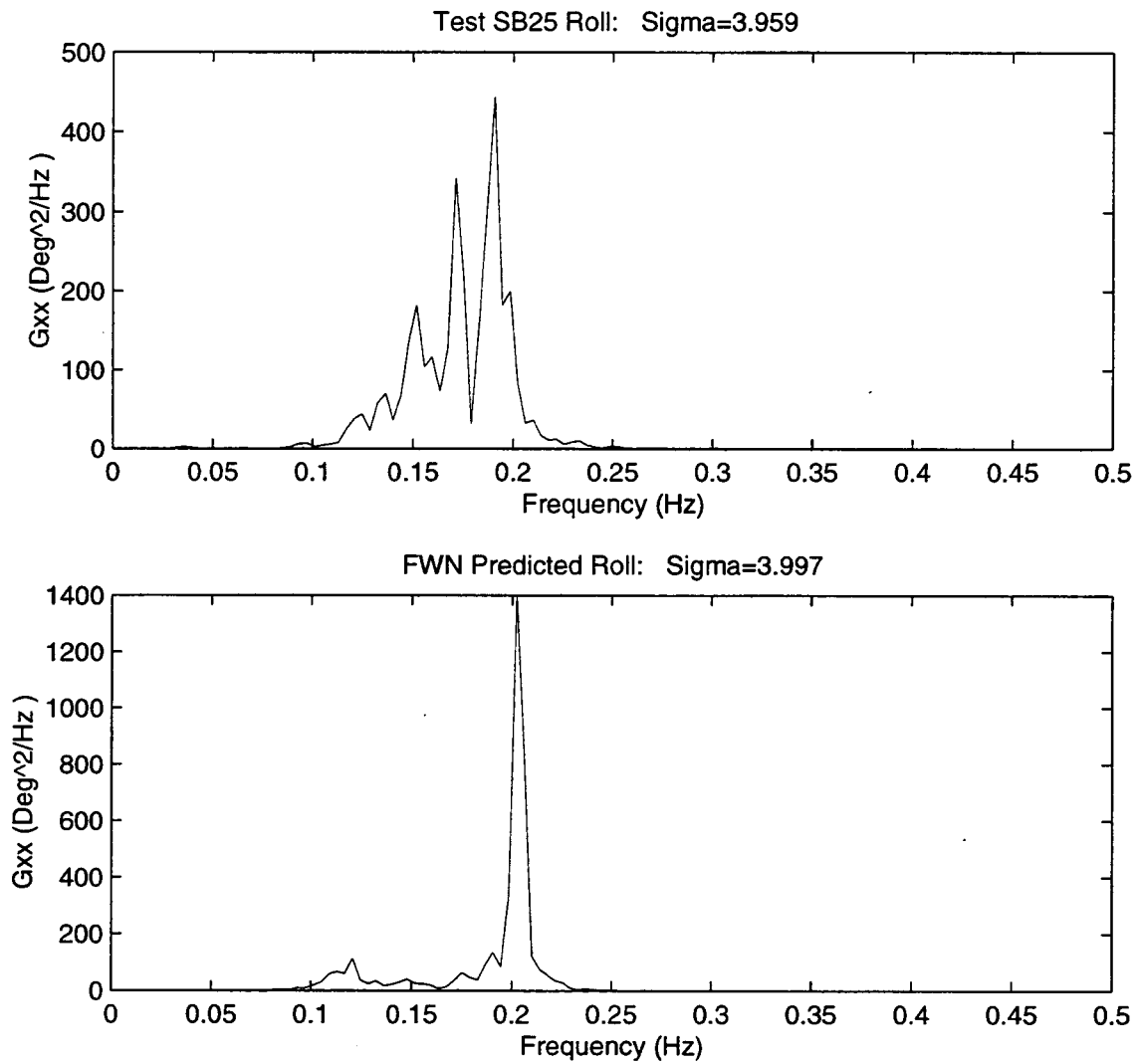


Figure E.20

Roll Spectral Densities, $H_s=4.7$ ft, $T_p=8.2$ s

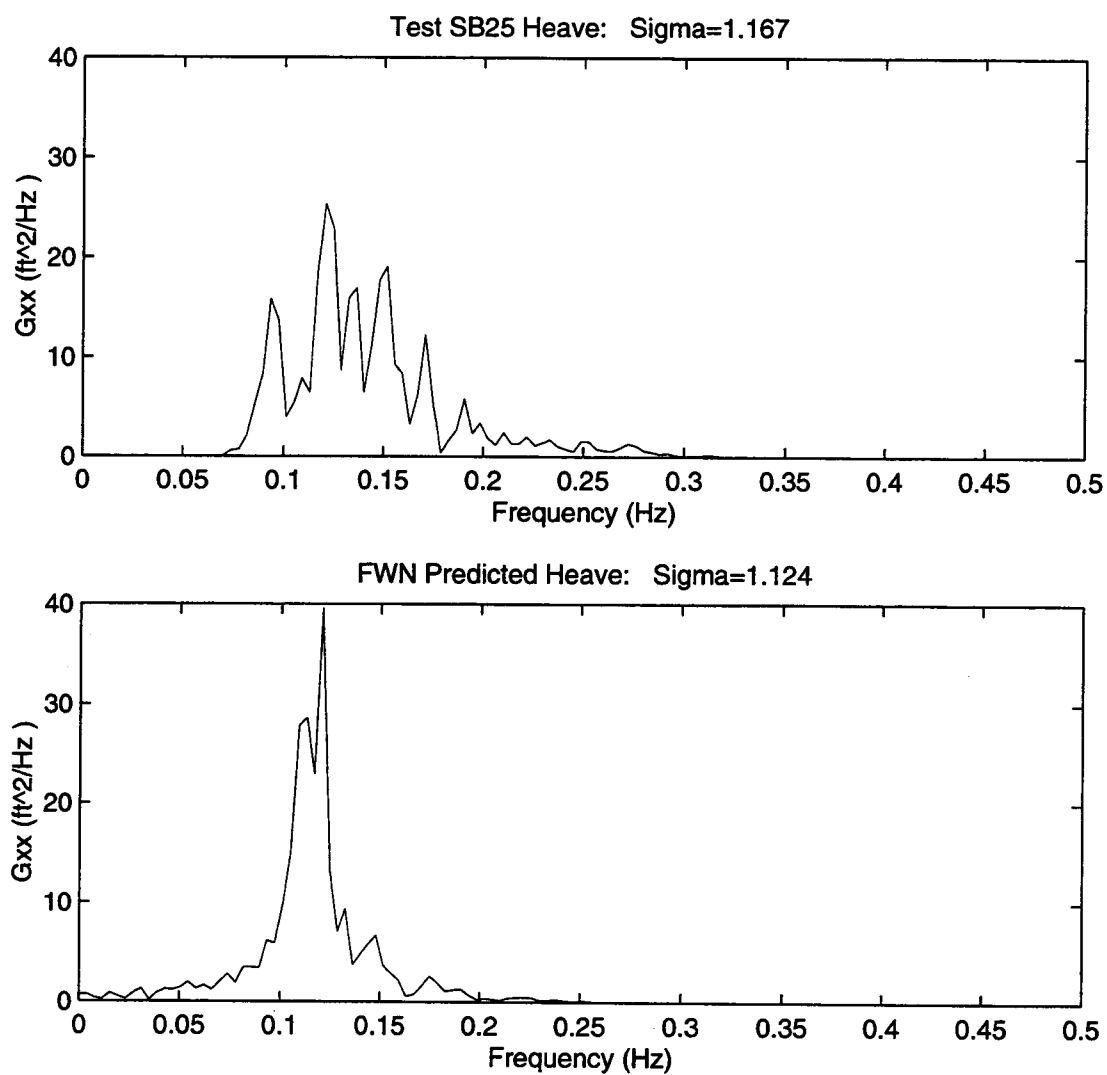


Figure E.21 Heave Spectral Densities, $H_s=4.7$ ft, $T_p=8.2$ s

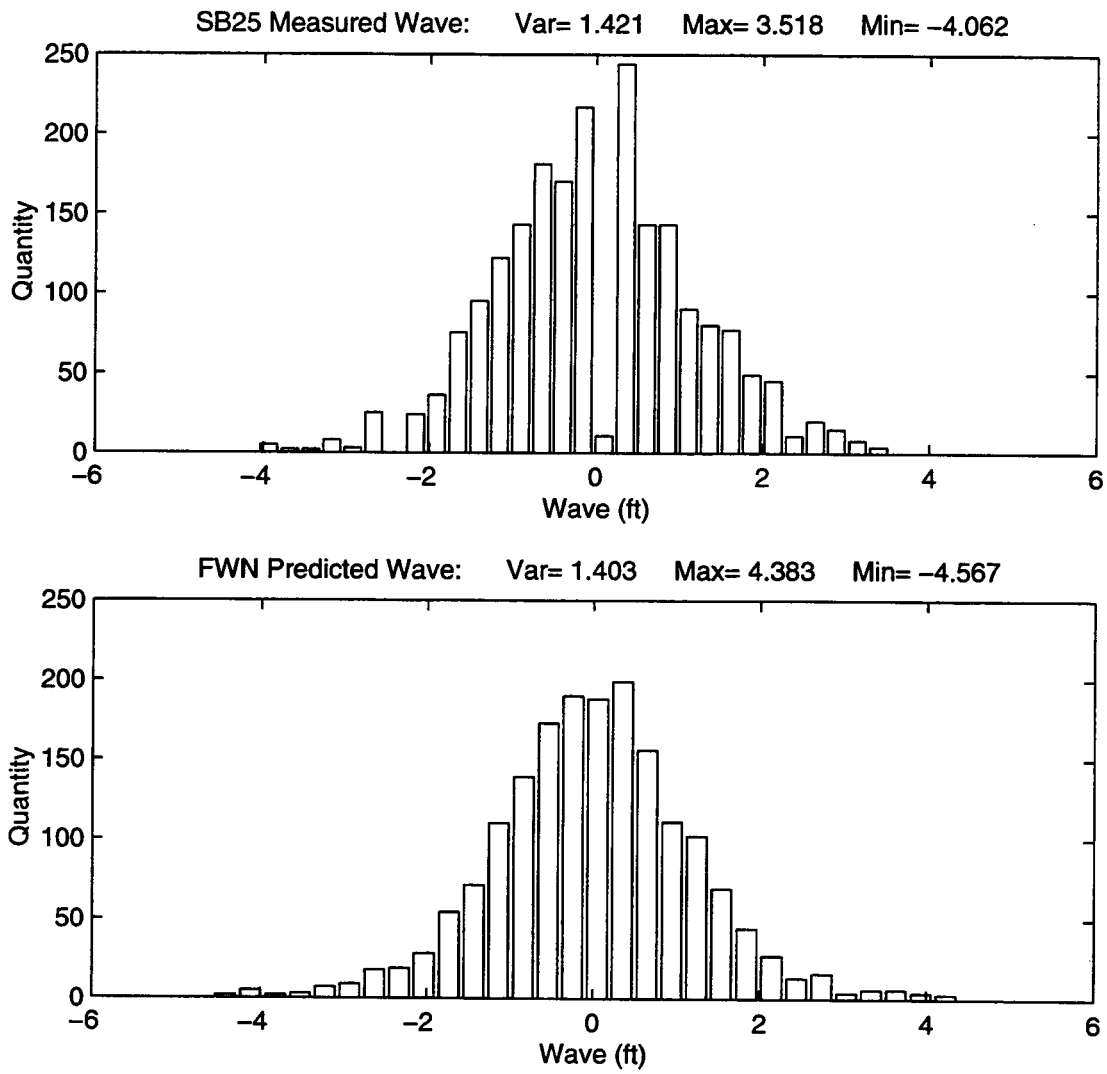


Figure E.22 Wave Histograms, $H_s=4.7$ ft, $T_p=8.2$ s

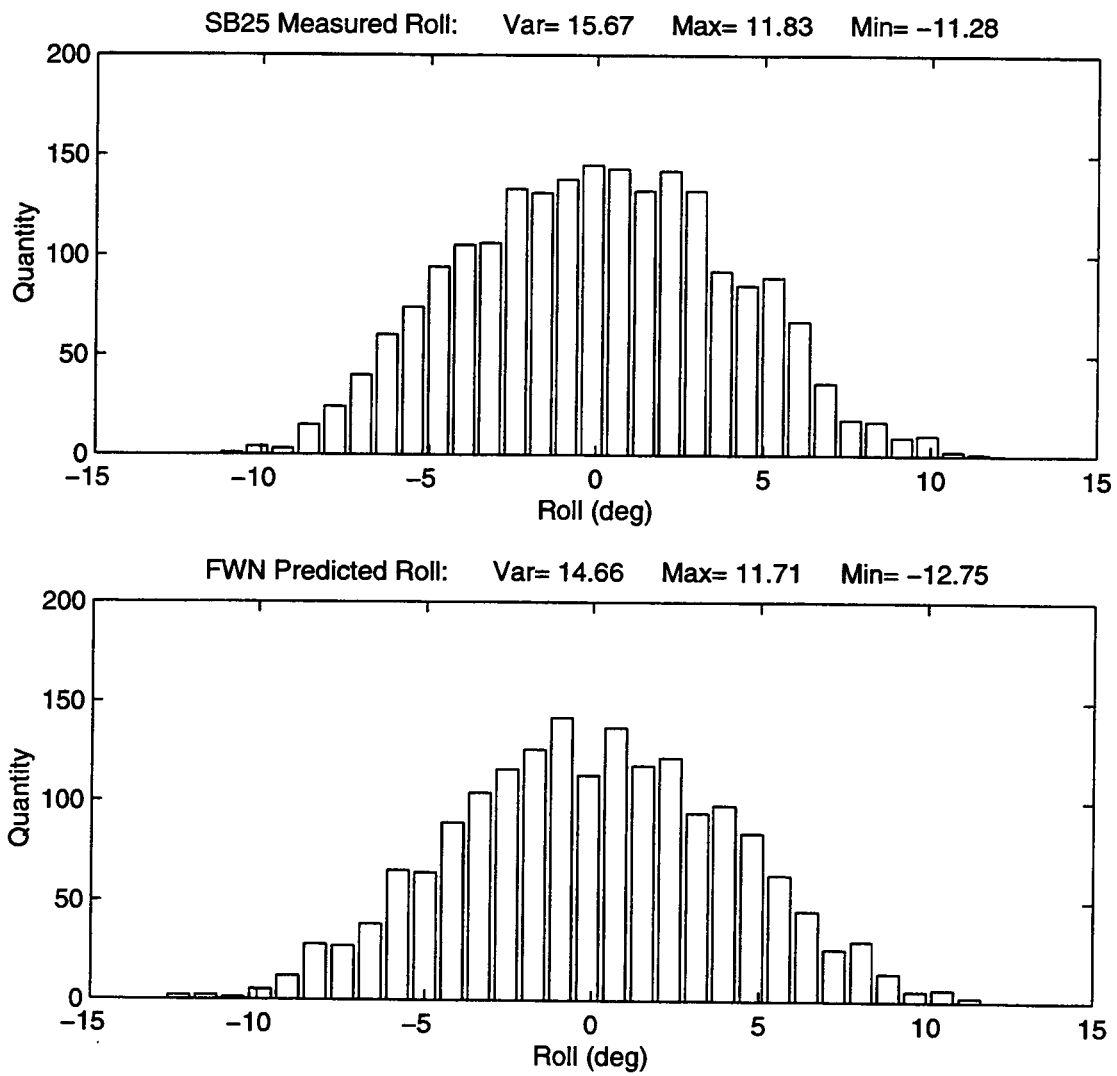


Figure E.23 Roll Histograms, $H_s=4.7$ ft, $T_p=8.2$ s

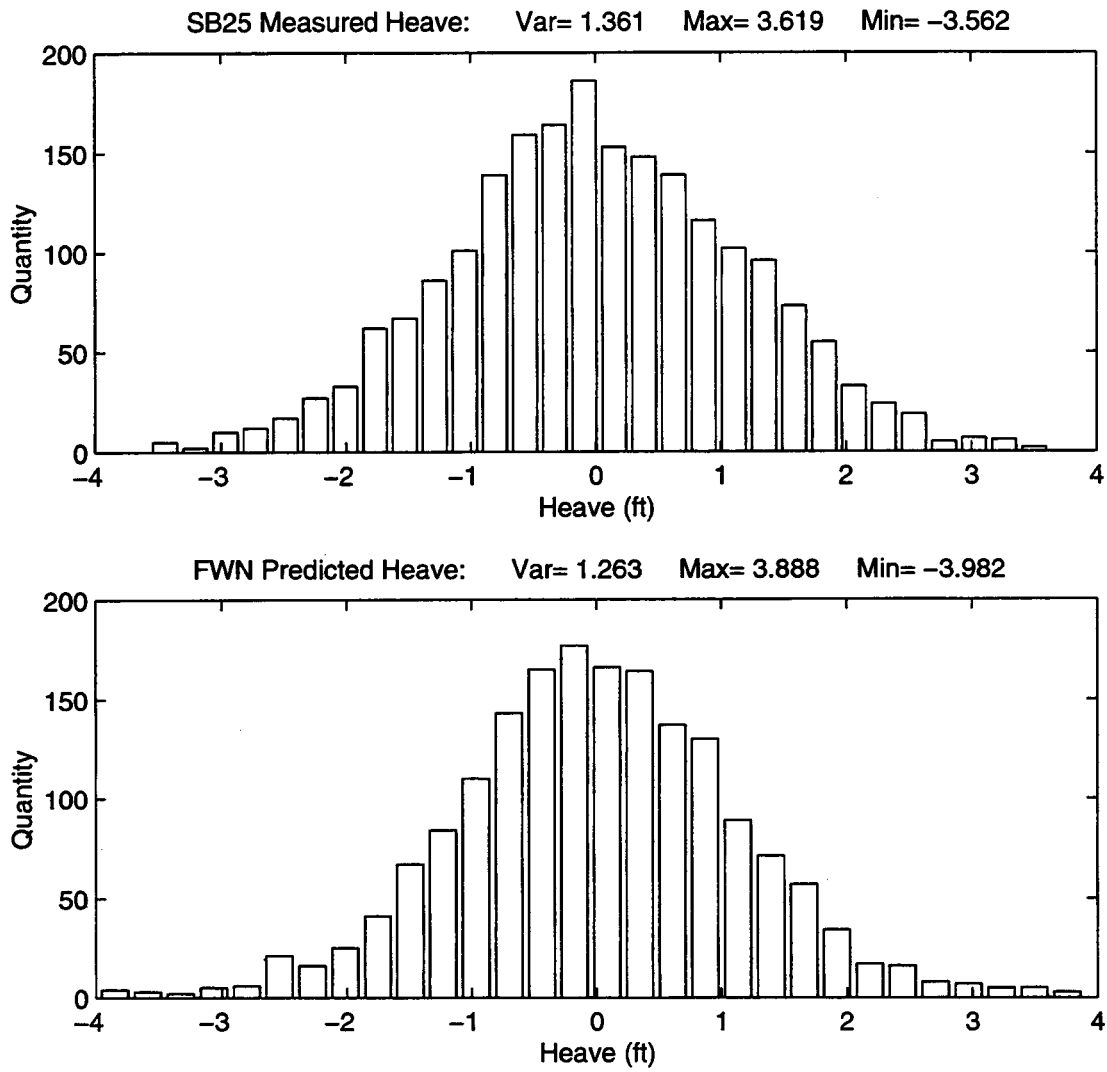


Figure E.24 Heave Histograms, $H_s=4.7$ ft, $T_p=8.2$ s